Injection and combustion dynamics in swirled spray flames and azimuthal coupling in annular combustors

Guillaume Vignat

université
PARIS-SACLAY

Injection and combustion dynamics in swirled spray flames and azimuthal coupling in annular combustors

Thèse de doctorat de l'Université Paris-Saclay

École doctorale n° 579, Sciences mécaniques et énergétiques, matériaux et géosciences SMEMAG.

Spécialité de doctorat: Combustion

Unité de recherche: Université Paris-Saclay, CNRS, CentraleSupélec, Laboratoire EM2C, 91190 Gif-sur-Yvette, France

Référent: CentraleSupélec

Thèse présentée et soutenue à Gif sur Yvette, le 3 juillet 2020, par

Guillaume Vignat

Composition du jury:

Christian Tenaud Directeur de recherche, CNRS (LIMSI), Université Paris-Saclay	Président
Françoise Baillot Professeure des universités, Université de Rouen (CORIA)	Rapporteur & Examinatrice
Thierry Poinsot Directeur de recherche, CNRS (IMFT)	Rapporteur & Examinateur
James Dawson Professeur, National Technical University of Norway	Examinateur
Stéphane Richard Ingénieur chef de groupe, Safran Helicopter Engines	Examinateur
Sébastien Candel Professeur des universités émérite, CentraleSupélec (EM2C), Université Paris-Saclay	Directeur
Daniel Durox Ingénieur de recherche consultant, CentraleSupélec (EM2C), Université Paris-Saclay	Co-Encadrant

Thèse de doctorat

NNT: 2020UPASC024

Remerciements

Je tiens tout d'abord à remercier les membres du jury. Grâce à eux, nous avons pu faire en sorte que la soutenance se passe dans les conditions les plus normales possibles malgré un contexte difficile et changeant. En premier lieu les rapporteurs, Pr Françoise Baillot et Dr Thierry Poinsot, qui ont pris le temps de lire en détail ce (long) manuscrit. Leurs rapports, commentaires et les échanges que nous avons eus pendant et après la soutenance ont permis de significativement améliorer les publications basées sur mes travaux de recherche. Je tiens également à remercier Dr Christian Tenaud, qui a pu se déplacer, assister et présider à la soutenance, ce qui a grandement allégé le fardeau de son organisation. Les échanges ont également été très riches et instructifs avec Pr James Dawson et Dr Stéphane Richard, qui ont pu assister à la soutenance à distance. Je fais également un petit clin d'œil à Dr Yoann Méry qui a pris un jour de congé pour faire le déplacement et avec qui nous avons eu des échanges imprévus et d'une grande qualité. Un grand merci également à tous ceux, très nombreux, qui m'ont aidé à organiser la soutenance: en particulier, Victor Boniou, qui a assuré la diffusion en mondo-vision et a géré les nombreux petits soucis techniques, Noï Lavaud et Brigitte Llobel, grâce à qui nous avons pu avoir un pot, Victorien Blanchard et Nicolas Minesi, qui m'ont aidé à gérer les restrictions d'accès pour les invités, et bien sûr toute ma famille qui a pu faire le déplacement.

Il me faut également remercier les organismes qui ont financé ces travaux de recherche: l'Université Paris-Saclay, CentraleSupélec et l'école doctorale SMEMAG, qui m'ont attribué une bourse de thèse financée par le ministère de l'enseignement supérieur et de la recherche; l'Agence Nationale de la Recherche, qui au travers du projet FASMIC (ANR16-CE22-0013) a financé le fonctionnement des installations expérimentales; les projets ANR TIMBER (ANR14-CE23-0009-01, chapitre 10) et PASTEC (ANR16-CE22-0005, chapitre 11) ; la Commission Européenne, qui dans le cadre du programme Horizon2020, finance le projet Annulight (grant 765998); SafranTech (groupe Safran) qui nous a accordé un soutien à l'expérimentation sur SICCA-Spray et MICCA-Spray et au développement de TICCA-Spray (contrat Safran NF5Z-5100); le Grand Équipement National en Calcul Intensif (GENCI), qui m'a donné accès à des ressources de calcul intensif sur le calculateur Occigen du Centre Informatique National de l'Enseignement Supérieur (CINES, allocation

2019-A0072B10315); le mésocentre commun à CentraleSupélec et l'École Normale Paris-Saclay (calculateurs Fusion et Ruche), financé par le CNRS et la région Île de France; et bien entendu le Centre National de la Recherche Scientifique (CNRS), cotutelle du laboratoire EM2C.

Tout ce travail n'aurait bien entendu pas été possible sans mes encadrants, avec qui il a toujours été un grand plaisir de travailler. Pr Sébastien Candel, toujours de bon conseil dans les moments difficiles, que ce soit pour rédiger, interpréter et comprendre des données qui semblent incompréhensibles au premier abord, développer de nouveaux modèles et concevoir et planifier des expériences. Sa grande culture scientifique, son immense puissance de travail, ses capacités à développer des modèles et ses talents rédactionnels sont une inspiration. Dr Daniel Durox bien sûr, que j'ai côtoyé au jour le jour. Toujours disponible et de bon conseil. Adepte des petits bricolages qui permettent aux « manips » d'avancer. Très pointilleux et rigoureux, et à raison, sur les articles et leur contenu scientifique. Ça a été un grand plaisir et un grand privilège que de pouvoir travailler avec eux pendant ces quelques années. Je tenais également à remercier trois enseignants-chercheurs du laboratoire EM2C avec qui il m'a été donné l'occasion de collaborer: Dr Antoine Renaud, de retour au laboratoire vers la moitié de ma thèse et avec qui j'ai travaillé sur nos expériences MICCA-Spray et SICCA-Spray, ainsi que sur l'analyse modale. Dr Aymeric Vié, d'un très grand secours pour les simulations numériques, en particulier pour les LES avec spray. Pr Ronan Vicquelin, pour les discussions sur les transferts thermiques pariétaux et leur modélisation, ainsi que pour le partage du code Agath.

Je tenais aussi à remercier les collègues doctorants avec qui j'ai travaillé: Dr Kevin Prieur bien sûr, avec qui j'ai partagé le début de ma thèse, Dr Théa Lancien et Dr Stefano Puggelli, qui ont travaillé sur les simulations LES d'allumage. Ermanno Lo Schiavo, Dr Davide Laera et Dr Laurent Gicquel, du CERFACS, avec qui j'ai collaboré sur la simulation LES des écoulements réactifs dans SICCA-Spray, dans le cadre du projet FASMIC. Également bien sûr, toujours dans le cadre du projet FASMIC, Pr Françoise Baillot, Clément Patat et Dr Marcos Caceres, avec qui nous travaillons en collaboration pour mieux comprendre l'effet du forçage acoustique transverse sur les flammes de spray. Je me dois également de mentionner Pr James Dawson, Pr Nicholas Worth et Håkon Nygård qui m'ont accueilli pour un court séjour dans le cadre du projet européen Annulight. J'ai aussi eu le plaisir de travailler sur la combustion assistée par plasma en compagnie de deux collègues avec une grande expertise dans ce domaine: Nicolas Minesi et Victorien Blanchard. Ce furent des expériences fructueuses et qu'il faudra poursuivre ! Enfin et surtout, je me dois d'abondamment remercier deux collègues doctorants avec qui j'ai eu le grand plaisir de travailler, avec de très beaux et nombreux résultats: Preethi Rajendram Soundadarajan, qui poursuit l'expérimentation sur MICCA-Spray, et Karl Töpperwien, qui a beaucoup partagé son immense expertise sur les simulations LES pour MICCA-

Spray et SICCA-Spray. Merci à vous deux, je vous dois beaucoup pour la réussite de la fin de ma thèse.

Un grand merci également à mes collègues et amis doctorants au labo, toujours de bon conseil, que se soit pour débugger AVBP, critiquer la LIF ou juste garder le moral. Je vous remercie tous bien sûr, et plus particulièrement Preethi, Karl, Livia, Kevin Torres, Léo, Yacine, Hernando et Victorien.

J'en viens maintenant à toute l'équipe du laboratoire. Il me faut bien sûr remercier notre directeur, Dr Sébastien Ducruix. Je voulais également remercier particulièrement notre efficace et merveilleuse équipe de gestion, Brigitte Llobel, Nathalie Rodrigues et Noï Lavaud, sans qui rien n'avancerait. Également l'atelier, Érika Jean-Bart et Yannick Le Teno, ainsi que le BE, Jérôme Beaunier, que j'ai (très) régulièrement sollicités, toujours avec succès. Et bien sûr Jean-Michel Dupays et Sébastien Turgis pour leurs conseils en informatique et le travail sur cluster. Merci également à Philippe Scouflaire et Clément Mirat pour leur aide avec l'équipement expérimental en salle de manip.

Enfin, je voulais également remercier ma famille, mes parents, mes grands-parents et mes sœurs, qui m'ont aidé et supporté au cours de ces années de thèse. Merci aussi d'avoir fait le déplacement vers la région parisienne pour la soutenance malgré la pandémie.

Résumé

Le déploiement de technologies à faibles émissions dans les moteurs d'avion ne nécessite pas seulement que les nouvelles conceptions émettent des quantités réduites de polluants, mais également que leur comportement dynamique (allumage, extinction et instabilités de combustion) soit compatible avec les normes de sécurité qui sont drastiques dans le domaine aéronautique. Ce travail de recherche se concentre sur ces derniers aspects. La chambre annulaire transparente MICCA-Spray, équipée de 16 injecteurs swirlés représentant à échelle réduite le foyer d'un moteur d'hélicoptère est utilisée conjointement avec un système à un seul secteur (SICCA-Spray) pour étudier les problèmes dynamiques. Théorie, expérimentation et simulation aux grandes échelles sont combinées pour examiner une gamme de questions ayant trait à la dynamique de l'injecteur et à la structure de l'écoulement et du spray.

Après avoir succinctement introduit les travaux antérieurs, une première étude est conduite sur le lien entre la chimiluminescence de la flamme et le taux de dégagement de chaleur. Il est généralement admis que ces deux quantités sont proportionnelles dans les flammes parfaitement prémélangées, ce qui conduit à utiliser la chimiluminescence comme indicateur du taux de dégagement de chaleur instationnaire. Les expériences réalisées montrent que cette proportionnalité est inexacte pour des flammes prémélangées swirlées, ce qui conduit à une erreur dans l'estimation du taux de dégagement de chaleur. Par ailleurs, cette erreur est du même ordre de grandeur pour les flammes parfaitement prémélangées et les flammes de spray dans l'expérience SICCA-Spray.

Une autre étude d'intérêt fondamental a été conduite dans le cadre des présents travaux de thèse. Le nombre de swirl est un nombre sans dimension couramment utilisé pour estimer le taux de rotation des écoulements swirlés. On retrouve dans la littérature de nombreuses formulations pour ce nombre, et cette grande variété de formulations est peut-être pour partie responsable de certaines inconsistances observées dans la littérature sur la valeur critique de ce nombre qui détermine le phénomène de "vortex break-down" dans les écoulements swirlés. Pour comparer ces différentes formulations, une simulation aux grandes échelles haute fidélité est réalisée sur une configuration générique, et les résultats de cette simulation sont utilisés pour examiner ces différentes formulations et leurs propriétés de conservation. Il apparaît que seule la formulation la plus complète, initialement proposée par Chigier and Beér (1964), assure la conservation du nombre de swirl dans un écoulement typique d'une chambre de combustion.

Pour conduire les travaux portant sur la dynamique de l'injection et de la combustion,

une base de données d'injecteurs est introduite et caractérisée pour étudier l'impact des paramètres d'injection sur la dynamique de la combustion. Ces injecteurs sont examinés dans des conditions stables et instables en combinant des diagnostics laser et des simulations permettant la caractérisation de comportements spécifiques à la dynamique du spray et du système d'injection. Deux résultats importants sont que la présence d'un film liquide formé sur la paroi de l'injecteur induit une distribution multimodale des vitesses des gouttelettes et que les injecteurs ayant un nombre de swirl élevé sont plus robustes aux imperfections éventuelles du système d'atomisation. Une nouvelle méthode est ensuite introduite pour examiner le comportement spatio-temporel de l'écoulement et de la flamme lorsque l'injecteur est soumis à des modulations axiales. Une étude du processus par lequel les perturbations convectives se couplent au champ acoustique permet d'examiner les délais qui contrôlent l'instabilité de combustion et d'identifier les rôles respectifs de la convection et de l'évaporation des gouttes. Pour le système SICCA-Spray opérant avec de l'heptane liquide comme combustible, il apparait que l'évaporation a lieu en même temps que la convection du combustible vers la zone réactive. Afin d'analyser la structure de la flamme à haute cadence, une technique tomographique novatrice reposant sur des particules d'oxide d'étain est développée. Il est montré qu'elle peut permettre une prise d'images à grande cadence (100 kHz). Elle fournit des résultats majeurs sur la structure du noyau tourbillonnaire en précession (PVC) et montre que, sous forçage acoustique, le PVC est modulé en fréquence et en amplitude. L'impact de la perte de charge de l'injecteur sur les instabilités de combustion est ensuite examiné à l'aide de plusieurs systèmes d'injection avec des niveaux de rotation semblables. Il est démontré que ce paramètre joue un rôle majeur dans le couplage entre la flamme et le plenum.

Les résultats précédents sont utilisés pour guider les expériences sur la chambre de combustion annulaire. L'accent est mis sur les oscillations de combustion de grande amplitude couplées par un mode azimutal stationnaire induisant une extinction de flamme au voisinage de la ligne nodale de pression. Le traitement des mesures microphoniques est réalisé grâce à une technique novatrice reposant sur le développement en série d'harmoniques azimutaux du champ de pression acoustique, ce qui permet de déterminer les conditions critiques conduisant aux extinctions de flammes. Le développement en série d'harmoniques azimutaux est ensuite étendu à l'évaluation de l'impact de déformations du champ de température sur les fonctions propres du champ de pression acoustique. On montre ainsi que les déformations du champ de température conduisent à une baisse de la fréquence propre acoustique et à une déformation du champ de pression. Enfin le taux d'amortissement acoustique est déterminé expérimentalement dans la chambre MICCA-Spray au moyen de deux méthodes complémentaires.

De nouveaux résultats sont également présentés sur la dynamique transitoire d'un injecteur lors de l'allumage: suite à son initiation, la flamme pénètre dans la zone de recirculation interne et s'établit dans l'injecteur pour une durée de quelques dizaines de millisecondes. Un modèle acoustique d'ordre réduit est développé et révèle le mécanisme conduisant à ce phénomène. Enfin, une preuve de concept de la possibilité d'étendre la limite d'extinction pauvre d'une flamme de spray par des décharges plasma nanosecondes est présentée.

Abstract

The deployment of low-emission technologies in aero-engines does not only require that new designs produce reduced amounts of pollutants, but also that their dynamical behavior (ignition, blow-off, and combustion instabilities) be compatible with the high safety standards prevailing in aeronautics. This research is focused on the latter aspect of combustor design. A transparent annular combustor equipped with 16 swirled spray injectors is used to represent at the laboratory scale the combustion chamber of a jet engine. This system is used in conjunction with a single sector rig to investigate dynamical issues. Theory, experimentation and large eddy simulation are combined to examine a range of items pertaining to the injector dynamics, flow structure, swirl number determination, spray characteristics, and coupling between injector flow and acoustic field. A database of injectors is introduced to investigate the impact of injection parameters on combustion dynamics. These injectors are examined under steady and unsteady conditions by combining laser diagnostics and high-fidelity simulations which allows the characterization of spray-specific behaviors of relevance to the dynamics of injection systems. One important result is that the presence of a liquid film formed on the wall of the injection unit gives rise to a multi-modal distribution of droplet velocities. A novel method is introduced to examine the space-time behavior of the flow and flame of a swirling injector submitted to axial modulations. A detailed investigation of the process by which convective perturbations couple with the acoustic field allows to examine the time lags that control combustion instabilities and sort out the respective roles of convection and fuel droplet evaporation. High speed tomography relying on SnO_2 microparticles provides major results on the Precessing Vortex Core structure and show its behavior under acoustic forcing. The impact of injector head loss on combustion instabilities is examined using several injection systems with similar levels of swirl. The head loss is shown to play a major role in the coupling between the flame and the upstream plenum. The previous results obtained in a single sector rig are used to guide experiments on the annular combustor. The focus is placed on high amplitude combustion oscillations coupled by a standing azimuthal mode inducing flame blow-off near the pressure nodal line. The deformation of the acoustic distribution is tracked using a novel expansion on azimuthal harmonics allowing the determination of the critical conditions leading to this phenomenon. New results are also presented about the transient dynamics of an injector during ignition and about lean blow out with a proof of concept extension of the LBO limit by nanosecond plasma discharges.

Contents

List of Tables

List of Figures

Publications

Articles in rank A journals

- *Investigation of transient PVC dynamics in a strongly swirled spray flame using high speed planar laser imaging of SnO_2 microparticles.*
  Vignat, Guillaume, Durox, Daniel, Renaud, Antoine, Lancien, Théa, Vicquelin, Ronan and Candel, Sébastien
  Combustion and Flame 2020, *In press.*

- *Combustion dynamics of annular systems.*
  Vignat, Guillaume, Durox, Daniel, Schuller, Thierry and Candel, Sébastien
  Combustion Science and Technology 192(7) (p. 1358-1388), 2020. doi.org/10.1080/00102202.2020

- *A joint experimental and LES characterization of the liquid fuel spray in a swirl injector.*
  Vignat, Guillaume, Rajendram Soundararajan, Preethi, Durox, Daniel, Vié, Aymeric, Renaud, Antoine and Candel, Sébastien
  Proceedings of the ASME TurboExpo 2020, ASME Paper GT2020-14935.
  Journal of Engineering for Gas Turbine and Power 2020, *In press.*

- *Effect of different fuels on combustion instabilities in an annular combustor.*
  Rajendram Soundararajan, Preethi, Vignat, Guillaume, Durox, Daniel, Renaud, Antoine and Candel, Sébastien
  Proceedings of the ASME TurboExpo 2020, ASME Paper GT2020-15123.
  Journal of Engineering for Gas Turbine and Power 2020, *In press.*

- *Large eddy simulation of flame dynamics during the ignition of a swirling injector unit and comparison with experiments.*
  Töpperwien, Karl, Collin-Bastiani, Félix, Riber, Éléonore, Cuenot, Bénédicte, Vignat, Guillaume, Prieur, Kevin, Durox, Daniel, Candel, Sébastien and Vicquelin, Ronan
  Proceedings of the ASME TurboExpo 2020. ASME Paper GT2020-16197.
  Journal of Engineering for Gas Turbine and Power 2020, *In press.*

- *Improvement of lean blow-out performance of spray and premixed swirled flames using nanosecond repetitively pulsed discharges.*
  Vignat, Guillaume, Minesi, Nicolas, Rajendram Soundararajan, Preethi, Durox, Daniel, Renaud, Antoine, Blanchard, Victorien, Laux, Christophe

and Candel, Sébastien
Proceedings of the Combustion Institute 2021, *In press.* doi.org/10.1016/j.proci.2020.06.136

- *Dynamics of a spray and swirling flame under acoustic oscillations: a joint experimental and LES investigation.*
Vignat, Guillaume, Lo Schiavo, Ermanno, Laera, Davide, Renaud, Antoine, Gicquel, Laurent, Durox, Daniel and Candel, Sébastien
Proceedings of the Combustion Institute 2021, *In press.* doi.org/10.1016/j.proci.2020.05.054

- *High amplitude combustion instabilities in an annular combustor inducing pressure field deformation and flame blow-off.*
Vignat, Guillaume, Durox, Daniel, Renaud, Antoine and Candel, Sébastien
Journal of Engineering for Gas Turbine and Power 142(1) (p. 011016), jan. 2020. doi.org/10.1115/1.4045515

- *An experimental study into the effect of injector pressure loss on self-sustained combustion instabilities in a swirled spray burner.*
Vignat, Guillaume, Durox, Daniel, Prieur, Kevin and Candel, Sébastien
Proceedings of the Combustion Institute 37(4) (p. 5205-5213), 2019. doi.org/10.1016/j.proci.2018

- *Flame and spray dynamics during the light-round process in an annular system equipped with multiple swirl spray injectors.*
Prieur, Kevin, Vignat, Guillaume, Durox, Daniel, Schuller, Thierry and Candel, Sébastien
Journal of Engineering for Gas Turbine and Power 141(6) (p. 061007), jan. 2019. doi.org/10.1115/1.4042024

Conferences with proceedings

- *Quantifying acoustic damping in a multi-injector annular combustor.*
Vignat, Guillaume, Durox, Daniel, Renaud, Antoine and Candel, Sébastien
9$^{\text{th}}$ European Combustion Meeting, Lisboa, Portugal, 2019.

- *Large-Eddy Simulation of Flame Dynamics during the Ignition of a Swirling Injector Unit and Comparison with Experiments.*
Töpperwien, Karl, Lancien, Théa, Vignat, Guillaume, Prieur, Kevin, Durox, Daniel, Candel, Sébastien and Vicquelin, Ronan
9$^{\text{th}}$ European Combustion Meeting, Lisboa, Portugal, 2019. hal-02497004

- *Large-Eddy Simulation of Flame Dynamics during the Ignition of a Swirling Injector Unit and Comparison with Experiments.*
Töpperwien, Karl, Lancien, Théa, Puggelli, Stefano, Vignat, Guillaume, Prieur, Kevin, Durox, Daniel, Candel, Sébastien and Vicquelin, Ronan
17$^{\text{th}}$ International Conference on Numerical Combustion, May 2019, Aachen, Germany. hal-02497007

- *Tomographie à très haute cadence de flammes turbulentes swirlées au moyen du*

dioxyde d'étain.
Vignat, Guillaume, Durox, Daniel, Prieur, Kevin, Lancien, Théa, Vicquelin, Ronan and Candel, Sébastien
16ème Congrès Francophone de Techniques Laser, Dourdan, France, 2018. hal-02098273

- *Experimental determination of flame describing function of swirling spray flames.*
Prieur, Kevin, Durox, Daniel, Vignat, Guillaume, Schuller, Thierry and Candel, Sébastien
Colloque INCA, Chateaufort, France, 2017. hal-02324581

Introduction

In a context of sustained growth of air travel, with a factor of 2.4 in the number of revenue passenger kilometer (RPK) between 2000 and 2019 (Airbus (2019)), and a further expected doubling in traffic in the next 15 years, the demand for new aircraft is expected to be in the order of 40 000 units for the next 20 years. Pollutant emissions by this growing sector have however become a global concern, and are affecting the future of the aviation industry. The European Aviation Safety Administration (EASA (2019)) estimated that in 2019 the aviation sector will be responsible for about 3% of the total greenhouse gas emissions of the European Union. However, the contribution of aviation to global warming is not restricted to its CO_2 emissions. It was estimated in 2005 that 40% of the radiative forcing associated with aviation arised from its CO_2 emissions. Other contributing factors include nitrogen oxides (NOx) emissions at altitude and their interactions with the ozone layer, soot nanoparticles, formation of contrails, high-altitude cirrus clouds, a phenomenon to which nanoparticles are suspected to contribute, and general modification of the cloudiness. It is generally considered that the level of scientific understanding is good for the impact of CO_2 emissions, but that the other mechanisms are still subject to large uncertainties (Lee et al. (2009)). In addition to these global consequences of air travel, NOx and soot nanoparticle emissions in the vicinity of airports also contribute to urban pollution and are detrimental to human health. Noise in the vicinity of airport is an additional challenge to the growth of aviation.

To meet these challenges in a context of growing air travel, regulators have set ambitious targets for improvement in aircraft performance regarding emissions. Since 2012, CO_2 emission for aircraft are included in the EU's carbon credit system. The International Civil Aviation Organization (ICAO) has set as a 2027 target to reduce NOx emissions below 54% of the current CAEP/8 regulations. Reaching these goals will require some difficult balancing. It is known for example that increasing the engine pressure ratio leads to higher efficiency and lower CO_2 emissions, but increases NOx emissions as the combustor inlet temperature is correspondingly higher. The Zeldovich mechanism for NOx formation indicates that the levels of these species increase exponentially with temperature. To overcome this fundamental issue, new combustor architectures have been introduced, many making use of Lean Premixed Prevaporized (LPP) combustion. This implies that air and fuel are premixed inside the injector in a homogeneous manner with an overall excess of air, thereby burning at lower temperatures with a minimal number of hot pockets. This injection strategy has shown great promise to reduce NOx emissions, and is already implemented in modern stationary power generating gas turbines (Tacina (1990); Lefebvre and Ballal (2010)). There are also more disruptive attempts

to decarbonate aviation by replacing the current gas turbines with electrical engines but such solutions cannot in the foreseeable future match the performance of current systems. Among the many issues that are raised by electrification, one of the most difficult is that of energy storage in batteries. The energy density in the best batteries is at this point lower than about 300 Wh/kg or about 1 MJ/kg while the energy content of kerosen is 42 MJ/kg. An A320 Neo with a maximum take-off weight of 80 t requires 20 t of kerosene to carry 160 passengers over a distance of 6300 km. With current technologies, an electrical aircraft with similar performance figures would require in the order of 280 t of batteries, equivalent to about 7 times the current empty mass of this aircraft. To keep the same wing loading the wing area will have to be multiplied by 5 and would then exceed 600 m^2, the wing area of an A380 being 845 m^2 for comparison. The power required to move this electrical aircraft would also have to be multiplied by about the same factor amounting to more than 130 MWe. However, the batteries would be far from being able to meet these power requirements. This rough reasoning indicates that the energy storage technology is not yet available for developing purely electrical transport aircraft that would match the performance of current airplanes. Other routes to reduce the carbon intensity of aviation that are more realistic include the integration of bio-fuels generated from agricultural products, or the addition of hydrogen in current engine technologies.

These requirements for improved emissions and the deployment of new combustion technologies that they imply must occur in a context where safety is a primary concern that cannot be compromised. In the context of combustor design, these concerns are generally discussed under the operability framework, and are related to combustion dynamics issues. These include phenomena such as water and particulate ingestion, ignition, lean blow out, and combustion instabilities. Changing the design of the combustor or the injectors in order to reduce emissions may lead to deterioration in the combustor's operability, and this topic is therefore quite relevant to the current effort aimed at reducing the environmental footprint of aviation.

Among the operability concerns, combustion instabilities have a singular place. They constitute problems that can remain undiscovered for the most part of an engine development project, and that may be manifested during its latter stages, when a near full scale engine is being tested. This is due to the highly sensitive nature of combustion instabilities: they are in particular sensitive to acoustic boundary conditions which are difficult to reproduce in reduced-scale development testing. They can thus generate delays in engine development projects. The problem is compounded by the fact that there is an overall lack of predictive tools and even of an in depth-understanding of the mechanims giving rise to these phenomena. Combustion dynamics constitutes a real challenge in engineering design.

This is specifically the case for the LPP combustion mode, which is quite promising for reducing NOx emissions but is also known to be sensitive to combustion instabilities. Lean premixed combustors require that a large amount of the available airflow be directed to the injector, reducing the size of the multi-perforated liners that are commonly used to cool combustor walls, and that contribute to the acoustic damping of the chamber. Addi-

tionally, this mode of operation is associated with high power densities that characterize high pressure ratio engines, and that favors the development of instabilities (Keller (1995); Méry (2018)). Combustion instabilities coupled by azimuthal modes in engine configurations featuring annular combustors are reported by Schuermans et al. (1999) and Krebs et al. (2002). This type of coupling is more complex in nature, and damped to a lesser extent by upstream and downstream boundary conditions. They are also more difficult to suppress using dampers, making for a bigger challenge.

The present research combines experimentation, modeling and simulation aimed at understanding and predicting combustion instabilities in annular systems. It is more specifically targeted on instabilities coupled by azimuthal modes. On the experimental level this work makes use of two facilities, the MICCA-Spray annular combustor test-rig and the single sector SICCA-Spray system. Both are operated at EM2C laboratory. With its annular geometry MICCA-Spray allows studies of instabilities coupled by azimuthal acoustic modes. It is designed to be as close as possible to an aero-engine configuration while being simple enough to maintain both a high degree of optical access for measurements, and a high degree of flexibility to be able to perform parametric studies on injectors, chamber geometry and fuel composition. A large set of experiments has been carried out in this set up and has brought considerable insight. Another set of experiments is carried out on a simpler, single sector rig (SICCA-Spray). This is mainly used to investigate flame dynamics in a framework where experiments carried out in both rigs nicely complement each other. In particular, SICCA-Spray allows for detailed measurements of the flame describing function and for an analysis of the coupling between the reactive flow and acoustic perturbations. It is also an excellent test bed for simulations of the dynamics of a single spray swirling flame. Numerous parametric studies on injector design have been carried out in this facility. An extended presentation of the thesis contents is given at the end of this introduction.

At this point it is worth reviewing work concerned with combustion instabilities in aeronautical systems, that is focused on annular combustors and spray flames. The present thesis includes investigations on other topics related to operability, such as ignition, lean blow-out and plasma assisted combustion, but these subjects will be reviewed latter on in the chapters where these items are discussed.

Combustion instabilities in annular combustion systems

This literature review is adapted from a review article accepted for publication to *Combustion Science and Technology*: Combustion dynamics of annular systems, by Guillaume Vignat, Daniel Durox, Thierry Schuller and Sébastien Candel.

A considerable amount of research in combustion deals with combustion instabilities. The early work of Lord Rayleigh (1878) on the so-called "singing flame" phenomenon left its mark in the field by pointing out the driving mechanism of thermoacoustic instabilities, that is combustion instabilities coupled by an acoustic oscillation on a resonant mode of the system. Heat release rate fluctuations must be in phase with pressure fluctuations

to drive the instability. These investigations were largely expanded after the 2nd world war, motivated by problems encountered during early developments of high performance devices such as liquid rockets and jet engines and more recently by difficulties in operating gas turbines featuring low NOx premixed combustor architectures. Pioneering work in the field of combustion instability was initiated in the early fifties by various groups and in particular by Luigi Crocco, a professor at Princeton, and his students and colleagues. Much of the early work of this period emphasized the existence of time lags in combustion processes associated for example with the vaporization of propellant droplets and the sensitivity of the corresponding delays to state variables (Crocco (1951); Tsien (1952); Crocco (1952); Marble and Cox (1953); Crocco and Cheng (1953); Crocco and Cheng (1956)). Many investigations were concerned with the effect of the nozzle and the associated boundary condition (Crocco and Sirignano (1966); Zinn and Crocco (1968)). Crocco (1965) also summarizes his and his groups' work on combustion instabilities driven by unsteady droplet combustion. Research by the Princeton group underlined the nonlinear features associated with the large amplitude perturbations arising under combustion instability, see for example Sirignano and Crocco (1964); Mitchell et al. (1969). The effort on liquid rocket engine combustion instability was synthesized in a report (NASA SP194) edited by Harrje and Reardon (1972). Many of the methods, tools and theories developed in these early works remain of high relevance to modern analysis of combustion instability phenomena. One such example is the widely used modal expansion framework for the low order analysis of complex thermoacoustic systems, formalized by Zinn and Powell (1970) and explored in great detail by Culick (1976); Culick (1988).

The current effort in the field of combustion instability is motivated by issues raised by gas turbine combustors (Candel (2002); Poinsot (2017)). Table 1 summarizes characteristics of high performance devices that influence their combustion dynamics. While rocket thrust chambers are cylindrical and terminated by a choked nozzle, combustors are annular in modern aero-engine and in most stationary gas turbines. The downstream boundary condition is formed by the turbine distributor which is generally choked. In most cases these devices feature an annular geometry and the combustion dynamics of such systems raises fundamental issues and in particular those associated with the coupling by azimuthal chamber modes. Operation under lean conditions and the relatively high energy density associated with the compact flame region and high pressure ratios promotes the development of such oscillations. The absence of perforated liners in partially premixed systems also reduces damping characteristics. In the annular geometry, one finds in addition to longitudinal instabilities, oscillations coupled by tangential modes that are less well damped. The problem is compounded by the fact that flames are likely to respond over a wide frequency range, and the modal density in the annular geometry can be quite high. If a resonant mode disappears because the combustion regime has been modified, or because the thermal or impedance conditions are changed, another acoustic mode may be initiated.

Many of these issues are considered in a book edited by Lieuwen and Yang (2005) while Huang and Yang (2009) provide an extensive review of multidimensional simulation efforts and low order dynamical modeling. Predictions are necessarily based on a flame

Table 1: *General characteristics of high performance devices of importance for their combustion dynamics analysis.*

System	Liquid rocket engines	Aero-engines	Gas turbines
Power density	Very high, $\simeq 50$ GW m^{-3}	High, $\simeq 1$ GW m^{-3}	High, $\simeq 1$ GW m^{-3}
Chamber pressure	Very high, $\simeq 10$ MPa	High, 3 to 5 MPa	High, 1.7 to 3.5 MPa
Combustion mode	Non premixed	Partially premixed	Essentially premixed
Chamber geometry	Cylindrical	Annular	Often annular
Upstream boundary	Propellant domes	High pressure compressor	High pressure compressor
Dowstream boundary	Choked nozzle	Turbine distributor	Turbine distributor
Injection	Shear coaxial, low swirl	Swirling injectors, hollow cone or multipoint atomizers	Swirling injectors
State of fuel and oxidizer	Liquid-liquid or liquid-gas. No diluent	Liquid fuel & air, nitrogen diluent in air stream	Gaseous fuel & air, nitrogen diluent in air stream

model. Early work used a time domain representation, for example using the sensitive time lag $(n - \tau)$ theory (Smith and Zukoski (1985); Zukoski (1988)). Some works also use a finite impulse response model (see for example Guo et al. (2019)). However, in general, predictions are carried out in the frequency domain and are based on measurements of the flame transfer function (FTF) which are combined with acoustic network representations of the system. This linear analysis gives access to stability maps, resonant frequencies and growth rates (Dowling and Stow (2003); Sattelmayer and Polifke (2003); Schuller et al. (2003); Durox et al. (2013)). This approach has become reasonably mature that it can be successfully applied to industrial configurations, even at elevated pressure as indicated for example by Schuermans et al. (2010). The linear approach can be extended to deal with nonlinear features by making use of the describing function, a concept used for example by Dowling (1997) to represent the dynamics of a ducted flame. The flame describing function (FDF) representing the flame response in combination with an acoustic network or in combination with a Helmholtz solver yields growth rates and frequencies depending on the amplitude of oscillation. As shown by Noiray et al. (2008); Boudy et al. (2011) this framework gives access to nonlinear phenomena like frequency shifting, mode switching triggering and hysteresis. The FDF has been applied more recently to instabilities oin systems equipped with a swirling injector (Palies et al. (2011); Silva et al. (2013); Cosic et al. (2014)) and to annular systems (Ghirardo et al. (2016); Laera et al. (2017); Yang et al. (2019)). Large eddy simulations have also been used to predict the dynamical processes in gas turbine combustors, either as input to low order models based on the FTF and FDF frameworks, or for direct simulation of unstable combustion systems. These subjects are reviewed by Gicquel et al. (2012) and Poinsot (2017).

In most gas turbine combustors flames are stabilized by swirling injectors. This has led to detailed examination of the dynamics of swirling flames. In these systems the flame is anchored by imparting an azimuthal component to the flow usually by passing the air stream through a swirler or through a set of swirlers. The rotation induced by these devices generates an inner recirculation zone (IRZ, also known as a central recirculation zone) and in many cases an outer recirculation zone (ORZ, also known as a corner recirculation zone) which are filled with hot combustion products which continuously ignite the fresh reactants injected in the combustor.

The dynamics of swirling flames thus constitutes a basic topic that has received considerable attention in recent years (see Candel et al. (2014) for a recent review). Swirling flames were found to be subject to a variety of direct and indirect excitation mechanisms. Under the effect of acoustic forcing, the annular jet formed in the swirling flow fluctuates, and the vortex breakdown bubble is dynamically displaced. This results in deformations of the flame front and oscillations of the flame anchor point (Thumuluru and Lieuwen (2009); Borghesi et al. (2009); Gatti et al. (2019)). If the fuel is injected close to or inside the swirler, a situation which is typically found in practical systems, acoustic perturbations at the injector generate fluctuations in the mixture ratio. These are convected to the flame and cause heat release rate fluctuations by modifying the burning velocity (Lieuwen et al. (2001)). Another indirect effect is related to the interaction of incident acoustic waves with the swirler. This process generates fluctuations in the azimuthal

velocity that perturb the flame after a convective delay (Huang and Yang (2009); Palies et al. (2010); Komarek and Polifke (2010); Albayrak et al. (2019)). The interference between perturbations propagating at acoustic and convective velocities leads to a specific frequency dependence of the flame response. Swirl flames are also receptive to transverse acoustic forcing and this may be relevant to azimuthal instabilities observed in annular combustors. Generally, the swirling flame response to transverse acoustic forcing depends on the orientation of the acoustic field (Baillot and Lespinasse (2014); O'Connor et al. (2015)). If a pressure antinode is located near the flame, axial acoustics will be excited and these axial fluctuations dominate the flame response. For the case of a transverse velocity antinode, it is found that non-axisymmetric shear layer modes are excited which interact with the flame. In swirling spray flames similar to those considered in the present work, Caceres (2019) observed that these non-axisymmetric perturbations take the form of an helical deformation of the flame front.

In practical cases the swirling flow is confined by lateral walls in a geometry which features in many cases an annular cross section and by transverse flows originating from lateral orifices. Given the highly sensitive nature of subcritical swirling flows commonly found in combustors (Escudier and Keller (1985); Li and Gutmark (2005); Terhaar et al. (2012)), the presence of these side walls, transverse jets and neighboring injectors has a significant impact on the flow structure complicating the analysis (Fanaca et al. (2010); Han and Morgans (2018); Worth and Dawson (2019)). Studies of a single injector placed in a single sector or in a cylindrical configuration provides useful information but only approximately represent the practical situation. This clearly underlines the necessity to work on fully annular configurations allowing azimuthal mode coupling.

A substantial amount of literature exists in the field of combustion instabilities but the majority of experimental investigations consider oscillations coupled by longitudinal modes in single injector configurations (see review articles by Putnam (1971); Culick (2001); Candel (2002); Huang and Yang (2009); Poinsot (2017)). The problem of azimuthal mode coupling in combustion instabilities is considered in recent theoretical investigations: Stow and Dowling (2001); Evesque et al. (2003); Pankiewitz and Sattelmayer (2003); Schuermans et al. (2003); Noiray et al. (2011); Noiray and Schuermans (2013b); Ghirardo and Juniper (2013); Bauerheim et al. (2014); Bauerheim et al. (2014); Bauerheim et al. (2015); Bauerheim et al. (2016); Ghirardo et al. (2016). A central issue is to account for the collective processes where neighboring flames interact and feed energy in the azimuthal modes.

Experimental investigations on well instrumented annular chambers are not common. Kopitz et al. (2005) used a network model to analyze the stability of an experimental annular combustor exhibiting two different instabilities depending on the operating conditions, a longitudinal mode and a first-order azimuthal mode. The flame response measured at stable conditions was extrapolated in flow rate and equivalence ratio to the unstable regime. Both modes could be identified in the model but only the instability coupled by a longitudinal mode was accurately captured. Moeck et al. (2010) explored azimuthal instabilities of an annular chamber equipped with twelve channels comprising

electrically heated Rijke tubes. Note that the Rijke tubes sucked air from the surrounding atmosphere and there was no plenum or upstream manifold. Depending on the electrical power injected, two azimuthal modes were observed in the form of a standing wave or a slowly spinning oscillation. Staging in the heating tubes was tested to see if this could help stabilize the system. It was found that some modes could be attenuated, while others were strengthened. An acoustic model was used to predict the dynamical behavior of the annular chamber and test the influence of staging. Krebs et al. (2002) were the first authors reporting detailed experimental data for the acoustic pressure distribution in an instrumented industrial gas turbine featuring self-sustained combustion oscillations coupled to one of the azimuthal modes of the combustion chamber. Their analysis places particular emphasis on the role of the acoustic boundary conditions and flame response in the development of spinning and standing modes.

In this general context it appears logical to consider the dynamics of annular configurations comprising multiple injectors. This review is based on experimental data gathered in two model scale annular combustor facilities developed in recent years. They both feature a transparent combustion chamber to see the flames over all the injectors regularly distributed along the azimuthal direction. In both cases the objective was to gather knowledge on ignition and azimuthal instabilities in annular configurations. The first described by Worth and Dawson (2013a) was initially designed in Cambridge. Interesting aspects of the dynamics of this annular system are explored in a series of articles: Worth and Dawson (2013b); Dawson and Worth (2014); Dawson and Worth (2015); Worth and Dawson (2017); Mazur et al. (2019). This team was also able to acoustically force the combustor along azimuthal modes in Worth et al. (2017a); Nygård et al. (2019). Ignition dynamics is also investigated in the Cambridge annular combustor both in a premixed combustion regime, and in non-premixed conditions by Machover and Mastorakos (2016); Machover and Mastorakos (2017a). Numerical simulations have also been performed by Machover and Mastorakos (2017b).

This experimental device, shown in Figure 4, has a relatively small chamber diameter of 17 cm. The number of injectors connecting the plenum to the chamber backplane can be changed. Experiments were carried out with 12, 15 or 18 units allowing a change in the spacing to diameter ratio. Injectors are swirled but the swirl number is moderate and there is a central bluff-body which occupies 50% of the injector exhaust section. The fresh gases are then exhausted through a thin annular slit. Azimuthal instabilities are obtained by operating with a mixture of ethylene and air, and by making use of an interior chamber wall shorter than the outer wall (13 cm and 17 cm respectively). For an equivalence ratio above 0.85, a strong azimuthal instability is observed taking the form of a spinning or standing wave depending on the spacing between injectors. The instability is enhanced when the flames are close giving rise to strong interactions between adjacent reactive layers. For pressure oscillations with an amplitude of 200 Pa in the chamber, the fluctuation in heat release rate quoted in Worth and Dawson (2013a) is around 10%.

Another experimental setup MICCA developed independently in our laboratory (Bourgouin et al. (2013)) provides additional information on instabilities coupled by azimuthal

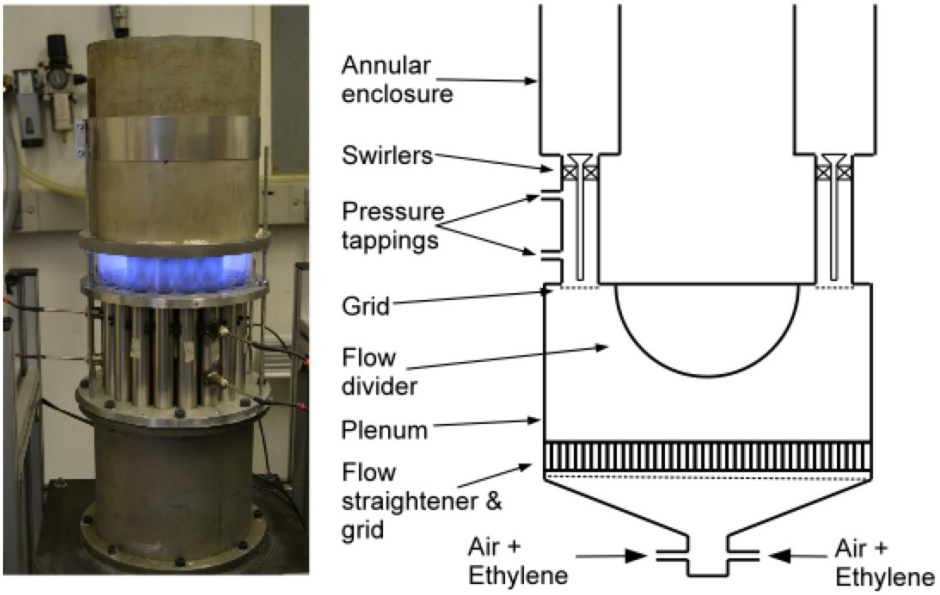

Figure 4: *Left : view of the system under operation. The mean diameter of the ring is 170 mm. Injectors comprise a central bluff body. Right : Schematic diagram of the setup. Reproduced from Worth and Dawson (2013a).*

modes. The geometry has some features in common with that of Worth and Dawson (2013a) but there are differences. The MICCA test facility was designed to identify the physical mechanisms driving instabilities of annular combustors and provide experimental data for model validation. Dimensions of MICCA differ from those used in Worth and Dawson (2013a), a choice guided by considerations of flame receptivity to flow perturbations. By selecting a large diameter, resonant frequencies corresponding to azimuthal modes are reduced and can be brought inside the range where the flame transfer function has a finite gain. In particular, the mean diameter of the MICCA combustor of 35 cm is close to that of a helicopter gas turbine and is twice that of the Cambridge experiment. The annular chamber is equipped with 16 swirl injectors. The swirl number is sufficiently high to allow flame anchoring without requiring a central bluff-body. The flame dynamics is then closer to that found in practical devices where combustion is stabilized aerodynamically by swirl in the absence of a central obstacle. The chamber operates at atmospheric pressure and it is fully transparent to allow observations with a high speed camera. Waveguide microphones are used to record pressure signals at the combustor injection plane and inside the annular plenum. Depending on operating modes, the system exhibits longitudinal or azimuthal instabilities (Bourgouin et al. (2013)).

The MICCA facility has evolved into a number of different versions as illustrated in Figure 5. The initial configuration was equipped with injectors fed by premixed reactants featuring a cylindrical exhaust section (Bourgouin et al. (2013); Bourgouin et al. (2013)). These injectors were later fitted with a conical cup and the corresponding configuration was designated as MICCA2 (Durox et al. (2016)). Swirling units were then replaced by matrix injectors comprising a periodic arrangement of small channels producing a multiplicity of small laminar flames. This version (MICCA3) has allowed investigations of

combustion instabilities coupled by azimuthal modes in the absence of complexities associated with turbulence and swirling flows (Bourgouin et al. (2015a); Bourgouin et al. (2015b); Prieur et al. (2017a); Laera et al. (2017); Moeck et al. (2019)). It was modified more recently to allow liquid fuel injection in the form of a spray using hollow cone atomizers. This configuration designated as MICCA-Spray is used in the present thesis, in continuation of the thesis work of Prieur (Prieur et al. (2017a); Prieur et al. (2018); Prieur et al. ()).

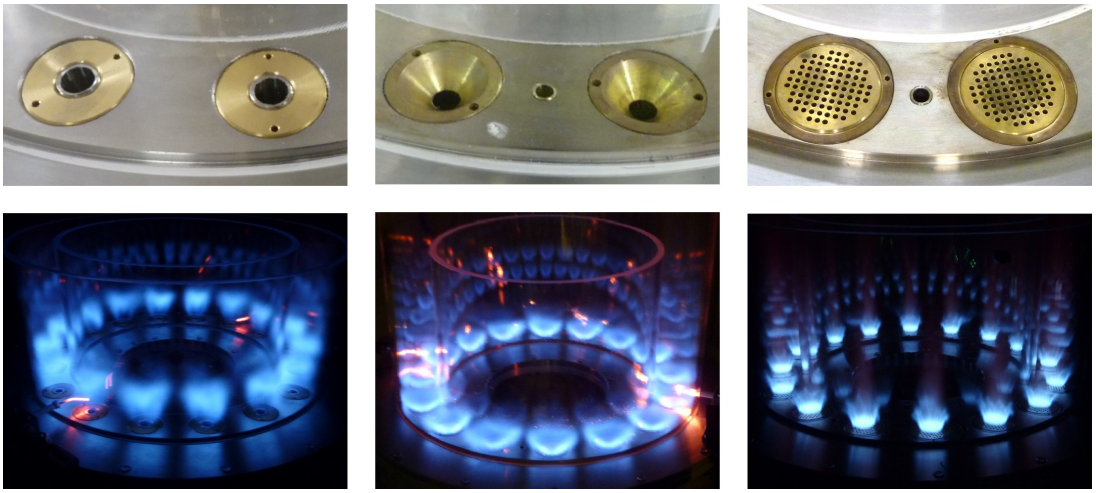

Figure 5: *Injector geometry and induced flame shape in the annular setup. Only the premixed flame MICCA version is shown. Left: MICCA, the injectors feature a swirler and a cylindrical exhaust channel. This configuration is used in the light-round investigation of Bourgouin et al. (2013). Center : MICCA2, the injectors feature a swirler and a conical cup. This geometry is used in the thermo-acoustics instability investigations of Durox et al. (2016). Right : MICCA3 with matrix injectors used to examine thermo-acoustics instabilities in an environment which features low levels of random perturbations (Bourgouin et al. (2015a); Prieur et al. (2017a); Laera et al. (2017); Moeck et al. (2019)).*

The present review essentially deals with fundamental items pertaining to, on the one hand, combustion instabilities of annular systems, and on the other hand, combustion dynamics of spray swirled flames. There is no intention to provide an exhaustive review but merely to give a synthesis of research that pertains to the type of combustion dynamics found in MICCA-Spray. The first item is specifically concerned with oscillations coupled by modes that span the circumference of the annulus. An experimental methodology is first introduced that combines single sector investigations targeted at injector characterization and selection with testing in the annular configuration (Section). Instabilities of annular systems equipped with premixed injectors are then discussed (Section). The premixed case is considered first because much of the recent work on swirling flames has been carried out in relation with the design of advanced premixed combustion technologies with the objective of reducing NOx emissions from gas turbines. These systems have achieved low pollutant levels but their operation has been hindered by dynamical phenomena. This is so because premixed flames are more compact and more sensitive to external perturbations. Also damping in lean premixed systems is reduced because the perforated liners

found in more standard designs are for the most part eliminated in modern premixed combustors. It is next interesting to examine situations where the fuel is injected as a liquid spray of droplets as in aero-jet gas turbine engines. This will be accomplished be first briefly reviewing the recent litterature concerned with the dynamics of spray swirled flame similar to those found in aero-engine configurations (Section). The case of annular combustors fed by swirl spray atomizers is then reviewed, with a particular focus on the MICCA-Spray configuration (Section).

Experimental methodology for combustion instability analysis

Experiments on annular configurations are possible but both for the atmospheric rigs MICCA at EM2C and the Cambridge combustor of Dawson and Worth, a major challenge was to design injectors and confinement geometries giving rise to combustion instabilities coupled by azimuthal modes. It was quickly found that some guiding ideas were needed about injector geometry selection. This guidance may be obtained from simulations or perhaps from single sector experiments providing information on the flame response through measurements of the flame describing function. The objective was to determine the gain and phase that could be used with a theoretical model to predict instability. The combination of single sector and multiple injector annular combustor testing is represented in Figure 6 for the case of MICCA.

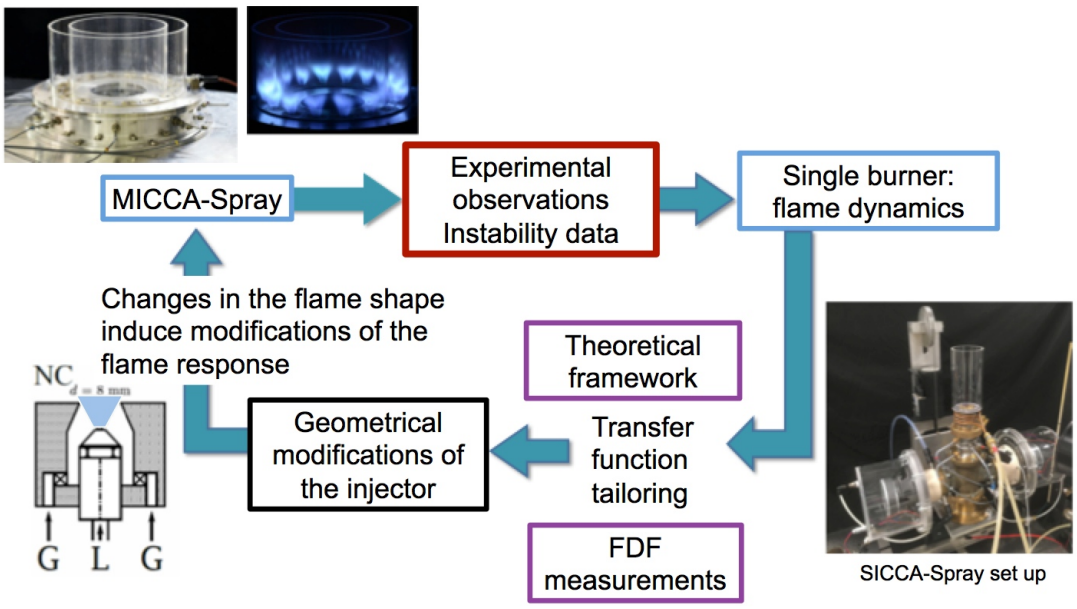

Figure 6: *Experimental methodology combining single sector measurements in the SICCA setup and annular combustor testing on MICCA.*

Results of single injector experiments are illustrated in Figure 7. In this case the injector is fitted with a conical "cup". Experiments carried out for different cup angles indicate notable changes in the flame geometry as the cup angle is augmented. This is also reflected in the flame describing functions with some notable modifications of the gain and

phase of these functions (Prieur et al. (2016)). This information could then be used in combination with a simplified theoretical framework to define the geometry giving access to instabilities in the annular chamber. The single sector experiments can thus be used to tailor the injector response in an iterative process. From an industrial point of view, the aim is of course just the opposite as one wishes to avoid naturally excited instabilities. The idea is then to work on the single sector configuration and, with the help of the theoretical framework, try to design an injector that will be less receptive to oscillations when arranged in an annular combustor system.

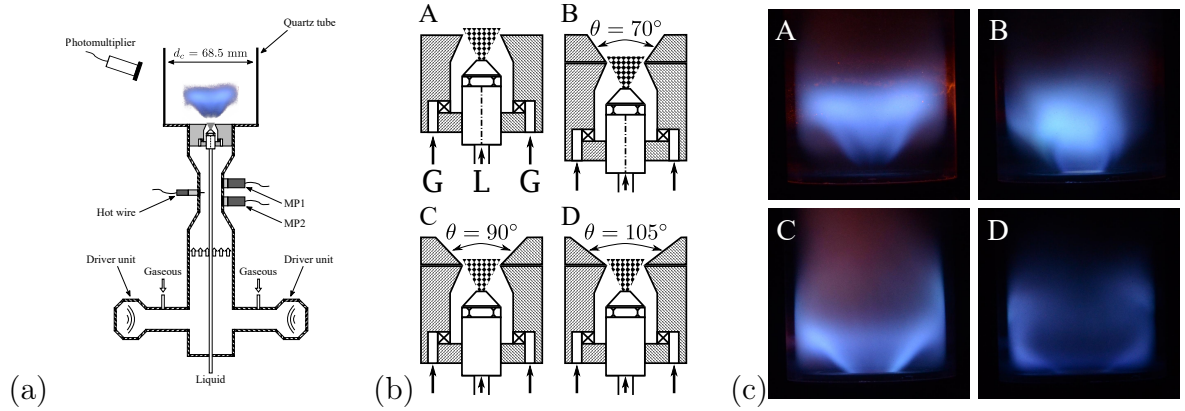

Figure 7: *(a) Schematic of the burner to determine the flame response. (b) Injector configurations. Case A: No cup is installed. Case B: a 70° cup is installed. Case C: a 90° cup is installed. Case D: a 105° cup is installed. G stands for gas and L for liquid. (c) Flame shapes with different injector configurations. Case A: injector without cup generates an M flame. Case B: injector with 70° cup generates an amphora flame. Case C: injector with 90° cup generates a V flame. Case D: injector with 105° cup generates a corner flame. From Prieur et al. (2016).*

Combustion instabilities of premixed annular systems

Before reviewing experimental data concerning instabilities in premixed annular burners it is first useful to examine the acoustic modes of annular devices. This will be done in the next subsection by considering an idealized geometry. We will then successively review experimental work on annular systems. The focus will be placed on well instrumented, laboratory scaled test rigs. We will first discuss results obtained on MICCA equipped with swirling injectors featuring an outlet cup (MICCA2), then on the Cambridge/NTNU burner and finally on an annular configuration comprising multiple matrix injection units (MICCA3).

Modal structures in annular chambers

The following discussion is concerned with the three configurations shown in Fig. 8. The first of these geometries (Fig. 8(a)) is formed by a cylindrical chamber with lateral walls of equal length l. The annular spacing and mean annular radius are d and R respectively. To be consistent with the conditions of the MICCA setup one may assume that the bottom plane and side walls are rigid while the exhaust section is open to the atmosphere and

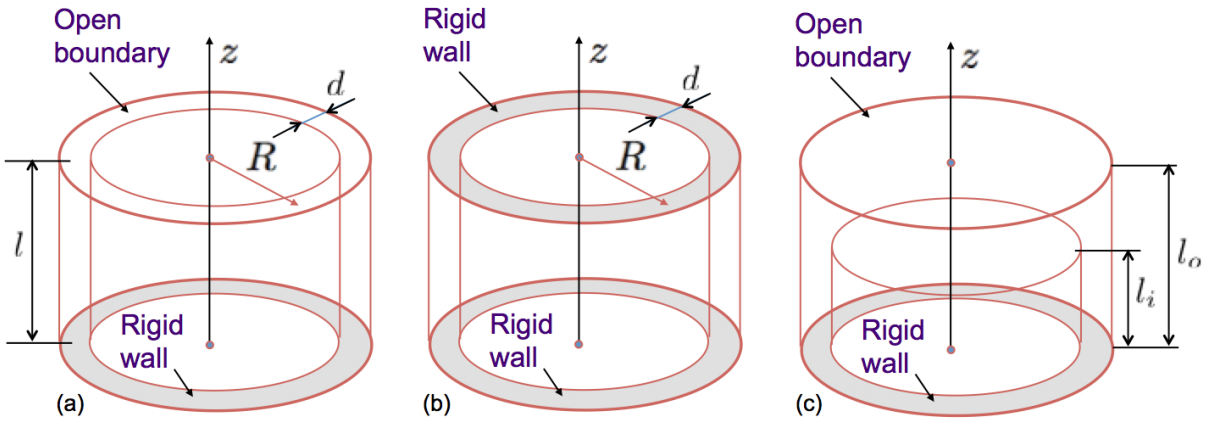

Figure 8: *Generic annular geometries. (a) Annular chamber with a rigid backplane, equal length side walls and an open boundary, (b) Annular chamber with a rigid backplane and a rigid wall boundary condition at the outlet, (c) Annular chamber with unequal side walls.*

corresponds to a pressure node. In fact the node is not exactly in the open section but at a distance from the outlet. One may assume for simplicity that this additional distance can be neglected. In practice this end correction is easily determined experimentally and can be added to the combustor length to improve the resonance frequencies estimations. To obtain simple analytical expressions it is also assumed that the sound velocity c is constant inside the system. It is also convenient to consider that the annular distance between the side walls is small compared to the mean diameter ($d << D = 2R$). One may then assume that the pressure waves in this configuration do not depend on the radial coordinate. Harmonic waves then satisfy a simplified Helmholtz equation:

$$\frac{1}{R^2}\frac{\partial^2 p}{\partial \theta^2} + \frac{\partial^2 p}{\partial z^2} + \frac{\omega^2}{c^2} p = 0 \tag{1}$$

This equation features purely azimuthal modes:

$$\psi_n(\theta) = a_n \exp(in\theta) + b_n \exp(-in\theta) \tag{2}$$

where a_n, b_n are constant amplitudes and the corresponding angular frequencies are $\omega_n = nc/R$. The eigenfrequencies are then given by $f_n = nc/\mathcal{P}$ where $\mathcal{P} = 2\pi R$ is the mean perimeter of this annular configuration and the pressures waves take the form:

$$p_n(\theta, t) = a_n \exp(in\theta - i\omega_n t) + b_n \exp(-in\theta - i\omega_n t) \tag{3}$$

The pressure appears as a combination of a wave propagating in the positive azimuthal direction and a wave propagating in the negative azimuthal direction. These two waves respectively travel conter-clockwise and clockwise. There are also purely axial modes which for the rigid bottom plane - open outlet take the form:

$$\psi_m(z) = a_m \cos(k_m z) \tag{4}$$

where $k_m = (m - 1/2)\pi/l$ where m is an integer. The angular frequencies are then of the form $\omega_m = (m - 1/2)\pi(c/l)$ and the corresponding eigenfrequencies ar such that $f_m = (2m - 1)(c/4l)$. The annular geometry with a rigid backplane and an open outlet only sustains mixed modes which satisfy all boundary conditions. The corresponding eigenfunctions are a combination of those given previously:

$$\psi_{mn} = [a_n \exp(in\theta) + b_n \exp(-in\theta)] \cos(k_m z) \tag{5}$$

and the corresponding eigenfrequencies are :

$$f_{mn} = \left[(2m-1)^2 \left(\frac{c}{4l}\right)^2 + n^2 \left(\frac{c}{\mathcal{P}}\right)^2 \right]^{1/2} \tag{6}$$

The lowest eigenfrequency corresponds to $m = 1$ and $n = 0$: $f_{10} = c/(4l)$. This eigenfrequency is that of the first (quarter wave) axial mode (1L). The next eigenfrequency pertains to the first azimuthal -first axial mode 1A1L: $f_{11} = [(c/4l)^2 + (c/\mathcal{P})^2]^{1/2}$. When the length l is large, the first term in this expression becomes small and this eigenfrequency tends to $c/\mathcal{P}$ which characterizes the first azimuthal mode. In the experiments carried out in MICCA2, i.e. premixed conditions with swirling injectors fitted with a cup as shown in Figure 5-center and in MICCA-Spray, combustion oscillations are essentially coupled by the 1L and by the 1A1L modes of the chamber. The 1A1L mode features the 1A azimuthal structure that is of central interest. In experiments carried out with MICCA3 in premixed conditions with matrix injectors as shown in Figure 5-right, the coupling involves the plenum through a 1A1L mode and the corresponding eigenfrequency takes a lower value because the sound velocity in the plenum is lower than in the chamber.

It was noted by a reviewer that the open end used in experimental facilities like MICCA does not quite represent the situation encountered in practical combustors where the chamber exhaust is formed by the turbine distributor which is generally choked. This imposes a choked nozzle boundary condition which may be approximated by an acoustically rigid wall condition sketched in Fig. 8(b). In this situation the system features purely azimuthal modes (1A,2A...) with eigenfrequencies $f_n = nc/\mathcal{P}$. This is less easy to reproduce in the laboratory because it requires operation under pressurized conditions. However, it is possible to approach this situation by augmenting the length of the combustor to reduce the axial contribution to the resonant frequency of the mixed mode (see Chapter 8 for a more in-depth discussion on azimuthal modes). For example the frequency of the 1A1L mode is only 11 % greater than the frequency of the 1A mode if the perimeter to length ratio is equal to 2. This explains why in many experiments carried out in MICCA the combustor has at least 0.5 m in length.

In the third configuration shown in Fig. 8(c) the sidewalls have unequal heights. This was used by Worth and Dawson (2013a); Worth and Dawson (2013b) to obtain unstable regimes of operation as their experiments using walls with equal heights did not give rise to unstable oscillations. Similarly many experiments at EM2C were carried out with unequal wall heights. The question about the effect of this arrangement and its influence on stability is not yet fully settled. It is possible that this configuration allows mixing

between the cool central stream of air and the burnt products which tends to reduce the speed of sound in the upper part of the annular system. This mighty be subsequently translated into a reduction in the eigenfrequencies corresponding to the acoustic modes in the system possibly shifting the resonant frequency in the range where the flame is sensitive to incoming perturbations. This issue is investigated in Chapter 8 where acoustic eigenmodes and eigenfrequencues are determined using a 3D Helmholtz solver.

Experiments with premixed swirl injection - MICCA2

The annular system MICCA is now employed to investigate instability issues and specifically those involving azimuthal chamber modes. The inner and outer tubes lengths are 200 and 400 mm respectively. The swirling injectors are equipped with 90° cups that are flush mounted in the chamber backplane. This system features a strong longitudinal combustion instability for an injector bulk velocity $u_b = 20\,\mathrm{m\,s^{-1}}$ and $\phi = 0.79$. This is characterized by an intense emission of sound. Figure 9(a) shows that the five microphones exhibit a strong sinusoidal signal at a frequency $f = 252\,\mathrm{Hz}$ and an amplitude $p' = 330\,\mathrm{Pa}$. A harmonic is present at a frequency $f = 504\,\mathrm{Hz}$ but with a significantly lower level (-25 dB). The pressure amplitude of the instability slowly varies in time in most cases between 280 Pa and 380 Pa. To extract the heat release rate oscillation pattern from the high-speed images, a dynamic mode decomposition (DMD) is used. This method introduced by Schmid (2010) relies on a large number of instantaneous images to extract a meaningful representation of the unsteady flow dynamics. It differs from the well-known proper orthogonal decomposition in that it is frequency selective. The camera records 12500 images per second corresponding to 49 images during one period of the instability. By processing 300 images at this sampling rate, one only has access to 6 periods. A value of about 20 periods would yield a better signal-to-noise ratio. This condition can be fulfilled by using only one image out of three in the calculation of the DMD modes. By processing 300 images, 18 periods are then considered with around 16 images per period. The DMD yields a frequency $f = 252\,\mathrm{Hz}$ which is close to that detected by the microphones. The DMD modes are presented in Figure 9(c)(e)(g)(i) which respectively pertain to the phases $\psi = 0$, $\psi = \pi/2$, $\psi = \pi$, and $\psi = 3\pi/2$. The phase $\psi = 0$ corresponds to the instant in the cycle where the maximum of heat release rate is reached. The flames are globally moving in phase and their motion is essentially that of a bulk oscillation. Some flames are desynchronized and two of them are even pulsating in phase opposition. The swirlers have been checked and no differences in the geometry have been observed. However, the flow dynamics downstream the swirlers is sensitive to the swirler geometries and even small differences in geometries can cause significant differences (Bourgouin et al. (2013)). Hydrodynamic instabilities in the plenum could also break the symmetry of the flow injection but their identification is not easy to perform. This dynamic mode decomposition also indicates that even if some flames are desynchronized, strong thermoacoustic instabilities can still occur in the chamber. The detuning imposed by these flames is not sufficiently effective to suppress the instability.

The study of azimuthal modes is more complicated because these modes are degenerate. An azimuthal mode can be interpreted as a superposition of clockwise and counterclockwise rotating components. In the results of Figure 9, the pressure amplitudes recorded by

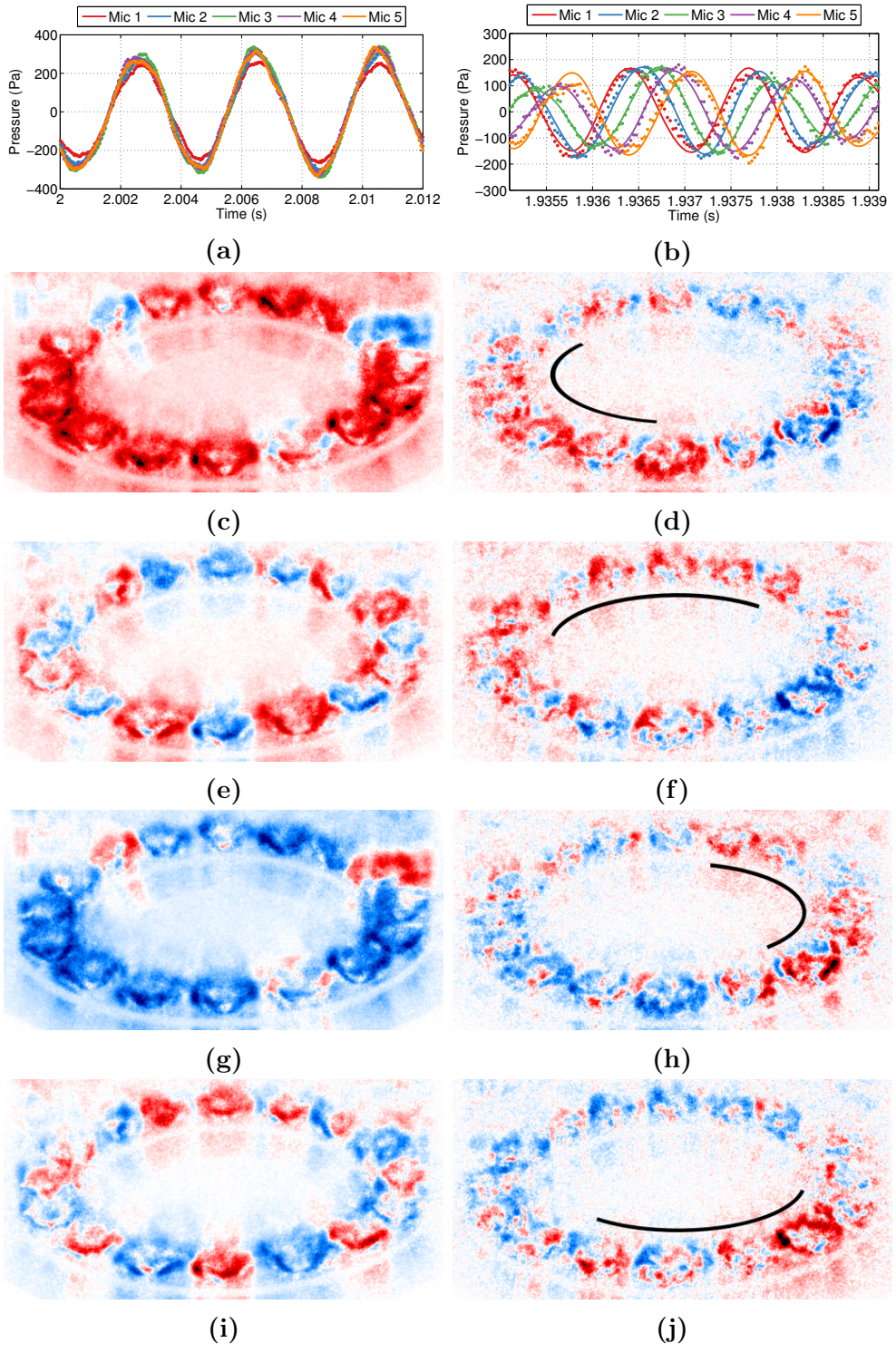

Figure 9: *Pressure signals recorded by microphones (a, longitudinal oscillation) and (b, azimuthal spinning oscillation). In (b) the continuous lines correspond to the reconstructed signals. (c), (e), (g), (i) : Dynamic mode decomposition (DMD) of 300 images recorded by the ICMOS camera for different phases for the longitudinal mode coupling at 252 Hz. (d),(f), (h), (j) : Dynamic mode decomposition (DMD) of 300 images recorded by the ICMOS camera for different phases for an azimuthal mode coupling at 792 Hz. The mode is essentially rotating* ($0.6 < s < 1.0$, *see Eq. 8). The black curves indicate regions where the heat release rate is maximum. Adapted from Bourgouin et al. (2013).*

the microphones are not constant in time and the modal structure is also varying. The clockwise and counterclockwise wave components are varying in time as well.

The clockwise and counterclockwise amplitudes may be deduced from the microphone signals. This is briefly explained in what follows. Near the backplane of the combustion chamber the acoustic pressure distribution only depends on the azimuthal angle θ and may be written as the sum of two waves:

$$p(\theta, t) = a \exp(i\theta - i\omega t) + b \exp(-i\theta - i\omega t) \tag{7}$$

Here a and b are respectively the complex amplitudes of the counterclockwise and clockwise rotating waves. When $b = 0$ the mode is counterclockwise, when $a = 0$, the mode is clockwise. When $|a| = |b|$ the mode is standing. Otherwise, the mode is neither purely rotating nor standing. The nature of the mode may be characterized in terms of a spin ratio:

$$s = \frac{|a| - |b|}{|a| + |b|} \tag{8}$$

The spin ratio s is such that $s = -1$, $s = 0$ and $s = 1$ respectively correspond to clockwise rotating, standing and counterclockwise rotating modes.

The pressure amplitudes of the five microphones are similar and there is a phase shift of about $\pi/8$ between each microphone in Figure 9(b). The signals recorded by the microphones suggest that the mode is rotating clockwise. This is confirmed by the determination of the spin ratio which varies between $-1 < s < -0.6$ with a mean spin ratio $\bar{s} = -0.8$. As a result, the mode is essentially rotating in the clockwise direction. The DMD represented in Figure 9(d)(f)(h)(j) also indicates a clockwise rotating motion which is consistent with the microphones signals. It is interesting to note that the DMD applied to a relatively short sequence reliably reconstructs standing and rotating modes. The azimuthal coupling described previously takes place at a relatively high frequency of 792 Hz corresponding to the 1A1L mode of the chamber. One may then ask whether the swirling flames established in the system are sufficiently receptive to perturbations in this frequency range. Swirling flames are generally sensitive to low frequency perturbations. However the frequency extent of this range scales like the exhaust velocity and like the inverse of a typical flame dimension. The gain of the FDF may still take large values at Strouhal numbers of the order of one. For an exhaust velocity of 40 m/s and a typical flame size of about 4 cm, the sensitive range of frequencies will reach 1 kHz and which includes the resonance frequency of the 1A1L mode. This is confirmed by measurements of the FDF in the single sector set up which indicate that the gain takes sizable values in a range extending to 850 Hz. In addition to this, the occurence of instability will also require conditions on the phase of heat release with respect to the pressure perturbation. The analysis of the two modes identified previously is carried out in further detail in Bourgouin et al. (2013); Bourgouin et al. (2015a); Bourgouin et al. (2015b).

Experiments with premixed swirl injection - Cambridge/NTNU annular combustor

The data gathered by Worth and Dawson (2013b) using the set up shown in Fig. 4 also features some interesting rotating mode patterns. These are obtained by high speed imaging with a miror set at 45° from the combustor axis allowing a direct view of the annular flame arrangement. The camera operates at 14400 fps and detects OH* emission from the flames allowing a suitable sampling of oscillations taking place at a frequency $f \simeq 1700$ Hz which corresponds to a 1A1L mode. The resonant coupling takes place at a frequency that is about double that found in MICCA because the diameter of the system is about half that of MICCA. The circumferential spinning mode displayed in Fig. 10 rotates in the counter-clockwise direction.

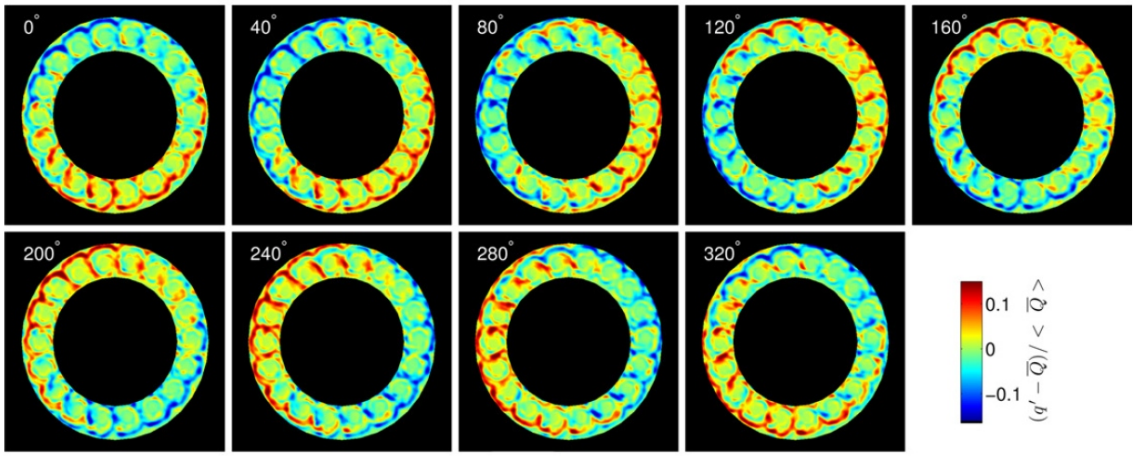

Figure 10: *Circumferential mode spinning in the counter-clockwise direction. OH* emission is detected by a camera operating at 14400 fps. The fluctuating light intensisty reflecting the heat release rate fluctutations is phase averaged. The patterns correspond to nine phases in a cycle. The system is fed with a mixture of air and ethylene at an equivalence ratio* $\phi = 0.85$*. Spacing between successive injectors* $S/D = 1.56$*. Reproduced from Worth and Dawson (2013b).*

Studies carried out in various configurations as well as theoretical investigations indicate that azimuthal coupling modes in turbulent annular systems vary with time, leading to intermittent switching between predominantly spinning or standing states with changes in orientation of the modes Noiray et al. (2011); Worth and Dawson (2013b); Ghirardo and Juniper (2013). Using loudspeakers, it was shown by Worth et al. (2017b) and by Nygård et al. (2019) that the modes could be controlled easing the analysis of the combustion dynamics during clock wise spinning (CW, $s = -1$), anti-clockwise (ACW, $s = 1$) or standing azimuthal modes ($s = 0$). These studies were used to infer the importance of local swirl direction and the role of the separation distance between the injectors on the local flame structure and its response to the flow perturbations when coupled to azimuthal modes. Figure 11 reproduced from Nygård et al. (2019) is an example where CW, ACW and standing modes could be triggered for the same operating conditions by forcing the system at $f_0 = 1690$ Hz.

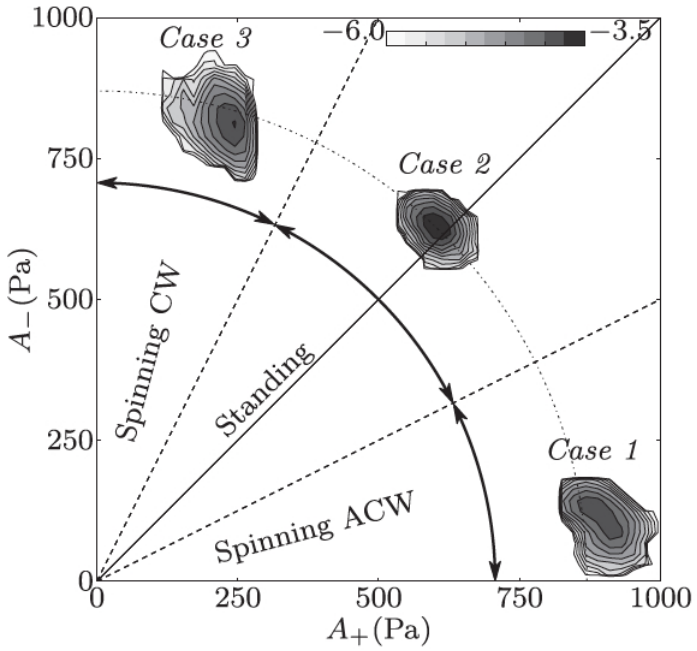

Figure 11: *Joint PDF of the azimuthal wave amplitudes A_+ and A_- respectively corresponding to a and b in Eq. 7 for three different cases, all using a forcing frequency $f_0 = 1690\,\mathrm{Hz}$. Dashed lines indicate $s = \pm 1/3$ and the solid line corresponds to $s = 0$. Case 1: $s = 0.9$. Case 2: $s = 0.0$. Case 3: $s = -0.6$. Reproduced from Nygård et al. (2019).*

Experiments with premixed matrix injectors - MICCA3

The swirling injectors induce a complex flow pattern in the annular combustor. It is then natural to try to reduce the complexity of the flow and for that replace the swirling units by matrix injectors establishing multiple conical flames and operating in a laminar regime. This configuration allows investigations of azimuthal coupling in the absence of swirl and turbulent fluctuations. In this new configuration it has been possible to examine stable limit cycles corresponding to a standing mode or to a rotating mode. As mentioned earlier, this simplicity allowed several new phenomena to be found. The "slanted" mode, combination of an azimuthal plenum acoustic mode and a longitudinal chamber mode, was identified by Bourgouin et al. (2015a). It was also found that in a certain region of the domain of operation, designated as the *"dual mode"* region, the two types of modes could occur for the same operating conditions (Prieur et al. (2017a)).

In that special region the nature of the oscillation depends on the path taken to reach the operating point (u_b , ϕ). If the equivalence ratio ϕ is increased, with the same air mass flow rate, from lean conditions to the target value, a rotating mode is obtained. If ϕ is decreasedfrom rich conditions, a standing mode is manifested at the target conditions. The rotating and standing modes do not switch from one to the other but instead when a mode arises, it is locked on. This experiment indicates that the nature of the mode (standing or spinning) is not only defined by the geometry or by some characteristics of the unstable regime but is also influenced by the history or more precisely by the path taken to reach the nominal operating point. Finally, it is worth mentioning that

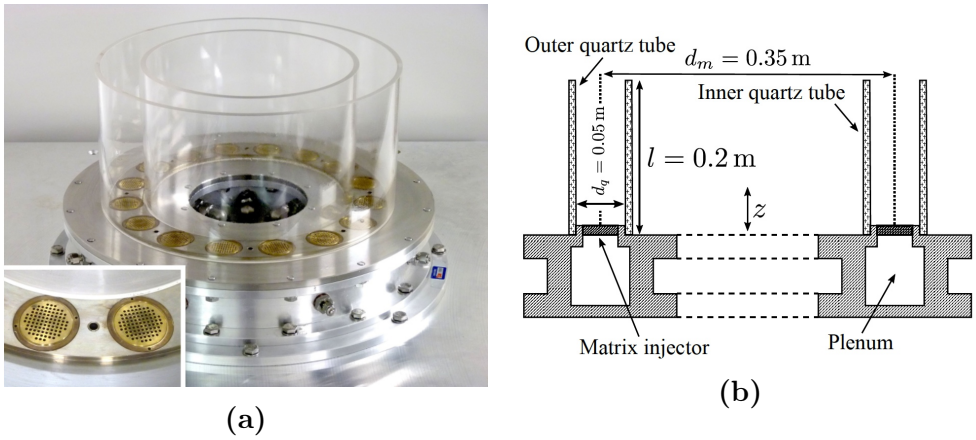

Figure 12: *(a) Photograph of the MICCA3 chamber equipped with matrix injectors. The injectors comprise 89 holes of 2 mm diameter spaced by 3 mm. The thickness of the injector plate is fixed to 6mm. The chamber formed by two cylindrical quartz tubes provides optical access to the flame region. (b) Lateral view of MICCA3. The length of the inner and outer quartz tubes are equal to $l = 0.2$ m, $d_q = 0.05$ m is the gap between the two quartz tubes and $d_m = 0.35$ m is the mean chamber diameter. Adapted from Prieur et al. (2017a).*

MICCA3 is the only annular configuration for which accurate prediction of instabilities by theoretical simplified models are found (Bourgouin et al. (2015b); Laera et al. (2017); Laera et al. (2017); Yang and Morgans (2018); Moeck et al. (2019)).

Combustion dynamics of spray swirled flames

This topic is reviewed by Lieuwen and Yang (2005), Candel et al. (2014) and more recently by Poinsot (2017). In the field of swirling spray flames, experimental diagnostics are a challenge, especially when time resolution is required. Experiments, even well-conducted and instrumented (Bernier et al. (2004); Eckstein et al. (2006); de la Cruz García et al. (2009); Renaud et al. (2017)), do not give access to all necessary variables. Large eddy simulations can be used in high fidelity calculations of combustion instabilities in engine like configurations as demonstrated by Staffelbach et al. (2009); Tachibana et al. (2015).

In addition to the dynamic phenomenon observed in premixed swirl flames and discussed earlier, specific effects of two phase flows and in particular evaporation on combustion instabilities exist, and were studied early on in the field of rocket propulsion (Crocco (1951); Crocco (1952)). Crocco (1965) reviews early results on the subject with a particular attention given to the behavior of burning droplets in acoustic fields. In this configuration, a strong interdependence exists between the flow, the inertia of the droplets, evaporation and combustion. Combustion can essentially occur in two modes for isolated droplets, depending mainly on the relative velocity of the droplet and the surrounding gaseous flow: either as a spherical flame surrounding the droplet, or as a wake. This is a very defavorable configuration where a high dependency of the combustion regime on the flow velocity and its fluctuation may be a driving factor for combustion instabilities.

In practical applications of swirling spray flame, the combustor is generally optimized to avoid isolated droplet combustion, a combustion mode that is very defavorable for both pollutant emissions and operability. The aforementioned effect is thus rarely predominant. The time lag concept is a useful first level of analysis in order to study the effect of spray on combustion instabilities. Lee et al. (2005) showed the validity of this concept for combustion instabilities in spray flames by using a Nanomizer, a controllable atomizer, to actively modify the size distribution of liquid fuel droplets, thereby modifying the associated time delay and "slowly" controlling an unstable combustion system. Yu et al. (1998) were also able to achieve active control of a combustion instability in a spray flame, but using a less elegant strategy of varying the fuel injection depending on the phase of the thermoacoustic cycle.

The significance of the evaporation time delay on the overall flame response is reported by several authors: Tachibana et al. (2015), in their simulation of a spray flame at elevated pressure, Kitano et al. (2016), in their LES of a simpler backward-facing step and naturally, Lee et al. (2005). On the contrary, Bernier et al. (2004), who experimentally studied an atmospheric pressure, n-heptane fueled swirl burner, noted that in their system, evaporation should not be accounted for in the overall time delay as it occurs concurrently to convection. Eckstein et al. (2006), in his amospheric pressure, kerosene fueled rich-quench-lean burner, and Apeloig et al. (2015), who studied the multi-point spray injector of an aeronautical combustor, noted that flow modulation could lead to fluctuations in atomization properties, and concurrently, to fluctuations in evaporation time delays. The numerical results of Zhu et al. (2000) show a similar mechanism. Gajan et al. (2007) and Kim et al. (2012) studied the spray in aeronautical injectors submitted to acoustic forcing in cold flow conditions. They observe that this forcing does affect the atomization properties, and that the modulation creates a propagating wave of droplet density.

Combustion instabilities of spray swirled flames in annular systems

Liquid fuel injection adds further complexity to experimentation and modeling but is nevertheless interesting because it comes closer to practical situations like those found in aero-engines where kerosene is introduced in the combustor as a spray of droplets. Publication presenting detailed results of combustion instabilities coupled by azimuthal acoustic modes in annular, liquid fuel combustors are scarce. The numerical simulation team of CERFACS was able to perform and analyze a full chamber compressible LES simulation of a thermoacoustic oscillation in an helicopter combustor (Staffelbach et al. (2009); Wolf et al. (2012); Wolf et al. (2012)). The oscillatory behavior of the system is successfully retrieved.

The annular combustor MICCA was fitted with a set of swirl spray injectors shown in Figure 13 in a configuration designated as MICCA-Spray as part of the thesis of Kevin Prieur. This setup is unique in the world due to its size, flexibility and optical access. This has allowed an examination of combustion instabilities coupled by azimuthal modes.

The system is sufficiently flexible to allow investigations under fully premixed gaseous, liquid heptane and liquid dodecane injection. The single sector test bed (SICCA) was also modified to accommodate liquid injection.

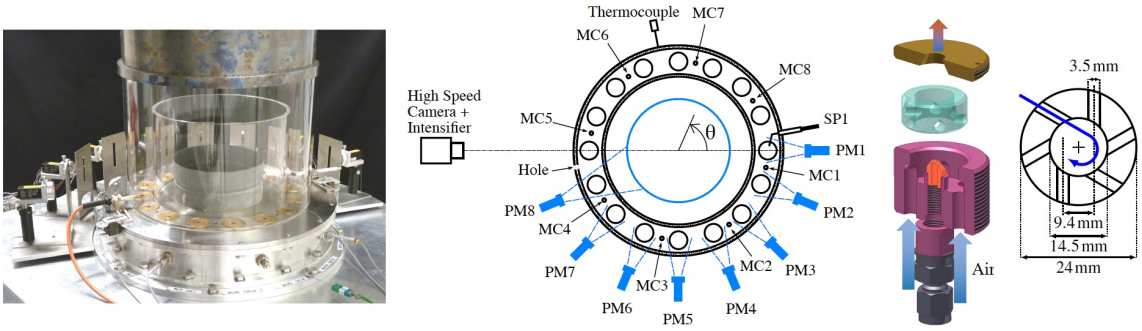

Figure 13: *From left to right: (1) Photograph of the MICCA-Spray test rig. (2) Schematic view of the chamber backplane showing the locations of the camera, thermocouple, chamber microphones MCx, plenum microphones MPx, photomultipliers PMx and of spark plug SP1. Dashed lines show the field of view of the photomultipliers. (3) Exploded view of the injector and its components. In purple, the main body, in orange the liquid fuel atomizer, in translucide teal the tangential air swirler and in gold the injector outlet, which is flush with the chamber backplane. (4) Schematic view of the swirler seen from above indicating the main dimensions of this component.*

Among the many experiments carried out in MICCA-Spray, those yielding very large combustion instability levels coupled to the 1A1L mode of the annular cavity have some unusual consequences. In many cases the oscillations take the form of long bursts with a repetition rate of approximately a few hertz. During these bursts, the acoustic pressure fluctuation in the chamber can reach up to 6% of the ambient pressure in the chamber corresponding to a peak level of approximately 6000 Pa. The type of instability, that arises under these circumstances is investigated in detail in Prieur et al. (2018). By determining the spin ratio one observes that this process occurs predominantly when the acoustic coupling mode is of the standing type.

Specific attention is given to the flame behavior at the nodal positions during the standing mode. Flames located in the neighborhood of this line are submitted to an intense transverse motion. When the pressure oscillation takes large values, the transverse velocity reaches a critical value which displaces the flow and disrupts the recirculation regions that stabilize the flame (Prieur et al. (2018)). The resulting flame dynamics is illustrated in Figures 14 and 15.

Thesis objectives and contents

The literature review presented in the previous pages is focused on some key issues and on results obtained in annular combustors, but does not cover all topics discussed in this thesis. For this reason, each chapter contains further reviews of the literature pertaining

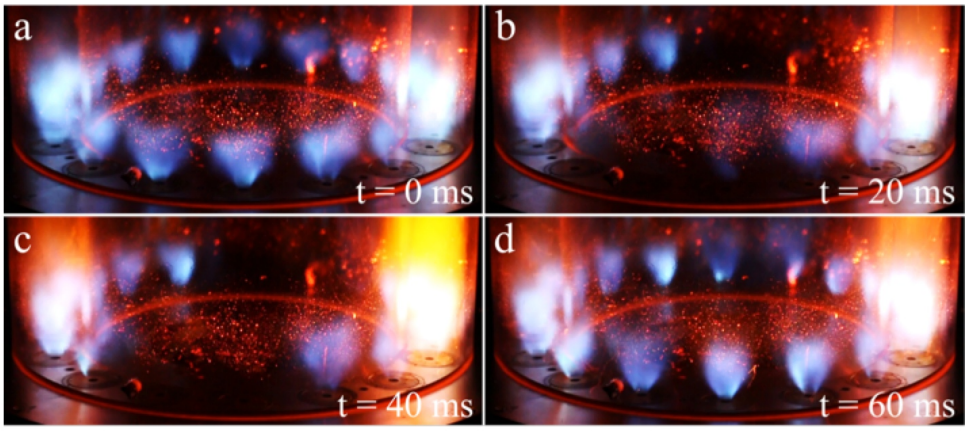

Figure 14: *True-color photographs of the annular chamber when six flames are blown-off for about 20 ms.* $\phi = 0.85, \mathcal{W} = 111\,kW$.

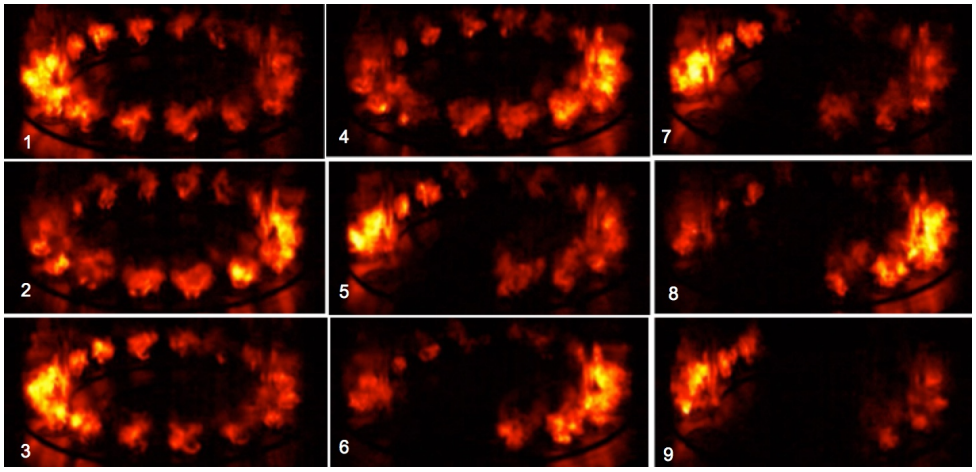

Figure 15: *Sequences of 9 images illustrating the partial flame blow off in MICCA-Spray in the presence of an azimuthal standing mode of high amplitude (4000 Pa peak).* $\phi = 0.85, \mathcal{W} = 111\,kW$

to the topic at hand.

Nevertheless, the previous review indicates that some fundamental issues of flame dynamics in aero-engine combustor are not yet fully understood. It is known in particular that injectors are a key component of combustors used in gas turbines and aero-engines. These units are selected for their steady state characteristics in terms of atomization, and head loss and in terms of flame anchoring, soot formation, pollutant emissions. However injectors also determine to some extent the dynamical properties of the combustor. Much of the present work is concerned with the swirler and injector influence with respect to combustion dynamics. This involves in particular variations in swirler design and investigations of their dynamical properties and of those of single sector and annular configurations featuring multiple injection units. Two questions are addressed in this work :

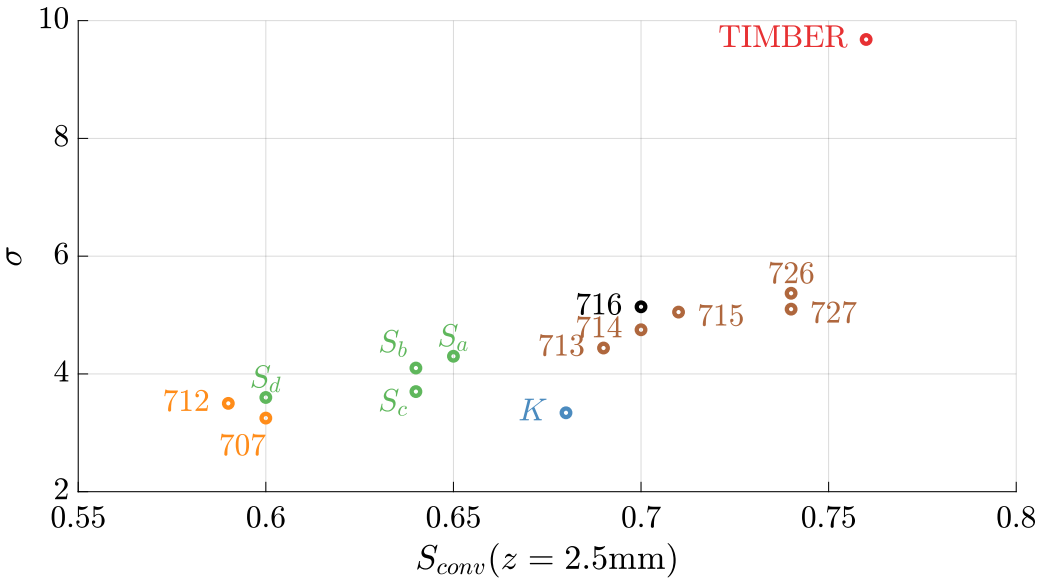

Figure 3.3: *Graphical representation for all swirlers of the swirl number $S_{conv}(x = 2.5\,\text{mm}$ measured at an air mass flow rate of $\dot{m} = 2.6\,\text{g}\,\text{s}^{-1}$ against the head loss coefficient σ. (repeated from page 91)*

- How should one characterize injectors used to establish swirled spray flames?
- How should one investigate their dynamics and the coupling between several injectors in an aero-engine type annular combustor to deal with the challenges of combustor operability?

To this end, several versions of the SICCA-Spray injector are used throughout this thesis. These injectors are characterized in detail in Chapter 3, and Fig. 3.3 is repeated here from this chapter to briefly introduce these different injection system. Forteen injectors have been qualified and characterized in SICCA-Spray, grouped in 6 generations (shown by the colors in Fig. 3.3). These injection systems span a wide range of swirl number and head loss coefficient. This variety of injection characteristics is employed in the present thesis to conduct parametric studies on these important design characteristics. In this large group it is worth distinguishing three of these injector designs and give further information on their use and limitations:

(G1): "TIMBER" swirler: this first generation of injector is introduced in Prieur et al. (2016) and Lancien et al. (2016). It is used in many studies and in particular in those concerned with ignition and blow out. However, MICCA-Spray equipped with this injection system is rather thermoacoustically stable.

(G2): K swirler: designed during the thesis of Kevin Prieur, and first introduced in Prieur et al. (2018), this injection system is unstable in MICCA-Spray. It was decided to phase-out this injection system due to manufacturing difficulties.

(G3): 716 swirler: this system replaces the K swirler. Featuring a level of swirl similar to that unit, and higher than those of 707 and 712, this injection system exhibits strong combustion instabilities in MICCA-Spray. Its design is one of the major result of

this thesis.

Throughout this work, numerical simulations will be carried out in combination with experiments and modeling to better understand mechanisms that drive instabilities or couple the flame dynamics to the acoustic modes. Contrary to what is commonly found, it was decided to avoid separating experimental and numerical investigations. These are combined in thematic chapters that are each dealing with a physical mechanism.

The manuscript is subdivided into five main parts.

In the first part, the experimental setup MICCA-Spray, and its corresponding single sector rig are presented. The iterative design loop introduced earlier is detailed with a particular emphasis on the representativity of SICCA-Spray. LES is used in the present thesis to investigate flame and flow dynamics. The numerical setups and models are presented. The experimental diagnostic tools are introduced, with a particular focus on flame chemiluminescence detection. An entire chapter and a set of experiments are dedicated to establishing the relationship between light emission from excited radicals and heat release rate. This issue has received considerable attention in the past but has not been extensively investigated in the case of spray flames. The objective is to see to what extent flame chemiluminescence can be an indicator of heat release rate in such flames. It is found in particular that light emission from excited radicals is not quite proportional to the flame heat release rate, in both a premixed and a spray flame. A calibration strategy, based on systematic measurements, is suggested.

The second part focuses on the steady state characterization of injectors and flames in the single sector system SICCA-Spray. The different injection systems are systematically characterized in Chapter 3. The setup for Large Eddy Simulations is also validated, and subsequently used to examine the effect of the confinement on the flow field. Several effects linked with the spray are investigated in some details: the azimuthal "patternation" (spray distribution) and the impact of the swirler thereon is examined. It is also found that the droplet velocity distribution is bimodal a feature that is well retrieved and explained numerically as being due to the liquid film forming on the conical section of the injector. Chapter 4 is concerned with the definition of the swirl number, based on a high fidelity Large Eddy Simulation of a very generic swirling injector. It is found that the commonly used simplifications employed to compute the swirl number may yield inaccurate estimates of the original formulation proposed by Chigier and Beér (1964). In practice, calculating this original swirl number from experimental data is difficult to implement. It is alternatively proposed to use a "conventional" formulation that is weakly linked to the original definition but is much easier to determine from experimental velocity profiles measured in the near vicinity of the injector outlet. This provides a measure of the rotation rate and may be used to categorize injection units.

The dynamics of the single sector system is examined in the context of thermoacoustic oscillations in Part III. Studies carried out on older generations of swirlers (G1 and G2) are first presented. In Chapter 5, high speed flame tomography using tin dioxide

particles, a technique that fell out of favor, is given a new spin. The technique itself is first briefly characterized by determining the flame isotherm that can be identified by the sublimation of these particles. Taking advantage of this technique to accomodate very high frame rate (40 kHz), it is used to investigate the dynamics of the precessing vortex core (PVC) formed in the swirling flow. The PVC appears as a double helix vortex precessing at 3.75 kHz. In steady flame conditions, it is found that during intermittent flame flashbacks, the PVC changes shape, switching successively to a single helix structures and then to a triple helix structure for a few milliseconds. When a strong combustion oscillation arises, it is also found that the PVC is strongly affected and that it is modulated, both in frequency and amplitude. In Chapter 6, a self-sustained combustion instability in SICCA-Spray is analyzed using LES in combination with Dynamic Mode Decomposition (DMD). The dynamics of the spray and the flame are compared to experimental data to validate the simulations. LES results are then post-processed using a 1D-1T representation designed to extract information on the propagation of perturbations in the flame. The convective nature of the motion of the flow, and its transition to acoustics near the top of the flame is demonstrated. It is also observed that several types of perturbation are combined to yield the dynamics of the flame: injector and liquid film dynamics, swirl number fluctuations, equivalence ratio fluctuations. One major conclusion is that, from a time delay standpoint, evaporation occurs simultaneously with convection of the droplets, and should not be accounted for separately. The impact of head loss on combustion instabilities in SICCA-Spray is then examined using a set of third generation (G3) 3D-printed injectors in Chapter 7. This set of injectors is designed to have identical velocity profiles, but different head loss levels to isolate the impact of the latter parameter. It is found that the stability map of SICCA-Spray equipped with this set of injectors is complex. In particular, two types of limit cycle oscillations can be observed depending on the injection system and the operating conditions. It is suggested that these two types of oscillations are associated with two different eigenmodes.

Coupling by azimuthal acoustic modes in the MICCA-Spray combustor is discussed in Part IV. It is useful to start by characterizing the structure of acoustic modes in annular systems. Following the brief discussion on this topic earlier in the present introduction, non-ideal situations actually encountered in MICCA-Spray, such as inhomogeneous temperature fields and walls of unequal lengths, are discussed. The acoustic damping in the combustor is then measured using time series of chemiluminescence and acoustic pressure during operation. In Chapter 9, experimental results of high amplitude flame oscillations coupled by a standing azimuthal acoustic mode are examined. The spatial structure of the acoustic field is reconstructed using a new high order method, and it is shown that during high amplitude oscillation, the modal structure is distorted. Furthermore, when the oscillation reaches a level of approximately 2 kPa peak, flames located near the pressure node are blown-off. The blow-off limit is quantified in terms of transverse acoustic velocity fluctuations.

Finally, Part V contains results of experiments pertaining to operability. These concern dynamical processes outside the domain of combustion instability. Issues in ignition are examined first by reviewing results obtained on the light-round of annular combustors.

One then examines the flame transient during ignition whereby the flame penetrates the injection unit because of an excursion in chamber pressure before lift-off and final stabilization at a distance from the injector outlet. Finally, in Chapter 11, a study where SICCA-Spray is equipped with a plasma assisted combustion apparatus is presented. Low frequency combustion disturbances are also observed close to the lean blow-out limit, and it is shown that the flame becomes more robust to these oscillations when the plasma assisted apparatus is operating. It is then possible to extend the lean blow-out limit, in particular when liquid fuels are used.

Part I

Experimental methods and numerical set-up

Chapter 1

Experimental systems, diagnostics and numerical set-up

The MICCA-Spray and SICCA-Spray experimental test rigs are described in this chapter. These set ups complement each other. MICCA-Spray is used to investigate processes that require a fully annular configuration with multiple injection units. SICCA-Spray corresponds to a single segment and comprises one injector placed in a cylindrical chamber. This configuration allows detailed investigations of the flame dynamics, analysis of the flow and structures and measurements of the flame describing function. The target configuration is always the annular combustor. In this chapter, the experimental diagnostic tools used in the test rigs are presented. The different setups and models for Large Eddy Simulations are also introduced.

Contents

In stationnary gas turbines, and jet and helicopter power plants, a central shaft traverses the engine. This is the major design constraint that dictates the use of annular combustors in such systems. Some early designs featured a can-annular combustion chamber, but this architecture was quickly phased out in aeronautical applications due to its higher weight and structural complexity. Several injectors are mounted in the combustor, with the aim of delivering a mixture of air and fuel featuring an azimuthal distribution that is as axisymmetric as possible in order to maximize the operational life of downstream turbine components. Many test rigs are dedicated to the study of steady and dynamic combustion for aero-engines, both in an academic environment (large optical access, modular design, Bernier et al. (2004); Eckstein et al. (2006); de la Cruz García et al. (2009); Malbois et al. (2019) for example) and in a semi-industrial environment (Konrad et al. (1998); Fanaca et al. (2010); Lecourt et al. (2011)), but they are in most cases equipped with a single injector. However, in practical combustors, injectors are found in close proximity to one another. Flames may interact with their neighbors (Durox et al. (2016); Smith et al. (2018); Lee et al. (2019); Worth and Dawson (2019)), and coupling of all flames within the chamber can also occur, mostly due to azimuthal acoustic modes. MICCA-Spray has some unique features that distinguishes this set up from other laboratory scale test rigs that have been developed to study azimutal coupling leading to combustion instabilities or light-round ignition processes. In what follows, MICCA-Spray is described in some details with a particular focus on its distinguishing features. SICCA-Spray, its complementary single sector rig, is also introduced. In Section 1.1.3, the modular injector design common to both rigs is presented. The experimental diagnostic tools are discussed in Section 1.2. In Section 1.3, a synthetic overview of the SICCA-Spray and MICCA-Spray experimental setups used in each chapter of the thesis is presented. Finally, Section 1.4 presents the setup used for LES simulations of SICCA-Spray.

1.1 MICCA-Spray and SICCA-Spray: a complementary set of experimental rigs

1.1.1 MICCA-Spray: an annular combustor representative of an aero-engine

MICCA-Spray is an annular laboratory scale combustor operated at atmospheric ambient pressure. It is designed to be representative of the combustor of a small helicopter engine while remaining simple enough to operate in a laboratory setting. Equipped with sixteen swirl spray injectors described in detail in Section 1.1.3, it is operated with either liquid heptane, liquid dodecane or a premixture of gaseous propane and air. As shown in Fig. 1.1, the system comprises a plenum, which is fed with air (or with a propane-air

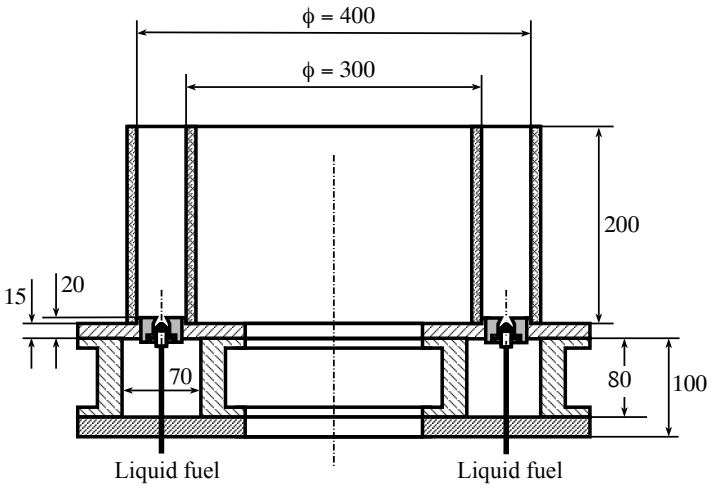

Figure 1.1: *Schematic cross-section of the MICCA-Spray combustor with dimensions in* mm. *The configuration corresponds to the photograph of Fig. 1.2(d).*

mixture) by eight regularly spaced tubes connected to two Bronkhorst EL-flow thermal mass-flow controllers with a relative accuracy better than 1%. Liquid fuel is supplied to the injectors using a pump controlled by a Bronkhorst CoriFlow mass-flow controller, with a relative accuracy better than 0.5%. The maximum fuel flow rate is currently $10\,\mathrm{kg\,h^{-1}}$, corresponding to a thermal power of 125 kW. The fuel is however not equally distributed between the different injectors due to small differences in the pressure characteristics of the fuel atomizers. The plenum is also annular and has a cross-section of 80 mm by 70 mm. The backplane of the combustor and the plenum are water-cooled. The combustion chamber itself is formed by two concentric tubes, forming an annulus with a mean diameter of 350 mm and a width of 50 mm. It naturally follows that the injectors are spaced by 69 mm. MICCA-Spray is unique: it has a large number of injectors and a large size, making it better suited to study combustion instabilities coupled by azimuthal modes as the frequency of these modes decreases with increasing combustor diameters. Since flames have a low-pass behavior, the larger size makes the system more likely to be acoustically unstable. As can be seen in Fig. 1.2, the bottom of the confinement is made of quartz for optical access. Steel prolongating tubes can be added to attain different chamber lengths as required to obtain unstable operating conditions. MICCA-Spray is ignited using a spark plug which creates a 25 mJ discharge at a repetition rate of 100 Hz in the periphery of an injector. To accommodate this plug, two 5 mm holes are drilled on opposite sides of the external quartz tube, 15 mm above the backplane of the combustor.

1.1.2 SICCA-Spray: a complementary single sector system

1.1.2.1 On the need for a single sector rig

Although MICCA-Spray has many positive features it also has some experimental limitations:

- Due to its large size and number of injectors, iterations on injector design are long

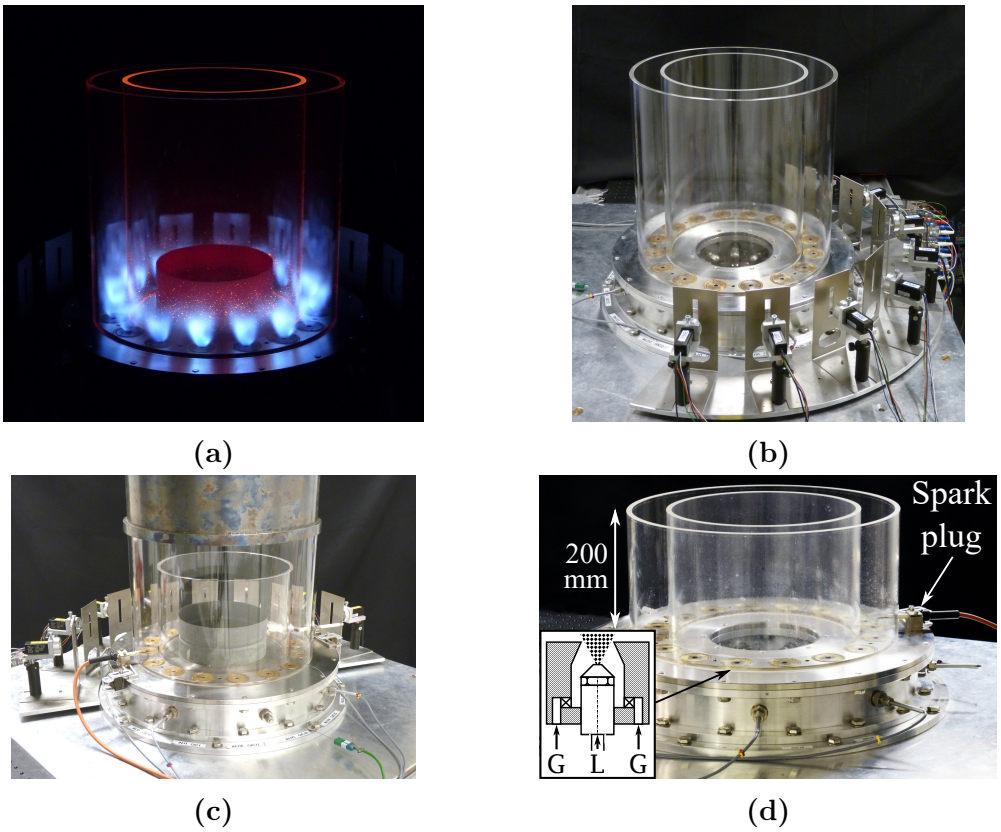

Figure 1.2: *Photographs of MICCA-Spray: (a) True color image of MICCA-Spray in operation; (b) MICCA-Spray with two equal-length* 400 mm *confinement walls and no spark plugs (Chapter 8); (c) MICCA-Spray setup with a* 700 mm *long outer confinement and* 200 mm *long inner confinement (Chapters 8-9); (d) MICCA-Spray configuration for ignition studies.*

and costly;
- Complex flame-flame interactions, and reduced control on acoustic coupling;
- Difficult implementation of laser diagnostics because of the annular shape and low optical quality of the quartz tube confinement;
- In its current configuration, MICCA-Spray cannot be acoustically forced.

It is then reasonable to operate MICCA-Spray in conjunction with the single sector rig SICCA-Spray and to make use of the design loop shown in Fig. 6. The underlying assumption is that for an azimuthal acoustic mode, the flames located near the acoustic pressure antinode constitute the main drivers of the instability and that in turn the dynamics of a single flame forced by longitudinal acoustic waves will give insights on the flame dynamics and on the likelyhood of combustion instabilities in the annular combustor MICCA-Spray.

The layout of this research closely follows the injector design loop for MICCA-Spray:
1. An injection system is first characterized in steady conditions in SICCA-Spray. Its swirl number, head loss and spray are measured, flame images are captured.
2. Its response to acoustic perturbations is examined in SICCA-Spray by either acoustic forcing and measurement of the Flame Describing Function, or by using a con-

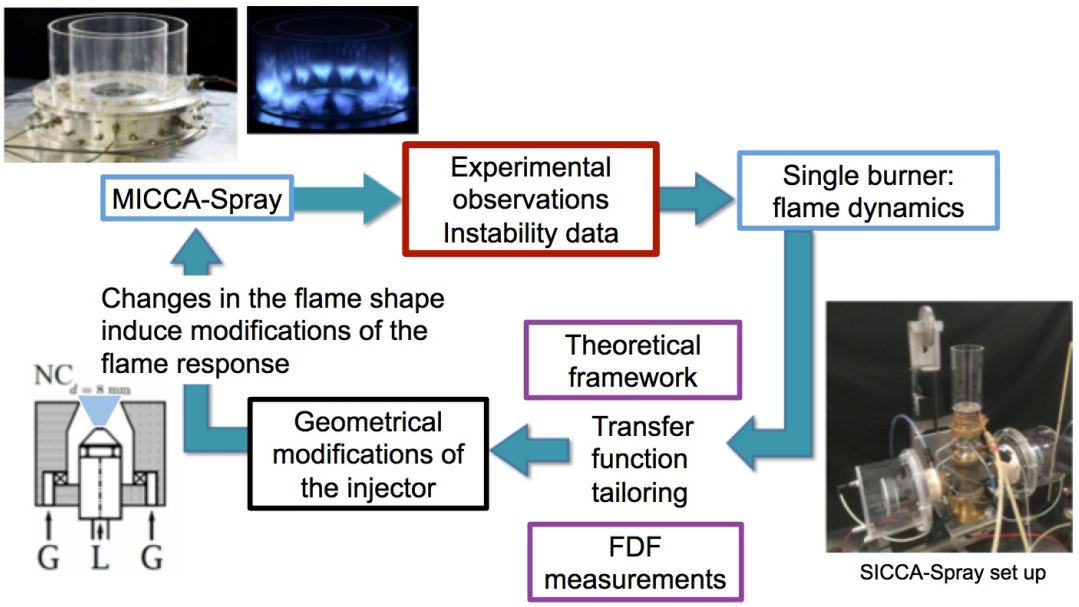

Figure 6: *Experimental methodology combining single sector measurements in the SICCA setup and annular combustor testing on MICCA. (repeated from page 11)*

figuration in which SICCA-Spray features self-sustained instabilities.

3. If it is deemed likely that this injector will be unstable in MICCA-Spray, a small series of injectors is manufactured for the annular rig, and tests are performed.
4. MICCA-Spray results are analyzed by making use of knowledge of the FDFs measured in SICCA-Spray.

1.1.2.2 SICCA-Spray: a versatile combustor

The SICCA-Spray set up consists in three main elements: a plenum, a single spray swirled injector from the MICCA-Spray test rig, and a cylindrical combustion chamber. The fuel and air flow rates are handled in a similar manner to MICCA-Spray, with Bronkhorst mass flow controllers (relative accuracy of 1%). Two versions of the plenum exist: the one shown in Fig. 1.4 has the form of a cross with two driver units (Monacor SP108-Pro) mounted in compartments to handle to pressure loss of the injector. The loudspeakers are driven by a standard audio amplifier and are used to acoustically modulate the flame or left passive for steady state or self-sustained instability studies (Chapters 4 - 5, 7, 10 and 11). A small cylindrical section near the top, located on the upstream side of the swirling injector, is used for acoustic measurements by microphones and a hot wire. The second plenum is a simple tube that replaces the loudspeakers cross. It is only used in Chapter 6. As in MICCA-Spray, the injector is water-cooled. The combustion chamber of SICCA-Spray is cylindrical. It is mostly made of quartz so that flame chemiluminescence and laser diagnostics can be implemented. A small section at the bottom of the combustion chamber is machined out of brass, so that a water-cooled waveguide for a microphone can be mounted near the backplane. If optical access to the base of the flame is required, this brass piece can be removed. The total length of the combustor can be easily varied

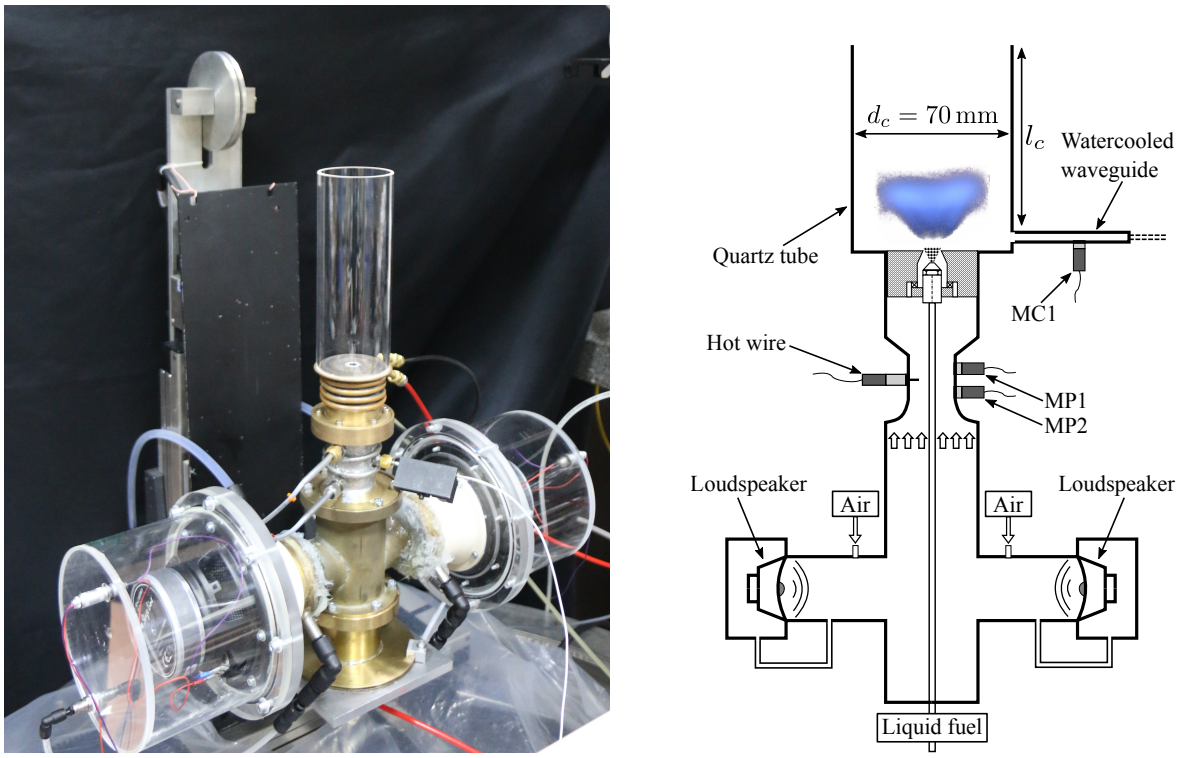

Figure 1.4: *SICCA-Spray: left, photography of the test rig. Right: schematic of the system.*

by changing the quartz tube or adding small metallic prolongating tubes. Although the diameter of the combustion chamber can also be easily varied, the confinement used in this thesis has an internal diameter of 69 mm (except in Chapter 4 where the confinement has a diameter of 50 mm). The quartz tube is 5 mm thick. SICCA-Spray is mounted on a 3-component displacement system, an important feature for point measurements such as Phase Doppler Anemometry.

1.1.2.3 Limitations of SICCA-Spray

The aim of SICCA-Spray is to be representative of the flame and flame dynamics that are found in MICCA-Spray. Whether this is the case or not can be decomposed in two main questions:

- Is the flame and the flow found in SICCA-Spray representative of what is found in MICCA-Spray?
- Is the response of the flame and the flow to acoustic perturbation representative of what is found in MICCA-Spray?

These questions are not yet fully settled but some partial answers may be deduced from experiments carried out during the present investigation, and from the literature.

For a given swirling injector design, it is known that the swirling flow will depend on the confinement and outlet boundary conditions. In the subcritical/supercritical categorization of swirling flows proposed by Escudier and Keller (1985), the MICCA-Spray injector belongs to the subcritical category. The near injector flow field can thus be affected by

outlet boundary conditions as shown in non-reactive conditions by Escudier and Keller (1985); Altgeld et al. (1983) and also in reactive conditions by Li and Gutmark (2005) and Terhaar et al. (2012). It is also known that the outlet affects the Precessing Vortex Core that is characteristic of swirling flows (Mason et al. (2019)). Detailed measurements on the impact of confinement on swirling jets are reported by Fu et al. (2005), showing a dramatic transition between a so-called "wall-bounded" regime and a "free jet" regime. Fanaca et al. (2010) considered, in addition to the results of Fu et al. (2005), effects of the azimuthal flow induced in annular systems on the transition between these two regimes. Their theory and correlation were used to determine the optimal confinement diameter of 69 mm for SICCA-Spray experiments. A second major difference between MICCA-Spray and SICCA-Spray pertains to the thermal boundary conditions that prevail in the two experimental rigs. Some items presented in Chapters 3 and 2 indicate that there are differences in the non-reactive flow fields corresponding to confined and unconfined SICCA-Spray configurations, a subject that is discussed in further details in these chapters.

Concerning the representativity of the flame response to incident perturbations in SICCA-Spray, there are two additional concerns.

- In SICCA-Spray, the flame is only submitted to longitudinal modulations. Flames in MICCA-Spray are also perturbed by transverse acoustic velocity fluctuations during oscillations coupled by azimuthal acoustic modes. In a first approach, the flame located near the pressure antinodes contribute most to the thermoacoustic energy balance and are not submitted to high levels of transverse fluctuations. Flames located near pressure nodes and velocity antinodes contribute the least. This indicates that in a first approach, a rig such as SICCA-Spray will give valuable insights into the dynamics of the annular system. There are however significant differences in the manner in which flames near the velocity antinode respond, such as asymetries induced by a helical perturbation as shown by Lespinasse et al. (2013) for laminar premixed "V" flames and by Caceres (2019) for swirling spray flames similar to those studied in the present thesis. This subject is reviewed in detail by O'Connor et al. (2015). O'Connor et al. (2013) used the annular combustor of Worth and Dawson (2013b) and the transversally forced facility at GeorgiaTech to compare the dynamics of flames located near the pressure node in the two rigs. Some discrepancies in the flame shape between these rigs exist, the flame having a "V" shape in one case and "M" in another, but differences can likely be attributed to different thermal conditions, a major difficulty in such long transversally forced rigs. The authors thus conclude that linear systems with transverse acoustic forcing can reproduce the dynamics of flames near the pressure node in annular combustors. The TACC facility at CORIA (Caceres (2019); Baillot et al. (2021)) is currently being adapted to accommodate MICCA-Spray injectors and perform such studies as part of the FASMIC ANR project.
- Acoustic forcing in SICCA-Spray is performed from the plenum. In experiments by Gaudron et al. (2019) on the NoiseDyn burner at EM2C laboratory, the Flame Transfer Function obtained by upstream and downstream forcing are compared. They show that the methods are equivalent if the reference of the FTF is the re-

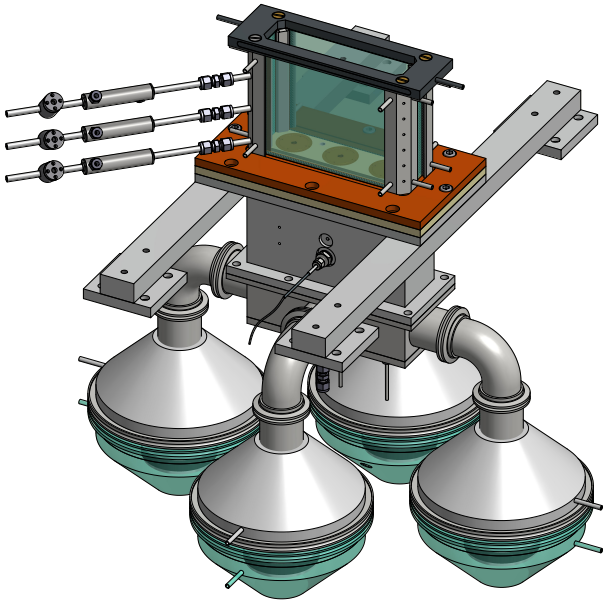

Figure 1.5: *3D rendering of the future linear, 3 injector combustion test rig TICCA-Spray.*

constructed acoustic velocity in the fresh gases upstream of the flame. The injector head loss of the MICCA-Spray injector is however an order of magnitude larger than that of the NoiseDyn burner, and the extensibility of the work of Gaudron et al. (2019) to the MICCA-Spray injector is an issue that is not yet settled.

In this situation it is natural to try to design a rig that will be more representative of MICCA-Spray at least in some aspects. This motivates the development of TICCA-Spray, a linear system comprising three injectors and a rectangular cross-section. A 3D rendering is displayed in Fig. 1.5. This rig specifically addresses concerns regarding the confinement and thermal conditions impacts on the flow field and on the flame dynamics, and its design draws on the large expertise acquired in MICCA-Spray and SICCA-Spray. An additional advantage of TICCA-Spray will be the flat side windows, that are better suited to laser diagnostics and planar light sheets than a cylindrical confinement. This new combustor will however be less versatile and flexible than SICCA-Spray and more costly to run. Although the design of TICCA-Spray was started early on, several unforeseen delays prevented the first experiments to be performed in time to be included in the present thesis.

1.1.3 A modular injector design

The injector is common to MICCA-Spray and SICCA-Spray. An exploded 3D view is shown in the left of Fig. 1.6. From bottom to top, it consists in fittings for the liquid fuel (gray), a main body (purple), a fuel atomizer (orange), a tangential hole swirler (translucent teal) and an end piece (gold). The main body threads into MICCA-Spray and SICCA-Spray, and houses all other components. Six axial holes are drilled into it, channeling air from the plenum to the tangential swirler. The swirler design is classical and schematically described in the left of Fig. 1.6. As indicated in the introduction,

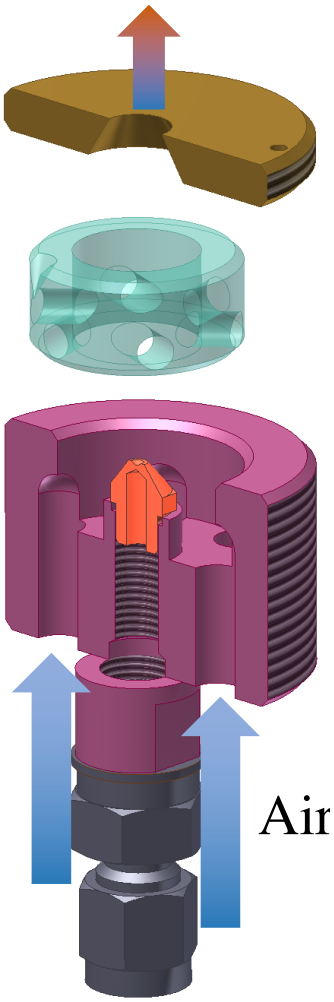

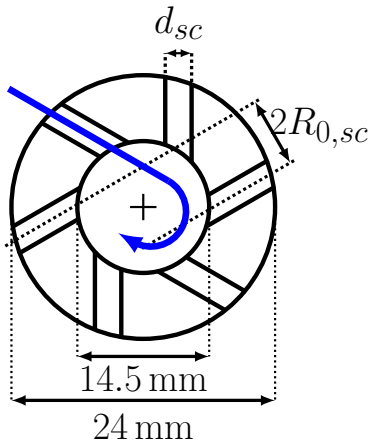

Figure 1.6: *Injector design. Left: exploded 3D view of the injection system and its components. Above: schematic cut of the swirler with key dimensions and nomenclature.*

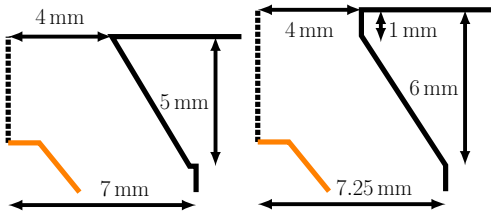

(a) *TP1.* **(b)** *TP2.*

Figure 1.7: *Design of the terminal plate (gold piece in Fig. 1.6). The atomizer is shown in orange for reference. Version TP1 is used with swirlers "TIMBER" and K, version TP2 with all other swirlers.*

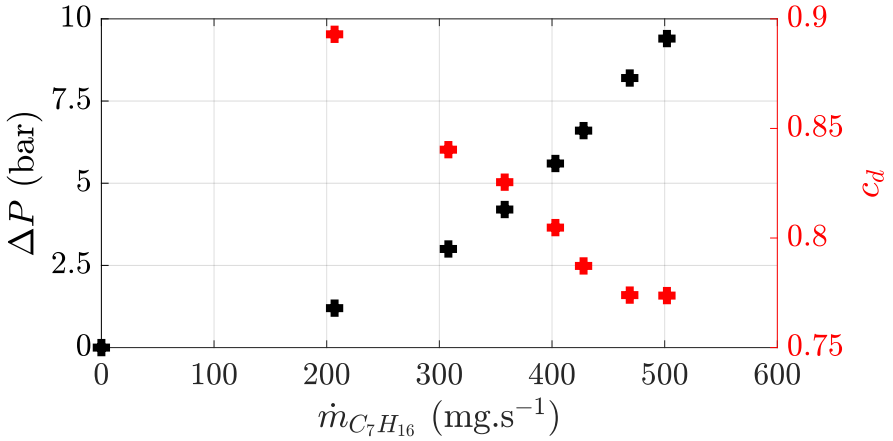

Figure 1.8: *Experimentally measured flow rate characteristic of the fuel atomizer. Measured with liquid heptane. The discharge coefficient is defined as* $c_d = \pi R_{at}^2 \left(2\rho_l \Delta P\right)^{0.5} / \dot{m}_l$*, where* ΔP *is the head loss across the injector,* $R_{at} = 40\,\mu\text{m}$ *the radius of the outlet of the atomizer,* ρ_l *the density of heptane, and* $\dot{m}_l$ *the mass flow rate of heptane (Lefebvre and Ballal (2010)).*

different versions are used in this thesis. More details on this topic are given in Chapter 3.

The fuel atomizer is a simplex pressure swirl design manufactured by ADIndustries Hydraulics (formerly MicroMécanique Pyrénéenne) under part number IJ2582-0-00. It is specified for a flow number of FN $= 0.261\,\text{l.h}^{-1}.\text{bar}^{-0.5}$ and an outlet radius of $R_{at} = 40\,\mu\text{m}$. The outlet of the atomizer is placed at the bottom of a small diverging cup with an included half angle of 59° and a final diameter of 1.5 mm. In Fig. 1.8, the relationship between the fuel flow rate and the atomizer head loss is plotted. One can observe that the discharge coefficient c_d is not quite constant with the flow rate, although it appears to begin to stabilize at a fuel flow rate of $500\,\text{g s}^{-1}$ which is typical of the operating points used in MICCA-Spray and SICCA-Spray. This change in discharge coefficient could be interpreted in two manners: in the inviscid theory of internal spray swirl atomizer flow reported by Lefebvre and Ballal (2010), the discharge coefficient is linked to the angle of the spray. If the inviscid theory applies, the change of discharge coefficient might be linked to a small change in spray angle. However, the Reynolds number of the heptane flow inside the atomizer is in the order of 4000-5000, which indicates that viscous effects might not be negligible and could account for some of the variation in discharge coefficient.

The golden plate on top is flush mounted with respect to the combustor backplane. It has a conical section before the outlet to avoid flame flashback. Two versions of this end piece exist and are depicted in Fig. 1.7. TP1, presented in Fig. 1.6 and 1.7(a), has a conical section with a large diameter of 14 mm and a final diameter of 8 mm for a thickness of 5 mm. It is used in conjunction with 1$^{\text{st}}$, 2$^{\text{nd}}$ and 3$^{\text{rd}}$ generation swirlers ("TIMBER" and K swirlers, see Tab. 3.1). The second version of this unit (TP2, Fig. 1.7(b)) has, on top of the conical section, a small 1 mm thick, 8 mm in diameter cylindrical section. This second version is used in conjunction with further generation swirlers. This change in terminal plate was made to remove the small corner at the bottom of the conical section. The thicker edge near the outlet of the atomizer is also more resilient and repeatable for

manufacturing.

The different versions of the injection system, easily obtained by changing the swirler, allow for parametric investigations in which the injection characteristics are varied. Two of these characteristics are of primary interest: the injector head loss, measured between the upstream and downstream sections, and its swirl number, which estimates the rate of rotation imparted to the flow.

1.2 Experimental diagnostics

This section details the experimental tools that are used to characterize the flow and flame in the present thesis. After introducing the instrumentation and its position on the test rigs, each experimental technique is briefly described.

1.2.1 Sensor implementation in MICCA-Spray

The positioning of sensors in MICCA-Spray is indicated in Fig. 13. The waveguides connected to the 8 chamber microphones MCx are placed at equidistant positions, and connected to the backplane of the combustor. 4 microphones are additionally mounted on the plenum. These 12 microphones allow to reasonably reconstruct azimuthal acoustic fields in both annular cavities. The 8 photomultipliers allow to investigate half of the 16 flames found in MICCA-Spray. They are equipped with masks to restrict their field of view to a single flame, and a small metallic tube is placed inside the chamber to hide the luminosity of flames located on the opposite side of the chamber. When the high speed camera is in use, it is aligned with the diameter of the combustor corresponding to the spark plug, and a high angle shot is used. This configuration allows to study standing oscillations, where the nodal line is often aligned with the spark plug, and ignition.

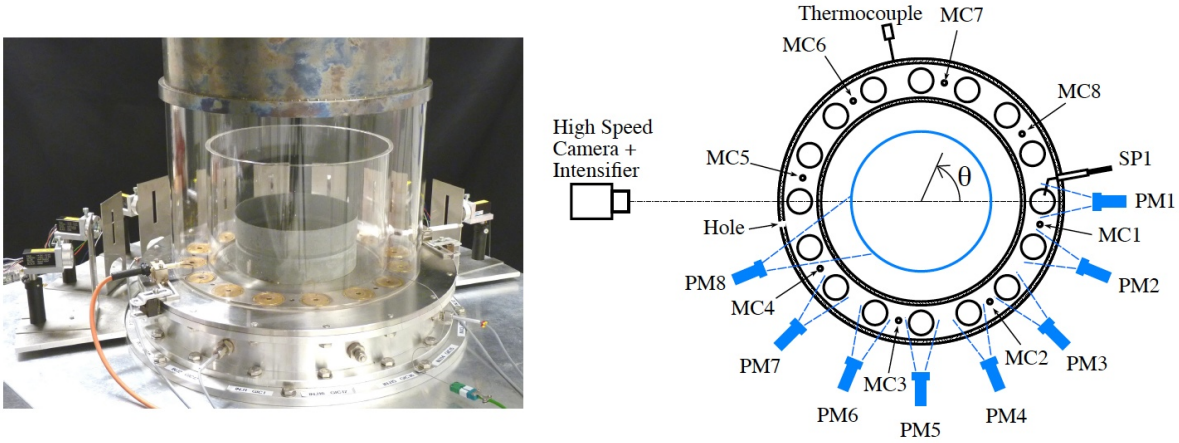

Figure 13: *From left to right: (1) Photograph of the MICCA-Spray test rig. (2) Schematic view of the chamber backplane showing the locations of the camera, thermocouple, chamber microphones MCx, plenum microphones MPx, photomultipliers PMx and of spark plug SP1. Dashed lines show the field of view of the photomultipliers. (repeated from page 22)*

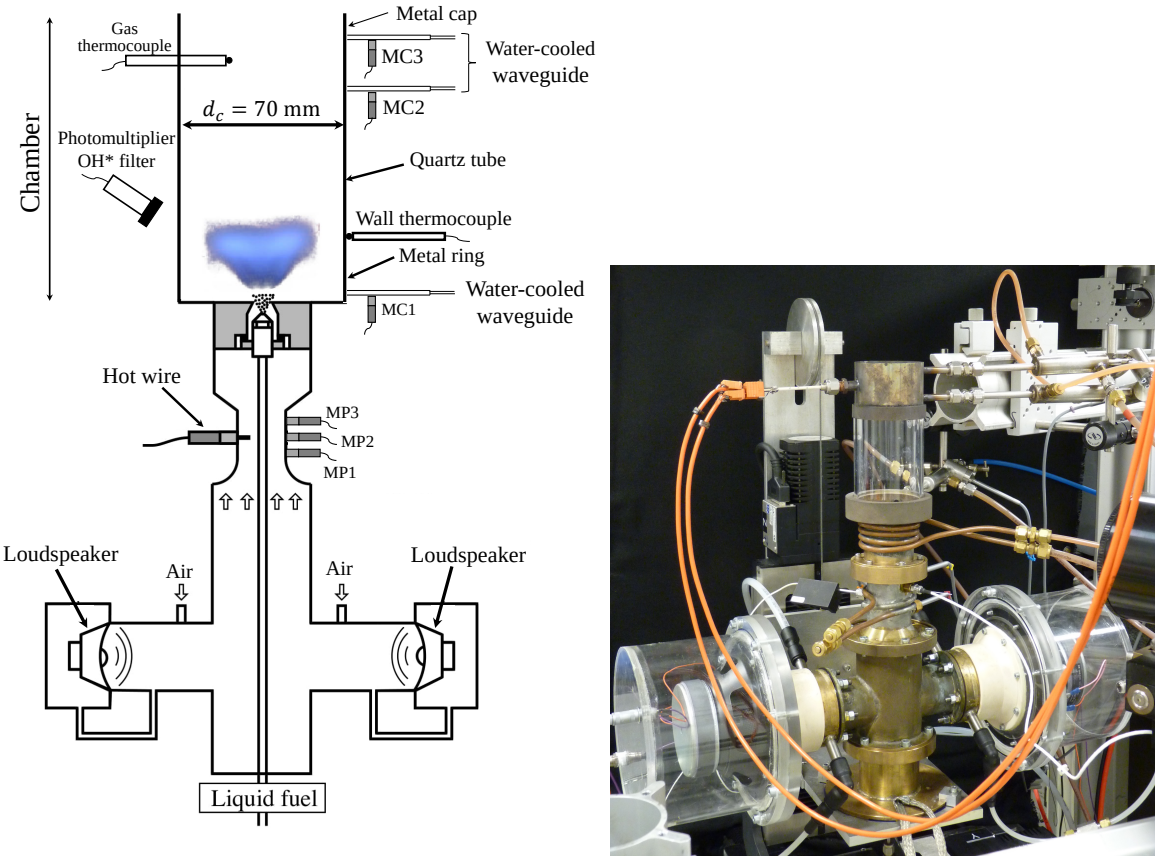

Figure 1.10: *Left: schematic of SICCA-Spray showing the implementation of most sensors that may be installed; Right: Photograph of this experimental setup*

1.2.2 Sensor implementation in SICCA-Spray

Being quick modular, it is difficult to give an exhaustive description of all possible versions and implementations of SICCA-Spray. Figure 1.10 gives an overview of the most heavily instrumented version of SICCA-Spray to display its versatility. Upstream of the injector, the plenum features a measurement section, positionned between a convergent and divergent to obtain 1D-velocity profiles. In this section are found a hot wire, three microphones MPx, spaced $\delta x \approx 20\,\text{mm}$ from each other, and a differential pressure measurement system. This apparatus allows to measure static and acoustic pressures, as well as flow rate fluctuations and acoustic velocities (using either the hot-wire or the two microphone method described in Tran (2009)). The quartz combustion chamber provides ample optical access for chemiluminescence measurements using photomultipliers, for flame imaging, for emission spectroscopy, for spray or tracer-based laser tomography and for PDA measurements. However, acoustic measurements using the waveguide-mounted microphones require the use of additional metallic pieces. A brass piece can be placed at the bottom of

the combustor for backplane acoustic pressure measurements using microphone MP1, but it impedes the optical access to the lower part of the flame. A stainless steel top piece can alternatively be placed on top of the quartz tube, near the outlet of the combustor. It is equipped with pressure taps so that two additional waveguide mounted microphones can be placed at this position. A thermocouple can also be positioned there to measure the temperature of the combustion products. It is mounted using a pass-through, air tight coupling on the upper stainless steel tube, and located 140 mm above the backplane of the combustor.

1.2.3 Thermometry

Although temperature is not the focus of the present work, it is an important parameter, mostly as an input for LES and acoustic simulations, but also to validate said simulations. Two temperature measurement techniques are employed in the present work. K-type thermocouples are quite systematically used for punctual measurement of the wall temperature of the quartz confinement tubes, mostly to control that a thermally steady state has been reached before acquiring data, as thermal transients have large impacts on flame shapes (Guiberti et al. (2015)), and naturally also on flame dynamics and combustion instabilities (Prieur et al. (2017b); Bonciolini et al. (2019)). In addition, double bead R-type thermocouples are used for gas temperature in SICCA-Spray. This gas temperature measurements are taken near the outlet of the combustor and are used as validation data for LES simulations, and as input for acoustic eigenmode determination. The double bead system allows to correct for radiation effects during the measurements (Lemaire and Menanteau (2017)). These are however found *a posteriori* to be negligible in the present case. For SICCA-Spray equipped with swirler 712 (see Tab. 3.1), and operated with heptane at an air flow rate of $2.3\,\mathrm{g\,s^{-1}}$ and a fuel flow rate of $0.5\,\mathrm{kg\,h^{-1}}$ ($\phi = 0.93$ and $P = 6.2\,\mathrm{kW}$), the temperature is measured using the gas thermocouple located near the outlet of the combustor at the axial section indicated in Fig. 1.10 ($z = 140\,\mathrm{mm}$), and at three radial positions:

- On the centerline: $T_{gas} = 1380\,\mathrm{K}$;
- At $r = 10\,\mathrm{mm}$: $T_{gas} = 1435\,\mathrm{K}$;
- At $r = 20\,\mathrm{mm}$: $T_{gas} = 1420\,\mathrm{K}$.

For the determination of wall temperatures used as input for LES, a thermochromic paint is used. These paints can be used to obtain an upper and lower bound for the maximum temperature reached at the wall during an experiment in the test rig. Experiments are conducted in SICCA with swirler 707 (see Tab. 3.1) at an operating point corresponding to an air flow rate of $2.3\,\mathrm{g\,s^{-1}}$ and a fuel flow rate of $0.5\,\mathrm{kg\,h^{-1}}$ ($\phi = 0.93$ and $P = 6.2\,\mathrm{kW}$). The temperature profiles on the inside wall of the quartz tube are measured for two combustor lengths (150 mm and 370 mm), the first corresponding to a steady flame, while combustion oscillations occur with the longer confinement. Results are reported in Fig. 1.11. With the shorter (150 mm) quartz tube, the maximum in wall temperature (1210 K) is reached at $z \approx 50\,\mathrm{mm}$, while with the longer (370 mm) quartz tube, and during a combustion instability, the wall temperature reaches 1250 K at $z \approx 80\,\mathrm{mm}$. The red curves are used as inputs for reactive LES simulations.

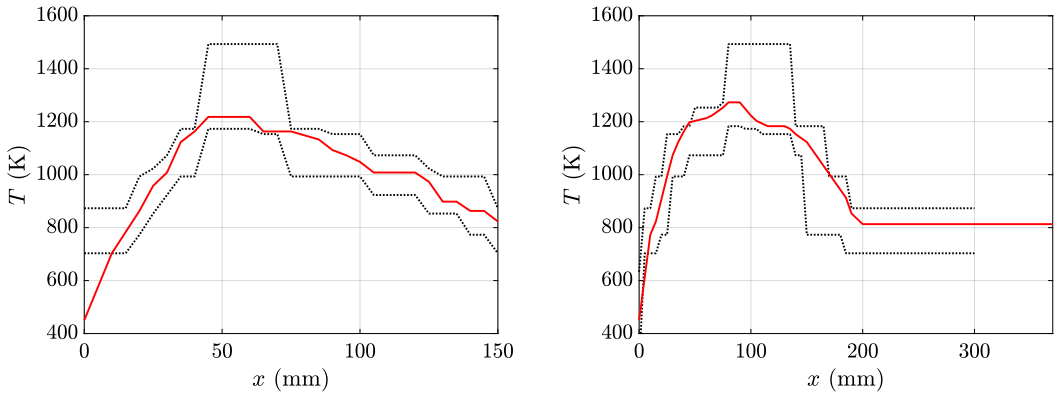

Figure 1.11: *Temperature measured with thermochromic paint in SICCA-Spray. Left:* 150 mm *long quartz; right:* 370 mm *long quartz. The dotted lines indicate the temperature bracket that is given by the thermal paint, the red curve is the interpolated temperature used for LES simulations.*

1.2.4 Static pressure measurements

The pressure drop across the injector is a parameter that receives a great deal of attention in the present thesis. In SICCA-Spray, it is measured using a differential pressure sensor (Kimo MP111, precision $\pm 0.5\% \pm 20\,\text{Pa}$) connected between the position of microphone MP1 in Fig. 1.10, and the atmosphere. It is assumed that the pressure drop inside the combustion chamber itself is very small and negligible compared to that of the injector.

1.2.5 Constant Temperature Anemometry

Constant Temperature Anemometry (CTA) is employed in the present thesis to measure the flow rate and its fluctuations immediately upstream of the injector. The hot wire (Dantec Dynamics 55P16) consists in a 5 µm diameter, 1.25 mm long tungsten wire welded to a pair of prongs and placed in an orthogonal direction to the flow. It is maintained at a constant temperature, higher than that of the air flow, by the electronic module (Dantec Dynamics MiniCTA). As the wire is continuously cooled down by the flow, the current fed to the wire to maintain its temperature constant is related to the velocity of the air stream. It can be measured using an electronic bridge, and the bridge voltage is related to the absolute velocity by King's law (King (1914)):

$$E^2 = a + bu^n \tag{1.1}$$

where E is the measured voltage across the bridge, u the velocity of interest, and a, b and n are constants obtained by a calibration on a reference air jet. Theoretically n must be equal to 0.5, but this value needs to be slighly corrected using the calibration. This measurement method is simple and straightforward to use, can be employed to measure velocities inside channels, and has a large bandwidth (up to 10 kHz with the system used in SICCA-Spray). There are however some limitations:

- Hot wires are unable to handle backflow, limiting their range of applications to situations where the relative amplitude of the fluctuating velocity is lower than $\approx 90\%$ peak;

- They should be placed orthogonal to the main direction of the flow;
- It is not quite a single point measurement;
- They are intrusive;
- The composition of the gas (in the case of premixed reactants for example), its temperature, and density fluctuations also affect the signal.

In the present work, constant temperature anemometry is used to estimate the fluctuations in flow rate upstream of the injector. The plenum of SICCA-Spray is designed with a profiled convergent duct (see Fig. 1.10) such that the hot wire probe is placed in a position where the velocity profile is one-dimensional. In this situation, many of the aforementioned drawbacks are no longer a consideration.

1.2.6 Acoustic pressure measurements

Acoustic measurement are conducted in this thesis using Brüel & Kjær type 4938 externally polarized capacitive microphones with type 2670 preamplifiers. Their relative accuracy is 1% and their cut-off frequencies are 70 kHz and 15 Hz. The microphone are driven using Brüel & Kjær type 2690-A Nexus signal conditioners. The microphone are systematically calibrated using a Brüel & Kjær type 4231 calibration source. Concerning the mounting method of these microphones, when the microphones are mounted inside a plenum, they are fixed flush to the wall. When measuring the acoustic pressure inside the chamber, a waveguide is employed to avoid exposing the microphone to high temperatures.

- In the case of MICCA-Spray, the waveguides are connected to the backplane of the combustor, and consist in a $\approx$ 25 m long, 6 mm internal diameter tube closed at the other end. This very long tube is designed to avoid acoustic reflexions. The microphone is mounted to the wall of the tube, 170 mm away from the dump plane of the combustor.
- In the case of SICCA-Spray, a water-cooled waveguide design is employed. It is described in details in the thesis of Gaudron (2018).

The waveguide system has its own transfer function, which was experimentally measured by Gaudron (2018) and during an earlier internal project by Moureau and Gurliat (2001). It was found that the phase of the transfer function can be adequately modeled by a constant delay corresponding to the travel time of the acoustic wave, which can easily be corrected in post-processing. The gain of the waveguide is not quite unity, but it is between 90% and 1 in the entire frequency range of interest (0 to 1 kHz). Although Gaudron (2018) suggest that the gain of the waveguide can be corrected in post-processing, the calibration can only be performed in cold flow conditions. Since the acoustic behavior of the junction between the waveguide and the combustor might be quite different between cold and hot reactive conditions, there are some doubts about the applicability of this procedure. In the present thesis, the gain of the waveguide is not corrected, which introduces an $\approx$ 10% uncertainty in the absolute value of pressure measurements. However, comparisons of measurements between different cases (i.e. comparison between 2 operating points, 2 swirlers, where the frequency is not too different...) are not affected by this uncertainty.

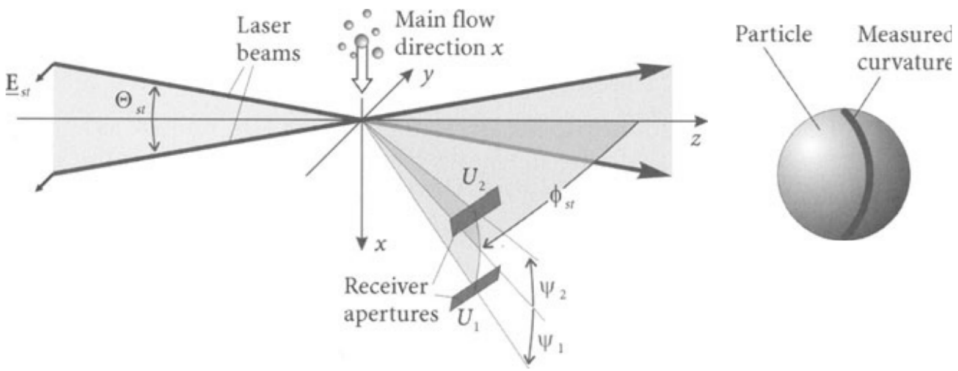

Figure 1.12: *Laser beams and associated angles in the PDA system. Figure from Albrecht et al. (2003).*

1.2.7 Phase Doppler Anemometry

Phase Doppler Anemometry (PDA) is a laser diagnostic that may be used to measure simultaneously the velocity and diameter of spherical droplets in a flow. This allows the measurement of liquid fuel droplet properties, but also of cold flow velocity profiles by seeding the flow with micro-meter sized oil droplets with a small Stokes number (Durox et al. (1999)). In what follows, the experimental setup and working principle of PDA are presented. Some elements regarding measurement uncertainties in the system are then discussed.

SICCA-Spray is equipped with a Dantec FlowExplorer 2-component PDA system, consisting in practice of two Laser Doppler Velocimetry systems placed orthogonally, and working with two lasers at different wavelengths (532 nm and 561 nm). One of them operates as the Phase Doppler Anemometer to measure droplet sizes. The system is coupled with an automated 3 axis motion system with a repeatability better than 0.01 mm. The system is aligned with the lasers with a parallelism better than 1.5 mm.m^{-1} on all axis. At the beginning of each measurement session, the system is aligned with respect to the injector. The positioning accuracy of the system is thus better than 0.13 mm in all axis in unconfined, non-reactive conditions. In confined conditions, due to the cylindrical nature of the confinement tube, the positioning uncertainty of the laser probe volume is higher.

The principle of Laser Doppler Velocimetry are described for example by Albrecht et al. (2003); Boutier and Most (2012). For a single channel system, the organization of the laser beams is shown in Fig. 1.12. The laser emission head creates two coherent laser beams using a Bragg cell. The Bragg cell acts as a beam splitter, but it also creates a frequency shift between the two beams. The beams then go through an optical system designed so that they intersect at a specific angle in the area of interest in the flow. At the intersection of the beams, an interference pattern is created. When a particle crosses that pattern, light is scattered with a modulation at a specific frequency which is simply related to the velocity of the flow by $u = d_f f$ where the inter-fringe spacing d_f is related to the

wavelength λ of the laser and the angle Θ_{st} of the two beams: $d_f = \lambda/(2\sin(\Theta_{st}/2))$. In the present case, $\Theta_{st} = 6.87°$, and $d_f = 4.45\,\mu m$. The frequency shift created by the Bragg cell allows for negative and zero velocities to be measured. The collection optic consists in a series of lenses, slots and optical bandpass filters designed to both minimize the size of the measurement volume ($0.14 \times 0.14 \times 0.23\,mm$ for the present setup), and reduce the noise in the optical signal which is received by photomultipliers. When a particle crosses the measurement volume, it appears as a gaussian shaped "Doppler burst" on the PM's signal. Inside the LDV processor system, complex, high frequency electronics are employed to process these signals. After going through a series of analog bandpass filters and amplifiers, whose settings dictate the range of velocities that can be measured, the signal goes through a burst detector, which detects whether a particle is present inside the measurement volume using signal correlation methods. If a droplet is detected, frequency analysis is performed using a Fast Fourier Transform, and the velocity of the droplet is recorded. In the two component LDV system employed in the present thesis, the laser emission head hosts two lasers at different wavelengths, and is designed such that all four laser beam intersect at the same location. Two interference patterns are thus created, whose fringes are orthogonal to each other. Each direction is associated with a laser wavelength, and is processed quite separately using distinct photomultipliers. Inside the processor, the only common piece of equipment is the coincidence computer, which detects whether bursts are detected simultaneously on both channels. If it is the case, the droplet is validated, and included in the data: two of its velocity components have been measured simultaneously. LDV is a very accurate, time resolved, absolute velocity measurement technique. The manufacturer certifies the measurement system (laser, optics and processor) at an uncertainty of 0.11% on the droplet or tracer velocities. The second major source of uncertainty besides the equipment is the computation of the statistical moments of the velocity. In the present case, the number of acquired data points (50 000) ensures that in the region of interest, the statistical uncertainty on the mean and RMS velocities are lower than 1.5% based on the 95% confidence intervals. Given these elements, it is reasonable to consider that measurement uncertainty on the velocity are less 2%. In regions of high velocity gradients, a gradient bias may exist which leads to an additional overestimation on the RMS velocity. This bias is associated with the finite size of the measurement volume, and may be easily understood in the following simplified scenario. Let us consider a velocity field $\mathbf{u}(\mathbf{x}, t)$. Using a first order Taylor expansion and a Reynolds decomposition, one may write in the measurement volume

$$\mathbf{u}_i(\mathbf{x}, t) = \overline{\mathbf{u}}_i(\mathbf{x_0}) + \nabla\,\overline{\mathbf{u}}_i(\mathbf{x_0}) \cdot (\mathbf{x} - \mathbf{x_0})_i + \mathbf{u'}_i(t) \tag{1.2}$$

where the subscript i designates a component of the velocity. If the turbulent velocity can be estimated to be constant within the measurement volume, and if a uniform probability is assumed for droplets crossing the measurement volume, it follows that the LDV system measures the RMS velocity at $\mathbf{x_0}$ as

$$\widetilde{\mathbf{u}'}_i(\mathbf{x_0}) = \mathbf{u'}_i(\mathbf{x_0}) + \delta x_j \frac{\partial \overline{\mathbf{u}}_i}{\partial x_j}(\mathbf{x_0}) \tag{1.3}$$

where Einstein's notation are used and δx_j designates the dimensions of the measure-

ment volume. In a typical configuration, the bias can be estimated to be of the order of $1.9\,\mathrm{m\,s^{-1}}$ for the axial velocity component. For more details on this bias, see Boutier and Most (2012) for example.

In Fig. 1.12, two apertures, associated with two photomultipliers U_1 and U_2, can be seen. This pair of sensors is used in the context of phase Doppler anemometry to measure the droplet diameter (Albrecht et al. (2003)). Let us consider a droplet as a perfect sphere. Let the ratio of the optical index of this sphere to that of the surrounding media be n_r. $n_r = 1.39 \pm 0.02$ for heptane droplets in air or in hot combustion products. The principle of phase Doppler anemometry is that the phase $\Delta\phi_{12}^{Mes.}$ between the Doppler bursts received by photomultipliers U_1 and U_2 is linked to the diameter of the droplet $D_{12}^{Mes.}$ by a linear relationship

$$\Delta\phi_{12}^{Mes.} + 2\pi q \equiv \frac{2\pi}{\lambda} D_{12}^{Mes.} (\beta_2 - \beta_1) \tag{1.4}$$

where q is an integer indicative of the 2π uncertainty of phase measurements and β_i is the phase factor for detector i, which can be estimated using geometrical optics as

$$\begin{aligned} \beta_i = &\sqrt{1 + n_r^2 - n_r\sqrt{2}\sqrt{1 + \cos\psi_i \cos\phi \cos\theta/2 + \sin\psi_i \sin\theta/2}} \\ &-\sqrt{1 + n_r^2 - n_r\sqrt{2}\sqrt{1 - \cos\psi_i \cos\phi \cos\theta/2 - \sin\psi_i \sin\theta/2}} \end{aligned} \tag{1.5}$$

These relationship are approximate, and may be more accurately predicted in the framework of the Generalized Lorentz-Mie Theory (Albrecht et al. (2003)). The angles ψ_i of the PDA setup are set by the manufacturer, and the scattering angle ϕ has been set to $71.5° \pm 3°$ so that the actual values of β_i match the aforementioned simplified formula as best as possible. The PDA system uses three photomultipliers organized in two pairs: one pair is close to each other so that $\beta_2 - \beta_1$ is small, the second is farther away so that $\beta_3 - \beta_1$ is larger. Using two pairs of photomultipliers with two different slopes for the phase-diameter relation allows to disambiguate the 2π uncertainty on the determination of the phase, and increases the measurement range of the instrument while conserving a high level of accuracy. This also allows to check the validity of measured diameters using a phase diagram: the diameter obtained using each pair of photomultipliers should be the same.

1.2.8 Flame chemiluminescence

Flame chemiluminescence can be used to estimate the instantaneous heat release rate in a flame. This is done by measuring the spontaneous light emission from certain chemical radicals present in the flame front, which emit at specific wavelengths. The relationship between heat release rate and chemiluminescence is examined in details in Chapter 2. The present section focuses on the experimental apparatus used to measure light emission.

To measure light emission in the ultraviolet range and in a time resolved manner, the photomultiplier tube (PM) is the best suited instrument. It integrates the light emission

over a large solid angle, which comprises the entire flame in our applications. The system, comprising the photomultiplier tube, a high voltage power supply and a current to voltage converter, outputs a voltage proportional to the incident light intensity, and its gain can be easily varied over a wide range, making it quite versatile. In SICCA-Spray, two PMs are used. For the emission of the OH^* radical, a Thorn EMI type QLF30F is equipped with an optical bandpass interference filter centered at 308 nm with a width at half peak of 10 nm. The temporal bandwidth of this PM can be set as high as 1 MHz. For the emission of the CH^* radical, a Hamamatsu H11902-10 integrated photosensor module (temporal bandwidth from DC to 20 kHz) is used in conjunction with a bandpass optical filter centered on 431 nm with a width at half peak of 10 nm. In MICCA-Spray, a new array of eight photomultiplier has been put in place as part of the present thesis. The photosensor modules are Hamamatsu H10722-110//001 equipped with optical bandpass filters centered around 307 nm with a width at half peak of 10 nm. Each photosensor module is additionally equipped with a mask (see Fig. 1.2(b) and 1.2(c)) so that the light emission from a single flame is captured.

To measure the time averaged flame emission spectra, an OceanOptics Maya Deep UV spectrometer is used in Chapter 2 and 11. The collection setup for the spectrometer consists in a spherical lens connected to an optical fiber, so that the light received by the spectrometer consists in the integrated emission of the flame. The spectrometer is calibrated in wavelength using a mercury spectral lamp. Its spectral resolution is 0.5 nm.

Flame images are acquired using an intensified CCD camera (PiMax 4) with a resolution of 1024×1024 pixels. An optical bandpass filter is placed in front of the fused silica lens to select the emission of a specific radical in a similar manner to the photomultipliers. The images are time-averaged. Since the signal is integrated along the line-of-sight, an Abel transform is generally used to obtain an approximate planar visualization of the flame, under the assumption of flame axisymmetry. Note that the PiMax camera can be synchronized to an external signal (such as a microphone) to perform phase averaging (Chapter 7).

1.2.9 High speed imaging

High speed imaging is a very versatile diagnostic tools for the analysis of flame dynamics. Chemiluminescence images can be acquired at a high frame rate (up to 20 kHz), to be post-processed using modal decomposition methods such as DMD (Schmid (2010)) or POD (Chatterjee (2000)). In the present thesis, a Photron FastCam APX-i2 intensified CMOS camera is employed in Chapters 5, 9 and 11. This system is capable of acquisition frequency up to 6 kHz for flame chemiluminescence. In Chapter 10, a PhantomHighSpeed V2512 camera is used to record chemiluminescence images in MICCA-Spray and SICCA-Spray with acquisition frequency up to 10 kHz. Finally, a color version of the same camera is made use of in Chapter 6 to simultaneously acquire flame chemiluminescence (blue, mostly CH^* emission), and light scattering on the spray (green signal from a Nd:YAG laser at 532 nm). In Chapter 5, a Photron FastCam SAX-2 is used to record light scattering on tin dioxide tracer particles from a 10 W continuous Nd:YAG laser at 532 nm at acquisition

frequencies up to 100 kHz.

1.3 Overview of MICCA-Spray and SICCA-Spray experimental setups

Two synthetic tables gather the main configurations of SICCA-Spray (Tab. 1.1) and MICCA-Spray (Tab. 1.2) used in the following chapters.

1.4 Numerical setup for LES

Experimental data are often incomplete and their interpretation may be difficult. It is then interesting to combine these data with numerical results. Calculations are carried out in the Large Eddy Simulation (LES) framework. The models and numerical setup used for these calculations of the single injector system SICCA are presented in this section. Simulation are carried out for two swirlers 707 and 712. The solver and numerical schemes are introduced in Section 1.4.1 together with the meshing and mesh adaptation strategies. The droplet spray is modeled using a Lagrangian particle tracking approach which is described in Section 1.4.2.

1.4.1 Cold flow configuration

1.4.1.1 Flow solver

The present work makes use of the 3D Navier-Stokes solver AVBP developed by CERFACS in collaboration with IFP Énergies Nouvelles (CERFACS (2020)). Its compressible nature allows for solving acoustic and reactive flows on unstructured meshes. Domain decomposition makes the solver highly parallel, a requirement for the highly CPU intensive simulations that are envisaged. The integration relies on TTGC, a two-step Taylor-Galerkin weighted residual central distribution scheme with a third order precision in space and time (Colin and Rudgyard (2000)). Its stabilization requires the use of artificial viscosity, which is added based on the sensor proposed by Colin and Rudgyard (2000). Artificial viscosity is also applied to avoid over and undershoots of species mass fractions. An adaptative time step based on a Courant Friedrichs Lewy criterion ($CFL_{crit} = 1$) is used. The diffusion operator is handled with the 2Δ scheme (Colin and Rudgyard (2000)). For multi-species simulations, the gaseous species are transported under an assumption of unity Lewis number. The SIGMA model proposed by Baya Toda et al. (2010) is specifically designed to handle swirling flows and is used to model the subgrid scales of the gaseous flow. The contribution of the subgrid scale turbulence to thermal and species diffusion is modeled under a constant turbulent Schmidt and Prandtl number assumption: $\mathrm{Pr}_t = \mathrm{Sc}_t = 0.6$.

The computational domain of SICCA-Spray used for LES is shown in Fig. 1.13. The plenum is cut at the position of the hot wire, which subsequently serves as the inlet. The use of a large volume to represent the ambient atmosphere is standard practice to

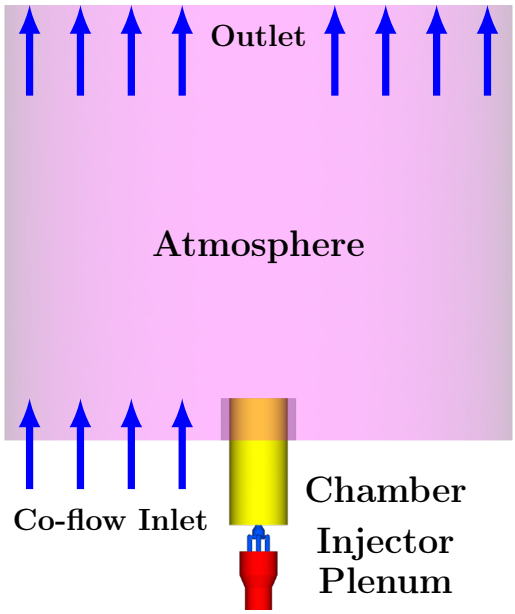

Figure 1.13: *Computational domain used for SICCA-Spray simulations. The combustion chamber is in this case* 165 mm *long.*

Table 1.1: *Synthesis of SICCA experimental setups*

Chapter	Chapter 2	Chapter 3	Chapter 4	Chapter 5
Purpose	Analysis of flame chemiluminescence	Steady state characterization of injectors	Best practices for swirl number measurements	Self-sustained instabilities and PVC
Type of study	Experiments	LES and experiments	LES and experiments	Experiments
Injection system	Swirler 707 and 716	Swirler 707, 712, 716	Injector of Bourgouin et al. (2013)	Swirler "TIMBER"
Setup images			Fig. 4.2 (p. 135)	Fig. 5.3 (p. 173)
Fuel	Heptane and premixed propane	Non reactive and heptane	Non reactive	Heptane
Combustor length	150 mm	None	200 mm	-
Combustor diameter	69 mm	None	50 mm	69 mm
Type of plenum	Passive loudspeakers	Passive loudspeakers	Passive loudspeakers	Passive loudspeakers
Diagnostics	PM, spectroscopy, pollutant emissions	LDV, PDA, differential pressure sensor, hot wire, intensified camera	LDV	SnO_2 high speed laser tomography
Air mass flow rate	-	-	$1.66\,g\,s^{-1}$	$1.94\,g\,s^{-1}$
Fuel mass flow rate	-	-	-	$440\,g\,h^{-1}$
Thermal power	-	-	-	5.4 kW
Equivalence ratio	-	-	-	0.95

Table 1.1 *(cont.)*: *Synthesis of SICCA experimental setups*

Chapter	Chapter 6	Chapter 7	Chapter 10	Chapter 11
Purpose	LES of a self-sustained instability and time-lag analysis	Effect of injector pressure loss	Ignition dynamics	Lean blow out with plasma assisted combustion
Type of study	LES and experiments	Experiments	Experiments	Experiments
Injection system	Swirler *K*	3D printed swirlers (3rd gen.)	Swirler "TIMBER"	Swirler "TIMBER"
Setup images	Fig. 6.1 (p. 198)	Fig. 7.2 (p. 213)	Fig. 10.13 (p. 288)	Fig. 11.1 (p. 302)
Fuel	Heptane	Heptane	Heptane	Heptane, dodecane and methane
Combustor length	300 mm	315 mm	150 mm	150 mm
Combustor diameter	69 mm	69 mm	69 mm	69 mm
Type of plenum	Straight tube	Passive loudspeakers	Passive loudspeakers	Passive loudspeakers
Diagnostics	High speed spray tomography and flame imaging, microphones	LDV, differential pressure sensor, hot wire, microphones, intensified camera	High speed flame imaging, constant temperature anemometry	PM, spectroscopy, high speed flame imaging
Air mass flow rate	$2.6\,\mathrm{g\,s^{-1}}$	-	$1.94\,\mathrm{g\,s^{-1}}$	-
Fuel mass flow rate	$520\,\mathrm{g\,h^{-1}}$	$500\,\mathrm{g\,h^{-1}}$	$400\,\mathrm{g\,s^{-1}}$	$400\,\mathrm{g\,s^{-1}}$
Thermal power	6.4 kW	6.2 kW	5.0 kW	5.0 kW
Equivalence ratio	0.85	-	0.87	-

Table 1.2: *Synthesis of MICCA experimental setups*

Chapter	Chapter 8	Chapter 9	Chapter 10
Purpose	Measurement of acoustic damping and acoustic characterization	Large amplitude oscillations coupled by standing azimuthal mode	Review of previous work on ignition
Injection system	Swirler 716	Swirler 716	Swirler "TIMBER" Injector of Bourgouin et al. (2013)
Setup images	Figs. 13 (p. 22) and 1.2(c) (p. 34)	Figs. 13 (p. 22) and 1.2(c) (p. 34)	Fig. 1.2(d) (p. 34)
Fuel	Heptane	Heptane	Heptane and premixed propane
Length of combustor walls	$l_{in} = 200\,\text{mm}$ $l_{out} = 700\,\text{mm}$	$l_{in} = 200\,\text{mm}$ $l_{out} = 700\,\text{mm}$	$l_{in} = 200\,\text{mm}$ $l_{out} = 200\,\text{mm}$
Ignition system Quartz tube	Fixed spark plug 2 holes	Fixed spark plug 2 holes	Fixed spark plug 2 holes
Diagnostics	PM and microphone arrays and simulations	Microphone array, high speed intensified camera	PM and microphone array, high speed camera

Table 1.3: *Operating conditions and boundary conditions for non-reactive LES simulations (except Chapter 4).*

	Plenum (Inlet)	Atmosphere (Inlet)	Atmosphere (outlet)
Type of BC	Imposed mass flow rate with relaxation	Imposed velocity with relaxation	Imposed pressure with relaxation
Target	$\dot{m} = 2.3\,\mathrm{g\,s^{-1}}$	$\overline{u}_z = 1\,\mathrm{m\,s^{-1}}$	$p = 99\,325\,\mathrm{Pa}$
Relaxation coefficient	$5000\,\mathrm{s^{-1}}$	$500\,\mathrm{s^{-1}}$	$500\,\mathrm{s^{-1}}$

avoid difficulties near the outlet boundary conditions (see for example Shum-Kivan et al. (2017)). Cases without confinement are also calculated for validation purposes, and use a similar large volume. Navier-Stokes characteristic boundary conditions as derived by Poinsot and Lele (1992) are used at the inlet. A 3D boundary condition accounting for vorticity (Granet et al. (2010)) is used at the outlet. Operating conditions and relaxation coefficients for the boundary conditions are gathered in Tab. 1.3. The relaxation coefficient are estimated following rules proposed by Poinsot and Veynante (2012). Walls are generally modeled using no-slip boundary conditions. The lateral boundary representing an unconfined situation is treated with a slip condition. Inside the injector, a logarithmic law of the wall is used (Jaegle et al. (2010)). This significantly improves the injector head loss prediction because in this unit the thickness of the laminar sublayer is around one tenth to one quarter of the size of near wall mesh elements. Wall resolved LES remains too expensive for this configuration.

1.4.1.2 Computational mesh

The adaptation strategy proposed by Daviller et al. (2017) is used to generate the mesh. This strategy is designed to improve head loss predictions for swirling injectors and is briefly described in what follows. The $LIKE$ (Loss in Kinetic Energy) metric is used to define the time averaged viscous dissipation

$$LIKE = \overline{(\mu + \mu_t)\left(\frac{\partial \tilde{u}_i}{\partial x_j} + \frac{\partial \tilde{u}_j}{\partial x_i}\right)^2} \tag{1.6}$$

where μ and μ_t respectively designate the dynamic and turbulent (subgrid scale model) viscosity, $\tilde{\mathbf{u}}$ the velocity. Einstein notations are used in this expression. By performing mesh refinement where this criterion is high, the weight of the subgrid scale model is reduced at these critical location, and the overall quality of the simulation is improved. The mesh creation thus follows the following procedure. A first mesh is generated from scratch, where relatively coarse element sizes are imposed. Note that the element sizes at this step are still sufficiently small to handle other simulation constraints, such as adequate resolution for the flame (using the thickened flame approach). A first LES simulation is

performed, and the statistically converged $LIKE$ field is used as a metric to isotropically refine the mesh at relevant locations. The process can be repeated until the quantities of interest reach mesh convergence. In the present work, these quantities are the mean and RMS velocity profiles, and the injector head loss. These items are validated against experimental measurements. In practice, using this approach, the time step of the simulations can decrease very rapidly as the mesh is refined, while only small improvements in the results are obtained. In the present work, the mesh refinement process is stopped when the smallest element size in the domain is of the order of 0.1 mm. This is reached after two refinement steps.

The sizes of mesh elements in the numerical model are displayed in Figure 1.14. Injector meshes are displayed in Figs. 1.14(d) and 1.14(e), after (1.14(d)) and before (1.14(e)) the adaptive refinement. Table 1.4 summarizes the typical mesh element size used in the simulations. A characteristic dimension is presented in each region of the geometry, to assess the mesh resolution. The two limiting features in terms of mesh sizes are the flame front, which is handled using a thickened flame approach, and the liquid fuel atomizer nozzle, featuring a very small outlet diameter of 80 µm (see Section 1.4.2). A typical mesh for swirler 707 and a combustor length of 165 mm comprises 30 million tetrahedral elements.

1.4.2 Droplet spray modeling using Lagrangian particle tracking

The characteristic mean droplet diameter in the spray is in the order of 5 to 10 µm while the characteristic length scales of the geometry are of the order of 0.1 m. Four orders of magnitude separate these two length scales. Direct numerical simulations of the liquid and gaseous phases would induce excessive numerical costs. This problem may be alleviated by simulating the gaseous, reactive flow field in an Eulerian framework, while the disperse liquid phase is calculated in a Lagrangian framework. Liquid fuel droplets are directly injected into the Eulerian fluid domain near the position of the atomizer, and are then transported. Primary atomization phenomena are only modeled, only spherical, individual fuel droplets are transported. Contrary to the Eulerian-Eulerian moment based method, the Lagrangian particle tracking approach facilitates the handling of polydisperse sprays such as those found in SICCA-Spray as concluded from calculations of laboratory scale aeronautical reported by Jaegle et al. (2011); Cunha Caldeira Mesquita et al. (2017) for example.

1.4.2.1 Solver setup

The numerical setup is similar to those previously used in well validated simulations carried out for spray flames in swirled laboratory scale combustors (Jaegle et al. (2011); Sanchez (2012); Tachibana et al. (2015); Paulhiac (2015); Shum-Kivan et al. (2017); Cunha Caldeira Mesquita et al. (2017); Collin-Bastiani et al. (2019)). The particle trajectories are integrated using a two-step Runge-Kutta scheme. The correlation of Schiller and Naumann (1935) is used to model the drag force on the particles. The two-way coupling between the disperse and gaseous phases is implemented using a second order linear interpolation. Particles are assumed to remain perfectly spherical, gravity and shear

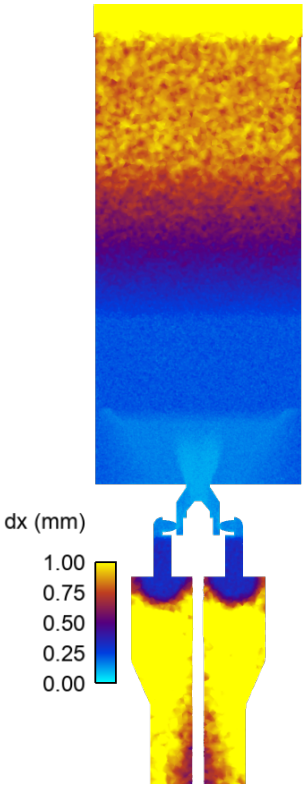

(a) *Plenum and combustion chamber.*

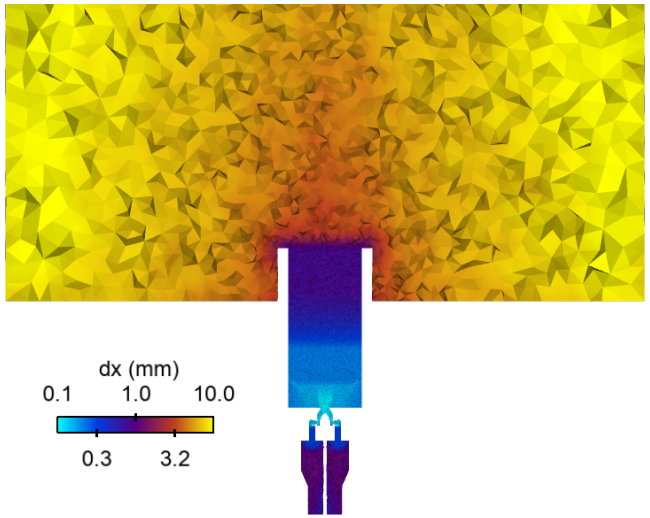

(b) *Element sizes in the whole domain. Log scale.*

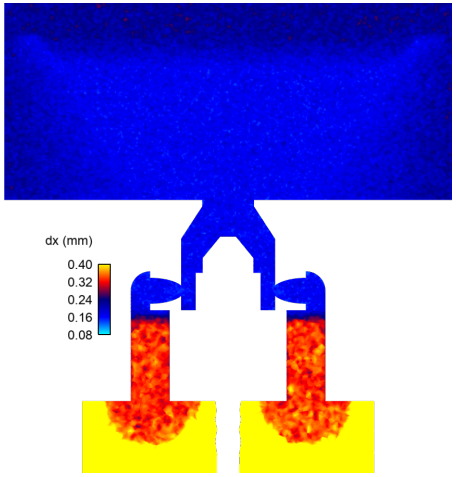

(d) *Plenum and combustion chamber (before AMR).*

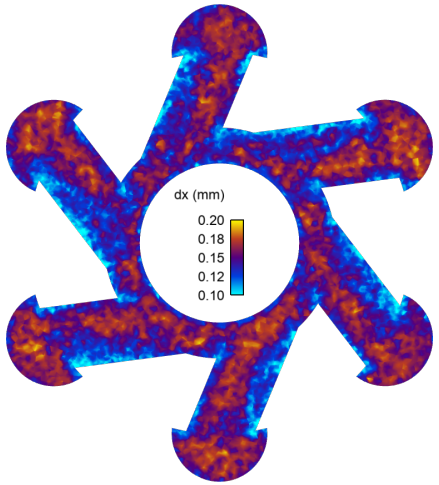

(c) *Transverse cut of the swirler.*

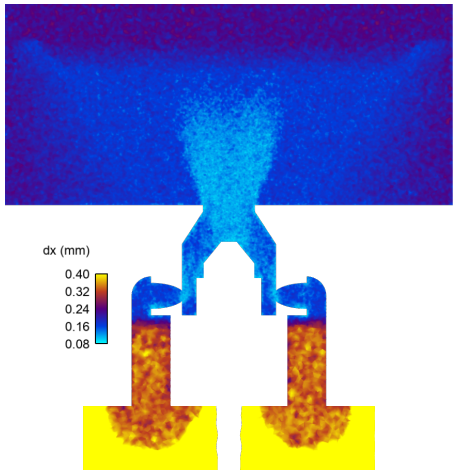

(e) *Plenum and combustion chamber.*

Figure 1.14: *Sizes of mesh elements dx for SICCA-Spray simulations with swirler 707 and a* 165 mm *long combustion chamber.* ***(a) - (c) and (e)*** *Mesh after two steps of adaptive mesh refinement, as used in the simulations.* ***(d)*** *Mesh before adaptive mesh refinement.*

Table 1.4: *Typical element size (dx) in the mesh after adaptive refinement (except Chapter 4). Sizes given in (*mm*).*

Location	max dx	average dx	Characteristic geometric size		Nb. of elements
Plenum	1.3	1	Diameter	31	30
Axial channels	0.35	0.35	Diameter	6	17
Tangential channels	0.15	0.1	Diameter	4	40
Atomizer tip	0.15	0.13	Nozzle diameter	0.08	< 1
Injector outlet	0.15	0.13	Shear layer thickness	1	8
Flame (root)	0.2	0.15	Flame front (thermal, premixed)	0.4	2.5
Flame (top)	0.4	0.3	Flame front (thermal, premixed)	0.4	1
Chamber (downstream)	1.0	0.75	Diameter	69	90
Atmosphere	10	10			

effects are neglected compared to drag. Secondary atomization is neglected as well. The effect of subgridscale turbulence on the trajectory of the particles is also neglected. This topic has been reviewed by Marchioli (2017), who indicates that this research topic is not mature and that many different modelling approaches are currently being investigated based on DNS simulations. He nonetheless conveniently defines a subgridscale Stokes number based on turbulent and droplet properties

$$\mathrm{Stk}_{SGS} = \frac{\tau_p}{(\Delta^2/\epsilon)^{1/3}} \tag{1.7}$$

where τ_p is a characteristic time for the droplets, Δ is the LES filter size and ϵ the turbulent kinetic energy dissipation rate. For $\mathrm{Stk}_{SGS} \gtrsim 10$, it is generally considered that coupling with the subgrid scale can be neglected.

Evaporation and heat exchanges between the gaseous and liquid phases is handled in the framework proposed by Abramzon and Sirignano (1989). For a given particle, its mass and uniform temperature follow

$$\frac{dm_p}{dt} = \dot{m}_p \tag{1.8}$$

$$\frac{dT_p}{dt} = \frac{1}{m_p c_{p,l}} \phi_p^c \tag{1.9}$$

where m_p and $\dot{m}_p$ designate the mass of the particle and evaporative mass transfer, T_p its temperature (assumed uniform), $c_{p,l}$ the specific heat of the liquid fuel and ϕ_p^c the conducive heat-flux. The closure proposed by Abramzon and Sirignano (1989) is based on the assumption of a single isolated droplet in a convective flow, and on a quasi-steady hypothesis. It writes

$$\dot{m}_p = -\pi d_p \mathrm{Sh}^* \rho_g D_g \ln(1 + B_M) \tag{1.10}$$

$$\phi_p^c = -\pi d_p \mathrm{Nu}^* \lambda (T_\infty - T_p) \frac{\ln(1 + B_T)}{B_T} \tag{1.11}$$

where d_p, ρ_g, D_g and λ are respectively the diameter of the droplet, the density of the gas, the binary diffusion coefficient, and the thermal conductivity, evaluated at a film temperature based on the one third rule (Hubbard et al. (1975)). B_M and B_T are dimensionless quantities introduced by Spalding (1953) and designated as Spalding transfer numbers. The dependency on the convective flow is introduced in the Nusselt and Sherwood numbers Nu^* and Sh^*. The AVBP code implements a correlation by Froessling (1938) for the dependency of evaporation on the flow field:

$$\mathrm{Sh}^* = 2 + \frac{0.552 Re_p^{1/2} Sc^{1/3}}{F(B_M)} \tag{1.12}$$

$$\mathrm{Nu}^* = 2 + \frac{0.552 Re_p^{1/2} Pr^{1/3}}{F(B_M)} \tag{1.13}$$

$$\mathrm{Re}_p = \frac{d_p \rho_g \left\| \mathbf{u_p} - \mathbf{u_g} \right\|}{\mu_g} \tag{1.14}$$

where a constant value is chosen for the Prandtl and Schmidt numbers: Pr = 0.976 and Sc = 1.343, determined using the method proposed by Sanchez (2012). Re_p designates the droplet's Reynolds number. F is a function introduced in Abramzon and Sirignano (1989). Abramzon and Sirignano (1989) suggest, following the work of Crocco (1965), that the use of the Froessling correlation for the dependency on the velocity field might lead to erroneous results, especially in the case of combustion instabilities. In Crocco's work concerning isolated droplets of liquid propellants burning in rocket engines, the response of the heat release rate associated with burning droplets placed in an acoustic field depends on $\partial \dot{m}_p / \partial \mathrm{Re}_p$, which grows to infinity as the Reynolds number goes to zero. In SICCA-Spray, this type of combustion regime and combustion/acoustic coupling does not represent a large contribution to the overall heat release rate, such that the simple correlation of Froessling (1938) may be used.

1.4.2.2 Boundary conditions

The present subsection focuses on droplet-wall interaction. This subject is reviewed in Lee and Ryu (2006); Chaussonnet (2014). The impact of an isolated droplet on a wall, which is the configuration of interest in this thesis, can be categorized as either:

- rebound: the droplet bounces on the wall and conserves its shape;
- stick: the droplet remains spherical, but is stuck to the wall;
- filming: the droplet forms a liquid film on the surface of the wall;
- splashing: the droplet creates several smaller droplets.

Wall boundary conditions are handled by three types of models depending on the surface being considered. In general, a simple elastic rebound model is chosen for its simplicity and numerical stability. Inside the injector however, the handling of the spray-wall interaction is critical, and more realistic models are applied to the wall formed by the conical convergent at the end of the atomizer. In Chapter 3, a comparison is made in non-reactive conditions between three wall model approaches:

- elastic rebound;
- slip;
- the film model presented by Chaussonnet et al. (2013).

This last model consist in a switching between the Lagrangian approach and the Eulerian approach close to the wall. In practice, this model imposes the velocity of particles close to the wall to form a group (the liquid film) based on the solution of a set of Saint Venant Eulerian equations for film thickness and momentum. Particles are then released in the gaseous stream when an edge sharper than 45° is encountered. No edge atomization or breakup model is used in this thesis. The injection strategy is presented in Chapter 3,

where the numerical setup for the spray is validated against experimental data.

Chapter 2

The relationship between chemiluminescence and heat release rate

The determination of the unsteady heat release rate is of considerable importance in combustion dynamics analysis. This quantity is generally deduced from the chemluminescence emission intensity of excited radicals like OH^* or CH^*. The relation between this signal and the heat release rate is well established for lean premixed flames but less well documented in the case of spray flames. This relation is investigated in the present chapter by making use of steady state experiments in which the fuel flow rate is systematically varied and the light intensities of OH^* or CH^* are measured. It is found in particular that the relation deviates from a linear dependancy and that it is necessary to use a quadratic fit. The deviation from linearity is found to be less important in the case of OH^* chemiluminescence. The fits derived from these experiments can be used to correct the measured light emission intensity to obtain a signal that more closely corresponds to the heat release rate signal integrated over the whole flame.

Contents

2.1 Introduction

The estimation of the instantaneous heat release rate integrated over the volume of the flame is of critical importance in the field of combustion dynamics. This can be seen for example by considering the linearized wave equation for reacting flows that may be written as (Poinsot and Veynante (2012))

$$\nabla \cdot \left[\bar{c}^2 \, \nabla p' \right] \; - \frac{\partial^2 p'}{\partial t^2} \; = \; - \left(\gamma - 1 \right) \frac{\partial \dot{\omega}}{\partial t} \tag{2.1}$$

where the aeroacoustic contribution is neglected, $\bar{c}$ designates the mean speed of sound, p' the acoustic pressure, γ the specific heat ratio, and $\dot{\omega}$ is the volumetric heat release rate. In practical systems, and in laboratory scale rigs such as SICCA-Spray and MICCA-Spray, the flame region can often be considered to be acoustically compact so that the wave equation may be simplified by considering that the contribution of combustion can be represented by a point source.

Early on, Hurle et al. (1968) proposed to use the chemiluminescence emission from premixed flames to estimate the instantaneous heat release rate. Considering that excited radicals such as C_2^*, CH^* and OH^* emit light at specific wavelengths, that these radicals are mostly localised in the flame front and that, reabsorption of the emitted light is negligible, it was assumed that the light collected at these specific wavelengths could be linked to the heat release rate in the flame. The light emission was observed with a photomultiplier placed far from the flame and with a large collection angle integrating the light radiated from the entire flame. This was then linked to the global heat release rate from the combustion process. In the case of premixed flames under lean conditions, this has been shown to provide an acceptable estimate of the instantaneous heat release rate.

Since the work of Hurle et al. (1968) however, many other studies of light emission from flames have been carried out, mainly as a way to obtain local measurements of flame properties, or as a way to implement active control of combustion systems. Work on flame chemiluminescence as a diagnostic tool is reviewed in Docquier and Candel (2002); Ballester and García-Armingol (2010). Many studies on canonical flames have served to assess the relation between flame chemiluminescence and heat release rate under different operating conditions. The chemiluminescence signal is sometimes collected inside a small region of the flame, using for example a Cassegrain optical set-up (Kojima et al. (2000); Hardalupas and Orain (2004)), or it can be integrated over the entire flame region (for example in Higgins et al. (2001); García-Armingol et al. (2014); Ding et al. (2019)). The focus is placed in these studies on premixed hydrocarbon-air flames. Kojima et al. (2000) show that the light emission from radicals is concentrated in the flame. Their detailed emission spectra also demonstrate that a fine spectral band is not necessary for chemiluminescence measurements as, for a given radical, the numerous peaks associated with each possible electronic transitions behave in the same manner with regards to the combustion parameters of interest (heat release rate, equivalence ratio, strain rate...).. The relationship between chemiluminescence and equivalence ratio has been characterized in

numerous studies as a mean to either evaluate and/or control combustion. For example, the ratio of CH^* to OH^* emission is often suggested as a metric for equivalence ratio determination (Docquier and Candel (2002); Ballester and García-Armingol (2010); Ding et al. (2019)). This property is for example used by Peterleithner et al. (2016) to identify a progressive equivalence ratio perturbation in a technically premixed burner submitted to acoustic modulation. The dependence of emission on equivalence ratio is examined by Hardalupas and Orain (2004) in premixed counterflow strained flames. These authors conclude that this ratio is a good indicator in the lean regime, but that the ratio C_2^* / OH^* is a better indicator under rich operating conditions. More importantly, one may observe in their configuration that CH^* chemiluminescence is quite sensitive to the equivalence ratio, while OH^* only varies by approximately 30 % when the equivalence ratio is increased from 0.7 to 1.1. This last result is also found by Kojima et al. (2000). The effect of the strain rate is also examined by Hardalupas and Orain (2004). For flames close to stoichiometry, and strain rates between 160 and 320 s^{-1}, OH^* chemiluminescence can vary by $\pm 10\%$. Non-adiabatic effects on flame chemiluminescence are studied by Ding et al. (2019) using a porous plug burner. The chemiluminescence properties of the flame are shown to depend on its distance from the porous plug. The effect of re-absorption of OH^* emission by ground state OH in the burnt gases is examined in the PhD thesis of Ding (2018) where it is shown that this effect can be non-negligible, with 45% re-absorption for a 10 cm long optical path in the burnt gases of a premixed methane-air flame at atmospheric pressure. As mentioned by Guethe et al. (2012), this problem is far greater in practical systems operating at elevated pressure. In such applications, chemiluminescence measurement should be based on CH^* emission to improve signal to noise ratios, as ground state CH is not present in the burnt gases.

The chemiluminescence of swirled flames is investigated by García-Armingol et al. (2014) in combination with 1D premixed methane-air flame simulations using detailed chemistry. The chemiluminescence kinetics is also included. It is shown that pre-heating and heat losses in the fresh stream strongly affect the chemiluminescence process. In a configuration where burnt gases are mixed with the fresh reactants with a dilution by burnt gases of 50% by volume, OH^* chemiluminescence is increased by approximately 25%, while CH^* chemiluminescence is multiplied by a factor of 3. A study carried out on an unconfined, turbulent, premixed methane-air flame by Lauer et al. (2011) combines chemiluminescence detection with detailed PIV measurements. Using a model for air entrainment, and 1D detailed chemistry simulations of strained flames, the authors are able to compensate for numerous non-ideal effects of flame chemiluminescence, and obtain an improved 2D reconstruction of the heat release rate field. To our knowledge, the only study dealing with the relationship of chemiluminescence and heat release rate in practical spray flames is that of Mirat et al. (2014). Using a steady state method it is shown that these quantities are linearly related. A further validation in a thermoacoustic analysis is reported by Mirat et al. (2015).

To overcome the limitations encountered with chemiluminescence techniques, other approaches have been developed in the combustion dynamics field to measure heat release rates in flames. A first category relies on density measurements. Li et al. (2012); Li et al.

(2013) suggest for example to estimate density fluctuations using ultrasonic waves propagating in a direction orthogonal to the flame axis. Their traveling time can be related to the density on the path of the wave if the shape of the flame is known a-priori. This line of sight integrated measurement system was validated against chemiluminescence measurements in modulated and unconfined conical laminar flames. Laser based interferometry can also be employed to estimate density fluctuations. This was implemented by Leitgeb et al. (2013) on a laminar flame burner but their demonstration had the same limitations as that of Li et al. (2012), requiring an unconfined configuration, and an a-priori knowledge of the shape of the flame to deduce the flame-integrated heat release rate fluctuations. Peterleithner et al. (2016) later used laser interferometry in a confined rig to compare flame transfer functions obtained with different methods to measure the heat release rate. The manual scanning of the combustor needed by laser interferometry is likely the reason for the limited number of operating conditions investigated with this method. For perfectly premixed flames, the global heat release rate fluctuations obtained using laser interferometry and OH^* chemiluminescence are in good agreement. This is not the case for a technically premixed case that was also examined, for which laser interferometry appeared to provide a better data set. Laser interferometry was recently improved by Greiffenhagen et al. (2019), with a full field measurement system using a high speed camera, demonstrated on an unconfined perfectly premixed swirled flame. This improvement in the applicability of the method opens the way to its more widespread use in the future. A second category of techniques for the determination of the unsteady heat release rate relies on laser induced fluorescence (LIF). A comprehensive comparison of chemiluminescence and LIF is reported by Najm et al. (1998), who compare chemiluminescence from numerous radicals (OH^*, CH^*, C_2^* and CO_2^*) to planar laser induced fluorescence (PLIF) as an indicator for local heat release rate. Their experiments on premixed methane-air "V"-flames are complemented by numerical simulations of a flame-vortex interaction with detailed chemistry. It is found that in highly curved flames, the formyl radical HCO PLIF signal is well correlated to the heat release rate, and constitutes a better measure of that quantity than OH^* chemiluminescence. It is sometimes argued in the thermoacoustic literature that it is possible to avoid measuring the heat release rate by making use of direct determinations of acoustic transfer matrices, based on multi-microphone techniques. This may be used to infer the flame dynamics by system identification (see the reference case of Greiffenhagen et al. (2019) for example). If the acoustics of the entire system can be adequately modeled, it is in principle possible to extract the flame transfer function as a black-box model. However, a non-acoustic based, direct measurement of heat release rate fluctuations is still desirable to check the black box result and to determine nonlinear features of the flame response.

In a system such as SICCA-Spray, the measurement methods presented in the last paragraph are not readily applicable: ultrasonic based measurements have only been applied in unconfined flames. In addition, the spray would disturb laser interferometry measurements, and fluorescence measurements such as HCO PLIF are difficult to implement because of the cylindrical geometry and a 2D slice would not give an adequate account of the strongly three dimensional nature of the flame. Chemiluminescence is the only practical option available. The present chapter aims at evaluating the applicability of

Table 2.1: *Operating conditions for experiments on chemiluminescence. Shown here for swirler 716 with heptane fuel. The same operating conditions are used with the other fuels and swirlers.* ***O*** *indicates operating points where measurements are performed (based on the operating range of the mass flow controllers).*

$\dot{m}_{C_7H_{16}}$	$350\,\mathrm{g\,h^{-1}}$	$400\,\mathrm{g\,h^{-1}}$	$450\,\mathrm{g\,h^{-1}}$	$500\,\mathrm{g\,h^{-1}}$	$520\,\mathrm{g\,h^{-1}}$	$550\,\mathrm{g\,h^{-1}}$
$\phi = 1.1$	**O**	**O**	**O**	**O**	**O**	**O**
$\phi = 1.0$	**O**	**O**	**O**	**O**	**O**	**O**
$\phi = 0.9$	**O**	**O**	**O**	**O**	**O**	**O**
$\phi = 0.8$	**O**	**O**	**O**	**O**	**O**	**O**
$\phi = 0.7$		**O**	**O**	**O**	**O**	**O**
$\phi = 0.6$				**O**	**O**	**O**

this diagnostic to spray flames. A quasi-steady approach is chosen in which the chemiluminescence intensity is recorded for different operating conditions of the burner. This serves to establish the relation between the thermal power and the chemiluminescence signal. After describing the experimental setup (Section 2.2), the combustion efficiency is determined (Section 2.3), and shown to be close to unity for lean and stoichiometric mixtures. One may then assume that, for the steady flames considered in this chapter, the integrated heat release rate of the flame is proportional to the fuel mass flow rate. In Section 2.4.1, OH^* chemiluminescence is assessed using swirler 716 and two fuels: heptane injected as a hollow cone spray of droplets, and premixed propane-air. The same assessment is performed for CH^* chemiluminescence in Section 2.4.2. The degree of generality of the conclusions drawn with a specfic swirler 716 is then assessed with measurements carried out with swirler 707 in Section 2.5. Practical conclusions are drawn in Section 2.6. In what follows, when heptane is employed as a fuel, the equivalence ratio designates the global equivalence ratio.

2.2 Experimental setup

Experiments are carried out in the SICCA-Spray test bench (see Fig. 1.4) equipped with swirler 716 for the cases discussed in Sections 2.3 - 2.5, and with swirler 707 in Section 2.5. The chamber is formed by a short (150 mm) quartz tube that avoids combustion instability. Both perfectly premixed propane-air, and the usual hollow cone spray of liquid heptane are used as fuel for experiments with swirler 716. The mass flow rate of propane is adjusted to obtain the same thermal power as the heptane cases (based on the lower calorific value). For swirler 707, test results are only given for liquid heptane injection. The experimental conditions used in the present chapter are gathered in Tab. 2.1.

In addition to the massflow meters for air and fuel, the test rig is equipped with an OceanOptics "Maya deep UV" spectrometer. A 525 nm shortpass filter is used with the spectrometer to eliminate thermal radiation from the burner. The collection optics consists in a spherical lens and a UV fiber, so that the field of view encompasses the whole flame area. The spectrometer is calibrated in wavelength using a mercury lamp, and a

nonlinearity correction is applied. Two photomultiplier modules are used to perform more quantitative measurements using a set-up described in Section 1.2.8. The photomultipliers are placed such that the light emission from the flame is entirely captured. One of the photomultipliers is equipped with an optical bandpass filter centered at 431 nm with a width at half maximum of 10 nm to capture the emission from the CH^* radical, while the other photomultiplier has another optical bandpass filter centered at 308 nm with a width at half maximum of 11 nm to capture the emission from the OH^* radical.

Measurement uncertainties are determined whenever possible by making use of the mass-flow meters uncertainties and by estimating the PM statistical uncertainties and those related to electronic noise and background light.

2.3 Combustion efficiency

The first step in this set of experiments consists in estimating the combustion efficiency. This is performed using a combustion flue gas analyzer (ECOM JKNPro). The gas analyzer probe is placed in the position of microphone MC2 in the schematic in Fig. 1.4 (p. 36), that is close to the end of the combustion chamber. The volume fractions of different species are measured using recently calibrated electrochemical cells. Given the low levels of carbon monoxide that have been detected, the combustion efficiency can be estimated in lean conditions from two methods: either from the remaining O_2 volume fraction which gives a lower bound, this method being sensitive to air leaking into the chamber; or from the unburnt hydrocarbons measurements, which give a rough estimate. Results are gathered in Tab. 2.2 for eight operating conditions corresponding to extreme values in terms of equivalence ratio and fuel flow rates. Measurements are carried out with swirler 716 and heptane. For all operating conditions, one may reasonably consider for the purpose of this chapter that the combustion efficiency is sufficiently close to unity so that the heat release rate in the flame can be considered to be proportional to the fuel mass flow rate.

2.4 Assessment of the chemiluminescence linearity

It is first useful to examine some emission spectra to determine the radical species that may be identified. Figure 2.1 shows that OH^* emits in the vicinity of 308 nm and that CH^* is found near 431 nm. Numerous bands are related to C_2^*. It is assumed that the emission from sodium near 589 nm is due to the presence of this species in the manufacturing process of the quartz tube. The broadband emission identified by the red line is associated with CO_2^* emission. The spectrum is limited to 650 nm to avoid the region of high thermal radiation of little interest in this thesis.

In Fig. 2.2, the emission spectrum of a lean propane-air flame is compared to the emission spectrum of a globally lean, spray heptane air flame. Both spectra have similar features, the two main differences being larger C_2^* peaks, and stronger overall emission (including thermal radiation, CH^* and CO_2^*) from the heptane flame.

Table 2.2: *Measurements of flue gas composition at the exhaust of SICCA-Spray equipped with swirler 716 and operated with heptane. Operating conditions correspond to extrema in Tab. 2.1. The combustion efficiency is subsequently estimated from either the O_2 volume fraction (and designated as η_{O_2}) or the unburnt hydrocarbon measurements (and designated as $\eta_{C_xH_y}$).*

ϕ -	$\dot{m}_{C_7H_{16}}$ $g\,h^{-1}$	X_{O_2} %	X_{CO} ppm	$X_{C_xH_y}$ %	X_{NO} ppm	X_{NO_2} ppm	η_{O_2} %	$\eta_{C_xH_y}$ %
1.1	550	0	sat.	0.35	51	1	-	97
	350	0	sat.	0.35	45	0	-	97
1.0	550	0.6	258	0.14	36	7	97	99
	350	1.0	251	0.23	26	5	95	98
0.8	550	4.8	25	0.17	8	3	96	98
	350	5.4	113	0.24	6	2	93	98
0.7	520	7.1	120	0.24	4	1	94	97
	350	7.4	77	0.24	2	1	93	97

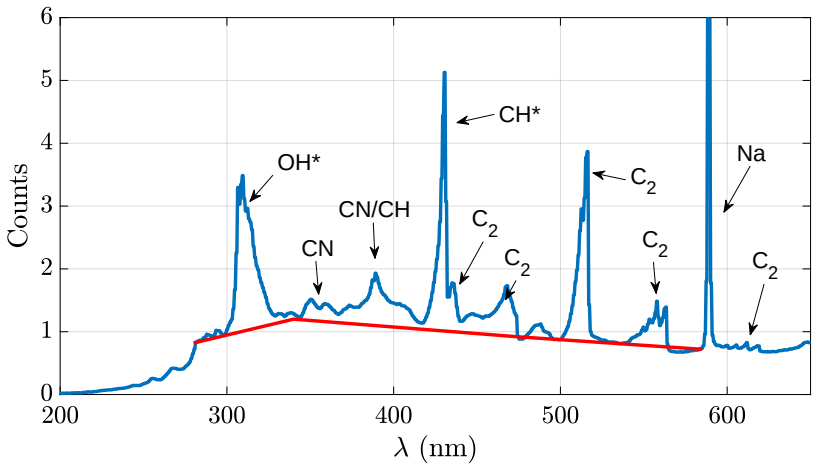

Figure 2.1: *Emission spectra of the perfectly premixed propane-air flame from swirler 716. Equivalence ratio of 1.1, thermal power of* 6.8 kW *(equivalent to an heptane mass flow rate of* $550\,g\,h^{-1}$*). Annotations indicate the species corresponding to each peak (Gaydon (1974)). The red line near the bottom roughly shows the baseline associated with broadband CO_2^* emission (see for example Gaydon (1974); Lauer et al. (2011)).*

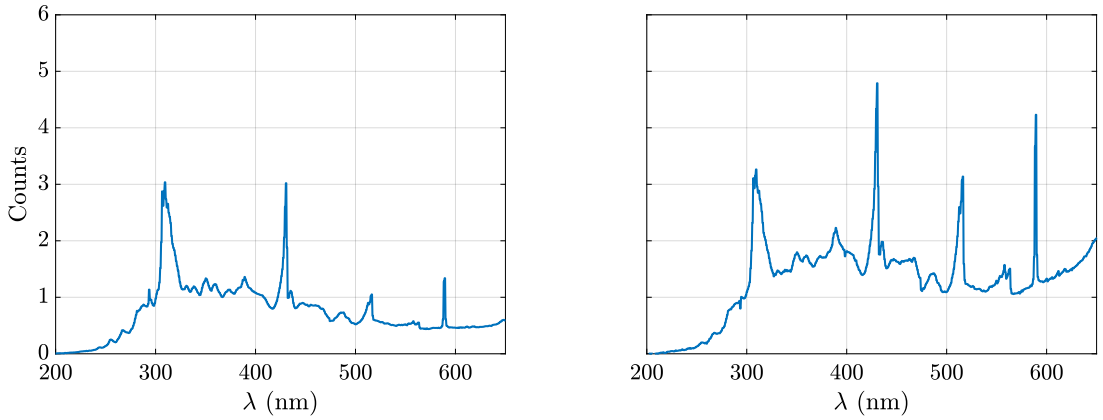

(a) *Premixed propane-air.* **(b)** *Spray heptane-air.*

Figure 2.2: *Comparison of emission spectra of a propane (left) and heptane (right) flames established by swirler 716. Equivalence ratio of 0.9, thermal power of* 6.8 kW *(equivalent to an heptane mass flow rate of* $550\,\mathrm{g\,h^{-1}}$*).*

In what follows, the non-linearity of the relationship between heat release rate and OH^* chemiluminescence is assessed using photomultiplier measurements (Section 2.4.1). The same study is then repeated with CH^* emission (Section 2.4.2). The potential bias arising from the setup of the collection optics, such as the impact of the CO_2^* baseline, or the transfer function of the optical filter, are finally discussed in Section 2.4.3.

2.4.1 Non-linearity in the relationship between $\dot{Q}$ and I_{OH}

Having established that the combustion efficiency is close to unity in SICCA-Spray, the linearity of the relationship between the integrated flame heat release rate and OH^* chemiluminescence signal can be assessed by plotting the light intensity measured by the OH^* photomultiplier against the fuel flow rate. In practice, both are normalized by their value at the maximum thermal power (6.8 kW), and a plot is made for each value of the equivalence ratio.

In Fig. 2.3, this is done for an heptane fueled flame at $\phi = 0.9$. Two fits are compared: the first is proportional, in the form $y = mx$, the second quadratic[1], $y = \alpha x(1+\beta x)$. The quadratic fit matches the data well, with a coefficient of determination $R^2 = 1$. What is demonstrated here in a single curve extends to all equivalence ratios investigated (as shown in Tab. 2.1), for both fuels and both swirlers. In what follows, the quadratic fit is systematically employed.

Given that a quadratic fit will be systematically employed in what follows, it is useful

[1] A linear fit $y = mx + p$ also matches the data well. However this relation is expected to cross the origin: an absence of flame corresponds to no I_{OH^*} signal. It is more natural to consider a relation of the general form $I_{OH^*}/\dot{m} = C$, where the correlation coefficient C might vary depending on the equivalence ratio and the fuel flow rate.

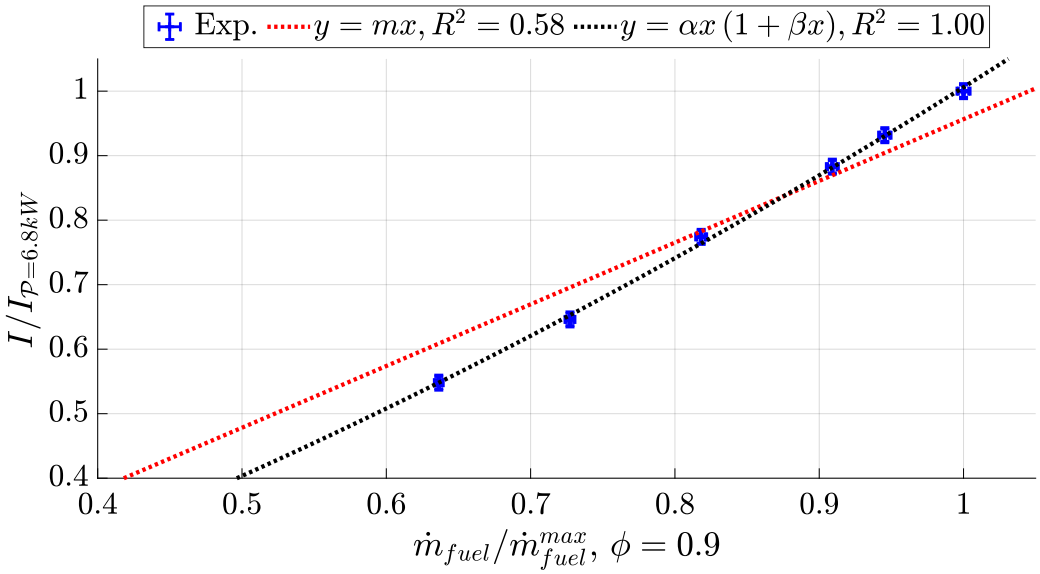

Figure 2.3: *Relationship of OH* chemiluminescence to fuel mass flow rate. The burner is operated with liquid heptane fuel at a global equivalence ratio of* $\phi = 0.9$*. The data is normalized by the values at the highest thermal power of* 6.8 kW*. A proportional and a quadratic fit are compared.*

to construct an index that measures the level of nonlinearity contained within the data. This is done here by considering the target application of the present investigation by considering a synthetic signal that represents the fluctuating heat release rate in the flame:

$$\dot{Q}(t) = \dot{Q}_0[1 + \kappa\cos(\omega t)] \tag{2.2}$$

This signal oscillates at an angular frequency ω, and the relative amplitude of oscillation is $\kappa = a_1/\dot{Q}_0$ where a_1 is the coefficient of the first harmonic in the Fourier series of $\dot{Q}(t)$. In typical experiments $\kappa \simeq 0.35$, corresponding to a heat release rate fluctuation level of about 25% rms.

Now, let us consider that the relation between the heat release rate and the light intensity takes the form of a quadratic function $y = \alpha x(1 + \beta x)$, that is let us assume that

$$\frac{I(t)}{I_{ref}} = \alpha\frac{\dot{Q}(t)}{\dot{Q}_{ref}}\left[1 + \beta\frac{\dot{Q}(t)}{\dot{Q}_{ref}}\right] \tag{2.3}$$

Inserting the heat release rate expression in this relation one may first determine the mean intensity level. A straightforward calculation yields :

$$\frac{\overline{I}}{I_{ref}} = \alpha\frac{\dot{Q}_0}{\dot{Q}_{ref}} + \alpha\beta\frac{\dot{Q}_0^2}{\dot{Q}_{ref}^2}\left[1 + \frac{1}{2}\kappa^2\right] \tag{2.4}$$

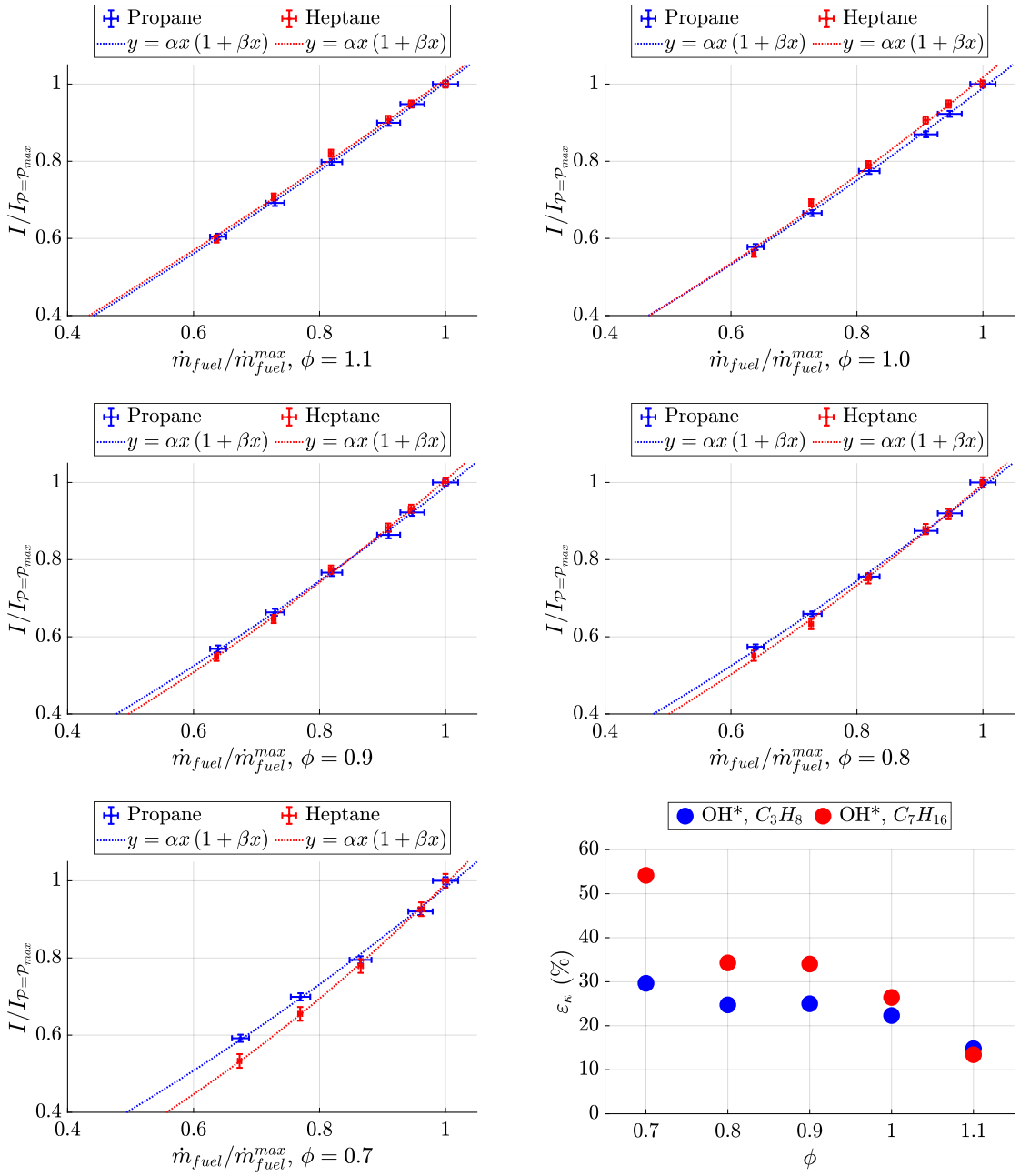

Figure 2.4: *OH* chemiluminescence intensity plotted against the fuel mass flow rate for several equivalence ratios (decreasing from left to right and top to bottom). Both are normalized by their respective values at the highest thermal power. For swirler 716, two fuels are considered: propane, premixed with air, and heptane, injected as a hollow cone spray. The last subfigure shows the value of the nonlinearity estimator ε_κ for the two fuels and different equivalence ratios.*

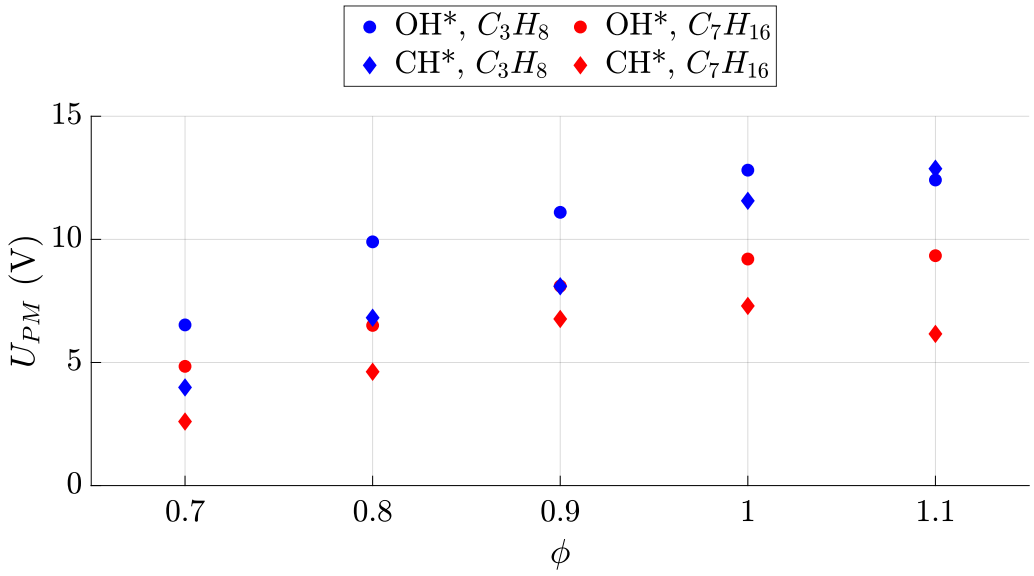

Figure 2.5: *PM signal as a function of equivalence ratio for a fuel flow rate of* $550\,\mathrm{g\,h^{-1}}$. *Both fuels (heptane and propane) are shown, as well as both chemiluminescence signals (OH* and CH*).*

One may next determine the Fourier coefficient of the first harmonic in $I(t)/I_{ref}$. One finds after a simple calculation:

$$b_1 = \kappa\alpha\frac{\dot{Q}_0}{\dot{Q}_{ref}}\left[1 + 2\beta\frac{\dot{Q}_0}{\dot{Q}_{ref}}\right] \tag{2.5}$$

The relative intensity oscillation at the angular frequency ω is then obtained by dividing the previous expression by the mean value of the intensity. This gives an estimate of the relative oscillation in heat release rate :

$$\kappa_{est} = b_1/[\overline{I}/I_{ref}] \tag{2.6}$$

It is then possible to compare this estimate with the relative level of heat release rate fluctuation κ by forming the ratio $\varepsilon_\kappa = (\kappa_{est} - \kappa)/\kappa$. One finds

$$\varepsilon_\kappa = \frac{\beta\frac{\dot{Q}_0}{\dot{Q}_{ref}}\left(1 - \frac{1}{2}\kappa^2\right)}{1 + \beta\frac{\dot{Q}_0}{\dot{Q}_{ref}}\left(1 + \frac{1}{2}\kappa^2\right)} \tag{2.7}$$

In what follows, $\kappa = 0.35$ and $\dot{Q}_0/Q_{ref} = 0.9$ are used, and ε_κ is used as a metric for nonlinearity.

Using the curves in Fig. 2.4, where the flame's OH* chemiluminescence signal intensity is plotted against the fuel mass flow rate at a constant equivalence ratio, it is possible to conclude that for global equivalence ratios between 0.8 and 1.1, the flame integrated OH*

chemiluminescence behaves in a similar manner for the perfectly premixed case and for the heptane spray flame. At a global equivalence ratio of 0.7, the OH^* chemiluminescence signal of the heptane flame is however more nonlinear than that of the premixed propane flame.

Finally, it is interesting to examine the dependence of the chemiluminescence intensity to the equivalence ratio at a fixed fuel flow rate. This is done in Fig. 2.5. In the range $\phi = 0.9$ to 1.1, the OH^* chemiluminescence signal is not very sensitive to the equivalence ratio with variations contained below 15%. Outside of this range, the dependence on equivalence ratio is stronger.

2.4.2 Assessment of CH^* chemiluminescence

The investigation of CH^* chemiluminescence is here performed in a manner similar to that of OH^* chemiluminescence presented in Section 2.4.2. Concerning the premixed propane-air flames (blue data points in Fig. 2.6), it appears that CH^* chemiluminescence behaves like OH^* chemiluminescence. However for the heptane spray flames, the nonlinearity is more pronounced. Additionally, Fig. 2.5 shows that, for the heptane spray flame, the CH^* chemiluminescence variability depending on the equivalence ratio is larger.

2.4.3 Measurement bias originating from the optical collection system

As mentioned by Docquier and Candel (2002); Peterleithner et al. (2016); Lauer et al. (2011) among others, the usual chemiluminescence experimental apparatus consisting of a bandpass optical filter attached in front of a photomultiplier or a camera does not exactly measure the emission of the targeted radical and introduces two sources of bias:

(I): Emission mostly due to CO_2^* constitutes a baseline level that combines with the peaks associated with OH^* and CH^* (see for example the spectra in Fig. 2.1 and Fig. 2.2). A common method to handle this limitation consists in adding a second photomultiplier / camera, equipped with a bandpass filtered centered on a band where only CO_2^* emits. Two spectral bands are commonly used for this purpose: 450 nm or 370 nm (Samaniego et al. (1995); García-Armingol et al. (2013)).

(II): The signal that is captured does not correspond to a single transition of OH^*, but rather to a combination of several transitions. It is also not optimal from a signal to noise ratio standpoint since the ≈ 15 nm-wide peak associated with OH^* is not necessarily captured in its entirety. Using their spectrally resolved data, Kojima et al. (2000) show that the emission at slightly different wavelengths associated with the different transitions of OH^* behave in the same manner when their dependence to flame parameter are compared. García-Armingol et al. (2013) warn of the dependence of quantitative chemiluminescence measurements to the spectral filter used. They show that some pitfalls can be avoided if calibration and measurements are carried out with the same optical filter set-up.

In the present case, the impact of these two sources of bias can be assessed using the data acquired with the spectrometer.

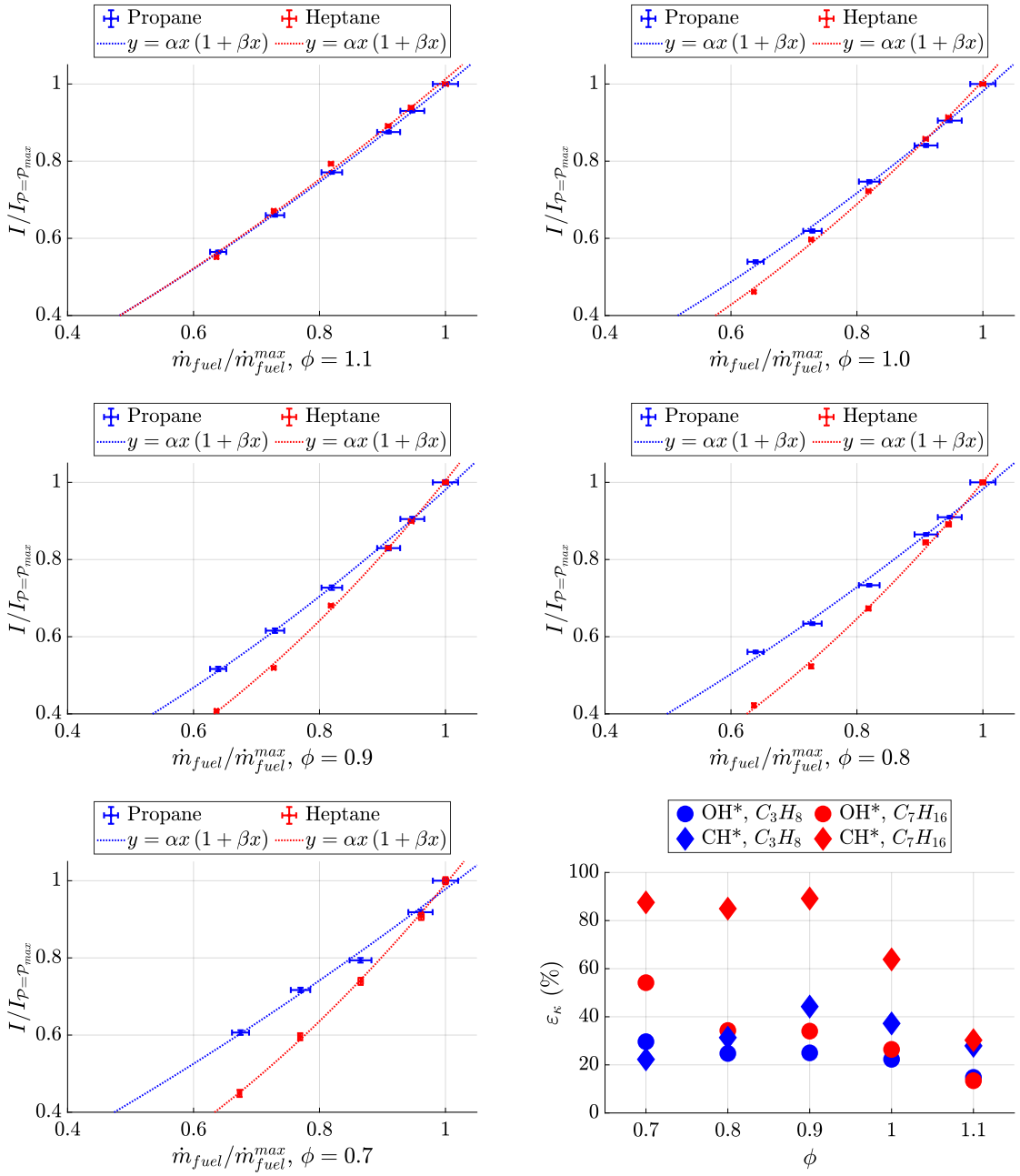

Figure 2.6: *CH* chemiluminescence intensity plotted against the fuel mass flow rate for several equivalence ratios (decreasing from left to right and top to bottom). Both are normalized by their respective values at the highest thermal power. For swirler 716, two fuels are considered: propane premixed with air, and heptane injected as a hollow cone spray. The last subfigure shows the value of the nonlinearity estimator ε_κ for the two fuels and different equivalence ratios. Values obtained for OH* chemiluminescence (Fig. 2.4) are repeated in this last plot for convenience.*

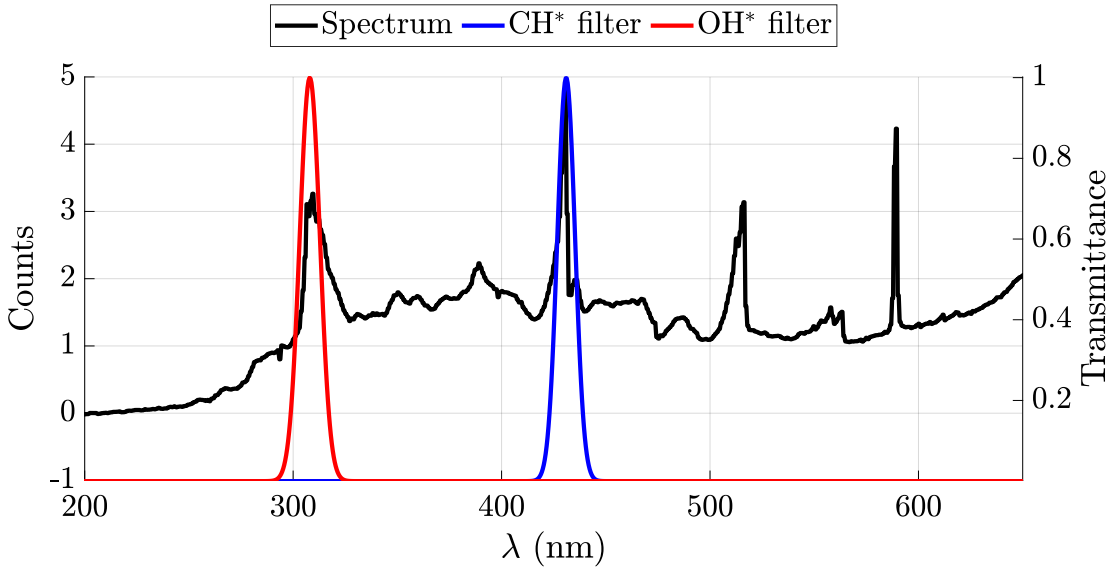

Figure 2.7: *Flame emission spectrum (heptane, $\phi = 0.9$) on which is superimposed the transmittance of the optical bandpass filters used on the photomultipliers. The wavelengths corresponding to the peak emission of the radical species are shown as well.*

It is achieved by integrating the emission spectra $\mathcal{S}(\lambda)$ to account for these non-ideal effects. Figure 2.7 shows, superimposed on a flame emission spectrum, the transmittance $T_{\mathrm{OH}^*}(\lambda)$ and $T_{\mathrm{CH}^*}(\lambda)$ of the bandpass filters used in the collection optics. To evaluate non-ideal effects in the photomultiplier setup, the emission spectra of the propane flames are measured at different equivalence ratios, and for a range of fuel flowrates. A simple polynomial interpolation is used to model $\mathcal{S}_{\mathrm{CO}_2^*}$, the baseline CO_2^* emission, in the manner of Lauer et al. (2011). The spectra are post-processed to obtain:

- A peak value: $\mathcal{S}(\lambda = 308\,\mathrm{nm})$.
- A peak without baseline: $\mathcal{S}(\lambda = 308\,\mathrm{nm}) - \mathcal{S}_{\mathrm{CO}_2^*}(\lambda = 308\,\mathrm{nm})$.
- Simulated filtered signal: $\int \mathcal{S}(\lambda) T_{\mathrm{OH}^*}(\lambda) d\lambda$.
- Simulated filtered signal without baseline: $\int \left(\mathcal{S}(\lambda) - \mathcal{S}(\lambda)_{\mathrm{CO}_2^*}\right) T_{\mathrm{OH}^*}(\lambda) d\lambda$.
- Photomultiplier signal for reference.

These quantities are naturally normalized by their respective value at the operating point with the highest fuel flow rate for their comparison. The same process naturally extends to CH^* emission, and the results are plotted in Fig. 2.8. In Fig. 2.8, these transmittance characteristics are used to integrate the flame spectra and evaluate the different non-ideal effects in the optical collection system. It is found that OH^* chemiluminescence is quite insensitive to imperfections in the collection system. The effects are more perceptible for CH^* chemiluminescence, especially at $\phi = 0.7$.

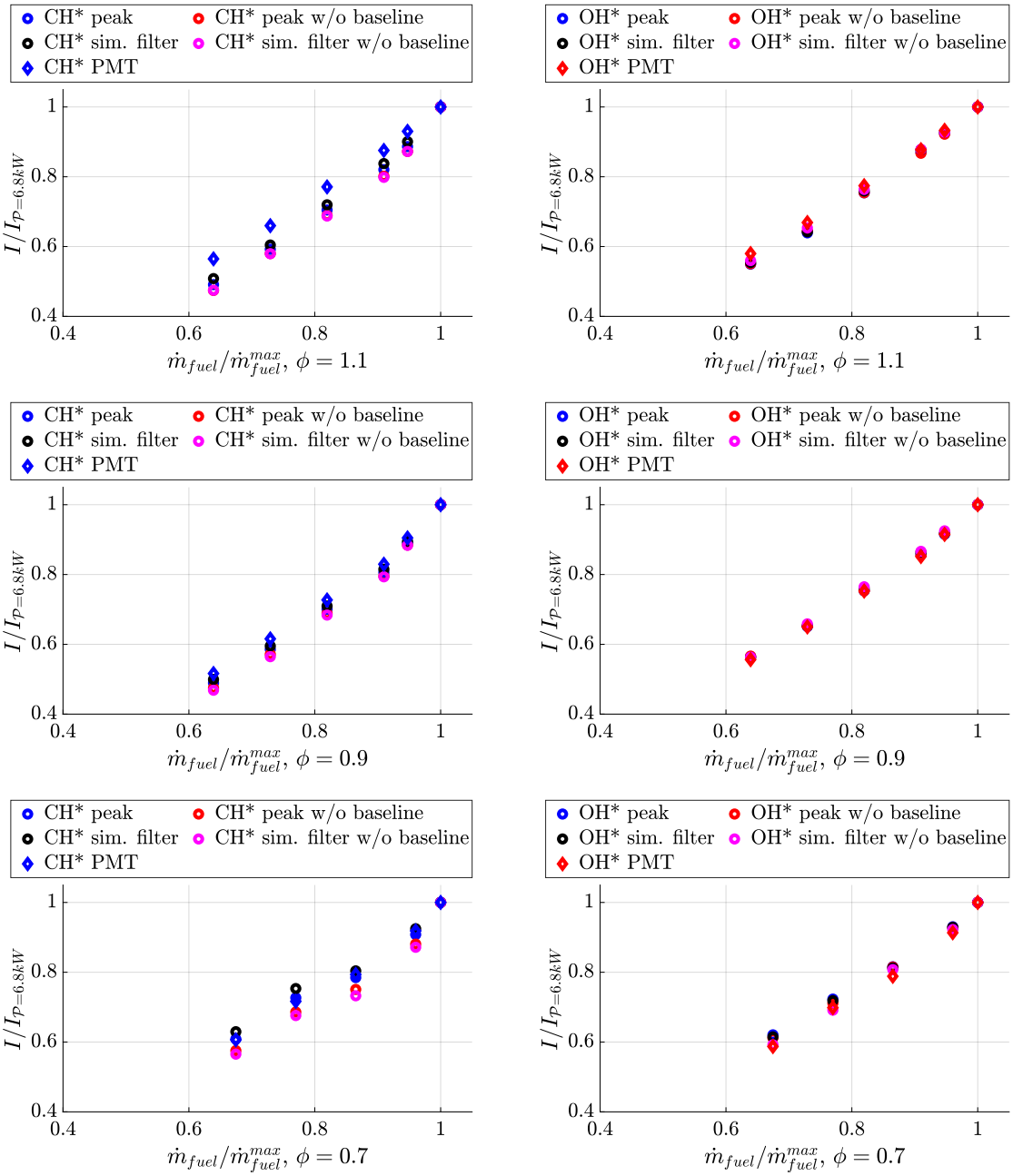

Figure 2.8: *Comparison of photomultiplier signals and reconstructed photomultiplier signals accounting for non-ideal effects. Propane flame.*

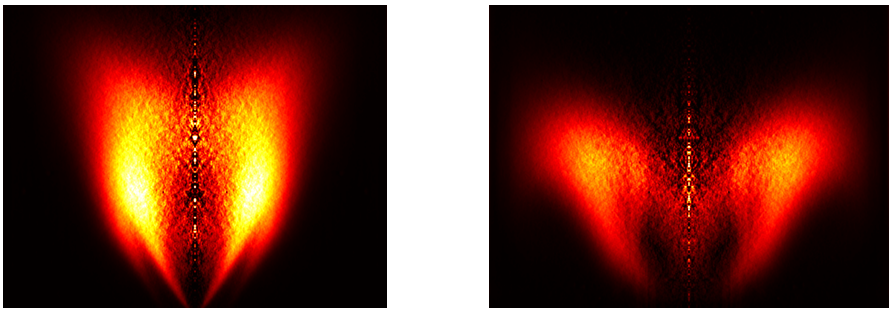

(a) *Swirler 707.* **(b)** *Swirler 716.*

Figure 2.9: *Comparison of chemiluminescence images between a flame formed by swirler 707 and 716. Burner operated with liquid heptane at a fuel flow rate of* $520\,\mathrm{g\,h^{-1}}$ *and an equivalence ratio of 0.85. An Abel-transform is used for easier visualization.*

2.5 Application to a different flame

In this section, the analysis is limited to liquid heptane injection. It is first interesting to examine flame shapes corresponding to the 716 and 707 swirlers (Figure 2.9). The Abel-transformed chemiluminescence images pertain to the same operating point in terms of heptane flow rate ($520\,\mathrm{g\,h^{-1}}$) and global equivalence ratio (0.85). The shapes of the flames formed by the two swirlers are quite different: while swirler 716 forms a fairly wide "M"-shaped flame, the flame formed by swirler 707 is narrower and closed like a "bowl". It is then natural to pursue the analysis by comparing results obtained for these very different flames formed by these two swirlers.

Chemiluminescence from OH^* is compared in Fig. 2.10, for the flames formed by swirler 707 and 716. The same general conclusion can be drawn for both injection system: I_{OH^*} is not excatly proportional to the integrated heat release rate. However, for a given global equivalence ratio, the level of nonlinearity can be significantly different for the two injection systems.

2.6 Discussion

The present chapter is focused on the practical applicability of flame chemiluminescence in the estimation of heat release rate in SICCA-Spray. Based on flue gas composition measurements, it is shown that the combustion efficiency of the system is close to unity, indicating that the heat release rate integrated over the volume of the flame is proportional to the fuel mass flow rate. A quasi-steady approach is employed, where the chemiluminescence signal of several flames operated at different thermal powers, but identical global equivalence ratios, are recorded. The relationship between the chemiluminescence signals and the thermal power is modeled using a quadratic equation in the form of $I = \alpha\dot{Q}(1 + \beta\dot{Q})$. The focus is now solely placed on OH^* chemiluminescence because its radiation in the near UV is less sensitive to parasitic light and because it was shown to be closer to a linear dependance on the heat release rate and less sensitive to imperfections in the optical collection system and its optical filter.

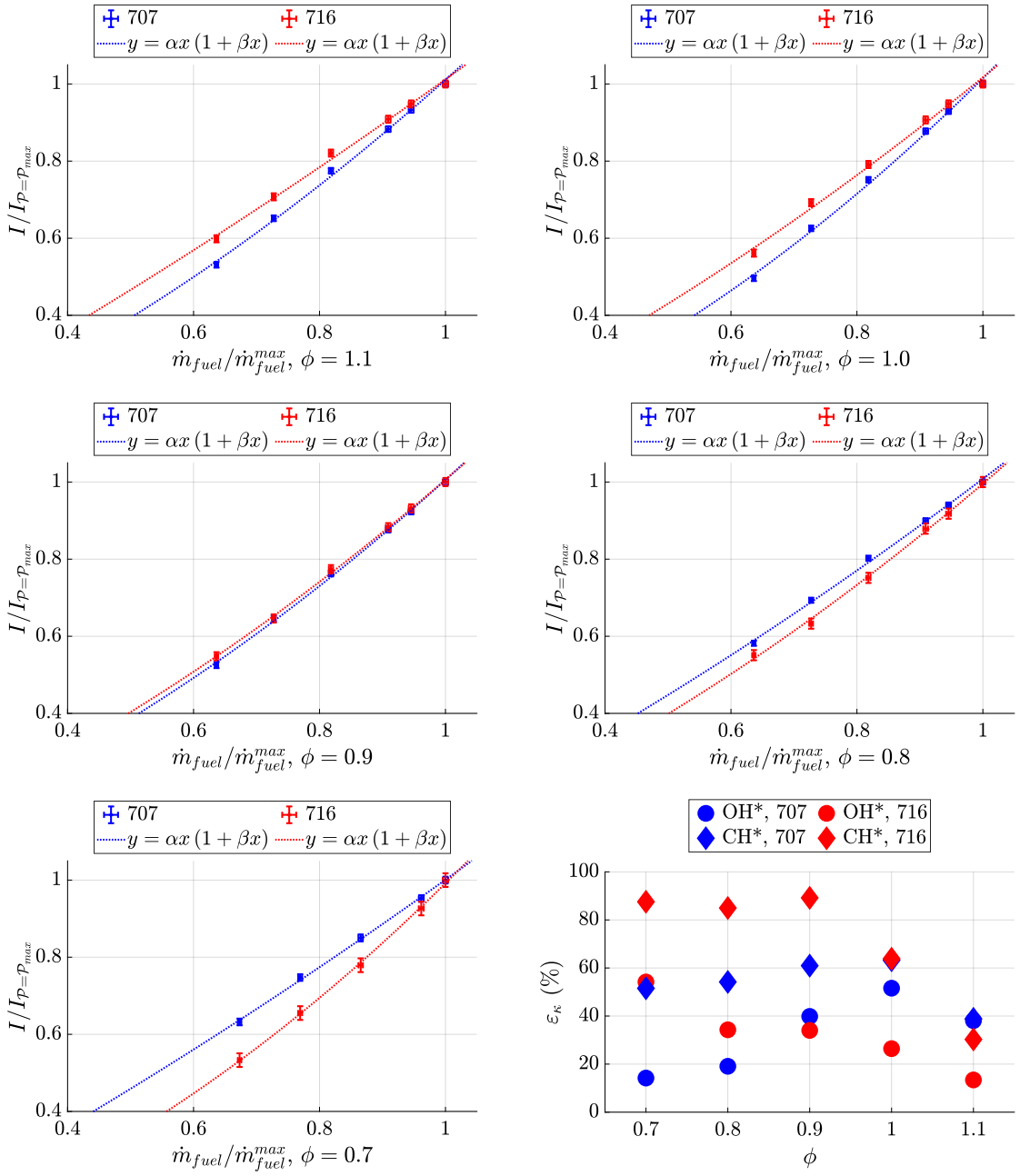

Figure 2.10: *OH* chemiluminescence signal plotted against the fuel mass flow rate for several equivalence ratios (decreasing from left to right and from top to bottom). Both are normalized by their respective values at the highest thermal power. The fuel is heptane, injected as a hollow cone spray. Swirlers 707 and 716 are compared. The last subfigure shows the values of the nonlinearity estimator ε_κ for the two swirlers and different equivalence ratios.*

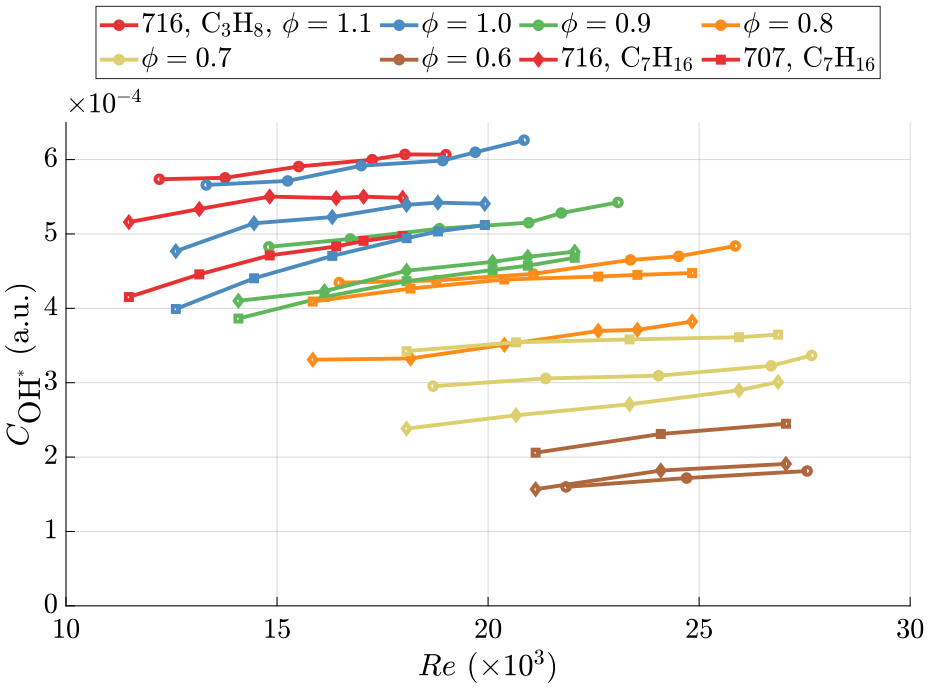

Figure 2.11: *Correlation coefficient of the integrated OH* chemiluminescence to the thermal power, plotted against the Reynolds number. Represented for two injection systems, and two fuel and injection conditions (symbols). The global equivalence ratio is shown in color.*

The literature review presented at the beginning of the present chapter indicates that three factors may lead to non-linearities in the chemiluminescence/heat release rate relation for perfectly premixed turbulent flames:

1. Turbulence: in highly turbulent regions, unsteady strain rates and flame curvatures affect the chemical pathways of the flame and may lead to deviation from linearity (Lee and Santavicca (2003); Lauer et al. (2011));
2. Preheating and mixing: mixing of fresh reactants with burnt products lead to changes in the composition and initial temperature of unburnt gases before combustion, which might strongly affect chemiluminescence (García-Armingol et al. (2014)).
3. In technically premixed flames, or in SICCA-Spray, which operates close to a lean premixed regime, the equivalence ratio and its inhomogeneities also affect flame chemiluminescence (Peterleithner et al. (2016)).

To investigate the first point, it is natural to study the dependency of the flame chemiluminescence to the Reynolds number at fixed equivalence ratios. In what follows, the Reynolds number is based on the bulk cold flow injection velocity $\mathrm{Re} = (\rho R_{inj} u_b)/\mu$ and the correlation coefficient C_{OH^*} is the ratio of the integrated OH^* chemiluminescence signal (taken as the photomultiplier signal) to the thermal power of the operating point. A constant value of the coefficient indicates proportionality between the two quantities.

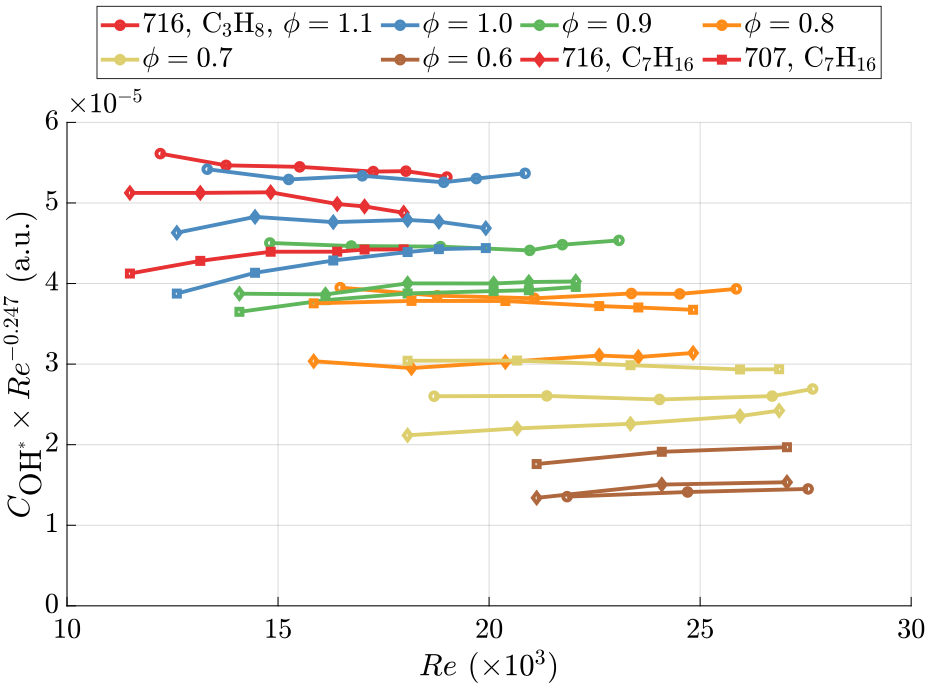

Figure 2.12: *Correlation coefficient of the integrated OH* chemiluminescence to the thermal power corrected by $Re^{0.25}$ and plotted against the Reynolds number. Represented for two injection systems, and two fuel and injection conditions. The global equivalence ratio is shown by the symbols colors.*

Figure 2.11 displays C_{OH^*} at all operating points presented in this chapter, corresponding to six global equivalence ratios, six thermal powers and two injection systems (707 and 716). Additionally, for swirler 716, two injection conditions (perfectly premixed propane air and spray of heptane) are investigated. For a given combination of equivalence ratio, injection system and fuel, C_{OH^*} increases monotonically with the thermal power and the Reynolds number and it appears from Fig. 2.12 that C_{OH^*} scales as $\mathrm{Re}^{0.247}$, except for liquid fuel operation in the rich or near stoichiometric regime. The value of 0.247 ± 0.05 for the exponent is obtained by fitting the surface $z = f(\phi)\mathrm{Re}^p$ to all available data points for each swirler and fuel type. This might indicate that turbulence is the main factor controlling the deviation from linearity.

Having established that the level of nonlinearity is most likely controlled by turbulence one may tentatively conclude on the applicability of a quasi-steady hypothesis concerning flame chemiluminescence in SICCA-Spray. The review of the literature and the analysis carried out in this chapter indicate that there is no experimental alternative that will allow the determination of the integrated heat release rate. It is reasonable to use the quasi-steady assumption to establish the relation between the chemiluminescence signal delivered by the photomultiplier and the integrated heat release rate. This relation is nonlinear but the nonlinearity is quite manageable and the relationship may be used to derive a corrected heat release rate signal from the measured emission intensity.

2.7 Conclusion

The relationship between integrated flame chemiluminescence and heat release rate is investigated in SICCA-Spray by employing a quasi-steady approach. After ensuring that the combustion efficiency is close to unity, systematic measurements are carried out for different injectors and two injection conditions: a liquid heptane spray, and a perfect premixture of propane and air. OH^* appears to be a better radical than CH^* for such measurements because it features a lesser deviation from linearity, and a reduced sensitivity to parasitic light. It is found that for both injection conditions (heptane as a spray and premixed propane-air), the chemiluminescence signal is not quite proportional to the heat release rate. A quadratic fitting method is thus established to correlate flame chemiluminescence and heat release rate. The consequence of the quadratic nature of the relationship between these two variables is a bias in the estimation of heat release rate fluctuations from experimental data. In the quasi-steady framework, this can be quantified, and one finds that the fluctuations may be overestimated by approximately 20% to 40 % in typical conditions. Finally, the physical mechanism causing the nonlinear behavior of the chemiluminescence signal is examined by first reviewing the existing literature, and correlating chemiluminescence, heat release rate and Reynolds number. Given the specifics of the flow and flame in SICCA-Spray, it is reasonable to assume that the relation between chemiluminescence and heat release rate obtained in quasi-steady experiments can be used to calibrate measurements pertaining to the unsteady combustion process appearing under unstable operation, and thus obtain a better estimate of heat release rate fluctuations.

Part II

Steady flow characterization of spray swirl injectors

Chapter 3

A database of fully characterized swirl injectors that can be used in a single sector and in an annular combustor

It is well known that the injection system plays a major role and in particular determines to a large extent many of the properties of the combustion process. This may be investigated by considering a set of injectors with different swirlers and examining the characteristics of the flow and spray under steady conditions and in a second stage exploring the dynamical properties of these units to identify parameters that favor the development of unstable oscillations. This chapter is focused on the steady state characteristics under cold flow conditions. After an overview of the set of swirlers, the analysis is focused on the flow and spray structures corresponding to three swirlers. Numerical modeling is used to complement experimental data and interpret specific features.

Contents

Section 3.4 of the present chapter has been accepted for presentation at the 2020 ASME TurboExpo as "A joint experimental and LES characterization of the liquid fuel spray in a swirl injector" by Guillaume Vignat, Preethi Rajendram Soundararajan, Daniel Durox, Aymeric Vié, Antoine Renaud and Sébastien Candel (GT2020-14935).

3.1 Introduction

A number of injection unit has been designed for systematic testing in the annular combustor MICCA-Spray and in the single sector system SICCA-Spray. The objective is to identify parameters that favor the developement of instabilities. The first step in a parametric study on injection systems is to characterize these units under steady operation. Results of this characterization carried out in SICCA-Spray are described in what follows.

An overview of the MICCA-Spray injection units is first presented. Fourteen swirlers are tested and their swirl number and head loss are determined (Section 3.2). Section 3.3 is focused on a subset of injectors, namely swirlers 707, 712 and 716. A combination of experimental measurements and high fidelity simulations are used to investigate relevant features of the flow: the precessing vortex core (PVC), the effect of confinement on the flow pattern and head loss. The spray of liquid fuel is then investigated under non reactive conditions in Section 3.4 for the same subset of swirlers (707, 712 and 716). Measurements are used to study the impact of the swirler design on the azimuthal distribution of the spray. Numerical modeling of the flow and spray injection conditions and spray-wall interaction are validated, and used to interpret features of the spray observed experimentally.

3.2 Overview of MICCA-Spray injector variants

The injector of MICCA-Spray is highly modular, and its modularity has been extensively used in this work and in that of Prieur (2017) to obtain desirable unstable behavior in the test rigs and study the impact of the injector on combustion dynamics. Figure 1.6 is repeated here to fix the ideas about the injector layout. The swirler (translucent teal) is changed by modifying the diameter of the channels (d_{sc}) in conjunction with the distance $R_{0,sc}$ separating the axis of two opposing channels. Changing these two dimensions allows to control the characteristics of the flow, which are mainly governed by the injector head loss and the swirl number.

These swirlers can be grouped in six generations:

(G 1): "TIMBER" swirler: this first generation of injector is introduced in Prieur et al. (2016) and Lancien et al. (2016). It is used in many studies and in particular in those concerned with ignition and blow out. However, MICCA-Spray equipped with this injection system is thermoacoustically stable.

(G 2): K swirler: designed during the thesis of Kevin Prieur, and first introduced in Prieur et al. (2018), this injection system is unstable in MICCA-Spray. It was decided to

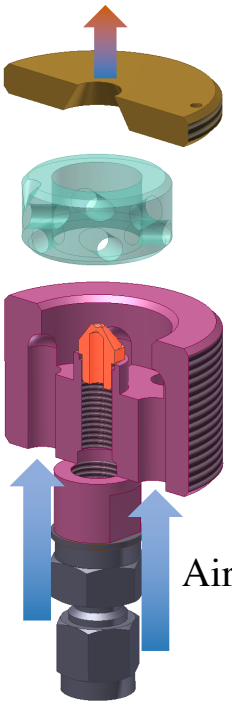

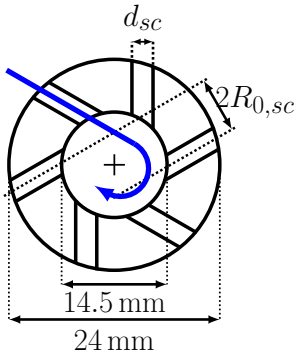

Figure 1.6: *Injector design. Left: exploded 3D view of the injection system and its components. Above: schematic cut of the swirler with key dimensions and nomenclature. (repeated from page 39)*

progressively phase-out this injection system due to manufacturing difficulties.

(G 3): 3D printed swirlers S_a to S_d: this generation is only used in Chapter 7, but served as the basis for the design of further swirler generations.

(G 4): 707 and 712 swirlers: these injection system are designed to present similar aerodynamic characteristics and in particular similar velocity profiles, but different head loss levels.

(G 5): 716 swirler: this injection system is the replacement of K swirler. Featuring a level of swirl similar to that of K swirler, and higher than those of 707 and 712, this injection system exhibits strong combustion instabilities in MICCA-Spray.

(G 6): 713 to 727 swirlers: these injection system are characterized here but will be part of planned future work in MICCA-Spray.

All of these swirlers will be briefly characterized in the present section. Further measurements pertaining to these swirlers are gathered in Appendix A. A detailed characterization of the flow (Section 3.3) and the spray (Section 3.4) is nonetheless presented for a small subset of injectors from the 4^{th} and 5^{th} generation swirlers. Table 3.1 synthesizes the results for all swirlers. Three air mass flow rates, corresponding to three commonly used operating conditions, are considered:

- $\dot{m} = 1.9\,\mathrm{m\,s^{-1}}$: this operating point is used in ignition studies in SICCA-Spray and the simulations thereof.
- $\dot{m} = 2.3\,\mathrm{m\,s^{-1}}$: this operating condition is used for many studies in SICCA-Spray involving third and fourth generation swirlers. It is in particular used for numerical simulations in this thesis.
- $\dot{m} = 2.6\,\mathrm{m\,s^{-1}}$: this operating point is used in the determination of the Flame Describing Function in Prieur et al. (2016); Prieur (2017). All swirlers have been

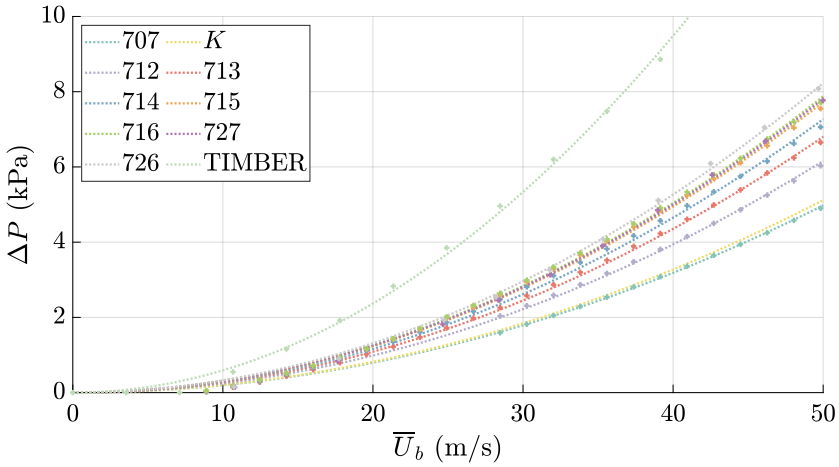

Figure 3.2: *Head loss characteristic measured for different swirlers in non reactive, unconfined conditions for different injector bulk velocity. The experimental points are shown with crosses, the quadratic correlation of Eq.* (3.1) *by the dotted lines. Injectors sorted by increasing level of head loss. See Fig. 7.5 for swirlers* $S_a - S_d$.

characterized at this operating point allowing comparisons between the different units.

The injector head loss is measured using a differential pressure sensor (see Section 1.2.4) placed between the plenum (hot wire position in SICCA-Spray) and the atmosphere. Measurements are carried out on an unconfined configuration by varying the air mass flow rate. Results are plotted in Fig. 3.2. It can be seen that the head loss is nicely correlated with the injector bulk velocity ($\overline{U}_b = \dot{m}/(\pi\rho R_{inj}^2)$) by the usual quadratic correlation

$$\Delta P = \frac{1}{2}\rho\sigma\overline{U}_b^2 \tag{3.1}$$

where σ is a dimensionless coefficient.

The three velocity components are also determined using Laser Doppler Velocimetry (LDV, see Section 1.2.7 for details on the setup) for all swirlers in unconfined conditions. The swirl number is calculated from these measurements. The conventional formulation S_{conv} (see Chapter 4 Eq. (4.30)) is useful as a reference as its use is widespread within the combustion community:

$$S_{conv} = \frac{\int_0^{2R_{inj}} \overline{U_\theta}\,\overline{U_x}\, r^2 dr}{R_{inj}\int_0^{2R_{inj}} \overline{U_x}^2 r dr} \tag{4.30 \textit{rep.}}$$

It is computed for all swirlers at a height of $x = 2.5\,\text{mm}$ above the backplane with an integration radius corresponding to twice the radius of the injector outlet. As discussed in Chapter 4, this formulation is less general and S_P^f should be preferred if possible. For MICCA-Spray injection systems, as for the MICCA injection system used in Chapter 4,

Table 3.1: *Synthesis of cold flow, unconfined characteristics for MICCA-Spray injectors. "Gen." designates the generation of swirler, TP the type of terminal plate employed (see Fig. 1.7), $\dot{m}$ the air mass flow rate, d_{sc} and $R_{0,sc}$ the dimensions specified in Fig. 1.6, S_{conv} the swirl number measured experimentally at $x = 2.5\,\mathrm{mm}$ near the backplane using Eq. (4.30), $S^f_{U,BL}$ the more universal swirl number discussed in Chapter 4 (Eq. (4.29)), σ the head loss coefficient of Eq. (3.1), ΔP the head loss of the injection system at the specified operating point, d_{10} and d_{32} an estimate for an overall mean and Sauter mean diameter of a non reactive, unconfined heptane spray (see Section 3.4).*

Swirler	Gen.	TP	$\dot{m}$	d_{sc}	$R_{0,sc}$	S_{conv}	S^f_U	σ	ΔP	d_{10}	d_{32}
-	-	-	$\mathrm{g\,s^{-1}}$	mm	mm	-	-	-	kPa	µm	µm
TIMBER	G1	TP1	1.9	3	5	0.77	-	9.68	6.1	10	21
			2.3			0.77	-		8.3	-	-
			2.6			0.76	-		10.8	-	-
K	G2	TP1	2.6	4.5	5	0.87	-	3.34	3.73	8	24
		TP2	2.3			0.68	-		2.86	-	-
			2.6			0.68	-		3.73	-	-
S_a	G3	TP1	2.6	2.9	2.3	0.65	-	4.3	4.87	-	-
S_b	G3	TP1	2.6	3.3	3.0	0.64	-	4.1	4.64	-	-
S_c	G3	TP1	2.6	3.6	3.5	0.64	-	3.7	4.19	-	-
S_d	G3	TP1	2.6	4.0	4.6	0.60	-	3.6	4.08	-	-
707	G4	TP2	2.3	4.0	4.6	0.60	2.4	3.25	2.81	10	26
			2.6			0.60	-		3.65	-	-
712	G4	TP2	2.3	3.0	2.3	0.60	2.5	3.5	3.4	12	29
			2.6			0.59	-		4.5	-	-

Table 3.1 *(cont.)*: *Synthesis of cold flow, unconfined characteristics for MICCA-Spray injectors.*

Swirler	Gen.	TP	$\dot{m}$	d_{sc}	$R_{0,sc}$	S_{conv}	S_U^f	σ	ΔP	d_{10}	d_{32}
-	-	-	$g\,s^{-1}$	mm	mm	-	-	-	kPa	µm	µm
716	G5	TP2	2.3	3.5	4.7	-	-	5.14	4.41	10	14
			2.6			0.70	-		5.74	8	15
713	G6	TP2	2.6	3.5	3.9	0.69	-	4.44	4.96	-	-
714	G6	TP2	2.6	3.5	4.1	0.70	-	4.75	5.30	-	-
715	G6	TP2	2.6	3.5	4.4	0.71	-	5.05	5.64	-	-
726	G6	TP2	2.6	3.5	5.5	0.74	2.8	5.37	6.00	-	-
727	G6	TP2	2.6	3.5	5.1	0.74	2.7	5.10	5.70	-	-

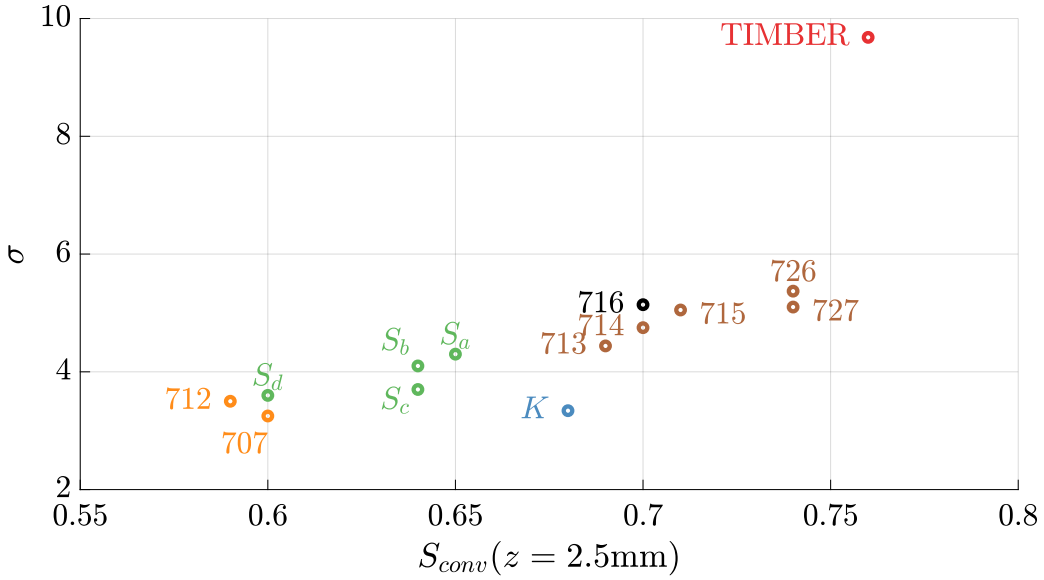

Figure 3.3: *Graphical representation for all swirlers of the swirl number* $S_{conv}(x = 2.5\,\text{mm})$ *measured at an air mass flow rate of* $\dot{m} = 2.6\,\text{g}\,\text{s}^{-1}$ *against the head loss coefficient* σ*. The swirlers are color-coded by generation.*

a good estimate of S_P^f can be obtained by employing the slightly simplified expression

$$S_{U,BL}^f = \frac{\int_0^\infty \rho \left(\overline{U_\theta}\,\overline{U_x} + \overline{u_\theta u_x}\right) r^2 dr}{R_{inj} \int_0^\infty \rho \left[\overline{U_x}^2 + \overline{u_x^2} - \frac{1}{2}\left(\overline{U_\theta}^2 + \overline{u_r^2} + \overline{u_\theta^2}\right)\right] r dr} \qquad (4.43\ \textit{rep.})$$

calculated at $x = 10\,\text{mm}$ above the backplane of the combustor in unconfined conditions. At this position, the quality of the LDV measurement is high, and it was found from both detailed LDV measurements and LES of several swirlers that the axial gradient of $\overline{u_x u_r}$ found in the general expression S_U^f (Chapter 4 Eq. (4.29)) could be neglected. Unfortunately, the required measurements could not be performed for all swirlers and operating conditions. Those for which it is available are reported in Tab. 3.1.

In addition to the data presented in Tab. 3.1, the different swirlers may be compared using the synthetic graphical representation displayed in Fig. 3.3 where their head loss are plotted as a function of their swirl number. This representation nicely shows the variety of injector characteristics that may be achieved in the MICCA-Spray test rig, with the ability to vary the head loss coefficient by a factor of four, and the swirl number between 0.57 and 0.77.

Comparing integrated values such as the swirl number is useful, but a direct comparison of the velocity profiles of different swirlers is also necessary. This is performed in Fig. 3.4 for swirlers "TIMBER", K, 707 and 716 which are the most widely tested in the present investigation. When comparing the axial velocity profiles of swirlers "TIMBER", K and 716, it is observed that an increasing level of swirl yields a broader inner recirculation

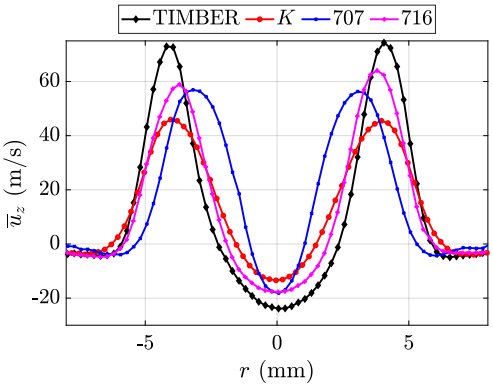

(a) *Mean axial velocity* $\overline{U_x}$.

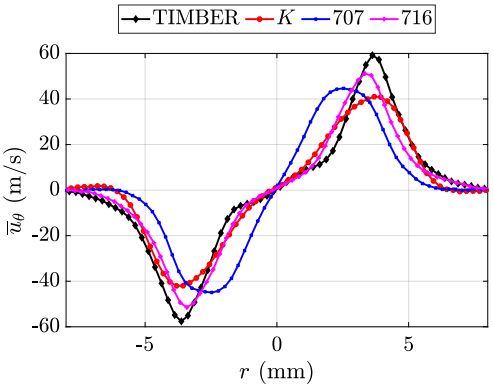

(b) *Mean tangential velocity* $\overline{U_\theta}$.

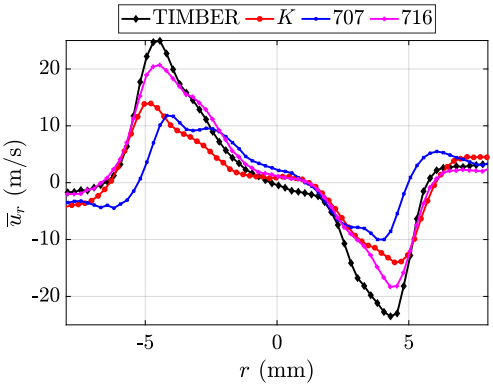

(c) *Mean radial velocity* $\overline{U_r}$.

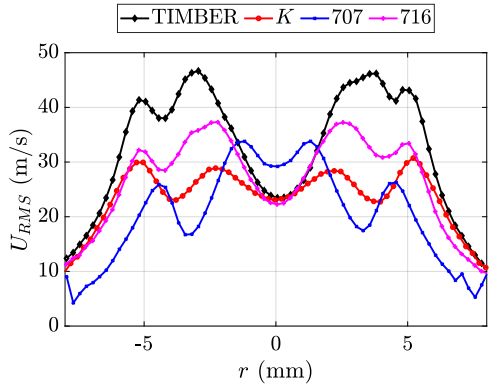

(d) *Mean turbulent velocity* $\left(\overline{u_x^2} + \overline{u_\theta^2} + \overline{u_r^2}\right)^{0.5}$.

Figure 3.4: *Mean velocity profiles measured* $x = 2.5\,\mathrm{mm}$ *above the backplane of the injector for swirlers TIMBER, K, 707 and 716 with an air mass flow rate of* $\dot{m} = 2.6\,\mathrm{g\,s^{-1}}$.

Table 3.2: *Experimentally measured and LES predicted injector head loss ΔP. Determined in unconfined cold flow conditions at an air mass flow rate of $\dot{m}_{air} = 2.26\,\mathrm{g\,s^{-1}}$, and measured between the position of the hot wire in the plenum and the atmosphere.*

Injector	ΔP (experimental) kPa	ΔP (LES) kPa
707	2.81	3.44
712	3.48	4.76

zone with augmented negative velocities on the centerline, and that the maximum of the axial velocity is also larger for higher swirl numbers. The velocity profiles are different, but their shape is quite similar. Considering the tangential velocity, again, the profiles for swirlers "TIMBER", K and 716 are quite similar: the central part of the flow ($r < 2\,\mathrm{mm}$) is in solid body rotation at the same rotation rate of $7.5\,\mathrm{ms^{-1}}$. In the outer regions of the flow, the maximum of the tangential velocity increases with higher swirl numbers. Naturally, higher levels of swirl are associated with higher levels of shear in the inner and outer shear layers of the swirling jet, which translates into higher levels of turbulent fluctuations in these regions. The velocity profiles of swirler 707 differ significantly from other profiles plotted in Fig. 3.4. In particular, the flow is also in solid body rotation for $r < 2\,\mathrm{mm}$, but the rotation rate is significantly higher at $22\,\mathrm{ms^{-1}}$, and no inflexion point is found around $r = 2\,\mathrm{mm}$ in the tangential velocity profiles. Instead, at the radial distance $r = 2\,\mathrm{mm}$, the tangential velocity reaches its maximum value. Although swirler 707's swirl number is smaller than that of swirler K, its axial velocity on the centerline is higher. But the size of its recirculation zone is also much smaller. One may tentatively conclude that the flow regimes will be different for swirler 707 and for the other three swirlers.

3.3 Detailed flow analysis for a subset of injectors

The focus is now placed on injectors 707, 712 and 716, which are predominantly used in this thesis. This section is focused on their steady state cold flow characterization. Numerical twins obtained by LES for swirlers 707 and 712 are validated against experimental data in Section 3.3.1. The effect of the confinement is investigated numerically in Section 3.3.2. Finally, to complement the experimental data presented in the previous section, the PVC is characterized.

3.3.1 Validation of numerical twins for swirler 707 and 712

In order to examine in details the dynamics of the flow and the flame, especially in region inaccessible using laser techniques (such as inside injector), numerical twins have been constructed for SICCA-Spray, equipped with 4^{th} generation injection system: swirler 707 and 712. These two injection system are specifically selected for their nearly identical velocity profiles. The parameters of the solver is described in details in Section 1.4.1, and are not repeated here.

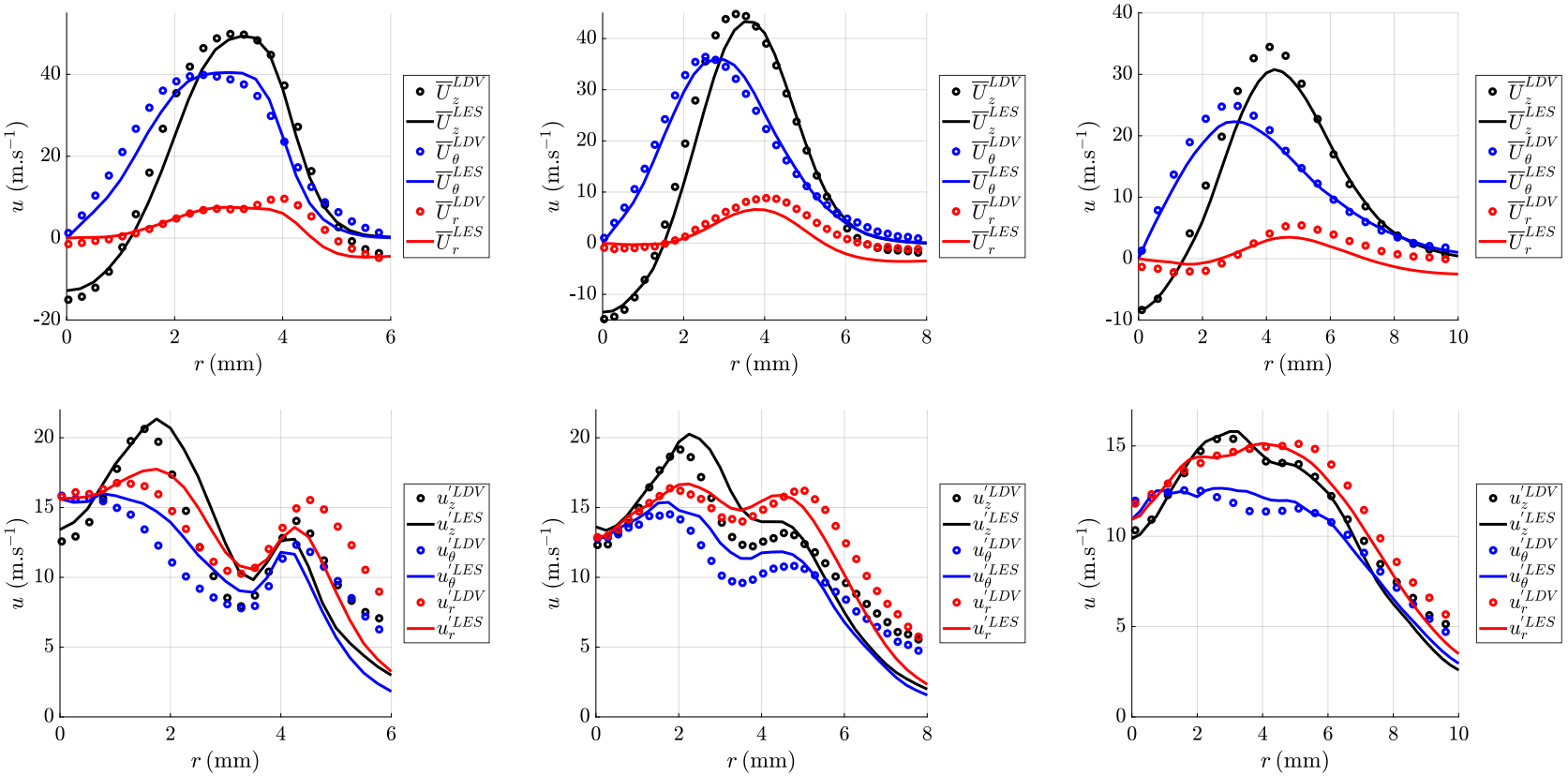

(a) $z = 2.5\,\text{mm}$ **(b)** $z = 5\,\text{mm}$ **(c)** $z = 10\,\text{mm}$

Figure 3.5: *Comparison of mean (top) and RMS (bottom) velocity profiles measured at three different heights above the backplane. LES results as a continuous line, LDV as circle markers. Swirler 707 in unconfined, non-reactive conditions with an air mass flow rate of* $\dot{m}_{air} = 2.26\,\text{g}\,\text{s}^{-1}$.

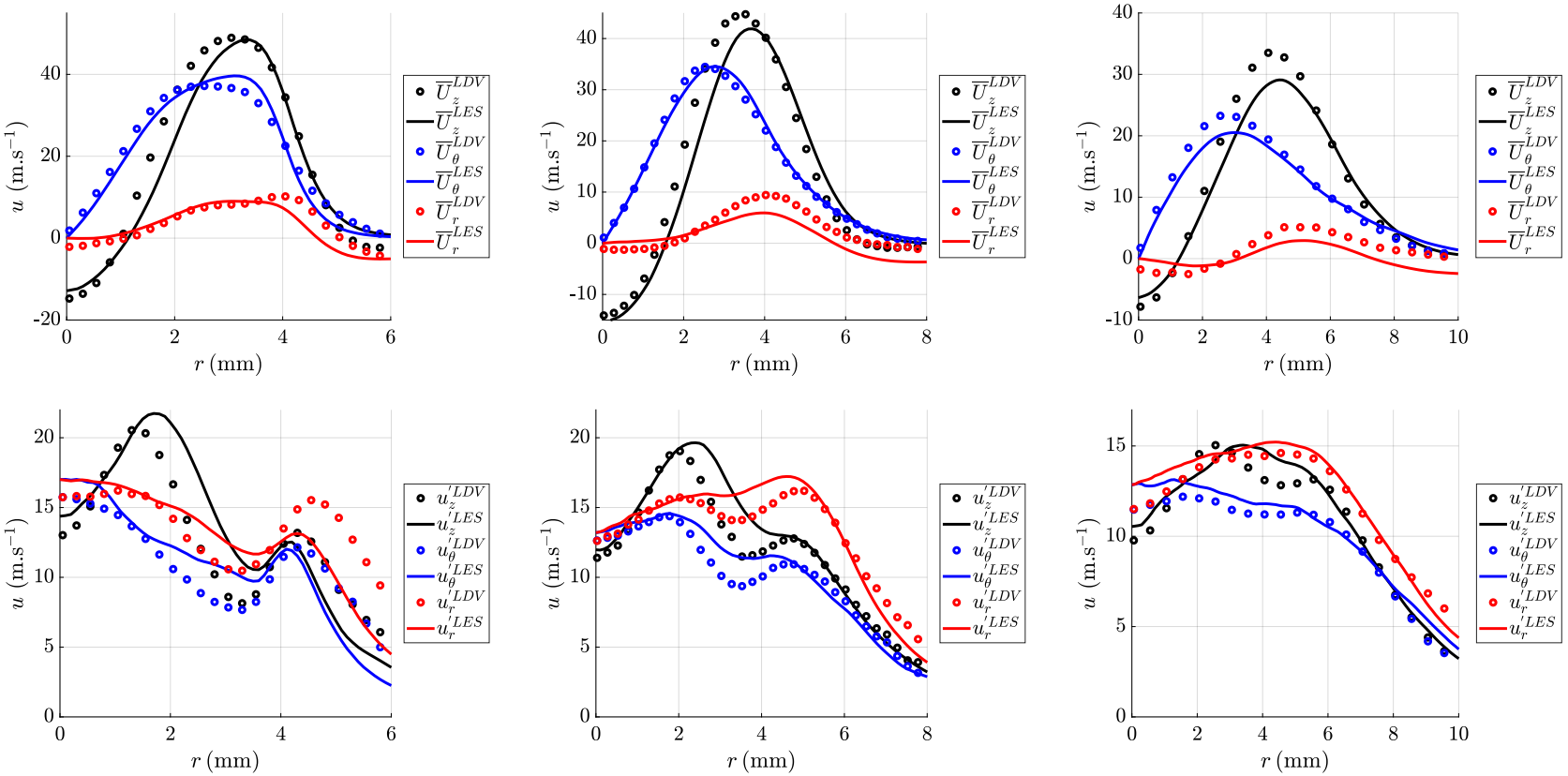

(a) $z = 2.5\,\mathrm{mm}$ **(b)** $z = 5\,\mathrm{mm}$ **(c)** $z = 10\,\mathrm{mm}$

Figure 3.6: *Comparison of mean (top) and RMS (bottom) velocity profiles measured at three different heights above the backplane. LES results as a continuous line, LDV as circle markers. Swirler 712 in unconfined, non-reactive conditions with an air mass flow rate of* $\dot{m}_{air} = 2.26\,\mathrm{g\,s^{-1}}$.

To begin the validation process, the reader is reminded that results presented in the present section are obtained after two steps of adaptive mesh refinement based on the $LIKE$ criterion (see Section 1.4.1). Mesh convergence was ensured by checking that an additional step of adaptive mesh refinement did not improve significantly the prediction of the injector head loss nor modify the predicted velocity profiles in a significant manner. In Fig. 3.5 (for swirler 707) and Fig. 3.6 (for swirler 712), the experimentally measured and numerically determined velocity profiles are compared. The agreement between the experiment and simulation is quite good at all measurement height and for all components. It can also be observed that the velocity profiles of swirlers 707 and 712 are very similar, which was the objective of their design. Tab. 3.2 reports the experimentally measured, and numerically predicted values of the injector head loss. As is often the case for complex swirled injectors with high velocities, the head loss is slightly over-predicted in the simulations, by 22% for swirler 707 and 35% for swirler 712. It has been checked that the combination of subgrid scale turbulence model (Sigma model, Baya Toda et al. (2010)) and wall model (logarithmic law of the wall, Jaegle et al. (2010)) provides the best possible prediction among all models for both the injector head loss and velocity profiles.

3.3.2 Effect of confinement on swirling flow

It is well known in the literature on swirling flows that confinement can strongly affect the topology of the velocity field. A number of work have demonstrated the impact of the combustor outlet condition on the injector near-field: Escudier and Keller (1985); Altgeld et al. (1983) demonstrated it in non-reactive conditions for subcritical swirling flows[1]. Li and Gutmark (2005); Terhaar et al. (2012) made a similar observation under reactive conditions. Fu et al. (2005) conducted a systematic study on this phenomenon by placing a swirling injector in a confinement with a square cross-section. The width of the cross-section was systematically varied with ratios of confinement size to injector outlet diameter varying from 1.8 to 3.6. An unconfined case was also investigated. A two-component LDV system was used to measure the velocity in the non-reactive flow. Although the velocity in the near-field of the outlet of the injector appeared unaffected by the size of the confinement, the downstream flow-field is very sensitive to this parameter. In particular, two main regimes can be distinguished: with a small confinement, the swirling jet is wall-bound, the inner recirculation zone is very large, occupies most of the confinement and extends far downstream. With a larger confinement, the swirling jet behaves similarly to the free, unconfined jet. The inner recirculation zone forms a bubble that closes up rapidly, and fairly large outer recirculation zones are present on the sides of the jet. The study of Fanaca et al. (2010) is concerned with the same question, but focuses on the difference between a single sector and an annular rig. The authors suggest a model based on mass and momentum budgets to determine the confinement size at which the swirling flow transitions from the free jet to the wall bound regime depending on the shape of the confinement. Their model accounts for the effect of induced

[1]Flows where perturbations can be convected upstream, typically flows featuring an inner recirculation zone extending up to the outlet.

azimuthal flow in annular combustor, and was used to select the size of the confinement tube in SICCA-Spray.

In the present subsection, the result of numerical simulations are presented for four configurations: with swirlers 707 and 712 in SICCA-Spray in unconfined and confined conditions. For the confined cases, the usual confinement of inner diameter 69 mm is used. The pressure, as well as the axial, tangential and radial velocity profiles at different heights are gathered in Fig. 3.8 for comparison. Injectors 707 and 712 were designed to have identical velocity profiles as measured by LDV in unconfined conditionned. At $z = 2.5\,\mathrm{mm}$, the profiles in these four configurations are remarkably similar, with a slightly higher radial velocity for swirler 712 compared to swirler 707. In the confined case, the flow is additionally in solid body rotation in the outer recirculation zone, which is not the case in unconfined conditions. At $z = 10\,\mathrm{mm}$, as could be expected the profiles differ between unconfined and confined conditions. One observes that the swirling jet is opening faster with the confinement. However, the profiles obtained with swirlers 707 and 712 remain remarkably similar for each confinement type. At $z = 20\,\mathrm{mm}$, what was observed at $z = 10\,\mathrm{mm}$ is confirmed: the flow obtained with swirlers 707 and 712 are quite similar, but the swirling jets opens much more readily in confined conditions. The topology of the flow in these four configurations is additionally shown in Fig. 3.9, with a blue to yellow colormap for the time averaged axial velocity, and white isocontours at $\overline{U_x} = 0$. The following conclusions can be drawn:

- In unconfined conditions, the swirling flow is a free jet, with an inner recirculation bubble that closes approximately $2R_{inj}$ downstream of the outlet.
- In confined conditions, the swirling jet is wall-bound and the inner recirculation extends up to the outlet of the confinement tube.
- Swirler 707 and 712 have been designed to have very similar velocity profiles in unconfined conditions.
- This property extends to confined conditions.

3.3.3 Precessing Vortex Core: characterization and mode intermittency

The PVC is an global hydrodynamic instability commonly found in strongly swirling flow. It consists in an helically shaped vortex precessing around the axis of the injector. As a review on this topic is presented at the beginning of Chapter 5, the reader is referred to this chapter for a more in-depth discussion of this phenomenon, its apparition and its significance for combustion dynamics. In the present section, the focus is placed on comparing the PVC observed with swirlers 707, 712 and 716.

The experiments are also conducted on the unconfined version of SICCA-Spray. A constant temperature anemometer is placed at the outlet of the injector, $z = 2.5\,\mathrm{mm}$ above the backplane, at a radial position of $r/R_{inj} = 0.75$. The operating conditions correspond to an air mass flow rate of $2.26\,\mathrm{g\,s^{-1}}$ and a bulk velocity of $37\,\mathrm{m\,s^{-1}}$. The power spectral density of the axial velocity measured by the hot wire are plotted in Fig. 3.7 for swirlers 707, 712 and 716. The Strouhal number based on the bulk velocity can be calculated

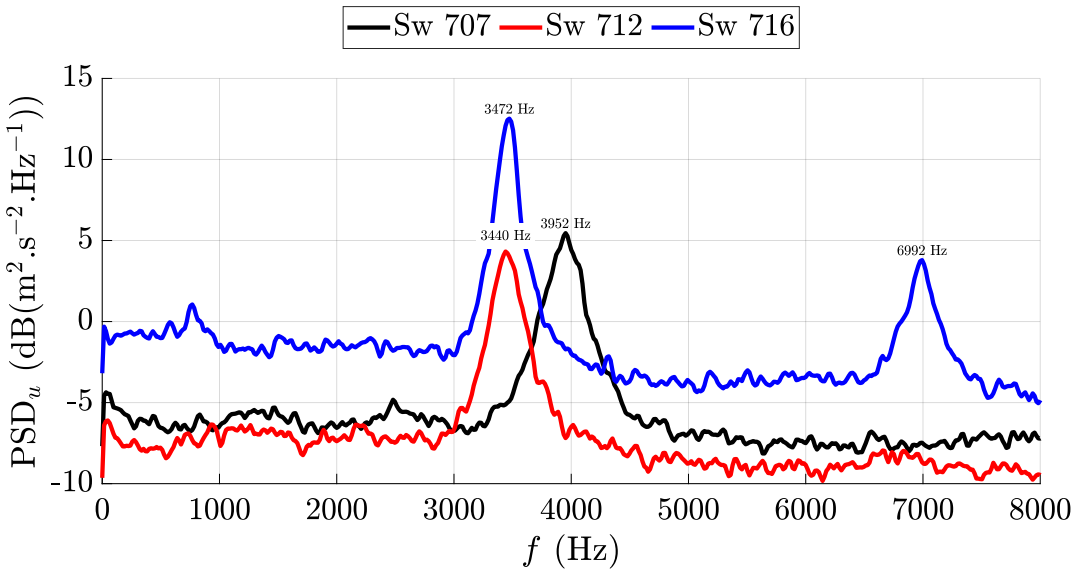

Figure 3.7: *Power spectral density of the axial velocity measured using constant temperature anemometry at the outlet of the injector ($z = 2.5\,\mathrm{mm}$, $r/R_{inj} = 0.75$) for swirlers 707, 712 and 716 at an air mass flow rate of $2.26\,\mathrm{g\,s^{-1}}$, corresponding to a bulk velocity of $37\,\mathrm{m\,s^{-1}}$.*

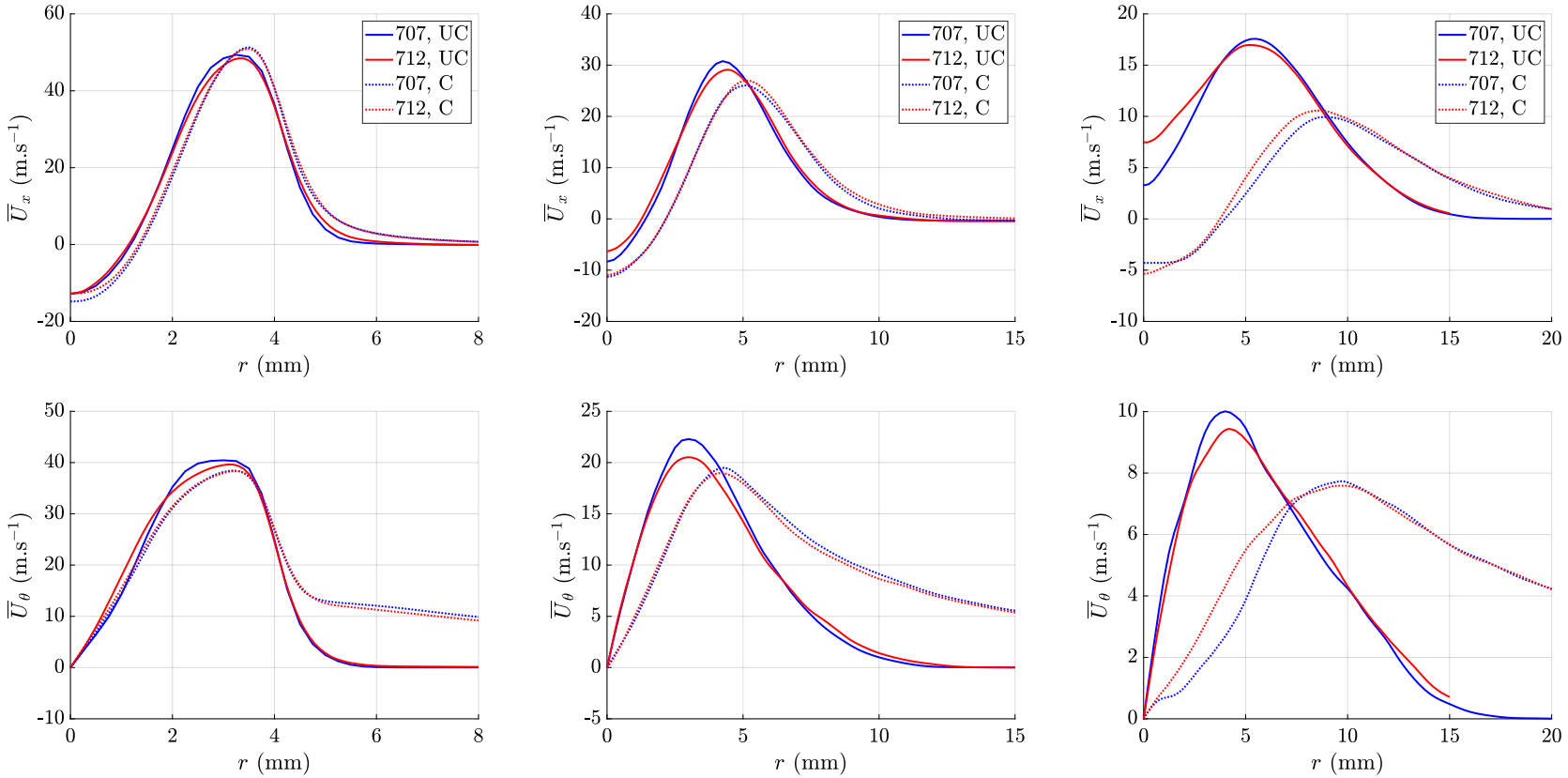

(a) $z = 2.5\,\mathrm{mm}$ **(b)** $z = 10\,\mathrm{mm}$ **(c)** $z = 20\,\mathrm{mm}$

Figure 3.8: *Comparison of the mean axial (top) and tangential (bottom) velocity profiles from the LES simulations at three different heights above the backplane for swirler 707 (blue) and 712 (red) in unconfined (UC, continuous lines) and confined conditions(C, dotted lines, $d_q = 69\,\mathrm{mm}$). Air mass flow rate of $\dot{m}_{air} = 2.26\,\mathrm{g\,s^{-1}}$.* *Continued on next page.*

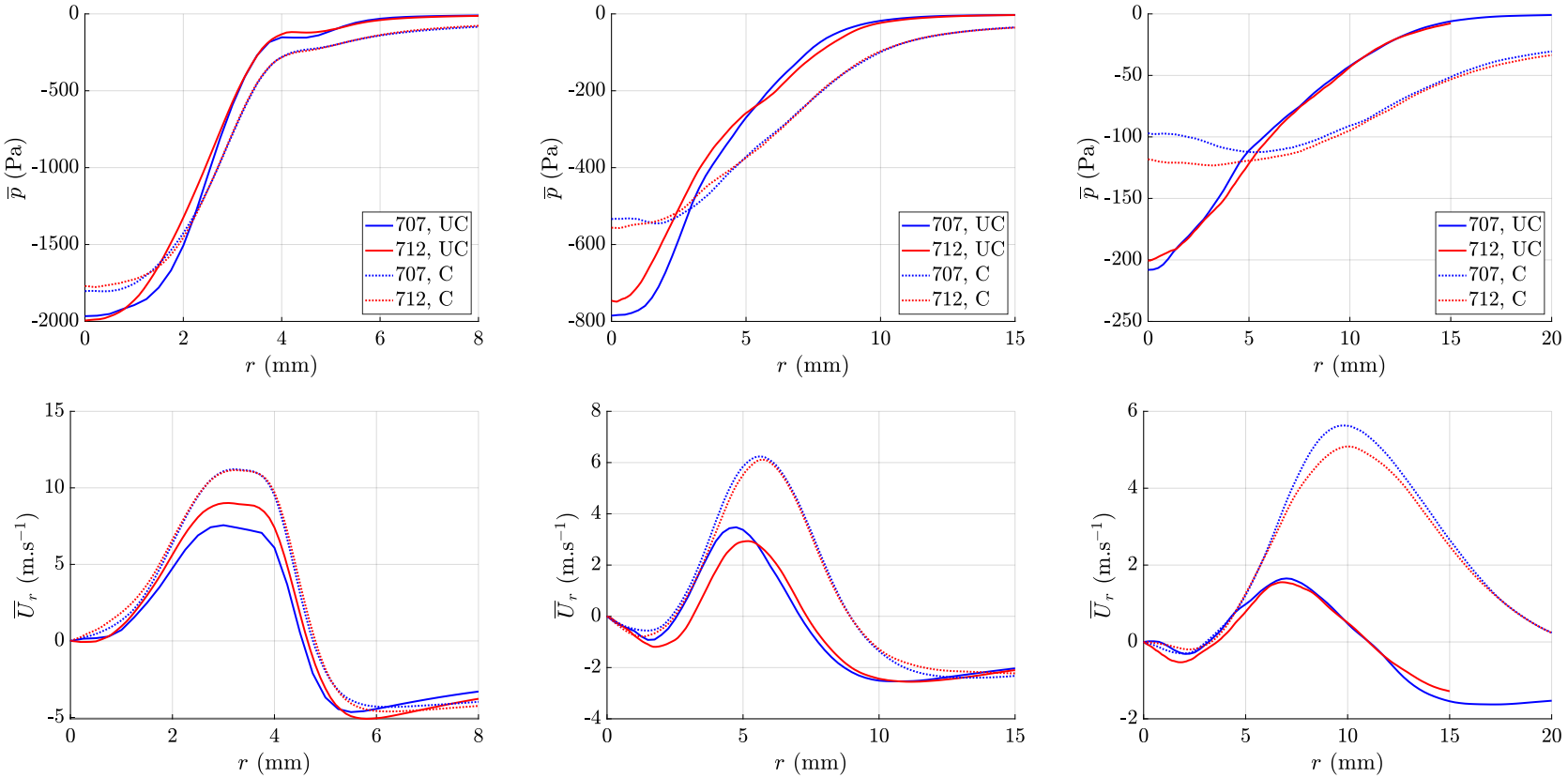

(d) *(cont.)* $z = 2.5\,\mathrm{mm}$ **(e)** *(cont.)* $z = 5\,\mathrm{mm}$ **(f)** *(cont.)* $z = 10\,\mathrm{mm}$

Figure 3.8 *(cont.)*: *Comparison of the mean pressure (top) and radial velocity (bottom) profiles from the LES simulations at three different heights above the backplane for swirler 707 (blue) and 712 (red) in unconfined (UC, continuous lines) and confined conditions(C, dotted lines,* $d_q = 69\,\mathrm{mm}$*). Air mass flow rate of* $\dot{m}_{air} = 2.26\,\mathrm{g\,s^{-1}}$.

as $\mathrm{St} = 2R_{inj}f/u_b = 0.74$ for swirlers 712 and the first peak of 716, and $\mathrm{St} = 0.85$ for swirler 707. This matches well with the Strouhal number of the PVC observed in reactive conditions with swirler "TIMBER" in Chapter 5 ($\mathrm{St} = 0.81$). In that chapter, the PVC is identified using high speed flame tomographies and advanced image processing. This value of the Strouhal number also matches well with values reported in the review by Syred (2006). All these elements clearly indicate that the peaks observed in the power spectral densities correspond to a precessing vortex core. The difference in PVC precessing frequency between swirlers 707 and 712 is quite striking given that their velocity profiles measured downstream of the outlet of the injector are quite similar. There is however some small differences with the profiles of $\overline{U_r}$. It is thus quite useful to refer to some recent publications concerned with the PVC. Using Linear Stability Analysis and Structural Stability Analysis, Tammisola and Juniper (2016); Vanierschot et al. (2020); Manoharan et al. (2020) have identified the location of the wavemaker of the PVC in configuration similar to the SICCA-Spray injector: they find that this wavemaker region, which controls the growth and decay of the PVC, is located near the top of the fuel atomizer, on either side. As can by seen in Fig. 3.9, the flow formed by swirler 707 does slightly differ from that formed by swirler 712 in this critical region.

It is then interesting to consider the case of swirler 716. Two peaks appear in the power spectral density of the velocity for this swirler, the second peak corresponding to twice the frequency of the first. It is reasonable to assume at this point that the first peak corresponds to a single helix, first order in azimuth ($m = 1$ with m the azimuthal wavenumber), while the second peak corresponds to a double helix, second order in azimuth ($m = 2$) PVC (for a detailed experimental study on double helix PVC in isothermal swirling flows, see Liang and Maxworthy (2005)). A time-frequency analysis of the hot wire signal is performed using the continuous wavelet transform with analytical Bump wavelets. The resulting scalogram (square of the coefficients of the continuous wavelet transform) is shown in Fig. 3.10 for a short time sequence. It appears that the velocity signal can exist in two states: either oscillating at $f \approx 3500\,\mathrm{Hz}$, or at twice that frequency. The transition between the two states occurs at a timescale in the order of a microsecond. It appears that, in SICCA-Spray equipped with swirler 716, two globally unstable hydrodynamic modes associated with PVCs at two azimuthal wavenumbers compete with each other. One or the other may be predominant at each point in time, but they do not coexist.

3.4 Features of the fuel spray

Liquid-fueled aero-engine injectors have to handle a wide range of fuel flow rates from engine idle to full power conditions (typically 1:40) while ensuring good atomization in order to maintain combustor performance levels, in terms of pollutant emissions and operability (ignition, blow out, combustion instabilities...). To this end, many larger engines use several atomizers, or even several injectors, one of which, dubbed "pilot", is designed to handle lower flow rates and ensure reliable operation under low power settings (Lefebvre (1995)). Pressure-swirl atomizers are often used for that purpose as they give access to the required performances by generating a spray of fine droplets in a hollow cone pattern with a large angle and a homogeneous circumferential liquid distribution even under low

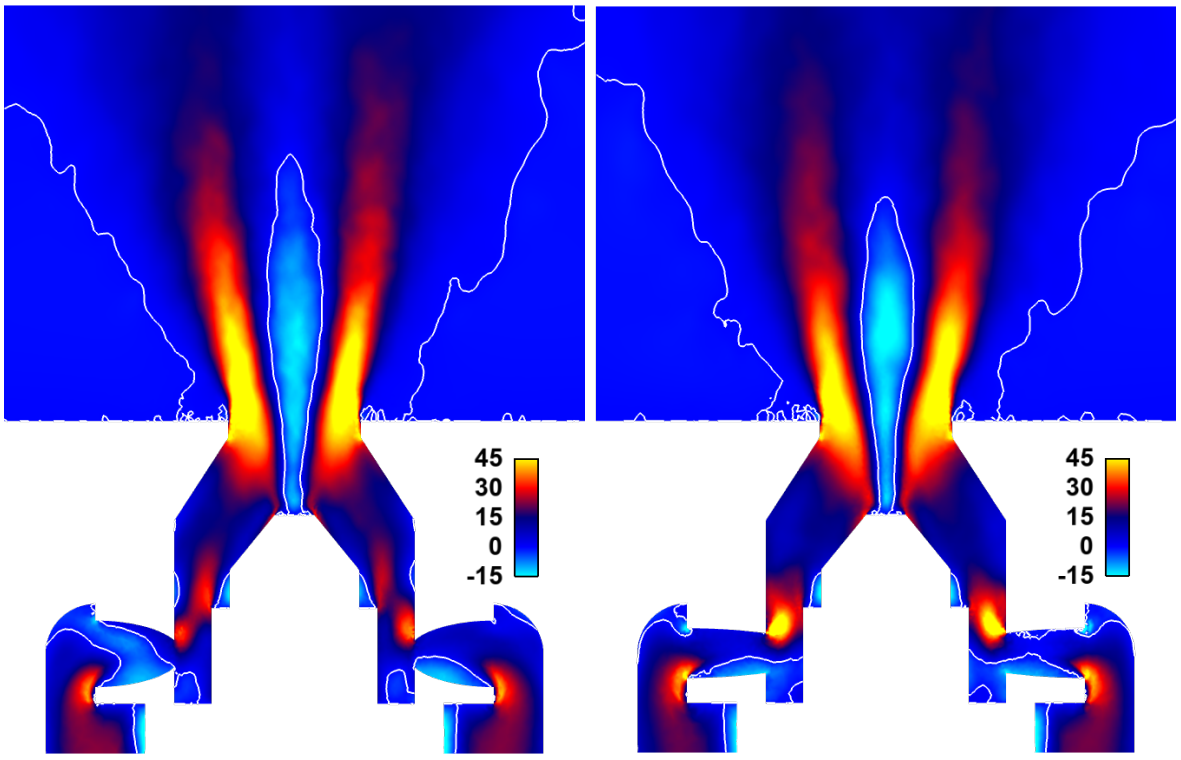

(a) *Swirler 707, unconfined.*

(b) *Swirler 712, unconfined.*

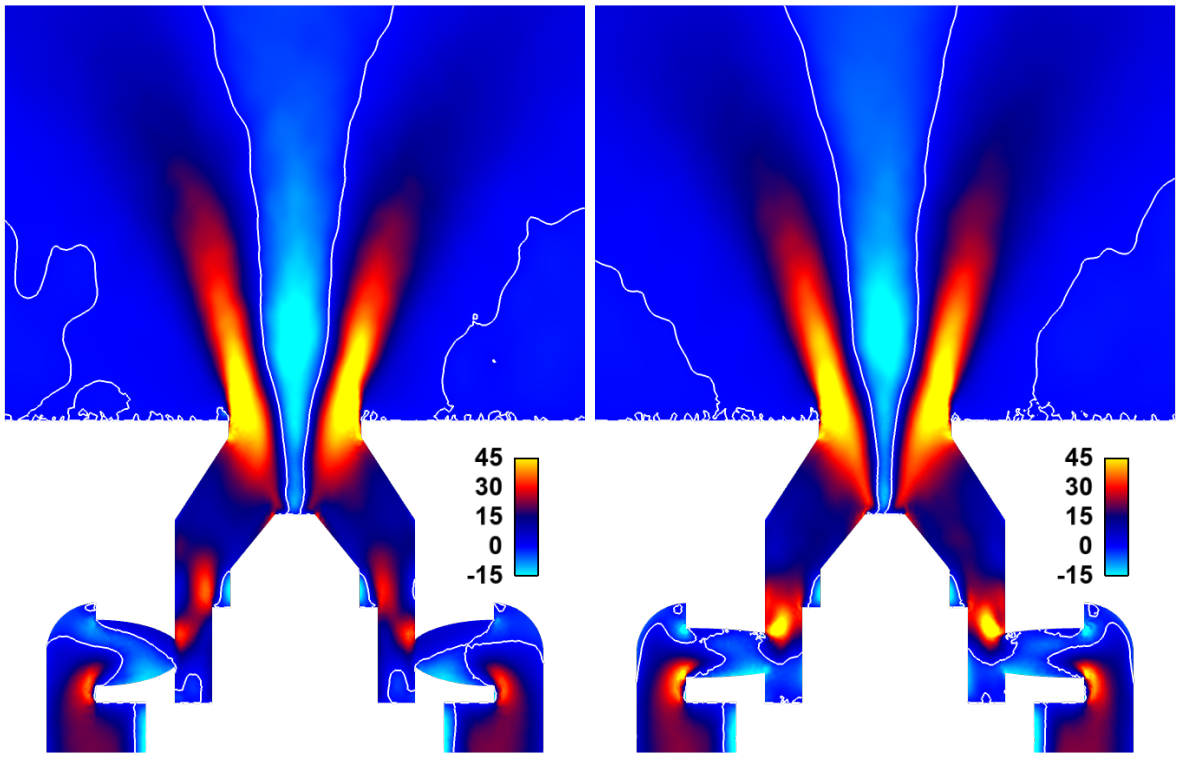

(c) *Swirler 707, confined.*

(d) *Swirler 712, confined.*

Figure 3.9: *Time-averaged axial velocity fields shown on a midplane with white isolines for* $\overline{U_x} = 0$. *The results are presented for four configurations corresponding to a combination of two swirlers (707 and 712) and confined and unconfined configurations.*

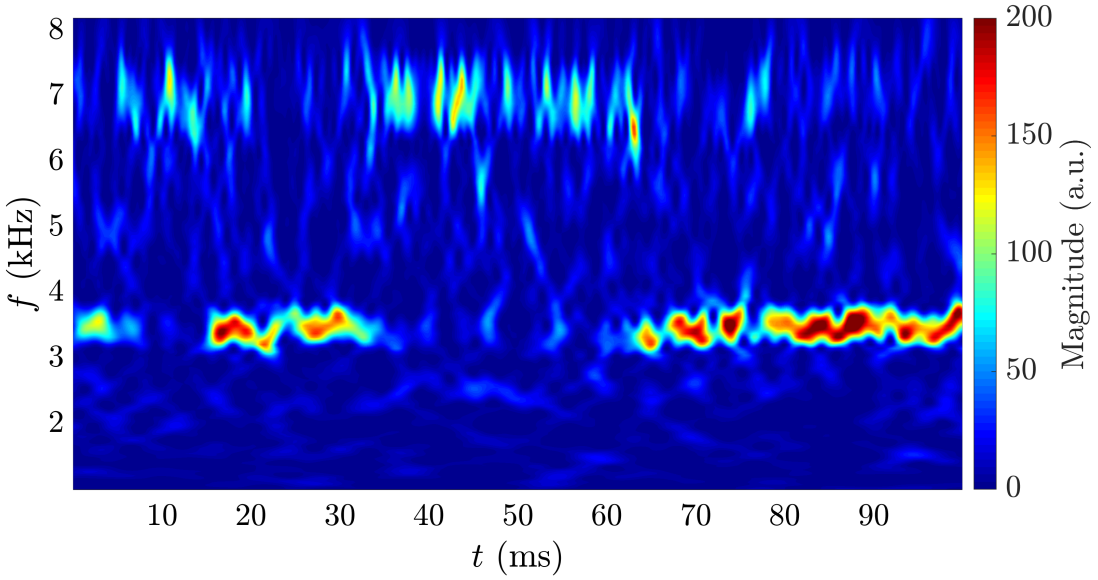

Figure 3.10: *Scalogram of the axial velocity measured by constant temperature anemometry at the outlet of the injector equipped with swirler 716.*

fuel pressure and flow rates (Lefebvre and Ballal (2010)).

The general objective of the present section is to investigate the complex interaction taking place inside the injector between the swirling flow, the droplet cloud produced by the pressure atomizer and the injector geometry. This question is examined by combining detailed experiments and simulations. On the experimental side attention is first focused on the impact of the injector design on the circumferential droplet size distribution. The velocity distribution is measured and its features are interpreted using Large Eddy Simulation (LES).
At this stage it is worth reviewing the literature dealing with these various issues. Early characterizations of pressure-swirl atomizers are reviewed by Lefebvre (1989). Much of the work was focused on obtaining correlations between injector geometrical dimensions and performance such as discharge coefficients, cone angle and overall droplet diameter. As atomizers are integrated inside injectors, interactions between the air flow and the spray must be considered. This is accomplished for example by Rajamanickam and Basu (2017) who study the interactions between the hollow cone liquid sheet formed by a simplex atomizer and a swirling air flow by systematically varying the air flow rate to investigate different flow regimes. Time resolved measurements show that the dominant mechanism for sheet break-up and primary atomization is driven by surface tension effects when the momentum of the liquid is large compared to that of the air. At higher air flow rates, the motion of the liquid is strongly coupled with that of the air leading to flapping and "catastrophic" break-up of the liquid sheet by vortices in the air flow. The angle of the spray also increases with increasing air flow rate, a result also reported in Sharma et al. (2019) where the spray angle of a simplex atomizer is shown to increase when the air flow rate and swirl number of the surrounding air coflow are augmented. The dynamics of the disperse phase is investigated for example in Hardalupas et al. (1992) where particle

dispersion takes place in a jet after a sudden expansion. Adding a swirling motion can lead to segregation depending on droplet size and associated Stokes number, and constitutes the working principle of cyclonic separation (Dring and Suo (1978); Kriebel (1961)). Detailed characterization of droplet size and velocity in laboratory scale aero-engine-type combustors have been made possible by advances in laser diagnostics, in particular by the development of the Phase Doppler Anemometer (PDA). An early application of this instrument by McDonnell et al. (1990) showed its potential for laboratory characterization of sprays formed by aero-engine injectors. More recently, PDA has been used by Lecourt et al. (2011) to fully characterize an aeronautical injector in non-reactive and reactive conditions and provide data that was then used to initiate numerical simulations (Jaegle et al. (2011); Guedot et al. (2018); Franzelli et al. (2013)). These studies explored Eulerian and Lagrangian particle tracking approaches to model spray combustion. One lesson learned from these investigations is that a complex interaction takes place between the spray and the Precessing Vortex Core (PVC). This helicoidal coherent vortical structure that is commonly found in strongly swirling flows is also present in aeronautical injectors. This interaction subsequently perturbs the flame. Recent experiments by Renaud et al. (2019) on spray-PVC interaction indicate that the PVC attaches at the tip of the atomizer, and produces a periodic disturbance of the fuel supply. Although the PVC vanishes at the injector outlet, the perturbation on the spray still influences the flame. A more detailed, joint experimental and numerical study on the interaction between a spray formed by a prefilming atomizer and a PVC was carried out by Keller et al. (2015). They compared several numerical simulation approaches and note that contrary to Unsteady Reynolds Averaged Navier Stokes (URANS), Large Eddy Simulation (LES) is better suited to predict interactions between droplets and vortical structures, leading to an improved modeling of fuel-air mixing. Their simulations also feature spray clustering: the larger droplets gather and form a helical shaped volume of higher liquid loading and equivalence ratio, in phase with the PVC, somewhat at variance with Franzelli et al. (2013) who find fuel loading perturbations that are delayed with respect to the PVC.

In the area of combustion dynamics, the response of droplets and of the fuel atomizer itself to acoustic perturbations is also found to play a key role in the flame response. Cold flow and spray response to acoustic perturbations of a swirl spray injector examined experimentally and with LES in Gajan et al. (2007) indicate that a slow convective wave of fuel loading is formed. This is attributed to the modulation of the droplet transport by the air flow, and to the modulation of the atomization process in the air-blast atomizer. Kim et al. (2012) used LES in a similar cold flow study. Eckstein et al. (2006) studied a self-excited oscillation in a single sector, laboratory scale, kerosene fueled aeronautical burner. They observe a modulation in droplet diameter and note that subsequent modulation of evaporation and of droplet acceleration delays may play a key role in the dynamics of their flame. The joint experimental and numerical (LES) investigation of Tachibana et al. (2015), carried out on a high pressure, kerosene fueled test rig, underlines the importance of the delay introduced by droplet evaporation on the thermoacoustic feedback loop. Finally, perhaps the best demonstration of the impact of liquid fuel injection properties on combustion instabilities is provided by Lee et al. (2005), who use an actively controlled Nanomiser^{TM}to vary the fuel droplet size of their injector, allowing them to move from a

stable to an unstable combustion regime of operation.

The present analysis is motivated by observations of combustion dynamical phenomena in an annular combustor "MICCA-Spray", an atmospheric test rig at EM2C laboratory used to investigate ignition and azimuthally coupled combustion dynamics. This system has been more recently converted to allow liquid fuel injection in order to be more representative of a small helicopter engine combustor (Vignat et al. (2020); Prieur et al. (2017b)). To better understand flame dynamics in this rig, it is necessary to take a closer look at fuel injection in this configuration and obtain information that may apply more generally to swirl injectors comprising a pressure atomizer.

The aim of this section is to present detailed measurements of cold flow spray that are necessary inputs to high fidelity simulations. These data are obtained on a single sector featuring a central injector "SICCA-Spray" (a sister test rig to "MICCA-Spray"). This configuration will first be introduced, along with the design of the injector and the diagnostic tools that have been employed. Several swirlers are used to assess the impact of swirler design and in particular that of the swirl number on the circumferential distribution of fuel. The spray is then characterized using laser tomography and Phase Doppler Anemometry. These data are then combined with Large Eddy Simulations. This is accomplished by first presenting the numerical setup, validating calculations with experimental results and finally gathering insights from the LES and experimental measurements to discuss key aspects of the injected spray.

3.4.1 Swirler design impact on fuel spray distribution

It is first interesting to examine the impact of the swirler design on the fuel spray circumferential pattern. A homogeneous circumferential distribution of the spray is usually desired to ensure symmetry of the flame and avoid formation of hot spots which may reduce the service life of the high pressure turbine distributor and increase pollutant emissions (Lefebvre and Ballal (2010)). This characteristic of the spray is however seldom studied in a laboratory setting. McDonnell et al. (1990) performed such a study on three methanol-fueled air-blast atomizer used in a helicopter engine, and showed the advantage of PDA against the more traditional patternator for such a study. However, only manufacturing dispersion was considered.

In the present section, the spray characteristics are examined for six variants of the injection system. Two different atomizers are used: the first designated as AG was observed to form a circumferentially homogeneous spray. The second, AD, damaged by repetitive electrical discharges during plasma assisted combustion experiments, features a spray pattern that is circumferentially skewed. The sprays formed with the two atomizers are characterized for three different swirlers: 707, 712 and 716. The operating point considered in what follows corresponds to a heptane mass flow rate of $500\,\mathrm{g\,h^{-1}}$ and an air flow rate of $2.3\,\mathrm{g\,s^{-1}}$.

The circumferential spray droplet size distribution is determined by moving the laser probe

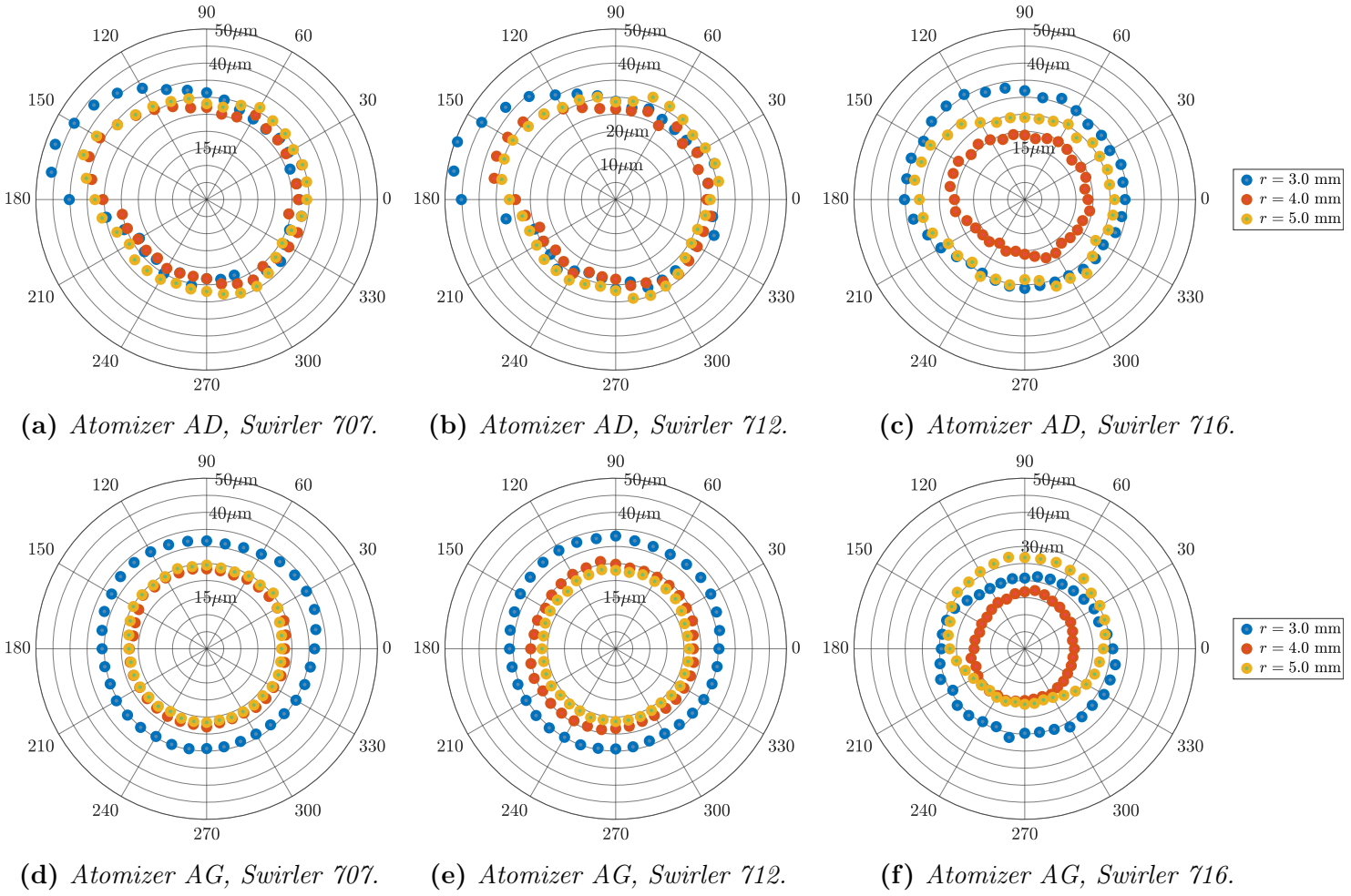

(a) *Atomizer AD, Swirler 707.* **(b)** *Atomizer AD, Swirler 712.* **(c)** *Atomizer AD, Swirler 716.*

(d) *Atomizer AG, Swirler 707.* **(e)** *Atomizer AG, Swirler 712.* **(f)** *Atomizer AG, Swirler 716.*

Figure 3.11: *Circumferential distribution of the Sauter mean droplet diameter d_{32}. For each data point the azimuthal angle on the graph corresponds to the azimuthal angle in the experiment, the color of the point to the radial coordinate of the measurement point, and the radial position in the graph corresponds to the value of d_{32} (the gray circles correspond to* 5, 10, 15... µm *as indicated in the graphs when this is possible). Measurements acquired at* $z = 2.5\,\mathrm{mm}$.

volume of the PDA system on a cylindrical mesh. The Sauter mean droplet diameters d_{32} are displayed in polar coordinates in Fig. 3.11 by placing a symbol at a distance from the center corresponding to the d_{32} value. The plots correspond to three radii with respect to the injector axis. The distributions pertaining to the damaged atomizer AD and swirlers 707 and 712, are not axisymmetric. This is confirmed in the polar plots of the mean diameter d_{10} corresponding to the same injection systems and operating conditions (not shown here). The circumferential Sauter mean droplet diameter distribution pertaining to swirler 716, with the damaged atomizer AD, is more regular. When atomizer AG is employed, the circumferential pattern of the spray is much more homogeneous for all three swirlers. A slight asymmetry is still present with swirler 716 and atomizer AG and found to be quite reproducible. From these observations, one concludes that the damaged atomizer AD is mainly responsible for the skewed circumferential distribution, while an undamaged atomizer AG creates a fairly homogeneous spray. One also finds that an injector with a higher level of swirl interacts with the spray such that the droplet pattern is more robust to defects in the atomizer. It is however not possible to conclude at this point about the physical processes that homogenize the spray distribution or create the slight asymmetry with swirler 716. The internal aerodynamics of swirler 716 are probably conducive to a higher level of turbulent mixing. It appears indeed from velocity data measured downstream of the injector (Figs. A.17 and A.25) that the turbulent intensity is higher with this swirler compared to 707 and 712. Another possibility may be that the interaction between the flow and the conical liquid sheet formed at the tip of the atomizer plays a role in the azimuthal distribution of droplet sizes. The higher swirl number of swirler 716 is creating a stronger recirculation zone near the tip of the atomizer. These features may have a direct impact on the atomization process itself (Rajamanickam and Basu (2017)). One reviewer also suggests that the PVC might be the cause of the asymmetry observed with swirler 716 and atomizer AG. Indeed, if the transition between the single and double helix PVC of this swirler happens preferentially at some azimuthal position, it may be the root of the deformed pattern that has been observed.

3.4.2 Detailed experimental characterization of the fuel distribution

The focus is now placed on the detailed analysis of PDA measurements obtained using atomizer AG and swirler 707. Figure 3.12 presents the mean (d_{10}) and Sauter mean (d_{32}) diameters at different distances from the injector dump plane. The droplet sizes appear relatively homogeneous across the radial dimension at $z = 5\,\text{mm}$. Typical values are then $d_{10} = 10\,\mu\text{m}$ and $d_{32} = 27\,\mu\text{m}$. Note that the mean diameters have a very high statistical uncertainty in a region around the injector axis ($r < 2.5\,\text{mm}$) as the number of droplets that travel in this region is quite low, as is well exemplified in the laser tomography image in Fig. 3.13. This is a common problem when computing Sauter mean diameters from PDA measurements as noted in McDonnell et al. (1994). In general, the droplet diameter profiles have a bowl shape with larger droplets on the outside, which is expected due to segregation based on the Stokes number in swirling flows Dring and Suo (1978); Kriebel (1961). One may note however that the difference between the profiles of d_{10} and those of d_{32} decreases sharply with the distance from the backplane, indicating that an originally

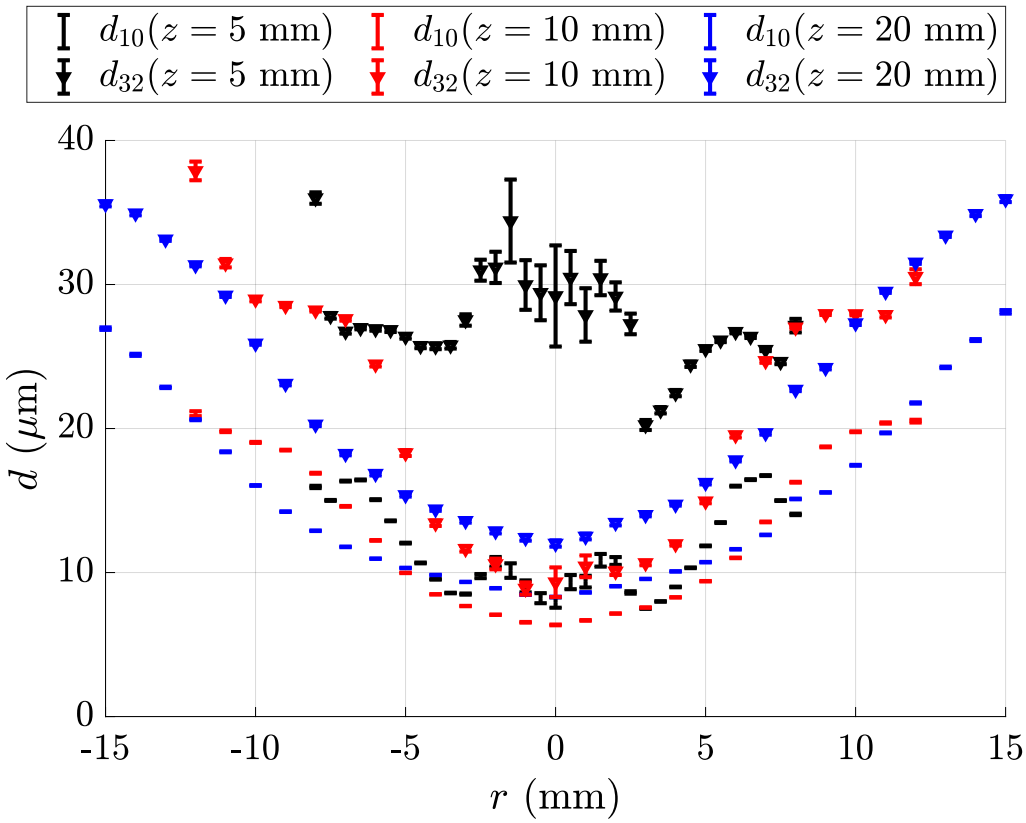

Figure 3.12: *Radial profiles of mean droplet diameter d_{10} and Sauter mean diameter d_{32} obtained at $z = 5$, 10 and 20 mm above the backplane (red dotted lines in Fig. 3.13). Swirler 707. Error bars indicate the 95% statistical confidence interval obtained from bootstrapping.*

highly polydisperse distribution at $z = 5$ mm becomes nearly monodisperse at $z = 20$ mm and that this is probably due to a combination of swirl induced particle segregation and vaporisation. Finally, one may also note that in the tomographic image of Fig. 3.13, the signal is very intense near the backplane around $r = R_{inj} = 4$ mm. In a previous study, it was visually observed in this system that a film of liquid droplets is formed on the conical convergent section of the injector, and that this film is being atomized in an air blast manner (Prieur (2017)). Droplet size histograms are shown in Fig. 3.14 for different radial positions at $z = 5$ mm. These positions correspond to areas where large numbers of droplets are present (see Fig. 3.13). The distributions are highly polydisperse, and essentially feature three peaks: the first, at approximately $d = 10 - 15$ µm appears small here in this volumic representation, but corresponds to the main peak of the droplet number distribution. The second is around $d = 30 - 40$ µm while the third represents a small number of relatively large droplets ($d \simeq 70$ µm). One may suspect that these multiple peaks arise from the different atomization processes taking place in the experiment, and result: from the flow interacting with the atomizer spray; from the liquid film escaping from the conical convergent; and from air-blast by the swirling air flow in the injector end-piece.

To further analyze the spray characteristics, the distribution of axial velocity conditioned

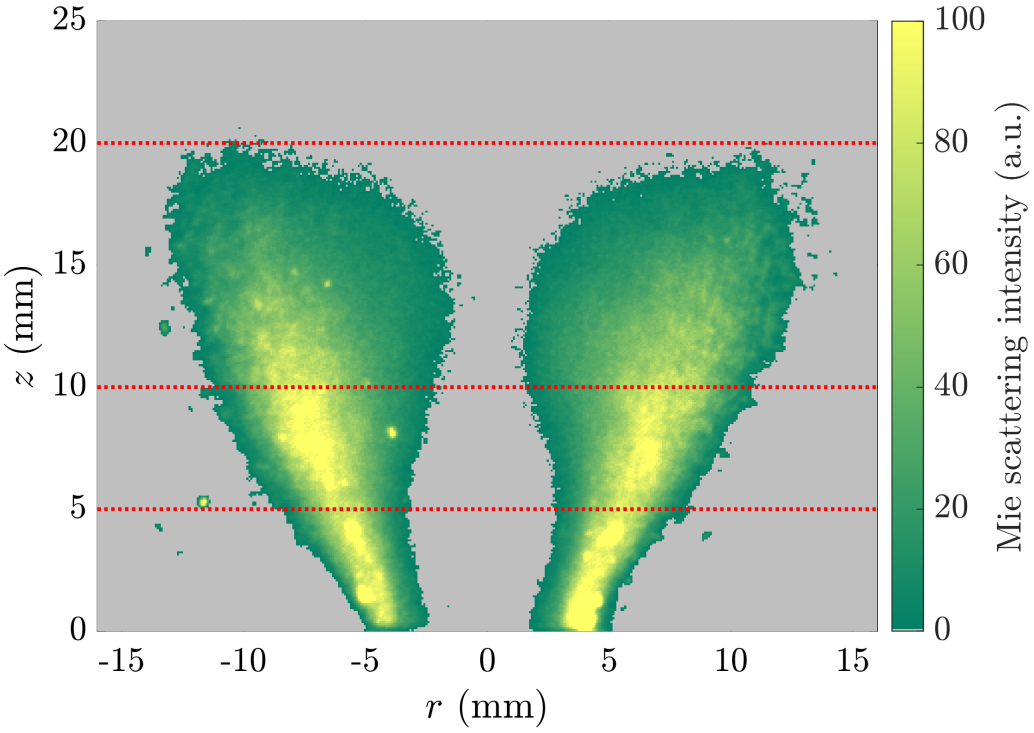

Figure 3.13: *Laser tomography of the spray above the dump plane, in the presence of flow. Swirler 707. Red dotted lines: PDA measurements heights.*

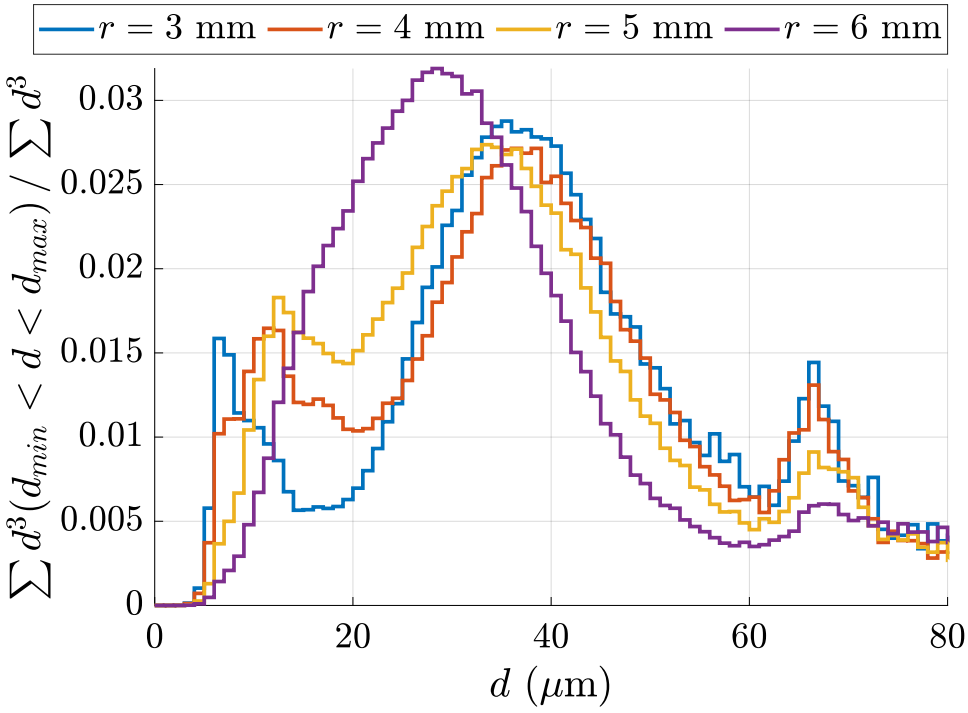

Figure 3.14: *Volumetric droplet size histograms measured at four radial positions $z = 5\,\mathrm{mm}$ above the backplane. The plots correspond to the fraction of the total liquid volume for each droplet diameter class in the histogram.*

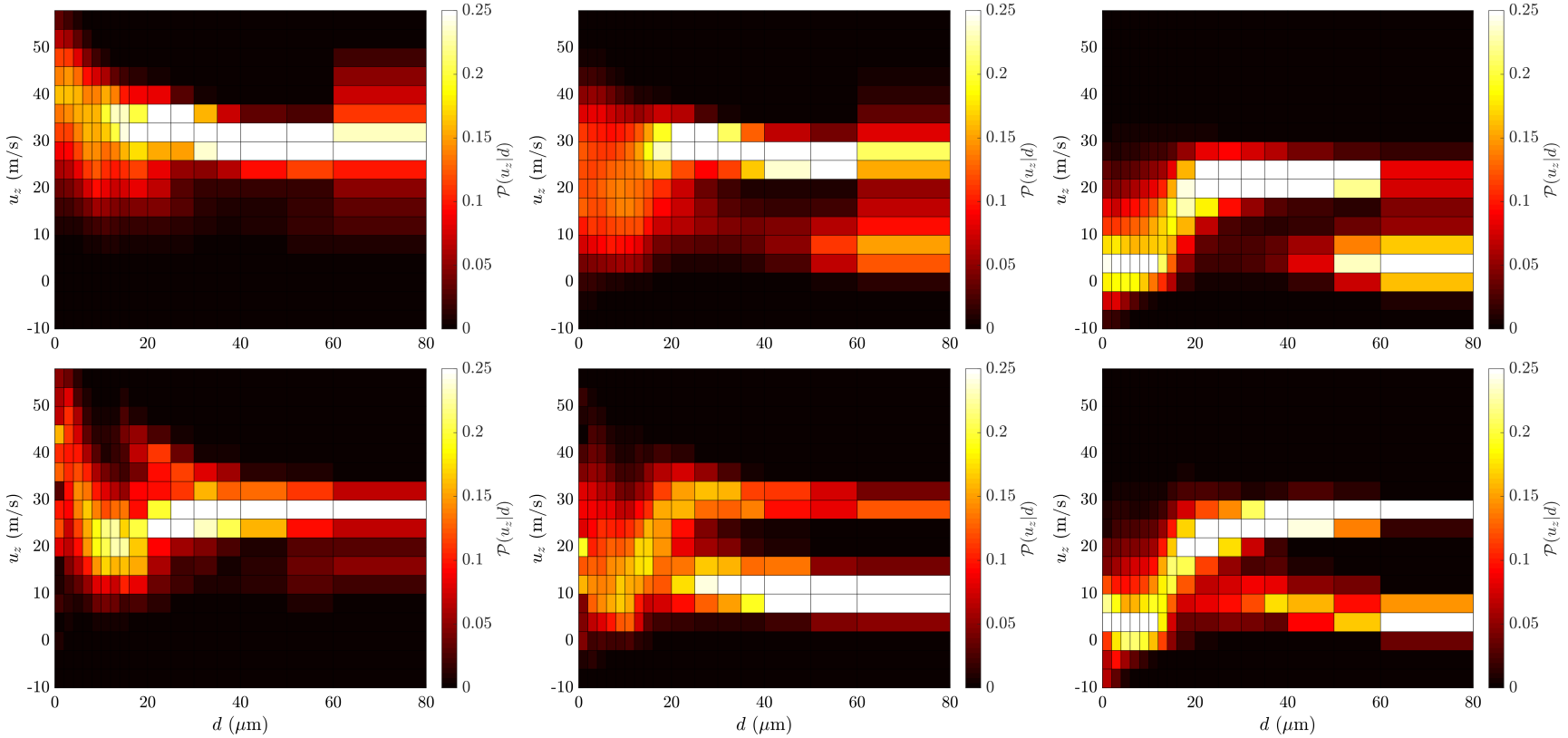

(a) $r = 4\,\text{mm}$. **(b)** $r = 5\,\text{mm}$. **(c)** $r = 6\,\text{mm}$.

Figure 3.15: *Probability of axial velocity conditioned by the droplet diameter at* $z = 5\,\text{mm}$ *and at radial positions* $r = 4$, 5 *and* $6\,\text{mm}$. *On the top row, experimental results measured by PDA. On the bottom row, simulation (LES) results that will be discussed in the LES section. In both cases, circumferential averaging is performed.*

by the droplet diameter is shown in Fig. 3.15. For smaller droplets, the distribution is fairly wide and continuous, as could be expected as these droplets behave essentially like tracers in a highly turbulent flow. For larger droplets, the velocity distribution is much narrower with a sharp peak around $29\,\mathrm{m\,s^{-1}}$. At $r = 5\,\mathrm{mm}$, a second peak seems to be present at a much lower velocity for larger droplets. This is confirmed by the velocity histograms plotted in red in Fig. 3.16. These velocity histograms pertain to droplets with a diameter larger than $45\,\mu\mathrm{m}$. At $r = 4\,\mathrm{mm}$ the histograms exhibit a single peak around $29\,\mathrm{m\,s^{-1}}$. At $r = 5$ and $r = 6\,\mathrm{mm}$ the distribution becomes bimodal with a second peak at a much lower velocity. The velocity statistics for the air flow at the same positions are shown in black alongside those of larger droplets in Fig. 3.16. These histograms feature a single very wide peak at a velocity that notably differs from that of the large fuel droplets.

Such a bimodal velocity distribution for large droplets is also identified by Wang et al. (1994) in the injector used in the CFM56 engines. In this two-stage counterswirling design, fuel is injected on the centerline in a hollow cone pattern and subsequently hits the wall of a venturi, forming a film. The authors attribute the bimodality of the velocity distribution to two possible and distinct droplet histories: those formed by the atomizer and those formed by the film have different velocities. Given that filming is also observed in the "SICCA-Spray" experiments, a similar explanation for the bimodality of the velocity distribution can be invoked here: some droplets directly originate from the atomizer while others are formed in the liquid fuel film located on the convergent section of the injector. However, in the present case, the highest velocity values correspond to the droplets from the atomizer. Indeed, using a simple mass and momentum balance on the atomizer, one concludes that droplets are injected with an axial velocity of the order of 30 to $50\,\mathrm{m\,s^{-1}}$ and, given their large size, their velocity does not change much when they reach the measurement section. This will be confirmed and complemented with the large eddy simulations carried out in what follows.

3.4.3 Large eddy simulation of the gaseous and dispersed phases

The reader is referred to Chapter 1 for a detailed description of the numerical setup.

3.4.3.1 Liquid injection model

A critical aspect of spray simulations in a Lagrangian framework is the specification of the initial position, size and velocity distributions for the particles. There are various models in the literature that describe pressure-swirl atomizers such as the FIMUR model (Sanjosé et al. (2011)). However these models do not yield velocity distributions that are consistent with what is known from the present measurements. Indeed, it can be experimentally observed, as shown in Fig. 3.17, that the atomizer and the air flow interact, leading to a drastic change in injection properties when air flow is present. Such drastic changes in the near atomizer flow field caused by addition of a swirling air flow are also reported in the literature: the term "explosive breakup" is coined for this phenomenon by Hopfinger and Lasheras (1996), who studied a round water jet in a swirling air flow. Above a certain critical value of the swirl number, the plain jet underwent a violent radial expansion, forming a hollow cone and dramatically improving atomization. In Muthuselvan et al.

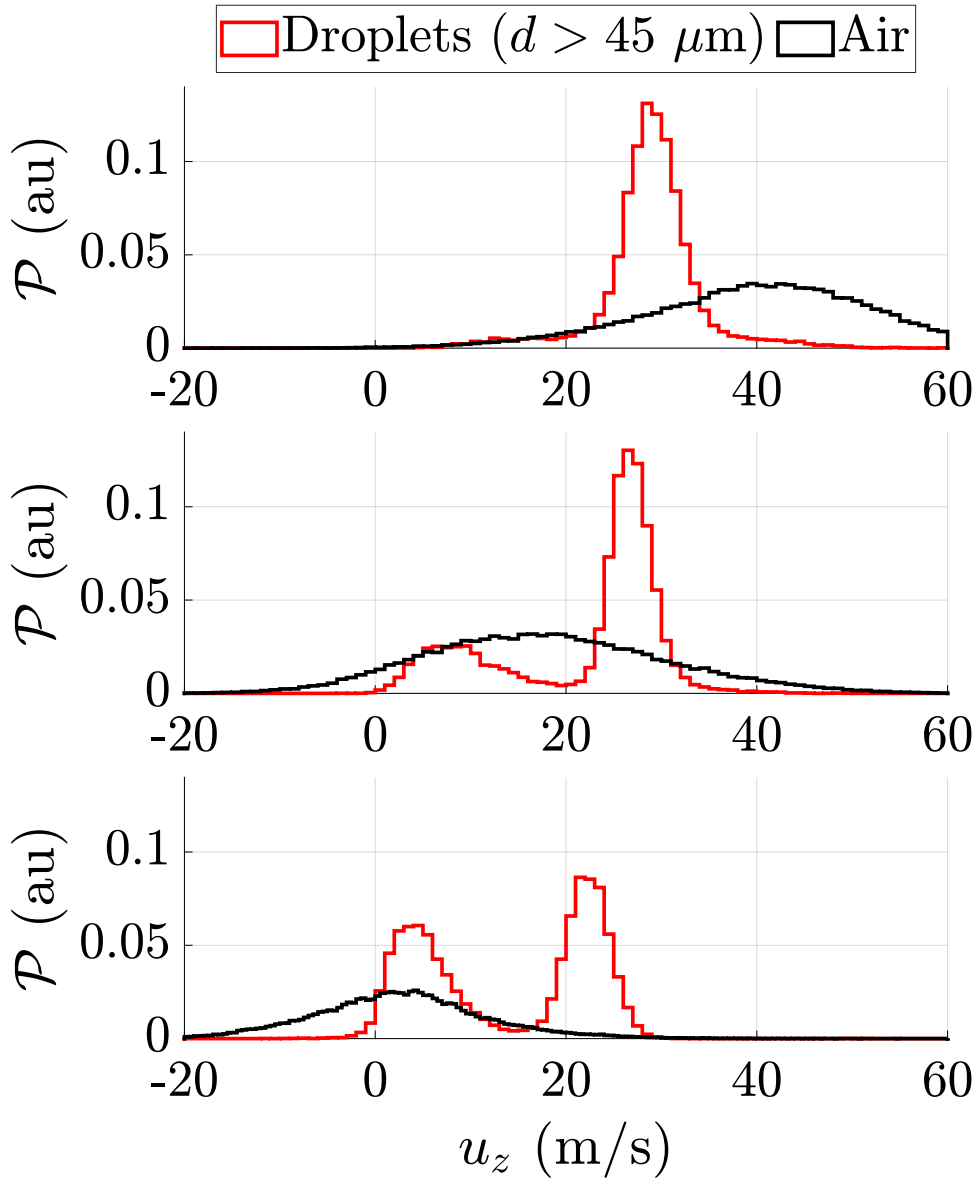

Figure 3.16: *In red, axial velocity histogram for large droplets (diameter greater than* 45 µm*) at 3 radial positions (from top to bottom,* $r = 4$, 5 *and* 6 mm*, all taken at* $z = 5$ mm*). In black, air axial velocity histogram from LDV measurements.*

(2018), the authors analyze the spray formed by a simplex atomizer in a swirling air flow, and observe a transition similar to that of Fig. 3.17 from a closed spray to a hollow cone as air flow is increased. They observe that this transition is affected by a strong hysteresis.

Thus, a dynamical injection model accounting for coupling with the air flow would be required. This is not attempted in the present simulations and a simpler uncoupled model is adopted in which the initial spray characteristics are adjusted by making use of experimental data obtained in the injector near field. Four main parameters must be determined: the position of fuel injection, the initial droplet size distribution, their velocity and injection angle.

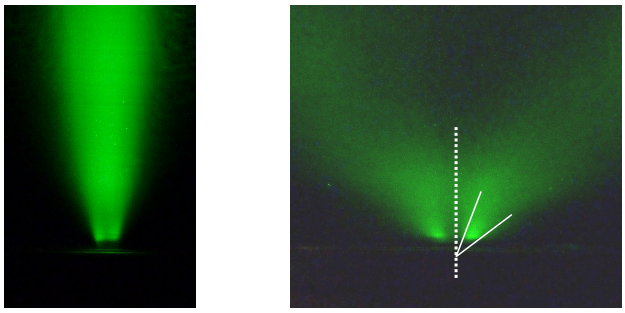

(a) $\dot{m}_{air} = 0$ **(b)** $\dot{m}_{air} = 2.3\,\mathrm{g\,s^{-1}}$

Figure 3.17: *Tomographic visualization of the spray at the tip of the atomizer. The spray is illuminated by a laser sheet just above the outlet of the atomizer. In this experiment, the end plate of the atomizer (golden disc in Fig. 1.6) is removed to gain optical access. The laser sheet crosses the atomizer on its centerline, and the spray image is obtained with a long exposure time. Left image : fuel injection without air flow. Right image : with air flow.*

The initial droplets are injected on a ring of inner radius 27 µm and outer radius 54 µm. The droplet size distribution is the one measured at $z = 5\,\mathrm{mm}$. This choice is driven by two reasons. First, there is at present no accurate model for the determination of droplet size distributions at the atomizer's exit, and there is no direct optical access to perform in situ experimental measurements. Second, several physical phenomena (secondary atomization, splashing, droplet-droplet interactions) are not accounted for in the simulation because of the lack of fully predictive models. By imposing the experimental distribution, one circumvents these issues, making the assumption that the corresponding physical processes only take place in the immediate vicinity of the atomizer and are characterized by short time scales. Simulations with diameter distributions from measurements at several different radial positions as input were performed, but using a droplet diameter PDF averaged over all experimentally available radial positions gave the best results. The injected distribution is corrected for evaporation between the atomizer and the PDA measurement section assuming that it follows a d^2 law. This correction is important for the smaller droplets, for which this simplistic evaporation law is acceptable as they behave as tracers in an isothermal flow Lefebvre (1989). A constant value of the d^2 law coefficient $\lambda_{d2} = 1.65 \times 10^{-8}\ \mathrm{m^2\,s^{-1}}$ given by Chauveau et al. (2019) is used for this correction. The time of flight of particles from the atomizer to the measurement point is estimated using LES. The histogram of the corrected distribution is shown in Fig. 3.18. One may observe that droplets initially smaller than approximately 5 µm are fully evaporated and cannot be recovered. In practice, this has a negligible impact as these droplets represent a small fraction of the total injected mass, and this will not bias the comparison between experiment and LES at the PDA measurement section. One side advantage is that the tracking of these droplets would have induced a high CPU cost.

To determine the axial injection velocity by taking advantage of experimental data, it is instructive to examine the dynamics of large droplets. Using a simplified model for the droplet dynamics, only accounting for viscous drag following Stokes' law, the velocity

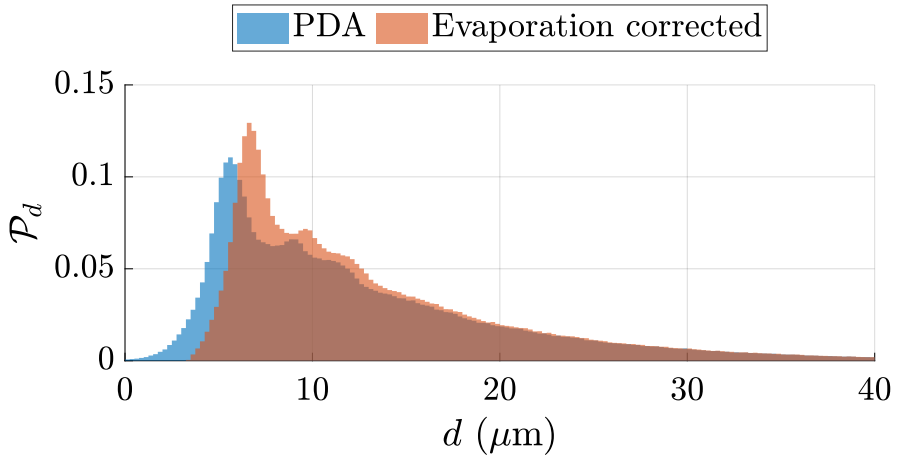

Figure 3.18: *Measured (blue) and injected (brown) droplet distribution. The injected distribution is corrected for evaporation.*

$\mathbf{u_d}$ of a droplet of diameter d in an air flow at velocity $\mathbf{u}$ is given by $\dot{\mathbf{u}}_\mathbf{d} = [\mathbf{u} - \mathbf{u_d}]/\tau_d$ where $\tau_d = (\rho_l d^2)/(18\mu)$ is a characteristic time for the droplet acceleration, with ρ_l the density of the liquid, d the diameter of the droplet, and μ the viscosity of air. For a given time of flight in a uniform air flow with velocity $\overline{U}_{air}$, an upper bound for this velocity change for a particle injected with the velocity $\overline{U}_{p,0}$ can be estimated from: $\delta\overline{U} \simeq \left(\overline{U}_{air} - \overline{U}_{p,0}\right)\left[1 - \exp\left(-St^{-1}\right)\right]$ where St_k is the Stokes number based on the particle time of flight, $St_k = \tau_d/\tau_{flight}$. For an upper bound of the air flow velocity $\overline{U}_{air} = 70\,\mathrm{m\,s^{-1}}$ and a flight time corresponding to the time taken by the largest particles ($d > 50\,\mu\mathrm{m}$) to travel from the atomizer to the PDA measurement volume, the increase in axial velocity for such a particle is less than $3\,\mathrm{m\,s^{-1}}$. Thus, the velocity of the larger droplets is roughly the same as their injection velocity. It is then reasonable to assign an initial value $29\,\mathrm{m\,s^{-1}}$ to all the initial droplets.

The injection angle of each droplet is randomly chosen by normally distributing its values with a mean θ_0 and a standard deviation $\delta\theta$. These two parameter are selected by conducting a parametric study of several LES and varying θ_0 and $\delta\theta$ to match the experimental droplet size and velocity measured conducted downstream using PDA. The initial values for these parameters are selected from the tomographic images of the spray with air flow (Fig. 3.17). These visualization are qualitative but give some indications as to the injection angle of large droplets After the LES parametric studies were conducted, $\theta_0 = 37\,\mathrm{deg}$ and $\delta\theta = 8\,\mathrm{deg}$, corresponding to the values inferred from the experimental visualization of Fig. 3.17, are found to be the optimal set of injection parameters.

3.4.3.2 Validation of the simulation

Volumetric cumulative distribution functions of droplet diameter are compared between LES and PDA measurements at two locations in Fig. 3.19. At $r = 5\,\mathrm{mm}$, the agreement is excellent. At $r = 4\,\mathrm{mm}$, the proportion of large droplets is overpredicted by about 20% by volume. Mean and Sauter mean diameters are compared with PDA measurements

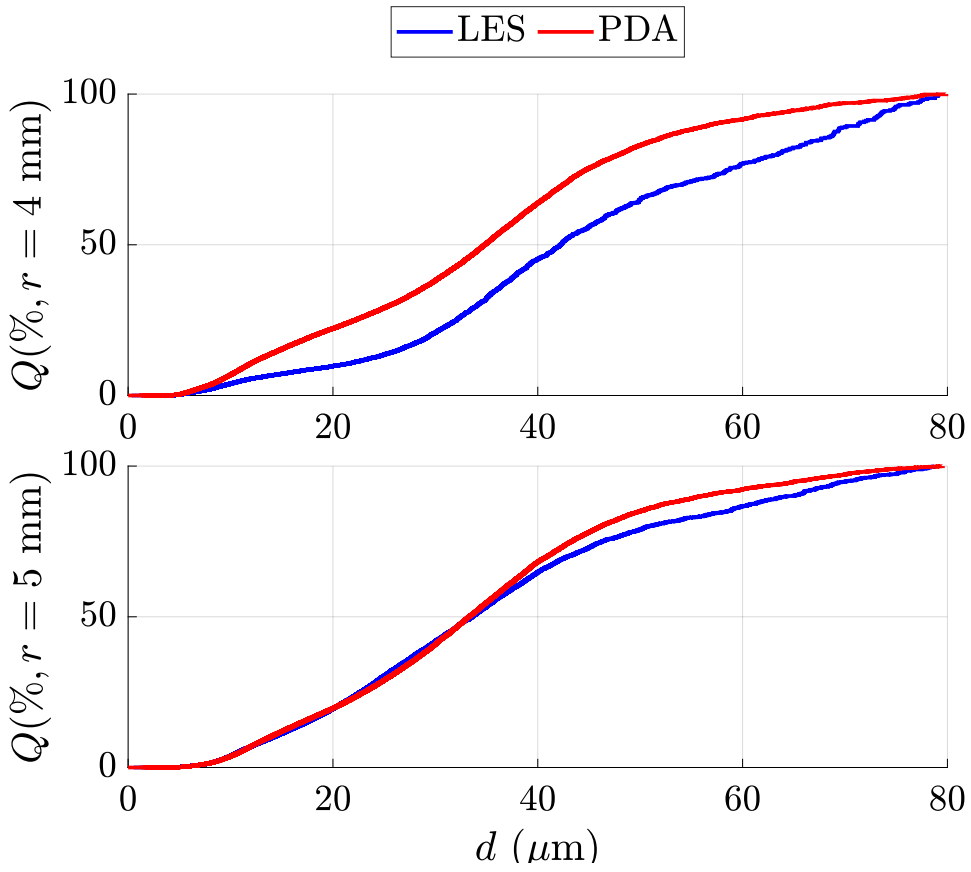

Figure 3.19: *LES and PDA volumetric cumulative distribution function of droplet sizes at* $r = 4$ *(top) and* $r = 5\,\mathrm{mm}$ *(bottom).* $z = 5\,\mathrm{mm}$.

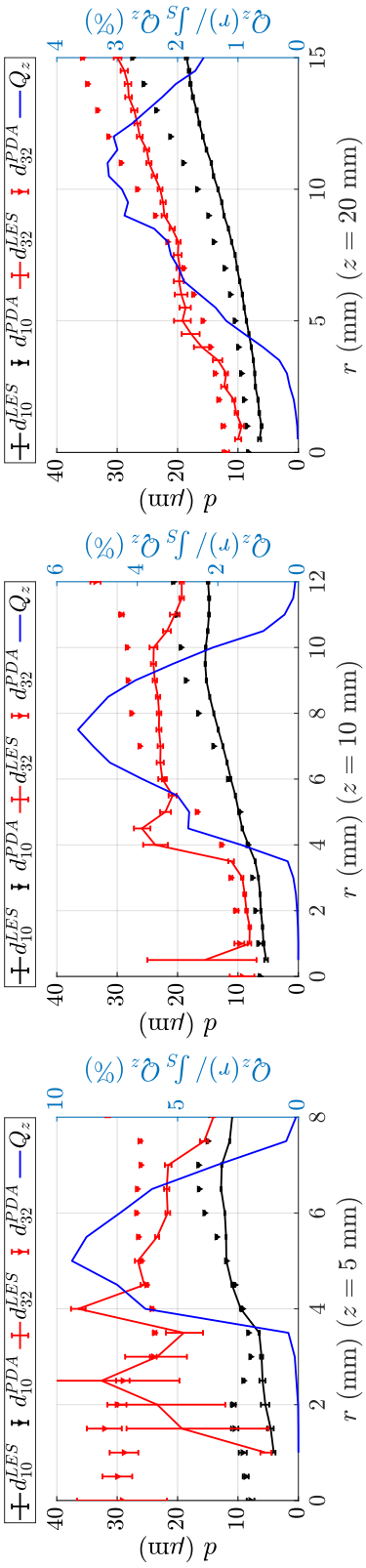

Figure 3.20: *Comparison of mean (black) and Sauter mean (red) diameters from the LES with PDA measurements. Three measurement sections are considered ($z = 5$, 10 and 20 mm). Azimuthal averages are performed in both cases. On the right axis, the radial distribution of the axial liquid volume flux is shown as a blue solid line.*

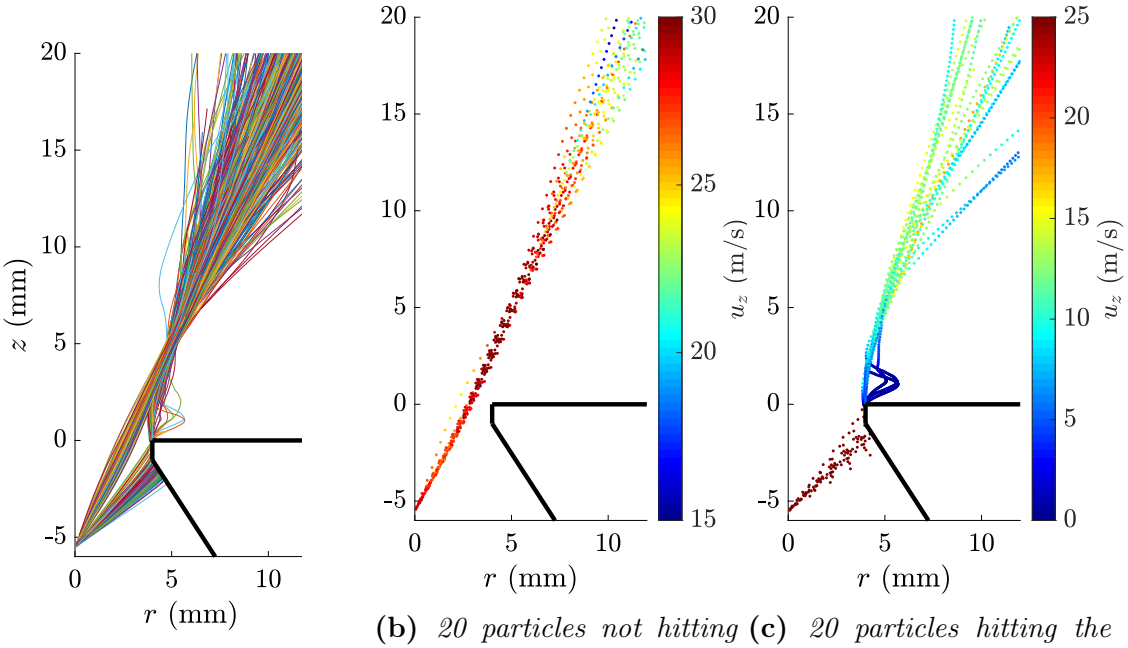

(a) *All particles.* **(b)** *20 particles not hitting the wall.* **(c)** *20 particles hitting the wall.*

Figure 3.21: *Backward - forward Lagrangian particle tracking of all droplets that pass inside the control volume (*0.5 mm *diameter torus around the point of interest at* $r = 5\,\text{mm}, z = 5\,\text{mm}$*). In black, geometry of the upper part of the injector. On the right, trajectories are colored by axial velocity.*

in Fig. 3.20. The agreement is fairly good, especially in the regions characterized by higher liquid volume fluxes that are of greatest practical interest. Some discrepancies are observed in the inner recirculation region at $z = 5\,\text{mm}$. This could be expected as the number of droplets in this region is very low, also leading to high statistical uncertainties. Overprediction of d_{32} around $r = 4\,\text{mm}$ are mainly due to the film model and the manner in which particles are shed at the edge of the conical convergent.

The probabilities of axial velocity conditioned by the droplet diameter are gathered in Fig. 3.15 for the points located at $r = 4$, 5 and 6 mm and at 5 mm from the outlet. The bimodality of the velocity distribution for large droplets observed experimentally at $r = 5\,\text{mm}$ is retrieved albeit overestimated. As is seen experimentally, this bimodality is also not observed at $r = 4\,\text{mm}$. The agreement between LES and experimental measurements is also excellent at $r = 6\,\text{mm}$. The locations of the velocity peaks are also well retrieved for all positions and for both peaks.

3.4.4 Discussion

Backward-forward Lagrangian particle tracking is employed in Fig. 3.21 to examine droplet histories from the LES data. Only droplets larger than $d > 40\,\mu\text{m}$ are considered. The following process is used. Droplet trajectories are projected on the (rz) axial plane. All droplets that pass in the vicinity of the control volume (0.5 mm diameter torus around the point of interest at $r = 5\,\text{mm}, z = 5\,\text{mm}$) are then extracted. In this manner, the

history of droplets whose behavior is examined in the center image of Fig. 3.15 can be analyzed.

Figure 3.21(a) presents the trajectories of all 516 large particles observed to travel in the vicinity of $(r, z) = (5, 5)$ mm during 5 ms of simulation, along with the geometry of the injector (in black). Two populations can be distinguished. Some droplets hit the conical convergent wall of the injector, others do not, and those two groups are well separated. The dynamics of 20 particles that do not collide with the wall is examined in more detail in Fig. 3.21(b). Their axial velocity at every point in the trajectory is shown by their color. These particles have a high initial axial momentum communicated at injection. They are slightly accelerated after the outlet of the injector and reach velocities of the order of $30\,\mathrm{m\,s^{-1}}$ in the vicinity of the point of interest $(r, z) = (5, 5)$ mm and stay close together over a long distance.

Figure 3.21(c) is focused on particles that form a film on the convergent section. As they hit the wall at a close to normal angle, their initial momentum is mostly dissipated at this point. They are released at the edge ($(r, z) = (5, 5)$) with a lower velocity of the order of $10\,\mathrm{m\,s^{-1}}$ and subsequently accelerated by the flow.

3.5 Conclusion

This investigation is concerned with issues of technical importance in the engineering of swirling injectors for jet engine applications. The study is carried out on a laboratory scale injector designed to emulate a small helicopter engine injector. This unit features a radial swirler and a pressure swirl simplex atomizer creating a hollow cone shaped spray of heptane droplets. The radial swirler can be easily changed and a total of 14 different versions of this component are presented and characterized. A more detailed analysis of the flow is carried out on three of these components using large eddy simulation. The focus is placed in particular on swirlers 707 and 712. It is found that these swirlers have very similar velocity profiles, both in confined and unconfined conditions, although the confined and unconfined flows differ significantly. It is also found that the frequency of their PVC is different. One observes in addition that the PVC formed by the flow of swirler 716 is bistable, and that it switches between a single helix and a double helical structure. Concerning the spray of liquid fuel, it is found that the geometry is such that some of the droplets in the spray hit the injector end piece inner surface forming a liquid film. Using an experimental characterization of the spray in the form of polar plots, it is shown that asymmetries in the spray can be identified, and that these features are linked to manufacturing variability or in the present case to a damaged atomizer. Tests with swirlers having different rate of rotation levels indicate that injector flows characterized by a higher swirl number tend to smooth out irregularities in the spray pattern. A second item of considerable importance in the numerical simulation of liquid spray injectors is that of size and velocity distribution of the droplets. It is shown that suitable choices of the size and velocity distributions imposed in the atomizer near field are needed to obtain a good match between experimental data and results of simulations. The injected

distributions are derived by optimizing the input set of parameters determined from laser tomographic visualizations of the spray and Phase Doppler Anemometry. This allows high fidelity LES simulations of the spray. It is shown in particular that an experimentally observed bimodality in the velocity distribution for large droplets is retrieved and that this feature can be linked to the droplet histories. Droplets forming the liquid film are slowed down and form a second, low velocity peak in the distribution. It is worth noting that the bimodal character of the velocity distribution in the spray of aeronautical injection systems was observed some time ago by McDonnell et al. (1990), and that their interpretation is confirmed by the present investigation.

Chapter 4

Revisiting swirl number formulations using LES

Swirling flows are of considerable practical importance. They are used for example to increase heat transfer in pipes or to stabilize flames at a distance from the injector unit by means of a central reverse flow that establishes an inner recirculation zone of hot combustion products. The level of swirl is governed by a dimensionless parameter designated as the swirl number, which essentially quantifies the ratio of the flow rate of the angular momentum axial component to the flow rate of axial momentum. This ratio controls to a great extent the structure of the swirling flow and its value determines whether an inner recirculation zone is established and whether a precessing vortex core (PVC) is formed in the flow. However, a major difficulty resides in calculating the swirl number from experimental measurements and over the last 50 years, several simplified formulas have been proposed to overcome this difficulty. The present study is aimed at using velocity and pressure profiles obtained by a large eddy simulation in a generic configuration to examine these simplified expressions and determine the conditions under which they may be applicable. The geometry comprises a cylindrical swirling injector, flush mounted in the back plane of a cylindrical combustion chamber. Although the swirl number is in principle constant when the flow is established in a duct with a constant cross-section, provided that viscous forces at the wall are negligible, one finds that this quantity varies substantially if inadequate approximations are made. Among the many possibilities one concludes that two swirl numbers should be distinguished. The first corresponding to the original definition features conservation properties, but is difficult to properly calculate from experimental data. The second is a highly simplified formulation that is commonly used today but does not share the conservation properties of the first formulation. Recommended practices are provided on how each of these swirl numbers should be calculated.

Contents

4.1 Introduction

Swirling flows are widely used in practice (Gupta et al. (1984)), whether to favor mixing at a jet outlet (Ribeiro and Whitelaw (1980); Chen and Driscoll (1989); Park and Shin (1993); Örlü and Alfredsson (2008)), to increase heat transfer in ducted flows (Chang and Dhir (1995); Steenbergen and Voskamp (1998)) or to stabilize flames in combustors (Syred et al. (1971); Beer and Chigier (1972); Syred and Beér (1974); Lilley (1977); Weber and Dugué (1992); Valera-Medina et al. (2011); Candel et al. (2014)). Early investigations indicated that it was worth defining a dimensionless group to classify swirling flows and

determine critical values for various phenomena. The Rossby number defined as the ratio of the mean axial velocity $< \overline{U}_x >$ to the azimuthal flow velocity ΩR

$$\mathrm{Ro} = \frac{< \overline{U}_x >}{\Omega R} \tag{4.1}$$

is commonly employed to analyze flows rotating at a rate Ω and featuring a typical scale R. The vortex breakdown phenomenon taking place in such flows was generally characterized in terms of this dimensionless number (Lucca-Negro and O'Doherty (2001); Spall et al. (1987); Billant et al. (1998); Liang and Maxworthy (2005)). This was adequate because in the relatively low Reynolds number flows that were investigated ($\mathrm{Re} < 10^3$), a solid body rotation could be assumed so that the Rossby number could be easily determined. In higher Reynolds number flows like those generated by combustor injectors, which are the main focus of the present article, the Rossby number is difficult to define in a precise manner because the flow is non uniform. This was noticed in some early studies on swirling injectors and a dimensionless group that had a greater degree of generality was proposed by Rose (1962); Beer and Chigier (1972); Chigier and Beér (1964); Chigier and Chervinsky (1967b); Chigier and Chervinsky (1967a). The swirl number concept was widely adopted as it essentially compares flow rates of moment of tangential momentum and of axial momentum

$$S(x) = \frac{1}{R(x)} \frac{G_\theta(x)}{G_x(x)} \tag{4.2}$$

where G_θ is the time average of the flow rate of the angular momentum axial component integrated over the axial cross-section, R is a characteristic radius of the swirling flow and G_x is the time average of the flow rate of axial momentum across the axial cross-section [1]. Independently of these early works, Reynolds **?** showed using a similarity analysis that the swirl number is the controlling parameter in the decay of swirling wakes and jets. As will be seen later, G_θ and G_x are conserved in free jets and in confined flows if the duct has a constant cross-section and viscous losses at the wall are negligible. These conservation properties enhance the degree of generality of the dimensionless number defined by Eq. (4.2) and this expression may be used with some confidence to characterize rotating flows. In axisymmetric configurations these fluxes may be written as follows (Gupta et al. (1984); Rose (1962); Chigier and Beér (1964); Chigier and Chervinsky (1967b))

$$G_\theta = 2\pi \int_0^\infty \rho r^2 \left(\overline{U_\theta}\, \overline{U_x} + \overline{u_\theta u_x} \right) dr \tag{4.4}$$

[1] As noted by Yajnik and Subbaiah Yajnik and Subbaiah (1973), the swirl number is related to the Rossby number with the following velocity U^* and rotation rate Ω^* scales:

$$\mathrm{Ro} = \frac{U^*}{\Omega^* R},\ G_\theta = \pi \rho U^* \Omega^* R^4,\ G_x = \pi \rho U^{*2} R^2 \tag{4.3}$$

$$G_x = 2\pi \int_0^\infty r \left[(\overline{p} - p_\infty) + \rho(\overline{U_x}^2 + \overline{u_x^2}) \right] dr \tag{4.5}$$

As G_θ and G_x are conserved, at least in certain types of flows, this is translated into a constant swirl number as underlined by Chigier and Beér (1964), a feature that is crucial for its accurate determination from measured velocity profiles. In practice however, the previously defined G_x and G_θ are replaced by simplified formulations but it is not easy to say if this does not reduce the degree of generality that was initially sought in defining the swirl number. The objective of the present work is to compare the various formulations and extract expressions that are most representative and are best suited to characterize flows formed by injectors in combustion systems.

The motivation of this investigation lies on the idea that flows which have the same swirl number and the same Reynolds number will also have similar dynamics. It is known for example that above a swirl number of 0.6, vortex breakdown takes place together with the formation of a recirculation zone around the jet axis (Lucca-Negro and O'Doherty (2001); Billant et al. (1998); Liang and Maxworthy (2005); Harvey (1962); Oberleithner et al. (2011)). This is at variance with other studies indicating that the critical value that leads to vortex breakdown is about 0.48 (Farokhi et al. (1989)), or 0.45 (Panda and McLaughlin (1994)), or 0.94 as in Toh et al. (2010). Some further studies indicated that the flow dynamics depends not only on the swirl number but also on the initial conditions (Farokhi et al. (1989); Gilchrist and Naughton (2005)). Escudier and Keller (1985) and Altgeld et al. (1983) further demonstrate that the outlet boundary conditions influence the near-field dynamics of subcritical non-reactive swirling flows, a result also observed in reactive conditions in Li and Gutmark (2005); Terhaar et al. (2012). The work of Weber and Dugué (1992) additionally suggests that in reactive flows, the strength of the inner recirculation zone can be estimated based on a swirl number accounting for the increase in temperature.

In practice, the variability of these results can be to some extent attributed to the different simplified formulations adopted to calculate the swirl number. It is thus worth re-examining the simplified swirl number formulations for isothermal flows and use large eddy simulations (LES) to compare the corresponding expressions, obtain swirl number estimates and analyze their behavior as the flow evolves in the axial direction.

This article is organized as follows. The next section contains a brief review of the different swirl number formulations derived from the Reynolds-averaged Navier-Stokes equations. This section includes the various combinations that may be deduced from the original definition and an expression that is most commonly used in practice that may be designated as "conventional". The computational geometry introduced in section 4.3 corresponds to a generic experimental configuration that is later used to validate the numerical simulations. The numerical set up is also briefly described in section 4.3. Experimental data are compared to the simulation results, and the general structure of the flow is examined in section 4.4. The various simplified formulations of the swirl

number, and the axial evolution thereof, are then compared in section 4.5. Section 4.6 specifically discusses a conventional swirl number formulation that is commonly employed in the literature. A few appendices are concerned with various practical aspects and some complementary analysis. Appendices C and D present recommended procedures that may be used in the practical computation of the swirl number from experimental or simulation data. Appendix E is concerned with the comparison of the flow and resulting swirl number obtained in a confined and unconfined configuration. The jump condition at a sudden expansion is discussed in appendix F. Finally, in appendix G, the conservation properties of non axisymmetric isothermal swirling flows are demonstrated.

4.2 A brief review of swirl number derivations and corresponding expressions

4.2.1 Free swirling jets

Formulations for the swirl number depend on the simplifications introduced to estimate the integrated fluxes defined previously. The method for writing the swirl number in terms of velocities and static pressure is described in Chigier and Chervinsky (1967b) and more recently in Örlü and Alfredsson (2008). The main steps are briefly reviewed to underline the main points in the most common simplifications.

Chigier and Chervinsky (1967b) employ the integral techniques used in shear flow theory. A similar process is used in what follows. It is convenient to begin with the Navier-Stokes equations for an axisymmetric, stationary, incompressible, newtonian flow. The Reynolds-averaged Navier-Stokes equations expressed in a cylindrical set of coordinates write

$$\frac{1}{r}\frac{\partial(r\overline{U_r})}{\partial r}+\frac{\partial\overline{U_x}}{\partial x}=0 \tag{4.6}$$

$$\begin{aligned}\overline{U_r}\frac{\partial\overline{U_r}}{\partial r}+\overline{U_x}\frac{\partial\overline{U_r}}{\partial x}-\frac{\overline{U_\theta}^2}{r}=&-\frac{1}{\rho}\frac{\partial\overline{p}}{\partial r}-\left[\frac{\partial\overline{{u_r}^2}}{\partial r}+\frac{\partial\overline{u_r u_x}}{\partial x}+\frac{1}{r}\left(\overline{{u_r}^2}-\overline{{u_\theta}^2}\right)\right]\\&+\frac{1}{\rho}\left[\frac{1}{r}\frac{\partial r\overline{\tau_{rr}}}{\partial r}+\frac{\partial\overline{\tau_{rx}}}{\partial x}-\frac{1}{r}\overline{\tau_{\theta\theta}}\right]\end{aligned} \tag{4.7}$$

$$\begin{aligned}\overline{U_r}\frac{\partial\overline{U_\theta}}{\partial r}+\overline{U_x}\frac{\partial\overline{U_\theta}}{\partial x}+\frac{\overline{U_r}\,\overline{U_\theta}}{r}=&-\left[\frac{\partial\overline{u_\theta u_x}}{\partial x}+\frac{1}{r^2}\frac{\partial(r^2\overline{u_r u_\theta})}{\partial r}\right]\\&+\frac{1}{\rho}\left[\frac{1}{r^2}\frac{\partial r^2\overline{\tau_{\theta r}}}{\partial r}+\frac{\partial\overline{\tau_{\theta x}}}{\partial x}\right]\end{aligned} \tag{4.8}$$

$$\overline{U_r}\frac{\partial\overline{U_x}}{\partial r}+\overline{U_x}\frac{\partial\overline{U_x}}{\partial x}=-\frac{1}{\rho}\frac{\partial\overline{p}}{\partial x}-\left[\frac{\partial\overline{u_x^2}}{\partial x}+\frac{1}{r}\frac{\partial(r\overline{u_r u_x})}{\partial r}\right]+\frac{1}{\rho}\left[\frac{1}{r}\frac{\partial r\overline{\tau_{rx}}}{\partial r}+\frac{\partial\overline{\tau_{xx}}}{\partial x}\right] \tag{4.9}$$

where the mean and fluctuating velocity components satisfy the following boundary conditions

$$\begin{aligned}\overline{U_x}(x,r=\infty)&=u_x(t,x,r=\infty)=0\\ \overline{U_r}(x,r=0)=\overline{U_r}(r=\infty)&=u_r(t,x,r=\infty)=0\\ \overline{U_\theta}(x,r=0)=\overline{U_\theta}(x,r=\infty)&=u_\theta(t,x,r=\infty)=0\\ \frac{\partial\overline{U_\theta}}{\partial r}(x,r=0)=\frac{\partial\overline{U_\theta}}{\partial r}(x,r=\infty)&=0\\ \overline{\tau}(x,r=\infty)&=\underline{\underline{0}}\end{aligned} \tag{4.10}$$

The balance for the flow rate of axial momentum G_x can be obtained by first multiplying Eq. (4.9) by r and integrating between $r=0$ and $r=\infty$. Using Eq. (4.6), this yields

$$\frac{d}{dx}\int_0^\infty r\left[(\overline{p}-p_\infty)+\rho(\overline{U_x}^2+\overline{u_x^2})\right]dr=\frac{d}{dx}\int_0^\infty r\overline{\tau_{xx}}dr \tag{4.11}$$

The viscous term appearing in the right hand side is usually neglected as swirling flows of interest are generally characterized by a high Reynolds number. The pressure at $r=\infty$, p_∞, is included in this expression in order for the integral to remain finite. This is specific to free swirling jet flows. Equation (4.11) then expresses the conservation of G_x:

$$\frac{dG_x}{dx}=\frac{dG^f_{x,P}}{dx}=2\pi\frac{d}{dx}\int_0^\infty \rho r\left[(\overline{p}-p_\infty)+\rho(\overline{U_x}^2+\overline{u_x^2})\right]dr=0 \tag{4.12}$$

The notation $G^f_{x,P}$ is introduced to indicate that G_x comprises the fluctuating (superscript f) and pressure (subscript P) terms, which are often neglected due to the difficulty involved in the determination of pressure inside the flow (see Gupta et al. (1984); Syred and Beér (1974)).

A convenient formulation removing the need for pressure measurements is derived in Chigier and Chervinsky (1967b). The Navier-Stokes equations, Eqs. (4.6) - (4.9), are first simplified by considering that in a swirling jet, viscous terms can be neglected and boundary layer assumptions can be adopted. For more details on the use of boundary layer assumptions in shear flows, see for example Pope (2000). Equation (4.7) simplifies into

$$-\frac{\overline{U_\theta}^2}{r}=-\frac{1}{\rho}\frac{\partial\overline{p}}{\partial r}-\left[\frac{\partial\overline{u_r}^2}{\partial r}+\frac{1}{r}\left(\overline{u_r}^2-\overline{u_\theta}^2\right)\right] \tag{4.13}$$

Multiplying Eq. (4.13) by r^2 and integrating the result between $r = 0$ and $r = \infty$ yields

$$\int_0^\infty r\,(\overline{p} - p_\infty)\,dr = -\frac{1}{2}\int_0^\infty \rho r\,(\overline{U_\theta}^2 + \overline{u_r^2} + \overline{u_\theta^2})\,dr \tag{4.14}$$

This result is sometimes combined with a simplified form of Eq. (4.13) where fluctuations are neglected (Chigier and Chervinsky (1967b); Mattingly and Oates (1986)). One may then write

$$\frac{\partial \overline{p}}{\partial r} \simeq \rho \frac{\overline{U_\theta}^2}{r} \tag{4.15}$$

Equations (4.14) and (4.11) can be merged into

$$\frac{d}{dx}\int_0^\infty \rho r \left(\overline{U_x}^2 - \frac{\overline{U_\theta}^2}{2} + \overline{u_x^2} - \frac{\overline{u_r^2} + \overline{u_\theta^2}}{2}\right) dr = 0 \tag{4.16}$$

To get a simplified version it is sometimes assumed that $\overline{u_x^2} - (\overline{u_r^2} + \overline{u_\theta^2})/2$ is negligible with respect to U_x^2 to obtain

$$\frac{d}{dx}\int_0^\infty \rho r \left(\overline{U_x}^2 - \frac{\overline{U_\theta}^2}{2}\right) dr = 0 \tag{4.17}$$

This last result (4.17) is used for example by Ribeiro and Whitelaw (1980) to define a simplified expression of G_x, that can be called $G^0_{x,U,BL}$, where the superscript 0 indicates that velocity fluctuations are neglected, and the subscript U, BL that a velocity expression is used to replace the pressure term under a boundary layer assumption:

$$G^0_{x,U,BL} = 2\pi \int_0^\infty \rho r \left(\overline{U_x}^2 - \frac{\overline{U_\theta}^2}{2}\right) dr \tag{4.18}$$

In distinction with Chigier and Chervinsky (1967b), Örlü and Alfredsson (2008) keep the fluctuating terms in their final result and express the conservation of the flow rate of axial momentum in the form

$$G^f_{x,U,BL} = 2\pi \int_0^\infty \rho r \left(\overline{U_x}^2 - \frac{\overline{U_\theta}^2}{2} + \overline{u_x^2} - \frac{\overline{u_r^2} + \overline{u_\theta^2}}{2}\right) dr \tag{4.19}$$

The simplified expressions (4.18) and (4.19) account for effects of static pressure within the swirling flow without direct measurements of the corresponding term. These expressions however assume a high Reynolds number and use an approximation of the radial pressure gradient in terms of the mean azimuthal velocity.

Consider now the axial flow rate of the angular momentum axial component G_θ defined

as

$$G_\theta = G_\theta^f = 2\pi \int_0^\infty \rho r^2 \left(\overline{U_\theta}\,\overline{U_x} + \overline{u_\theta u_x}\right) dr \tag{4.20}$$

Here again, the superscript f indicates that the fluctuations are kept in G_θ^f. By multiplying Eq. (4.8) by r^2 and integrating between 0 and ∞, the following expression can be obtained for the balance of the flow rate of the angular momentum axial component

$$\frac{d}{dx}\int_0^\infty \rho r^2 \left(\overline{U_\theta}\,\overline{U_x} + \overline{u_x u_\theta}\right) dr = \frac{d}{dx}\int_0^\infty r^2\,\overline{\tau_{\theta x}}\,dr \tag{4.21}$$

As for Eq. (4.11), the viscous term in the right hand side is generally neglected. Keeping the fluctuating term, Örlü and Alfredsson (2008) obtain the following expression

$$\frac{d}{dx}\int_0^\infty r^2 \left(\overline{U_\theta}\,\overline{U_x} + \overline{u_\theta u_x}\right) dr = 0 \tag{4.22}$$

When the cross-correlation of the fluctuating velocities is neglected (Chigier and Chervinsky (1967b)), the previous expression simplifies to

$$\frac{d}{dx}\int_0^\infty r^2\,\overline{U_\theta}\,\overline{U_x}\,dr = 0 \tag{4.23}$$

Equations (4.11), (4.16) and (4.17) correspond to conservation relations for G_x under various simplifying assumptions and similarly, Eqs. (4.22) and (4.23) to conservation relations for G_θ. These results may then be combined in various ways to yield a set of expressions for the swirl number defined by Eq. (4.2). In the remainder of the paper, the swirl number will be notated as S_{sub}^{super}. The superscript f is used to indicate that the fluctuating terms $\overline{u_\theta u_x}$ and $\overline{u_x^2}$ are kept, while the superscript 0 indicates that they are neglected. The subscript P is used to indicate that the pressure term $\overline{p} - p_\infty$ is kept, while the subscript 0 indicates that it is neglected, and the subscript U, BL that $\overline{p} - p_\infty$ is replaced with the velocity formulation introduced in Eq. (4.19). The same notation is used for simplified formulations for the integrated fluxes G_x and G_θ.

The most complete formulation for the swirl number S_P^f takes into account both the static pressure term and the velocity fluctuations. The reference radius R used in the swirl number definition for free jets (Eq. (4.2)) is the injector radius at its oulet.

$$S_P^f = \frac{G_\theta^f}{R G_{x,P}^f} = \frac{\int_0^\infty \rho \left(\overline{U_\theta}\,\overline{U_x} + \overline{u_\theta u_x}\right) r^2 dr}{R\int_0^\infty \left[(\overline{p} - p_\infty) + \rho\left(\overline{U_x}^2 + \overline{u_x^2}\right)\right] r dr} \tag{4.24}$$

If the turbulent fluctuations terms are deleted one has

$$S_P^0 = \frac{G_\theta^0}{R G_{x,P}^0} = \frac{\int_0^\infty \rho\,\overline{U_\theta}\,\overline{U_x}\,r^2 dr}{R\int_0^\infty \left[(\overline{p} - p_\infty) + \rho\,\overline{U_x}^2\right] r dr} \tag{4.25}$$

Since static pressure and density are difficult to measure inside the flow, their variations are often neglected in the expression of the swirl number and the following expression is widely used

$$S_0^0 = \frac{G_\theta^0}{RG_{x,0}^0} = \frac{\int_0^\infty \rho\,\overline{U_\theta}\,\overline{U_x}\,r^2dr}{R\int_0^\infty \rho\,\overline{U_x}^2\,rdr} \tag{4.26}$$

To get closer to the original formulation S_P^f, but to avoid measuring the static pressure, it is possible to write the conservation of the axial flow rate of axial momentum expressed in terms of velocities only (Eq. (4.16)). Under boundary layer assumptions, the expression of the swirl number then takes the form

$$S_{U,BL}^f = \frac{G_\theta^f}{RG_{x,U,BL}^f} = \frac{\int_0^\infty \rho\,(\overline{U_\theta}\,\overline{U_x} + \overline{u_\theta u_x})\,r^2dr}{R\int_0^\infty \rho\left(\overline{U_x}^2 - \frac{1}{2}\overline{U_\theta}^2 + \overline{u_x^2} - \frac{1}{2}(\overline{u_r^2} + \overline{u_\theta^2})\right)rdr} \tag{4.27}$$

If the fluctuation terms are neglected, this becomes

$$S_{U,BL}^0 = \frac{G_\theta^0}{RG_{x,U,BL}^0} = \frac{\int_0^\infty \rho\,\overline{U_\theta}\,\overline{U_x}\,r^2dr}{R\int_0^\infty \rho\left(\overline{U_x}^2 - \frac{1}{2}\overline{U_\theta}^2\right)rdr} \tag{4.28}$$

A new swirl number formulation is introduced in the present article (section 4.5.3). Similarly to $S_{U,Bl}^f$, it expresses the conservation of the axial flow rate of axial momentum in terms of velocities only, but it does no rely on a boundary layer simplification. It writes

$$S_U^f = \frac{G_\theta^f}{RG_{x,U}^f} = \frac{\int_0^\infty \rho\,\left(\overline{U_\theta}\,\overline{U_x} + \overline{u_\theta u_x}\right)\,r^2dr}{R\int_0^\infty \rho\left[\overline{U_x}^2 + \overline{u_x^2} - \frac{1}{2}\left(\overline{U_\theta}^2 + \overline{U_r}^2 + \overline{u_r^2} + \overline{u_\theta^2}\right) + \frac{r}{2}\frac{\partial}{\partial x}\left(\overline{U_x}\,\overline{U_r} + \overline{u_x u_r}\right)\right]rdr} \tag{4.29}$$

These six formulations use different levels of simplification, and the aim of this article is to examine the impact of these simplifications on the calculated swirl numbers. It is also natural to add to these formulations an expression that will be designated as "conventional"

$$S_{conv} = \frac{\int_0^{R_{lim}} \rho\,\overline{U_\theta}\,\overline{U_x}\,r^2dr}{R\int_0^{R_{lim}} \rho\,\overline{U_x}^2\,rdr} \tag{4.30}$$

The reference radius R is taken equal to the injector radius while the radial limit of integration R_{lim} needs to be specified on physical grounds. We will see that this may be defined by considering the evolutions of the flow rates $G_{x,0}^0$ and G_θ^0.

4.2.2 Confined flows

In the previous developments all integrations were carried out from 0 to ∞, but it is evident that these integrations stop at a place where the jet velocity has essentially vanished,

or at a radial distance R_c if the flow is confined by a duct of radius R_c.

It is thus logical to examine swirling flows confined in a duct of constant radius R_c. A no-slip boundary condition is used at the duct wall and Eq. (4.10) is then

$$\begin{aligned} \overline{U_x}(x, r = R_c) &= u_x(t, x, r = R_c) = 0 \\ \overline{U_r}(x, r = 0) = \overline{U_r}(r = R_c) &= u_r(t, x, r = R_c) = 0 \\ \overline{U_\theta}(x, r = 0) = \overline{U_\theta}(x, r = R_c) &= u_\theta(t, x, r = R_c) = 0 \end{aligned} \tag{4.31}$$

The definition of G_x is then

$$G_x = G^f_{x,P} = 2\pi \int_0^{R_c} r \left[(\overline{p} - p_{ref}) + \rho(\overline{U_x}^2 + \overline{u_x^2}) \right] dr \tag{4.32}$$

and Eq. (4.11) writes

$$\frac{dG^f_{x,P}}{dx} = 2\pi \frac{d}{dx} \left(\int_0^{R_c} r \overline{\tau_{xx}} dr \right) + 2\pi R_c \, \overline{\tau_{rx}}|_{r=R_c} \tag{4.33}$$

A reference pressure is not strictly required but is included to keep formulations similar to those derived for free swirling jets allowing direct comparisons between confined and unconfined cases. Furthermore, the pressure term $\overline{p} - p_{ref}$ then has the same order of magnitude as that of the velocity term $\rho(\overline{U_x}^2 + \overline{u_x^2})$, a feature of practical interest. There is no widespread consensus on the choice of the reference value p_{ref}. It is often suggested that it may be taken equal to a pressure at the wall as this yields relatively simple expressions for the swirl number (Mattingly and Oates (1986); Weber and Dugué (1992)). This point will be considered in subsection 4.5.2. The right hand side term in Eq. (4.33) comprises viscous terms, accounting for dissipation in the flow and at the wall. Mattingly and Oates (1986) derived the following balance while neglecting the turbulent fluctuating terms and working under a high Reynolds number assumption except at the wall

$$\frac{d}{dx} \int_0^{R_c} r \left[(\overline{p} - p_{ref}) + \rho \overline{U_x}^2 \right] dr = R_c \, \overline{\tau_{rx}}|_{r=R_c} \tag{4.34}$$

Here, the right hand side is the axial component of the wall shear stress. Using the method of Chigier and Chervinsky (1967b), Mattingly and Oates (1986) propose an equation similar to Eq. (4.14) for confined flows

$$\int_0^{R_c} r \, (\overline{p} - p_{ref}) \, dr = \frac{1}{2} R_c^2 (\overline{p}|_{r=R_c} - p_{ref}) - \frac{\rho}{2} \int_0^{R_c} r \, (\overline{U_\theta}^2 + \overline{u_r^2} + \overline{u_\theta^2}) \, dr \tag{4.35}$$

This leads to the following balance equation for the flow rate of axial momentum

$$G_x = G^f_{x,U,BL} = 2\pi \int_0^{R_c} r\rho \left[\overline{U_x}^2 - \frac{1}{2} \overline{U_\theta}^2 + \overline{u_x{}^2} - \frac{1}{2} \left(\overline{u_r{}^2} + \overline{u_\theta{}^2} \right) \right] dr + \pi R_c^2 (\overline{p}|_{r=R_c} - p_{ref}) \tag{4.36}$$

$$\frac{dG^f_{x,U,BL}}{dx} = 2\pi R_c \, \overline{\tau_{rx}}|_{r=R_c} \tag{4.37}$$

The axial flow rate of moment of angular momentum is defined as

$$G_\theta = G^f_\theta = 2\pi \int_0^{R_c} \rho r^2 \left(\overline{U_\theta} \, \overline{U_x} + \overline{u_r u_\theta} \right) dr \tag{4.38}$$

and its changes in the axial direction may be deduced from the momentum balance equation (Eq. (4.8))

$$\frac{dG^f_\theta}{dx} = 2\pi \frac{d}{dx} \int_0^{R_c} \rho r^2 \left(\overline{U_\theta} \, \overline{U_x} + \overline{u_r u_\theta} \right) dr = 2\pi \frac{d}{dx} \left(\int_0^{R_c} r^2 \, \overline{\tau_{\theta x}} \, dr \right) + 2\pi R_c^2 \, \overline{\tau_{r\theta}}|_{r=R_c} \tag{4.39}$$

The viscous losses in the flow are neglected by most authors. Mattingly and Oates (1986) however keep the wall shear stress term $R_c^2 \, \overline{\tau_{r\theta}}|_{r=R_c}$. Equations (4.24) to (4.29) can then be adapted to confined flows in ducts with a radius R_c which now constitutes the upper limit of integration.

$$S^f_P = \frac{G^f_\theta}{R_c G^f_{x,P}} = \frac{\int_0^{R_c} \rho \left(\overline{U_\theta} \, \overline{U_x} + \overline{u_\theta u_x} \right) r^2 dr}{R_c \int_0^{R_c} \left[(\overline{p} - p_{ref}) + \rho \left(\overline{U_x}^2 + \overline{u_x^2} \right) \right] r dr} \tag{4.40}$$

$$S^0_P = \frac{G^0_\theta}{R_c G^0_{x,P}} = \frac{\int_0^{R_c} \rho \, \overline{U_\theta} \, \overline{U_x} \, r^2 dr}{R_c \int_0^{R_c} \left[(\overline{p} - p_{ref}) + \rho \, \overline{U_x}^2 \right] r dr} \tag{4.41}$$

$$S^0_0 = \frac{G^0_\theta}{R_c G^0_{x,0}} = \frac{\int_0^{R_c} \rho \, \overline{U_\theta} \, \overline{U_x} \, r^2 dr}{R_c \int_0^{R_c} \rho \, \overline{U_x}^2 r dr} \tag{4.42}$$

$$S^f_{U,BL} = \frac{G^f_\theta}{R_c G^f_{x,U,BL}} = \frac{\int_0^{R_c} \rho \left(\overline{U_\theta} \, \overline{U_x} + \overline{u_\theta u_x} \right) r^2 dr}{R_c [\int_0^{R_c} \rho \left(\overline{U_x}^2 - \frac{1}{2} \overline{U_\theta}^2 + \overline{u_x^2} - \frac{1}{2} (\overline{u_r^2} + \overline{u_\theta^2}) \right) r dr + \frac{1}{2} R_c{}^2 \left(\overline{p}|_{r=R_c} - p_{ref} \right)]} \tag{4.43}$$

$$S^f_U = \frac{\int_0^{R_c} \rho \left(\overline{U_\theta} \, \overline{U_x} + \overline{u_\theta u_x} \right) r^2 dr}{R_c \int_0^{R_c} \rho \left[\overline{U_x}^2 + \overline{u_x^2} - \frac{1}{2} \left(\overline{U_\theta}^2 + \overline{U_r}^2 + \overline{u_r^2} + \overline{u_\theta^2} \right) + \frac{r}{2} \frac{\partial}{\partial x} \left(\overline{U_x} \, \overline{U_r} + \overline{u_x u_r} \right) \right] r dr + \frac{R_c^3}{2} \left(\overline{p}|_{r=R_c} - p_{ref} \right)} \tag{4.44}$$

One may note that many authors employing Eq. (4.43) use a reference pressure equal to

the pressure at the wall in the axial section where the swirl number is measured, thereby eliminating the term $\frac{1}{2}R_c^2\left(\overline{p}|_{r=R_c} - p_{ref}\right)$ (Chen et al. (1989); Weber and Dugué (1992); Mattingly and Oates (1986); Chen et al. (1990)). The reference pressure then varies with the axial position in the system. This assumption together with the suppression of the turbulent terms yields a fairly simple expression

$$S_{U,BL}^0 = \frac{G_\theta^0}{R_c G_{x,u}^0} = \frac{\int_0^{R_c} \rho\, \overline{U_\theta}\, \overline{U_x}\, r^2 dr}{R_c \int_0^{R_c} \rho \left(\overline{U_x}^2 - \frac{1}{2}\overline{U_\theta}^2\right) r dr} \tag{4.45}$$

Finally, it is worth noting that the conservation properties that have been demonstrated here for G_θ^f, $G_{x,P}^f$ and the swirl number S_P^f in a cylindrical duct extend to all confinements with a constant cross-section as shown in appendix G.

4.2.3 Geometrical formulations

The previous expressions require measurements of velocity profiles that are not always available. They are often replaced by algebraic expressions based on the injector geometry. The present section focuses on expressions suited for the geometry presented in Fig. 4.1, where a radial swirler is placed at the bottom of a cylindrical injection duct. Some assumptions are always placed on the shape for the velocity profiles, which may not necessarily be realistic. One such expression for the swirl number of radial swirlers fed by tangential channels only involves the swirler outlet diameter D, the radial distance R_0 separating the axis of each tangential channel from the injector axis and A_t the total cross-section area of these channels (Claypole and Syred (1981); Zhang et al. (2005))

$$S_{geo,1} = \frac{\pi D_{sw} R_0}{2A_t} \tag{4.46}$$

This expression is deduced from expression S_0^0 (Eq. (4.26)), by considering a flat velocity profile for the velocity $\overline{U_x}$, that is to say independent of r, and by assuming that the azimuthal velocity component $\overline{U_\theta}$ is constant over the entire radius of the injector. The latter hypothesis may be acceptable with tangential channel holes which are very large, of the order of magnitude of the radius of the injector, but not with tangential holes having a diameter much smaller than the radius of the injector. Durox et al. (2013) compared this equation with experimental results and it was shown to yield values that overestimate results obtained by integrating velocity profiles and making use of expression S_{conv}. To correct this effect, it was suggested by Durox et al. (2013) that the azimuthal velocity profile could be represented by a solid body rotation, with $\overline{U_\theta}$ depending linearly on r, yielding an expression $S_{geo,2}$ that was one half of $S_{geo,1}$

$$S_{geo,2} = \frac{\pi D_{sw} R_0}{4A_t} \tag{4.47}$$

In Durox et al. (2013), this expression was found to be in better agreement with experimental determinations of the conventional swirl number S_{conv}.

Chigier and Chervinsky (1967b) proposed a simplified expression, based on $S^0_{U,BL}$ (Eq. (4.28)), which indirectly takes into account the pressure correction, via $\overline{U_\theta}$. For a solid body rotation with a uniform axial velocity in the duct, they obtained

$$S_{geo,3} = \frac{(1/2)G}{1-(1/4)G^2} \tag{4.48}$$

where $G = (\mathrm{Max}\,\overline{U_\theta})/(\mathrm{Max}\,\overline{U_x})$ is the ratio between the maximum values of $\overline{U_\theta}$ and $\overline{U_x}$ in a section of the flow.

Another expression derived by Sheen et al. (1996) for a radial swirler with variable pitch blades is particularly appealing because the swirl number is given in terms of volumetric mean values of the azimuthal and axial velocities

$$S_{geo,4} = \frac{3}{4}\frac{<\overline{U_\theta}>}{<\overline{U_x}>} \tag{4.49}$$

In many cases the swirl number is deduced from geometrical parameters pertaining to the blades that serve to turn the flow, or to the injection holes of the tangential flow in the channel (Gupta et al. (1984); Syred et al. (1971); Lilley (1977)). However, the many geometrical expressions that can be found in the literature are derived by assuming a certain flow field and lead to swirl number estimates that often differ from values determined from experimental velocity profiles.

4.2.4 Limitations in using the various formulations

This review of the literature on swirl number formulations indicates that much effort has been made to define a characteristic dimensionless number that will be constant throughout the flow. An important point to note however, is that depending on the formulation, the different equations for the swirl number (Eqs. (4.24) to (4.28) and (4.40) to (4.45)) require a set of assumptions to ensure the same invariance properties as S^f_P (Eq. (4.24)). The high Reynolds number hypothesis is widely used, and justifies that the viscous terms are neglected. It is quite suitable in the case of injectors used in combustors. However, in many practical injectors, there are reductions or expansions in cross-section. In this case, the balance equations (Eqs. (4.11), (4.21), (4.33) and (4.39)) are no longer valid inside the injector. Choi et al. (2018); Degenève et al. (2019) present models for the evolution of the swirl number in such configurations.

To calculate the swirl number using integral expressions, it is necessary to know the profiles of the different velocity components and the static pressure distribution in the flow. In certain formulations (Eqs. (4.25), (4.26) and (4.28)), the turbulent fluctuations and/or static pressure are eliminated. Some studies (Ribeiro and Whitelaw (1980); Chigier and Beér (1964); Toh et al. (2010); Sislian and Cusworth (1986); Mahmud et al. (1987)) have tried to quantify the importance of the neglected terms. Concerning turbulent fluctuations, in Ribeiro and Whitelaw (1980); Toh et al. (2010) the authors have shown

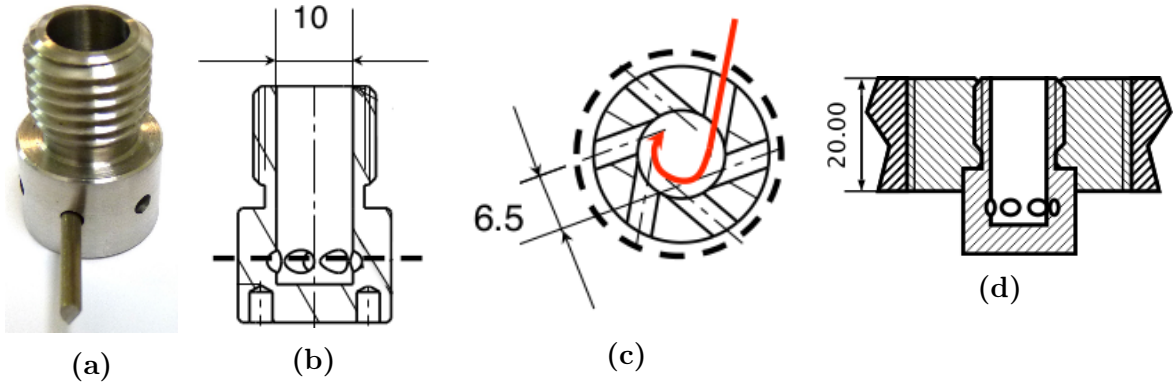

Figure 4.1: *The swirler comprises six tangential channels, which are* 3 mm *in diameter. (a) Photograph of the swirler. A small rod is placed in one of the holes, (b) Axial cut, (c) Transversal cut at the height indicated by the dashed line in (b). The red arrow shows the air path. (d) Swirler mounted in the combustion chamber backplane. Adapted from Durox et al. (2016).*

experimentally that for high swirl numbers, terms that are usually neglected take significant values. The fluctuations u_r, u_θ and u_x are small but not necessarily negligible compared to the average velocities. It is concluded in these two studies that the turbulent fluctuations could significantly contribute to the axial flow rates used to compute the swirl number. The same authors also investigated the static pressure correction in some peripheral regions of the swirled flow, estimated indirectly using Eq. (4.15). They found that the static pressure correction could be of the same order of magnitude as $\rho \overline{U_x}^2$. Direct measurements of the static pressure are performed in Chigier and Beér (1964); Mahmud et al. (1987) using Pitot tubes, and it is shown that the oftentimes neglected pressure term is important to assure the swirl number invariance property. Despite these previous studies, there is still a need to get a precise evaluation of these terms.

Given the experimental difficulties, it is interesting to examine these issues using numerical tools. Because Large Eddy Simulation (LES) methods are considered mature for computing swirling flows, it is timely to carry out a study of a turbulent swirling flow and discuss the various expressions of the swirl number. This is accomplished by examining a generic case in which a swirler is placed in a cylindrical injector connected to a cylindrical chamber. It is thus possible to examine the flow inside the injector unit, in the immediate vicinity of its outlet and in the chamber. The data obtained from calculations will be first validated with Laser Doppler Velocimetry (LDV) measurements.

4.3 Geometry of the generic swirl injector and description of the numerical scheme

The geometry used in this study corresponds to that of the SICCA combustor, a single injector system operating at EM2C laboratory. The swirling flow can be used to stabilize premixed swirling flames as in Bourgouin et al. (2013); Candel et al. (2012); Moeck et al. (2012); Palies et al. (2009). In the present study, all tests are carried out in an isothermal,

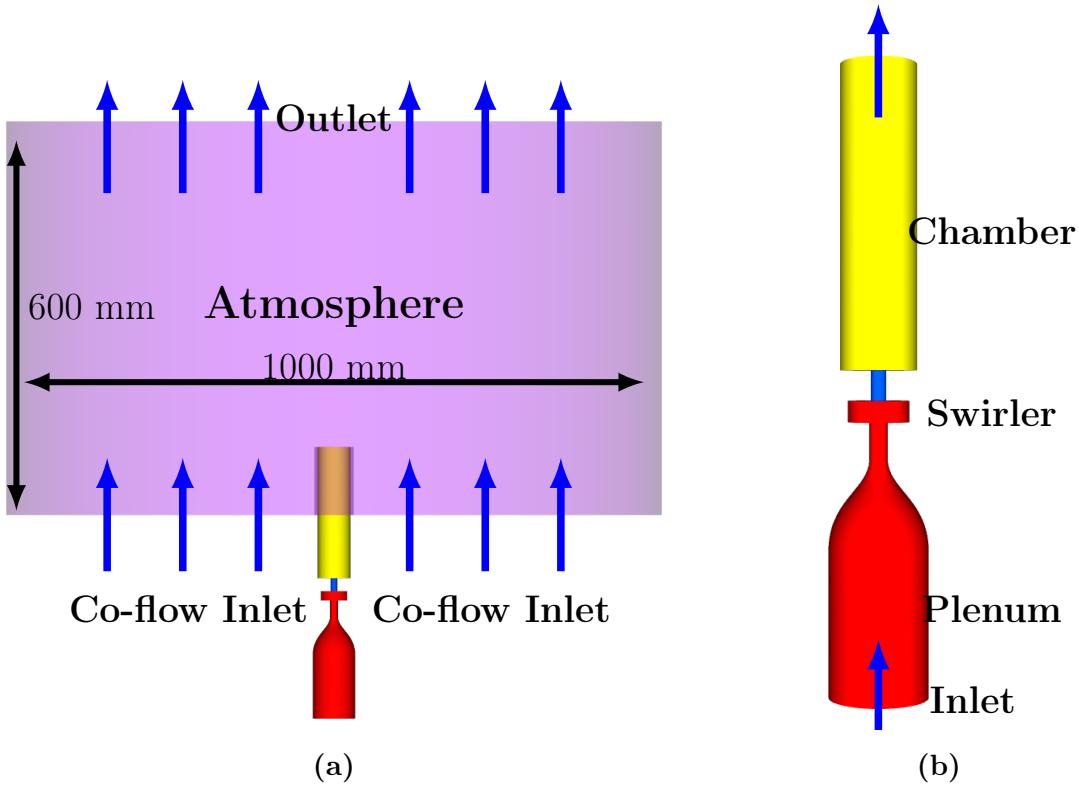

Figure 4.2: *Computational domain; (a) Full domain showing the atmosphere and associated co-flow; (b) Close-up view of the plenum, swirler and combustion chamber; further details may be found in Philip (2016). This figure is adapted from this reference.*

cold flow configuration, only using air at ambient conditions.

The experimental setup comprises a plenum fed with compressed air through a Bronkhorst EL-Flow mass flow controller, with a relative accuracy better than 0.75%. The plenum ends in a convergent section leading to the swirler. The injector (Fig. 4.1) comprises a cylindrical channel, of diameter $D_{sw} = 10\,\text{mm}$ and length $L_{inj} = 26\,\text{mm}$, flush mounted on the backplane of the combustion chamber. At the inlet of the swirler, the flow passes through six cylindrical tangential channels of internal diameter $D_{ch} = 3\,\text{mm}$. The axis of the channels is $R_0 = 3.25\,\text{mm}$ away from the axis of the cylinder, and it is located at $x_{channel} = 3.5\,\text{mm}$ above the bottom of the swirler. The combustion chamber is formed by a quartz tube of inner diameter $D_Q = 50\,\text{mm}$ and length $L_Q = 200\,\text{mm}$. A Dantec 2-component Phase Doppler Velocimetry system provides the axial, radial and tangential velocity components.

Application of Eqs. (4.46) and (4.47) yields the following geometrical swirl number values:

$$\begin{aligned} S_{geo,1} &= 1.2 \\ S_{geo,2} &= 0.60 \end{aligned} \tag{4.50}$$

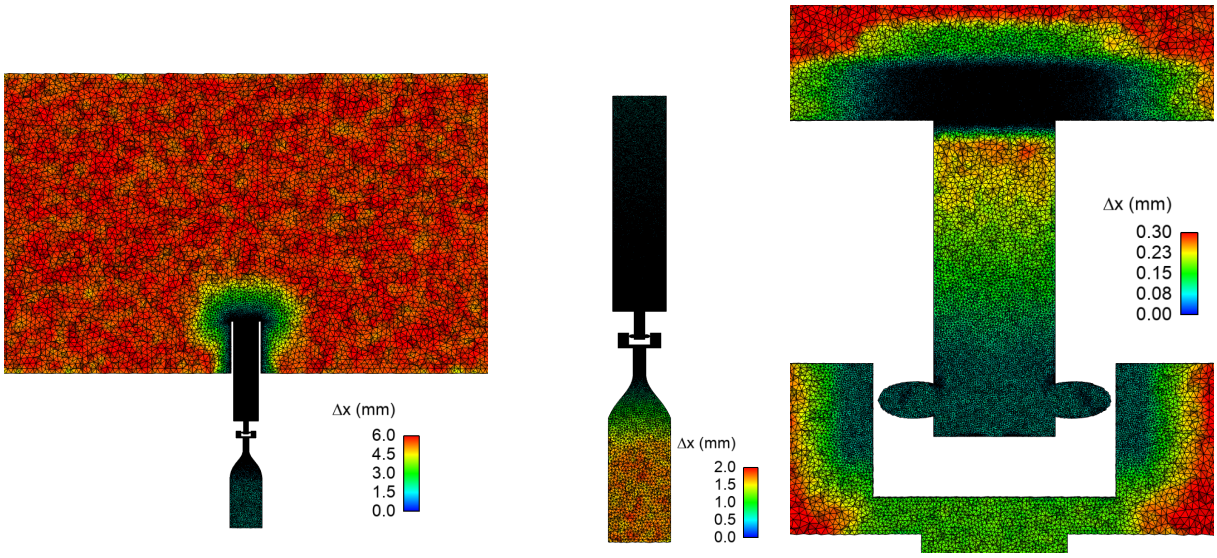

Figure 4.3: *Mesh used for the simulation and element size Δx; (a) Axial cut showing a typical element size of* 6 mm *in the atmosphere; (b) Axial cut showing element sizes in the plenum ($\Delta x =$ 2 mm at the inlet to $\Delta x = 0.3$ mm in the injector). In the chamber, the cell size $\Delta x = 0.25$ mm near the backplane grows quasi linearly to $\Delta x = 0.6$ mm at the chamber outlet; (c) Detailed view of the mesh inside the injector. At the injector outlet the typical cell size is $\Delta x = 50$ µm.*

For swirling injectors, the Reynolds number is commonly based on the average axial velocity at the nozzle exit and the orifice diameter (Billant et al. (1998); Toh et al. (2010)):

$$\mathrm{Re} = \frac{\langle \overline{U_x} \rangle D_{sw}}{\nu} = 1.11\ 10^4 \tag{4.51}$$

Numerical simulations are carried out using AVBP, a compressible Navier-Stokes solver developed by CERFACS (https://www.cerfacs.fr/avbp7x). The third order in time and space numerical scheme TTGC (Colin and Rudgyard (2000)) is used relying on a two-step Taylor-Galerkin weighted residual central distribution scheme. Subgrid scale turbulence is represented by the SIGMA model described in Baya Toda et al. (2010). Navier-Stokes Characteristic Boundary Conditions (NSCBC) (Poinsot and Lele (1992)) are employed and set according to the values used in the experiment. The inlet air temperature is set to 298 K, the outlet pressure to $p_{atm} = 101\,325$ Pa. The mass flow rate at the inlet upstream of the swirler is $1.61\,\mathrm{g\,s^{-1}}$. A logarithmic law of the wall is applied on the solid boundaries (high Reynolds number approach: $u^+ = \ln(9.2y^+)/0.41$ following the implementation described in Jaegle et al. (2010)). This treatment is preferred to a no-slip condition as the thickness of the laminar sublayer near the wall is estimated to be around $0.1\Delta x$ to $0.25\Delta x$ within the injector, and $0.5\Delta x$ in the chamber (Δx being the characteristic size of a mesh element). Comparison of velocity profiles obtained using the wall law and no slip approach (not shown here) confirmed the choice of the logarithmic law of the wall model.

The computational domain, presented in Fig. 4.2, comprises the plenum, swirler and combustion chamber. An atmosphere with a slow co-flow is added. The mesh is adapted from Philip (2016). The adaptive mesh refinement (AMR) method of Daviller et al. (2017) is used to refine the mesh. Based on the Loss in Kinetic Energy (LIKE) criterion, this AMR method is designed to capture the head loss of swirled injection systems in LES. It is also found in the present configuration to greatly improve the quality of the velocity profiles at the outlet of the injector. A total of 5 steps of AMR are used for this simulation, the parameters for the AMR, defined in Daviller et al. (2017), are $\alpha = 60$ and $\epsilon = 0.7$. The final mesh comprises a total of 33.55 million tetrahedral elements. The sizes of mesh elements are indicated in Fig. 4.3.

4.4 Numerical results and comparison with experiments

4.4.1 Validation of the simulation

It is first important to ensure that the simulation is reliable by comparing velocity profiles with experimental data acquired with an LDV system downstream of the injector. The injector flow is seeded with micronic silicon oil droplets. Profiles are determined at three heights from the injector outlet, respectively $0.25D_{sw}$, $0.5D_{sw}$ and D_{sw}. The average and RMS velocity are measured every 0.25 mm for each of the three components. With the cylindrical quartz confinement and its high curvature, LDV measurements can only by conducted up to a radial position of $r = 10$ mm, and are additionally very challenging for the radial velocity component, which could not be adequately measured for radial positions exceeding $r = 7$ mm.

The same velocity profiles are extracted from the Large Eddy Simulation, by time averaging over 250 ms. A sample is taken every 20 µs. Assuming that the mean flow is axi-symmetric, a further averaging is performed by rotation around the axis. Comparison between the LES and LDV measurements are shown in Fig. 4.4, where mean (black) and RMS (red) values of the axial, tangential and radial velocities are compared in three axial sections.

The agreement between the mean LDV velocity data and the simulation results is quite good. Concerning the axial velocity U_x, at $x = 0.25D_{sw}$, the velocity peak is predicted at a slightly smaller radius by the simulation, $r^{peak}_{LES} = 5.2$ mm as it is measured by LDV, $r^{peak}_{LDV} = 5.45$ mm. The difference approximately corresponds to the resolution of the LDV measurements. The peak velocity at $x = 0.25D_{sw}$ is underpredicted by 4.7%. This small error is still present at $x = 0.5D_{sw}$ but becomes vanishingly small further downstream. The peak of the tangential velocity is also predicted 0.45 mm closer to the centerline by the LES, and is overestimated by 6.2% at $x = 0.25D_{sw}$. Further downstream, the agreement is very good for the mean velocities, although the RMS values are underestimated at $x = D_{sw}$. The radial velocities are well predicted by LES, with only a very slight underprediction at the highest axial positions.

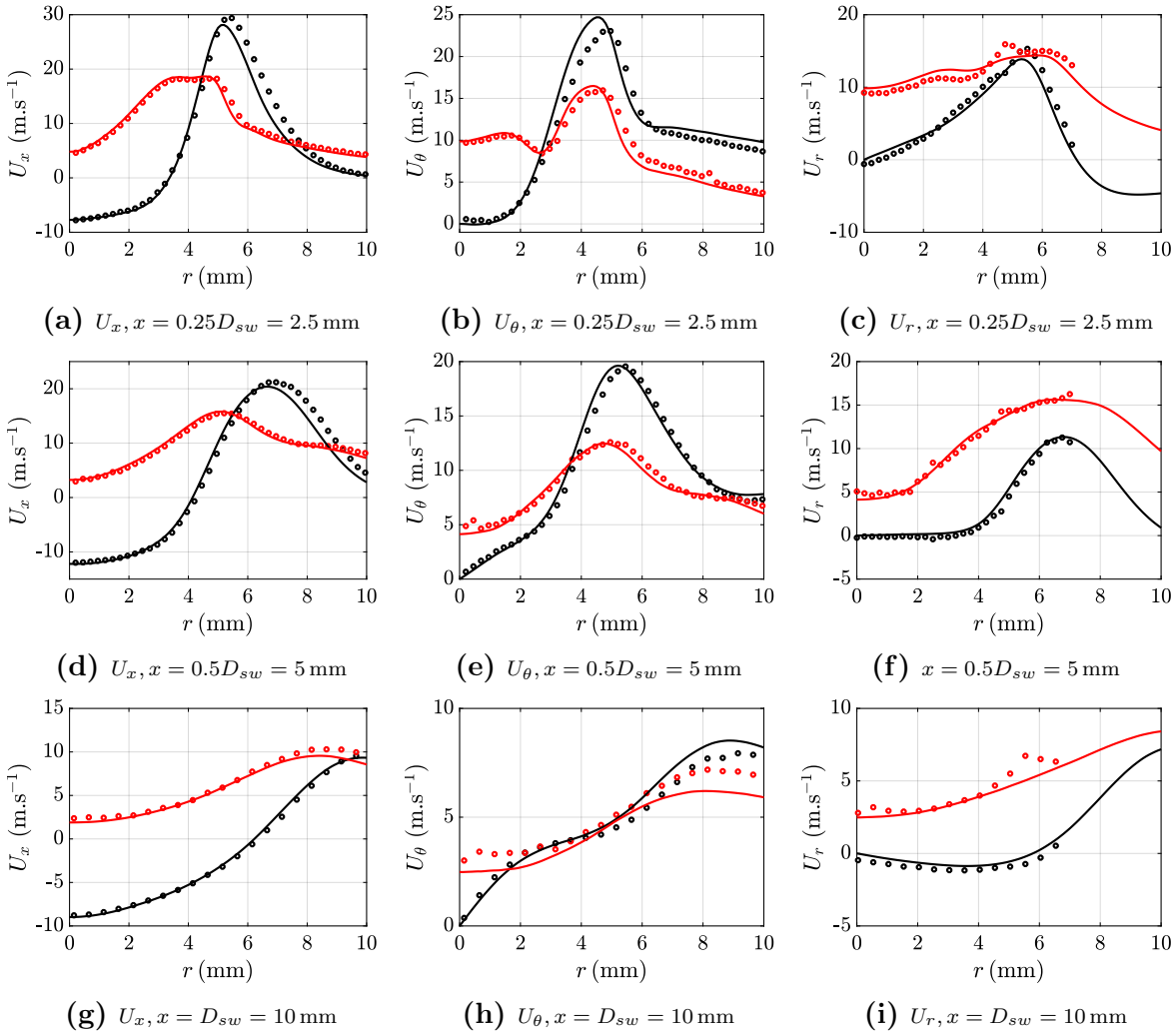

Figure 4.4: *Time averaged velocity profiles obtained using LES (continuous lines) and measured with LDV (symbols). Both mean (in black) and RMS (in red) values are shown at three distances from the combustor backplane. From left to right: axial, tangential and radial velocity profiles. Due to the cylindrical geometry of the confinement that the LDV light beams have to cross, measurements are only available up to a radius of* 10 mm *for* U_x *and* U_θ*, and* 7 mm *for* U_r*.*

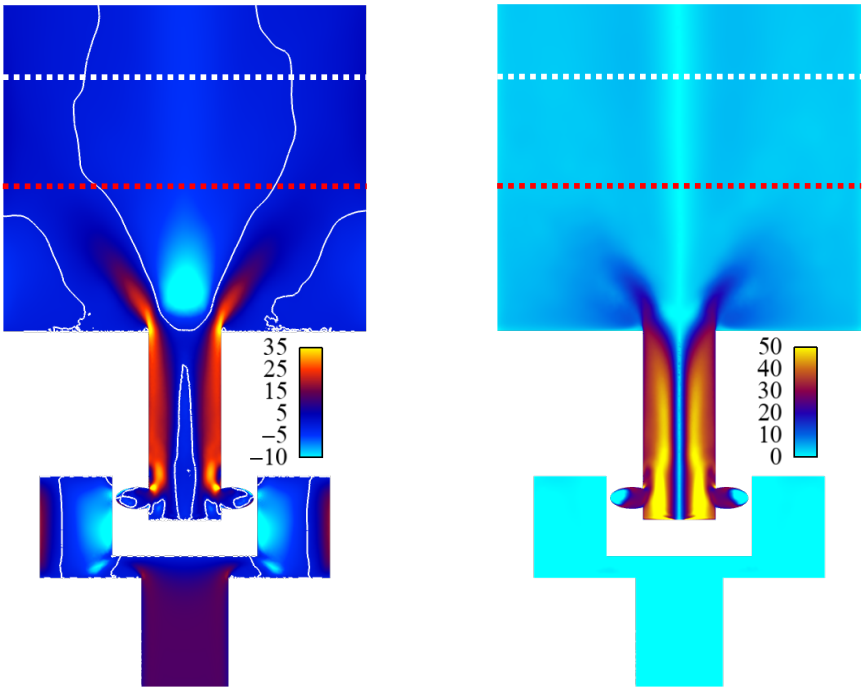

(a) $\overline{U_x}$ $(\mathrm{m\,s^{-1}})$ (b) $\overline{U_\theta}$ $(\mathrm{m\,s^{-1}})$

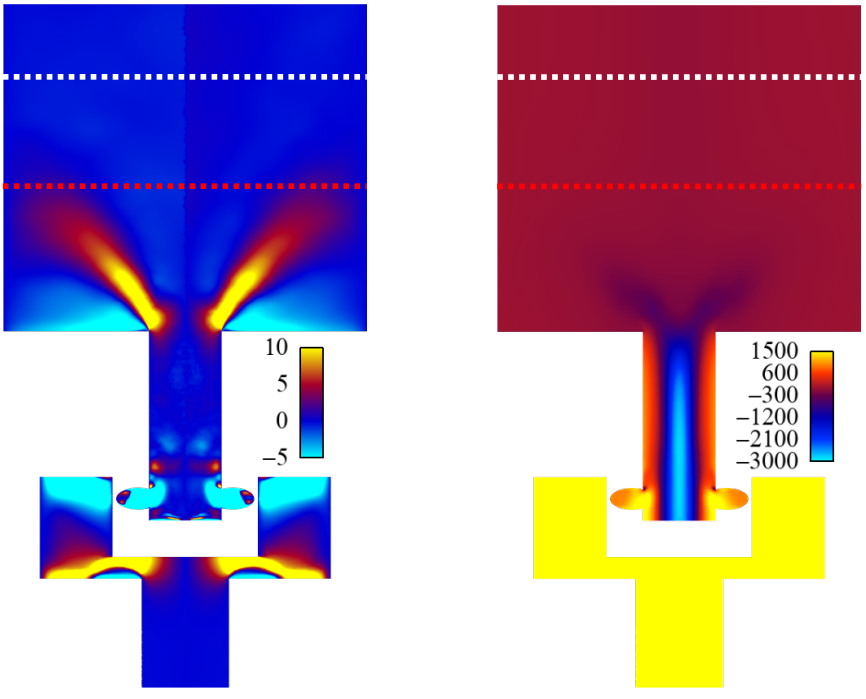

(c) $\overline{U_r}$ $(\mathrm{m\,s^{-1}})$ (d) $\overline{p} - p_{atm}$ (Pa)

Figure 4.5: *Axial cut showing the local time-averaged values of the three velocity components and of the pressure. On the top left image (a), the white isocontour corresponds to* $\overline{U}_x = 0$*. For the radial velocity* $\overline{U_r}$*, the values were saturated at* $15\,\mathrm{m\,s^{-1}}$*. Values above this level were only reached in the swirler feeding manifold, which is of little interest for this study. The pressure evolution is represented by* $\overline{p} - p_{atm}$*. It is saturated at* $1500\,\mathrm{Pa}$ *as higher values are only reached upstream in the plenum. The red dotted line corresponds to a distance* $x = 20\,\mathrm{mm}$ *from the backplane, and the white dotted line to* $x = 35\,\mathrm{mm}$*.*

4.4.2 General structure of the flow

Colormaps illustrating the general structure of the isothermal flow (Fig. 4.5) display the three components of the velocity ($\overline{U_x}$, $\overline{U_r}$ and $\overline{U_\theta}$) as well as the pressure ($\overline{p}$), both inside the injection system and in the combustion chamber. Inside the injector, high axial and tangential velocities are found near the periphery. These two components slightly decrease inside the injector. A central low pressure area can be found in the core of the flow. The simplified momentum balance of Eq. (4.15) explains this nicely. The radial component of the velocity is negligible inside the injector (see Fig. 4.5(c)).

Near the backplane of the combustor, a hollow cone shaped swirling jet is formed with a recirculation zone at its center. This is well illustrated both in Figure 4.5(a) and by the black solid line in Fig. 4.6, which shows the evolution of the axial velocity on the combustor centerline. The recirculating flow is quite strong near the backplane, but starts to decay at $x = 8\,\text{mm}$. This vortex breakdown appears to be of the bubble type as category of Billant et al. (1998). An outer recirculation zone is also present near the backplane, underneath the jet. Around $x = 20\,\text{mm}$, the outer layer of the conical jet reaches the side wall. This position is illustrated in Fig. 4.5 by a red dotted line. At $x = 35\,\text{mm}$ (white dotted line in Fig. 4.5), the jet has finished impacting the wall, and the flow starts to stabilize in a slowly evolving state. The pressure mean and wall values in the cylindrical chamber are close to p_{atm}, but still differ by several pascals from each other (Fig. 4.6). The recirculated massflow rate is shown as the red curve in Fig. 4.6. No recirculation is found in the injector. A strong recirculation develops immediately downstream of the injector, and the recirculated massflow rate presents a local minimum at $x = 16\,\text{mm}$. At the same position, the wall pressure has a local maximum, indicating the location of the vortex breakdown. This feature is reminiscent of the results published by Sarpkaya (1971) who finds a wall pressure evolution similar to that of Fig. 4.6, and relates a local maximum in wall pressure to the location of vortex breakdown.

4.4.3 Instantaneous flow field

The instantaneous velocity and pressure fields within the injector shown in Fig. 4.7 present the same overall features as the averaged field of Fig. 4.5. However, they reveal the highly turbulent nature of the flow, and the presence of a precessing vortex core (PVC) within the injector at a frequency of 1740 Hz. The velocity and pressure in the chamber, up to the outlet, are shown in Fig. 4.8. An important flow feature is the inner, lower pressure recirculation zone extending from the injector up to the outlet of the cylindrical combustor, indicating that the flow is subcritical in the whole domain. The theory of subcritical/supercritical swirling flows introduced by Escudier and Keller (1985) distinguishes two swirling flows categories depending on the ability of perturbation to propagate in the upstream direction. In subcritical flows, a central recirculation zone with negative velocities allows for such propagation. Additionally, the transverse cut of Fig. 4.8(c) shows that the instantaneous recirculation zone is not axisymmetric, but is also another precessing vortex core.

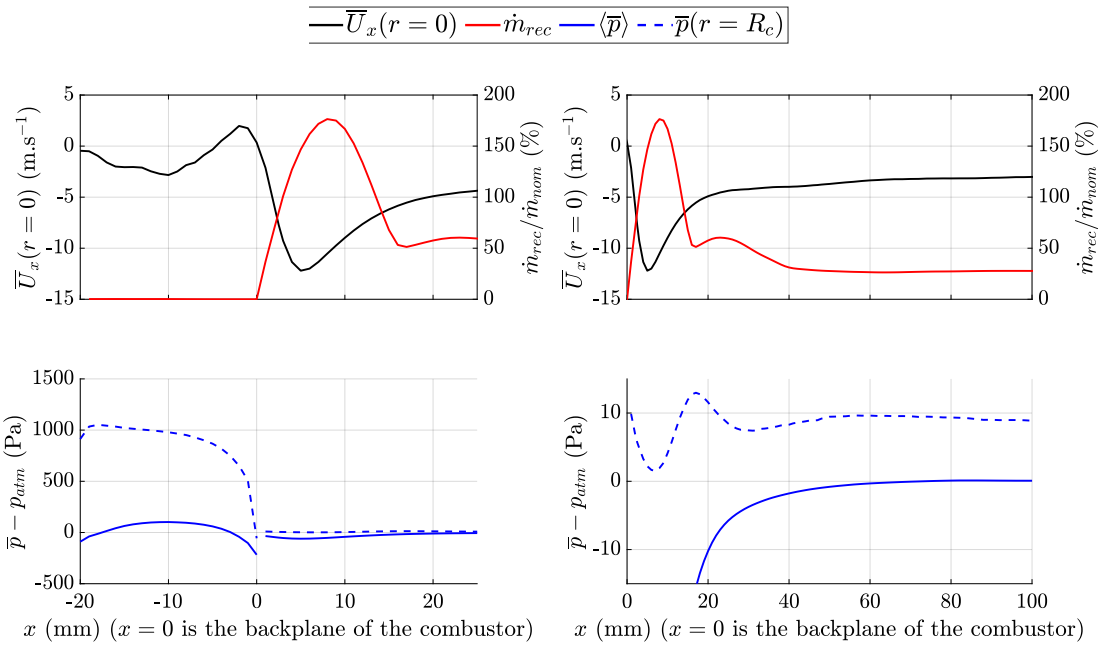

(a) *Inside the injector and near-field.* **(b)** *Downstream of the injector.*

Figure 4.6: *Top plot, left axis: evolution of the mean axial velocity $\overline{U_x}$ on the centerline (black line); top plot, right axis: recirculating mass flow rate normalized by the nominal flow rate (red line); bottom plot: axial evolution of the section-averaged pressure $\langle\overline{p}\rangle - p_{atm}$ (blue line) and of the pressure at the wall $\overline{p}(r=R_c) - p_{atm}$ (blue dashed line).*

4.4.4 Axial evolution of flow variables

Figure 4.9 shows the axial evolution of the velocity inside the injector and downstream of the dump plane. Four variables are shown: $\overline{U_x}$, $\overline{U_\theta}$, $\overline{U_r}$ and $\overline{p}$. The four plots on the left (Fig. 4.9(a)) show radial variations at five locations inside the injector $x = -15\,\text{mm} = -1.5D_{sw}$, $x = -10\,\text{mm} = -D_{sw}$, $x = -5\,\text{mm} = -0.5D_{sw}$, $x = -1\,\text{mm} = -0.1D_{sw}$, and $x = 0$. Strong variations can be observed: for $\overline{U_x}$, the first three profiles ($x = -15...-5\,\text{mm}$) are quite similar, but close to the injector outlet, the inner stagnation zone, precursor to the inner recirculation, widens, and the peak value of the axial velocity strongly increases near the outer wall. $\overline{U_\theta}$ features a similar pattern. Close to the injector outlet and outside the boundary layer, the flow is nearly in solid body rotation. At $x = -15...-5\,\text{mm}$, this solid body rotation behavior can only be seen up to about half the injector radius, with a slow axial decay. As observed in Fig. 4.5, the radial velocity $\overline{U_r}$ is quite small in the injector. It slightly increases near the outlet. A strong low pressure inner core is present and it rapidly decays near the outlet.

The four plots on the right in Fig. 4.9(b) display the same variables in six sections on the downstream side of the dump plane: $x = 1\,\text{mm} = 0.1D_{sw}$, $x = 2.5\,\text{mm} = 0.25D_{sw}$, $x = 5\,\text{mm} = 0.5D_{sw}$, $x = 10\,\text{mm} = D_{sw}$, $x = 20\,\text{mm} = 2D_{sw}$ and $x = 80\,\text{mm} = 8D_{sw}$. $\overline{U_x}$ is characteristic of a hollow cone jet. The radial position of the velocity maximum moves outwards and its value decreases as the distance from the dump plane increases. The inner recirculation zone intensifies up to $x = 5\,\text{mm}$ before slowly decaying, as shown

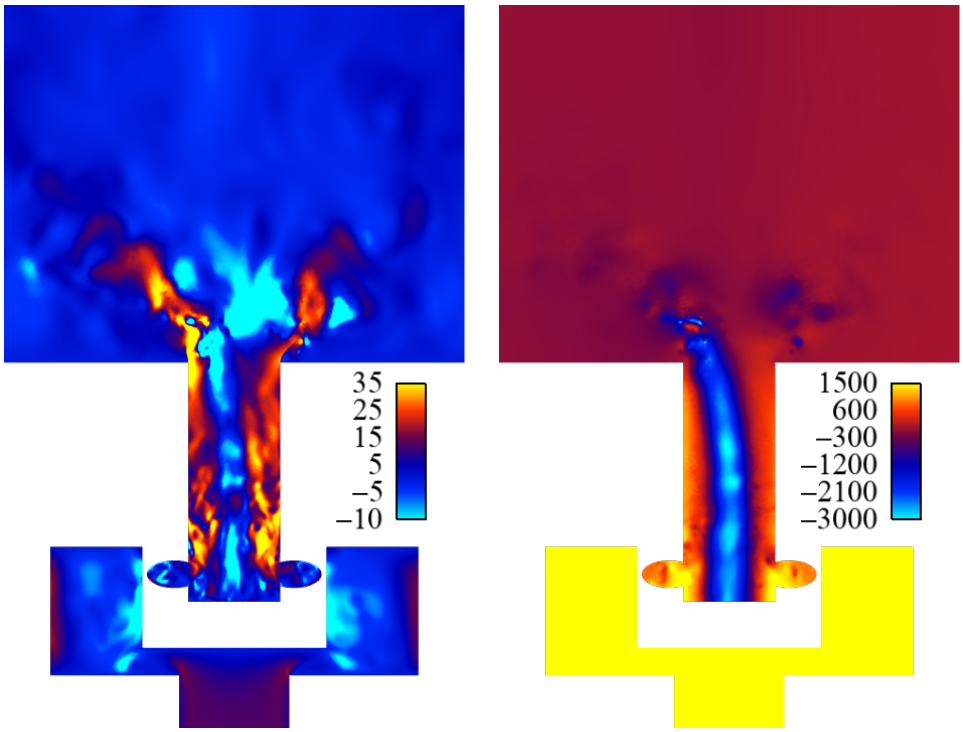

(a) u_x $(\mathrm{m\,s^{-1}})$. **(b)** p (Pa).

Figure 4.7: *Axial cut showing instantaneous values of the axial velocity and of the pressure in the injector. Concerning the pressure, the atmospheric pressure* $p_{atm} = 101\,325\,\mathrm{Pa}$ *has been substracted, and it is saturated at* $p_{atm} + 1500\,\mathrm{Pa}$ *as higher values are only reached upstream in the plenum.*

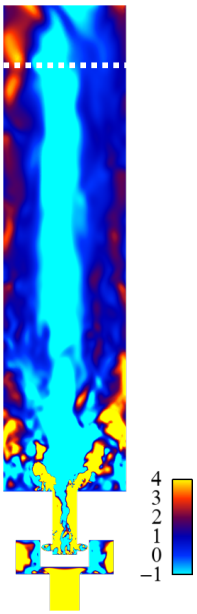

(a) u_x $(\mathrm{m\,s^{-1}})$.

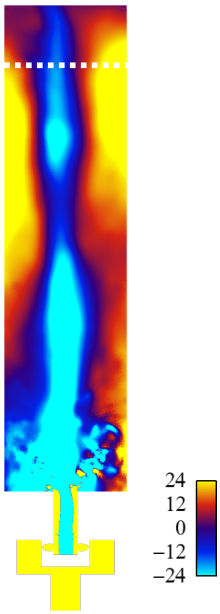

(b) p (Pa).

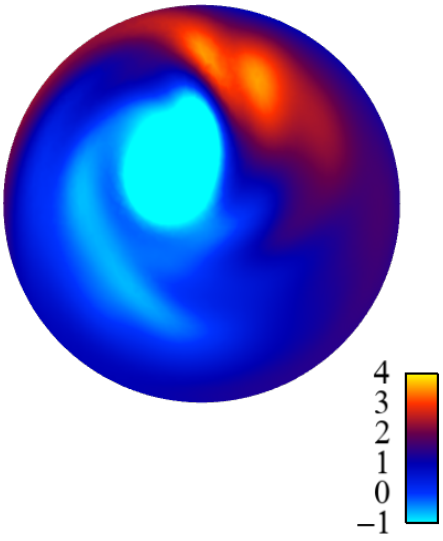

(c) u_x $(\mathrm{m\,s^{-1}})$. *Transverse cut of the chamber at* $x = 175\,\mathrm{mm}$.

Figure 4.8: *Axial cut showing the local instantaneous values of the axial velocity (a) and of the relative pressure,* $p - p_{atm}$ *(b) in the chamber. The white dotted line in the chamber corresponds to* $x = 175\,\mathrm{mm}$*, where a transversal cut showing the axial velocity near the outlet is taken and shown in (c).*

in Fig. 4.6. A weak outer recirculation zone is also slowly forming near the outer wall. $\overline{U_\theta}$ similarly decays and its peak moves outwards as x increases. At $x = 1\,\mathrm{mm}$ and $x = 2.5\,\mathrm{mm}$, a strong, outwardly oriented radial velocity is present near the axis, up to $r = 7\,\mathrm{mm}$, where a strong shear region is established. On the contrary, from this point to the outer wall, a recirculation is present, with an inwardly oriented velocity component. At $x = 5\,\mathrm{mm} = 0.5D_{sw}$ and $x = 10\,\mathrm{mm} = D_{sw}$, the inner recirculation zone weakens, and the radial velocity near the centerline becomes small and oriented inwards. The radial velocity is strongly positive inside the jet and becomes negative in the outer recirculation zone. At $x = 20\,\mathrm{mm} = 2D_{sw}$, the $\overline{U_r}$ velocity profile is much more uniform with a small peak corresponding to the spreading jet and it is completely flat at $x = 80\,\mathrm{mm} = 8D_{sw}$. The profiles at $x = 20\,\mathrm{mm}$ and $x = 80\,\mathrm{mm}$ are quite similar for all four variables under consideration. Looking at the mean pressure in Fig. 4.5(d), or comparing the two bottom plots in Fig. 4.9, the low pressure area at the core of the jet decays rapidly near the injector outlet. At $x = 1, 2.5$ and $5\,\mathrm{mm}$, the pressure profiles reach their minimum in the shear layer formed between the inner recirculation zone and the jet, away from the centerline. This is probably due to the precessing vortex core. Pressure inhomogeneities quickly decay further downstream, leading to a nearly flat pressure profile at $x = 20\,\mathrm{mm}$ and $x = 80\,\mathrm{mm}$.

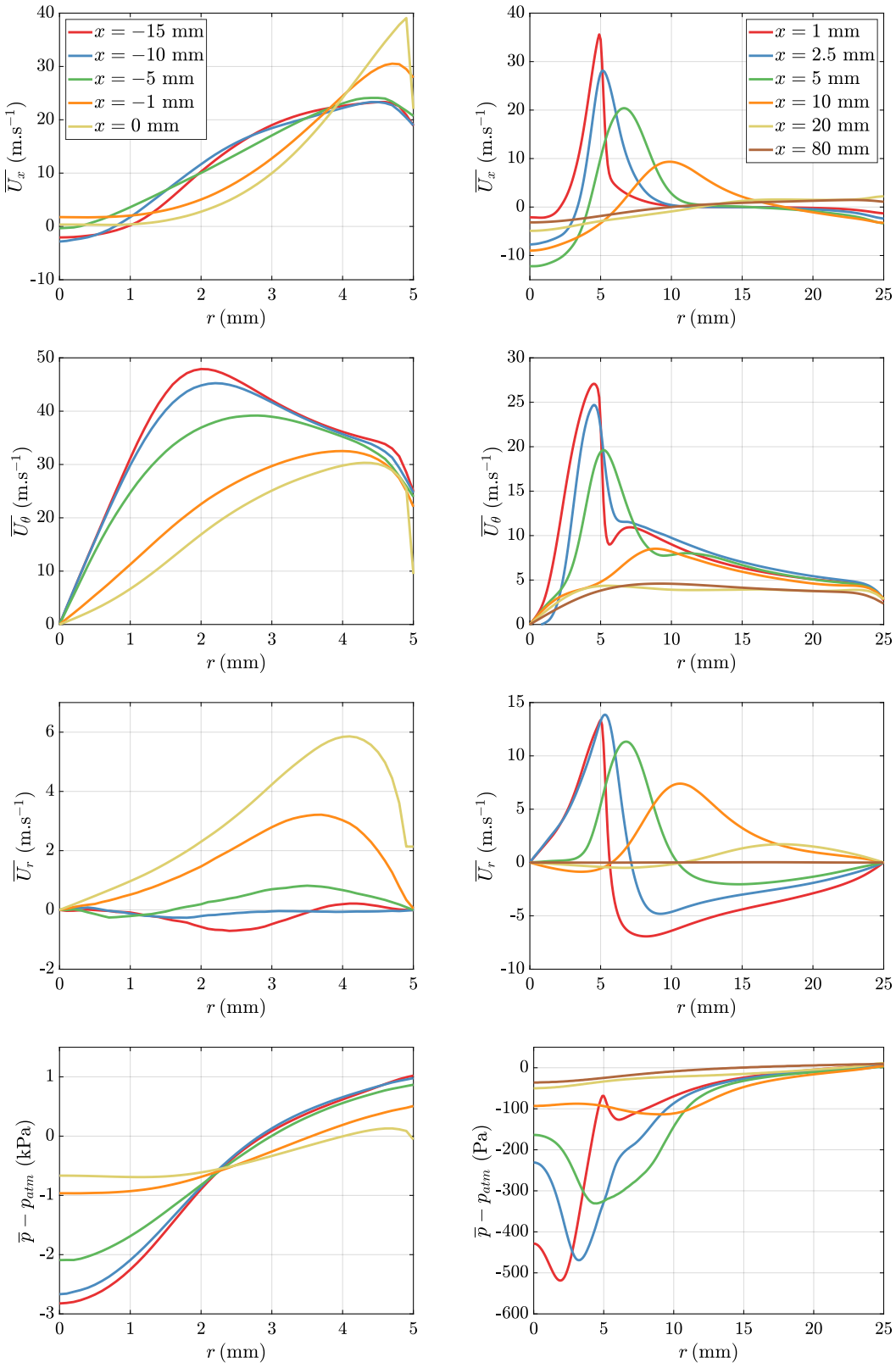

(a) *Inside the injector.* **(b)** *Downstream of the injector.*

Figure 4.9: *Radial profiles of the mean axial velocity $\overline{U_x}$, tangential velocity $\overline{U_\theta}$, radial velocity $\overline{U_r}$ and pressure $\overline{p} - p_{atm}$. The four plots on the left show these variables for five axial locations inside the injector, the four plots on the right for six axial sections in the chamber.*

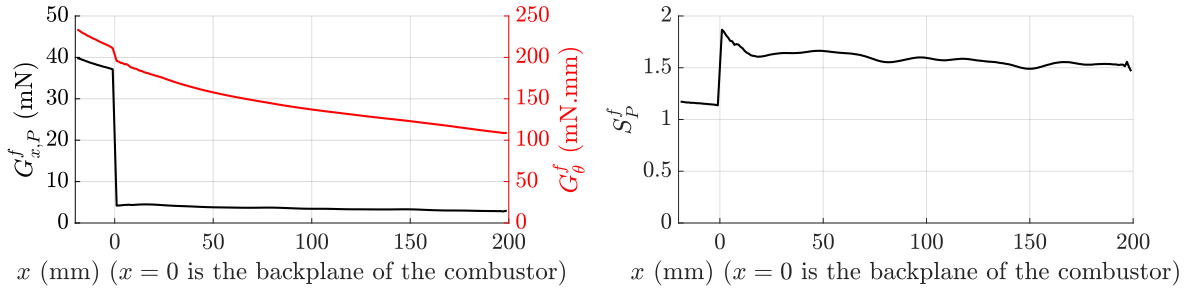

Figure 4.10: *Evolution of the flow rate of axial momentum $G^f_{x,P}$ (left subfigure, left axis, black), of the flow rate of the angular momentum axial component G^f_θ (left subfigure, right axis, red), and the swirl number S^f_P (right subfigure). The reference pressures are set to $p_{ref} = 101\,325.3$ Pa in the chamber ($x > 0$) and $p_{ref} = 101\,405$ Pa inside the injector ($x < 0$). The reference radius is the radius of the confinement: $R = R_c = 5$ mm for $x < 0$ and $R = R_c = 25$ mm for $0 < x < 200$ mm.*

4.5 The confined flow case

It is now possible to analyze the various expressions used to determine the swirl number and evaluate the simplified formulations presented in Sec. 4.2. It is first interesting to examine the quasi-invariance of the swirl number in the cylindrical chamber and show that this is only assured if the pressure term is accounted for (subsection 4.5.1). The second item to consider is that of the determination of the reference pressure p_{ref}. For confined flows, the determination of p_{ref} is not straightforward, a point discussed in subsection 4.5.2. Since static pressure measurements inside the flow are difficult it is interesting to evaluate alternatives based on velocity measurements (subsection 4.5.3). Fluctuating velocity terms that are often neglected are evaluated in subsection 4.5.4. The question of the limits to use for integration is considered in subsection 4.5.5. These results are finally summarized in subsection 4.5.6 leading to practical conclusions.

4.5.1 Axial evolution of the swirl number S^f_P and viscous losses

In this first analysis of the evolution of the swirl number it is convenient to use a reference pressure that is equal to $p_{ref} = 101\,325.3$ Pa in the chamber ($x > 0$), and $p_{ref} = 101\,405$ Pa in the injector ($x < 0$). The reasoning behind this choice will be discussed in the next section 4.5.2. One may note that this arbitrary choice of reference pressure does not affect the results and reasoning presented in what follows.

One may first consider the axial flow rates and swirl number as originally defined in Rose (1962) and in Chigier and Beér (1964) without any simplifying assumptions. $G^f_{x,P}$, G^f_θ and S^f_P are defined in Eq. (4.40) for a confined isothermal configuration. Their evolutions are shown in Fig. 4.10. The system comprises two cylindrical tubes of different diameters (see Fig. 4.2), the radius is constant in the injector ($x < 0$) and in the chamber ($0 < x < 200$ mm) with a sudden expansion between these two at $x = 0$. In this section, the reference radius used for the computation of the swirl number is taken as the actual radius of the confinement at the axial position under consideration: $R = R_c = 5$ mm for $x < 0$ and $R = R_c = 25$ mm for $0 < x < 200$ mm. There is a sizable jump in $G^f_{x,P}$, and a

Table 4.1: *Decay in G_θ^f and $G_{x,P}^f$ along with viscous losses at the wall in the injector and in the chamber.*

	ΔG_θ^f (mN mm)	$2\pi R_c^2 \int \overline{\tau_{r\theta}}\|_{r=R_c}$ (mN mm)	$\Delta G_{x,P}^f$ (mN)	$2\pi R_c \int \overline{\tau_{rx}}\|_{r=R_c}$ (mN)
Injector: $-20\,\text{mm} < x < 0$	-23	-17	-2.8	-2.8
Chamber: $0 < x < 200\,\text{mm}$	-87	-66	-1.3	-1.3

very small jump in G_θ^f at the position of sudden expansion ($x = 0$). These two quantities slowly decay in the constant section ducts. Correspondingly S_P^f also features a jump at $x = 0$ and then slowly diminishes in the axial direction reflecting the observed reductions in G_θ^f and that of $G_{x,P}^f$.

At this point it is interesting to discuss the decay observed in the flow rate of the angular momentum axial component by first reviewing studies dealing with turbulent swirling flows decay in tubes. This topic is covered for example by Steenbergen and Voskamp (1998) who review different formulas for this evolution, but give their results in terms of swirl angle instead of swirl number. The linearized theory in Kreith and Sonju (1965) for established turbulent swirling flows in long pipes indicates a typical decay of 10 to 20% on a distance of 50 pipe diameters. The decay rate increases at lower Reynolds number. Scott and Bartelt (1976) note the invariance of the velocity profiles in the axial direction in an experiment on a annular duct with a swirling air flow. Kitoh (1991) provides an experimental assessment of the wall shear stress impact and concludes that it governs the decay of the swirling motion which is generally found to be exponential. Another relevant feature from these studies is that the decay of flow rate of the angular momentum axial component G_θ^f predominates over that of the flow rate of axial momentum $G_{x,P}^f$.

In this respect it is worth recalling the rates of change balances of G_θ^f and $G_{x,P}^f$ established in section 4.2, Eqs. (4.33) and (4.39). These expressions indicate that the decay rates of G_θ^f and $G_{x,P}^f$ are governed by the shear stresses at the wall. The order of magnitude of these stresses is such that the decay rate of G_θ^f is much larger than that of $G_{x,P}^f$.

It is next interesting to examine the decay of G_θ^f and $G_{x,P}^f$ in the injector and in the chamber, as well as the friction losses at the wall, reported in Tab. 4.1. As the literature suggests, it appears that friction losses associated with wall stresses determine the slow axial decay of the swirl number.

4.5.2 Impact of the static pressure on the swirl number and selection of the reference pressure

Let us now evaluate the impact of the pressure term on $G_{x,P}^f$. This issue was considered in the past by Chigier and Beér (1964) and Mahmud et al. (1987) who used Pitot tubes to measure velocity and static pressure profiles in free swirling jets. It was found in these previous studies, in agreement with the theoretical equation Eq. (4.11), that the pressure term had to be included to ensure the axial conservation of $G_{x,P}^f$. This question may now

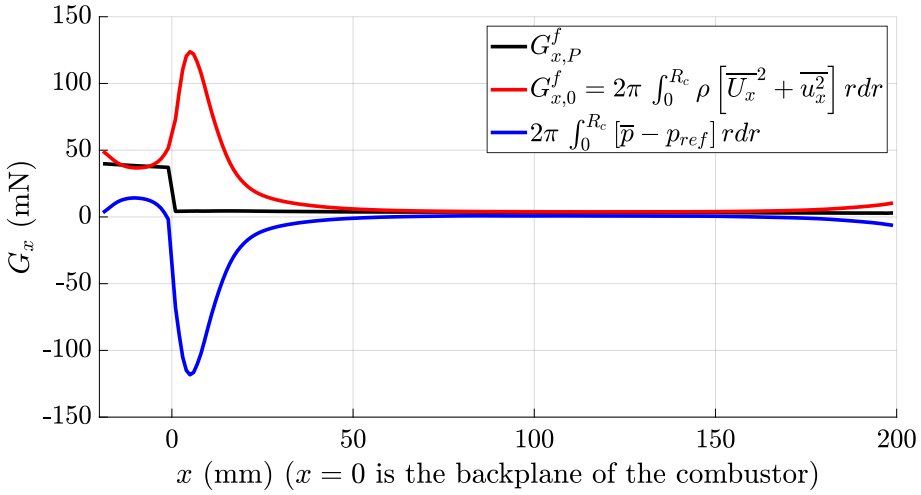

Figure 4.11: *Evolution of $G^f_{x,P}$ and its constituents (Eq. (4.52)) in the axial direction. The sudden expansion corresponds to $x = 0$. The reference pressures are set to $p_{ref} = 101\,325.3$ Pa in the chamber ($x > 0$) and $p_{ref} = 101\,405$ Pa inside the injector ($x < 0$).*

be examined with the present simulation thus avoiding intrusive pressure measurements. It is interesting to separate $G^f_{x,P}$ in its constituents

$$\underbrace{G^f_{x,P}}_{\text{(black)}} = \underbrace{2\pi \int_0^{R_c} \rho \left[\overline{U_x}^2 + \overline{u_x^2}\right] rdr}_{\text{Velocity term (red)}} + \underbrace{2\pi \int_0^{R_c} [\overline{p} - p_{ref}]\, rdr}_{\text{Pressure term (blue)}} \tag{4.52}$$

Figure 4.11 indicates that $G^f_{x,P}$ and $G^f_{x,0} = 2\pi \int_0^{R_c} \rho \left[\overline{U_x}^2 + \overline{u_x^2}\right] rdr$ nearly coincide in the injector ($x = -20$ to 0 mm) and in the downstream region of the chamber ($x = 50$ to 175 mm) with the choice of p_{ref} that is employed here. However, as observed in Mahmud et al. (1987), these quantities take different values in the vicinity of the area changes. Near $x = 0$, $G^f_{x,0}$ features a peak and sizable variations caused by the recirculation region generated by vortex breakdown. The pressure term $2\pi \int_0^{R_c} [\overline{p} - p_{ref}]\, rdr$ also features a strong negative peak at this position. The two peaks compensate each other when the two terms are summed up in $G^f_{x,P}$. This indicates that the pressure term is of considerable importance close to area changes ($0 < x < 50$ mm) to ensure conservation, but that this term can be omitted where the flow is established ($-20 < x < 0$ mm and $50 < x < 175$ mm).

The selection of a reference pressure is rarely considered in the previous literature but a suitable choice needs to be made because $G^f_{x,P}$ is sensitive to changes in reference pressure with a first order impact on the swirl number value. For the purpose of swirl number calculations, $\rho\left(\langle\overline{U_x}\rangle^2 + \langle\overline{u_x}^2\rangle\right)$ gives the order of magnitude for the sensitivity of the swirl number to the reference pressure. In the present configuration, $\rho\left(\langle\overline{U_x}\rangle^2 + \langle\overline{u_x}^2\rangle\right) \approx 0.5$ Pa in the confinement tube. From a practical standpoint, Mattingly and Oates (1986) propose to use a pressure at the wall somewhere in the duct as reference pressure, but with no

theoretical justification. One may note that, from Fig. 4.6, the pressure at the wall varies as a function of the axial position x, and that the difference between the section averaged pressure $\langle\overline{p}\rangle$, and the wall pressure $\overline{p}(r = R_c)$ is approximately $\overline{p}(r = R_c) - \langle\overline{p}\rangle \approx 9\,\text{Pa}$ for $x > 40\,\text{mm}$, that is one order of magnitude larger than $\rho\left(\langle\overline{U_x}\rangle^2 + \langle\overline{u_x{}^2}\rangle\right)$. The practice of taking the reference pressure as a wall pressure without selecting a suitable section in the flow is inadequate, in particular for flows with changes in cross-section. This leads to variable or even sometimes negative swirl number values (Weber and Dugué (1992)) depending on the position adopted to infer the reference pressure.

The following analysis is dedicated to defining a better practice for this choice. The following properties are desirable for the reference pressure p_{ref}:

[P1] Its definition should be consistent with that used for unconfined flows,

[P2] Its value might vary with area changes, but should remain constant in the system elements having a constant cross section,

[P3] Its determination should be straightforward using conventional measurement techniques,

[P4] Its value should be such that $G^f_{x,P} \simeq G^f_{x,0}$ at a distance from the area change where the flow is established as illustrated in Fig. 4.11.

If it is to have properties [P4], the reference pressure must be defined as the sectional average of the static pressure

$$p_{ref} = \langle\overline{p}\rangle = \frac{1}{\Sigma}\int_{\Sigma}\overline{p}dA \tag{4.53}$$

where Σ designates the cross-section where the reference pressure is computed. In this expression, if Σ becomes infinitely large, for example if an unconfined swirling jet is considered, the reference pressure will simply tend to the pressure at infinity p_∞.

$$\lim_{\Sigma\to\infty} p_{ref} = p_\infty = \overline{p}(r \to \infty) \tag{4.54}$$

The definition of the reference pressure proposed in Eq. (4.53) is thus consistent with Chigier's definition for unconfined swirling jets and satisfies property [P1]. Property [P2] imposes that this sectional average be taken at a single axial location in each part. In the present configuration, the sectional average of static pressure is nearly constant in the downstream part of the duct after an establishment distance roughly corresponding to the confinement diameter. This property can most likely be generalized to many constant pressure combustion applications featuring constant cross-sections due to the high Reynolds number and small length to diameter ratios that are generally found in combustors.

The reference pressure is thus taken as the mean value of the cross-section averaged static pressure at positions ($-15 < x < -5\,\text{mm}$ for the injector and $50 < x < 175\,\text{mm}$ for the chamber), that is at least one diameter downstream of area changes and at a distance from an outlet to avoid end effects. This yields $p_{ref}(-) = 101\,405\,\text{Pa}$ in the cylindrical injector and $p_{ref}(+) = 101\,325.3\,\text{Pa}$ in the downstream duct. Figures 4.10 and 4.11 use

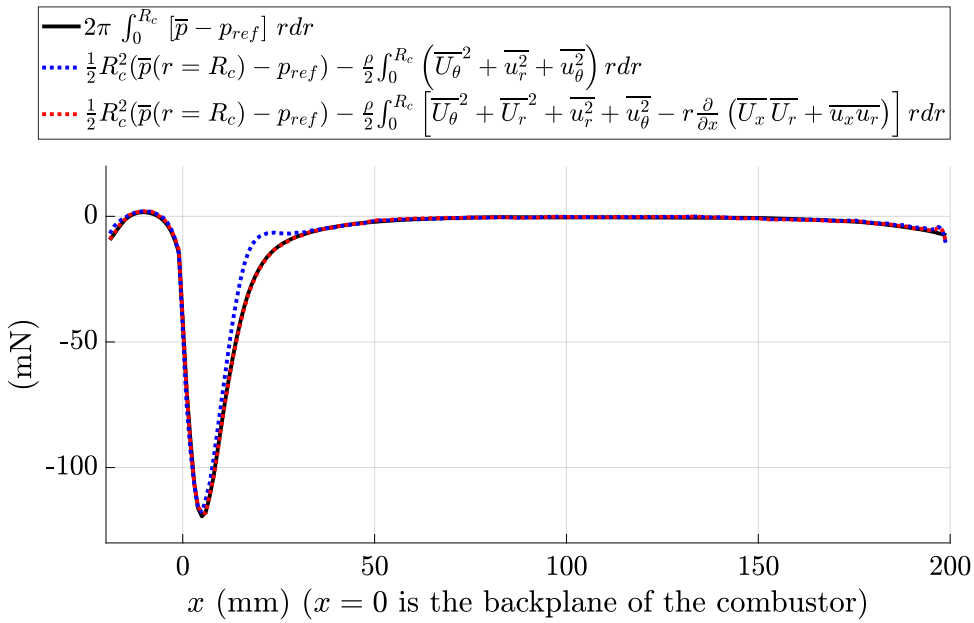

Figure 4.12: *Axial evolution of different pressure correction expressions. Blue, Eq.* (4.35)*; red, Eq.* (4.55)*. The reference line is in black.* $p_{ref} = 101\,325.3\,\text{Pa}$ *in the chamber* ($x > 0$) *and* $p_{ref} = 101\,405\,\text{Pa}$ *inside the injector* ($x < 0$).

the previous reference pressures and show that $G^f_{x,P}$ and G^f_θ evolve in the axial direction in the expected manner and that $G^f_{x,P}$ and $G^f_{x,0}$ collapse where the flow is fully developed.

4.5.3 Expressing the static pressure in terms of the velocity field and wall pressure

It is not always easy to measure the static pressure inside the flow with a sufficient resolution to correctly evaluate the pressure term in Eq. (4.52). Among the methods that can be used to replace this by an expression that only uses velocity information, it is interesting to examine that originally proposed by Chigier and Chervinsky (1967b) for free swirling jets and extended by Mattingly and Oates (1986) for confined configurations. It is expressed in Eq. (4.35), which is repeated here for convenience. It is worth noting that, in confined flows, this approach still requires a wall pressure measurement $\overline{p}|_{r=R_c}$.

$$\int_0^{R_c} r\,(\overline{p} - p_{ref})\,dr = \frac{1}{2}{R_c}^2(\overline{p}|_{r=R_c} - p_{ref}) - \frac{\rho}{2}\int_0^{R_c} r\,(\overline{U_\theta}^2 + \overline{u_r^2} + \overline{u_\theta^2})\,dr \quad (4.35\ rep.)$$

It is useful at this point to recall that the previous expression is derived from the simplified Navier-Stokes equations with boundary layer assumptions (Eq. (4.13)) and that terms that

depend on the radial velocity may also be included to get a more general expression

$$\begin{aligned}\int_0^{R_c} r\,(\overline{p}-p_{ref})\,dr &= \frac{1}{2}{R_c}^2(\overline{p}|_{r=R_c}-p_{ref})\\ -\frac{\rho}{2}\int_0^{R_c} r\left[(\overline{U_\theta}^2+\overline{U_r}^2+\overline{u_r^2}+\overline{u_\theta^2})-r\,\frac{\partial}{\partial x}\left(\overline{U_x}\,\overline{U_r}+\overline{u_x u_r}\right)\right]dr\end{aligned} \tag{4.55}$$

Figure 4.12 shows the axial evolution of $\int_0^{R_c} r\,(\overline{p}-p_{ref})\,dr$ and the two expressions appearing in Eqs. (4.35) and (4.55). Equation (4.35), commonly found in the literature, yields suitable results except between $x = 5\,\text{mm}$ and $30\,\text{mm}$, where the boundary layer assumptions do not apply. Given the sensitivity of the computation of the swirl number to the pressure, it is then preferable to use Eq. (4.55) in this region of the flow.

4.5.4 Fluctuating terms

It is now worth asking whether the terms corresponding to the fluctuating velocities need to be included. It is shown by Toh et al. (2010) using PIV data that neglecting these terms only induced a 3% in the swirl number because the errors in the numerator and denominator compensate each other. It should be noted that these authors did not have access to all the necessary components in the Reynolds stress tensor.

It is then worth examining this issue by isolating the fluctuating terms in the calculation of $G_{x,P}^f$ and G_θ^f:

$$\underbrace{G_{x,P}^f}_{\text{(black)}} = \underbrace{2\pi\int_0^{R_c}\left[\rho\overline{U_x}^2+\overline{p}-p_{ref}\right]rdr}_{\text{Mean term } G_{x,P}^0 \text{ (red)}} + \underbrace{2\pi\int_0^{R_c}\rho\overline{u_x^2}rdr}_{\text{Fluctuating term (blue)}} \tag{4.56}$$

$$\underbrace{G_\theta^f}_{\text{(black)}} = \underbrace{2\pi\int_0^{R_c}\rho\overline{U_\theta}\,\overline{U_x}rdr}_{\text{Mean term (red)}} + \underbrace{2\pi\int_0^{R_c}\rho\overline{u_\theta u_x}rdr}_{\text{Fluctuating term (blue)}} \tag{4.57}$$

These components are shown in Fig. 4.13. The integral of the fluctuating term $2\pi\int_0^{R_c}\rho\overline{u_x^2}rdr$ is nearly of the same order of magnitude as $G_{x,P}^0$ between $0 < x < 35\,\text{mm}$. For the flow rate of the angular momentum axial component G_θ, the fluctuating term represents up to 25% of G_θ^f. In view of their importance in the computation of the swirl number and the fact that hot wires or laser velocimetry give access to fluctuating velocities it appears advisable to include the corresponding terms in swirl number calculations, especially for systems such as combustion injectors which operate at high Reynolds numbers.

The experimental determination of $\overline{u_\theta u_x}$ may be based on cross hot wires, two component LDV systems or three component stereo-PIV. The standard 2D-PIV cannot be used to determine this cross-correlation. To overcome this difficulty with this last technique it is suggested in Toh et al. (2010) to simply replace $\overline{u_\theta u_x}$ by $\overline{u_r u_x}$. This possibility is

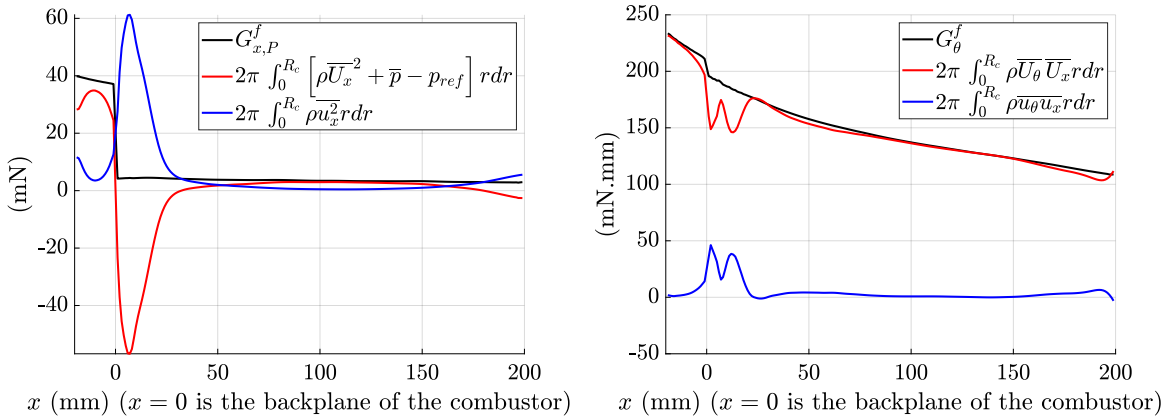

Figure 4.13: *The different components of the flow rate of momentum (left) and flow rate of moment of tangential momentum.* $p_{ref} = 101\,325.3\,\text{Pa}$ *in the chamber* ($x > 0$) *and* $p_{ref} = 101\,405\,\text{Pa}$ *inside the injector* ($x < 0$).

assessed in Fig. 4.14, which compares $2\pi \int_0^{R_c} \rho \left[\overline{U_\theta U_x} + \overline{u_\theta u_x}\right] rdr$, $2\pi \int_0^{R_c} \rho\, \overline{U_\theta U_x} rdr$ and $2\pi \int_0^{R_c} \rho \left[\overline{U_\theta U_x} + \overline{u_r u_x}\right] rdr$. This plot indicates that it is clearly preferable to drop the correlation $\overline{u_\theta u_x}$ than to try to replace it by $\overline{u_r u_x}$.

4.5.5 Integration limits

Up to now, the integrals defining $G^f_{x,P}$ and G^f_θ have been calculated over the entire cross-section of each element. It is now worth estimating the impact of stopping the computation of the integral at an earlier point. One may consider for that purpose Fig. 4.15 where $G^f_{x,P}$ and G^f_θ are calculated by integrating to an arbitrary radius R_{lim}:

$$G^f_{x,P}(x, R_{lim}) = 2\pi \int_0^{R_{lim}} \left[\rho \left(\overline{U_x}^2(x,r) + \overline{u_x^2}(x,r)\right) + \overline{p}(x,r) - p_{ref}\right] rdr \tag{4.58}$$

$$G^f_\theta(x, R_{lim}) = 2\pi \int_0^{R_{lim}} \rho \left(\overline{U_x}(x,r)\overline{U_\theta}(x,r) + \overline{u_x u_\theta}(x,r)\right) r^2 dr \tag{4.59}$$

Depending on the axial position at which the computation is performed, two regimes can be found. For $x = 2.5, 5$ and $10\,\text{mm}$, Fig. 4.9 indicates that the flow behaves as a jet with an outer recirculation zone. At $x = 20$ and $80\,\text{mm}$, the flow is wall-bounded and there is no outer recirculation zone. At $x = 2.5, 5$ and $10\,\text{mm}$, the flow rate of axial momentum $G^f_{x,P}$ is initially negative before strongly increasing at the radial position of the jet. It then decays again before increasing to its final value near the wall. G^f_θ has a similar behavior, with a strong increase at the radial position of the jet, followed by a plateau and a decay to its final value in the outer recirculation zone near the wall. At $x = 20$ and $80\,\text{mm}$, both $G^f_{x,P}$ and G^f_θ reach their final values in the last 5 to $10\,\text{mm}$ of the confinement. These calculations indicate that in the case of a confined configuration, especially when an outer recirculation zone is established, the computation of the swirl

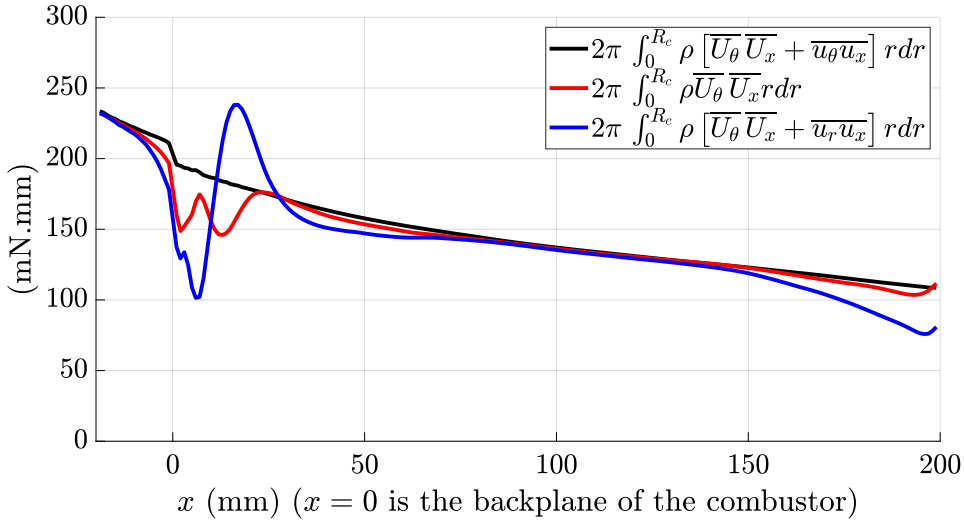

Figure 4.14: *Effect of integration limit on the calculated flow rates $G^f_{x,P}$ (left) and G^f_θ (right) at five axial positions. The integral terms are computed by stopping the integration at various distances r, and then normalizing by the integral taken over the entire cross-section.* $p_{ref} =$ 101 325.3 Pa.

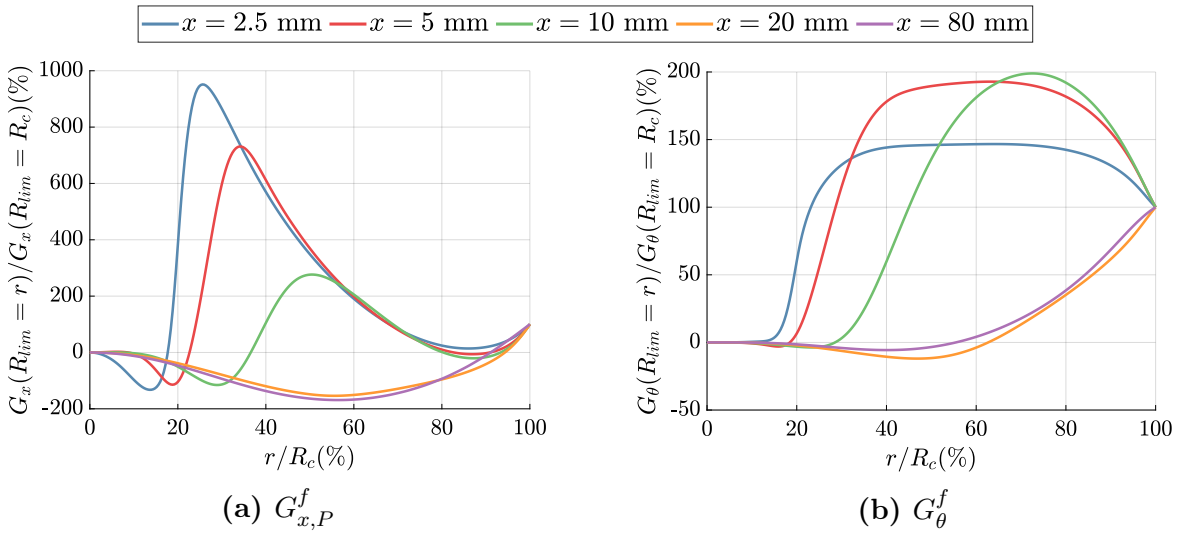

(a) $G^f_{x,P}$ **(b)** G^f_θ

Figure 4.15: *Effect of integration limit on the calculated flow rates $G^f_{x,P}$ (left) and G^f_θ (right) at five axial positions. The integral terms are computed by stopping the integration at various distances r, and then normalizing by the integral taken over the entire cross-section.* $p_{ref} =$ 101 325.3 Pa.

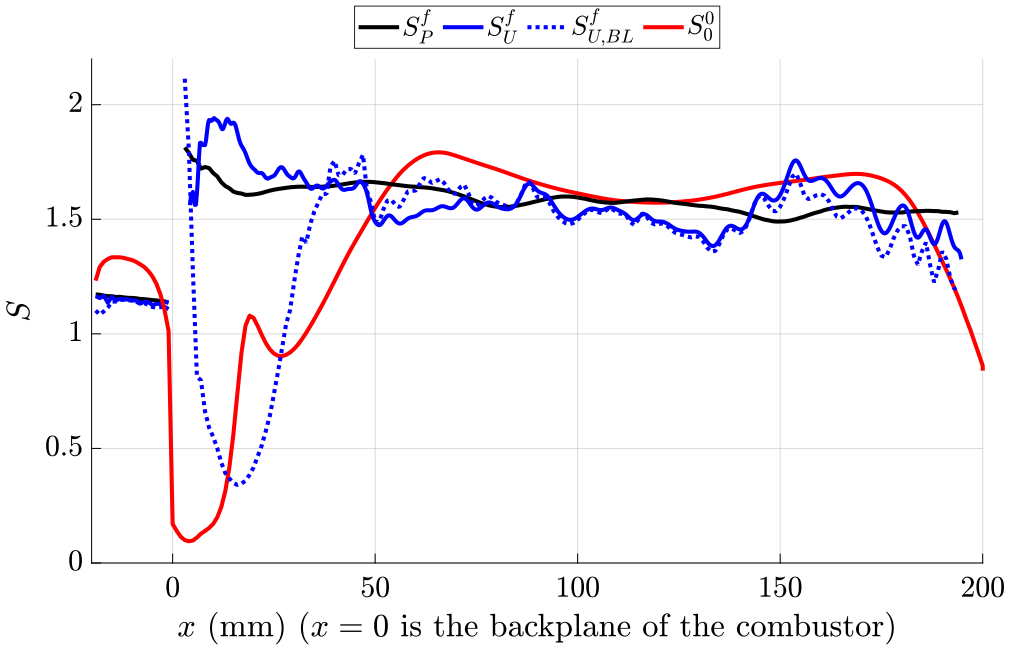

Figure 4.16: *Comparison of 5 formulas for the swirl number.*

number S_P^f needs to be carried out by integrating over the entire cross-section.

4.5.6 Direct comparison of 5 swirl number formulations

Finally, we compare in this section the swirl numbers calculated with the different formulations. The reference pressures are those determined previously in section 4.5.2. The reference swirl number S_P^f was defined by Rose (1962); Chigier and Beér (1964); Chigier and Chervinsky (1967b); Chigier and Chervinsky (1967a).

$$S_P^f = \frac{G_\theta^f}{RG_{x,P}^f} = \frac{\int_0^{R_c} \rho \left(\overline{U_\theta}\,\overline{U_x} + \overline{u_\theta u_x}\right) r^2 dr}{R_c \int_0^{R_c} \left[\rho \left(\overline{U_x}^2 + \overline{u_x^2}\right) + (\overline{p} - p_{ref})\right] r dr} \qquad (4.40\ rep.)$$

It includes the pressure and fluctuation terms and appears as a solid black line in Fig. 4.16. This quantity has the nice feature of being nearly constant in the injector and slowly diminishing in the chamber.

In the second formulation S_U^f the pressure term is replaced by velocity term and the pressure at the wall.

$$S_U^f = \frac{\int_0^{R_c} \rho \left(\overline{U_\theta}\,\overline{U_x} + \overline{u_\theta u_x}\right) r^2 dr}{R_c \int_0^{R_c} \rho \left[\overline{U_x}^2 + \overline{u_x^2} - \frac{1}{2}\left(\overline{U_\theta}^2 + \overline{U_r}^2 + \overline{u_r^2} + \overline{u_\theta^2}\right) + \frac{r}{2}\frac{\partial}{\partial x}\left(\overline{U_x}\,\overline{U_r} + \overline{u_x u_r}\right)\right] r dr + \frac{R_c^3}{2}\left(\overline{p}|_{r=R_c} - p_{ref}\right)} \qquad (4.44\ rep.)$$

This expression put forward in the present investigation does not appear in the literature. Its derivation relies on the balance put forward in Eq. (4.55). The boundary layer simplifying assumptions are not needed in this case so that S_U^f, shown as a solid blue line in Fig. 4.16, takes values that are close to the reference swirl number (black line).

On the other hand, the simplified formulation of Mattingly and Oates (1986), $S_{U,BL}^f$, relies on boundary layer assumptions.

$$S_{U,BL}^f = \frac{\int_0^{R_c} \rho \left(\overline{U_\theta}\,\overline{U_x} + \overline{u_\theta u_x}\right) r^2 dr}{R_c \int_0^{R_c} \rho \left[\overline{U_x}^2 + \overline{u_x^2} - \frac{1}{2}\left(\overline{U_\theta}^2 + \overline{u_r^2} + \overline{u_\theta^2}\right)\right] r dr + \frac{R_c^3}{2}\left(\overline{p}|_{r=R_c} - p_{ref}\right)} \quad (4.43\ rep.)$$

Plotted as a dotted blue line in Fig. 4.16, $S_{U,BL}^f$ is in good agreement with the reference swirl number S_P^f, except in the vicinity of the sudden expansion.

The commonly used, highly simplified expression S_0^0 appears as a red line in Fig. 4.16.

$$S_0^0 = \frac{\int_0^{R_c} \rho\,\overline{U_\theta}\,\overline{U_x}\, r^2 dr}{R_c \int_0^{R_c} \rho\,\overline{U_x}^2\, r dr} \quad (4.42\ rep.)$$

With the definition of the reference pressure proposed in the present work, it is close to S_P^f at axial positions that are far away from area changes. It is also close to S_P^f at $x = 0$, but exhibits large variations in the downstream flow and substantially differs from the reference value S_P^f.

The fairly common expression S_U^0 (where the pressure is replaced in terms of the velocity field, velocity fluctuations are neglected and the reference pressure is set equal to the wall static pressure)

$$S_U^0 = \frac{\int_0^{R_c} \rho\,\overline{U_\theta}\,\overline{U_x}\, r^2 dr}{R_c \int_0^{R_c} \rho \left(\overline{U_x}^2 - 1/2\overline{U_\theta}^2\right) r dr} \quad (4.45\ rep.)$$

is not plotted in Fig. 4.16 because it becomes negative at some axial sections and its value often exceeds the limits set for the y-axis in this figure. As previously noted by Weber and Dugué (1992), this expression is highly variable near the sudden expansion and becomes negative in the downstream section, indicating that the reference pressure is not well chosen. Overall, this is not a suitable approximation of the original swirl number S_P^f.

One may draw the following conclusions from the analysis conducted so far:

- The swirl number S_P^f is a well defined quantity that has desirable conservation properties in many isothermal configurations.
- Although it can be easily determined from numerical simulations its determination from experimental velocity measurements in practical configurations is challenging.
- S_U^f is the most general approximation of S_P^f. The simpler expression $S_{U,BL}^f$ consti-

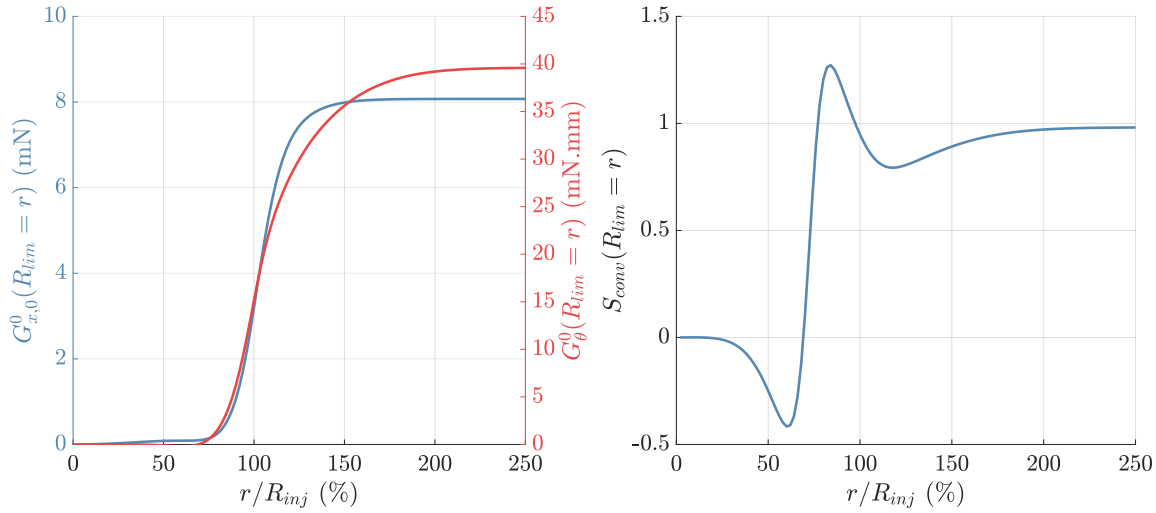

Figure 4.17: *Choice of the integration limit R_{lim} for the computation of the conventional swirl number S_{conv} (Eq. (4.30)). Velocity profiles are taken at $x = 2.5\,\text{mm}$. On the left, $G^0_{x,0}$ and G^0_θ are plotted for different integration radii. On the right, the conventional swirl number S_{conv} is plotted in a similar manner.*

tutes a good alternative in regions where the flow is established.

- In confined flows, care should be taken to properly define the reference pressure p_{ref}.

4.6 The conventional swirl number and its estimation

Given the complexity involved in the accurate estimation of the original swirl number S_P^f, it is now interesting to consider the conventional swirl number formulation (Eq. 4.30) that is widely used in practice to deduce an estimate from velocity profiles measured as close as possible to the injector outlet.

$$S_{conv} = \frac{\int_0^{R_{lim}} \rho\, \overline{U_\theta}\, \overline{U_x}\, r^2 dr}{R_{inj} \int_0^{R_{lim}} \rho\, \overline{U_x}^2 r dr} \qquad (4.30\ \textit{rep.})$$

In Eq. (4.30) the reference radius is that of the injector outlet and the integration is stopped at a radial distance R_{lim}. A critical aspect is the suitable choice of this limit. This may be guided by plotting $G^0_{x,0}$, G^0_θ and S_{conv} calculated in the vicinity of the outlet for different integration radii. Figure 4.17 indicates that these three quantities become independent of the integration radius as soon as $R_{lim} > 2R_{inj}$. Although the specific value of $R_{lim} = 2R_{inj}$ may depend on the configuration, one may expect that S_{conv} will be independent of the integration radius if R_{lim} is large enough, since the axial velocity component $\overline{U_x}$ vanishes close to the backplane at large radial positions ($r \gg R_{inj}$). In the section located at $x = 2.5\,\text{mm}$, one finds that S_{conv} takes a value of 0.98 that is close to that obtained for S_P^f near the injector outlet on the upstream side: $S_P^f = 1.14$.

It is clear from the elements presented in the previous section that S_{conv} is weakly related

to the original definition and that it does not have the same degree of generality as S_P^f. It is quite dependent on the configuration and on the height above the backplane at which the velocity profiles are measured. This measurement position should be systematically specified along with the integration limit R_{lim} when S_{conv} is quoted. However, since S_{conv} is close to the value of S_P^f inside the injector it may serve to classify injectors and in this sense constitutes a useful characteristic number and a practical alternative to S_P^f.

One should note that the geometrical formula of Claypole and Syred (1981); Zhang et al. (2005) $S_{geo,1} = 1.2$ (Eq. (4.46)) which is designed for this specific swirler arrangement and does not rely upon an assumption of a certain shape for the velocity profile, gives a result that is close to S_P^f inside the injector, but also to the conventional swirl number $S_{conv} = 0.98$.

4.7 Conclusion

This article deals with the determination of the swirl number in practical flows. The analysis is based on a large eddy simulation of a generic system comprising an injector having a circular cross-section, a cylindrical chamber and a sudden expansion between these two elements. This allows a detailed analysis of the various terms involved in the definition of the swirl number. The analysis is first carried out on the swirl number S_P^f originally defined as the ratio of the axial flow rate of angular momentum axial component G_θ^f to the axial flow rate of axial momentum $G_{x,P}^f$. It is found that the axial flow rate of axial momentum $G_{x,P}^f$ is nearly constant when the duct section is constant. The decay of the flow rate of angular momentum axial component G_θ^f is controlled by the moment of tangential shear stress at the duct wall. The analysis indicates that the swirl number S_P^f defined by Rose (1962); Chigier and Beér (1964); Chigier and Chervinsky (1967b); Chigier and Chervinsky (1967a) needs to account for the pressure term that is often neglected. In practical confined flows this requires the inclusion of a reference pressure. It is shown that this quantity needs to be adapted to each duct element composing the system. The analysis also indicates that it is important to include terms corresponding to turbulent fluctuations in the flow and that these terms correspond to non negligible contributions to the integrated fluxes appearing in the definition of the swirl number. It also appears that all integrations should be carried out up to the wall of the system. The commonly used formula S_U^0 (Eq. (4.45)) is found to yield inadequate results in the entirety of the system, while $S_{U,BL}^f$ (Eq. (4.43)) and S_0^0 (Eq. (4.42)) can only be used at a distance from area changes, in regions where the flow is established. Given these elements, the determination of the original swirl number from experimentally measured velocity profiles is quite challenging and requires the use of the complex expression S_U^f (Eq. (4.29)), introduced in the present study. Calculating S_U^f requires the measurement of the axial gradient of $\overline{U_x U_r}$ and the wall pressure as well as the determination of a reference pressure. In this respect, numerical simulations, which have shown their capability to model swirling flows, appear better suited to the task of determining the original swirl number S_P^f than using formulations that try to approximate the original expression. A highly simplified

expression for a conventional swirl number S_{conv} obtained by eliminating the pressure term and the turbulent fluctuation stresses may constitute a practical alternative when the swirl number has to be determined from experimental data. Although it is only weakly linked to the original definition, and does not have the same degree of generality, this conventional swirl number provides an estimate of the degree of swirl and may serve to categorize injectors. Appendices C and D contain a synthesis of recommended practices for the computation of the swirl numbers S_P^f and S_{conv} from experimental measurements and numerical simulations.

Part III

Flame and injector dynamics in a single sector rig (SICCA-Spray)

Chapter 5

Investigation of transient PVC dynamics in a strongly swirled spray flame using high speed SnO_2 tomography

Contents

The Precessing Vortex Core (PVC) dynamics is investigated in a laboratory scale swirl stabilized spray combustor. This helical structure commonly found in swirling flows used to stabilize flames in many combustion systems has a notable impact on the structure of the flow, spray and flame formed by the injector unit. The dynamics of the PVC is examined by combining laser sheet illumination of flame front tracers filmed with a high speed camera, Proper Orthogonal mode Decomposition (POD) and wavelet analysis. In distinction with most applications of laser sheet illumination, in which the flow is seeded with oil droplets that vanish at a relatively low temperature when crossing the flame front, the present implementation relies on micronic tin oxide (SnO_2) particles that vanish at much higher temperatures. This is well suited to flows where fresh reactants are already at high temperature or where hot gases are recirculated as is the case in most swirling injection configurations. A first set of experiments carried out with stagnation point premixed flames is used to determine the temperature ($T_v \approx 1770\,\mathrm{K}$) at which the tin dioxide vanish and to identify the chemical reaction that controls this process. Because the light scattered by the solid particles is quite intense, the method can be used at very high repetition rates. It is then applied at a 100 kHz frame rate to a swirling injection configuration in a situation where the flame is well stabilized and the combustor does not exhibit thermo-acoustic instabilities. It is found that the PVC takes the form of a double helix with brief intermittent switching to a single, followed by a triple helicoidal geometry. The POD-wavelet analysis indicates that these moments correspond to flashback events that randomly occur and during which the PVC characteristics change for a few milliseconds at a time. In a second set of experiments the chamber length is augmented giving rise to a combustion instability coupled by a longitudinal acoustic mode at a frequency that is an order of magnitude lower than the PVC frequency. The planar slices of the flame reveal a large cyclic motion of the lower edge of the flame in the inner recirculation zone. It is found that the PVC is modulated both in amplitude and frequency, the modulating frequency corresponding to that of the thermoacoustic oscillation. The double helix PVC is also observed to vanish in a random manner.

A part of this chapter (more specifically Section 5.1 to 5.3.2) was presented at the 2018 Congrès Francophone de Techniques Laser in Dourdan, France as Tomographie à très haute cadence de flammes turbulentes swirlées au moyen du dioxyde d'étain by Guillaume Vignat, Daniel Durox, Kevin Prieur, Théa Lancien, Ronan Vicquelin and Sébastien Candel.

5.1 Introduction

Swirling flows are commonly used in many combustion systems to stabilize the flame at a distance from the combustor walls by recirculation of hot gases around the axis of the burner and in outer regions adjacent to the stream of fresh reactants. The corresponding flames are relatively compact and fairly stable. To assist engineering design, it is important to characterize their structure and dynamical behavior and identify mechanisms that control their sensitivity to perturbations and determine the position of the flame edge in the injector near field to avoid hot spots, flashback, extinctions and combustion instabilities. It is logical to examine the behavior of these flames in representative configurations and use spatially resolved imaging tools that allow high frame rate operation to examine these flows. The present investigation illustrates one possible method consisting in illuminating the flame with a continuous planar laser sheet and seeding the flow with tracers which disappear in the flame front. Images acquired at up to 100 kHz allow to identify the structure of the precessing vortex core (PVC) in a swirling flow, examine its transient dynamics and accompanying flame motion and characterize modulations of the PVC induced by combustion instabilities.

It is worth at this point briefly reviewing optical techniques that might allow high rate imaging and could be used to investigate practical swirling reactive flows. One possibility would be to use fast imaging of the chemiluminescent emission. The light signal emitted by flames is generally not of a sufficient level for exposure durations corresponding to frame rates of the order of ten kHz or more. Using current imaging technology, visualizations of light emission from conventional hydrocarbon flames at atmospheric pressure may be achieved up to a sampling rate of about 6 kHz (e.g. Kypraiou et al. (2016); Prieur et al. (2017b); Ebi and Clemens (2016); Prieur et al. ()). Density gradients can be visualized using back-lighting and full-field interferometry at very high repetition rates: 200 kHz in Greiffenhagen et al. (2020). However, these techniques only give access to line-of-sight integrated images, which complicate the signal interpretation and the extraction of the flame front dynamics. Another powerful method is planar laser induced fluorescence (PLIF) of chemical species like OH. This radical appears near the end of the reactive zone and it persists in the burnt gases thus marking the flame front. Recently developed high repetition rate lasers allow a temporal resolution of the motion of the OH layer at rates of the order of 10 kHz. OH-PLIF imaging, widely used in combustion, has been applied to the study of the dynamics of swirled flames (e.g. Cavaliere et al. (2013); Osborne et al. (2017); Stöhr et al. (2018a); Yin and Stöhr (2020)). This method requires the use of pulsed, tunable lasers, and at high repetition rate the energy per pulse is fairly low, limiting the signal to noise ratio in the recorded images. Additionally, in high pressure applications, higher collisional quenching rates further reduce the fluorescence signal. Simpler flame front visualization methods based on tomography have been used for many years. The first objective of this chapter is to explore this standard path by specifically considering issues raised by the tracer's characteristics and by examining the possible use of particles featuring relatively high vanishing temperatures.

The availability of fairly powerful continuous lasers allowed the first developments of pla-

nar laser tomography aimed at visualizing flame fronts. The technique consists in seeding the reactive flow with a tracer which either appears or vanishes when crossing the flame front. In 1980, Boyer (1980) suggested using micronic oil droplets to seed the reactive flow. These tracers mark the flame front boundary on the fresh stream side (Durox and Ducruix (2000)), and the isotherm where these droplets vanish corresponds to approximately 570 K, with some small variations depending on the type of oil (Dumont and Borghi (1986); Miles and Gouldin (1998); Ebi and Clemens (2016)). This technique has been used extensively to analyze the dynamics of simple flame fronts (Hertzberg et al. (1984)) and time tracking was achieved in the 1990s with pulsed lasers operating at high repetition rates such as copper vapor lasers delivering light pulses at a rate of a few kilohertz in combination with fast film cameras (Mouqallid et al. (1994)). One advantage of flame tomography is its straightforward combination with PIV measurements to simultaneously determine the position of the flame front, its velocity and the velocity of the stream of fresh gases (e.g. Lecordier et al. (1994); Miles and Gouldin (1998); Balusamy et al. (2011)). Upton et al. (2011) expanded on this method by performing a 3D reconstruction of a turbulent premixed jet flame. The position of the flame front was determined by the disappearance of oil droplets used as seeders. Ebi and Clemens (2016) also performed a 3D reconstruction in a combustor featuring a lean-premixed swirling flame with a higher acquisition rate of 5 kHz. Simultaneous stereoscopic PIV was used to determine the three components of the velocity in the fresh stream.

However, in many applications where combustion is confined, the temperature of the fresh reactants can be higher than 570 K and in those cases the tracer oil droplets would be vaporized before reaching the flame front. This is the case, for example, in many systems operated above atmospheric pressure, in certain swirling flames with strong recirculation typical of gas turbines, in industrial furnaces equipped with heat recovery systems, in automobile engines just before ignition. It is then no longer possible to use oil droplets. This observation led to exploring seeding with titanium tetrachloride ($TiCl_4$) injected into the fresh stream in liquid form. $TiCl_4$ reacts with the water vapor formed during combustion to produce micronic particles of TiO_2 (Chen and Roquemore (1986)). A laser can then be used to visualize the reaction zone: its light is scattered by the titanium oxide particles conveyed in the burnt stream, thus marking the location of hot combustion products. This technique provides high quality planar images, but has the drawback of producing hydrochloric acid during the reaction, which limits its practical application. The possible use of other solid tracers that vanish when crossing a flame front was reviewed early on by Dumont and Borghi (1986) who quote temperatures at which particles disappear, either by sublimation, or through liquefaction. Some of these solid tracers are notably toxic while others modify the flame color, such as phosphorus pentaoxide P_2O_5, molybdenum trioxide MoO_3, zinc sulfide ZnS, or antimony trioxide Sb_2O_3. Among the particles used to seed reactive flows, titanium dioxide TiO_2 and zirconium dioxide ZrO_2 are often favored by experimenters, because they are resistant to high temperatures (> 2300 K), but they are generally not suitable for tracing the reaction fronts of hydrocarbon-air flames. According to Dumont and Borghi (1986) tin dioxide SnO_2 particles appear particularly interesting in cases where the fresh stream is brought to a high temperature of a few hundred degrees. The particle size of tin dioxide is in the micronic range and the distribution of particle

sizes is relatively narrow. Dumont and Borghi (1986) suggest that SnO_2 particles vanish at a temperature of 1820 K, while the PubChem database Pub () reports that its melting temperature is around 1900 K and its boiling temperature is in the range 2070−2170 K.

It is clear that tin dioxide tracers merit some attention and its use is explored in what follows with the aim of examining strongly swirled flame dynamics. These flames are stabilized in the vicinity of a spray swirled injector of the type used to study the circular ignition ("light round") in a transparent annular chamber (MICCA-Spray) representative of an annular combustor (Prieur et al. (2017b); Lancien et al. (2018); Prieur et al. ()). The swirl number measured at the injector outlet is relatively high (0.68) (Prieur et al. (2017b)), imposing a strong recirculation of burnt combustion products on the axis. This high level of swirl makes it likely that one or two precessing vortex structures exist in the flow. In the case considered in what follows experiments indicate that there are two helical structures for the Precessing Vortex Core (PVC), a feature that is also retrieved in a large eddy simulation and that will be studied in some detail using the SnO_2 tomographic technique.

It is worth at this point briefly reviewing the literature on PVCs in swirling flows and swirl-stabilized flames. This topic is discussed in isothermal conditions in the review on vortex breakdown by Lucca-Negro and O'Doherty (2001), and in flames in the reviews of Syred (2006) and Candel et al. (2012); Candel et al. (2014). In combustion applications, swirling injectors are used to aerodynamically stabilize the flame at a distance from the combustor walls. This is possible because, for a sufficiently high level of swirl, the flow undergoes vortex breakdown, a phenomenon whereby an inner recirculation zone forms on the centerline of the flow. As the swirl number is increased, a spiraling vortex structure appears in the vicinity of the inner shear layer as a result of a super-critical Hopf bifurcation (Liang and Maxworthy (2005); Oberleithner et al. (2011); Manoharan et al. (2020)). This structure established between the inner recirculation zone and the main flow (Selle et al. (2004); Liang and Maxworthy (2005); Wang et al. (2005); Stöhr et al. (2011); Stöhr et al. (2018b); Manoharan et al. (2020)) precesses in the same direction as the flow but is winding in the opposite direction (Liang and Maxworthy (2005)). The PVC is a global mode of instability (Gallaire et al. (2006); Oberleithner et al. (2011); Wang et al. (2017)). It creates a fully synchronized motion in the entirety of the flow, at a frequency that increases linearly with the flow rate (Lucca-Negro and O'Doherty (2001); Syred (2006); Ghani et al. (2016)) and is also related to the swirl number S (Cassidy and Falvey (1970); Lucca-Negro and O'Doherty (2001)). Manoharan et al. (2020) have recently shown that this dependency is of the form $f_{PVC} \propto S - S_c$ where S_c is a critical swirl number. Naturally, the amplitude of this helical disturbance decays downstream of the injector, and vanishes after one to two nozzle outlet diameters (Selle et al. (2004); Stöhr et al. (2011)).

It is generally possible to associate an azimuthal wavenumber m to the PVC that reflects the angular periodicity of this coherent structure. A single helix structure corresponds to an azimuthal wavenumber $m = 1$ and is observed in many studies of swirling injectors (Froud et al. (1995); Selle et al. (2004); Roux et al. (2005); Wang et al. (2005); Kuenne

et al. (2011); Stöhr et al. (2011); Moeck et al. (2012); Terhaar et al. (2015); Stöhr et al. (2018b); Rajamanickam and Basu (2018)). In some instances, more complex structures associated with higher azimuthal wavenumbers have been observed. In laminar flows in solid body rotation with a flat axial velocity profile, Billant et al. (1998) and Liang and Maxworthy (2005) report observing intertwined periodic helical structures associated with higher wavenumbers $m = 2$ and $m = 3$. Liang and Maxworthy (2005) also observe weak structures associated with even higher wavenumbers ($m = 4, 5$), and show that the precession frequency of the PVC, f_{PVC}, is strongly tied to the rotation rate of the flow Ω by $m\Omega = f_{PVC}$. Vanierschot et al. (2020) studied specifically single- and double-helix PVCs in a radial swirler with a central bluff-body, using time-resolved PIV, POD and linear stability analysis (LSA). They concluded in particular that the frequency of the double-helix is not necessarily the double of that of the single helix-structure. Vigueras-Zuñiga et al. (2012) present some striking images of a flame stabilized inside a double helix PVC ($m = 2$). Structures of this type have been reported in other experimental investigations of swirled flames (Froud et al. (1996); Syred (2006); Stöhr et al. (2018b); Yin and Stöhr (2020)).

The effect of a flame on a preexisting PVC is complex: in some cases, the PVC is suppressed by the flame (Selle et al. (2004); Roux et al. (2005); Kuenne et al. (2011)), while in others it persists and its strength may be enhanced (Froud et al. (1995); Syred (2006); Moeck et al. (2012)). In other conditions, these two outcomes are observed depending on the operating conditions and associated flame shapes (Terhaar et al. (2015); Stöhr et al. (2018b)). The injection of fuel on the centerline of the injector can also affect the PVC (Syred and Beer (1972); Rajamanickam and Basu (2018)). Yin and Stöhr (2020) used multi-resolution POD (MRPOD) to study the PVC in a bistable swirled premixed flame. They found that the PVC observed when the flame was stabilized in its "M"-shape was strongly damped and essentially vanished when the flame was established as a "V"-shape in the inner shear layer of the IRZ. In this regard, Terhaar et al. (2015) performed an interesting parametric study in a premixed confined swirled burner. By modifying operating conditions such as fuel type, equivalence ratio, preheating temperature, steam dilution and injection bulk velocity, they were able to stabilize the flame in four distinct shapes. Depending on the flame shape, the existence and frequency of the PVC were varied. By using a local LSA on the mean flow field, measured by PIV (velocity) and quantitative light sheet determination of the density, these authors were able to retrieve the frequency and location of the PVC. Their analysis indicates that the relationship between PVC, rotation rate and flame shape is complex, and that the backflow velocity and density gradients in the inner shear layer between the IRZ and the jet play a major role.

The present study comprises four parts. In the first, the objective is to obtain the temperature value T_v at which particles of SnO_2 vanish. This is accomplished by making use of a set of atmospheric pressure hydrocarbon-air flames operating at different equivalence ratios. In the second part, the dynamics of the swirling spray flame is examined. The air used in this combustion process is seeded with fine tin dioxide particles. It is shown that SnO_2 microparticles allow to detect the flame front, but also to identify the PVC. In the third part, POD image processing and wavelet analysis are employed to analyze the

dynamics of this helical structure. It is found that the PVC forms a double helix structure, that switches to a single and then triple helical structures during short intermittent flashback events. Finally, in Section 5.5, the combustion chamber is lengthened into a configuration giving rise to combustion instabilities coupled by a longitudinal acoustic mode. The shape of the flame in the IRZ is determined for different phase instants during the thermoacoustic cycle. It is also demonstrated that the PVC is modulated by the combustion oscillation, both in terms of intensity and precession frequency.

5.2 Measurement of the temperature at which tin dioxide particles vanish

Tin dioxide is a material of high technical importance to a number of industries. Its application as a flame front tracer is however not well documented. The aim of the present section is to see if SnO_2 can be used in this application, and to determine the temperature at which it vanishes. This is accomplished by examining methane-air laminar flames formed in a stagnation point flow in a well controlled configuration used to obtain images of the particles trajectories with planar laser illumination. By varying the equivalence ratio, it is possible to change the temperature at the end of combustion in the flame zone and deduce from images whether the solid particles disappear or not when crossing the flame front. For each equivalence ratio, the temperature profile in the flame is determined using a 1D simulation with a detailed chemistry. This gives access to the characteristic temperature at which the SnO_2 particles vanish in a typical hydrocarbon-air flame at atmospheric pressure.

5.2.1 Experimental set up

A diagram of the stagnation point burner used for this measurement is shown in Fig. 5.1. This system has a flat cooled copper wall 90 mm in diameter and 10 mm thick, placed perpendicular to the burner axis. The burner outlet diameter is 22 mm. The distance from the plate to the burner outlet is also 22 mm. Methane and air are premixed prior to entering the burner. Bronkhorst ELFlow mass flow meters are used to adjust the mixture mass flow rates. Their relative precision is 0.2% in the range of interest. A flow of $0.3\,\mathrm{L\,min^{-1}}$ of water circulates in a coil to cool the copper plate. A K-type thermocouple is placed in the center of the plate. During the experiments, the temperature of the plate stays between 318 and 324 K. Without flame, but with air flow, the temperature is 285 K. A vertical laser sheet about 50 mm high traverses the flow from the left of the burner to the right in an axial plane. This sheet is formed by a continuous laser operating at 532 nm with a power of 1 W. The optical assembly includes a cylindrical lens with a short focal length and a spherical lens with 300 mm focal length. Micronic SnO_2 particles are injected into the air stream, well upstream of the burner using a cyclonic system. The number distribution for the diameter of the tin dioxide particles is given by the manufacturer as follows: $10\% < 0.39\,\mu m$; $50\% < 1.04\,\mu m$; $90\% < 2.86\,\mu m$. The average particle diameter is $d_{10} = 1.38\,\mu m$. The tests are carried out for a fixed air flow rate and the equivalence

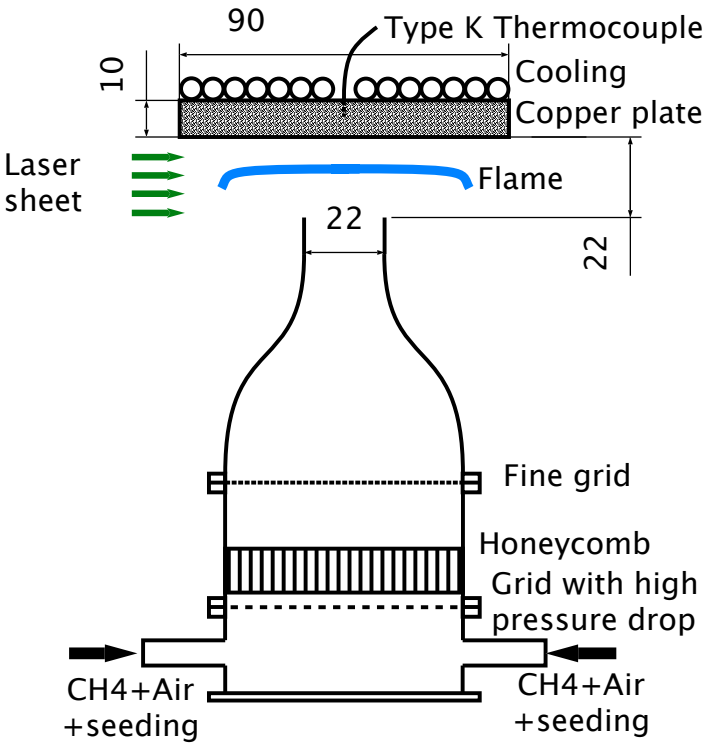

Figure 5.1: *Schematic diagram of the burner used for the study of the temperature T_v at which tin dioxide particles vanish. A plate is placed* 22 mm *above and parallel to the burner nozzle, such that a flat, stagnation point laminar flame is formed. The plate is water cooled to maintain a constant temperature at all equivalence ratios.*

Table 5.1: *Operating conditions and temperatures at the end of combustion.*

Test	1	2	3	4	5	6
$U_b\,(\mathrm{m\,s^{-1}})$	0.778	0.777	0.776	0.775	0.774	0.773
ϕ	0.705	0.691	0.677	0.662	0.648	0.634
$T_c\,(\mathrm{K})$	1842	1819	1795	1770	1745	1721

ratio of the mixture is set by adjusting the methane flow rate. The mixture velocity at the outlet of the burner varies between 0.773 and 0.778 $\mathrm{m\,s^{-1}}$ and the equivalence ratio ϕ between 0.634 and 0.705. Under these conditions, the flame is detached from the burner and established in the central part. It is nearly flat and parallel to the cooled plate.

5.2.2 Results

The test conditions are indicated in Tab. 5.1. The bulk velocity at the burner outlet (U_b) slightly varies because the methane flow rate is changed but this does not affect the results. The maximum temperature reached during combustion T_c is determined with the 1D flame simulation code "Agath", developed in house at EM2C laboratory, using a skeletal kinetic scheme GRI-Mech for methane-air combustion (Smith et al.). In these counterflow simulations, the uniform bulk velocity and the temperature of the fresh stream of 293 K are set at the burner exit while null velocities and 322 K are prescribed at the plate.

Typical flame images are displayed in Fig. 5.2. The flow is seeded with SnO_2 microparticles, which are illuminated by a laser sheet. The flame stabilizes at the point where the laminar burning velocity is equal to the axial component of the flow velocity. At the top left the flame is furthest away from the plate because this configuration corresponds to the highest value of the equivalence ratio and correspondingly to the greatest laminar burning velocity. By decreasing the equivalence ratio, from left to right and from top to bottom, the burning velocity decreases and the flame approaches the plate since the flow velocity at the nozzle has hardly changed. For equivalence ratios between 0.705 and 0.677, the tin dioxide particles completely vanish when crossing the flame front. In the image at the bottom left ($\phi = 0.662$), some particles succeed to cross the flame front, but there is a notable difference in brightness between the particle traces in the fresh stream and in the burnt gases. In the last two images all particles cross the flame front and remain visible in the hot stream. According to Tab. 5.1, one may consider that below 1745 K the particles do not vanish. At 1770 K some of the particles vanish, but some do not, most probably those featuring the largest initial diameters. One may conclude from these data that the tin dioxide particles mark an isotherm that approximately corresponds to a temperature of 1770 K for typical hydrocarbon-air flames at atmospheric pressures. This is slightly lower than the temperature indicated by Dumont and Borghi (1986) and much lower than the temperature quoted in the PubChem database ?? ().

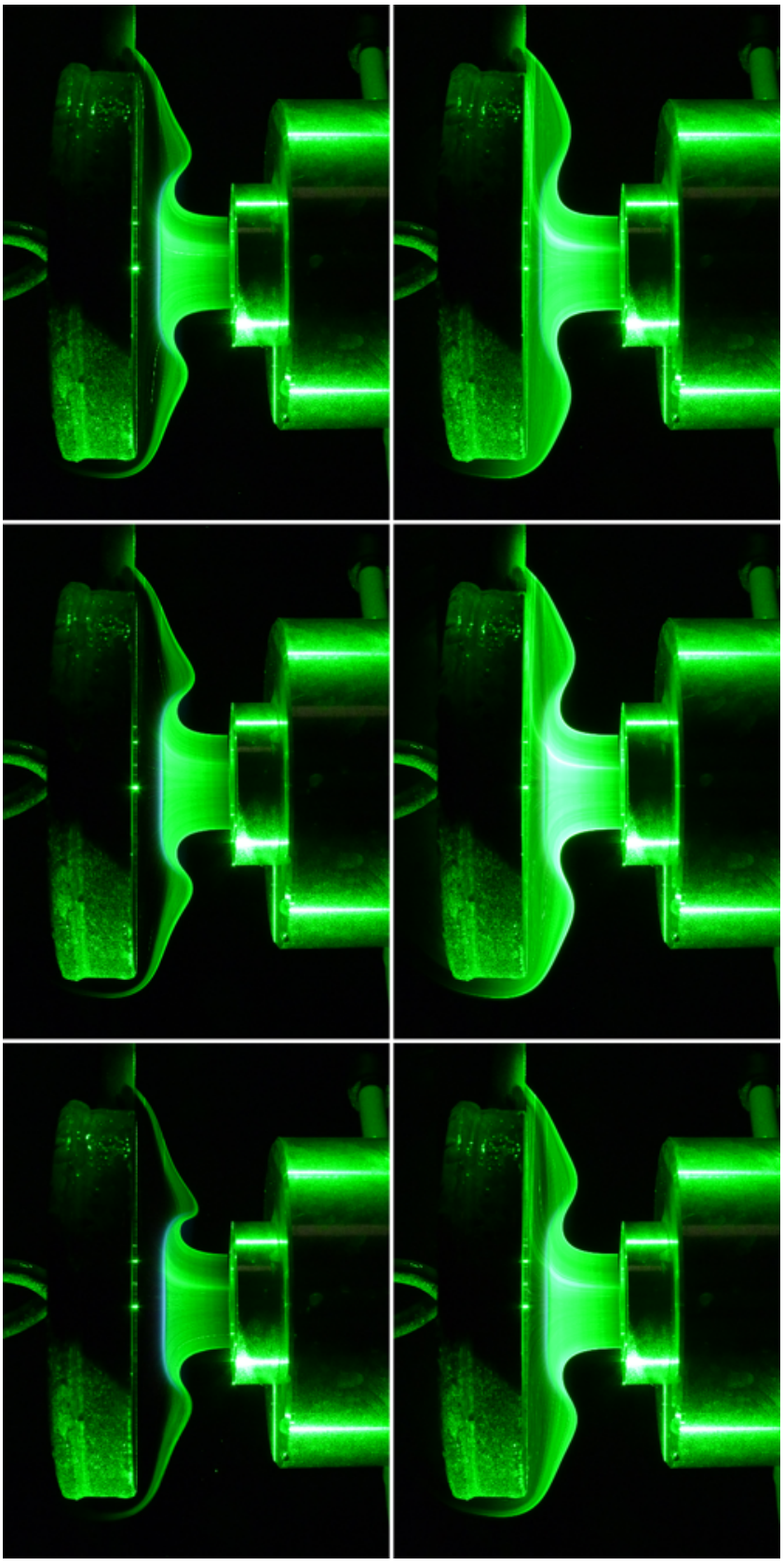

Figure 5.2: *Laser tomographies obtained by seeding the reactive flow with tin dioxide particles. The flame can be distinguished by a slight blue color. The green laser sheet illuminates the particles. A co-current annular nozzle surrounds the burner, but is not operated in this study. From left to right, and from top to bottom, the equivalence ratio is:* $0.705, 0.691, 0.677, 0.662, 0.648$ *and* 0.634.

5.2.3 Discussion

It is first useful to note that there is some debate as to the melting point of SnO_2. A value of 1903 K is often quoted (Pub (); Lamoreaux et al. (1987); Schofield (2020)). This contrasts with the experiments of Galazka et al. (2014) who suggest that the melting point is higher than 2370 K from experiments conducted at partial pressures of O_2 closer to those found in combustion applications. In any case, both these temperatures notably exceed the vanishing temperature obtained in the present work with a flat flame.

Thin films of SnO_2 are quite often formed using chemical vapor deposition (CVD). One of the first application of CVD for SnO_2 has been published by Marley and MacAvoy (1961). Their process involves heating very pure SnO_2 at 1923 K to vaporize this compound before crystallization at a lower temperature further down the furnace. The authors note that the chemical composition of the gases in the furnace is of great importance to the process. In an atmosphere devoid of oxygen, in addition to evaporation, solid SnO_2 may be decomposed as

$$SnO_2(s) \rightleftharpoons SnO(g) + \frac{1}{2}O_2(g) \tag{5.1}$$

Articles published later on confirmed that this reaction is an important process for the disappearance of SnO_2 in a high temperature environment (Hoenig and Searcy (1966); Lamoreaux et al. (1987); Schofield (2020)). Of specific interest to the present application as a flame tracer is the partial pressure of O_2 at equilibrium determined experimentally by Hoenig and Searcy (1966) for this reaction:

$$\log\left(p_{O_2}^{eq}\right) = 3.72 - \frac{20050}{T} \tag{5.2}$$

This was determined in a vacuum chamber using a Langmuir experimental apparatus. In this correlation, $p_{O_2}^{eq}$ is given in Pa. At atmospheric pressure and for $T = 1770$ K, one finds a volume fraction of O_2 at equilibrium of $X_{O_2}^{eq} = 2.5 \times 10^{-3}$, which is significantly smaller than the O_2 mass fraction in the burnt gases of the lean premixed flames used in the previous section. This indicates that the dissociation reaction (5.1) is not important in the stagnation point flames shown in Fig. 5.2.

In contrast, Galazka et al. (2014) suggest that, in the presence of gaseous CO and CO_2, another reaction may prevail:

$$SnO_2(s) + CO(g) \rightleftharpoons SnO(g) + CO_2(g) \tag{5.3}$$

For an ambient gas made of CO_2 at 1 bar, they calculate for this endothermic reaction an equilibrium temperature of $T_{eq} = 1759$ K. This is quite close to the vanishing temperature determined using the flat flame apparatus, and one may tentatively conclude that this process controls the disappearance of SnO_2 particles in hydrocarbon-air flames.

This analysis allows to identify which type of configurations may benefit from using SnO_2 as flame tracers. First it is worth underlining that the 1770 K disappearance temperature

Table 5.2: *Operating parameters for experiments using SnO_2 seeding in SICCA-Spray. Three slightly different configurations are used in this chapter. l_c is the length of the quartz confinement chamber, ϕ the global equivalence ratio of the combustible mixture, $\dot{m}_{C_7H_{16}}$ the fuel mass flow rate, u_b the bulk velocity at the outlet of the injector: $u_b = \dot{m}/(\pi\rho_{cold}r_{inj})$, with $\dot{m}$ the air mass flow rate, ρ_{cold} the density of the unburnt mixture and r_{inj} the radius of the injector outlet. Concerning the imaging apparatus, $\mathcal{P}_{LASER}$ designates the power of the continuous 532 nm laser, the high speed camera can be equipped with two different lenses, with different apertures f_{lens}. The sampling frequency of the camera is noted f_s, and the exposure time δt.*

Section	5.3	5.4	5.5
l_c(mm)	200	200	300
ϕ	0.87	0.95	0.95
$\dot{m}_{C_7H_{16}}$(g h^{-1})	400	440	440
u_b(m s^{-1})	32	32	32
$\mathcal{P}_{LASER}$(W)	10	15	15
Lens	25 mm	60 mm	60 mm
f_{lens}	f:0.95	f:2.8 (axial) or f:4 (normal)	
f_s(kHz)	100	40	40
δt(µs)	8.38	12.5	12.5
Resolution	384 × 264	512 × 512	512 × 512

only applies to hydrocarbon-air flames at ambient pressure. Several parameters may affect the exact value of that temperature, such as the chemical composition of the reactive mixture, ambient pressure... The impact of these parameters could be further assessed by performing chemical equilibrium simulations. Second, one may also ask whether the temperature is influenced by the particle size. Two batches of SnO_2 particles from different suppliers have been tested, indicating that the size of SnO_2 particles does not affect the disappearance temperature for particle sizes less than 2.5 µm. To tentatively conclude, SnO_2 should be used to trace flame fronts when oil droplet seeding would be ineffective because of premature disappearance. For hydrocarbon-air flames, SnO_2 can reliably be used if the burnt gas temperature is significantly higher than 1770 K.

5.3 Application to a highly swirled spray flame

5.3.1 Experimental set up

The SICCA-Spray swirled burner is used in this chapter (see Vignat et al. (2019) for more details on this experimental rig). It is displayed in Fig. 5.3, on the left. A quartz tube, open to the atmosphere, forms the combustion chamber. The tube has an inner diameter of 69 mm and its length l_c, alongside other experimental parameters, is reported in Tab. 5.2. The injector placed in this system is identical to that used in previous investigations on light round ignition in the MICCA-Spray annular chamber (Prieur et al. (2017b); Lancien et al. (2018); Prieur et al. ()). Components that make up this unit are shown on the right of Fig. 5.3. The fuel atomizer forms a hollow cone spray of liquid

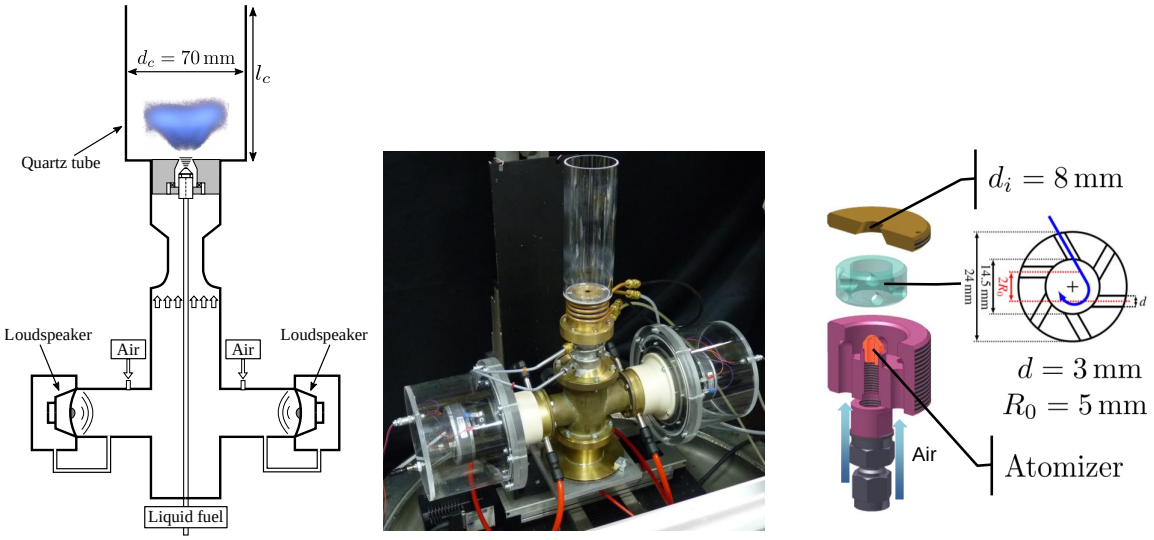

Figure 5.3: *Left, schematic view and photography of the experimental rig with its cylindrical quartz flame tube* 200 mm *long and* 70 mm *inner diameter. Right, injector components : the air distributor in purple, the hollow cone atomizer in orange, the swirler in green and the end plate in brown color. This plate features a conical converging hole having a* 14 mm *diameter inlet and an* 8 mm *diameter outlet. Adapted from Vignat et al. (2019); Vignat et al. (2020).*

heptane on the axis of the burner. The mean Sauter diameter in the droplet spray d_{32} equals 27 µm (Prieur et al. (2017b)). A swirler, marked in teal in Fig. 5.3, sets the air in rotation around the axis. This swirler consists of 6 holes tangentially connected to the annular space surrounding the atomizer. The diameter of each hole is 3 mm and the distance between two axes of parallel holes is 10 mm. An end plate, with a converging conical hole, blocks the swirler in its housing. The central hole forming the outlet has a diameter of 8 mm. This results in a swirl number experimentally determined immediately downstream of the injector of 0.68 (Prieur et al. (2017b)). Two driver units are plugged on the system to modulate the flame by means of harmonic waves but they are not operated in the present study.

In the present chapter, three different experimental configurations have been investigated, and are detailed in Tab. 5.2. Note that the bulk velocity and air flow rates are kept constant for all three experimental configurations. The first operating conditions, used in the present section, match those of previous experiments and LES (Prieur et al. (2017b); Lancien et al. (2018); Prieur et al. ()). In section 5.4, the operating conditions are slightly richer and transient PVC dynamics are examined in conditions where the system is thermoacoustically stable. In section 5.5, the air and fuel flow rates are identical to Sec. 5.4, but a longer combustion chamber is used and a combustion oscillation, coupled by a longitudinal acoustic mode, occurs.

As in section 5.2 the flow is investigated using planar laser imaging. The laser sheet traverses the burner perpendicular to the axis or parallel to the axis along a diameter. The emission optics for the laser sheet is the same as in Section 5.2, with a laser sheet height of approximately 50 mm. The flow is seeded with tin dioxide micronic particles which

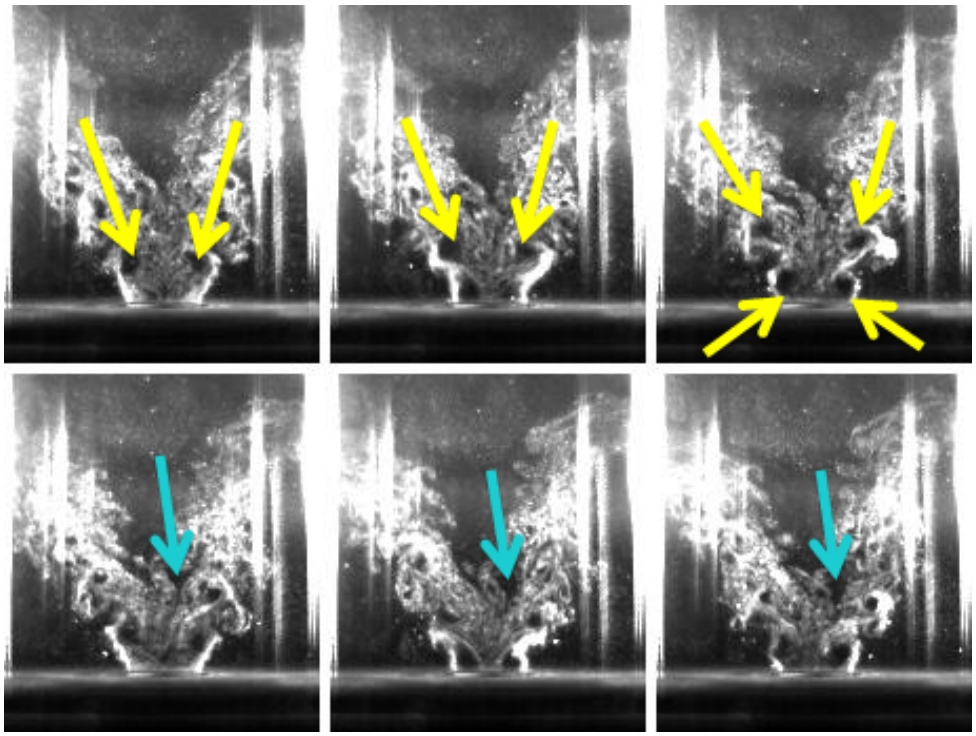

Figure 5.4: *Successive flame images with SnO_2 seeding and illumination by a vertical laser sheet. The sequence is read from left to right and from top to bottom. Compared to the recorded sequence only one image out of 5 is displayed, which corresponds to a rate of 20 000 fps. Yellow arrows indicate the low pressure regions corresponding to the branches of the PVC. The blue arrows indicate the lower edge of the flame in the inner recirculation zone.*

quickly vanish at the temperatures reached with a heptane-air flame near stoichiometry. The dynamics of the flame front is visualized with a Photron FASTCAM SA-X2 high speed camera at a frame rate of 100,000 fps with an exposure time of $\delta t = 8.38\,\mu s$ for each image. At this frame rate, one may hope to capture the flame front motion and distinguish hot regions where temperatures are higher than 1770 K from cooler regions. The images displayed in Figs. 5.4 and 5.5 only show one image out of 5 selected from complete sequences to exhibit the dynamics of flow structures, therefore at an effective sampling rate corresponding to 20 kHz.

5.3.2 Swirling flame front dynamics

Axial (vertical) planar laser visualization are displayed in Fig. 5.4. Near the combustion chamber backplane, in the lower corners of the images, there are no SnO_2 particles indicating that these areas are occupied by recirculating burnt gases that are hot. On each side of the injector outlet the images are quite bright, because of the light scattered by the spray of heptane droplets that are shed from the periphery of the outlet hole. Downstream, on the axis, one observes a large triangular area that is quite dark, indicating that tin dioxide particles are absent. This is an area filled with burnt gases recirculating towards the low pressure region formed around the centerline by the swirling flow. In

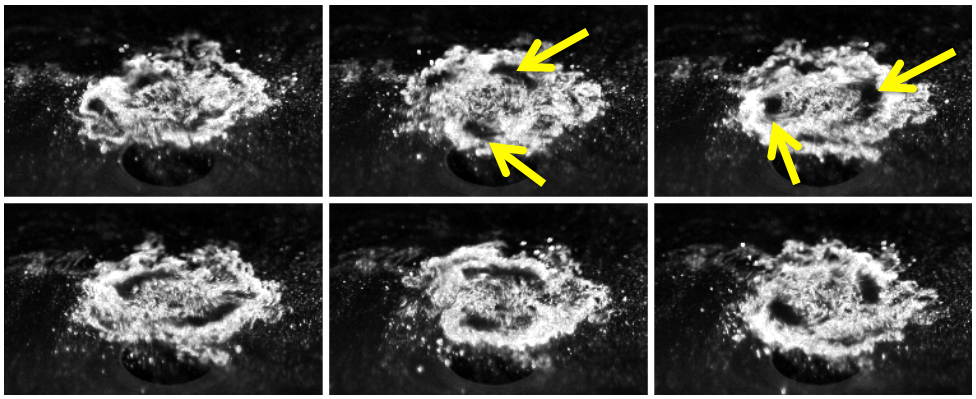

Figure 5.5: *Successive flame images with SnO_2 seeding and illumination by a horizontal laser sheet, at $z = 5$ mm from the injector outlet. Photographs are taken with a high elevation angle of approximately 45°. The sequence is read from left to right, then from top to bottom. Compared to the recorded sequence only one image out of 5 is displayed, which corresponds to a rate of 20 000 fps. The yellow arrows indicate the low pressure regions corresponding to the arms of the two helicoidal cores.*

each image in the second line, the lowest point of this region is indicated by a blue arrow. The flame penetrates deeply in the neighborhood of the central axis but the flame edge is also found to move downstream to a distance of 20 mm from the combustor backplane.

The external boundary of the spray and tin dioxide particles, near the injector outlet, sometimes features undulations induced by the vortices generated at the injector lip. The frequency of these vortices is high, but does not cause a specific flame motion. One distinguishes in these images dark areas that are symmetrical with respect to the axis of the burner and marked by yellow arrows in Fig. 5.4. They correspond to locations without particles that are surrounded by seeded areas. The absence of particles may be interpreted by considering that these dark areas correspond to a strong vortex from which particles are centrifuged. It is known that swirling flows may give rise to hydrodynamic instabilities taking the form of narrow and intense helical vortices with a precessing motion around the injector axis (PVC). If there is a single helix PVC ($m = 1$) the planar laser visualization would reveal unseeded spots with an alternate arrangement with respect to the central axis (e.g. Stöhr et al. (2011)). In the present case, however, the spots are symmetrical indicating that this could be due to the presence of two helical structures that are diametrically opposed (PVC with an azimuthal wavenumber $m = 2$, e.g. Liang and Maxworthy (2005).

To see if this is indeed the case it is logical to observe what is happening in the normal (horizontal) direction. This may be done by placing a laser sheet parallel to the backplane at a distance $z = 5$ mm from the outlet (Fig. 5.5). The corresponding images show two opposite dark spots that rotate around the injector axis in the clockwise direction. These spots are marked with yellow arrows. One deduces from the horizontal and vertical visualizations that the flow features two helical structures nested one inside the other. This double helix configuration ($m = 2$) is less common than the single core PVC ($m = 1$)

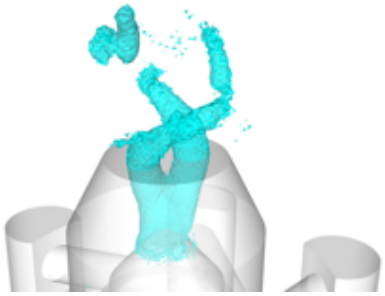

Figure 5.6: *Large eddy simulation of the flow inside and at the outlet of the swirling injector. A pressure isosurface corresponding to* 99 400 Pa *is displayed showing the winding of the two helicoidal PVCs.*

but is manifested in swirling flows characterized by high rotation rates as can be seen for example in Liang and Maxworthy (2005) where the instantaneous vorticity field in a non-reactive flow with a high level of swirl features a double helix structure. The images presented by Liang and Maxworthy (2005) are strikingly similar to those displayed in Fig. 5.4.
Using the images of Fig. 5.5, it is possible to determine the precession frequency of each arm. This is found to be of 3.25 kHz corresponding to a Strouhal number St $= 2R_{inj}f/u_b = 0.81$, which falls in the typical range reported by Syred (2006).

To understand the origin of the deficits in tin dioxide particles in areas where the temperature is normally low, it is natural to seek an estimate of the vorticity level in these low pressure regions. This however would require measurements of the velocity field which is difficult to measure with PIV because the particles are absent from high vorticity regions. To get an estimate of the vorticity level one may use large eddy simulations of the same flow. The calculations carried out by Lancien et al. (2018) give access to this information. Results corresponding to conditions selected for the experiments appear in Fig. 5.6 which shows details of the injector geometry and an isosurface of the pressure field that materializes the helicoidal winding of the two vortex cores.

One may clearly see in the left side of Fig. 5.7 two low pressure regions corresponding to slices through the two PVCs wound as a double helix. On the right, the vorticity field in this same plane shows that the levels of vorticity reach of the order of $2.0\,10^5\,s^{-1}$. It is then possible to know if particles are circulating in the vortex by examining their Stokes number Stk_ω in this region. This number can be defined by $Stk_\omega = \tau_b/\tau_\omega$, where τ_ω is a characteristic residence time of a particle in the vortex and τ_b is the classical momentum relaxation time for particles featuring a low Reynolds number

$$\tau_b = \frac{\rho_b d_b^2}{18\mu_f} \tag{5.4}$$

where ρ_b, d_b are the particle density and diameter and μ_f designates the dynamical viscosity in the surrounding gaseous stream.

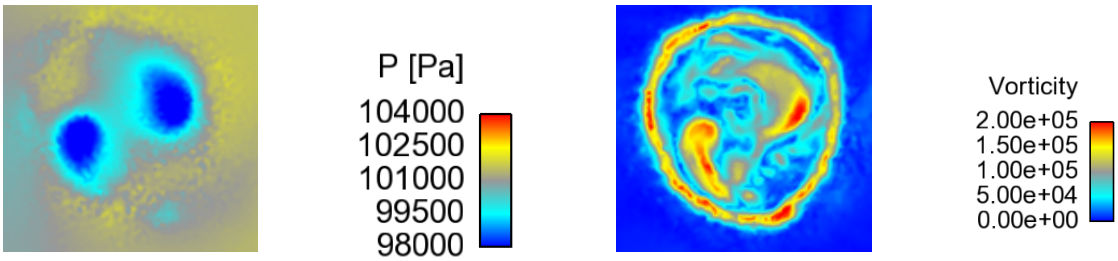

(a) (b)

Figure 5.7: *(a) Instantaneous pressure field in a plane located at $z = 1\,\text{mm}$ above the injector outlet. (b) Instantaneous vorticity field in the same section. Values are given in s^{-1}. Two spots of low pressure and high vorticity are visible, and correspond to the intersection of the two PVC helicoidal structures with the viewing plane.*

Table 5.3: *Calculation of the Stokes number Stk_ω for tin dioxide particles in air in the presence of a vorticity of $2.0\,10^5 \text{s}^{-1}$.*

$d(\mu\text{m})$	0.39	1.04	1.37	2.86
$\tau_b(\mu\text{s})$	3.23	22.9	39.8	174
Stk_ω	0.64	4.6	8.0	35

The characteristic residence time in a vortex featuring a vorticity level ω is inversely proportional to this level: $\tau_\omega \simeq \omega^{-1}$ (Kriebel (1961); Dring and Suo (1978)). This can be used to estimate the Stokes number Stk_ω for tin dioxide particles in places where the vorticity level reaches maximum values. Results gathered in Tab. 5.3 indicate that the finest particles have a Stokes number smaller than unity. They can theoretically follow the flow inside the vortex. However, the number of these small particles is relatively small (less than 10% of the total number of particles), their light scattering cross section is also small so that they will only contribute in a minor way to the light intensity measured by the camera. The particles having a diameter of the order of magnitude of one micron already have a Stokes number that is larger than 1, indicating that these particles will be centrifugated by the vortex structure. Thus more than 90% of the population will leave the zone where the vorticity is of $2.0\,10^5\,\text{s}^{-1}$. It is therefore normal to observe a deficit of tin dioxide particles in the vortex core. This lack of particles is obviously inconvenient for velocity measurements in these areas, but it has the advantage of allowing the spatial localization of strong vortical structures such as a PVC.

5.4 PVC dynamics during intermittent flame flashbacks

5.4.1 POD based image processing

It is now interesting to implement a processing method for the analysis of the dynamics of the flame and PVCs. The present method features two steps: first, a Proper Orthogonal

Decomposition is applied to the images. This statistical processing consists in expanding the images $\psi(x, y, t)$ onto a series of M modes $\Psi(x, y)$ in the spatial domain.

$$\psi(x, y, t) \approx \overline{\psi}(x, y) + \sum_{k=1}^{M} a_k(t)\Psi_k(x, y) \tag{5.5}$$

where a_k are temporal coefficients corresponding to the projection of ψ onto the mode Ψ_k and $\overline{\psi}$ is the mean value of ψ. If the number of modes M is equal to the number of images on which the POD is performed, then Eq. (5.5) is exact. The basis formed by the modes Ψ_k is orthogonal. The POD process allows to isolate dominant spatial structures. Thresholding for improved brightness and contrast is the only pre-processing applied prior to the POD.

The second step of the processing consists in the spectral analysis of the coefficients $a_k(t)$. This is performed by first computing their power spectral density using Welch's periodogram method. This step is useful to identify the dominant frequency of a structure, but transient dynamics are hidden by this type of processing. In a second step, time-frequency analysis is performed by means of a continuous wavelet transform based on an analytical Morlet wavelet (Delprat et al. (1992)). The conversion of the scale of the wavelet transform to a frequency is based on an approximation whereby the center frequency f_{CM} of the mother Morlet wavelet is divided by the scale a: $f = f_{CM}/a$. he temporal resolution of the continuous wavelet transform is evaluated as the width at half height of the scalogram of an impulse. At a given frequency f, it corresponds to $\delta t = 1.56/f$. Results of this processing are plotted in the form of a scalogram in time-frequency coordinates. The color scale indicates the squared magnitude of the continuous wavelet transform, which is akin to a power spectral density plotted as a function of time and frequency. Note that Yin and Stöhr (2020) exploit a similar approach (multi-resolution POD (MRPOD)), to study, among other things, the state of the PVC in a bi-stable flame.

In the present section, the operating conditions of the burner are slightly modified to match those that will be used in Section 5.5 to investigate the flame dynamics during a combustion instability. All relevant experimental parameters are gathered in Tab. 5.2. Compared to Section 5.3, the fuel flow rate is increased by 10% while the air flow rate is kept constant, corresponding to a global equivalence ratio of 0.96, and a thermal power of 5.4 kW. The image acquisition rate is set at 40 kHz with an exposure time of 12.5 µs.

Figure 5.8 shows the results of the POD analysis performed on a normal (horizontal) slice similar to that presented in Fig. 5.5. The energy distribution of the POD modes (Fig. 5.8(a)) reveals two dominant modes displayed in Fig. 5.8(b). Their shape corresponds to a set of two opposing holes (the $m = 2$ PVC located in the inner shear layer between the inner recirculation zone and the swirling jet), surrounded by two periodic bean shapes in the outer shear layer. These outer structures are fully synchronized with the precessing motion and are reported in several previous studies carried out in non-reacting conditions (Liang and Maxworthy (2005); Oberleithner et al. (2011); Stöhr et al. (2011)). The

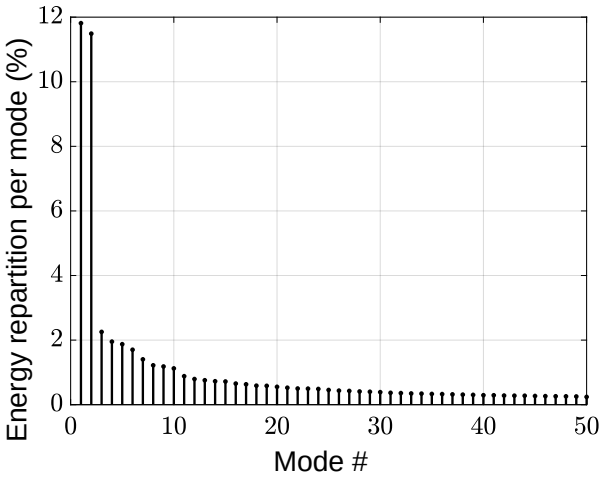

(a) *Energy distribution in POD modes.*

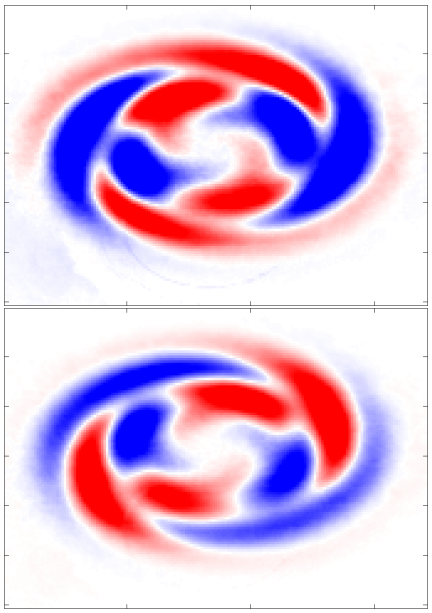

(b) *POD modes 1 and 2.*

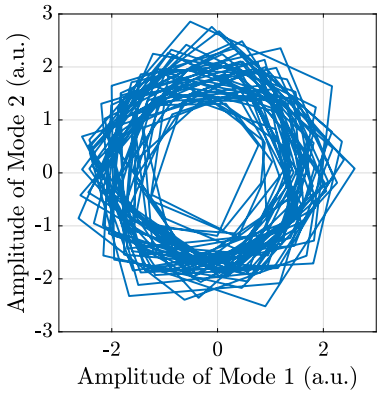

(c) $a_2^h(t)$*, amplitude of POD mode 2, plotted against* $a_1^h(t)$*, amplitude of POD mode 1.*

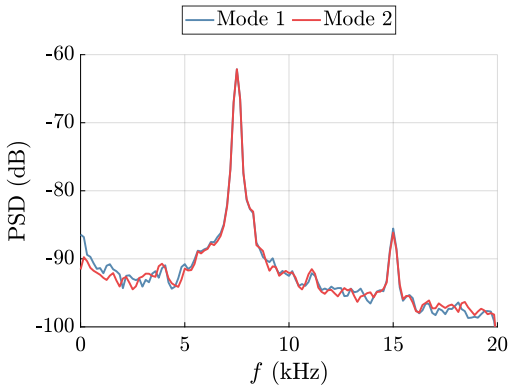

(d) *Power spectral density of* $a_1^h(t)$ *and* $a_2^h(t)$*.*

Figure 5.8: *POD processing of images recorded with a horizontal laser sheet illumination at* $z = 5\,\text{mm}$ *above the backplane with a high viewing angle of approximately* 45° *with respect to the vertical direction. 5458 images are used for this processing.*

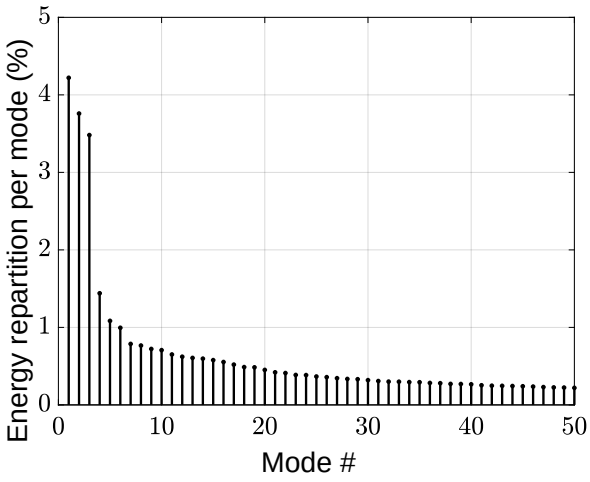

(a) *Energy distribution in the POD modes.*

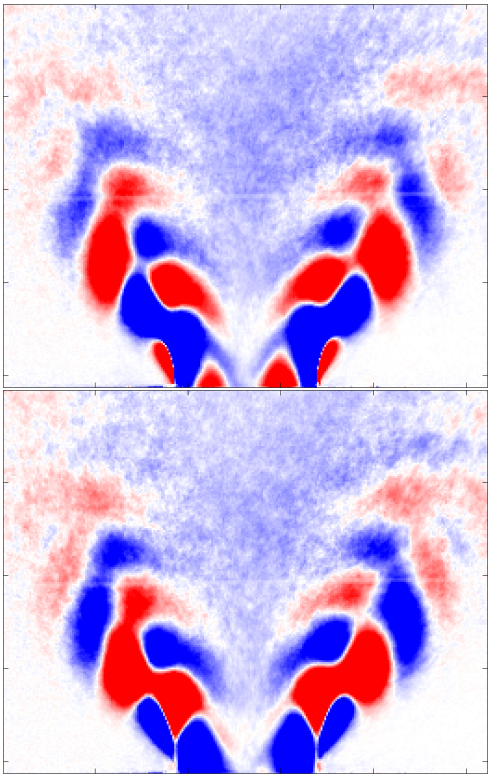

(b) *POD modes 1 and 2.*

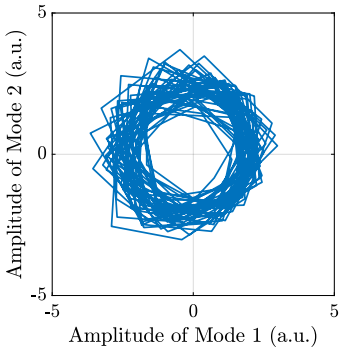

(c) $a_2^v(t)$, *amplitude of POD mode 2, plotted against* $a_1^v(t)$, *amplitude of POD mode 1.*

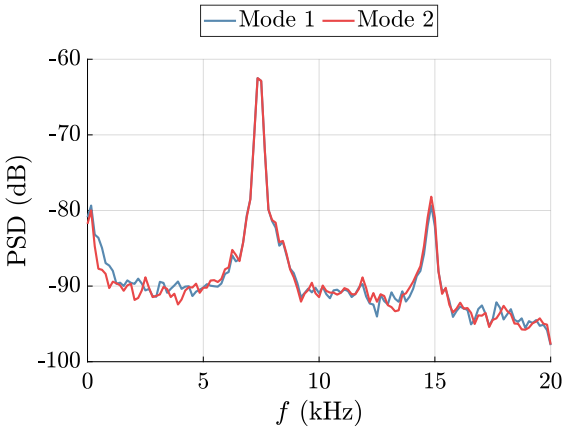

(d) *Power spectral density of* $a_1^v(t)$ *and* $a_2^v(t)$.

Figure 5.9: *POD processing of particle images with vertical laser sheet illumination. 4366 images are used for this processing.*

second mode is similar to the first mode, with a $\pi/4$ rad rotation. The power spectral density of the coefficients (Fig. 5.8(d)) shows that the POD coefficients are harmonic with a frequency of 7.5 kHz, corresponding to a precession frequency of 3.75 kHz for each arm. The temporal coefficients a_1^h and a_2^h, where the superscript h is used to denote the result of horizontal slices, form a set of circles in a Lissajous diagram (Fig. 5.8(c)), indicating that the two POD modes are highly correlated and in phase quadrature. These elements constitute the typical signature of a periodic, progressive rotating pattern extracted using POD. Given the shape and spectral signature associated with the pair of POD modes, one concludes that these two modes correspond to the double helix PVC shown in Fig. 5.6. For a detailed discussion on the reconstruction of a PVC using POD, which further substantiate the elements that have been presented, one may refer to Stöhr et al. (2011).

The same processing is now applied to axial (vertical) tomographic images similar to those presented in Fig. 5.4, leading to the results shown in Fig. 5.9 which confirm the presence of two POD modes in quadrature. The first two modes that the POD exhibits also correspond to the double helix PVC. It is next interesting to perform a time-frequency analysis of this double helix PVC signal. This is done by making use of an analytical wavelet transform, performed on the $a_1^v(t)$ coefficient of the first POD mode from the vertical tomographic images. Figure 5.10 shows the resulting scalogram for a 110 ms recording. The frequency around 7.5 kHz is dominant, but one observes during certain short periods of time of a few milliseconds, that the signal corresponding to the double helix PVC vanishes. This intermittency manifests itself six times during the 110 ms long recording, and its duration varies between 2 ms and 7 ms. The intermittent disappearance of this double helix structure is studied in more detail in the next section.

5.4.2 Changes in PVC regimes during intermittent flame flashbacks

To analyze the intermittent gaps in the scalogram of Fig. 5.10, one may first examine the raw images in the time interval corresponding to one of these gaps. The focus is thus placed on the longest intermittency found in Fig. 5.10 between $t = 70$ and $t = 76.5$ ms. The images of Fig. 5.11 show the evolution of the flow during this period of time. Note that these images are not equally spaced in time. Keeping in mind that the tin dioxide particles vanish while crossing the flame front, and referring to the images of Fig. 5.4, one sees that in the images corresponding to $t = 70$ and $t = 76.5$ ms, the flame is "M"-shaped with an Inner Recirculation Zone (IRZ) filled with hot combustion products. This state of the flame is by far the most commonly observed during the 110 ms recording, but the images of Fig. 5.11 focus on a transient flame flashback phenomenon that happens intermittently. Note that in the present work, the term "flashback" is not used to designate a full flashback where the flame would propagate upstream up to the air plenum, but rather an event where the flame propagates in the IRZ and penetrates further upstream than the outlet of the injector. From $t = 70.5$ to $t = 72.3$ ms, only a very small number of tin dioxide particles is found in the IRZ. The leading point of the flame (blue arrows) is descending towards the outlet of the injection unit. From the first image, and approximately up to $t = 71.3$ ms, a symmetric trail of holes can be found on either side

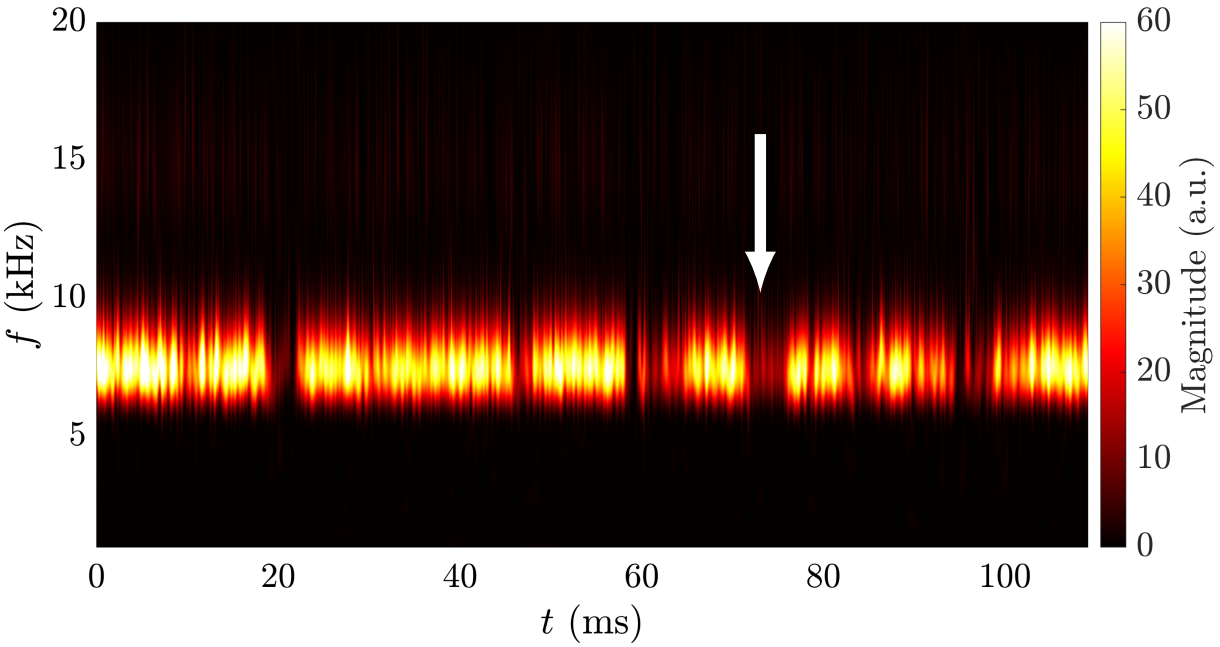

Figure 5.10: *Scalogram of the POD coefficient $a_1^v(t)$, associated with the double helix, $m = 2$ PVC mode in the visualization with a vertical laser sheet illumination. Indicated by a white arrow is the gap in the scalogram that is studied in Section 5.4.2.*

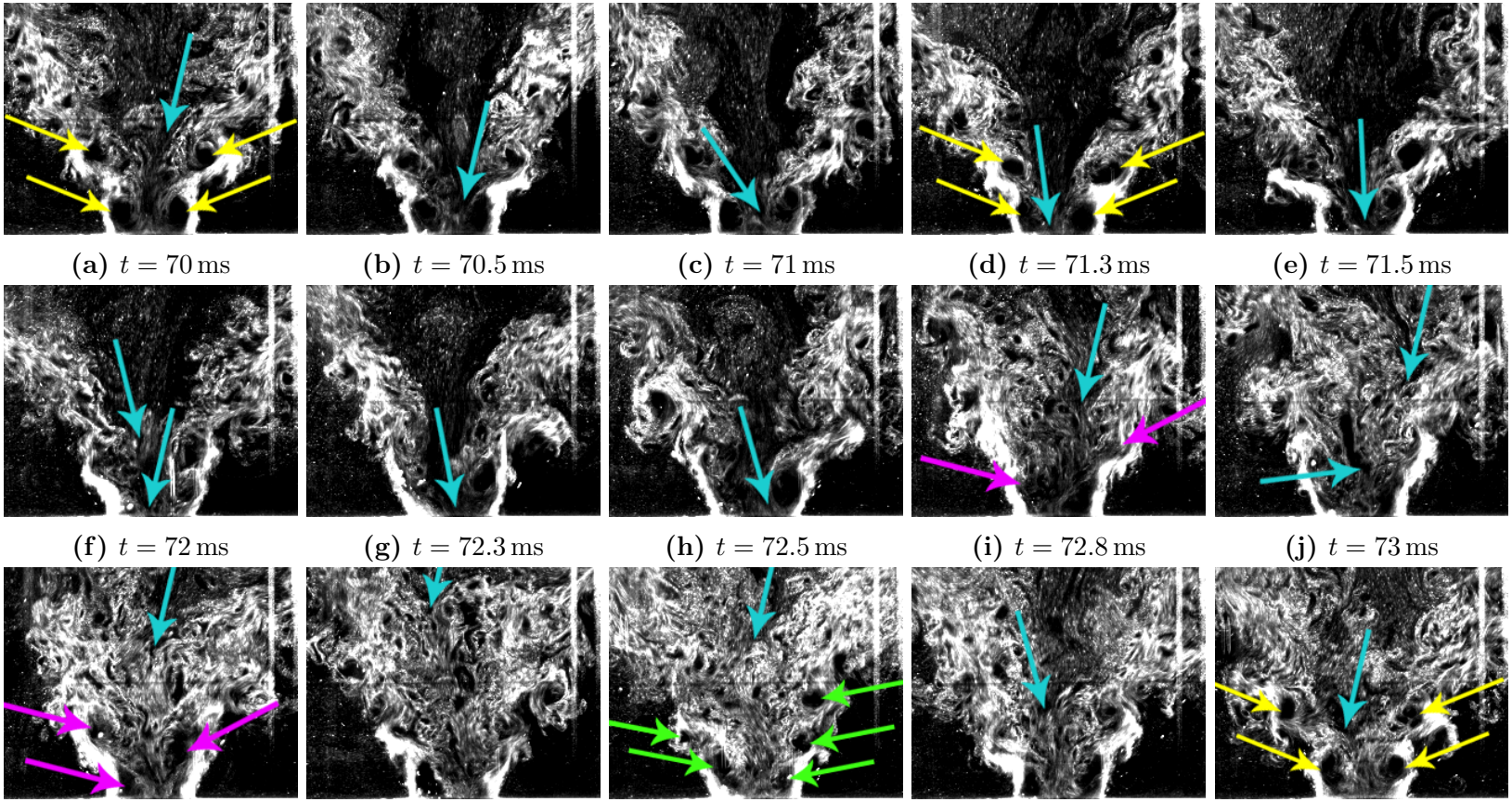

(a) $t = 70\,\text{ms}$ **(b)** $t = 70.5\,\text{ms}$ **(c)** $t = 71\,\text{ms}$ **(d)** $t = 71.3\,\text{ms}$ **(e)** $t = 71.5\,\text{ms}$

(f) $t = 72\,\text{ms}$ **(g)** $t = 72.3\,\text{ms}$ **(h)** $t = 72.5\,\text{ms}$ **(i)** $t = 72.8\,\text{ms}$ **(j)** $t = 73\,\text{ms}$

(k) $t = 73.4\,\text{ms}$ **(l)** $t = 74.5\,\text{ms}$ **(m)** $t = 75.5\,\text{ms}$ **(n)** $t = 76\,\text{ms}$ **(o)** $t = 76.5\,\text{ms}$

Figure 5.11: *Particle images with illumination by a vertical laser sheet. Images extracted between* $t = 70$ *and* $t = 76.5\,\text{ms}$*. The sequence is arranged from left to right and from top to bottom. Note that the images are not equally spaced in time. The highly luminous regions on the side of the spray near the outlet of the injector can be associated with light scattered by the fuel droplets. Blue arrows indicate the location of the lowest position of the flame in the IRZ, and magenta (respectively yellow and green) arrows show areas devoid of seeding caused by a single (respectively double and triple) helix PVC. The interpretation of these raw Mie scattering images may be helped by also examining Fig. 5.14 for a better identification of the flame shape.*

of the swirling jet of cold gases (yellow arrows). It corresponds to a vertical cut of the double helix PVC associated with the $m = 2$ azimuthal wavenumber. Between $t = 71.5$ and $t = 72.5$ ms, holes indicative of strong vortices are still present, but the pattern is asymmetric. The upstream motion of the hot gases in the IRZ has destroyed the $m = 2$ structure. At $t = 72.5$ ms, cold gases start to penetrate the IRZ which is filled with particles by $t = 73$ ms. This state is maintained more or less until $t = 76$ ms when hot gases start appearing inside the IRZ near the top of the image. At $t = 76.5$ ms, the flame returns to its nominal "M"-shape and one can again identify the symmetric trail of holes characteristic of the $m = 2$ PVC.

In order to examine the vortical structure associated with the PVC, the time-frequency analysis is now continued by performing another POD with images taken only during the instants bounding the flame flashback ($t = 70$ ms to $t = 78$ ms) and with a smaller region of interest focusing on the injector near-field. Results corresponding to the time sequence presented in Fig. 5.11 are shown in Fig. 5.12 for images with illumination from a vertical laser sheet. From top to bottom, the first mode (Fig. 5.12(a)) indicates the presence (negative $a_1^v(t)$ coefficient) or absence (positive $a_1^v(t)$ coefficient) of particles in the inner recirculation zone. From this mode and the images of Fig. 5.11, one may consider that a limited flashback occurs between $t = 70.5$ and $t = 72.5$ ms. The second mode (Fig. 5.12(b)) is similar to those displayed in Fig. 5.9, and correspond to a double helix ($m = 2$) PVC. One observes from the scalogram that its amplitude is small between $t = 71.5$ and $t = 76$ ms. The third and fourth POD modes of Fig. 5.12 correspond to structures in phase opposition on either side of the outlet of the injector. The frequency content of the third POD mode (Fig. 5.12(c)) is centered around 3.7 kHz, indicating that it corresponds to a first order ($m = 1$), single helix PVC. It is present between $t = 71$ and $t = 74$ ms, and subsequently vanishes at $t = 74.7$ ms. The signature of this structure is also visible in Fig. 5.11 where it is marked by magenta arrows at $t = 72.8$ and $t = 73.4$ ms. Concerning the last mode (Fig. 5.12(d)), its frequency content is centered around 11 kHz, indicating that the POD modes pertain to a triple helix PVC ($m = 3$). This mode appear at $t = 73.7$ ms and is quite strong between $t = 74.5$ and $t = 75.8$ ms. Its signature can also be seen on the images of Fig. 5.11 at $t = 75.5$ ms among others: three holes are located on the right side of the jet, two on its left side, all indicated by green arrows. These holes are staggered, and the spacing between the holes is smaller than that observed with the $m = 2$ PVC holes (yellow arrows). This further confirms the interpretation of the POD and wavelet processing as the signature of a triple helix PVC during these instants. This structure can additionally be observed on horizontal slices from a separate recording and shown in Fig. 5.13. During a short time period, three holes rotating around the axis can also be distinguished.

The analysis presented in Fig. 5.12 is also performed on four other intermittent flashback events identified in Fig. 5.10, and on horizontal laser sheet visualization as well (two events), with similar results that are not included here for the sake of brevity. The analysis reveals that three states of the Precessing Vortex Core can exist in this system, and that these three states are linked to different stages in intermittent flashback events:

- The double helix PVC ($m = 2$) discussed in Section 5.3.2 is by far the most common

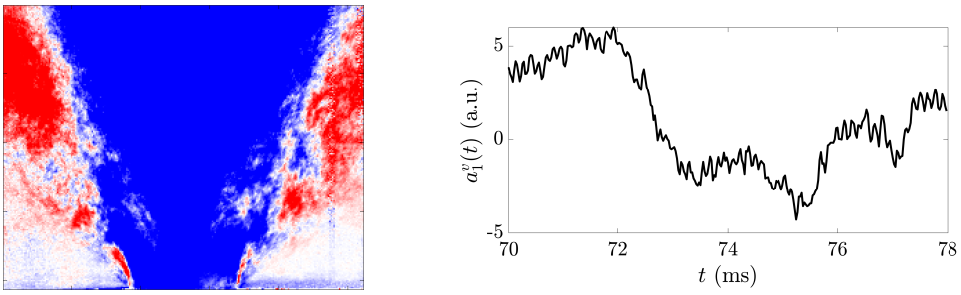

(a) *POD mode associated with the presence of particles in the IRZ. A positive temporal coefficient $a_1^v(t)$ (graph on the right) indicates that the IRZ is devoid of particles, while a negative coefficient $a_1^v(t)$ corresponds to an IRZ filled with particles.*

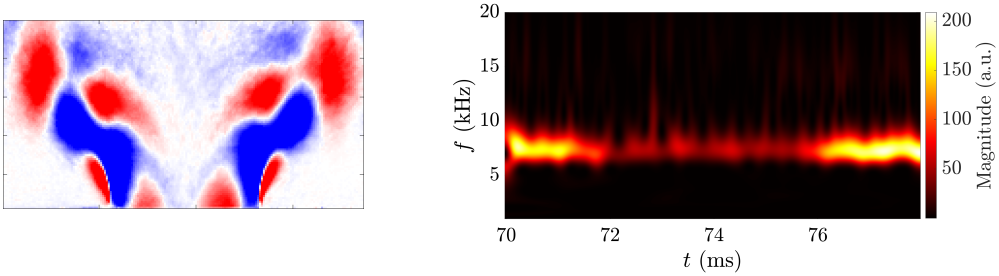

(b) *POD mode associated with a double helix ($m = 2$) PVC. Its shape is symmetric and its frequency is* 7.5 kHz.

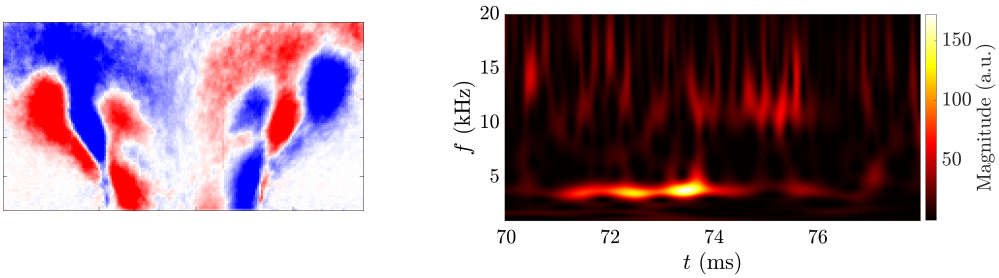

(c) *POD mode associated with a single helix ($m = 1$) PVC. Its shape is asymmetric and its frequency is found around* 3.7 kHz.

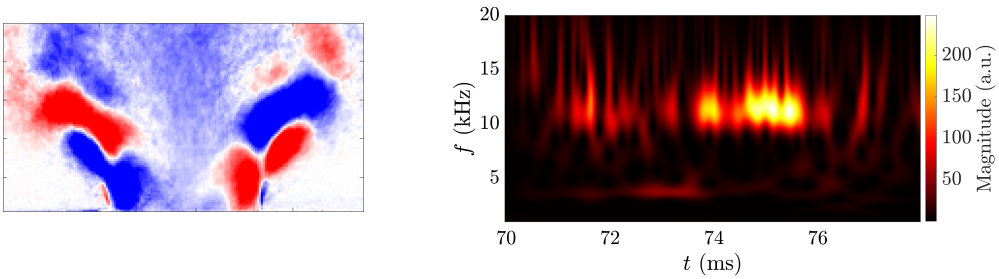

(d) *POD mode associated with a triple helix ($m = 3$) PVC. It is characterized by its asymmetric structure and a frequency content centered around* 11 kHz.

Figure 5.12: *Spatial shape of the POD modes (left), and associated scalograms (right). The processing is performed between $t = 70$ and $t = 78$ ms, corresponding to the images of Fig. 5.11.* **(a)** *POD mode showing whether the IRZ is filled or devoid of particle during the flashback.* **(b-d)** *POD modes associated with coherent helical structures. Each structure is naturally associated to a pair of POD modes in quadrature with each other as in Fig. 5.9. Here, only one mode per structure is plotted for the sake of brevity.*

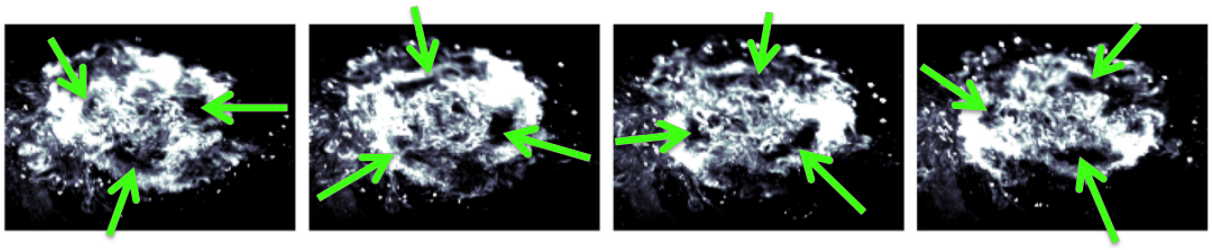

Figure 5.13: *Horizontal slices illustrating a $m = 3$ PVC. These 4 selected images are separated by* 25 µs.

structure in this flow, and is most often present.

- A PVC of azimuthal wavenumber $m = 1$ precessing at a frequency of 3.75 kHz can also be observed for short periods of time. This structure appears during intermittent flame flashbacks in the IRZ, while the flame and the IRZ penetrate inside the injection unit, and may be maintained for up to a millisecond after the end of flashback.
- A PVC of azimuthal wavenumber $m = 3$ appearing at a frequency of 11.1 kHz in the processed signal. This structure has the shape of three intertwined helices.

During seven intermittent flashback events that have been studied, the azimuthal wavenumber was always found to follow the sequence $m = 2$ followed by $m = 1$ and by $m = 3$, before returning to the steady state $m = 2$.

One may then try to explain these transitions from a theoretical viewpoint. It is known from recent stability analysis of the PVC (e.g., Manoharan et al. (2020)) that the wavemaker region which controls the amplitude and growth rate of this structure is located slightly upstream of the vortex breakdown bubble. The same conclusion is reached by Tammisola and Juniper (2016) using a structural linear analysis of a Turbomeca helicopter engine injector. These studies are mainly concerned with single helix ($m = 1$) PVCs. Contrary to the $m = 1$ PVC, the $m = 2$ mode has two wavemaker regions: one slightly upstream of the vortex breakdown bubble, and a second one further upstream (Vanierschot et al. (2020)). It is also noted by Terhaar et al. (2015) that the PVC may be damped by changes in the velocity and density distributions. These elements suggest that the changes in the flow structure in the wavemaker region accompanying the intermittent flashback may induce damping of certain PVC modes and growth of others.

5.5 Analysis of flame and PVC dynamics during a combustion instability

An important research question concerns the fate of the PVC during strong acoustic oscillations in the flow. Recent work in reactive flows are reviewed by Huang and Yang (2009); Candel et al. (2014) and in the introductions of Terhaar et al. (2016); Renaud et al. (2019). A first topic of interest is the energy transfer between the helical and acoustic modes. As the PVC is a helical instability, in perfectly axisymmetric flames, it does not directly feed acoustic energy into the thermoacoustic oscillation (Moeck et al.

(2012)). However, Acharya and Lieuwen (2020) suggest that, if the flame is not perfectly axisymmetric, the helical mode might feed energy into a longitudinal acoustic mode. In the case of high frequency combustion instabilities driven by transverse acoustic modes (so called "screech"), Ghani et al. (2016) indicate that the PVC can strongly interact with the acoustic field and drive the instability. In some experimental and LES studies, it is found that acoustic forcing suppresses the PVC (e.g. Syred (2006); Iudiciani and Duwig (2011); Alekseenko et al. (2012); Moeck et al. (2012); Terhaar et al. (2016)). In the study of Renaud et al. (2019) carried out in a liquid-fueled burner, the PVC is not observed in the gaseous flow downstream of the injector but its presence can be detected as it perturbs the liquid fuel spray, and consequently, the flame. The perturbation caused by the PVC also vanishes under high forcing amplitudes. On the other hand, in some studies, the PVC is enhanced by the acoustic forcing (Giauque et al. (2005)). In acoustically forced flows where a PVC can be detected, spectral analysis generally reveals a peak at $f_{PVC} - f_a$, the difference between the frequency of the PVC and that of the acoustic forcing (Moeck et al. (2012); Terhaar et al. (2016); Renaud et al. (2019); Yin and Stöhr (2020)), indicating that the helical structure is modulated by the acoustic perturbation. One should note that, in the aforementioned studies, the acoustic frequency is often higher, or of the same order of magnitude as that of the PVC. Terhaar et al. (2016) propose a classification of PVC-acoustic interaction, distinguishing between "mean flow correction", that is a change in the mean flow caused by acoustic fluctuations that subsequently modifies the PVC through the mechanisms presented in their previous study (Terhaar et al. (2015)), and "mean flow modulation", where the PVC is modulated. They suggest that the latter scenario can be modeled using a parametrically forced oscillator.

This section is focused on the dynamics of the flame under the operating conditions defined previously (Section 5.4.1), but with a longer combustion chamber of total length $l_c = 300\,\text{mm}$. This gives rise to thermoacoustic oscillations at a frequency of 473 Hz, such that the frequency f_{PVC} of the PVC is approximately one order of magnitude larger than f_a, the frequency of the acoustic oscillation, a situation not commonly examined in the previous literature. Photomultiplier measurements of excited OH^* radical emission give an indication as to the level of unsteady heat release rate fluctuations. It reaches $I'_{OH^*}/\overline{I_{OH^*}} = 23.4\%$ (RMS).

The present section is organized as follows: firstly, phase-averaged tin dioxide images with planar laser illumination are used to examine the dynamics of the inner recirculation zone during the oscillation cycle (Sec. 5.5.1); then the dynamics of the PVC interacting with the thermoacoustic instability is examined (Sec. 5.5.2) and intermittency in the azimuthal wavenumber of the PVC is discussed (Sec. 5.5.3).

5.5.1 Dynamics of the inner recirculation zone

In order to investigate the dynamics of the inner recirculation zone during the combustion oscillation, slices obtained by illuminating the flow and flame seeded with micronic SnO_2 particles with a vertical laser sheet are acquired at a sampling rate of 40 kHz. The addition of SnO_2 microparticles does not significantly affect the flame as the mean value

(a) $\varphi = 0$. **(b)** $\varphi = \frac{\pi}{4}$. **(c)** $\varphi = \frac{\pi}{2}$. **(d)** $\varphi = \frac{3\pi}{4}$.

(e) $\varphi = \pi$. **(f)** $\varphi = \frac{5\pi}{4}$. **(g)** $\varphi = \frac{3\pi}{2}$. **(h)** $\varphi = \frac{7\pi}{4}$.

Figure 5.14: (a - h) *Estimate of the phase averaged progress variable* $\overline{C}$. $\overline{C} \approx 0$ *indicates a region with a high probability of observing* SnO_2 *particles,* $\overline{C} \approx 1$ *regions with a low probability of observing* SnO_2 *particles. A black isocontour at* $\overline{C} = 0.35$ *is added to the images. Some reflections of the laser sheet are visible on the images due to the cylindrical shape of the quartz tube. The largest ones are hidden by gray rectangles. Note that a bias is introduced in areas where the PVC is strong due to the absence of particles in the core of the vortex. Only the very bottom part of the images is affected by the PVC, on either side of the centerline.*

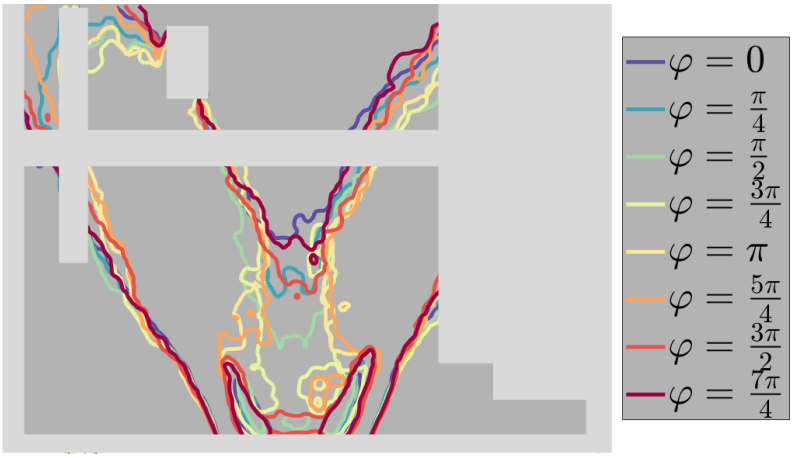

Figure 5.15: *Isocontours at* $\overline{C} = 0.35$ *plotted for 8 phase instants. Some reflections of the laser sheet are visible on the images due to the cylindrical shape of the quartz tube. The largest ones are hidden with a lighter shade of gray. Note that a bias is introduced in areas where the PVC is strong due to the absence of particles in the core of the vortex. Only the very bottom part of the images is affected by the PVC, on either side of the centerline.*

and amplitude of the PM signal remain unchanged. The images are then processed as follows: a Gaussian filter with a kernel size of 3×3 pixels and a standard deviation of 0.5 is first applied to remove noise. The images are then binarized to distinguish regions where SnO_2 particles are present (fresh gases and laser reflections) and those where they have vanished (hot combustion products and strong vortices). The non-parametric method of Otsu (1979) is used to determine the threshold. In this method, the threshold is independent of the exposure and seeder density in a particular image, which allows a reliable comparison between different configurations and phase instants. This method has been used with success in combustion applications to process particle, chemiluminescence and PLIF images (e.g., Balusamy et al. (2011); Degenève et al. (2019); Rock et al. (2020)). Phase averaging is then performed with bins of $\pi/8$ rad. The reference signal for the phase averaging process is the temporal coefficient $a_1^v(t)$ of the first POD mode which mostly captures the flame motion related to the combustion oscillation.

Results are shown in Fig. 5.14 as a color map featuring the phase averaged progress variable $\overline{C}$. The inner recirculation zone oscillates during the cycle: between $-\pi/2 < \varphi < \pi/2$, the bottom of the recirculation zone of hot combustion products is located several injector outlet diameters above the backplane. Between $3\pi/4 < \varphi < 5\pi/4$, the leading edge of the flame in the inner recirculation zone is located much closer to the outlet of the injector and is indistinguishable from the area where the PVC is strong. In addition isocontours at $\overline{C} = 0.35$ are plotted for different phase instants in Fig. 5.15. The movement of the upper part of the flame is unfortunately mostly hidden by laser reflections. One may only faintly distinguish in the upper left corner that the tip of the flame is slightly longer for $5\pi/4 < \varphi < 2\pi$ than at other phase instants. On the other end, in the vicinity of the outer recirculation zone, all isocontours $\overline{C} = 0.35$ are clearly visible. They are superimposed, indicating that there is no lateral motion of the flame front.

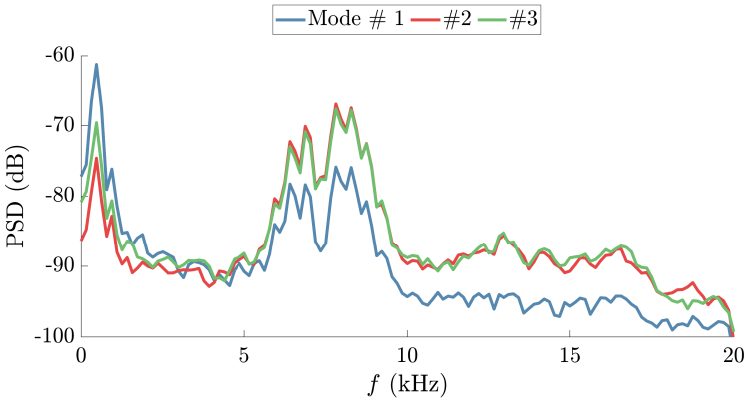

(a) *Power spectral density of a_1^v, a_2^v and a_3^v.*

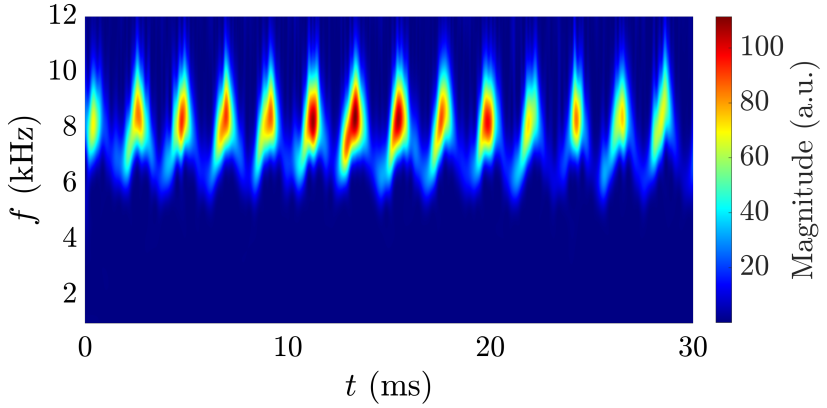

(b) *Scalogram of POD mode # 2.*

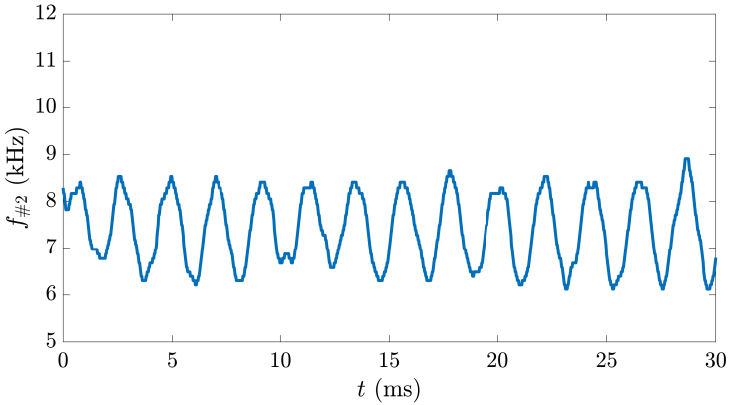

(c) *Instantaneous frequency of POD mode # 2 (from wavelet analysis).*

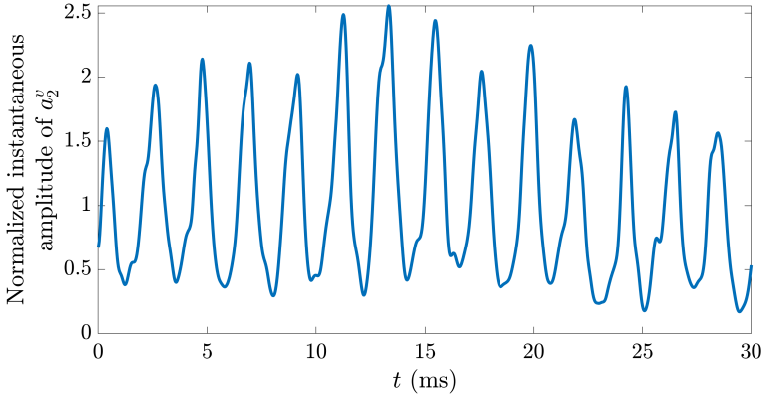

(d) *Instantaneous amplitude of POD mode # 2 (from wavelet analysis). The instantaneous amplitude is normalized by the mean amplitude of a_2^v.*

Figure 5.16: *Time-frequency analysis of POD mode of vertical tin dioxide planar laser illumination images taken during a combustion instability. The focus is mainly placed on POD mode # 2, associated with a double helix PVC. The POD processing was performed on 4366 images.*

5.5.2 Analysis of the PVC modulated by a combustion instability

The POD and wavelet based processing method used in Section 5.4.1 is now employed to analyze the same axial (vertical) slices acquired during combustion instability. Results presented in this section focus on the time-frequency analysis of one of the POD modes corresponding to a double helix PVC.

Figure 5.16 displays the results of the POD processing. Three POD modes contain most of the energy, and Fig. 5.16(a) shows the power spectral density of their temporal coefficients. Mode #1 corresponds to the motion of the flame caused by the combustion instability (hence its previous use as a reference for phase averaging). Its power spectral density has a strong peak at the frequency of the oscillation (473 Hz). Modes #2 and #3 have a shape corresponding to a double helix ($m = 2$) PVC. Their frequency content is centered around 7.4 kHz. The shape of their power spectral density is however peculiar, with a valley at 7.4 kHz surrounded by several peaks. Carrying a wavelet-based time-frequency analysis on mode #2 allows to understand this shape. The scalogram of a_2^v (POD coefficient of mode #2, shown in Fig. 5.16(b)) shows a repetitive motive of "hat-like" patterns. The instantaneous frequency of a_2^v extracted from the scalogram (center frequency associated with the scale at which the coefficient is largest at a given instant, shown in Fig. 5.16(c)) oscillates between approximately 6.3 and 8.4 kHz. Similarly, the instantaneous amplitude of a_2^v (largest coefficient of the scalogram at a given instant, shown in Fig. 5.16(d)) also oscillates at the frequency of the instability. The modulation of the PVC can be further characterized by calculating the power spectral densities of the instantaneous frequency $f_{\#2}$ and amplitude A_2^v extracted from the wavelet analysis (not shown here). Both of these power spectral densities are characterized by a prominent peak at 468 Hz, the frequency of the combustion oscillation. One may then conclude that the PVC is modulated by the combustion oscillation, both in frequency and in amplitude.

In SICCA-Spray, the very large difference in frequency between the acoustic mode and the precessing frequency of the PVC allows to clearly identify the mean flow modulation effect on the helical structure that was proposed by Terhaar et al. (2016). However, their theoretical model based on a parametrically forced oscillator predicts that acoustic forcing at a very small frequency ($10 f_a \approx f_{PVC}$) would result in the complete destruction of the helical structure. This is not observed in the present configuration.

In numerous experiments reviewed by Syred (2006) and conducted without acoustic forcing, the frequency of the PVC has been found to be linearly correlated with the injector bulk velocity. This corresponds to a constant value of the Strouhal number St $= 2R_{inj}f/u_b$. During the combustion instability studied in the present section, the frequency of the PVC is modulated with a peak-to-peak amplitude of 2.2 kHz. Under a quasi-stationary hypothesis, one may then tentatively estimate that the amplitude of fluctuation of the injector bulk velocity is in the order of $u'_b/\overline{u}_b \approx 11\%$ RMS.

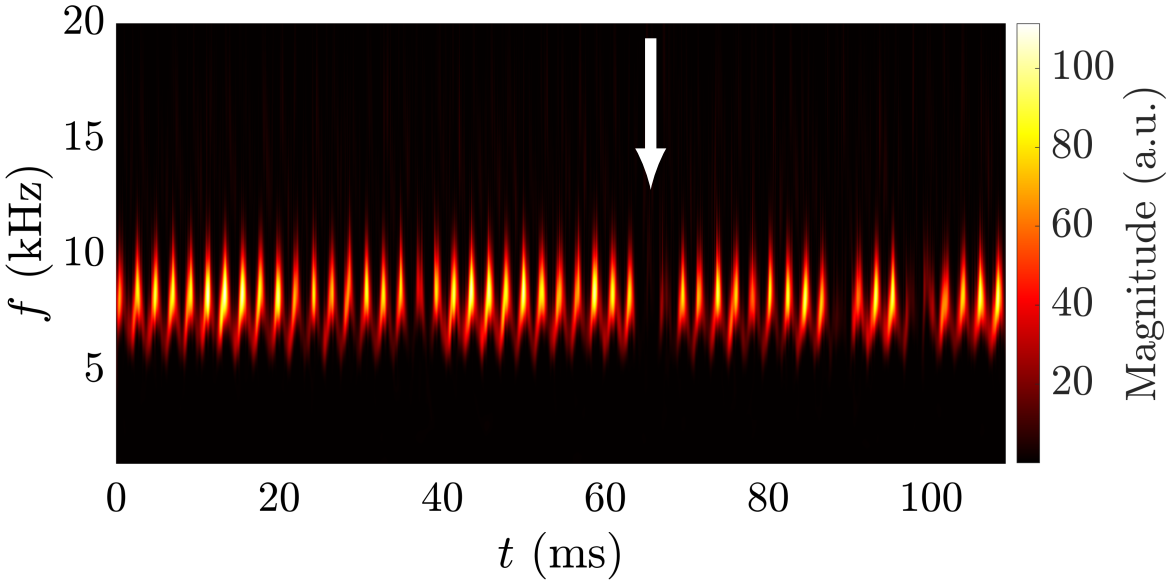

Figure 5.17: *Scalogram of POD coefficient $a_2^v(t)$, associated with the double helix, $m = 2$ PVC mode in the vertical slices during a combustion oscillation. Indicated by a white arrow is a gap in the scalogram.*

5.5.3 PVC intermittency during a combustion oscillation

Figure 5.17 is similar to Fig. 5.16(b): it shows the scalogram of the POD coefficient $a_2^v(t)$ associated with the $m = 2$ wavenumber PVC, but over a longer time duration. It presents gaps. The same analysis as that conducted in Fig. 5.10 (not detailed here for the sake of brevity) shows that the gaps occur in a similar manner during combustion oscillations and in thermoacoustically stable conditions: at the beginning of the gaps, the inner recirculation of hot combustion products penetrates deeper within the injection unit, and this leads to the disappearance of the $m = 2$ PVC. Then, a single helix structure with an azimuthal wavenumber $m = 1$ is observed, followed by a return to the usual $m = 2$ structure. However, the helical structure of azimuthal wavenumber $m = 3$ is never observed during the combustion oscillation.

Another important difference between thermoacoustically stable and unstable operation is the duration of the gaps. In Fig. 5.17, the gaps appear to have a duration corresponding to one or two acoustic periods. The histogram of gap durations normalized by the acoustic period (Fig. 5.18) shows that these gaps have a duration that is a multiple of the acoustic period, indicating that the thermoacoustic oscillation is able to lock the state of the PVC for one or more acoustic periods.

5.6 Conclusion

This chapter explores a high repetition rate flame imaging method using tin dioxide particles and its application to a strongly swirled spray flame. These particles are interesting as flow tracers because the temperature at which they vanish is much higher than that of

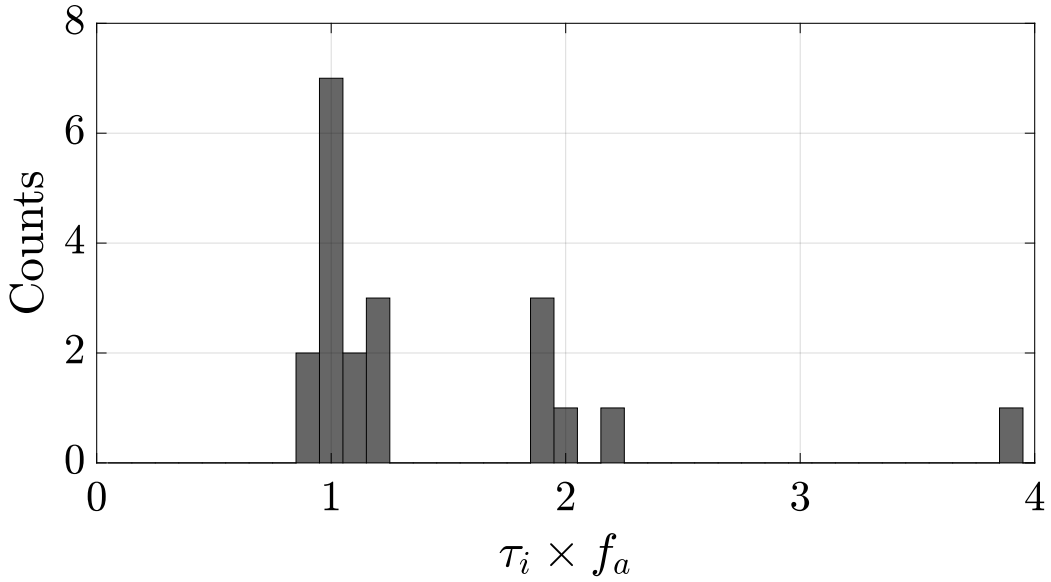

Figure 5.18: *Histogram showing the duration τ_i of gaps in the signal associated with the $m = 2$ PVC. The duration of the gap is normalized by the acoustic period. Statistics are gathered over several recordings for a total of 20 events. To determine τ_i, the instantaneous amplitude of the POD coefficient a_2^v is processed using the peak finding algorithm of Matlab to calculate the width at half prominence of peaks corresponding to the gaps.*

the oil droplets commonly used to locate flame fronts in combustion studies. It is shown that these particles when seeded in the flow and illuminated by a laser sheet give access to structural features in the flow and can be used to determine the structure and dynamics of flame fronts under conditions where the temperature of the gases feeding the flame is already high and would lead to the vaporization of many other types of tracers like oil droplets.

The first part of this study is aimed at specifying the temperature T_v at which the tin dioxide particles vanish. This is accomplished by means of a methane-air stagnation point flame configuration. Experiments in combination with calculations yield a value of approximately $T_v = 1770\,\mathrm{K}$ for the disappearance temperature. This indicates that the particles vanish by the chemical reaction $\mathrm{SnO_2}(s) + \mathrm{CO}(g) \rightleftharpoons \mathrm{SnO}(g) + \mathrm{CO_2}(g)$.

Laser illumination with tin oxide particles and illuminated by a planar laser sheet to identify precessing vortex cores formed by a swirled injector and to study the dynamics of flames formed by this injector. High speed visualization at 100 kHz reveal the presence of a double helicoidal structure. Although this structure dominates the flow, a time frequency-analysis based on POD reveals a more complex behavior. Intermittent flame flashback, during which the flame and the IRZ penetrate into the injector, randomly occur during steady operation of the burner. During these events, the double helix PVC is damped and vanishes to leave place to a single helix structure. This state of the flow is not stable, and fresh gases subsequently fill the inner recirculation zone. At these instants, the PVC features a triple helix structure. The flow and flame then return to their normal

state with a double helix PVC.

The experimental method in combination with time-frequency-analysis is finally used to study the dynamics of the PVC during a combustion instability characterized by an acoustic frequency an order of magnitude smaller than the frequency of the PVC. Phase averaged images of SnO_2 laser illuminated slices reveal the dynamics of the inner recirculation zone during the combustion oscillation and indicate that the leading edge of the flame in the IRZ has a strong axial motion during the thermoacoustic cycle. It is also found that the double helix PVC is the dominant PVC mode. The large difference in frequency between the PVC and the acoustic forcing allows the determination of the instantaneous frequency and amplitude of the PVC and shows that it is modulated, both in amplitude and in frequency. The modulation frequency is that of the thermoacoustic oscillation. The oscillating mass flow rate at the outlet of the injector is most likely the cause of the modulation of the PVC. Limited flashback events into the IRZ are also observed during the combustion instability and lead to changes in the azimuthal wavenumber of the PVC.

Chapter 6

Space-time analysis of a spray swirling flame under acoustic oscillations combining experiments and LES

The dynamics of spray swirling flames is investigated by combining experiments on a single sector generic combustor and large eddy simulations of the same configuration. Measurements and calculations correspond to a self-sustained limit cycle operation where combustion coupled by an axial quarter wave acoustic mode induces large amplitude oscillations of pressure in the system. A detailed analysis of the mechanisms controlling the process is carried out first by comparing the measured and calculated spray and flame dynamics. Considering in a second stage that the spray and flame are compact with respect to the acoustic wavelength the analysis can be simplified by defining state variables that are obtained by taking averages over the combustor cross section and representing the behavior of these average quantities as a function of the axial coordinate and time. This reveals a first region in which essentially convective processes prevail. The convective heat release rate then couples further downstream with the pressure field giving rise to positive Rayleigh source terms which feed energy in the axial acoustic mode. In the convective region, the swirl number features oscillations around its mean value with an impact on the flow aerodynamics and flame radial displacement. Fluctuations in the fuel flow rate are initiated at the injector exhaust and likewise convected downstream. The total mass flow rate that exhibits strong convective disturbances is dominated further downstream by the acoustic motion. This information provides new insights on the convective-acoustic coupling that controls the heat release rate disturbances and reveals the time delays governing the combustion oscillation process.

This chapter reproduces an article submitted to Proceedings of the Combustion Institute as "Dynamics of Spray and Swirling Flame under Acoustic Oscillations: A Joint Experimental and LES Investigation". It results from a collaboration with CERFACS. Authors of the original article are Guillaume Vignat, Ermanno Lo Schiavo, Davide Laera, Antoine Renaud, Laurent Gicquel, Daniel Durox and Sébastien Candel. The simulation was performed at CERFACS. A reader aware of what is presented in the introduction and in Chapter 1 may wish to skip the introductory material and go to the last paragraph of the introduction.

Contents

6.1 Introduction

Combustion instabilities have many undesirable consequences in terms of life duration and operability and are a source of risk in high performance systems like jet engines or industrial gas turbines (e.g., Konrad et al. (1998); Eckstein et al. (2006)). Their prediction, control and reduction require an understanding of the flame dynamics and the coupling with the resonant modes of the combustion system. Experiments, even well conducted and instrumented (e.g., Bernier et al. (2004); de la Cruz García et al. (2009); Eckstein et al. (2006)), do not give access to all necessary variables. Large Eddy Simulation (LES) can be used in high fidelity calculations of combustion oscillations in engine like configurations (Huang and Yang (2009); Tachibana et al. (2015)).

It is at this point worth briefly reviewing progress made in the simulation of spray flame dynamics under acoustic coupling or under acoustic forcing. Much of the numerical modeling effort has been carried out so far with unsteady RANS calculations (e.g., Zhu et al. (2005); Innocenti et al. (2017)). General trends are captured but mismatch with experimental data are also noted. Recent articles, among others Jones et al. (2014); Shum-Kivan et al. (2017) report LES results for gas turbine model combustors powered by swirled spray flames with detailed validations with experimental data for the mean variables, but the flame dynamics is not investigated. Tachibana et al. (2015) use LES to simulate a spray swirled flame at elevated pressure under self-sustained instability, and observe a good overall agreement with experimental data. They note the importance of the time delay introduced by droplet evaporation on the combustion instability coupling, an effect also described by Kitano et al. (2016) from LES of the reactive flow in a backward facing step configuration. Eckstein et al. (2006) indicate that in air assisted atomization systems, droplet diameter fluctuation will ensue from velocity fluctuations within

the injector. These fluctuations create unsteadiness in the fuel supply to the flame and contribute to the instability.

The present investigation focuses on flame dynamics in the swirl spray atmospheric single sector combustor "SICCA-Spray". This device features strong longitudinal oscillations in a limit cycle regime at a frequency (474 Hz) representative of the investigations conducted on the annular combustor "MICCA-Spray" (Prieur et al. (2017b)). Experiments and LES are combined to contribute to the validation of LES of swirl spray flame dynamics under acoustic interaction, and extract informations on the fundamental mechanisms of flame dynamics. The essence of this analysis is to consider that the flame is compact with respect to the acoustic wavelength. The multidimensional complexity of the problem may then be reduced but it is important to retain the capacity to describe the convective motion in the combustion region and to examine its coupling with the acoustic motion. This may be accomplished by considering variables that are integrated over the combustor cross section. In practice, it is more convenient to use variables that are integrated over an elementary volume $\Delta V = S_c \Delta z$ having as a base the combustor cross section S_c and extending over a small Δz in the axial direction:

$$\widehat{\psi}(z,t) = \int_z^{z+\Delta z} \int_{S_c} \psi(r,\theta,z,t)\, dV \tag{6.1}$$

where r, θ, z are the radial, tangential and axial coordinates. In what follows $\Delta z = 1\,\text{mm}$. It is also sometimes more physical to use variables integrated over the cross section for example when one considers mass flow rates. Such variables will appear as $\widetilde{\psi}$. It is known that combustion instabilities arise when the delay resulting from injection, convection, vaporization and chemical conversion is of the order of a multiple or half multiple of the acoustic period (Crocco and Cheng (1956)). The variables associated with these processes are perturbed in cascade during the oscillation, and end up creating heat release rate fluctuations which drive the combustion instability. The flame delay mostly results from the longitudinal phase velocity of these perturbations. The space-time analysis based on the integrated variables defined previously allows to identify these perturbations and their velocity.

6.2 Experimental and Numerical Setup

The experimental configuration "SICCA-Spray" shown schematically in Fig. 6.1(a), is an atmospheric single sector test rig designed for combustion dynamics experiments with swirl spray injectors. It comprises a cylindrical plenum equipped with two Brüel & Kjær type 4938 microphones with type 2670 preamplifier for acoustic pressure and velocity measurements upstream of the injector. The radial swirler design is that of swirler K and features a swirl number of $S_0^0 = 0.63$ measured at $z = 2.5\,\text{mm}$. Liquid n-heptane is injected by a simplex fuel atomizer creating a hollow cone shaped spray on the centerline. The mean droplet diameter is $d_{10} = 8\,\mu\text{m}$ and the Sauter mean diameter $d_{32} = 30\,\mu\text{m}$

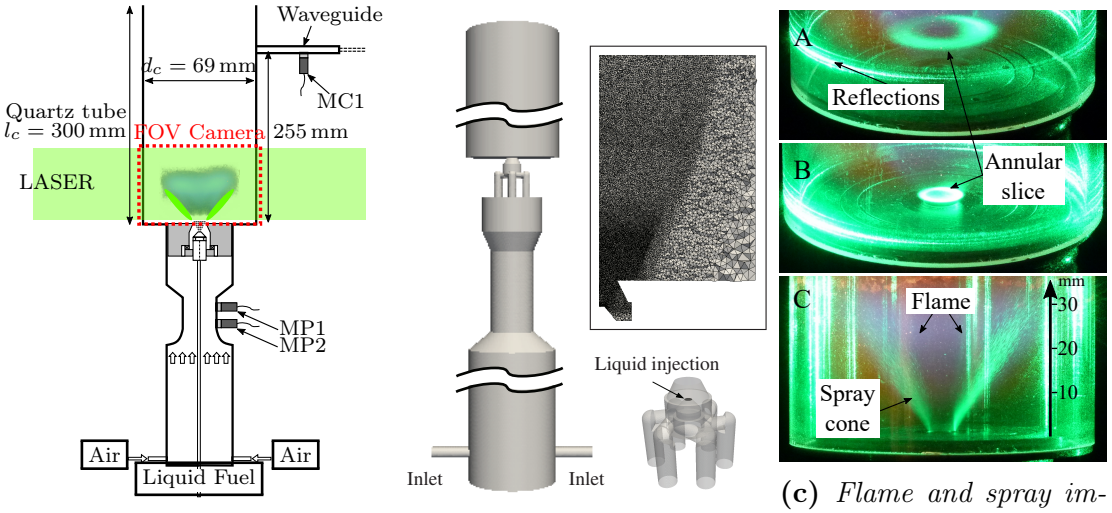

(a) *"SICCA-Spray" test rig.* **(b)** *LES domain and mesh.* **(c)** *Flame and spray images.*

Figure 6.1: ***(a)****: Schematic view of "SICCA-Spray". The green plane depicts the laser sheet used for spray tomography. The field of view (FOV) of the camera is indicated by a red contour.* ***(b)****: Numerical domain and mesh in the flame region.* ***(c)****: Color image with flame (blue) and spray laser tomography (green) showing the position of the flame with regards to the hollow cone spray. Adapted from Prieur et al. (2016).*

(Prieur et al. (2017a)). The combustion chamber is a cylindrical quartz tube with an upper metallic section on which a microphone "MC1" is mounted with a watercooled waveguide at $z_{MC1} = 255\,\text{mm}$ above the backplane. The waveguide creates a 640 µs delay that is compensated to retrieve the pressure signal in the chamber. The burner is operated at a global equivalence ratio of $\phi_{nom} = 0.85$ and a thermal power of $\mathcal{P} = 6.4\,\text{kW}$, corresponding to an air flow rate of $\dot{m}_{air,nom} = 2.58\,\text{g}\,\text{s}^{-1}$ (measured by a Bronkhorst EL-Flow) and a fuel flow rate of $\dot{m}_{fuel,nom} = 520\,\text{g}\,\text{h}^{-1}$ (monitored by a Bronkhorst CORI-Flow). A continuous 532 nm 0.5 W laser is used to generate a laser sheet for tomographic visualization of the liquid spray. The laser sheet is orthogonal to the backplane of the combustor and passes through the centerline. A high speed color camera (Phantom V2512) is used for simultaneous visualization of the droplet light scattering (green) and flame chemiluminescence (blue). The camera is operated at a frame rate of 10 kHz.

LES of this configuration is performed using the AVBP solver developped by CERFACS (http://www.cerfacs.fr/avbp7x) with the modeling strategy of Shum-Kivan et al. (2017). A third order accurate in time and space Taylor-Galerkin scheme (TTGC) is used along with non-reflecting Navier-Stokes Characteristic Boundary Conditions imposing an atmospheric pressure on the far-field outlet. The SIGMA subgrid scale model is used (Baya Toda et al. (2010)). A Lagrangian framework is adopted for the liquid spray description by injecting fuel droplets using the FIM-UR model with a constant mass flow rate and distribution (Rosin-Rammler). The droplet-wall interaction inside the injector is modeled using the film approach of Chaussonnet et al. (2013). No model is used for inter-particle interaction as the smallest inter-particle distance exceeds 10 droplet diameters shortly downstream of the injector outlet ($z > 5\,\text{mm}$). Particle interaction with subgrid scale

eddies is also neglected as the subgrid scale Stokes number $\mathrm{St_{SGS}}$ (Urzay et al. (2014)) is estimated to be of the order of 3×10^3. The chemistry is described with the global two-step 6-species scheme $2S\_C_7H_{16}\_DP$ with Pre-Exponential Adjustment (PEA) for rich mixtures (Paulhiac (2015)). The mesh comprises approximately 20 million tetrahedra with refinement up to $\Delta x \simeq 150\,\mu\mathrm{m}$ at the flame root and $\Delta x \simeq 200 - 300\,\mu\mathrm{m}$ further downstream. As the typical flame thickness is $\delta_{l,\phi=1} = 410\,\mu\mathrm{m}$, dynamic flame thickening (TP-TFLES) is used depending on the local equivalence ratio and only in the premixed regime identified by positive Takeno index values. The evaporation term is also thickened as recommended by Paulhiac (2015). The quality of the LES is evaluated by considering the ratio of turbulent to laminar viscosity, which at maximum and very locally reaches 50. After convergence, a physical time of 43 ms (20 cycles) was simulated under steady oscillations to acquire statistics at a sampling rate of 9.4 kHz.

6.3 Data Processing for LES Validation

Experimentally, the frequency of the oscillation obtained from the power spectral density (PSD) of the acoustic pressure p'_{MC1} measured by the chamber microphone is (474 ± 19) Hz (where the uncertainty is evaluated as sum of width at half height and frequency resolution), for an amplitude of 768 Pa (RMS). At the same position, the LES results show that the pressure oscillation reaches 618 Pa (RMS) for a frequency of (461 ± 42) Hz. The focus of the present section is now placed on the validation of flame and spray dynamics.

The number of cycles that can be simulated is not very large and will not provide statistically well converged phase averages. It is then more appropriate to use the Dynamic Mode Decomposition (DMD) (Schmid (2010)) to extract this kind of information. Using this method, and a 200 ms sequence of high speed camera images, it was found that a converged mode shape could be obtained from as little as 20 oscillation cycles, with less than 5% variation in frequency and no visible differences in the spatial structure. This powerful method is used to plot the images shown in Fig. 6.2. The same processing sequence is applied to the numerical and experimental data. In the experiment, the line of sight integrated chemiluminescence signal recorded by the blue channel on the camera mainly corresponds to emission from excited CH^* radicals within the flame, and may be assumed to be a qualitative indicator of heat release rate. In the simulation, the heat release rate is integrated over the line of sight before DMD is performed. Pseudo-phase averaged images are reconstructed from the 0 Hz and 461 Hz modes. This latter mode corresponds to the thermoacoustic oscillation and dominates the spectrum. These images are then Abel transformed. The phase reference is set by the pressure signal using the snapshot method. Care is taken to keep the same signal duration in the processing of LES and of experimental data. The common DMD processing ensures that no bias is introduced in comparing numerical results and experimental data. The flame exhibits a classical "M" shape. The agreement between LES and experiments is relatively good, although the flame appears to be slightly more opened and a bit longer in the experi-

Figure 6.2: *Top: experimental phase averaged chemiluminescence and spray tomography (Mie scattering) images. Bottom: LES phase averaged images of heat release rate, and spray liquid volume fraction multiplied by liquid density $\rho_l \alpha_l$. Spray images are zoomed in. The common reference for the phase is the acoustic pressure signal at microphone MC1.*

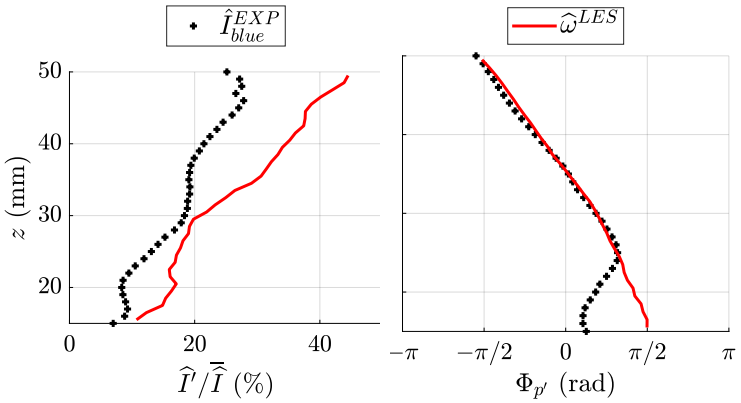

Figure 6.3: *Validation of flame dynamics. From the experiment (black), chemiluminescence signal. From LES (red), heat release rate. Left: axial evolution of the relative amplitude. Right: axial evolution of the phase with respect to acoustic pressure.*

ment. During the cycle, one observes very little motion at the flame root. A small phase difference can be observed between LES and experiment. The bulk of the flame motion happens at the tip of the flame and is reminiscent of that executed by laminar "M" flames responding to incident velocity perturbations (Durox et al. (2009)): a toroidal structure periodically forms at the tip, separates from the main flame while the fresh reactants enclosed by the toroidal flame surface are rapidly converted into products producing a heat release pulse. This process is observable in the experimental images, for example one observes the beginning of the decay of the toroidal flame structure between $\Phi = \pi/3$ and $2\pi/3$. Pseudo-phase average spray quantities are also shown in green in Fig. 6.2. The experimental data corresponding to Mie scattering from the fuel droplets features oscillations in angle and in intensity that are most visible in the vicinity of the injector. Similar features can be observed in the LES results although to a lesser extent. The liquid density weighted by liquid volume fraction $\rho_l \alpha_l$ is shown as it is more physically meaningful. In coherence with the flame shape, the angle of the spray also appears to be slightly under predicted.

To obtain a more quantitative view of flame dynamics, it is interesting as indicated in the introduction to consider variables integrated over a small cross-section of thickness $\Delta z = 1\,\text{mm}$ ($\widehat{\psi}$, Eq. (6.1)). Figure 6.3 depicts heat release rate relative fluctuations from LES and relative intensity fluctuations of light emission by CH* radicals captured by the high speed camera. The phase with respect to pressure is well captured by the LES. The relative amplitude fluctuations are in fair agreement. To examine the spray dynamics in Fig. 6.4, a pseudo Mie scattering signal is estimated from the discrete lagrangian particles in the LES. Downstream of $z = 25\,\text{mm}$ the experimental signal is affected by reflections of the laser sheet. Again, LES and experiment do not perfectly agree. One cannot expect to match the amplitudes, but the phase evolution is retrieved and the phase velocity of the spray disturbances is only slightly underestimated in the LES.

The validation with experiments is important in order to give weight to the findings from the LES. In this article, the phase and space resolved comparison of the dynamics of

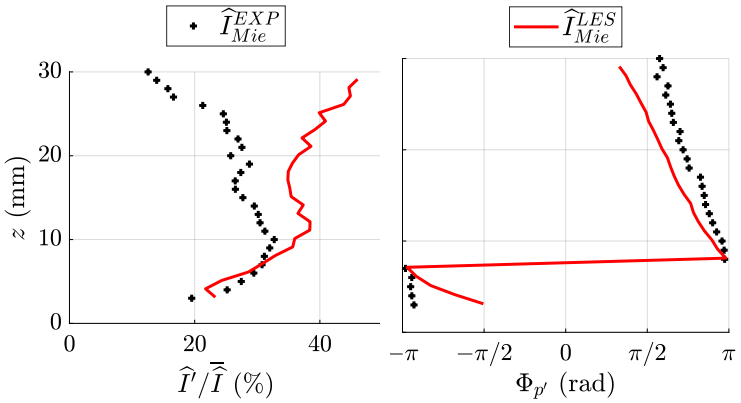

Figure 6.4: *Validation of spray dynamics. Black: experimental Mie scattering on droplets. Red: reconstructed Mie scattering from LES.*

the spray and flame in the simulation and in the experiment goes much further than what is found in previous studies dealing with similar issues (e.g., Zhu et al. (2005); Innocenti et al. (2017); Tachibana et al. (2015); Kitano et al. (2016)). It is first found that phase average chemiluminescence patterns agree well with the phase averaged heat release rate distributions. While the agreement is not perfect, it is acceptable (Fig. 6.2). The experimental and LES spray patterns are somewhat different but one could not expect a perfect match. The axial extent of the spray is suitably retrieved but there is a difference in the angular behavior. In the experiment the spray angle opens during the first two phases while this is not retrieved in the simulation. This weakness of the modeling indicates that further improvements are needed in this respect, requiring a better description of the injector near field. For the driving variables of combustion dynamics namely the heat release rate distribution and pressure, a good agreement is obtained between experiments and calculations (Fig. 6.3). Again, the agreement is not perfect but it is acceptable. The experimental light scattering from the spray is compared with a signal reconstructed from the LES by multiplying the number density by the mean droplet diameter squared to mimic the Mie scattering process. Even for the spray dynamics the amplitudes differ but the agreement is adequate in terms of phase (Fig. 6.4). Thus, the calculations reproduce many dynamical features to a reasonable degree allowing to deploy the methodology exposed in the next section. Some additional analysis and validation of the present modeling strategy for LES can be found in Lo Schiavo et al. (2020).

6.4 Analysis of the driving mechanisms

The focus is now placed on the detailed analysis of the LES. Throughout this section, a space-time representation is used in which time t and position z are horizontal and vertical coordinates respectively. Variables are integrated over the elementary volume V or over the cross section S_c as defined previously ($\widehat{\psi}$ and $\widetilde{\psi}$ respectively, Eq. (6.1)). It is

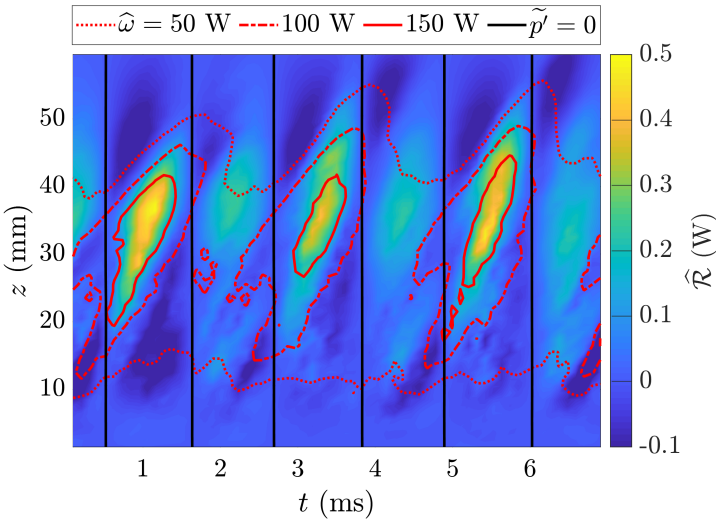

Figure 6.5: *Space-time representation of the evolution of the Rayleigh source term* $\hat{\mathcal{R}}$ *during three cycles.* $t = 1\,\text{ms}$ *corresponds to an acoustic pressure maximum,* $t = 2\,\text{ms}$ *to an acoustic pressure minimum.*

first interesting to consider the Rayleigh source term:

$$\widehat{\mathcal{R}}(z,t) = \frac{\gamma - 1}{\gamma p_0} \int_z^{z+\Delta z} \int_{S_c} p'\omega' \, dS dz \tag{6.2}$$

where p' is the acoustic pressure and ω' the heat release rate fluctuations. This term is plotted alongside isocontours of acoustic pressure (black) and locally integrated heat release rate $\widehat{\omega}$ in Fig. 6.5. As expected the source term is globally positive which is necessary for feeding energy into the oscillation to compensate damping. Pressure and heat release rate fluctuations are in phase. Driving is concentrated in the upper section of the flame, between $20 < z < 40\,\text{mm}$. Heat release rate perturbations exhibit a convective motion, and the delay between pressure and heat release rate perturbations corresponds to one acoustic period.

It is next interesting to examine time histories of different variables in the active region at $z = 30\,\text{mm}$ plotted in Fig. 6.6. Heat release rate $\widehat{\omega}$ and Rayleigh source term $\widehat{\mathcal{R}}$ are plotted in the bottom subfigure. The acoustic pressure $\widetilde{p'}$ and section averaged axial velocity $\widetilde{u_z}$ shown in the top subfigure, are in phase quadrature, as expected for a standing acoustic wave. The total mass flow rate $\widetilde{\dot{m}_{tot}}$ and the flow rate of axial momentum $\widetilde{\mathcal{F}_z}$ appear in the second row. These two variables are in near quadrature with the axial velocity. While the axial velocity reflects the acoustic motion, the mass and momentum flow rates still feature a convective nature. The next subfigure shows the vaporization mass transfer $\widehat{\dot{m}_{vap}}$ between liquid and gas. Its fluctuations are ahead of the heat release rate. The equivalence ratio ϕ_g of the gas phase (formulation by Bilger et al. (1990)) is plotted alongside. Its values are only considered in regions where the volumetric heat release rate exceeds a threshold of 1% of its maximum. The equivalence ratio is not constant and reaches its minimum values when the heat release rate is at its maximum. The next

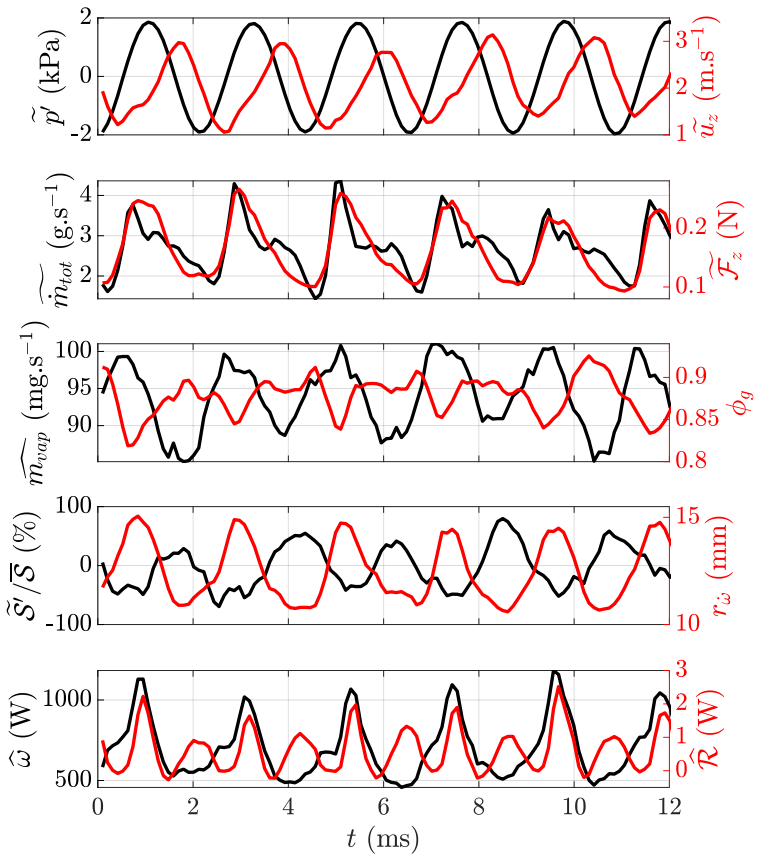

Figure 6.6: *Temporal evolution of several flow variables integrated / averaged ($\widehat{\psi}$ or $\widetilde{\psi}$, Eq. (6.1)) between $z = 27.5$ and 32.5 mm (for this figure, $\Delta z = 5$ mm).*

subfigure shows the relative fluctuations of the instantaneous swirl number defined as the ratio of the axial flow rates of moment of tangential momentum $\widetilde{\mathcal{F}_\theta}$ and axial momentum $\widetilde{\mathcal{F}_z}$ (Palies et al. (2010)):

$$\widetilde{\mathcal{S}}(z,t) = \frac{\widetilde{\mathcal{F}_\theta}}{R\,\widetilde{\mathcal{F}_z}} = \frac{\int_{S_c} \rho u_z u_\theta r \, dS}{R \int_{S_c} \rho u_z^2 \, dS} \tag{6.3}$$

It fluctuates in phase opposition to the pressure. The same graph also shows the radial position of the barycenter of heat realease rate which oscillates in phase with the heat release rate.

It is now instructive to examine the formation and convection of these swirl number perturbations. Figure 6.7(a) shows the time and space evolution of $\widetilde{\mathcal{F}_z}$. Strong fluctuations are released from the injector region in near phase quadrature with pressure. They are then convected downstream. The fluctuations of heat release rate (red isocontours) are in phase with $\widetilde{\mathcal{F}_z}$ and likewise convected by the flow (Fig. 6.7(a) and 6.7(c)). The relative fluctuations of swirl number $\widetilde{\mathcal{S}'}/\overline{\mathcal{S}}$ plotted in Fig. 6.7(b) reach about 32 % (RMS) in the lower flame region in phase opposition with these fluxes. In the upper flame region,

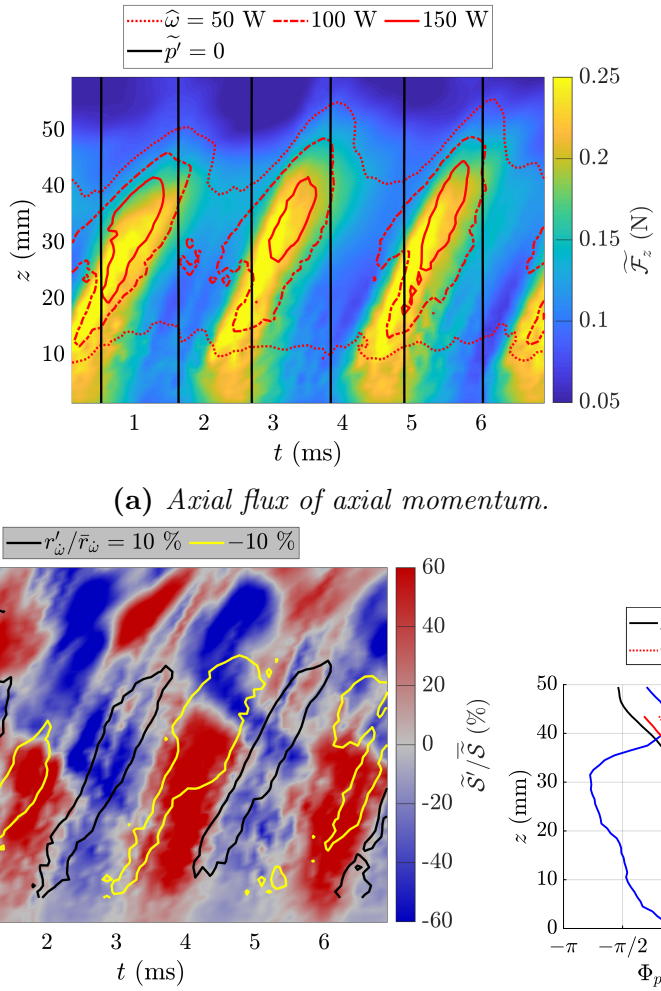

(a) *Axial flux of axial momentum.*

(b) *Swirl number fluctuations.*

(c) *Phase plot.*

Figure 6.7: *Analysis of swirl number fluctuations.* ***(a)*** *1D-1T colormap of axial flux of axial momentum* $\widetilde{\mathcal{F}_z}$ *with isocontours of heat release rate* $\widetilde{\omega}$ *and acoustic pressure* $\widetilde{p'}$. ***(b)****: 1D-1T colormap of fluctuations of instantaneous swirl number* $\widetilde{\mathcal{S}}$ *with isocontours of heat release rate barycenter fluctuations* $r'_{\dot{\omega}}/\overline{r_{\dot{\omega}}}$. ***(c)*** *Axial evolution of the phase related to pressure for* $\widetilde{\mathcal{F}_z}$, $\widetilde{\mathcal{S}}$, $\widehat{\omega}$ *and* $r_{\dot{\omega}}$.

the swirl number fluctuations are as intense, but in phase with the heat release rate. The perturbation is initiated in the vicinity of the injector and convected downstream. Oscillations in the flame position (black and yellow isocontours) are in phase opposition with the swirl number in the lower part of the flame, which appears to dictate their position further downstream. This differs from what was found in a previous study on premixed bluff-body swirl stabilized V-flames (Palies et al. (2010)), where flame opening was in phase with swirl number fluctuations at the base of the flame. Fluctuations further downstream were not examined. The phase of the different perturbations with respect to pressure is plotted as a function of the axial position in Fig. 6.7(c). Downstream of the injector, $\Phi_{p'}\left(\widetilde{\mathcal{F}_z}\right) = 3\pi/4$. The phase velocity of the perturbation decelerates in the first 15 mm to reach a quasi-steady value of $v_\Phi\left(\widetilde{\mathcal{F}_z}\right) = 27\,\mathrm{m\,s^{-1}}$ between $z = 20$ and 40 mm.

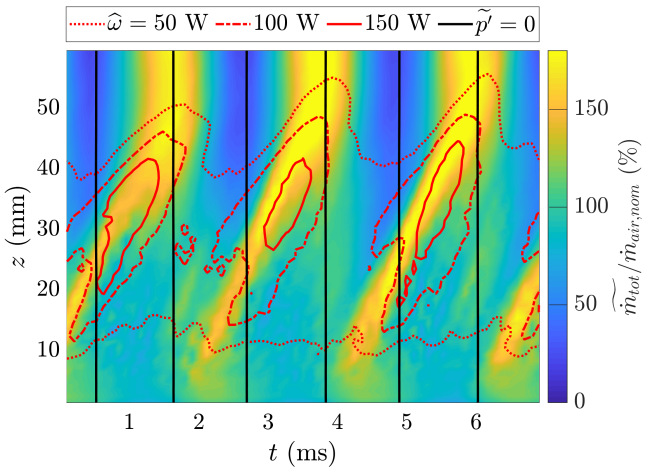

(a) *Normalised gaseous total mass flow rate.*

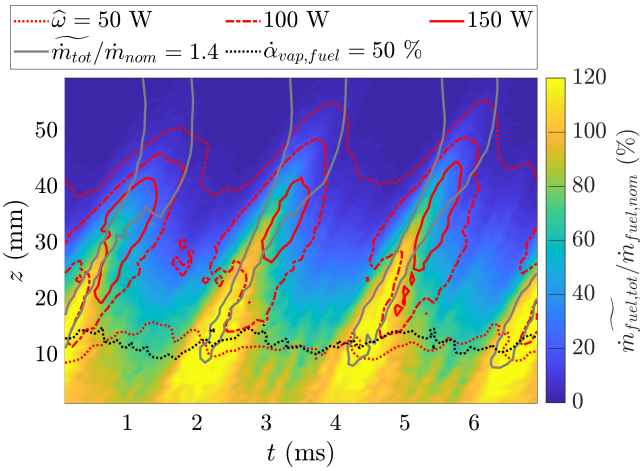

(b) *Normalised total fuel mass flow rate.*

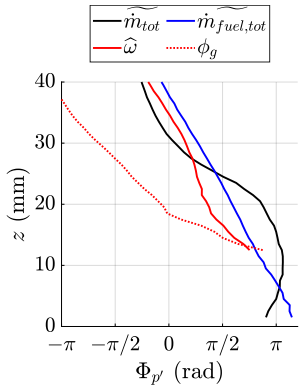

(c) *Phase plot.*

Figure 6.8: *Analysis of mass flow convective patterns.* ***(a)*** *1D-1T colormap of total mass flow rate $\widetilde{\dot{m}_{tot}}$ normalized by the nominal air mass flow rate. Isocontours of heat release rate $\widehat{\omega}$ and acoustic pressure $\widetilde{p'}$.* ***(b)****: 1D-1T colormap of total fuel mass flow rate $\widetilde{\dot{m}_{fuel,tot}}$ normalized by the nominal fuel flow rate. Isocontours of integrated heat release rate $\widehat{\omega}$, total mass flux $\widetilde{\dot{m}_{tot}}$ and fuel flow rate vapor fraction $\dot{\alpha}_{vap,fuel}$.* ***(c)*** *Axial evolution of the phase with respect to pressure for $\widetilde{\dot{m}_{tot}}$, $\widetilde{\dot{m}_{fuel,tot}}$, $\widehat{\omega}$ and ϕ_g.*

This corresponds to about half the cold flow jet velocity (Prieur et al. (2017b)).

It is next interesting to examine the total mass flow rate (Fig. 6.8(a)). It adopts a striking behavior: its perturbations released by the injector in phase opposition to pressure are convected up to the flame region ($z \simeq 35\,\text{mm}$). Further downstream its behavior is dominated by acoustics with vertical alternating bands characteristic of velocity fluctuations in quadrature with pressure of the quarter wave mode. Figure 6.8(b) displays the total fuel flow rate. Although the injected fuel flow rate in the atomizer is constant, the dynamics of the injector creates 10 % (RMS) fluctuations in the fuel flow rate at the outlet of the injector, in a process most likely similar to that presented by Eckstein et al.

(2006) and further discussed by Lo Schiavo et al. (2020). The phase to acoustic pressure is $\Phi_{p'}\left(\widetilde{\dot{m}_{fuel,tot}}\right) = -7\pi/8$. This perturbation is convected at $v_\Phi\left(\widetilde{\dot{m}_{fuel,tot}}\right) \simeq 28\,\mathrm{m\,s^{-1}}$, essentially the same phase velocity as the swirl number fluctuations. The phase plots in Fig. 6.8(c) complement the heat release rate isocontours in Fig. 6.8(a) and 6.8(b). There is a time delay between the fuel flow perturbation and the heat release rate which varies as a function of the axial position. One finds for example that $\tau_{ch}(z = 20\,\mathrm{mm}) = 0.25\,\mathrm{ms}$ and $\tau_{ch}(z = 30\,\mathrm{mm}) = 0.12\,\mathrm{ms}$. These values are typical of combustion delays under similar conditions (Bernier et al. (2004)).

This analysis now allows to estimate the various delays in the process. This can be decomposed into three contributions: firstly, the response of the injector which produces aerodynamic disturbances and flowrate fluctuations with a delay $\tau_{inj} = 0.95\,\mathrm{ms}$. Secondly, the perturbation is convected at a phase velocity $v_\Phi \simeq 28\,\mathrm{m\,s^{-1}}$ to the flame zone, located approximately 35 mm downstream in the high Rayleigh source term region (Fig. 6.5). This corresponds to a second delay $\tau_{cv} = 1.25\,\mathrm{ms}$. Thirdly, the combustion delay discussed previously must be accounted for. The total delay

$$\tau_t = \tau_{inj} + \tau_{cv} + \tau_{ch} \simeq 2.32\,\mathrm{ms} \tag{6.4}$$

is approximately equal to the delay between pressure fluctuations acting on the injector and heat release rate fluctuation which is about equal to the acoustic period 2.17 ms. Surprisingly the vaporization delay does not contribute to the total delay. This is because vaporization occurs simultaneously with convection. This is confirmed in Fig. 6.8(b) where the black dotted isocontour shows the region downstream of which more than 50 % of the fuel flow rate is being convected in gaseous form: $\dot{\alpha}_{vap,fuel} = \widetilde{\dot{m}_{fuel,vap}}/\widetilde{\dot{m}_{fuel,tot}}$. This contour is around $z = 12\,\mathrm{mm}$. This also substantiates what was inferred in Bernier et al. (2004) for a lean premixed prevaporized injector.

6.5 Conclusion

Large Eddy Simulation (LES) and experiments are combined to analyze acoustically coupled combustion oscillations in a generic configuration equipped with a swirling spray injector. The calculations essentially retrieve the frequency and amplitude of oscillation and are in fair agreement with the observed flame and spray dynamics. Comparisons of the flame and spray dynamics are performed using identical post-processing of experimental and numerical data, making use of the dynamic mode decomposition to analyze the oscillations. The data produced by the simulation is then processed to extract the mechanisms responsible for the intertwined response of the flame and the spray to the acoustic perturbation. This is done by noting that the flame is compact with respect to the acoustic wavelength and by making use of variables integrated over the combustor cross section. This gives access to the space time representation of central variables that are not easily measured experimentally and from which one observes that :

1. Sizable swirl number fluctuations are generated by the acoustic motion and convected by the jet. They have a strong impact on the aerodynamics of the flow and induce radial oscillations in the flame location.

2. Fluctuations of fuel flow rate are initiated in phase opposition to these swirl number fluctuations and likewise convected.

3. The total mass flow rate features a peculiar behavior: from the chamber backplane to the end of the combustion region it presents a convective motion while further downstream its fluctuations are dominated by the acoustic motion.

These various mechanisms contribute to the shaping of the heat release perturbations and the associated delay with respect to the pressure. This delay combines the response time of the injector to pressure disturbances, the convection time to the flame zone and the chemical conversion characteristic time while the vaporization time needs not to be included because it takes place simultaneously with convection.

Chapter 7

Investigating the effect of pressure loss on self-sustained instabilities

Combustion instabilities depend on a variety of parameters and operating conditions. It is known, mainly from experience in the field of liquid rocket propulsion, that the pressure loss of an injector has an effect on its dynamics and on the coupling between the combustion chamber and the fuel manifold. However, its influence is not well documented in the technical literature dealing with gas turbine combustion dynamics. Effects of changes in this key design parameter are investigated in the present chapter by testing different swirlers at constant thermal power on a broad range of injection velocities in a well controlled laboratory scale single injector swirled combustor using liquid fuel. The objective is to study the impact of injection pressure losses on the occurrence and level of combustion instabilities by making use of a set of injectors having nearly the same outlet velocity profiles, the same swirl number and that establish flames that are essentially identical in shape. It is found that combustion oscillations appear on a wider range of operating conditions for injectors with the highest pressure loss, but that the pressure fluctuations caused by thermoacoustic oscillations are greatest when the injector head loss is low. Four types of instabilities coupled by two modes may be distinguished: the first group features a lower frequency, arises when the injector pressure loss is low and corresponds to a weakly coupled chamber-plenum mode. The second group appears in the form of a constant amplitude limit cycle, or as bursts at a slightly higher frequency and is coupled by a chamber mode. Spontaneous switching between these two types of instabilities is also observed in a narrow domain.

Contents

This chapter reproduces an article published in Proceedings of the Combustion Institute as "An Experimental Study into the Effect of Injector Pressure Loss on Self-Sustained Combustion Instabilities in a Swirled Spray Burner". Authors of this article are Guillaume Vignat, Daniel Durox, Kevin Prieur and Sébastien Candel. Readers informed about the SICCA-Spray experimental rig may wish to skip Section 7.2.

7.1 Introduction

Combustion instabilities induced by an acoustic coupling are a recurring problem in high performance devices like aero-engines, liquid rocket motors and gas turbines for energy production. A substantial research effort has been dedicated to the understanding of the driving mechanisms and to the development of models, predictive tools and design control methods that could be used to avoid or suppress these dynamical phenomena. Much of the early work was motivated by spectacular failures of liquid rockets (Sutton and Biblarz (1949); Summerfield (1951); Harrje and Reardon (1972); Yang and Anderson (1995)). Research in the recent period has focused on issues related to gas turbines operating in the premixed mode (see for example the reviews of Candel (2002); Poinsot (2017)). The effort in control has mainly been aimed at increasing the acoustic damping rate in the chamber using quarter wave tubes, Helmholtz resonators, acoustic liners, bias flow perforated plates, etc. (Tang and Sirignano (1973); Bellucci et al. (2001); Zhao and Morgans (2009); Noiray and Schuermans (2012); Zhao and Li (2015); Yang and Anderson (1995); Lieuwen and Yang (2006)). An alternative route has been used that consisted in changing the acoustic mode structure and resonance characteristics of the system by placing baffles in the chamber. This method has been widely used in rocket engines to remove transverse oscillations (see for example Oefelein and Yang (1993)). A segmentation of the annular plenum of the combustor has also been used to reduce instabilities coupled by azimuthal modes in an industrially produced gas turbine by Tiribuzi (2007). Other studies have explored the possibility of changing the flame pattern and flame dynamics to reduce their sensitivity to perturbations and diminish the gain of the process that drives the instability, leading to the suppression of the unstable acoustic-combustion coupling (Lieuwen and Yang (2006); Noiray et al. (2011); Wolf et al. (2012); Durox et al. (2013)). A significant research effort has also been made to develop active control methods for combustion instability reduction (Lang et al. (1987); McManus et al. (1993)), with successful laboratory scale demonstrations and industrial application in some gas turbines (Lieuwen and Yang (2006)) but these methods have generally been considered to be too complex for a generalized implementation.

One method that has been extensively exploited in rocket engines has consisted in implementing a pressure drop in the injection elements to decouple the upstream manifold

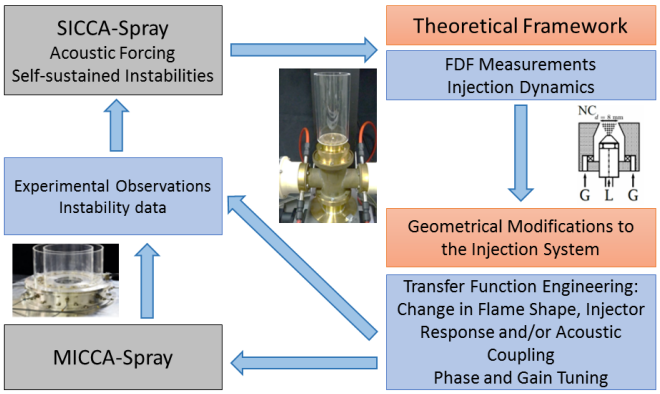

Figure 7.1: *Test methodology combining experiments on a single injector system and on the annular model scale combustor MICCA-Spray. The objective is to guide experimentation by tailoring the dynamical response.*

dynamics from those of the thrust chamber (Sutton and Biblarz (1949); Summerfield (1951); Harrje and Reardon (1972)). Relative injector pressure drop values of the order of 10 to 15% are typically adopted in engineering practice. Such head losses cannot be used in gas turbines, because of their impact on the overall engine thermodynamic efficiency. It is however important to examine effects of injector pressure losses on combustion instability and see how this parameter influences the stability of the system, an issue that has not been extensively investigated. In gas turbine combustors, the injection pressure of the liquid fuel is much higher than the chamber pressure to promote atomization and one may assume that the fuel manifold is insensitive to pressure perturbations in the chamber. However, pressure losses in the air stream have relatively low values of the order of a few percent (typically 3 to 4%). When modifying the head loss level in a swirled premixed burner by varying the pressure drop across the swirling injector Polifke et al. (2003) observed that for certain operating conditions, an increase in air flow rate in the injector led to the triggering of an instability. They also noted that this corresponded to a change in the slope of the operating line linking the air flow rate to the pressure drop and attributed this effect to a change in the recirculation zone at the injector outlet and thus to a change of flame geometry that in turn led to a change in the flame response to perturbation promoting instability.

The question that can be raised is whether an increase in the pressure drop of the air stream across injectors, without any significant change in flame shape and dynamics, can change the stability characteristics of the system possibly reducing or suppressing instabilities. This question is investigated in the present article. It is of course linked to the possible acoustic coupling between the upstream plenum and the combustion chamber. It is known that these cavities are weakly coupled if there are large changes in cross sections (Schuller et al. (2012); Poinsot and Veynante (2012); Bauerheim et al. (2014); Bourgouin et al. (2015b)). The coupling may also be changed by the injector pressure drop that modifies the injector impedance. It is then worth considering injectors with different head losses but similar swirl numbers conserving the flame shape and examining the flame dynamics and corresponding self-sustained oscillations. A single injector

configuration is used in the present investigation (designated as "SICCA-Spray") but the analysis is carried out in a framework where tests on this geometry are used to prepare investigations on a more complex multiple injector annular configuration "MICCA-Spray" at EM2C laboratory. Strong azimuthally coupled combustion instabilities have already been observed in MICCA-Spray (Prieur et al. (2017b)) and it was shown that injectors operating near the pressure antinodes were essentially driven by velocity perturbations induced by the injector response to the azimuthal mode. It is then logical to use the iteration loop shown in Fig. 7.1 to characterize the dynamics of injectors, measure flame describing functions (FDF) using acoustic forcing or examine the dynamics of the system under self-sustained, longitudinally coupled, combustion oscillations. The FDF can then be included in the stability analysis as exemplified by Noiray et al. (2008) in a configuration featuring longitudinal acoustic modes or implemented in combination with a Helmholtz solver as explored by Laera et al. (2017). The pressure loss across the injector is here considered as a design parameter that can be varied to promote or reduce unstable oscillations. Results obtained in single element tests can be used to guide experimentation on the MICCA-Spray annular system.

This article describes experiments carried out only on the single injector spray swirled burner SICCA-Spray. This configuration is briefly described in Sec. 7.2. Four different injectors are designed (Sec. 7.3) with the same swirl numbers, in order to have identical flame shapes, but different pressure drops (up to 30% difference). A stability map of this system is constructed in Sec. 7.4 by keeping the thermal power constant and exploring a broad range of injection velocities. Results are interpreted in Sec. 7.5.

7.2 Experimental Setup

The SICCA-Spray experiment is sketched in Fig. 7.2. This single injector version of the MICCA-Spray annular combustion chamber comprises a combustion chamber, a plenum, fed with compressed air, and an injector fed with air from the plenum and with liquid n-heptane fuel. The chamber is formed by a quartz tube of length $l_c = 315\,\text{mm}$. The base of the chamber has a 15 mm high section made of brass. The injection system comprises a main body (grey), an interchangeable swirler and an atomizer for the liquid fuel. The atomizer produces a hollow cone shaped spray of liquid fuel droplets. Their Sauter mean diameter measured 2.5 mm above the injector outlet is $d_{32} = 35\,\mu\text{m}$ (Prieur et al. (2016)). The injector ends in a conical convergent section, with an exit radius of $R_{inj} = 4\,\text{mm}$. The swirler is manufactured using a stereolithography 3D printer. It consists in a hollow cylinder with six tangential cylindrical channels. Key dimensions and notations are shown in Fig. 7.3. Two Monacor SP-6/108 Pro driver units are mounted on the plenum. They are not used in this study, and their electrical circuit is left open. A straight tubular section upstream of the injector is used for measurements in the plenum. The fuel mass flow rate is measured using a Bronkhorst mini CORI-FLOW mass flow meter of relative accuracy $\pm 0.4\,\%$, and similarly, the air mass flow rate is measured using a Bronkhorst El-Flow thermal mass flow meter of relative accuracy $\pm 0.9\,\%$. In this article, the bulk

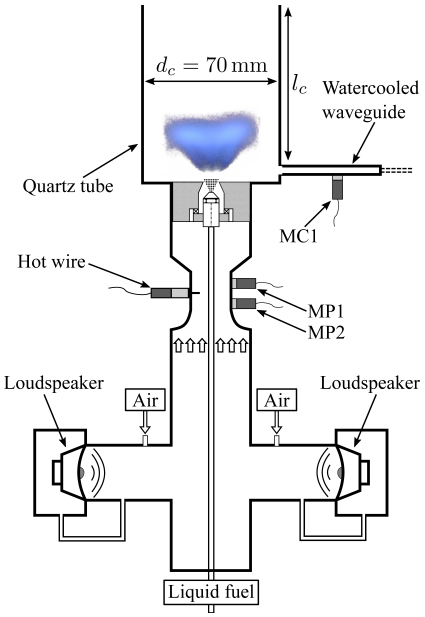

Figure 7.2: *Schematic representation of the SICCA-Spray setup.*

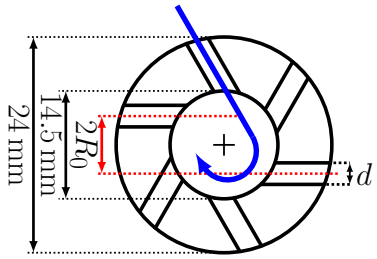

Figure 7.3: *Schematic view of the swirler seen from above indicating the main dimensions of this component. d is the diameter of the small cylindrical tangential channels, and R_0 is the distance between the axis of the channels and the swirler centerline.*

velocity $u_b = \dot{m}/(\pi\rho R_{inj}^2)$ is defined as the 1D velocity at the injector outlet under cold flow conditions.

Head loss is measured using a Kimo MP111 differential pressure gauge, with a 1% relative precision. Three Bruel & Kjaer type 4938 microphones with type 2670 preamplifier detect acoustic pressure signals. Their relative accuracy is 1% and their cut-off frequency of 70 kHz is far greater than the sampling frequency of 16 384 Hz used for data acquisition. Microphone MC1 is used to measure the pressure at the backplane. It is mounted on a water-cooled wave guide. This microphone is at 290 mm from the chamber backplane. Microphones MP1 and MP2 are mounted flush to the wall of a straight tubular section of the plenum upstream of the injector. They are separated by 50 mm. Combined with a Dantec Dynamics miniCTA constant temperature hot wire anemometer (cutoff frequency 10 kHz), they are used to measure acoustic pressure and velocity upstream of the injector. A Dantec Dynamics FlowExplorer two component Laser Doppler anemometer (LDA) measures velocities 2.5 mm downstream the combustor backplane, under non-reactive conditions and without the quartz tube. The theoretical optical probe volume of this LDA system measures 0.14 mm × 0.14 mm × 0.23 mm. Measurements are spaced every 0.25 mm. Uncertainty on the measured mean velocities, taking statistical uncertainties into account, is less than $0.8\,\text{m}\,\text{s}^{-1}$. Finally, a Princeton Instruments PiMax4 camera is

Table 7.1: *Dimensions and characteristics of the swirlers considered in this study.*

	d (mm)	R_0 (mm)	$\mathcal{S}$	σ
S_a	2.9 ± 0.1	2.3 ± 0.1	0.65	4.3
S_b	3.3 ± 0.1	3.0 ± 0.1	0.64	4.1
S_c	3.6 ± 0.1	3.5 ± 0.1	0.64	3.7
S_d	4.0 ± 0.1	4.6 ± 0.1	0.60	3.6

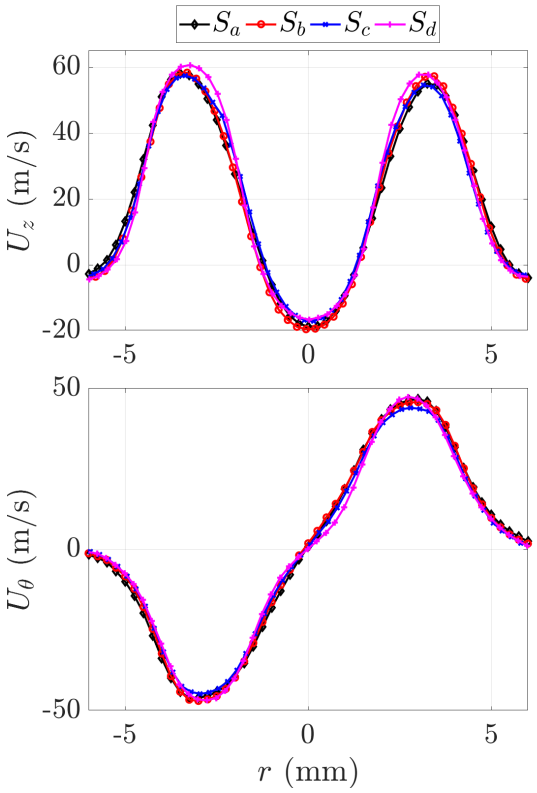

Figure 7.4: *Mean axial (U_z, top) and azimuthal (U_θ, bottom) velocity profiles measured* 2.5 mm *downstream of the injector under cold flow conditions outlet using LDA.* $u_b = 43\,\mathrm{m\,s^{-1}}$.

used for flame visualization. An optical bandpass filter centered on $\lambda = 430\,\mathrm{nm}$ is used to restrain visualization to light emitted by CH*.

7.3 Design of the injectors

Four injection systems were designed by changing the swirler units, while trying to keep the same flame shape and outlet velocity profiles as the reference injector used in (Prieur et al. (2017a)). To do so, a large parameter sweep was performed on parameters d and R_0 of the swirlers (see Fig. 7.3). A total of 38 swirlers were manufactured, the velocity profile at their outlet were measured using the LDA system and the flame shape was determined using CH* chemiluminescence. Their experimental swirl number $\mathcal{S}$ is calculated using the

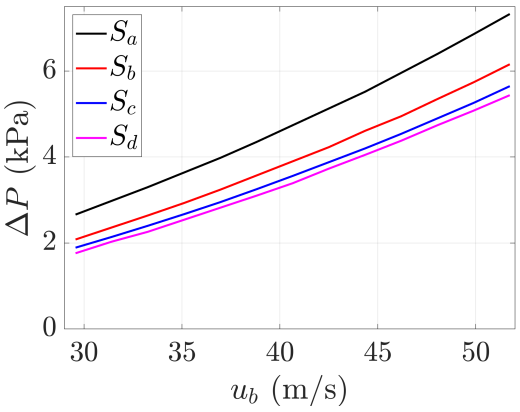

Figure 7.5: *Head loss ΔP of each swirler for the range of bulk air velocity used in this study. It is the difference between the pressure in the plenum, measured at position MP2, and the ambient pressure, in the absence of combustion.*

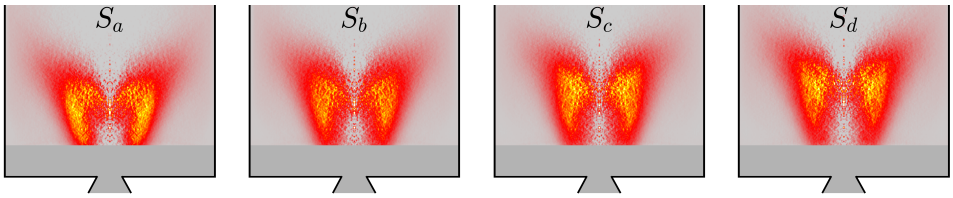

Figure 7.6: *CH* chemiluminescence image of the stable flame obtained by reducing the combustion chamber length to* 165 mm. *The line-of-sight integrated images obtained by the PiMax4 camera are Abel transformed. Yellow and white correspond to high light intensities while gray corresponds to no light. No information is available near the backplane due to the opaque brass section at the bottom of the combustion chamber. Positions of the quartz confinement tube and conical injector outlet are also indicated. Swirler S_a to S_d. Operating condition:* ($\mathcal{P} = 6.2\,\mathrm{kW}, \phi = 0.98, u_b = 36\,\mathrm{m\,s^{-1}}$).

conventional expression

$$\mathcal{S} = \frac{\int_0^{2R_{inj}} \overline{U_\theta}\,\overline{U_x}\, r^2 dr}{R_{inj} \int_0^{2R_{inj}} \overline{U_x}^2 r dr} \tag{7.1}$$

Among the 38 swirlers, four were selected and named S_a to S_d. Table 7.1 gathers key geometrical characteristics and aerodynamic performances. These four swirlers have very similar swirl numbers, and a nearly identical outlet mean velocity profile, shown in Fig. 7.4. The RMS velocity profiles (not presented here) show only a very small difference between the different swirlers. The injector head loss ΔP is shown in Fig. 7.5 for each swirler. Its evolution with the bulk velocity follows the usual scaling law: $\Delta P = 1/2\,\rho\sigma u_b^2$. The value of σ for each swirler is indicated in Tab. 7.1.

Figure 7.6 shows a direct visualization of CH* chemiluminescence from the four flames at ($\mathcal{P} = 6.2\,\mathrm{kW}, \phi = 0.98, u_b = 36\,\mathrm{m\,s^{-1}}$). These four images are obtained by averaging over 900 frames with 0.1 ms exposure time each. It shows that the four flames have similar "M"-shapes and this has been verified for wide range of operating points.

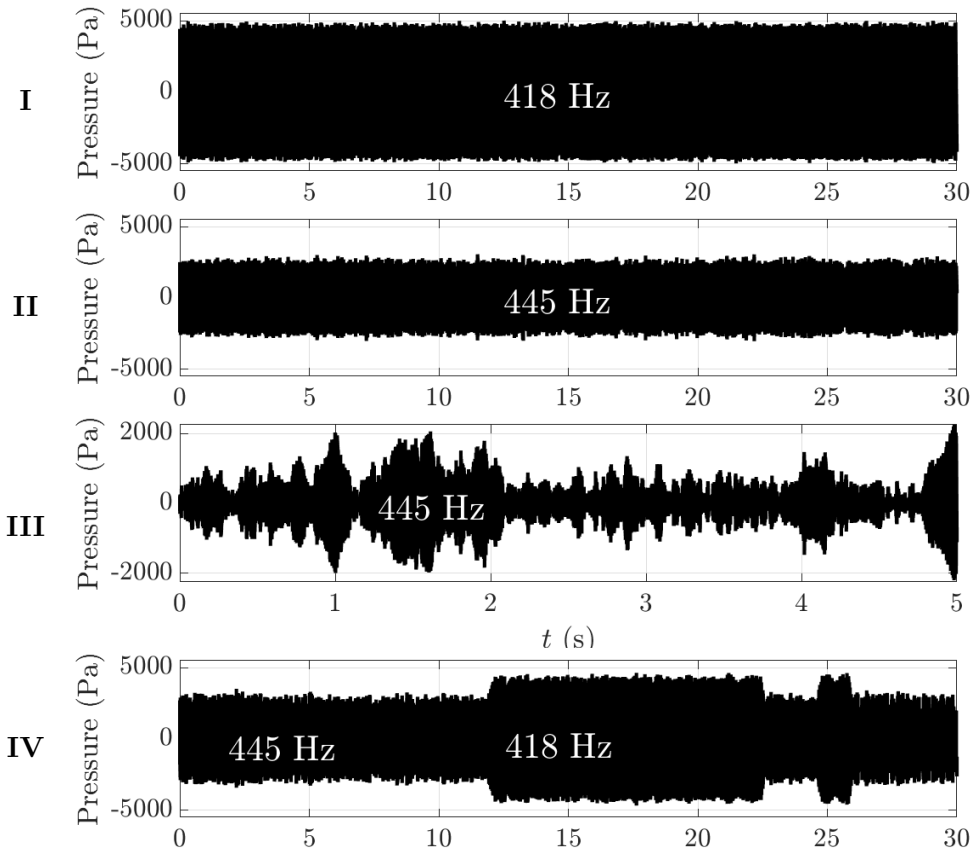

Figure 7.7: *Typical pressure records p_c measured by microphone MC1 at the combustor backplane illustrating type (I) to (IV) instabilities, as indicated on the left of each graph. The power is kept constant $\mathcal{P} = 6.2\,\mathrm{kW}$. Type (I) instability is mainly observed with swirlers S_b, S_c and S_d; type (II) instability is observed with the four swirlers; type (III) instability is observed with the four swirlers near the borders of the unstable domain; type (IV) instability is only observed with swirler S_c.*

7.4 Different types of combustion dynamics

The presence of self-sustained combustion instabilities in the SICCA-Spray experiment is investigated for each of these injection systems. The thermal power is kept constant at $\mathcal{P} = 6.2\,\mathrm{kW}$, while the air mass flow rate is varied, so that u_b varies between 29 and $51\,\mathrm{m\,s^{-1}}$, corresponding to global equivalence ratios between $\phi = 1.18$ and 0.69. The acoustic pressure near the combustor backplane p_c is measured by microphone MC1.

Five distinct types of dynamical regimes may be distinguished depending on the injection system and operating point:

(I) Limit cycle at approximately 418 Hz;

(II) Limit cycle at approximately 445 Hz;

(III) Bursts;

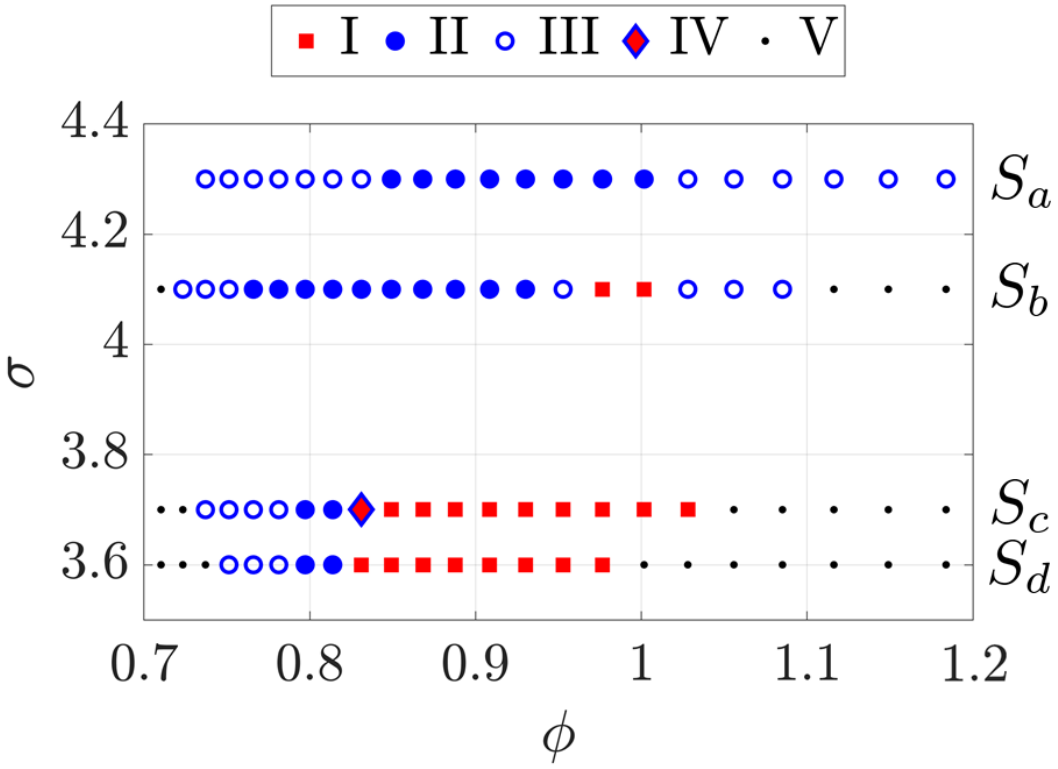

Figure 7.8: *Instability map showing the different types of combustion instabilities observed as a function of equivalence ratio ϕ and head loss coefficient σ of the swirlers. Red square: Limit cycle at 418 Hz, Open blue circle: Limit cycle at 445 Hz, Solid blue circle: Bursts, Red diamond: Switching between type I and type II, Dot: No oscillation.*

(IV) Spontaneous and irregular switching between type I and II instabilities;

(V) No oscillations or low amplitude perturbations : the peak acoustic pressure level in the chamber is less than 300 Pa.

Typical examples of pressure signals recorded near the combustor backplane are shown in Fig. 7.7 to illustrate these behaviors. The frequency of the burst regime is closest to 445 Hz, but it does vary on a wide range depending on the operating conditions, reaching as low as 425 Hz.

Figure 7.8 shows the type of instability that was observed for each swirler in SICCA-Spray when varying the air mass flow rate while keeping the power constant at $\mathcal{P} = 6.2\,\text{kW}$. Great care was taken to wait for the experiment to reach thermal equilibrium in order to eliminate the thermal environment impact on stability, an effect that is well known (see for example Prieur et al. (2017a)). No hysteresis phenomena were observed.

Swirler S_a with the highest head loss is unstable over a wider range of operating conditions.

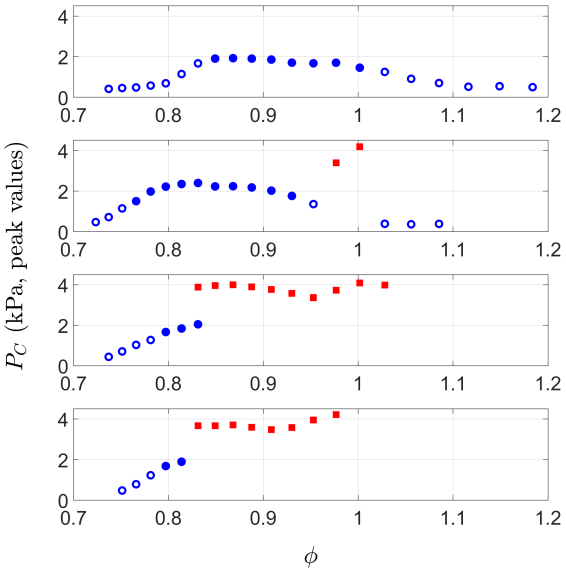

Figure 7.9: *Acoustic pressure amplitudes measured at the combustor backplane during thermoacoustic oscillations. Symbols are identical to those used in Fig. 7.8.*

Only type (II) and (III) instabilities at $f = 445\,\text{Hz}$ are observed with this swirler. The burst regime appears for both the leanest and the richest operating points. As the head loss decreases with swirlers S_b, S_c and S_d, the range of unstable operating conditions narrows. For swirler S_b, the first oscillations are in the burst regime, before switching to a limit cycle at 418 Hz near the stoichiometry. However, the instability rapidly switches to 445 Hz as the air flow rate is increased. For swirler S_c, the first unstable point appears at stoichiometric conditions, and a limit cycle at 418 Hz is observed. This type (I) instability arises over a broad range of operating conditions. Switching between 418 Hz and 445 Hz limit cycles takes place for $\phi = 0.83$. For leaner operating conditions, as for the other swirlers, a 445 Hz limit cycle is established giving rise to bursts at lower air flow rates. Swirler S_d, compared to swirler S_c, behaves similarly, but has a slightly narrower range of unstable conditions.

Figure 7.9 shows the amplitude of the acoustic pressure near the combustor backplane for the operating points appearing in Fig. 7.8. The level is always higher when the thermoacoustic oscillation frequency is around 418 Hz (red squares on Fig. 7.9). It reaches a peak level between 3400 and 4200 Pa while it is always inferior to 2400 Pa when the frequency is around 445 Hz (blue circles in Fig. 7.9).

7.5 Discussion

The coexistence of two types of combustion instabilities in a system can often be attributed to the coexistence of two flames having a different shapes and dynamical responses (Polifke et al. (2003); Hermeth et al. (2014); Renaud et al. (2017)). To investigate this point, phase-averaged CH* chemiluminescence imaging of swirler S_c at operating condition ($\mathcal{P} = 6.2\,\text{kW}, \phi = 0.83, u_b = 42\,\text{m}\,\text{s}^{-1}$) was used. At this operating point, type (IV) instabilities with alternating limit cycles were observed (see Fig. 7.7).

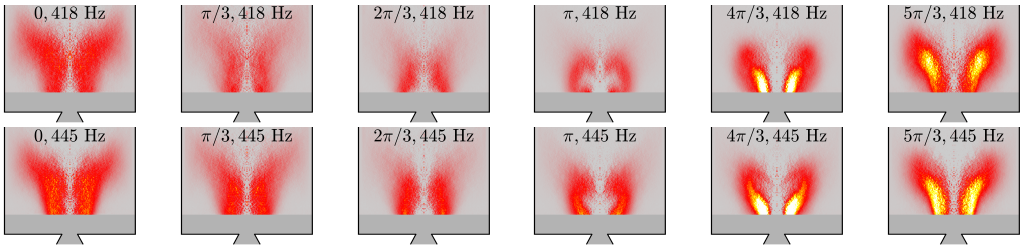

Figure 7.10: *Phase averaged CH* chemiluminescence image of the flame in type (V) instability. The PiMax4 camera is triggered using the MP2 microphone signal. The averaging is conditioned by the frequency of the limit cycle oscillations, with the* 418 Hz *limit cycle at the top, and the* 445 Hz *limit cycle at the bottom. As the oscillation stays at each frequency for several seconds between switchings, well separated acquisition can be easily performed for each frequency. The images are obtained in the same manner as in Fig. 7.6. Swirler S_c at* ($\mathcal{P} = 6.2\,\mathrm{kW}, \phi = 0.83, u_b = 42\,\mathrm{m\,s^{-1}}$).

In Fig. 7.10, the phase averaging is conditioned with respect to the thermoacoustic oscillation signal. This allows a direct comparison of flame shapes between the two combustion instabilities at a single operating point. The flames appear identical in the two types of oscillations, indicating that the coexistence of the two instabilities is not caused by a change in flame shape.

It is then natural to inquire if this may be linked to the acoustic eigenmodes of the system by making use of the Helmholtz solver of COMSOL Multiphysics. The geometry includes an end correction for the quartz confinement tube $\Delta l = 0.4 \times d_c$ where d_c is the diameter of the tube (see Fig. 7.2). At that distance from the chamber exit, the acoustic pressure vanishes. The passive loudspeakers in the plenum are not well characterized acoustically. In order to evaluate the influence of the plenum on the acoustic structure of the system, the acoustic impedance of the whole plenum was experimentally measured by making use of the three microphone method described by Chung and Blaser (1980a); Chung and Blaser (1980b). A third microphone replaces the hot wire in this experiment, and the combustion chamber and injector are replaced by a loudspeaker mounted at the end of a tube used to generate plane waves in the system. The impedance is reconstructed in a plane defined by the hot wire position in Fig. 7.2. The plenum can then be replaced by an impedance boundary condition in the simulations. All other boundary conditions correspond to rigid walls. The speed of sound and fluid density are assumed to be uniform in the chamber and the plenum respectively.

Acoustic response simulations are compared with experimental data in Tab. 7.2 for swirler S_d. In these experiments, a loudspeaker placed next to the SICCA-Spray setup provides acoustic excitation. In a first case, in the left column of Tab. 7.2, the experiment is carried out with air at room temperature in the absence of flow. In the second (third column of Tab. 7.2), the combustion chamber is filled with a mixture of helium and air in a suitable proportion that yields a speed of sound coinciding with that prevailing under hot fire conditions. Experimental data (columns 1 and 3) are in reasonably good agreement with simulation results (respectively columns 2 and 4). The frequency differences are less than 30 Hz in these two cases.

Table 7.2: *Acoustic simulation for swirler S_d: acoustic modes are determined experimentally by exciting the SICCA-Spray experiment with an external loudspeaker. Three operating conditions are considered: in the first column of the table, the plenum and the combustor are filled with air at room temperature, in the third column, the combustor is filled with a mixture of* 24.4% *air and* 75.6% *helium by volume such that the sound speed in this mixture is identical to that of the average temperature of the hot gases in the chamber (*1000 K*). Column 5 corresponds to acoustic simulations performed by considering that the combustor is filled with combustion products at a mean temperature of* 1000 K*. The experimental data resolution is* $\Delta f = \pm 14$ Hz*.*

Air		Air & Helium		Hot fire
Experimental	Simulation	Experimental	Simulation	Simulation
250	248	260	246	240
284	273	434	464	461
		490	480	478
534	541	657	646	647
744	744	914	892	

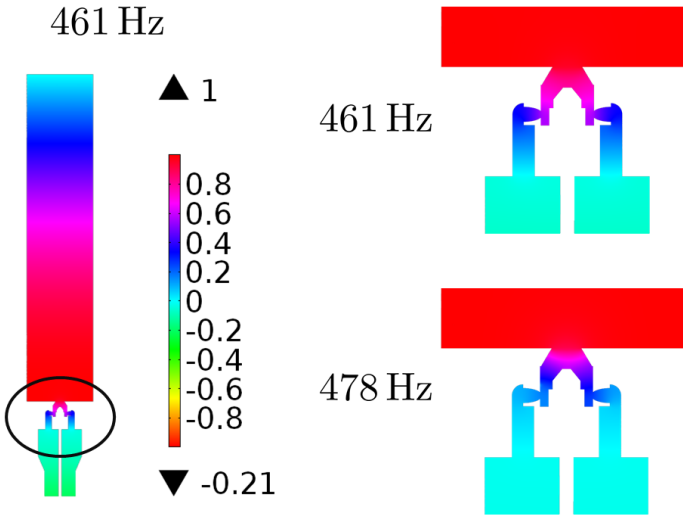

Figure 7.11: *Acoustic pressure amplitude obtained in the simulations. The simulated domain is shown on the left for a frequency* 461 Hz*. On the right, the injector is shown in detail for the two eigenfrequencies of interest. The acoustic pressure is normalized by the acoustic pressure at the pressure antinode of each mode.*

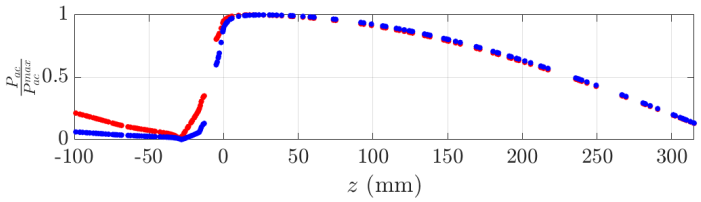

Figure 7.12: *Axial evolution of the acoustic pressure amplitude for the two modes. The acoustic pressure is normalized by its maximum in order to have the same scale for both curves.* 461 Hz *mode in red,* 478 Hz *mode in blue.* $z = 0$ *corresponds to the combustor backplane.*

One may then calculate the eigenfrequencies under hot fire conditions by considering swirler S_d and assuming a mean temperature $T = 1000\,\mathrm{K}$ in the chamber. This yields two eigenmodes at 461 Hz and at 478 Hz. These frequencies are not quite those observed experimentally but this could be expected since the instability frequencies are displaced with respect to the modal frequencies by the flame response. The two modes have nearly the same spatial structure. However the lowest eigenfrequency (461 Hz) corresponds to a mode that is coupled with the upstream plenum while the higher eigenfrequency (478 Hz) essentially pertains to a chamber mode (see the details Fig. 7.11). The higher amplitude of the acoustic pressure in the plenum is confirmed in Fig. 7.12 where the axial evolution of the acoustic pressure amplitude is shown.

This acoustic simulation indicates that two closely spaced acoustic modes coexist in the system. The lower frequency mode has a higher relative amplitude in the plenum. When the coupling between the plenum and the combustion chamber is strengthened, that is when the injector pressure loss is low, instabilities can more easily lock on this lower frequency mode, coupled with the plenum, leading to type (I) and type (IV) oscillations. In the experiment this pertains to the lower frequency oscillations at 418 Hz. When the injector pressure loss is higher, coupling between the cavities is diminished, leading to instabilities preferentially locking on the higher frequency, inducing type (II), and (III) combustion instabilities. These are manifested in the experiment at a frequency 445 Hz with in some cases a possible switching between the two eigenfrequencies (type (IV) oscillations).

7.6 Conclusion

Effects of injector pressure losses are investigated in this article to see how changes in this parameter modify the combustion dynamics of a generic system. Four injectors are tested in a single element combustor fed with liquid fuel and air. The velocity profiles at the injector outlets are quite similar and the corresponding swirl numbers are nearly the same. Thus the steady flame shapes obtained with these four injectors are close to each other. However, their pressure losses vary by about 30%.

This setup allows to study the influence of the head loss as a design parameter while

keeping the other conditions constant. The instability map of the burner is determined by examining the dynamical regimes and recording the various types of oscillations. The pressure loss in the injector has an impact on the occurrence, type and intensity of thermoacoustic instabilities. In this system, the range of global equivalence ratio corresponding to an unstable regime is wider for injectors with higher pressure loss. Four types of instabilities, coupled by two acoustic modes (418 Hz and 445 Hz) are observed. Calculations of the acoustic eigenmodes of the system indicate that two modes, that are close in frequency, coexist in this system. Both appear to have a quarter wave like structure. Oscillation at a frequency around 418 Hz, generally occurs when the injector pressure loss is low, and corresponds to a mode that weakly couples the chamber with the plenum. The second, at a frequency around 445 Hz, arises when the head loss is larger, and corresponds to a chamber mode. In a narrow domain, one also observes a random switching between the two modes. This bistable behavior might have been attributed to a change in flame response. However the flame shape is essentially identical in both types of instabilities and switching is linked to the existence of the two eigenmodes.

Part IV

Flame and injector coupling by azimuthal modes in the MICCA-Spray annular combustor

Chapter 8

Acoustic eigenmodes in annular combustors

In addition to the injector and flame dynamics it is important to examine the acoustic modes that couple oscillations, define the possible resonances and play a central role in the stability analysis of the system. Three items are examined in this chapter. We first examine the acoustic eigenmodes of an annular cavity with a focus on effects of unequal side walls. The asymmetric configuration with an inner wall that is shorter than the outer wall has been used in MICCA as well as in the Cambridge-NTNU facility to obtain combustion instabilities. Structures of acoustic eigenfunctions and eigenfrequencies are examined in this configuration and compared with those corresponding to of a system having side walls of equal sizes. Contrary to what was expected, it is found that eigenfunctions and eigenfrequencies are quite close for these two relatively different set-ups. The second item is concerned with effects of non-uniform temperature fields on the azimuthal structure of acoustic eigenfunction and on the corresponding eignefrequencies. This study is motivated by observations made under very high amplitude oscillations in MICCA-Spray which resulted in partial flame blow-off. In these experiments, reported in the next chapter, it is found that the azimuthal pressure distribution in the chamber is notably modified as the flames are blown out. This feature is investigated by analyzing the deformation of acoustic eigenfunctions induced by temperature non-uniformity. The third point is concerned with the determination of the damping rate in the annular system. The two methods explored in this chapter use simultaneous microphone and flame chemiluminescence measurements to estimate the acoustic damping level in MICCA-Spray.

Contents

The estimation of the acoustic damping in MICCA-Spray has been presented at the 9th European Combustion Meeting in Lisbon, Portugal, 2019, under the title "Quantifying acoustic damping in a multi-injector annular combustor" by Guillaume Vignat, Daniel Durox, Antoine Renaud and Sébastien Candel.

8.1 Introduction

This chapter deals with some acoustic issues involved in combustion instability analysis. it is worth recalling a few theoretical results concerning eigenmodes and their use in combustion dynamics analysis. This is often based on a wave equation for the acoustic pressure which may be written in the low Mach number framework in the form (Poinsot and Veynante (2012)):

$$\nabla \cdot \left[\bar{c}^2 \, \nabla p \right] - \alpha \frac{\partial p}{\partial t} - \frac{\partial^2 p}{\partial t^2} \;=\; -\left(\gamma - 1\right) \frac{\partial \dot{\omega}}{\partial t} \tag{8.1}$$

where p designates the acoustic pressure, $\overline{c}$ is the mean sound velocity, α is a volumetric acoustic damping coefficient, γ is the specific heat ratio and $\dot{\omega}$ represents the instantaneous volumetric heat release rate. One method for solving this equation that has been extensively exploited in the analysis of combustion instabilities consists in expanding the pressure field in terms of the normal modes, an approach initially introduced by Zinn and Powell (1970) to the field of thermoacoustics and notably explored by Culick (1988); Culick (2001). In this framework, it is assumed that the shape of the eigenmodes of the thermoacoustic system is close to that of the acoustic eigenmodes $\Psi_n(\mathbf{x})$ determined in the absence of the heat release rate source term. The acoustic pressure field is then projected onto a basis formed by the set of acoustic eigenmodes $\Psi_n(\boldsymbol{x})$:

$$p\left(t, \mathbf{x}\right) = \sum_{n=0}^{\infty} \eta_n(t) \Psi_n\left(\mathbf{x}\right) \tag{8.2}$$

The acoustic eigenmodes can be computed by solving

$$\nabla \cdot \left[\bar{c}^2 \, \nabla \Psi_n(\boldsymbol{x}) \right] \; + \omega_n^2 \, \Psi_n(\boldsymbol{x}) \;=\; 0 \tag{8.3}$$

together with a set of boundary conditions. In general these conditions correspond to rigid walls (the normal velocity vanishes at the wall), or to an open boundary (the pressure vanishes at the open end or at a distance of that end taking into account the end correc-

tion). The eigenmodes are then orthogonal and this greatly simplifies the projection[1].

For an orthogonal basis Ψ_n, the modal amplitudes η_n are solution to a second order inhomogeneous ordinary differential equation

$$\frac{\partial^2 \eta_n}{\partial t^2} + 2\xi\omega_n \frac{\partial \eta_n}{\partial t} + \omega_n^2 \eta_n = \frac{1}{\|\Psi_n\|_2} (\gamma - 1) \int_V \frac{\partial \dot{\omega}}{\partial t} \Psi_n dV \tag{8.4}$$

where ξ is a damping coefficient into which both the volumetric damping and acoustic flux at the boundary are bundled together, ω_n is the eigenfrequency of the n^{th} eigenmode, and $\|\Psi_n\|_2$ is the 2-norm of the eigenmode.

$$\|\Psi_n\|_2 = \int_V \Psi_n^2 dV \tag{8.5}$$

It clearly appears from the previous expression that the determination of both the acoustic eigenmode and the acoustic damping are of critical importance in the analysis of the stability of a thermoacoustic system. These items are considered in the following order. Section 8.2 is concerned with the eigenmodes and eigenfrequencies of annular cavities and specifically considers geometries in which the lateral walls have different length. In one configuration the inner wall is shorter than the outer wall while in a reference configuration the side walls have equal lengths. The second item examined in Section 8.3 pertains to effects of temperature inhomogeneities on the acoustic eigenmode azimuthal structure. This study is motivated by observations reported in the next chapter. It is found that when the level of instability is very high, of the order of a few percent of the ambient pressure, some of the flames in the annular combustor are blown out inducing a temperature inhomogeneity near the combustor backplane. The pressure distribution corresponding to the coupling mode is also distorted. It is then natural to calculate distortions that may be caused by the temperature nonuniformity. The third item (Section 8.4) pertains to the determination of the damping rate in annular systems. This problem is explored with two methods which both use time-series data recorded in MICCA-Spray during a combustion oscillation.

8.2 Acoustic eigenmodes of annular cavities

It is natural to examine the three generic annular geometries displayed in Figure 8. The analytical determination of the eigenmodes for the open-closed (Fig. 8(a)) and closed-closed configurations is discussed in the general introduction of the present document. In the following developement we analyze the differences in eigenmodes and eigenfrequencies between the open-closed configuration (Fig. 8(a)) and the annular chamber with unequal side walls (Fig. 8(c)). As already indicated the latter configuration has been used in the Cambridge-NTNU and in the MICCA laboratory scale annular combustors to obtain

[1] It is worth noting that Laurent et al. (2019) suggest to use an overcomplete, non-orthogonal basis to perform this projection. The overcomplete basis is composed by joining the solutions of Eq. (8.3) obtained with rigid walls boundary conditions and those obtained with an open boundary condition. This allows in particular to represent boundaries with an arbitrary impedance.

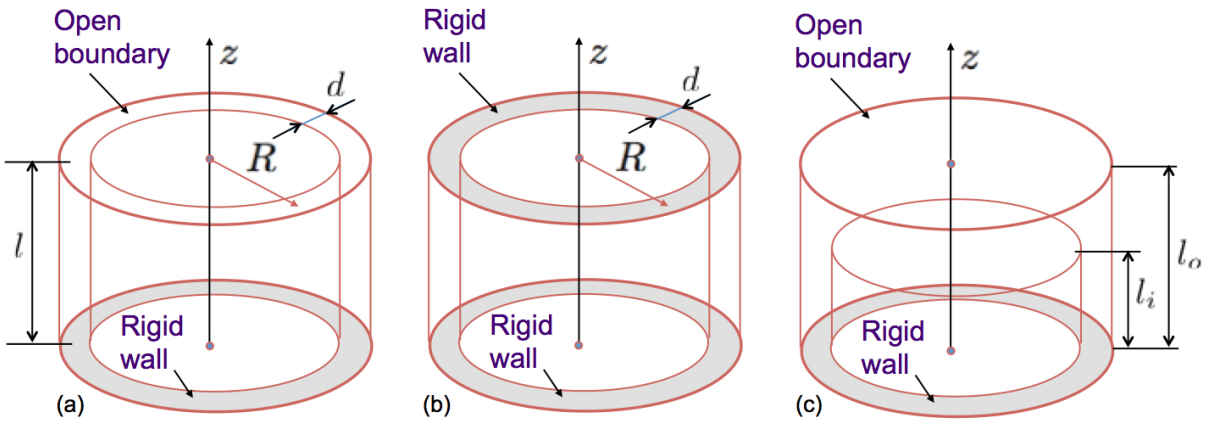

Figure 8: *Generic annular geometries. (a) Annular chamber with a rigid backplane, equal length side walls and an open boundary, (b) Annular chamber with a rigid backplane and a rigid wall boundary condition at the outlet, (c) Annular chamber with unequal side walls. (repeated from page 13)*

combustion oscillations.

The analysis, carried out with the commercial Helmholtz solver COMSOL, provides the acoustic eigenmodes for the two configurations. It was decided to use the specific geometries tested in MICCA-Spray. The first configuration comprises two confinement walls with an equal length of $l_o = l_i = 700\,\text{mm}$. The second has two confinement walls of unequal length, the inner wall being $l_i = 200\,\text{mm}$ long, the outer $l_o = 700\,\text{mm}$, corresponding to the configuration used in chapter 9. In this second case, the geometry comprises the internal volume found inside the annulus of MICCA-Spray and filled with cold gases. In both cases, the geometry also comprises the plenum and a simplified representation for the 16 injectors. All boundary conditions are rigid walls, except the outlets which are modeled as pressure nodes with end conditions. In the case of the two walls of equal length, the end condition corresponds to $\Delta l = 0.4 d_h = 40\,\text{mm}$, where d_h is the hydraulic diameter of the annulus. In the case of the two walls of unequal length, the end conditions have been measured by Bourgouin (2014), and these measurement correspond to the usual value of $\Delta l = 0.4d$. The temperature of unburnt gas is set to 350 K, that of the burnt gases to 1400 K which corresponds to the gas temperature measured in SICCA-Spray and presented in chapter 1 (p. 43). In the case of the unequal side walls geometry, the turbulent mixing between the burnt and unburnt gases is modeled by a mixing layer expanding with an half angle of 7.5°. The geometries are shown in Fig. 8.2. The sound velocity used for the simulations is shown in the top row, the shape of the acoustic pressure corresponding to the 1A1L eigenmode is displayed in the middle row, that of the 0A1L mode in the bottom row. The eigenfrequencies of the 1A1L eigenmode are close: 744 Hz in the configuration with equal side walls, and 734 Hz with unequal side walls. There are no notable differences in the shape of the acoustic pressure eigenmode in the first 200 mm of the combustor. The two first longitudinal modes are shown in Fig. 8.3. For the 0A1L (first order longitudinal mode, quarter wave mode), the difference in eigenfrequency is larger than for the azimuthal mode: 287 Hz in the configuration with equal side walls,

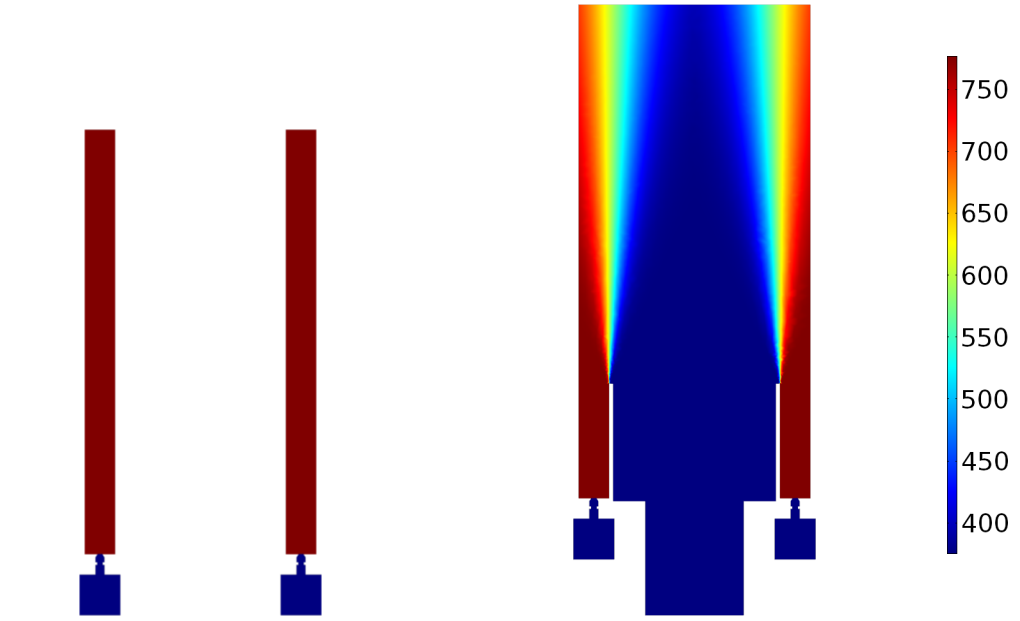

(a) $\bar{c}$ *(*$\mathrm{m\,s^{-1}}$*), equal side walls.* **(b)** $\bar{c}$ *(*$\mathrm{m\,s^{-1}}$*), unequal side walls.*

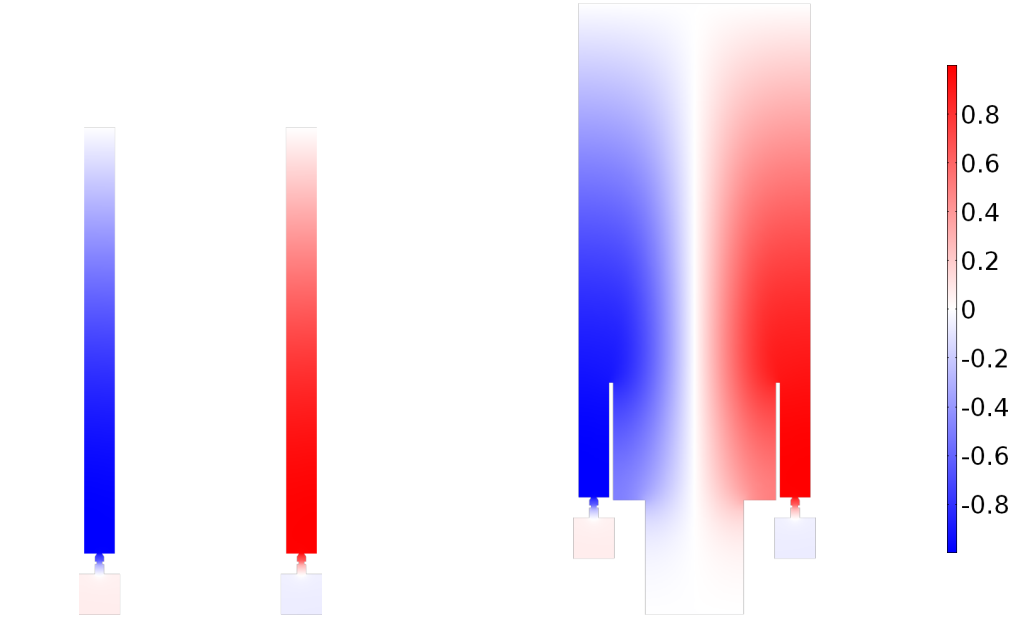

(c) Ψ_{1A1L}*, equal side walls.* **(d)** Ψ_{1A1L} *(*$\mathrm{m\,s^{-1}}$*), unequal side walls.*

Figure 8.2: *Top: sound speed used for the simulations. Bottom: acoustic pressure field corresponding to a 1A1L eigenmode. 2 geometries are considered: on the left, equally long side walls of the same length (*700 mm*); on the right, the unequal side walls (*700 mm *long external wall,* 200 mm *long internal wall) corresponding to the experiments of chapter 9.*

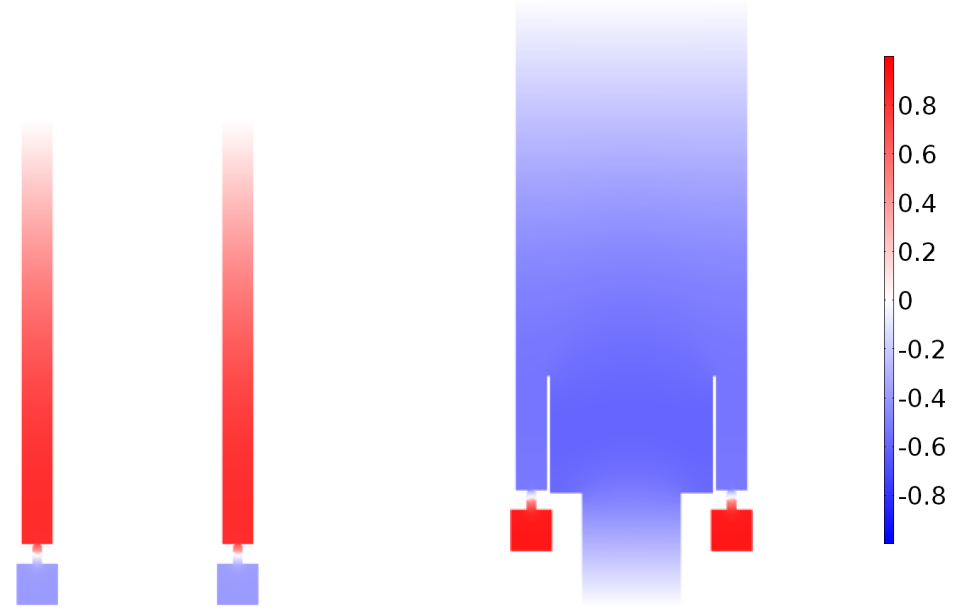

(a) Ψ_{0A1L}, *equal side walls.* **(b)** Ψ_{0A1L} $(\mathrm{m\,s^{-1}})$, *unequal side walls.*

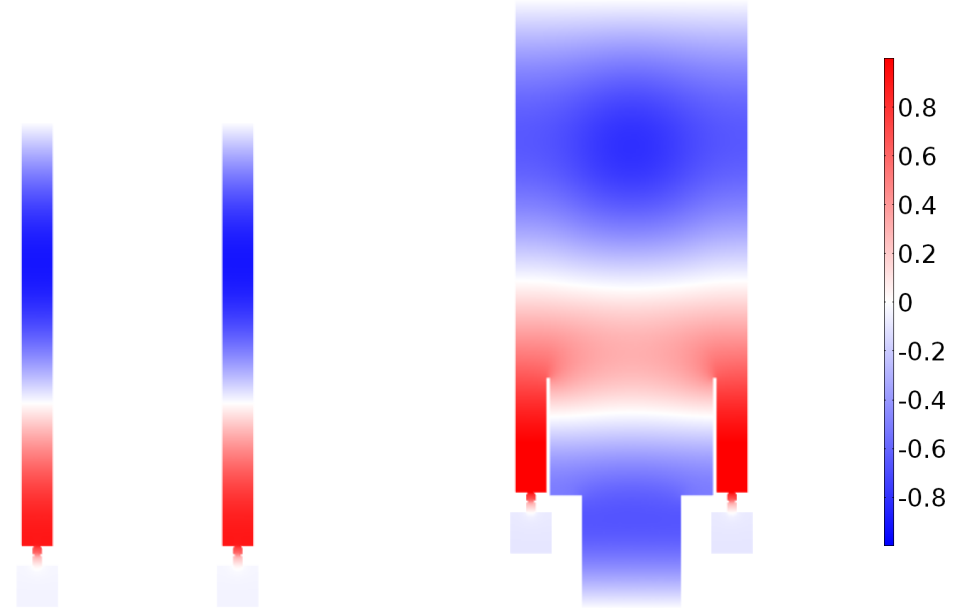

(c) Ψ_{0A3L}, *equal side walls.* **(d)** Ψ_{0A3L} $(\mathrm{m\,s^{-1}})$, *unequal side walls.*

Figure 8.3: *Top: acoustic pressure field corresponding to a 0A1L eigenmode. Bottom: acoustic pressure field corresponding to a 0A3L eigenmode.*

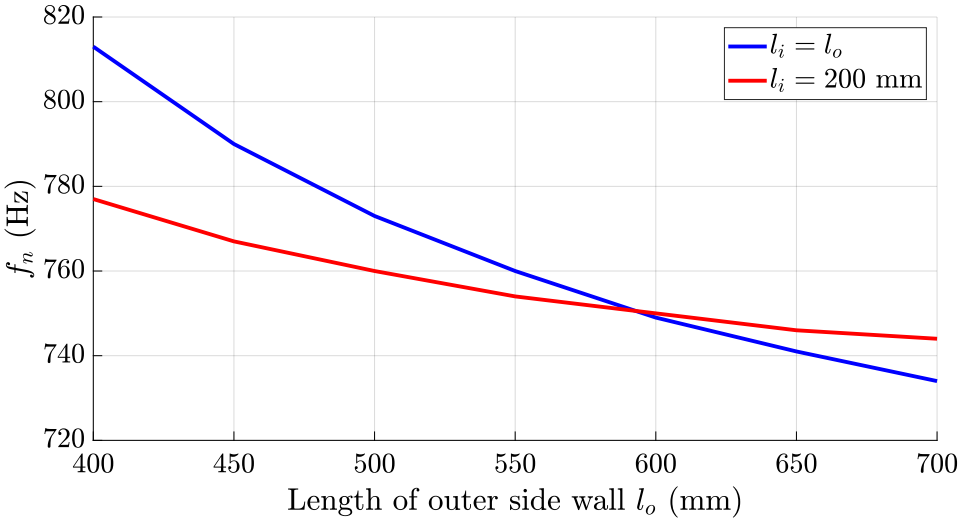

Figure 8.4: *Effect of the length of the combustor on the eigenfrequency of the 1A1L acoustic mode in MICCA. Two cases are shown: for the blue curve, the side walls are of equal; for the red curve, the length l_o of the outer side wall is varied from* 400 mm *to* 700 mm *while the length of the inner side wall is kept constant at* $l_i = 200$ mm.

and 205 Hz with unequal side walls. The difference is even more exacerbated for higher order modes (0A3L, three quarter wave mode): 816 Hz in the configuration with equal side walls, and 600 Hz with unequal side walls.

Another comparison, focused on azimuthal eigenmodes, is carried out in Fig. 8.4. The eigenfrequencies obtained for different lengths l_o of the outer confinement wall are plotted for two cases: in blue, the length of both side walls is identical ($l_i = l_o$), in red, the inner side wall is shorter and its length is kept constant at $l_i = 200$ mm. For $l_o = 400$ mm, these eigenfrequencies are respectively 813 in the equal side wall case and 777 Hz with the shorter inner wall. One observes that the shift in frequency associated with the use of an inner wall which is shorter than the outer wall is more sizable when the length of the outer wall is shorter. For very long confinements, an open-closed annulus behaves similarly to a closed-closed annulus from an acoustic standpoint. Using different length side walls then has a limited impact on the acoustical behavior.

This analysis indicates that the eigenfrequency corresponding to the 1A1L mode is moderately reduced in the unequal side walls geometry. This might perhaps bring this modal frequency in the band of instability and explain the observation that this asymmetric geometry is more favorable to the development of instabilities as observed in MICCA-Spray and in the annular combustor of Worth and Dawson (2017). However the shift in frequency is small and the modal structure in the chamber nearly coincides with that of the equal side walls case. It is possible that the greater propensity to unstable operation might be due to a reduced level of damping associated with the reduced lateral surface damping in the unequal side walls geometry.

8.3 Effect of temperature inhomogeneities

Effects of inhomogeneities in the temperature field are now examined. This is done by solving Eq. 8.3 in the case of an annular combustor with a temperature field featuring azimuthal distortions.

8.3.1 An efficient resolution method

In the present section, for the sake of readability, the notation will be simplified by dropping the index n of the eigenmode: $\Psi_n = \Psi$ and $\omega_n = \omega$. For an annular combustor, that is sufficiently narrow, one may use the mean radius R and recast the differential operator of Eq. (8.3) in the form

$$\frac{1}{R^2}\frac{\partial}{\partial\theta}\left(\bar{c}^2(\theta,z)\,\frac{\partial\Psi}{\partial\theta}(\theta,z)\right)+\frac{\partial}{\partial z}\left(\bar{c}^2(\theta,z)\,\frac{\partial\Psi}{\partial z}(\theta,z)\right)+\omega^2\,\Psi(\theta,z)=0 \tag{8.6}$$

Bourgouin (2014) indicates that, for the first order in azimuth mode, the error in eigenfrequency associated with this approximation is less than 1 % if the ratio d/R is smaller than 0.5. For simplicity, one may consider that the axial variations of sound velocity are negligible. An infinite Fourier series expansion, with coefficient b_m is then used to represent its variation with θ:

$$\bar{c}^2(\theta,z)=\bar{c}^2(\theta)=c_0^2\sum_{m=-\infty}^{+\infty}b_m\,e^{im\theta} \tag{8.7}$$

with $b_0 = 1$, implying that $c_0^2 = \frac{1}{2\pi}\int_0^{2\pi}\bar{c}^2(\theta)d\theta$.

Let us assume that the pressure eigenfunction can also be written in the form of a Fourier series expansion in the θ direction, multiplied by an eigenfunction g in the z direction:

$$\Psi(\theta,z)=f(\theta)\,g(z)=\left(\sum_{k=-\infty}^{+\infty}a_k\,e^{ik\theta}\right)\,g(z) \tag{8.8}$$

Separation of variables is possible:

$$\frac{g''(z)}{g(z)}+\frac{\omega^2}{\bar{c}^2(\theta)}+\frac{1}{R^2}\frac{f''(\theta)}{f(\theta)}+\frac{1}{R^2}\frac{f'(\theta)}{f(\theta)}\frac{(\bar{c}^2)'(\theta)}{\bar{c}^2(\theta)}=0 \tag{8.9}$$

So that $g(z)$ is solution to the standard equation

$$\frac{d^2g}{dz^2}=-k_z^2g \tag{8.10}$$

and f is solution to another differential equation

$$\frac{1}{R^2}\frac{d}{d\theta}\left(\bar{c}^2\,\frac{df}{d\theta}\right)+\left(\omega^2-k_z^2\bar{c}^2\right)\,f=0 \tag{8.11}$$

This may be solved by exapnding f in an azimuthal Fourier series

$$f(\theta) = \sum_k a_k e^{ik\theta} \tag{8.12}$$

One then obtains the following system of equations for the Fourier coefficients of f:

$$\omega^2 \sum_k a_k e^{ik\theta} - \sum_k \sum_m \left[\frac{c_0^2}{R^2} k\,(k+m)\, a_k\, b_m + c_0^2\, k_z^2\, a_k\, b_m \right] e^{i(k+m)\theta} = 0 \tag{8.13}$$

If a finite Fourier series expansion of order M is used, the system can be recast in matrix form and becomes a standard eigenvalue problem that can be solved numerically :

$$\frac{c_0^2}{R^2} \left(\mathcal{D}\mathcal{B}\mathcal{D} + k_z^2 R^2 \mathcal{B} \right) \mathcal{A} = \omega^2 \mathcal{A} \tag{8.14}$$

With $\mathcal{A}$ the $2M+1$ vectors of the Fourier series of Ψ :

$$\mathcal{A} = \begin{pmatrix} a_{-M} \\ \vdots \\ a_0 \\ \vdots \\ a_M \end{pmatrix} \tag{8.15}$$

and the square $2M+1$ matrix $\mathcal{B}$ is a Toeplitz matrix formed by the coefficients of the Fourier series expansion of $\bar{c}^2$:

$$\mathcal{B} = \begin{pmatrix} b_0 & b_{-1} & \dots & b_{1-M} & b_{-M} & 0 & \dots & 0 & 0 \\ b_1 & b_0 & \ddots & b_{2-M} & b_{1-M} & b_{-M} & \ddots & \vdots & \vdots \\ \vdots & b_1 & \ddots & \vdots & \vdots & b_{1-M} & \ddots & 0 & 0 \\ b_{M-1} & \vdots & \ddots & b_0 & b_{-1} & \vdots & \ddots & b_{-M} & 0 \\ b_M & b_{M-1} & \ddots & b_1 & b_0 & b_{-1} & \ddots & b_{1-M} & b_{-M} \\ 0 & b_M & \ddots & \vdots & b_1 & b_0 & \ddots & \vdots & b_{1-M} \\ \vdots & 0 & \ddots & b_{M-1} & \vdots & \vdots & \ddots & b_{-1} & \dots \\ \vdots & \vdots & \ddots & b_M & b_{M-1} & b_{M-2} & \ddots & b_0 & b_{-1} \\ 0 & 0 & \dots & 0 & b_M & b_{M-1} & \dots & b_1 & b_0 \end{pmatrix} \tag{8.16}$$

$\mathcal{D}$ is a $2M+1$ diagonal matrix of diagonal coefficients $\{-M, ..., -1, 0, 1, ..., M\}$:

$$\mathcal{D} = \begin{pmatrix} -M & 0 & \dots & \dots & \dots & \dots & 0 \\ 0 & 1-M & \ddots & & & & \vdots \\ \vdots & \ddots & \ddots & \ddots & & & \vdots \\ \vdots & & \ddots & 0 & \ddots & & \vdots \\ \vdots & & & \ddots & \ddots & \ddots & \vdots \\ \vdots & & & & \ddots & M-1 & 0 \\ 0 & \dots & \dots & \dots & \dots & 0 & M \end{pmatrix} \tag{8.17}$$

8.3.2 Application

Uniform temperature field Let us first consider the special case where the sound velocity is uniform in the combustor: $b_0 = 1$ and $b_m = 0$ for $m \neq 0$. Equation (8.14) translates into

$$\forall\, k \in \mathbb{Z},\ \omega^2 a_k = \frac{k^2 c_0^2}{R^2}\, a_k + c_0^2\, k_z^2\, a_k \tag{8.18}$$

This can only be met if

$$\omega^2 = \frac{k^2 c_0^2}{R^2} + c_0^2 k_z^2 \tag{8.19}$$

In terms of eigenfrequencies, this translates into

$$f_n^2 = n^2 \frac{c_0^2}{\mathcal{P}^2} + c_0^2 \left(\frac{k_z}{2\pi}\right)^2 \tag{8.20}$$

where $\mathcal{P}$ is the perimeter of the annulus. In the case of a rigid-open configuration in the axial direction:

$$\frac{k_z}{2\pi} = (2q-1)\,\frac{1}{4l} \tag{8.21}$$

where q is an integer and l is the length of the annulus in the axial direction. The eigenfrequencies become:

$$f_{nq}^2 = n^2 \frac{c_0^2}{\mathcal{P}^2} + (2q-1)^2 \left(\frac{c_0}{4l}\right)^2 \tag{8.22}$$

and exactly correspond to those of an annular system with uniform temperature.

First order sound velocity field We now consider the case where $b_0 = 1, b_1 = b_{-1} = \varepsilon$, and $\forall\, m \notin \{-1, 0, 1\}\,, b_m = 0$. This translates to

$$\bar{c}^2(\theta) = c_0^2\,(1 + 2\varepsilon \cos\theta) \tag{8.23}$$

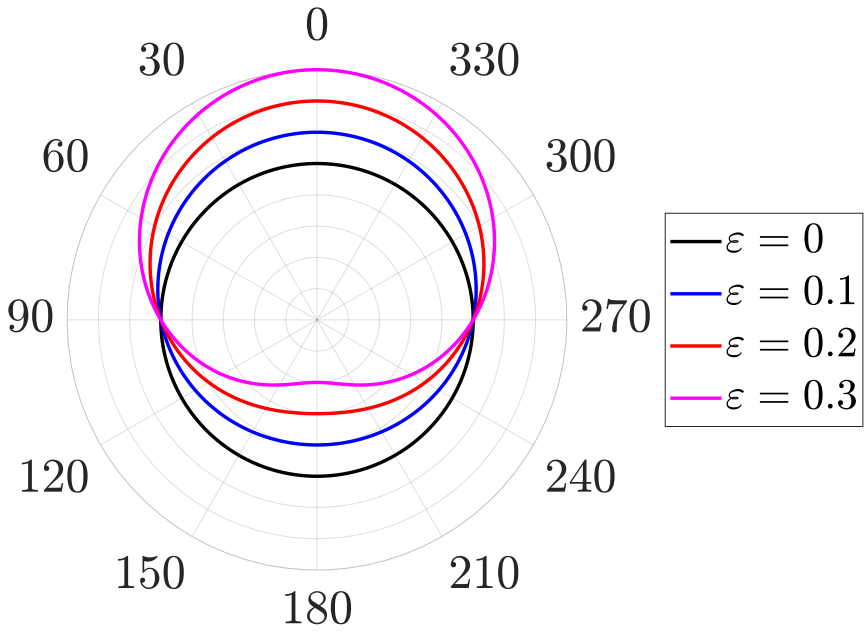

Figure 8.5: *Sound velocity given by* $\bar{c}^2 = c_0^2(1 + 2\varepsilon cos(\theta))$ *for different values of* ε*. 5 circles in radius corresponds to* c_0^2*.*

Figure 8.5 shows the azimuthal shape of the field of $\bar{c}^2$. In a worst case scenario, where some flames within the combustor would be blown-off and the sound velocity field would take on this shape, the minimal sound velocity in the chamber would be that of the fresh unburnt mixture c_u, while the maximal sound velocity would be reached in the burnt gases c_b. c_0 and ε can then be determined as:

$$c_0^2 = \frac{c_u^2 + c_b^2}{2}, \quad \varepsilon = \frac{c_b^2 - c_u^2}{4c_0^2} \tag{8.24}$$

Using this remark, one finds that for a typical flame in MICCA-Spray (heptane-air at an equivalence ratio of $\phi = 1$) $\varepsilon < 0.37$. In the present section, we use $c_0 = 800\,\mathrm{m\,s^{-1}}$, $R = 175\,\mathrm{mm}$ and vary ε between 0 and 0.4. Equation (8.14) becomes a tridiagonal system

$$\omega^2 a_k = \frac{k c_0^2}{R^2}\left\{k a_k + \varepsilon(k-1)a_{k-1} + \varepsilon(k+1)a_{k+1}\right\} + c_0^2\, k_z^2\left\{a_k + \varepsilon\left(a_{k-1} + a_{k+1}\right)\right\} \tag{8.25}$$

Closed-Closed configuration Let us now consider a closed-closed acoustic configuration. In this particular case, we have:

$$\frac{k_z}{2\pi} = \frac{2q}{4l} \tag{8.26}$$

where q, an integer, is the longitudinal order of the mode. Let us consider the case of a purely azimuthal mode, with $q = 0$. Equation (8.14) writes in this case

$$\frac{c_0^2}{R^2}\,\mathcal{D}\mathcal{B}\mathcal{D}\,\mathcal{A} = \omega^2\mathcal{A} \tag{8.27}$$

and the matrix $\mathcal{B}$ is atridiagonal Toeplitz matrix

$$\mathcal{B} = \begin{pmatrix} 1 & \varepsilon & 0 & \dots & 0 \\ \varepsilon & 1 & \ddots & \ddots & \vdots \\ 0 & \ddots & \ddots & \ddots & 0 \\ \vdots & \ddots & \ddots & 1 & \varepsilon \\ 0 & \dots & 0 & \varepsilon & 1 \end{pmatrix} \tag{8.28}$$

A short numerical study is performed to determine the impact of the value of the parameter ε on the eigenfrequencies of the mode and shape of the mode. Figure 8.6 shows the evolution of the frequency of the first four acoustic eigenmodes as a function of ε, in a dotted line for the closed-closed configuration. An increase in the parameter ε leads to a decrease in the eigenfrequencies, although the azimuthal average of $\bar{c}^2$ does not change. Figure 8.7 shows the azimuthal shape of the acoustic eigenmodes for $\varepsilon = 0, 0.1, 0.2$ and 0.3. The pressure distribution becomes asymmetric, with a higher pressure values on the side of the combustor where $\bar{c}^2$ is decreased. The higher order mode appears more sensitive to the deformation of the sound velocity field.

Open-Closed configuration Let us then consider a open-closed acoustic configuration. In this particular case, we have

$$\frac{k_z}{2\pi} = \frac{2q-1}{4l} \tag{8.29}$$

where q, an integer, is the longitudinal order of the mode. Let us consider the first longitudinal mode, with $q = 1$, of higher interest to the MICCA-Spray combustor. For MICCA-Spray, the length of the combustor is $l = 700\,\text{mm}$. An end correction must be taken in account. It was measured by Bourgouin Bourgouin (2014) at $\Delta l = 150\,\text{mm}$, and corresponds to the usual value $\Delta l = 0.4 d_m$ where d_m is the diameter of the combustion chamber. Equation (8.14) writes in this case

$$\frac{c_0^2}{R^2}\left(\mathcal{D}\mathcal{B}\mathcal{D} + \pi^2\frac{R^2}{4\left(l+\Delta l\right)^2}\mathcal{B}\right)\mathcal{A} = \omega^2\mathcal{A} \tag{8.30}$$

And here, matrix $\mathcal{B}$ is the tridiagonal Toeplitz matrix of Eq. (8.28). Again, a short numerical study is performed to determine the impact of the value of the parameter ε on the eigenfrequencies of the mode and shape of the mode. The results are reported as continuous lines in Fig. 8.6 and 8.7. The effect of the parameter ε are the same as in the closed-closed configuration, but they are slightly more pronounced.

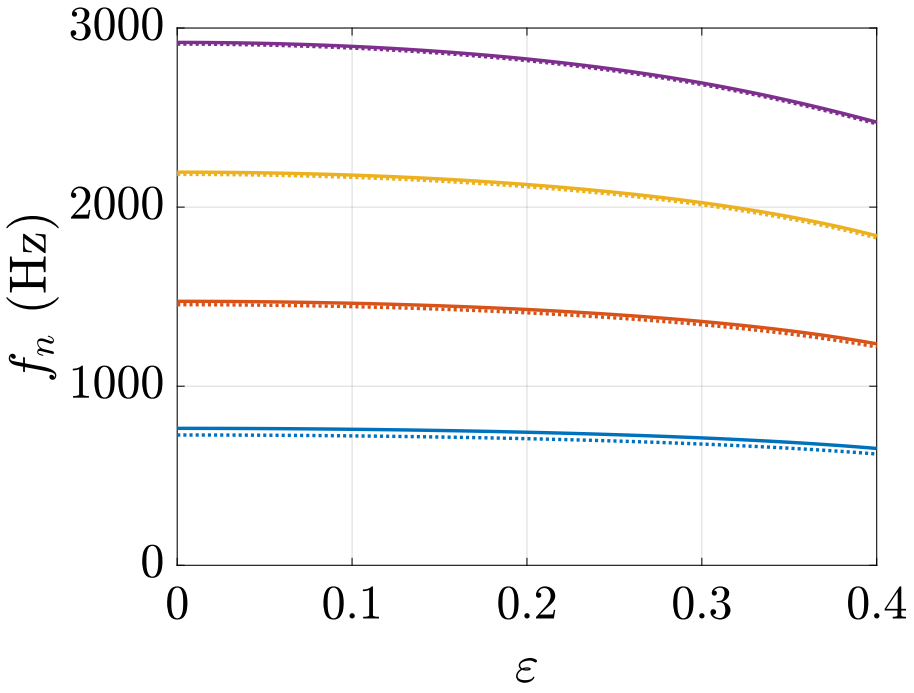

Figure 8.6: *Eigenfrequencies of the first four acoustic eigenmodes of a closed-closed annular cavity with a sound velocity given by* $\bar{c}^2 = c_0^2(1+2\varepsilon cos(\theta))$. *Dotted line: closed-closed configuration (xA0L modes), continuous line: open-closed configuration (xA1L modes).*

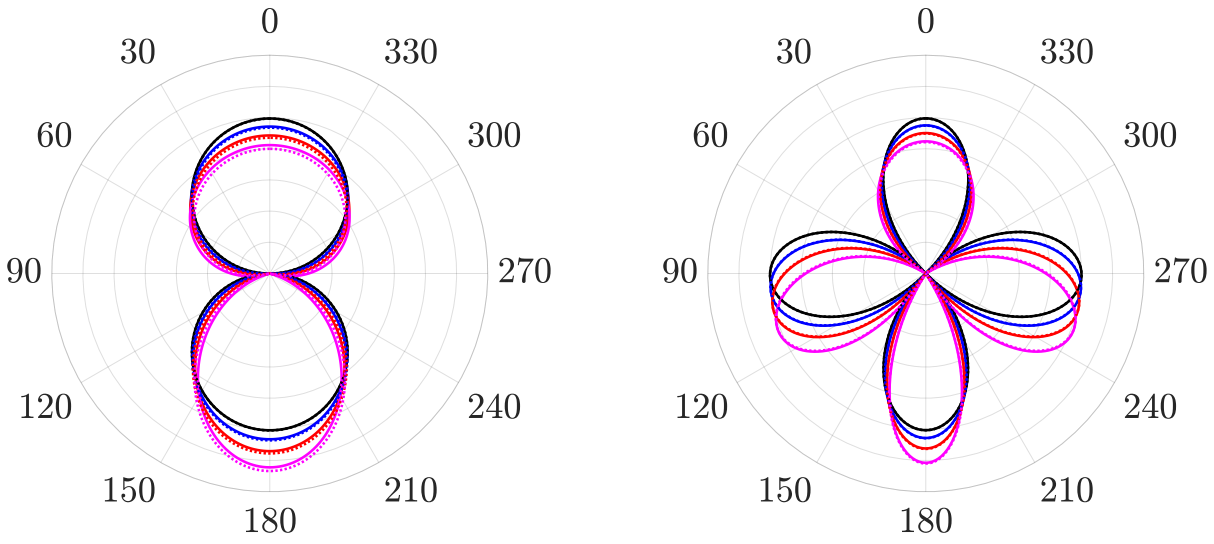

Figure 8.7: *Mode shape of the 1AxL (left) and 2AxL (right) acoustic eigenmodes with the pressure fields presented in Fig. 8.5. Dotted line: closed-closed configuration (xA0L modes), continuous line: open-closed configuration (xA1L modes).*

Table 8.1: *Geometrical dimensions used for the COMSOL Multiphysics simulations.*

	Closed-Closed	Open-Closed
Length l	200 mm	850 mm
Inner radius R_i	150 mm	150 mm
Outer radius R_o	200 mm	200 mm
$\Psi(\theta, z = 0)$	Rigid wall	Rigid wall
$\Psi(\theta, z = l)$	Rigid wall	$\Psi(\theta, z = l) = 0$

Validation against a Helmholtz solver In order to validate the methodology presented in this section 8.3.2, 3D simulation are performed with the Helmholtz solver COMSOL Multiphysics. Both the closed-closed, and the open-closed configurations are considered. The geometry is that of Fig. 8 (see Introduction of the thesis). The dimensions and boundary conditions are given in Tab. 8.1.

A parametric sweep is performed on ε, and the eigenfrequencies computed with COMSOL, and the eigenfrequencies computed using the method presented in this chapter (numerically solving for Eq. (8.27) and Eq. (8.30)) are compared. The comparison between the two methods is quite favorable, the difference between the methods being at most 0.4%. This confirms, in particular, that dropping the radial dependence to write Eq. (8.6) is acceptable.

8.4 Determination of acoustic damping in MICCA-Spray

The present section focuses on an operating point where a stochastic limit cycle oscillation, coupled by a longitudinal acoustic mode, is observed in MICCA-Spray. This limit cycle is characterized by a mean amplitude of oscillation with random fluctuations around this mean value. Other types of oscillation in the annular chamber are described in chapter 9. The objective of the present investigation is to get an estimate of the damping rate inside this device. This is important because the damping rate intervenes in the stability analysis of the system. If the gain exceeds the damping rate then the system is unstable. The damping rate also enters in the energy balance that governs the amplitude level when the system has reached a limit cycle. It is however not easy to obtain the value of this parameter. One possibility which has been employed in some previous studies at EM2C consisted in measuring the resonance curve of the device under investigation (Palies et al. (2011)). The measure of the width at half maximum of the resonance curve Δf gives access to the quality factor $Q = f/\Delta f$ and this may be related to the damping rate by assuming that the device behaves like a second order system. There are however difficulties in applying this method to a system under hot fire conditions because the flame itself has a gain and what is being measured is an apparent damping rate that represents the difference between the damping rate and the gain of the flame.

Two methods are explored in the present chapter. The first relies on the acoustic energy balance equation. The second is founded on a system identification procedure put forward

in a recent article by Boujo et al. (2016). Because the two methods are quite different it is interesting to compare their results and see if they match. If this is the case one may then use the results with more confidence.

It is interesting at this point to consider the acoustic energy balance (Durox et al. (2009)) and integrate this balance over the volume of the annular combustor:

$$\frac{d\langle E\rangle}{dt} = \langle S\rangle - \langle D\rangle - \int_{\Sigma} \boldsymbol{F}\cdot\boldsymbol{n}dA \tag{8.31}$$

In this expression $\langle E\rangle$ designates the acoustic energy averaged over a period and integrated over the volume of the system, $\boldsymbol{F}$ the acoustic flux, averaged over a period and here integrated over the system's boundary Σ, $\langle S\rangle$ the thermoacoustic source term, and $\langle D\rangle$ the acoustic damping, both averaged over a period and integrated over the volume of the system. The thermoacoustic source term can be estimated using combined pressure and flame chemiluminescence measurements by assuming that the flame is compact with respect to the acoustic wavelength. The acoustic losses corresponding to damping and to outgoing acoustic fluxes

$$\langle D\rangle + \int_{\Sigma} \boldsymbol{F}\cdot\boldsymbol{n}dA \tag{8.32}$$

must be known in order to determine the stability limits of the system.

After introducing the experimental setup and briefly characterizing the thermoacoustic oscillations under consideration, two methods are explored to obtain estimates of the acoustic losses within the system. The damping rates that can be deduced from these two methods are then compared.

8.4.1 Experimental setup

Experiments are carried out in the MICCA-Spray annular combustor equipped with sixteen spray swirl injectors. The confinement walls are made of quartz to allow optical access to the flames. The configuration is quite similar to that used in chapter 9: the inner confinement tube is 200 mm long while the outer tube is 700 mm high. Its upper section is a steel tube for practical design considerations. The injectors equipped with swirler 716 are mounted so that their outlet is flush with the backplane of the combustor. The liquid fuel, in the present experiments n-heptane, is injected as a hollow cone spray by the fuel atomizer. Its outlet is set 7 mm in recess with respect to the backplane of the combustor.

The test rig is equipped with an array of eight equally spaced microphones MCx. They are placed on 25 m long waveguides which are plugged to the combustor backplane. The microphones are located at 170 mm from the dump plane, and this mounting system induces a time lag of $\tau_{m-b} = 0.46$ ms. An array of eight photomultipliers (PMx) equipped with optical pass-band filters centered at the wavelength 308 nm are also used in these

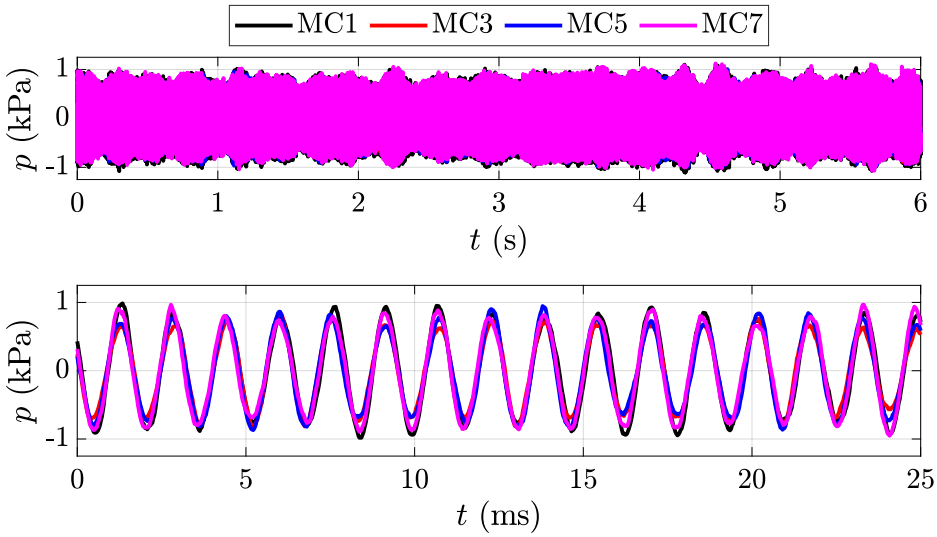

Figure 8.8: *Temporal evolution of the pressure signal from microphones MC1, MC3, MC5 and MC7.*

experiments. A spatial filter assures that each PM only captures the light emitted by a single flame within the combustor. All signals are acquired at a sampling frequency of 32 768 Hz. A K-type thermocouple placed in-between two injectors, 36 mm above the backplane, on the outer wall of the combustion chamber, provides a measure of the wall temperature T_{wall}.

8.4.2 Longitudinal thermoacoustic oscillations

The data presented in this study were obtained while the combustor was operated at a thermal power $\mathcal{P} = 114\,\text{kW}$, with a global equivalence ratio of $\phi = 1.0$, and a bulk injection velocity of $u_b = 37\,\text{m}\,\text{s}^{-1}$. The pressure signals measured by microphones MC1, MC3, MC5 and MC7 are shown in Fig. 8.8. The pressure traces are typical of thermoacoustic oscillations coupled by a longitudinal acoustic mode. The stochastic limit cycle features a mean amplitude of 510 Pa (RMS).

Figure 8.9 shows the power spectral densities of the pressure signals recorded by microphones MC1, MC3, MC5 and MC7. All have a strong peak at 640 Hz. A second peak arises at 750 Hz. It is 20 dB lower in amplitude than the main peak. All other peaks in the spectrum are smaller than the secondary peak by at least 15 dB. The frequency of the main peak corresponds to that of the three quarter wave mode of the combustion chamber (0A3L): $f_{0A3L} = 3c/(4(L + \Delta L)) \approx 657\,\text{Hz}$ with c the speed of sound (evaluated here for a gas temperature of 1400 K), $L = 700\,\text{mm}$ the length of the confinement tube and $\Delta L = 150\,\text{mm}$ corresponds to an end correction (measured experimentally in Bourgouin (2014)). This estimate is confirmed by the 3D COMSOL simulations shown in Fig. 8.3. The frequency of the secondary peak corresponds to that of the first azimuthal first longitudinal mode (1A1L): $f_{1A1L}^2 = (c/\mathcal{P})^2 + (c/(4(L+\Delta L)))^2$, so that $f_{1A1L} \approx 721\,\text{Hz}$.

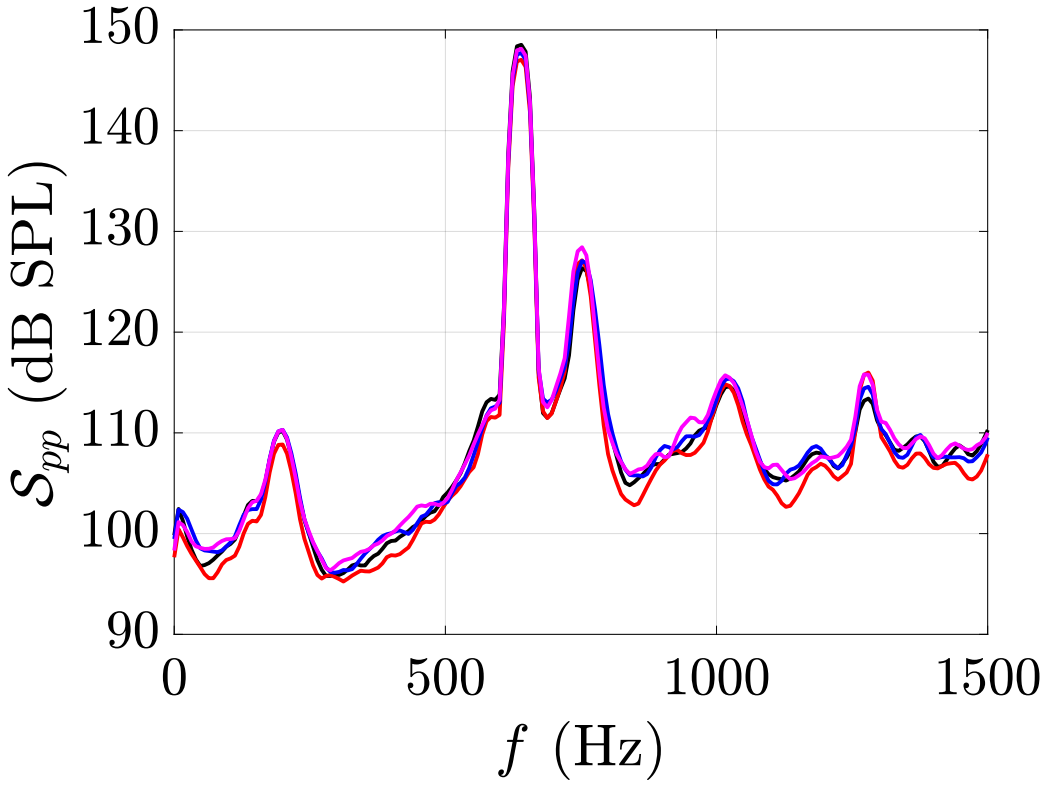

Figure 8.9: *Power spectral density of the pressure signal from microphones MC1, MC3, MC5 and MC7. The Welch method is used, with a flat top window, an overlap of* 50% *and a total recorded duration of* 6.2 s*. The frequency resolution is* 8 Hz*. Legend is identical to Fig. 8.8.*

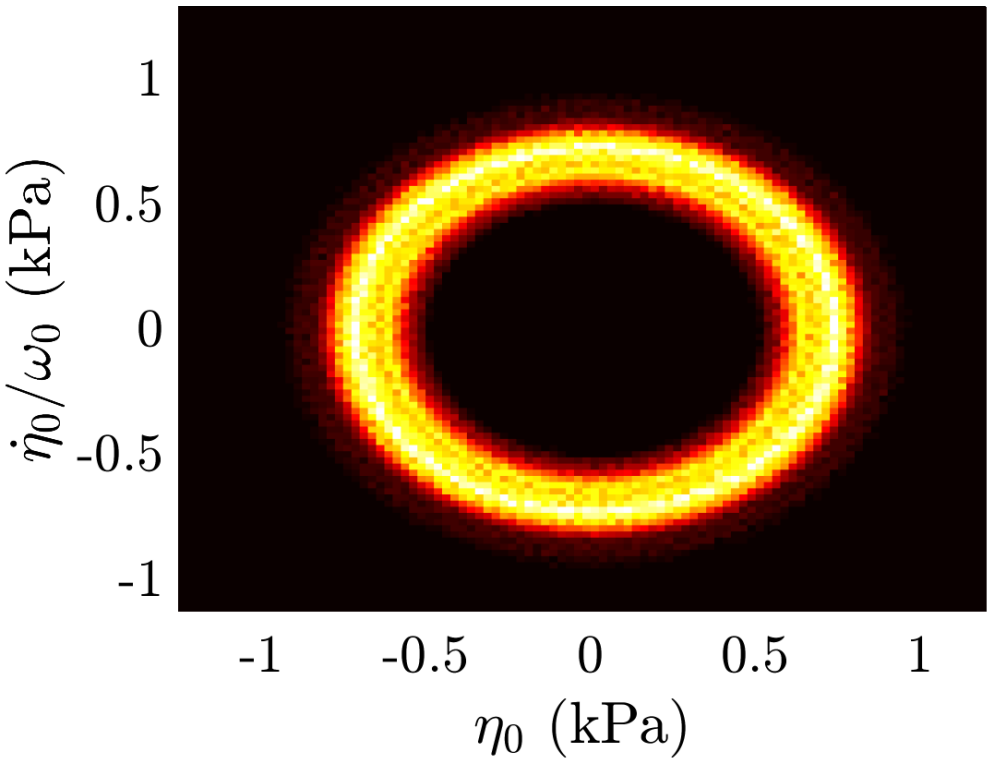

Figure 8.10: *Bivariate probability density function of η_0 and $\dot{\eta}_0/\omega_0$. White indicates a high probability while black indicates a zero probability. This shape is characteristic of a stochastic limit cycle exhibiting random fluctuations around a mean value Noiray and Schuermans (2013a).*

This identification based on the frequency is confirmed when reconstructing the acoustic field in terms of longitudinal and azimuthal components, using the method described in chapter 9. The acoustic pressure is written as the sum of waves travelling in the counterclockwise and clockwise directions

$$p(\theta, t) = \sum_{m=-1}^{1} \exp(im\theta)\, \eta_m(t) \tag{8.33}$$

The longitudinal component η_0 is a harmonic signal at frequency $f_0 = 640\,\text{Hz}$, the clockwise and counter-clockwise, first order in azimuth spinning components, η_1 and η_{-1} have a peak at 752 Hz. Figure 8.10 shows the joint probability density of η_0 and its time derivative $\dot{\eta}_0/\omega_0$. The gaussian ring shape obtained in this way is characteristic of a limit cycle oscillation with superimposed stochastic forcing caused by turbulent combustion Noiray and Schuermans (2013a).

8.4.3 Estimation of the acoustic losses using an acoustic energy balance

Although the flame dynamics is nonlinear, it is reasonable to assume that damping is linear Eq. (8.31) and can be taken to be proportional to the acoustic energy integrated over the volume (Durox et al. (2009)):

$$\frac{d\langle E\rangle}{dt} = \langle S\rangle - 2\xi\omega_0\langle E\rangle \tag{8.34}$$

where ξ is the damping factor of the system, including the acoustic fluxes across the boundaries. Given the limit cycle nature of the oscillation, the acoustic energy density integrated over a period of oscillation can be simplified as

$$E = \frac{1}{2}\frac{p_{rms}^2}{\rho_0 c^2} + \frac{1}{2}\rho_0 v_{rms}^2 \tag{8.35}$$

where p_{rms} and v_{rms} are the local RMS amplitudes of the acoustic pressure and velocities inside the volume. In the present case, the spatial pressure and velocity distributions correspond to the three quarter wave longitudinal mode. This energy density may be integrated over the volume of the chamber $V = \pi(L + \Delta L)(r_o^2 - r_i^2)$ where r_o and r_i designate the outer and inner radii of the annulus. One obtains

$$\langle E\rangle = \frac{|\eta_0|^2 V}{4\rho_0 c^2} = \frac{|\eta_0|^2 V}{4\gamma p_0} \tag{8.36}$$

where γ is the specific heat ratio and p_0 the pressure in the chamber which is very close to the ambient pressure. The thermoacoustic "Rayleigh" source term appearing in the integrated acoustic energy balance writes

$$\langle S\rangle = \frac{\gamma - 1}{\rho_0 c^2}\frac{1}{T}\int_T\int_V p\dot{q}' dV dt \tag{8.37}$$

with T the period of the oscillation, p the acoustic pressure and $\dot{q}'$ the unsteady volumetric heat release rate. In a compact flame framework, if an individual flame is considered, and assuming that the acoustic pressure does not change much in a control volume encompassing that flame

$$\int_T\int_{flame\,volume} S\, dV = \frac{\gamma - 1}{\gamma}\dot{Q}_0\frac{1}{T}\int_T \frac{p}{p_0}\frac{\dot{Q}'}{\dot{Q}_0}\, dt \tag{8.38}$$

with p_0 the ambient pressure, $\dot{Q}_0$ the mean heat release rate of the flame, and $\dot{Q}'$ the unsteady heat release rate of the flame. In practice, the instantaneous source term for a given flame is computed at each instant as

$$S_{flame} = \frac{\gamma - 1}{\gamma}\dot{Q}_0\,\frac{1}{2}\mathcal{R}\left(\mathcal{H}\left[\frac{p}{p_0}\right]\mathcal{H}\left[\frac{\dot{Q}'}{\dot{Q}_0}\right]^*\right) \tag{8.39}$$

$\mathcal{R}$ being the real part function, $\mathcal{H}$ the analytical signal (obtained by means of a Hilbert transform) and * the complex conjugate. The mean heat release per unit time $\dot{Q}_0$ is obtained from the fuel flow rate, assuming a 100% combustion efficiency, p/p_0 is reconstructed from the microphone measurements using the method described in chapter 9, and $\dot{Q}'/\dot{Q}_0$ is taken as the ratio between the unsteady signal from a photomultiplier and its mean value. $\langle S \rangle$, the overall acoustic source term in the combustor is taken as twice the sum of the eight individual flame contributions measured by the eight photomultipliers. The overall damping term can then be evaluated as

$$\overline{\langle D \rangle} + \int_\Sigma \overline{\boldsymbol{F}} \cdot \boldsymbol{n}\, dA = \overline{\langle S \rangle} - \frac{V}{4\gamma p_0} \overline{\frac{d|\eta_0|^2}{dt}} \tag{8.40}$$

The numerical value yields $\overline{\langle S \rangle} = 23.2\,\mathrm{W}$ so that:

$$\overline{\langle D \rangle} + \int_\Sigma \overline{F} \cdot n\, dA = 23.2\,\mathrm{W} \tag{8.41}$$

The second term on the right hand side of Eq. (8.40) is negligible, being three orders of magnitude smaller than the "Rayleigh" source term. The damping factor can then be evaluated and is found to be

$$\xi = \overline{\langle S \rangle}/(2\omega_0 \overline{\langle E \rangle}) = 59\,10^{-3} \tag{8.42}$$

The stochastic nature of the limit cycle only has a limited impact on the acoustic energy balance in the present case.

8.4.4 Estimation of the acoustic losses using system identification

It is now interesting to exploit a second method to determine the damping rate. This is based on ideas developed by Boujo et al. (2016) and relies on a system identification procedure. In the present situation, the acoustic pressure is formed by a single mode, identified as the 0A3L acoustic mode. One then assumes that the amplitude η_0 corresponds to the output of a forced, damped harmonic oscillator governed by an equation of the form

$$\ddot{\eta_0} + 2\xi\omega_0\dot{\eta_0} + \omega_0^2\eta_0 = \beta\dot{Q} \tag{8.43}$$

where $\omega_0/2\pi$ is the natural angular frequency of the mode, ξ is a positive factor representing the damping rate accounting for losses at the boundaries and volumetric damping, and $\beta\dot{Q}$ is the thermoacoustic forcing term caused by the unsteady heat release of the flames. The method of Boujo et al. (2016) consists in evaluating the damping term ξ by fitting the acoustic transfer function of the system to the model equation (8.43)

$$H(s) = \frac{\hat{\eta_0}(s)}{\hat{\dot{Q}}(s)} = \frac{\beta}{s^2 + 2\xi\omega_0 s + \omega_0^2} \tag{8.44}$$

with s the Laplace variable, and $\hat{\eta_0}$ designates the Laplace transform of η_0. By fitting the experimentally measured transfer function, and identifying the pole λ associated with the frequency of the thermoacoustic oscillation, the damping coefficient ξ can be estimated as $\xi \approx -\mathcal{R}(\lambda)/\mathcal{I}(\lambda)$.

In principle, the transfer function linking the pressure fluctuation to the heat release rate may be deduced from power and cross-power spectral densities. The standard method consists in forming the ratio of the cross power spectral density $\mathcal{S}_{\dot{Q}\eta_0}$ and dividing this quantity by the power spectral density of the input $\mathcal{S}_{\dot{Q}\dot{Q}}$. The transfer function is then be given by

$$H(f) = \mathcal{S}_{\eta_0\dot{Q}}/\mathcal{S}_{\eta_0\eta_0} \tag{8.45}$$

It is however proposed by Boujo et al. (2016) to use other expressions, among which one formed by the ratio of the power spectral density of the output by the cross spectral density of the output and input

$$H_m(f) = \mathcal{S}_{\eta_0\eta_0}/\mathcal{S}_{\eta_0\dot{Q}} \tag{8.46}$$

It is argued by Boujo et al. (2016) that these two expressions are identical. The presence of the power spectral density of the pressure in the numerator in Eq. (8.46) might perhaps allow a better extraction of the acoustic modes of oscillation of the system. However, the equivalence of expressions (8.46) and (8.45) may require some additional conditions and the first expression (8.45) is adopted in what follows.

Now the cross-power spectral density $\mathcal{S}_{xy}$ of x and y is obtained by making use of Welch's method of periodograms and applying a Blackman-Harris window of 2048 samples, and an overlap of 50%, yielding a frequency resolution of 16 Hz. The duration of the signal is 6.2 s. In the present study, given the available length of the time record, good statistical convergence was favored over frequency resolution. The amplitude of the acoustic mode η_0 is obtained by averaging the signals from all eight chamber microphones MCx. The unsteady heat release rate of the flames is taken as twice the sum of all eight photomultiplier signals.

This experimentally measured transfer function can be fitted with an ARMA (auto regressive moving average) transfer function comprising 15 poles and 15 zeros. The gain and phase of the measured transfer function and its fit are shown in Fig. 8.11. The fitted and measured transfer function are in good overall agreement, both in terms of phase and gain. One may then examine the poles and zeros of the fitted transfer function plotted in the complex plane in Fig. 8.12. Two pairs of conjugate poles $\lambda_1 = -265 \pm 3856i$ and $\lambda_2 = -50 \pm 4309i$ are close in frequency to the thermoacoustic oscillation being studied. As suggested by Boujo et al. (2016), the pole with the highest damping is retained, and it is then possible to estimate the damping rate $\xi \simeq 265/3856 = 69\,10^{-3}$. This value does not exactly match that obtained previously using the acoustic energy balance but it is sufficiently close to gain confidence in this estimate of the damping coefficient.

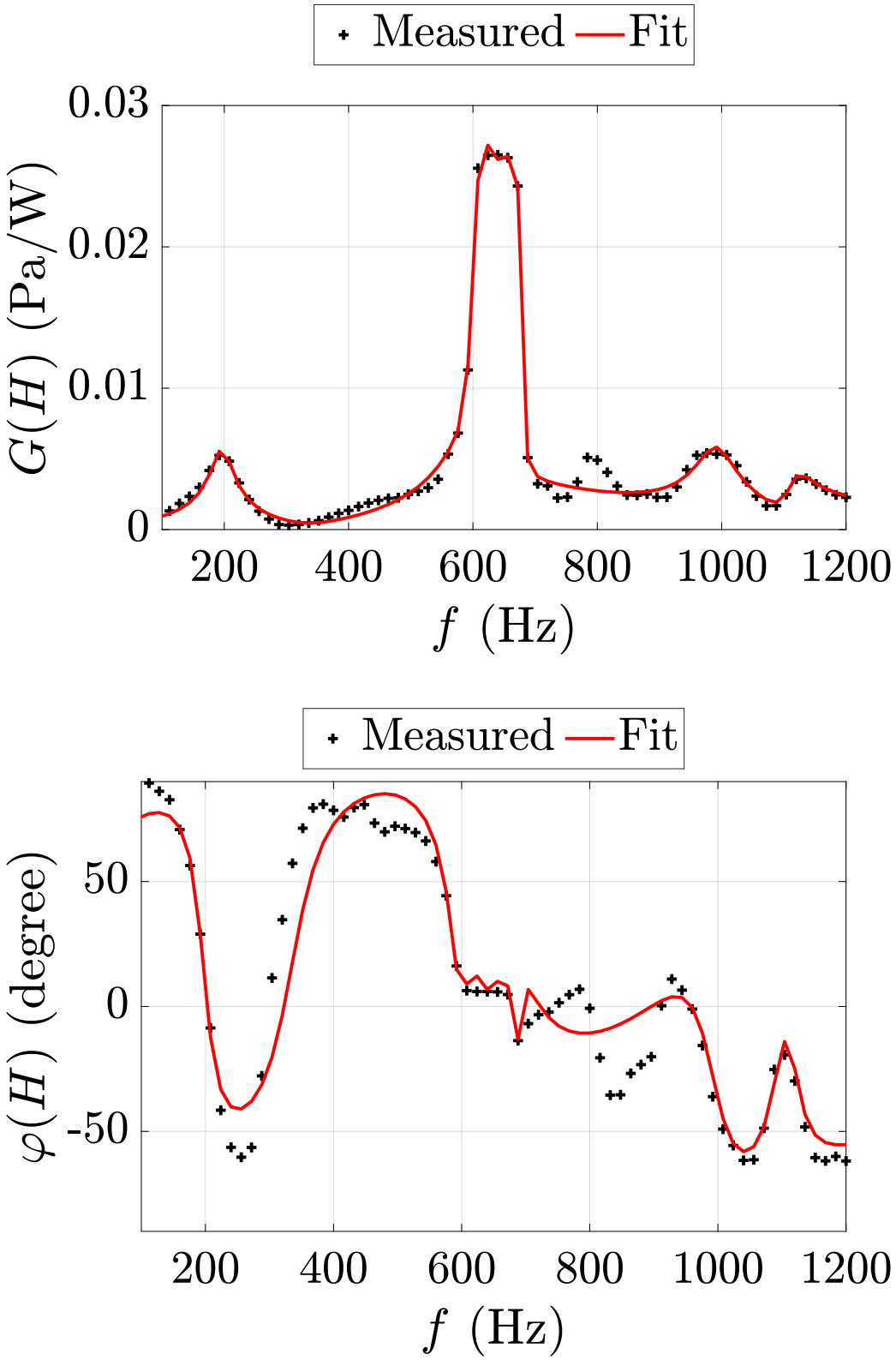

Figure 8.11: *Gain (upper) and phase (lower) of the experimentally measured acoustic transfer function H (in black) and its fit (in red).*

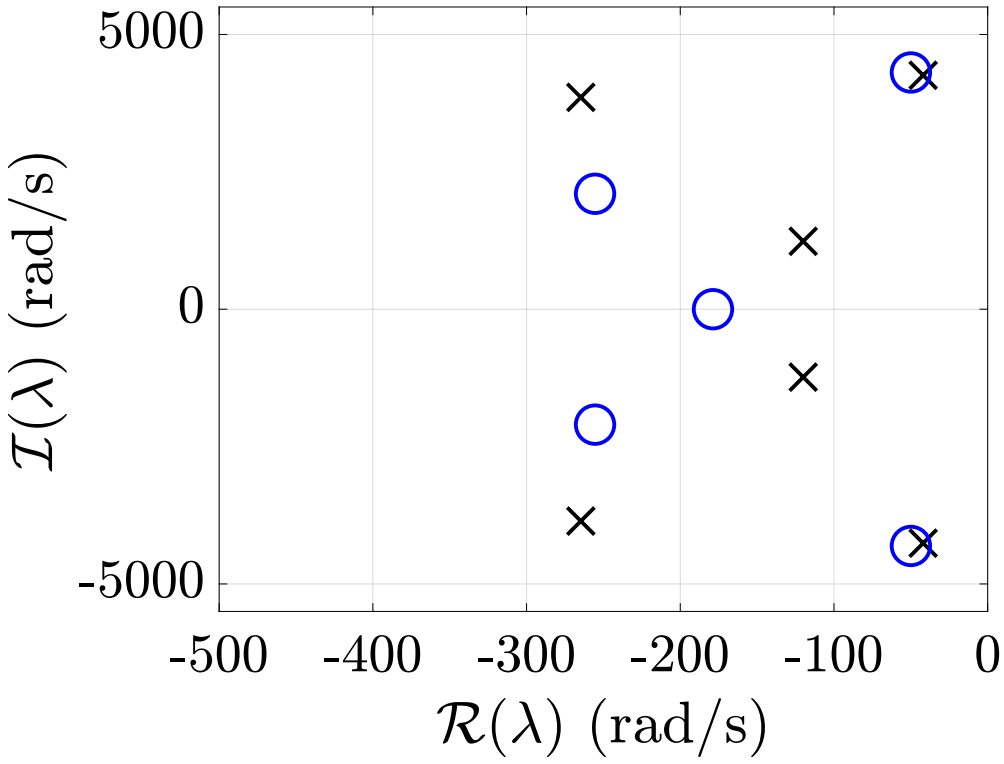

Figure 8.12: *Poles (black crosses) and zeros (blue circles) of the fitted transfer function in the frequency range of interest. These poles and zeros are shown in the complex plane.*

8.5 Conclusion

The structure of the acoustic eigenmodes and the corresponding eigenfrequancies play a key role in combustion instability analysis. This chapter considers three issues of direct interest to the annular combustor MICCA-Spray. A first analysis of the effect of using unequal side walls indicates that this geometry does not significantly change the 1A1L modal structure and only brings a moderate reduction in the corresponding eigenfrequency. It is then inferred that the greater propensity of the unequal side wall geometry to develop instability might be sought in other effects and might perhaps be linked to a reduced damping rate associated with the reduction in solid surface area. The effect of azimuthal inhomogeneities in the temperature field on acoustic eigenmodes is investigated in a second stage. A computationally efficient method is developed to obtain the acoustic eigenstructure and validated with respect to a direct numerical solution with a Helholtz solver.For a constant value of the mean temperature in the annulus, increasing the level temperature inhomogeneities leads to a decrease in the acoustic eigenfrequency and to a distortion of the acoustic field. These findings are useful in the analysis of very high amplitude instabilities which lead to a partial flame extinction in the annular combustor and subsequent development of a nonuniform temperature distribution near the combustor backplane. The third item covered in this chapter pertains to the determination of the damping rate in MICCA-Spray. Estimates of this important quantity are obtained by making use of signals recorded during instability experiments in which combustion is coupled by a longitudinal acoustic mode. A first method relies on the balance of acoustic energy in the system while the second uses a system identification procedure. The two methods yield similar results increasing the degree of confidence in the estimates obtained for this important parameter.

Chapter 9

High amplitude combustion instabilities in MICCA-Spray inducing pressure field deformation and flame blow off

Experiments carried out on the MICCA-Spray annular combustor equipped with 716 swirler and two concentric cylindrical quartz tubes of unequal length are reported. Injector 716 is experimentally characterized. For a wide range of operating conditions, strong combustion instabilities are observed, but the focus of this chapter is placed on very high amplitude combustion instabilities coupled by a standing azimuthal mode. New results are obtained using a higher order reconstruction method for the pressure field: its shape is shown to be modified during high amplitude oscillation, leading to asymmetries of the pressure distribution in the system. Flame blow off occurs near the pressure nodal line when a critical level of oscillation is reached. A method is proposed to reconstruct the acoustic velocity field just before blow off occurs and in this way determine the blow off threshold. It is found that the pressure distribution, velocity field and blow off pattern become asymmetric as the amplitude of oscillation increases and that this process is accompanied by a rapid shift in frequency of oscillation. Another notable result is that the heat release rate in the flames on the same side of the nodal line are not perfectly in phase and that the phase differences become larger as the amplitude of oscillation increases.

Contents

This chapter reproduces an article published in the Journal of Engineering for Gas Turbines and Power 142(1) in January 2020 as "High Amplitude Combustion Instabilities in an Annular Combustor Inducing Pressure Field Deformation and Flame Blow Off" by Guillaume Vignat, Daniel Durox, Antoine Renaud and Sébastien Candel.

9.1 Introduction

New regulations concerning the pollutant emission of aero-engines are pushing manufacturers towards new combustor designs. Burning fuel in a lean, premixed, prevaporized mode has been shown to reduce emissions of harmful nitrogen oxides and soot particles (Lefebvre and Ballal (2010)). Swirling injectors are most often adopted to ensure aerodynamic flame stabilization at a distance from boundaries. However, these technological choices lead to a more compact flame, they increase the power density, and reduce the acoustic damping, all factors promoting combustion instabilities.

A large body of research has been dedicated to the investigation, analysis and modeling of the dynamics of swirling flames inside simple combustion systems, and is well summed up in recent reviews: Poinsot (2017); Candel et al. (2012); Candel et al. (2014). The mechanisms involved are fairly complex and interlinked: flow instabilities, equivalence ratio and turbulence fluctuation downstream of an injector will induce fluctuations in the heat release rate of the flame. This unsteady heat release rate constitutes an acoustic source. It will also generate entropy waves. These sources will feed a resonant mode of the system and pressure fluctuation in the chamber will ensue. If one of these modes feeds back perturbations to the flames, it may eventually give rise to oscillations at a frequency that is close to that of the so-called coupling mode. If the process becomes self-sustained one can say that it results from an azimuthal mode coupling when the acoustic mode involved features an azimuthal structure.

Within gas turbine combustors a further degree of complexity is introduced. The combustion chamber in these systems is often annular. The greatest physical dimension of the chamber is then its perimeter, and combustion-acoustic coupling by the first azimuthal acoustic eigenmode of the chamber can occur. These azimuthal combustion instabilities have been observed in the two laboratory-scale annular test rigs investigated in the literature, MICCA at EM2C laboratory (Bourgouin et al. (2015b); Prieur et al. (2017b)), and the annular rig of the team of Dawson and Worth at Cambridge and later at NTNU (Worth and Dawson (2013a); Worth et al. (2017b)). This kind of coupling was also widely

observed in practical gas turbine applications (Krebs et al. (2002); Noiray and Schuermans (2013b); Bothien et al. (2013)). It has been shown that large eddy simulations (LES) could be used to retrieve azimuthally coupled thermoacoustic oscillations in industrial systems (Wolf et al. (2012); Wolf et al. (2012); Staffelbach et al. (2009)). These experimental and numerical studies have shown the existence of several degenerate acoustic modes by which coupling can occur: standing, clockwise or counterclockwise spinning, slanted. This behavior is conveniently characterized by the spin ratio (Bourgouin et al. (2015b); Prieur et al. (2017b); Mazur et al. (2019)), or by plotting the joint probability density function of the amplitude of the clockwise and counterclockwise spinning acoustic components (Mazur et al. (2019); Worth and Dawson (2013b)). Another characteristic present in all the aforementioned studies featuring swirling injection systems is the intermitent behavior of the resonant mode involving a growth and a decay of the oscillations, as well as switching between spinning and standing modal dynamics.

Compared to longitudinally coupled combustion instabilities, the modeling of such azimuthally coupled systems presents numerous challenges. Reduced order models, either in the form of acoustic network models (Bauerheim et al. (2015); Bauerheim et al. (2014); Bourgouin et al. (2015b); Ghirardo and Juniper (2013); Orchini et al. (2019); Moeck et al. (2019)) or Helmholtz solvers (Laera et al. (2017); Laera et al. (2017); Mensah et al. (2019)), have been used. Both approaches retrieve limit-cycle instabilities observed in the laminar, matrix burner version of the MICCA rig (Bourgouin et al. (2015b); Laera et al. (2017); Orchini et al. (2019); Moeck et al. (2019)), but more complex configurations remain a challenge. This modeling work requires an a-priori knowledge of the flame response, usually in the form of a flame describing function (FDF). Its determination may be done by acoustically forcing a flame. In annular burners, especially near the natural frequency of the annulus, this remains a challenge (Worth et al. (2017b)). Usually, a single injector system is used to measure the FDF subject to the assumption that the flames in both systems have the same response. As combustion instabilities are quite sensitive to small changes in flame response as shown analytically by Juniper and Sujith (2018) and also with LES by Bauerheim et al. (2015), a number of parameters, each having a potentially large influence on the flame response, have to be carefully controlled: confinement configuration (Fanaca et al. (2010); De Rosa et al. (2015)), wall temperature (Prieur et al. (2017b); Bonciolini et al. (2019)), injector geometry (Durox et al. (2013); Bourgouin et al. (2013)). In a compact flame framework, the response of a flame at a pressure antinode can be modeled using an experimentally determined FDF. This requires measuring the flowrate perturbation of the injector, or alternatively, determining its acoustic impedance. However, flames submitted to transverse velocity perturbation, near the pressure nodal line, have a very different response in the non-linear regime, a topic reviewed by O'Connor et al. (2015). Small variations in flame response, as well as symmetry breaking features also need to be considered, in particular to capture the spinning or standing nature of the mode (Juniper and Sujith (2018); Bauerheim et al. (2014); Bauerheim et al. (2016); Ghirardo and Juniper (2013); Bauerheim et al. (2015)).

Ghirardo and Juniper (2013) show for example that annular systems featuring large transverse velocity fluctuations favor standing acoustic modes by taking into account the effect

of these velocity fluctuations in their model. This is coherent with experiments presented by Prieur et al. (2017b), where standing acoustic modes appear preferentially when the amplitude reached by the oscillation is high. Additionally, this previous study carried out on the MICCA-Spray configuration indicates that upon reaching a certain value, flame blow off is observed near the pressure nodal line. This behavior is also found by Baillot and Lespinasse (2014) in a transversally forced geometry.

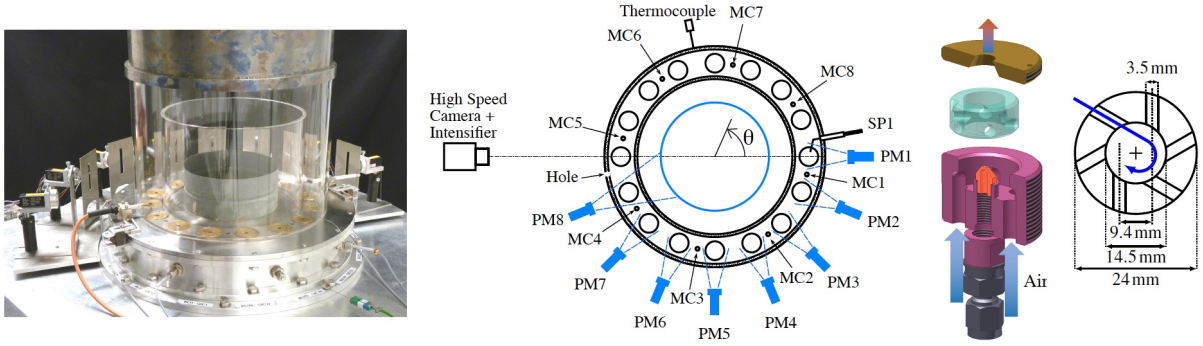

Figure 13: *From left to right. From left to right: (1) Photograph of the MICCA-Spray test rig. (2) Schematic view of the chamber backplane showing the locations of the camera, thermocouple, chamber microphones MCx, plenum microphones MPx, photomultipliers PMx and of spark plug SP1. Dashed lines show the field of view of the photomultipliers. (3) Exploded view of the injector and its components. In purple, the main body, in orange the liquid fuel atomizer, in translucide teal the tangential air swirler and in gold the injector outlet, which is flush with the chamber backplane. (4) Schematic view of the swirler seen from above indicating the main dimensions of this component. (repeated from page 22)*

The present investigation is carried out on the MICCA-Spray annular combustor (Prieur et al. (2017b)). This test rig is an idealized representation of aero-engine combustor configurations. Two major improvements were made to the set-up used in the previous study of Prieur et al. (2017b): an array of eight photomultipliers equipped with OH* narrowband optical filters gives access to the instantaneous heat release rate of one half of the flames in the combustor. Additionally, a new set of injectors, designed after numerous trials, is introduced. A full characterization of this swirled injection system is presented, including measurements of the fuel spray characteristics. The system exhibits a wide range of unstable operating conditions, in terms of thermal power, equivalence ratio and injector bulk velocity, giving rise to many types of thermoacoustic oscillations. Depending on the operating point, either a longitudinal oscillation or an azimuthal oscillation occurs. Limit cycles are observed in the case of the longitudinal oscillation. In other regions of the operating map, azimuthal oscillations take the form of bursts, with lower amplitudes sometimes coupled to spinning modes and with higher amplitudes only under standing mode coupling. The focus is placed in the present article on the analysis of very high amplitude, long bursts coupled by a standing azimuthal mode. The shape of the acoustic field near the backplane of the combustor is investigated using a higher order reconstruction method. Flame blow off during high amplitude standing thermoacoustic oscillations are once again observed. They are studied using high speed chemiluminescence imaging,

and dynamic mode decomposition. The instantaneous azimuthal acoustic velocity field is reconstructed and the critical velocity value leading to flame blow off is determined. It is shown that flame blow off induces temperature distribution inhomogeneities that in turn modify the modal structure in the annular combustor. The phase between the instantaneous heat release rate in each flame and the acoustic pressure is examined and it is shown that this quantity changes from flame to flame on the same side of the nodal line and that these variations in phase become larger as the amplitude of oscillation increases.

9.2 Experimental setup

In this section, we successively describe the MICCA-Spray test rig, the injection units and the resulting velocity distributions and the diagnostic tools.

9.2.1 MICCA-Spray Test Rig

The MICCA-Spray test rig (Fig. 13) comprises an annular combustor with spray and swirled injectors meant to be representative of the combustor of a small helicopter engine. However, this device operates at atmospheric pressure. Previous studies on combustion instabilities in this rig include Prieur et al. (2017b) in the spray flame configuration, and Bourgouin et al. (2015b); Durox et al. (2016); Prieur et al. (2017a) in a previous propane-air configuration. The rig comprises an annular plenum, fed with air at ambient temperature by eight evenly distributed channels, and closed on the top and the bottom by water-cooled stainless steel plates. The plenum is 80 mm high, and has an inner diameter of 280 mm and an outer diameter of 420 mm. Sixteen injectors are mounted on the upper plate of the plenum, which also forms the backplane of the combustion chamber. The combustor itself is an open-ended annulus with two concentric cylindrical vertical walls. The inner vertical boundary of the combustor is a quartz tube, 8 mm thick, 200 mm high, with an outer diameter of 300 mm. The outer wall, 700 mm high and with an inner diameter of 400 mm, is made in two parts: the bottom is a 300 mm long quartz tube, 6 mm thick; the upper is a 400 mm long heat resistant steel tube. The air flow to the experiment is metered using two Bronkhorst EL-Flow mass flow controller, leading to a relative accuracy better than 1%. The fuel flow is measured by a Bronkhorst CORI-Flow controller, with a relative accuracy of 0.5%. 9 mm holes are drilled in the outer quartz tube, 15 mm above the back plane, to accommodate spark plugs (see Fig. 13). For the experiment presented in this paper, spark plug SP1 is plugged in and used for ignition, while the opposite hole is left empty. The tip of the spark plug is placed approximately 15 mm from the center of an injector.

9.2.2 Injectors

The spray swirl injection system used in this study is a modified version of the injector used by Prieur et al. (2017b). It includes the 716 swirler, designed to obtain a higher

swirl number of $S = 0.71$. This is assumed to favor stronger self-sustained combustion instabilities on a wider range of operating conditions. In the exploded view of the injection system shown in Fig. 13 the air of the plenum flows from the bottom, passes through six axial channels 6 mm in diameter, and then through the six tangential channels of the swirler, depicted schematically with dimensions in the rightmost part of Fig. 13. The air is set in a rotational motion at this stage, and exits to the combustor through a small conical section, with an 8 mm diameter at the outlet of the injector. Liquid n-heptane is injected by an atomizer set 7 mm in recess with respect to the dump plane. A hollow cone spray is formed by this device.

The experimental characterization of the injector has been performed on a single injector rig, at an operating point corresponding to ($\mathcal{P} = 111\,\mathrm{kW}, \phi = 0.85, u_b = 42.7\,\mathrm{m\,s^{-1}}$) in MICCA-Spray, where the bulk velocity through an injector is defined as the 1D averaged velocity at the injector's outlet under cold flow conditions $u_b = \dot{m}/(\pi\rho R_{inj}^2)$.

The swirl number of these injectors is deduced from velocity profiles measured 2.5 mm above the dump plane in the absence of any confinement, under non-reactive conditions, and in the absence of fuel. The air is seeded with oil droplets approximately 2 µm in diameter, and the velocities are measured using a two-component Dantec Dynamics FlowExplorer Phase Doppler Anemometer. The theoretical optical probe volume of this system measures 0.14 mm × 0.14 mm × 0.23 mm. Measurements are spaced every 0.25 mm. Uncertainty on the measured mean velocities is less than $0.8\,\mathrm{m\,s^{-1}}$. The mean velocity profiles for this injection system are shown in Fig. 9.2. The experimental swirl number $S = 0.71$ is calculated using the conventional expression (see chapter 4):

$$S_{conv} = \frac{\int_0^{2R_{inj}} \overline{U_\theta}\,\overline{U_x}\, r^2 dr}{R_{inj} \int_0^{2R_{inj}} \overline{U_x}^2 r dr} \tag{9.1}$$

Droplet size measurements are also performed on the fuel spray, 2.5 mm above the dump plane in the absence of any confinement, and under non-reactive conditions. The Sauter mean particle diameter is $d_{32} = 18.0\,\mu\mathrm{m}$, while the mean particle diameter is $d_{10} = 4.5\,\mu\mathrm{m}$. The head loss of the injection unit was also characterized under non-reactive conditions, using a Kimo MP111 differential pressure gauge, with a 1% relative precision. The pressure loss across the injector follows the standard scaling law $\Delta p = 1/2\,\rho\sigma u_b^2$, with $\sigma = 5.1$ being the head loss coefficient. Figure 9.3 shows chemiluminescence images of stable flames in the combustion chamber. The upper part of the outer boundary of the combustor (steel prolongating tube) has been removed to suppress the thermoacoustic oscillation.

9.2.3 Diagnostic Tools

In addition to the diagnostic tools found on the single injector rig, and presented in the previous section, the MICCA-Spray experimental rig is equipped with several sensors for the analysis of self-sustained thermoacoustic oscillations. The sensor positions are indi-

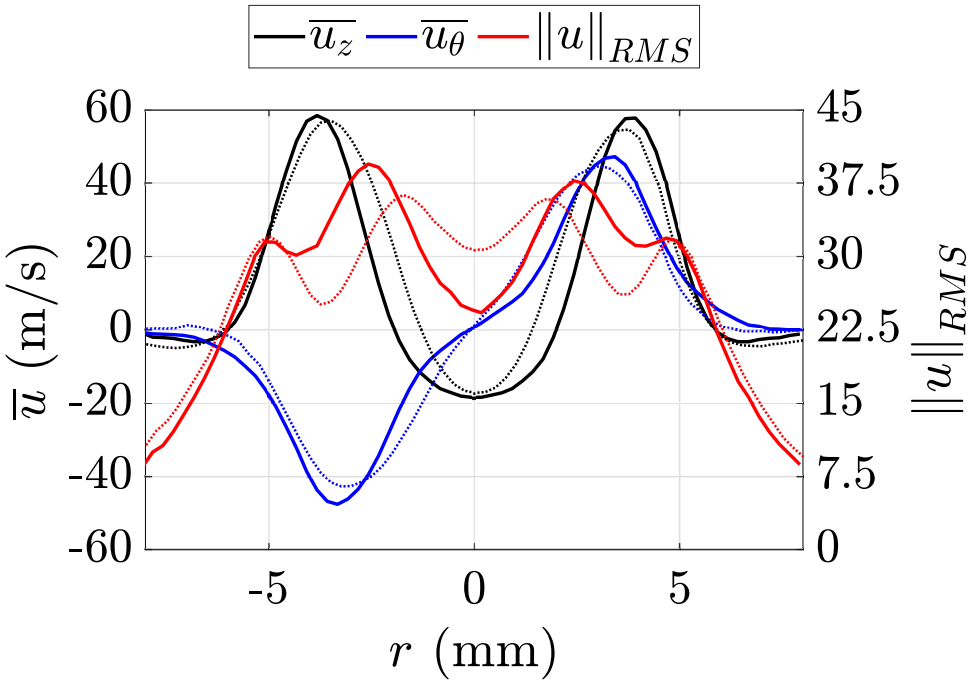

Figure 9.2: *Left axis: mean velocity profiles measured* 2.5 mm *downstream of the injector outlet using LDV. The axial component is shown in black, the tangential component in blue. Right axis: overall turbulent velocity. The profiles for the injector used in the present study are shown in solid lines, those for the injector used by Prieur et al. (2017b) in dotted lines. The injector used in this study features a swirl number* $S = 0.71$*, the one used by Prieur et al. (2017b)* $S = 0.68$*. These swirl numbers were determined from the profiles that are presented here.*

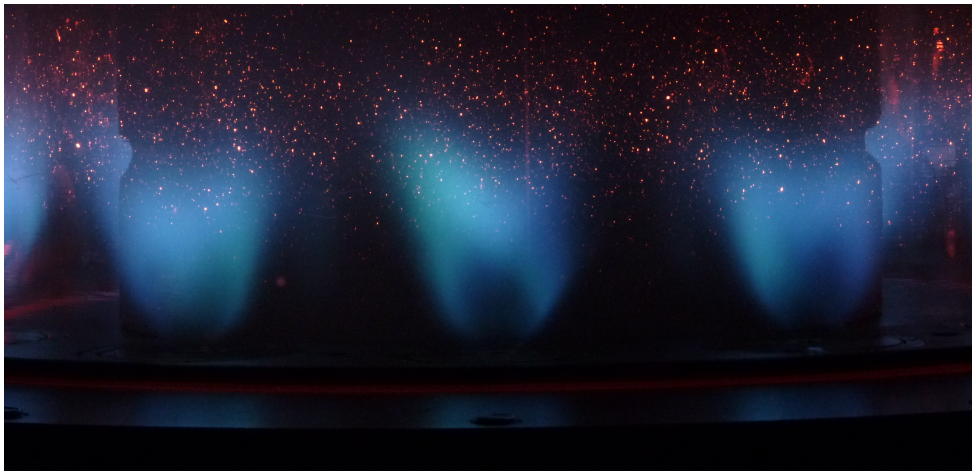

Figure 9.3: *Direct chemiluminescence image of several stable flames in MICCA-Spray at operating point* ($\mathcal{P} = 107\,\mathrm{kW}, \phi = 1.04, u_b = 33.4\,\mathrm{m\,s^{-1}}$)*. The exposure time is* 100 ms *so that the images are time-averaged. The flames have a typical "M"-shape. Slight differences can be observed from one flame to the other. The system is not perfectly rotationally symmetric due to the presence of the spark plugs, and differences in fuel atomization between each injector.*

cated in Fig. 13.

A total of 12 Bruel & Kjaer type 4938 microphones with type 2670 preamplifiers are used to measure acoustic pressure signals. Their relative accuracy is 1% and their cut-off frequencies are 70 kHz and 15 Hz. All signals are sampled at 32 768 Hz. Four of these microphones, designated as MP1 to MP4, are plugged onto the plenum, and eight of these sensors, designated as MC1 to MC8, are mounted on waveguides. These are connected to the backplane of the combustion chamber with their orifices set at equal distance of two injectors. The waveguides are terminated by a 25 m long flexible tube to avoid acoustic reflexions from the downstream end of the device. The microphones are located at 170 mm from the dump plane of the combustor. This arrangement induces a time lag $\tau_{m-b} = 0.46$ ms that can be estimated by taking into account the temperature prevailing inside the plenum, which was measured at 55 °C. This delay is taken into account when synchronizing the signals recorded during experiments. The signals delivered by these microphones are used to reconstruct the acoustic pressure field at each azimuthal position within the chamber and plenum. An array of eight photomultipliers also equips the experimental rig. They are positioned outside the annulus. Each photomultiplier is pointing at an individual flame, and is equipped with a mask acting as a spatial filter. A steel tube, 90 mm high and 205 mm in diameter, is placed within the inner quartz tube of the chamber (see the photography in Fig. 13). This tube and these masks ensure that each photomultiplier only detects light emitted by a single flame. Each photomultiplier is equipped with an optical filter centered on the chemiluminescence band of the OH* radical. These are pass-band filters centered on 308 nm with a bandwidth at half maximum of 12 nm. The light emission signal measured by these instruments can be used to roughly estimate the instantaneous heat release rate of each flame. It is worth noting that, even under these non-premixed conditions, one may assume that the PM signal intensity provides to some extent an indication on the combustion intensity, which is linked to the flame luminosity. This was shown experimentally using a quasi-steady approach by Mirat et al. (2014) and successfully applied in Mirat et al. (2015). A K-type thermocouple is also present on the outer wall of the combustor to measure the local temperature T_{wall}, in-between two injectors, 36 mm above the backplane.

The global motion of the flame is captured using a high speed intensified camera, without any optical filter. The camera, a Photron FastCam APX-i2, uses a CMOS sensor with a 512×256 pixels resolution, and an 8-bit gray level resolution. Recordings are performed at 6000 frames per second with an exposure time of 166 µs. The camera is positioned as shown in Fig. 13 in order to have a bird's eye view of the whole rig. Its axis is aligned with the position of the spark plugs, which are close to the nodal line during oscillations coupled by a standing azimuthal mode.

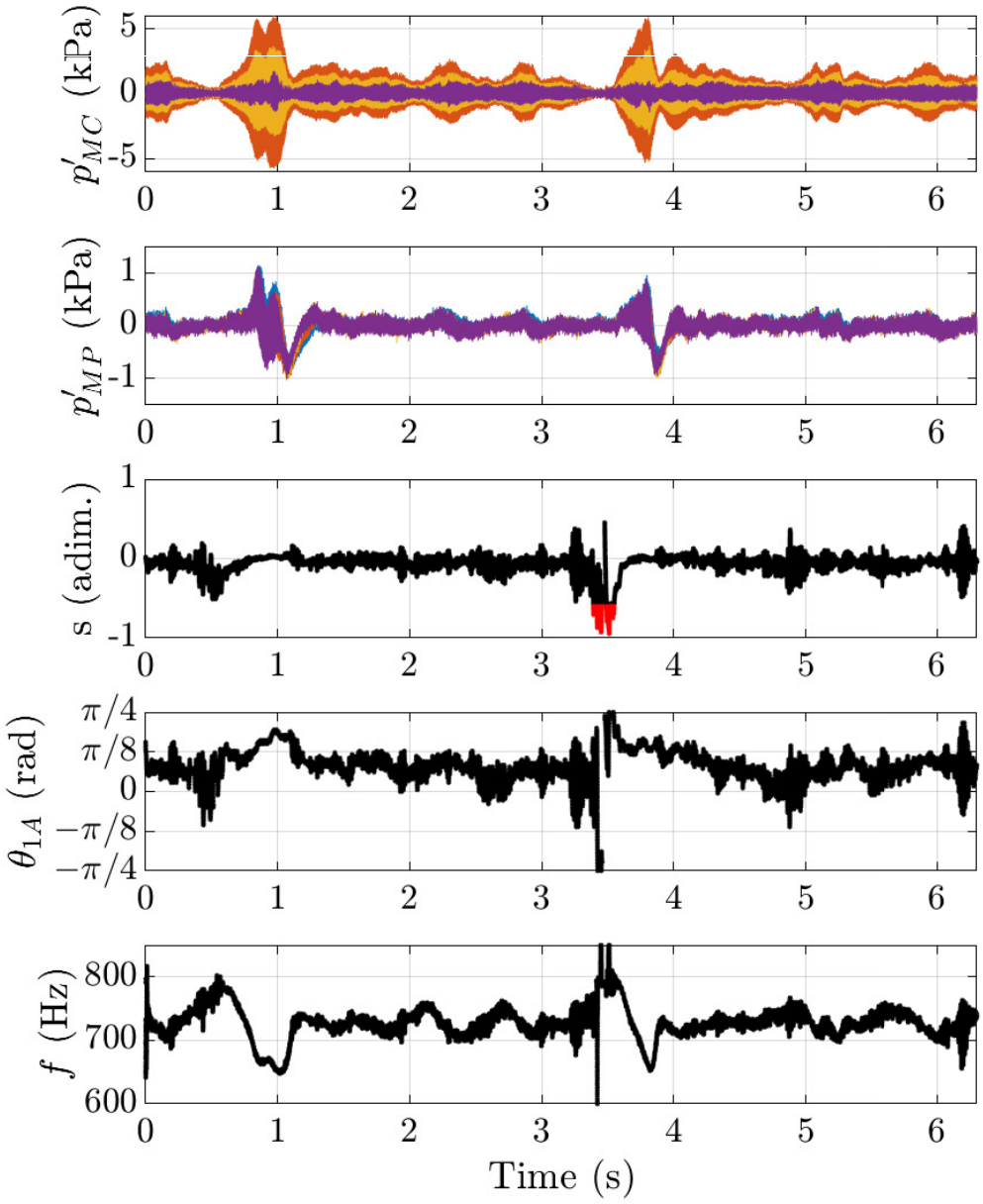

Figure 9.4: *Typical time series of thermoacoustic oscillations in the MICCA-Spray rig for operating conditions* ($\mathcal{P} = 128\,\mathrm{kW}, \phi = 1.11, T_{wall} = 828\,\mathrm{K}$). *On top, the raw acoustic pressure signals in the chamber* p'_{MC} *are shown for microphones MC1-MC4. Then the raw acoustic pressure signals in the plenum* p'_{MP}*, followed by the time evolution of the spin ratio* s*, calculated according to Eq. (8). The position of the pressure nodal line of the first in space azimuthal acoustic mode* θ_{1A} *is shown using the angle* θ *defined in Fig. 13. The instantaneous frequency* f *of the pressure signal is presented at the bottom. The colors for microphones MCx and MPx are shown in Fig. 9.5.*

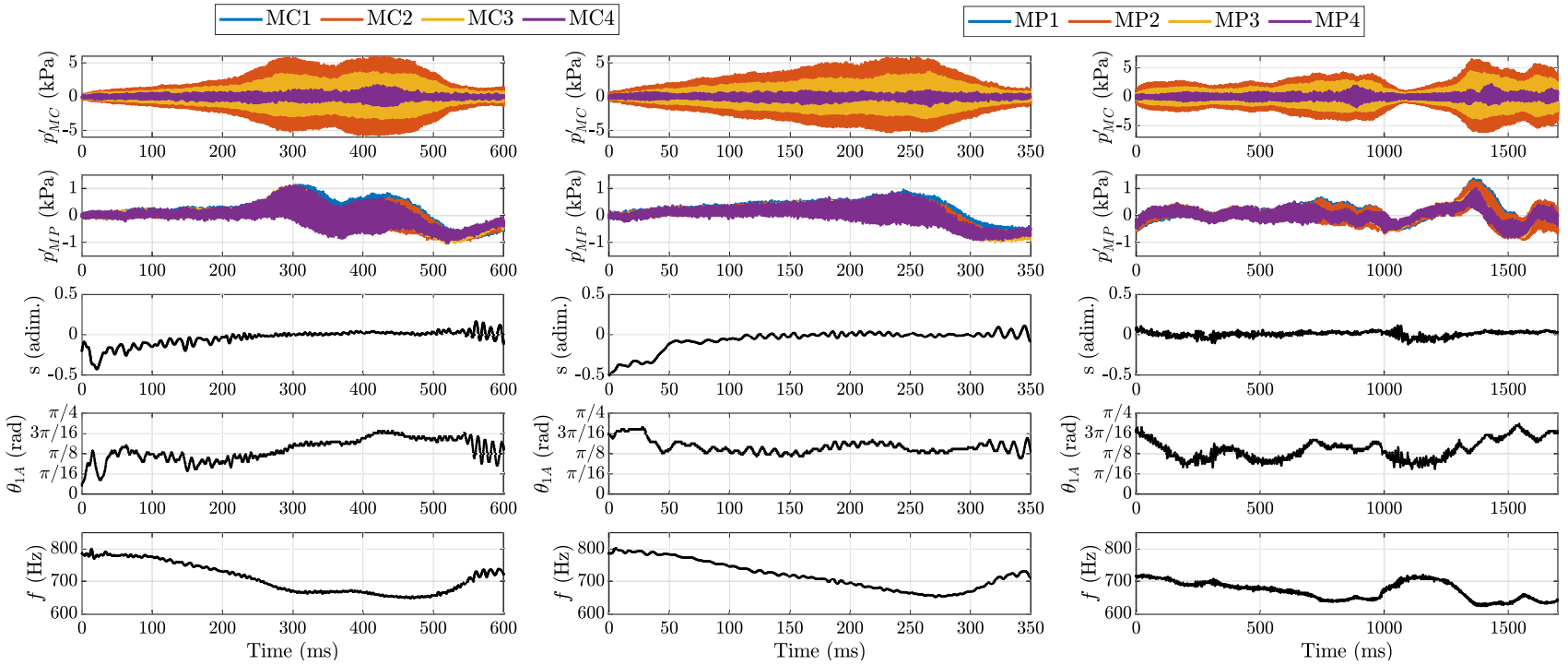

(a) ($\mathcal{P} = 128\,\mathrm{kW}, \phi = 1.11, T_{wall} = 828\,\mathrm{K}$) **(b)** ($\mathcal{P} = 128\,\mathrm{kW}, \phi = 1.11, T_{wall} = 828\,\mathrm{K}$) **(c)** ($\mathcal{P} = 117\,\mathrm{kW}, \phi = 1.09, T_{wall} = 811\,\mathrm{K}$)

Figure 9.5: *Three thermoacoustic oscillation bursts coupled by a standing acoustic wave. The operating condition is indicated underneath each sequence. Note that sequences (a) and (b) are two distinct time sequences obtained at the same operating conditions, extracted from the longer time series in Fig. 9.4. For sequences (a) and (b), the photomultiplier array was used to acquire flame chemiluminescence data, while for sequence (c), the high speed camera was used.*

9.3 Thermoacoustic oscillations coupled by a standing azimuthal mode

Thermoacoustic oscillations coupled by a standing azimuthal acoustic mode are observed in the MICCA-Spray configuration for numerous operating conditions. The corresponding intermittent oscillations take the form of long bursts several hundred millisecond long. The present article focuses on this mode of oscillation which features relatively low growth rates allowing time resolved processing of the microphone and photomultiplier signals. A typical time series recording is presented in Fig. 9.4, where pressure signals in the chamber (dubbed MCx) are shown at the top while pressure signals in the plenum (MPx) appear directly underneath. The bottom part of this figure displays the instantaneous frequency of the pressure signals in the chamber. The instantaneous frequency is computed from the pressure signal detected by the chamber microphone MC1, filtered using a bandpass 8th order Butterworth filter, with cut-off frequencies 600 Hz and 950 Hz. The analytical signal is then deduced with a Hilbert transform. The frequency is obtained by differentiating the phase of this analytical signal. This method compares quite favorably with time resolved spectrograms obtained using short-time Fourier transforms (not shown here). These spectrograms feature a peak that is shifting in time from 800 to 620 Hz. This peak is dominant by at least 20 dB over the other components in the spectrum. Figure 9.5 shows three representative, zoomed in sequences. Sequences (a) and (b) are extracted from the longer sequence displayed in Fig. 9.4, while sequence (c) originates from a separate experiment during which the high speed camera was used.

As already observed by Prieur et al. (2017b), the instantaneous frequency is consistently found to decrease during the growth of a thermoacoustic oscillation, and to increase as the amplitude of the thermoacoustic oscillation decreases. The spin ratio presented in Fig. 9.5 is that of the first azimuthal component, and is calculated using the definition and method derived by Bourgouin et al. (2015b)

$$s = \frac{\|a_{+1}\| - \|a_{-1}\|}{\|a_{+1}\| + \|a_{-1}\|} \qquad \text{(8 repeated)}$$

where a_{+1} and a_{-1} respectively designate the amplitudes of the counterclockwise and clockwise spinning components of the first azimuthal acoustic mode (defined in Eq. (9.3)). All three bursts are coupled by a standing mode. Figure 9.5 also displays the position of the pressure nodal line of the first azimuthal acoustic mode. It is found to move slightly during a thermoacoustic burst, by approximately $\pi/8$ rad, which corresponds to the angle between two injectors. The nodal line is nearly aligned with the diameter on which the spark plug and the opposing hole are found (see Fig. 13). This behavior is also found when two opposing spark plugs are present in the combustor. This characteristic is used in practice to freeze the position of the nodal line, and adequately position the high speed camera.

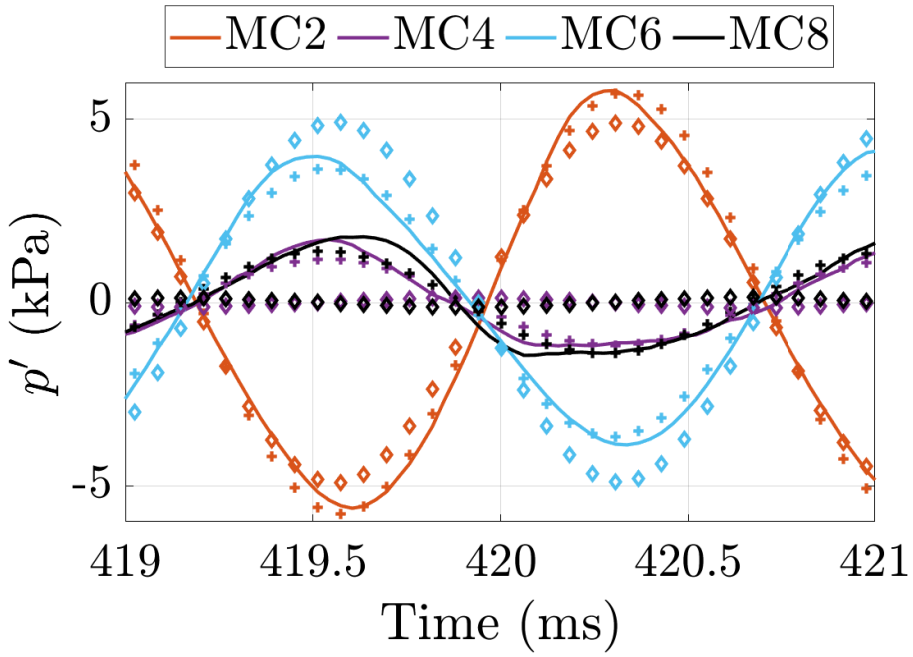

Figure 9.6: *Pressure signals from Seq. (a) of Fig. 9.5. At this instant, the thermoacoustic oscillation executes a quasi limit cycle, and the nodal line of the first azimuthal mode is nearly aligned with microphones MC4 and MC8. The measured pressure signals are shown in plain lines, the signals reconstructed using the first order in space method of Bourgouin et al. (2015b); Prieur et al. (2017b) appear as diamond symbols, the signals reconstructed using the third order in space method used in the present article are plotted as cross symbols.*

9.4 Spatial structure of the acoustic pressure field

Using the eight bandpass-filtered (600 Hz $< f <$ 950 Hz) pressure signals MC1-MC8, the spatial structure of the acoustic pressure field in the chamber can be reconstructed in the form of a Fourier series. For the present work, this reconstruction is carried out up to order three in azimuthal angle. In this framework, the analytical signal of the acoustic pressure field $p'(\theta, t)$ near the backplane of the combustor is represented as a finite Fourier series

$$p'(\theta, t) = \sum_{m=-M}^{M} \exp(im\theta)\, \eta_m(t) \tag{9.2}$$

where M is the number of Fourier components (in the present application, $M = 3$), θ is the azimuthal coordinate defined in Fig. 13, and taken positive in the counterclockwise direction. $\eta_m(t)$ is the projection of the analytical signal $p'(\theta, t)$ (determined by means of a Hilbert transform) on the Fourier basis. In practice, in the case of combustion instabilities examined in this paper, the power spectral density of the pressure signals (not shown here) presents a strong peak corresponding to the first azimuthal - first longitudinal, 1A1L acoustic mode. This peak dominates by at least 20 dB over other frequencies, so

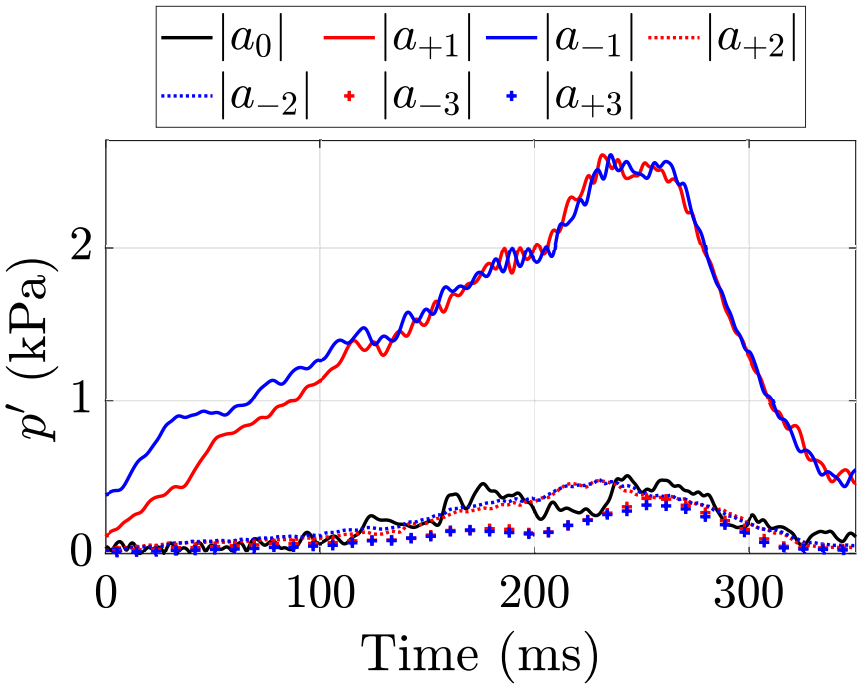

Figure 9.7: *Seq. (b) of Fig. 9.5. Time evolution of the amplitude of the seven reconstructed acoustic components defined in Eq. (9.2).*

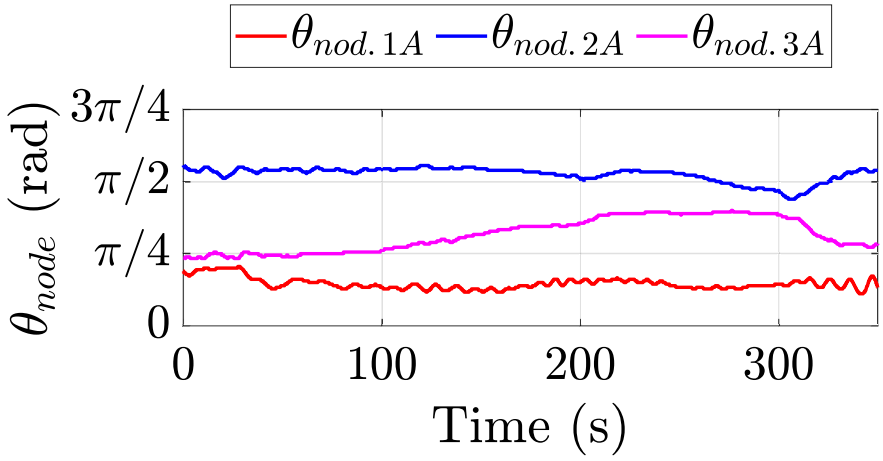

Figure 9.8: *Seq. (b) of Fig. 9.5. Time evolution of the position of the nodal line associated with each standing component. For the m^{th} order component, m nodal line co-exist. θ_{node} refers to the angular position of the pressure node in the interval $[0; \pi/2m[$ rad.*

that Eq. (9.2) can be simplified into

$$p'(\theta, t) = \sum_{m=-3}^{3} a_m(t) \exp\left(i\left[m\theta - 2\pi f(t)t\right]\right) \tag{9.3}$$

Complex amplitudes $a_m(t)$ are defined for each m$^{\text{th}}$ order spatial component. $f(t)$ is the instantaneous frequency of the signal. The least squares method used in previous works Bourgouin, Durox, Moeck, Schuller, and Candel (2015b); Prieur, Durox, Schuller, and Candel (2017b) is adapted for this higher order reconstruction. This higher order approach notably improves the fidelity of the pressure field reconstruction during high amplitude oscillations. For the thermoacoustic instabilities presented in Fig. 9.5, the time-averaged Pearson product-moment correlation coefficient between the measured and reconstructed pressure signals is $R^2_{1A} = 97.3\%$ using the first order reconstruction method, and $R^2_{3A} = 99.7\%$ using the third order spatial reconstruction introduced in the present article. Although the value of R^2_{1A} might appear perfectly acceptable at first, Fig. 9.6 shows that there are reconstruction errors when using a first order reconstruction method (diamonds in Fig. 9.6). This is particularly true in the vicinity of the nodal line, close to microphones MC4 and MC8 in the present case. The third order method (crosses in Fig. 9.6) greatly improves the reconstruction of the spatial structure of the pressure mode. Additionally, the root mean square acoustic pressure in the annulus, defined as the spatially averaged RMS value of the pressure, is easily computed using Eq. 9.4.

$$p'_{RMS}(t) = \frac{1}{\sqrt{2}}\Big[\sum_{m=-M}^{M} a_m^2(t)\Big]^{1/2} \tag{9.4}$$

The time evolution of the amplitude of the reconstructed waves is shown in Fig. 9.7. For all three orders, the amplitude of the clockwise and counterclockwise spinning components are nearly equal, indicating that a mostly standing acoustic wave with spin ratio close to zero is found. During very high pressure oscillations ($p'_{RMS} > 4\,\text{kPa}$), the sum of the peak amplitudes of the second and third order components is found to be of the order of 20 to 30% of that of the first order wave. All acoustic components have the same instantaneous frequency, that of the first order wave, shown at the bottom of Fig. 9.5.

Figure 9.8 shows the position of the nodal line for each standing component. These lines are staggered. In Fig. 9.6, microphones MC4 and MC8 are found to be very close to the nodal line of the first order azimuthal component. Yet, pressure fluctuations at their location reach an amplitude of 1.7 kPa. This is a consequence of the staggered nature of the nodal lines: flames at the pressure nodal line of the first component will be submitted to transverse velocity fluctuations from this first component, but also to pressure fluctuations from the higher order components; flames at the pressure antinode of the first component will be submitted to pressure fluctuations from this first component, but also to transverse velocity fluctuations from the higher order components.

9.5 Flame blow off during large amplitude thermoacoustic oscillations

In a previous work (Prieur et al. (2017b)), it was found that large amplitude thermoa-

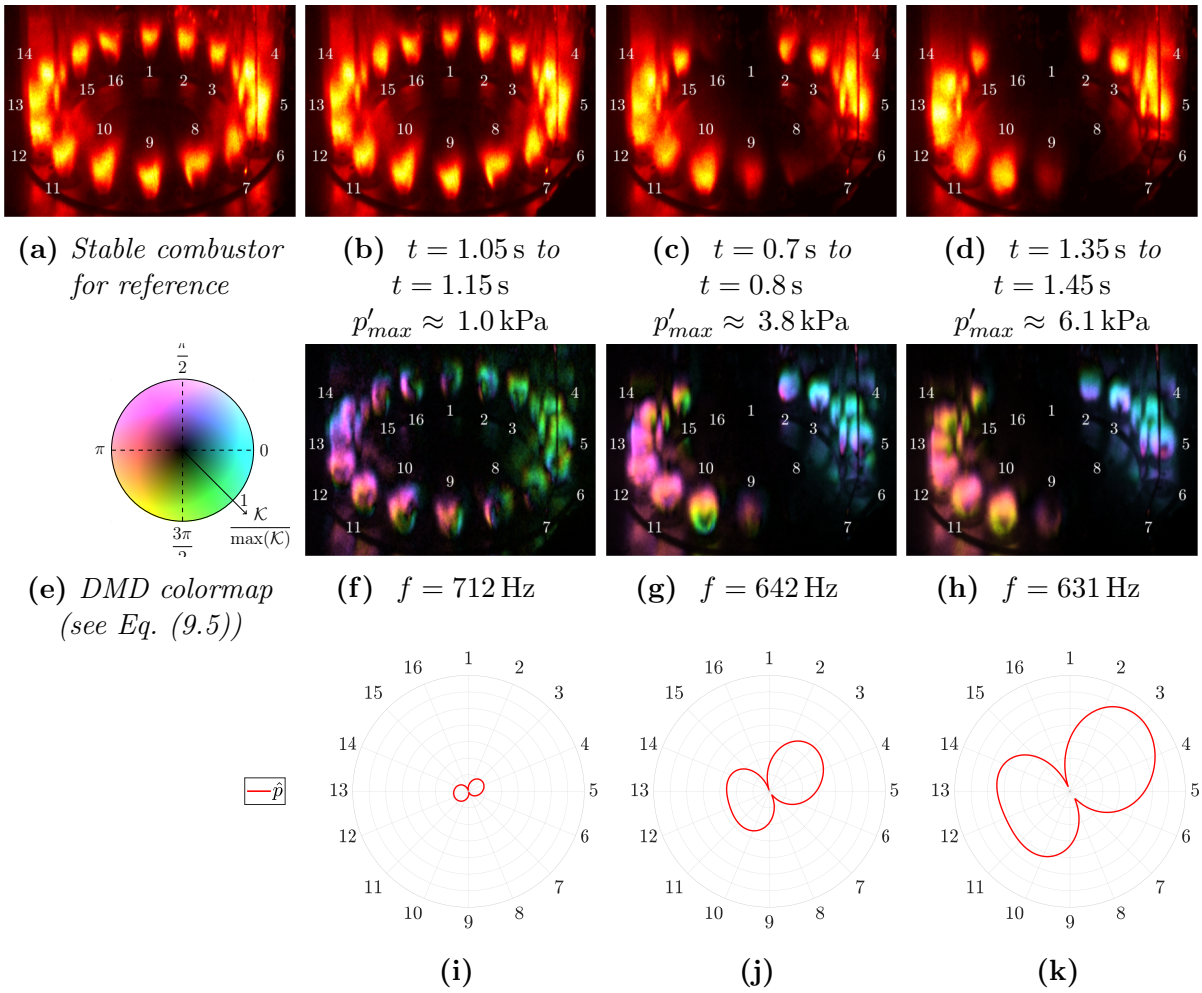

Figure 9.9: *Data is extracted from sequence (c) of Fig. 9.5.* ***(a)*** *Time averaged chemiluminescence image of the combustor in the absence of thermoacoustic oscillations. The flames are numbered from* 1 *to* 16*, flame* 1 *corresponding to the flame near the spark plug in Fig. 13.* ***(b)-(d)*** *Time averaged chemiluminescence image of the combustor. Three* 100 ms *long sequences are isolated. These correspond to carefully chosen periods during which the oscillation is constant in amplitude and frequency.* ***(f)-(g)*** *Spatial representation in amplitude and phase of the most energetic DMD mode of each image sequence. The phase reference is set by the pressure signal from microphone MC2 located between flames 2 and 3.* ***(i)-(k)*** *Spatial structure of the acoustic pressure $\hat{p}$. It is reconstructed using the method described in Eq. (9.2). The numbers in azimuth correspond to the injectors seen in the images. The amplitude is shown by the radial position of the curve, each circle represents* 1 kPa.

coustic oscillations coupled by a standing acoustic mode could destabilize flames formed by injectors located near the pressure nodal line and that this could lead to partial blow off. The pressure nodal line corresponds to an antinode of the acoustic azimuthal velocity component inducing a strong transverse motion of the flame and its root. A theoretical framework was also proposed to evaluate the blow off limit. Blow off of flames located near the pressure nodal line was also found to occur in the new configuration of the MICCA-Spray combustor investigated in the present article, under oscillations coupled

by a standing acoustic mode. Thus, this analysis is continued here by first examining high speed chemiluminescence images, by next estimating the critical velocity fluctuation threshold corresponding to blow off, and finally by considering the consequences of blow off in terms of modal distortion.

9.5.1 High speed imaging

In this section, sequence (c) from Fig. 9.5 will be analyzed in some details using high speed chemiluminescence imaging. In Fig. 9.9, three short sequences, each 100 ms long, are isolated. They feature a stable, quasi limit-cycle oscillation at three different amplitudes. Average chemiluminescence images are shown in the top of Fig. 9.9. In Fig. 9.9(b), none of the flames are blown-off, but flame 1 appears to be weaker compared to the others. The amplitude of the pressure oscillation is much higher in Fig. 9.9(c), and flames 1, 6, and 7 are blown-off. Flames 8 and 16 are nearly blown-off as well. The highest amplitude is reached in Fig. 9.9(d), where a total of five flames are blown-off: 1, 6, 7, 8, and 16. An asymmetry in the flame behavior can already be observed.

In order to go further in the analysis of these images, it is convenient to use the dynamic mode decomposition (DMD) introduced by Schmid (2010). A DMD mode is written as:

$$\mathcal{M}(\boldsymbol{x}, t) = \mathcal{K}(\boldsymbol{x})\, \mathrm{e}^{i\varphi(\boldsymbol{x})}\, \mathrm{e}^{(a+2i\pi f)t} \tag{9.5}$$

where $\mathcal{K}$ is the local amplitude of the mode at position $\boldsymbol{x}$, φ its local phase, a its growth rate and f its temporal frequency. All DMDs are obtained by processing 600 images, corresponding to 0.1 s. The most energetic mode, corresponding to the thermoacoustic oscillation at the frequency of the standing acoustic wave, is shown in the second row of Fig. 9.9. The spatial part of the mode is displayed with both the amplitude $\mathcal{K}(\boldsymbol{x})$ and phase $\varphi(\boldsymbol{x})$ using the colormap in Fig. 9.9(e). The color indicates the phase of the mode, the light intensity its amplitude.

9.5.2 Estimation of the critical velocity threshold

Blow off is first observed for peak acoustic pressure fluctuations reaching 2 kPa to 2.5 kPa in the combustor. As this phenomenon occurs near the pressure nodal line, which is an acoustic velocity antinode, it is particularly relevant to determine the azimuthal acoustic velocity. A method to do so from pressure measurements is described in Appendix B. As this method requires the density field to be known, the analysis is limited to the instants just before the blow off of the first flame, as a uniform temperature field hypothesis can then be made.

Figure 9.10 shows the acoustic pressure and velocity fields computed at $t = 106$ ms for sequence (c) from Fig. 9.5. This is just after blow off of flame 1 a situation identified in the high speed images. All other flames are still attached, so that the acoustic velocity can be retrieved using a uniform temperature model. The acoustic pressure appears to be asymmetric between the two sides of the nodal line, and the acoustic velocity is even

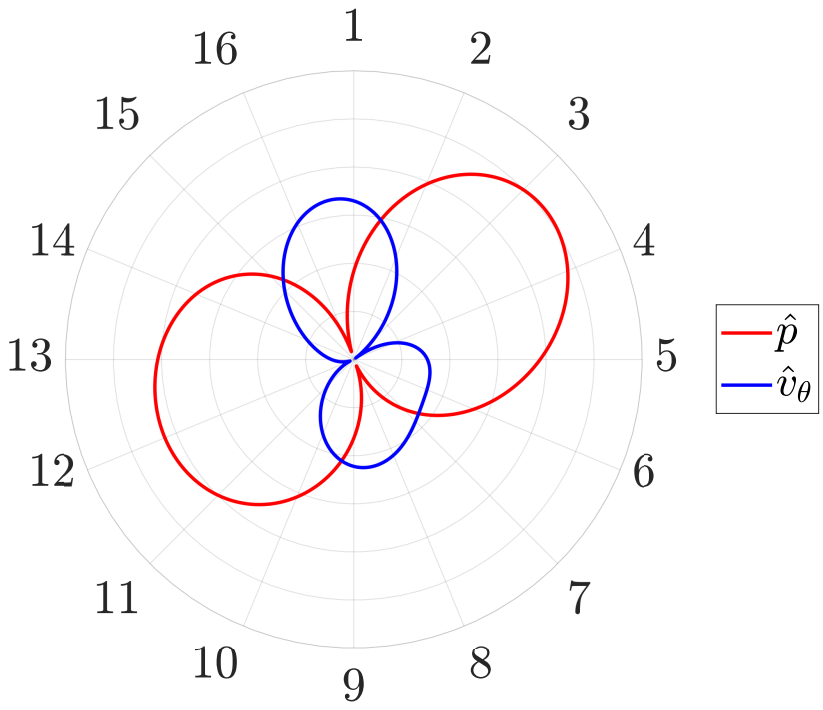

Figure 9.10: *Spatial structure of the acoustic pressure and azimuthal velocity fields at* $t = 106\,\mathrm{ms}$. *The blue curve* $\hat{v}_\theta$ *corresponds to the azimuthal velocity field assuming a uniform temperature* $T = 1550\,\mathrm{K}$ *in the combustion chamber. The velocity reconstruction method is detailed in Appendix B. The amplitude is shown by the radial position of the curve. For the velocity, each circle represents* $5\,\mathrm{m\,s^{-1}}$, *for the pressure, each circle represents* $500\,\mathrm{Pa}$.

more asymmetric, being 35% higher near injector 1 than near injectors 8 or 9. These velocity fields asymmetries are also found during other similar blow off events.

The critical blow off velocity $\hat{v}_\theta^{bo}$ at which flame 1 will be extinguished can be determined from Fig. 9.10. From this figure, the blow off velocity of flame 1 is estimated at $\hat{v}_\theta^{bo} \approx 16\,\mathrm{m\,s^{-1}}$ for $T = 1550\,\mathrm{K}$. T is not well know. $T = 1550\,\mathrm{K}$ is estimated from the frequency of the thermoacoustic oscillation. However, one may reasonably consider that T lies within the range $1500 - 1800\,\mathrm{K}$, leading to $15.5\,\mathrm{m\,s^{-1}} < \hat{v}_\theta^{bo} < 18.5\,\mathrm{m\,s^{-1}}$. This blow off limit is most likely strongly dependent on the injector design, and may be lower in a different thermal environment, at a different operating point, or in other combustors. This point is briefly discussed in the theoretical analysis presented in Prieur et al. (2017b).

9.5.3 Modal distortion associated with flame blow off

It is now interesting to examine the pressure field as it evolves after the first flame blow off event. The acoustic pressure and velocity fields reconstructed in Fig. 9.9 and Fig. 9.10 indicate that there is an asymmetry between the two sides of the nodal line. Nonlinear low order modeling of combustion instabilities often relies on the modal expansion approach first introduced by Zinn and Powell (1970), and explored by Culick (1976); Culick (1988).

In this framework, it is assumed that the spatial eigenmodes shapes are close to those of the acoustic eigenmodes of the system $\Psi_n(\boldsymbol{x})$. These modes are usually determined by assuming a low-Mach number flow with uniform mean pressure and no source or damping terms. The eignenmodes $\Psi_n(\boldsymbol{x})$ are then obtained as solutions to Eq. (9.6) (Poinsot and Veynante (2012)) together with boundary conditions at the chamber walls, inlet plane and outlet.

$$\nabla \cdot \left[\bar{c}^2 \, \nabla \Psi_n(\boldsymbol{x}) \right] \; + \omega_n^2 \, \Psi_n(\boldsymbol{x}) \; = \; 0 \tag{9.6}$$

In the present study, combustion oscillations are coupled by a 1A1L mode that is first order in the azimuthal direction and also first order in the axial direction. When all the flames are stabilized, the mean temperature in the annular chamber and the sound velocity are uniformly distributed. For a rigid backplane and open outlet the 1A1L eigenmode is

$$\Psi_{1A1L}(\theta, z) = (A\cos(\theta) + B\sin(\theta))\cos\left(\pi z / 2l\right)$$

where A, B are two real valued coefficients, l is the length of the annular cavity, and z the axial coordinate Poinsot and Veynante (2012). The spatial structure for the pressure field is that obtained in Fig. 9.9(i) for a relatively low level of oscillation. However, as the amplitude is increased and flames are blown off, the mean temperature distribution becomes non uniform and the modal structure is distorted.

In that situation the analytical solution of Eq. (9.6) leads to writing the eigenmode as a Fourier series with a fundamental and higher order coefficients. The link to the Fourier coefficients of the temperature field is discussed in Chapter 8. This is one of the reasons why the higher order coefficients in the pressure expansion increase as the flames are blown off and indicates that this observation is a direct consequence of the inhomogeneity of the temperature distribution that arises from the blow off phenomenon.

In Chapter 8, a short study is presented where the eigenfunction Ψ and the eigenfrequency of acoustic modes in an open-closed annulus are computed. In this study, the azimuthal average of the sound velocity squared $\bar{c}^2$ is kept constant, but this field is deformed: $\bar{c}^2 = c_0^2 \, [1 + 2\varepsilon\cos(\theta)]$. The eigenfunction $\Psi_{1A1L}(\theta)$ is shown for different values of ε. It is distorted, and becomes asymmetric. Additionally, it is found that the eigenfrequencies monotonically decrease as the parameter ε is increased. It is known from previous studies (Noiray et al. (2008)) that nonlinear features in the flame response can lead to shifts in the frequency of thermoacoustic oscillations. In distinction with standard modal expansion methods used in combustion instabilities analysis, it is found here that for large amplitudes of oscillations changes in the mean state of the system can distort the modal structures themselves, and shift the corresponding acoustic eigenfrequencies.

9.6 Phase of the flame response to the pressure perturbation

It is known that the phase between the heat release rate in the flames and the local pres-

sure plays plays a major role in combustion instability studies. When pressure and heat release rate are in phase energy is fed into the coupling mode. It is then interesting to determine the phase of the different flames with respect to the pressure. To this purpose one assumes that even in the spray combustion conditions that prevail in MICCA-Spray, most of the chemical conversion takes place in premixed flame elements and the light emission in the form of chemiluminescence is an approximate indicator of instantaneous heat release rate. Now, if the system were operating linearly one would find a uniform phase distribution which would remain uniform during the process. This is essentially the case at low amplitude levels, but the situation changes when the amplitude increases. The DMD images of Fig. 9.9 give an overall view of the phases for different amplitude levels. The evolution as the oscillation amplitude increases is clearly visible. It is also possible to obtain a direct quantitative time evolution of the phase from the different PM signals.

The phase reference in the DMD images of Fig. 9.9(f)-9.9(h) is provided by microphone MC2, located in-between injectors 2 and 3 (see Fig. 13). In Fig. 9.9(f), flames 1 to 8 are green, indicating that the phase of the flame chemiluminescence to the acoustic pressure is approximately $-\pi/4$ rad for these flames. Flames 9 to 16 are pink, in phase opposition to flames 1 to 8, as expected since the thermoacoustic oscillation features a standing azimuthal acoustic wave.

As the amplitude of the thermoacoustic oscillation increases, some flames are blown-off in the combustor. In Fig. 9.9(g)-9.9(h), the phase of the flames on the right side of the combustor (flame 2-5) increases and becomes positive ($\Phi \approx \pi/6$). Flames on the opposite side of the combustor are still in phase opposition. One may however observe from the color in the DMD, that flames 2, 5, 10 and 15 appear to be out of phase with respect to their neighbors. For example, the phase of flame 2 is $0.48\,\text{rad} \approx \pi/6\,\text{rad}$ in Fig. 9.9(g), and $0.93\,\text{rad} \approx \pi/3\,\text{rad}$ in Fig. 9.9(h), while the phase of flame 3 is $0.38\,\text{rad} \approx \pi/8\,\text{rad}$ in Fig. 9.9(g), and $0.54\,\text{rad} \approx \pi/6\,\text{rad}$ in Fig. 9.9(h).

This analysis of the DMD images is now complemented by examining the PM signals from sequence (a) of Fig. 9.5. In Fig. 9.11, the phases of the PM signals with respect to the pressure are shown for injectors 2, 3 and 4. They are deduced from a time resolved correlation method with blocks 16 ms long. The reference pressure amplitude plotted in the same figure indicates the overall level of the thermoacoustic oscillation. Flame 2 is blown-off between $t = 0.82\,\text{s}$ and $0.92\,\text{s}$.

As observed in the DMD images, the phase between the chemiluminescence signal and the pressure is slightly negative when the level of the oscillation is low, positive when it is very high. All injectors feature roughly the same phase between chemiluminescence and pressure for lower levels of oscillation (during the first $0.75\,\text{s}$ and the last $0.2\,\text{s}$ of the sequence). During very high amplitude oscillations, around $0.8 - 1.1\,\text{s}$, injectors 2 and 3 have nearly the same phase, but it is higher than that of injector 4. Again, after $t = 1.1\,\text{s}$, the phase of injector 2 is often higher than that of injectors 3 and 4.

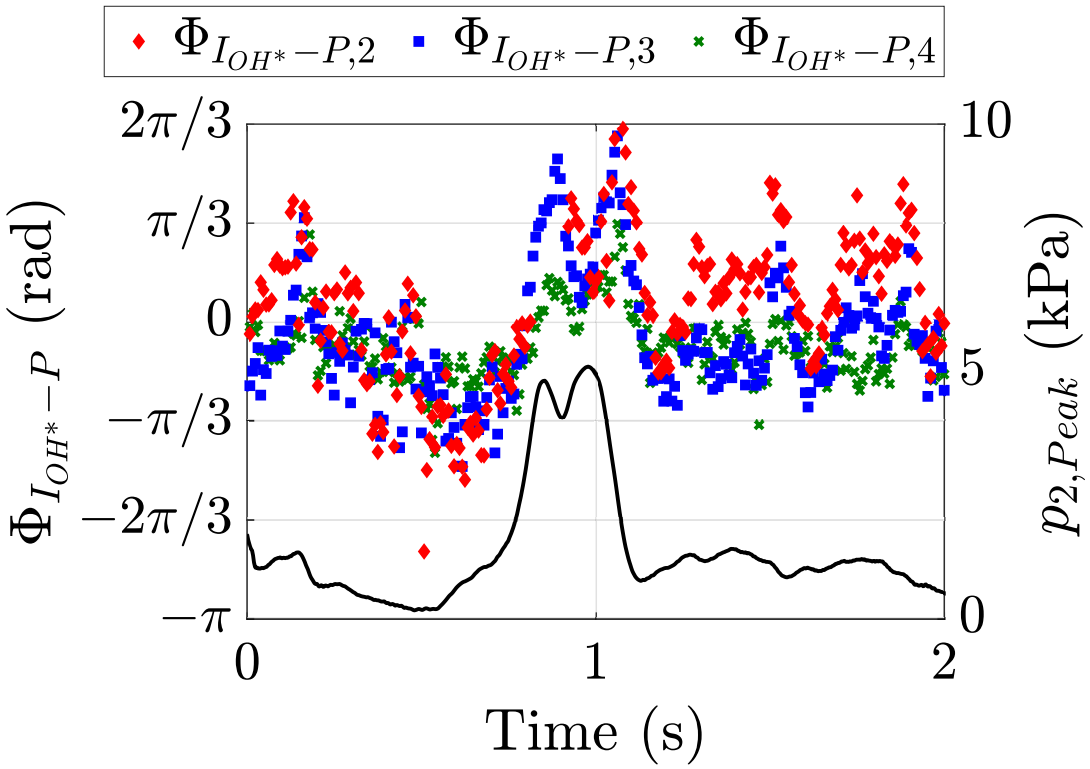

Figure 9.11: *Data for this figure are extracted from Fig. 9.4. The solid black line (right axis) is the instantaneous amplitude of the pressure at the location of injector 2. The dots show the time resolved phase between the photomultiplier signal and the pressure for injectors 2 (red, diamonds), 3 (blue, squares) and 4 (green, crosses). Flame 2 is blown-off during* $0.82\,\mathrm{s} < t < 0.92\,\mathrm{s}$*, so that no phase data is available.*

Similar observations can be made on other sequences featuring the same type of very high amplitude oscillations induced by a standing acoustic mode, using either the photomultiplier array, or the high speed imaging system. At lower oscillation amplitudes, the phase between chemiluminescence and pressure is slightly negative, and it becomes positive at higher oscillation amplitudes. In all cases flames on the same side of the nodal line do not all feature the same phase when the amplitude of the oscillation becomes large. The phase distribution is clearly affected by the amplitude of oscillation, a nonlinear feature that can be modeled in the Flame Describing Function Noiray, Durox, Schuller, and Candel (2008) framework. It is also likely that the change in phase results from the transverse velocity fluctuations and maybe perhaps from the presence of nearby extinguished flames.

9.7 Conclusion

This chapter describes experiments carried out on a laboratory scale annular combustor comprising multiple injectors fed with liquid fuel. This investigation is concerned with dynamical phenomena observed when the system features a coupling between combustion and azimuthal acoustic modes giving rise to thermoacoustic oscillations. Experiments re-

veal a broad variety of dynamical features. In particular, very high amplitude oscillations coupled by the standing first azimuthal mode 1A1L of the annular system are described. The azimuthal mode coupling is intermittent and gives rise to intense bursts featuring peak amplitude levels of 6 kPa to 7 kPa. These pressure excursions are sufficiently high to induce an extinction of flames located near the pressure nodal line. This phenomenon already observed in our previous experiments is here analyzed by combining pressure oscillation measurements and images of the flames.

It is found in this case that the frequency of oscillation sweeps a range of values extending more than 10 % around the nominal modal frequency (from 800 Hz to 620 Hz for a typical frequency of 730 Hz). During these high amplitude oscillations, the spin ratio remains at zero, indicating that the coupling mode is standing with some slight displacements of the nodal line. A new result is that the acoustic pressure field is distorted as the amplitude increases. Using the signals delivered by the waveguide microphone array plugged on the chamber backplane, it is possible to expand the pressure up to third order in spatial components to account for this distortion which leads to a relatively asymmetric acoustic field.

Flame blow off is observed for peak acoustic pressure amplitudes above 2 kPa. During a large amplitude oscillation reaching 6.1 kPa, five of the sixteen flames of the combustor are blown off. An important result is that the blow off pattern is also not symmetric, and it appears strongly linked to asymmetries in the acoustic field. A method to reconstruct the acoustic velocity field is proposed, providing a first estimate of the critical threshold value. The phases of the heat release rates in the different flames with respect to the local pressure are also not uniform among all flames on each side of the nodal line. Flame blow off creates temperature inhomogeneities within the combustor, which are shown to be one of the contributing factors to the observed shift in frequency and to the deformation of the acoustic mode. At high amplitude of oscillations, it is important to consider distortions of the modal distributions induced by inhomogeneitites in the mean flow characteristics, notably those affecting the temperature and the sound velocity.

In summary, the key points of this chapter are:

1. A mechanism of flame blow off induced by large amplitude oscillations in an annular combustor;
2. An evolution of the pressure distribution as flames are extinguished, shown using higher order spatial harmonics for reconstruction;
3. An estimation of the transverse velocity fluctuation that induces the initial flame blow off;
4. And a demonstration of the impact of perturbations in the mean sound velocity field on the acoustic eigenfunctions.

Part V

Ignition and blow-out dynamics

Chapter 10

Ignition dynamics

Ignition raises many fundamental and pratical issues. The research effort on this topic is reviewed with specific attention to investigations of the light round process in annular systems. The analysis is then focused on the transient dynamics of an injector after ignition by the travelling flame branch. This process is first documented with experiments in the annular configuration. It is shown that the flame reaches its final shape and position after a certain delay which is here of the order of 50 ms. After the passage of the traveling flame, the newly ignited flame flashes back into the injector during a few milliseconds, (5 ms for the conditions that are tested) in a configuration that may be detrimental to the injector service life. The flame is then lifted off. This process is investigated in further detail by making use of the single segment combustor SICCA-Spray. A model is proposed to represent the pressure excursion induced by the fast combustion of the fresh reactants originating from the injector. This positive excursion induces a sudden reduction in the mass flow rate which then relaxes back to the nominal value by oscillating at one of the resonant frequencies of the system. The model suitably retrieves the velocity waveform recorded by a hot wire placed in the upstream plenum.

Contents

*The second section of this chapter reproduces the ignition literature review of an article published in Combustion Science and Technology in March 2020 as "Dynamics of Annular System" by Guillaume Vignat, Daniel Durox, Thierry Schuller and Sébastien Candel. The third section presents my contribution to the modeling of a combustion dynamics phenomena occuring during ignition. This was included in an article published in the Journal of Engineering for Gas Turbine and Power **141**(6) as "Flame and spray dynamics during the light-round process in an annular system equipped with multiple swirl spray injectors" by Kevin Prieur, Guillaume Vignat, Daniel Durox, Thierry Schuller and Sébastien Candel.*

10.1 Introduction

In the general context of operability of aero-engines, the topic of ignition raises many issues that need to be considered and that have already been extensively investigated in the technical literature. Research has been concerned with a variety of topics such as conditions at the spark plug like minimum spark energy (Lewis and Elbe (1987); Ballal and Lefebvre (1975)), influence of gas velocity, equivalence ratio, gas stream heterogeneity (Lefebvre and Ballal (2010); Ballal and Lefebvre (1977); Ballal and Lefebvre (1978b); Ballal and Lefebvre (1979); Ahmed and Mastorakos (2006); Ahmed et al. (2007)), ambient pressure (Ballal and Lefebvre (1978a)), conditions of formation of a spherical flame kernel leading to a successful initiation of a flame (Deshaies and Joulin (1984); Champion et al. (1986); Champion et al. (1988)), ignition probability in turbulent flows (Ahmed and Mastorakos (2006); Ahmed et al. (2007); Neophytou et al. (2012); Cordier et al. (2013)), or effects of fuel spray characteristics on the ignition delay (Ballal and Lefebvre (1981); Neophytou et al. (2012)). Many other aspects of forced ignition of spray flames are reviewed by Mastorakos (2017). These contributions provide considerable insight on forced ignition that can be used in the engineering design of aeronautical combustors and indicate that the process follows three main steps: (1) creation of a flame kernel by the ignition source, (2) establishment of the flame at an injector that is closest to the ignition source and (3) burner-to-burner propagation of the flame, designated light-round ignition in the case of annular combustors. Many experiments are available on steps (1) and (2), mainly based on ignition of a single injector under a variety of conditions. Simulations have also been used quite successfully to reproduce ignition processes, mainly again for a single sector. Some recent work present experiments and related numerical simulations of step (3) in a linearly arranged multiple swirling injector combustor. This is exemplified in Barré et al. (2014) with results concerned with the impact of injector spacing on the flame propagation under premixed conditions. Experiments where fuel is injected as a spray of liquid fuel droplets are simulated by Collin-Bastiani et al. (2019). Light round ignition of annular combustors was until recently not well documented. There was however a remarquable simulation by Boileau et al. (2008) of the ignition sequence in an annular combustor of a helicopter engine, comprising eighteen injectors but with no experimental validation. While many ignition correlations have been established from experiments on complete combustors, see for example Lefebvre and Ballal (2010) or Naegeli and Dodge (1991), there was a lack of detailed experimental data on the ignition and subsequent flame spreading in annular devices. The topic was clearly less well covered than ignition

of single injector configurations, as indicated in the literature review developed in Section 10.2. One aspect that has also received little consideration is that of the transient dynamics of a particular injector when it is initiated by the sweeping flame or by the initial combustion region formed by the spark plug. Observations made during ignition tests on MICCA-Spray, indicated that there is a transient adjustemnt of the flow before the flame is fully established and that there is a delay before the flame adopts its final shape and position at a distance from the combustor backplane. The process observed in the annular configuration is also present in the single sector configuration. Section 10.3 describes experiments carried out on this rig. A model is also derived to represent the initial stages of the the transient and its results are compared with experimental data.

10.2 Ignition dynamics in annular configurations: a brief review

The present section focuses on recent results obtained on the subject of the light-round in laboratory scale annular combustors. Subsection 10.2.1 focuses on results obtained under premixed conditions in three experimental rigs, while subsection 10.2.2 is concerned with the reproduction of these experimental results using LES. Subsection 10.2.3 discusses the light-round studies performed with liquid spray fuel injection in the MICCA-Spray combustor. The injector transient dynamics observed in MICCA-Spray and examined in subsection 10.2.4. gives rise to a change in flame shape after initiation by the sweeping flame branch.

10.2.1 Light round under premixed conditions

Data on light round in annular systems have become available from the relatively recent work of Bourgouin et al. (2013). This was obtained with MICCA equipped with swirled injectors and operated in perfectly premixed conditions. Investigation of the light round mechanism has also been carried out in Cambridge, both under premixed (Bach et al. (2013); Machover and Mastorakos (2017a)) and non-premixed conditions (Machover and Mastorakos (2016)). More recently another annular combustion facility has been developed with a design close to that of MICCA in China and ignition studies have also been performed under premixed conditions in this facility, but for lower injection velocities, see for example Ye et al. (2018).

The light round process taking place during the ignition of an annular system equipped with multiple swirling injectors is investigated with the arrangement shown in Fig. 10.1. The system (MICCA) comprises an upstream plenum closed at the top by a plate comprising sixteen swirling injectors and a combustion chamber made of two cylindrical concentric quartz tubes mounted on the annular plate which serves as a chamber backplane. The diameters of the inner and outer quartz tubes are 30 cm and 40 cm respectively. The length of the inner and outer tubes can be varied. It is set at 40 cm in the ignition experiments.

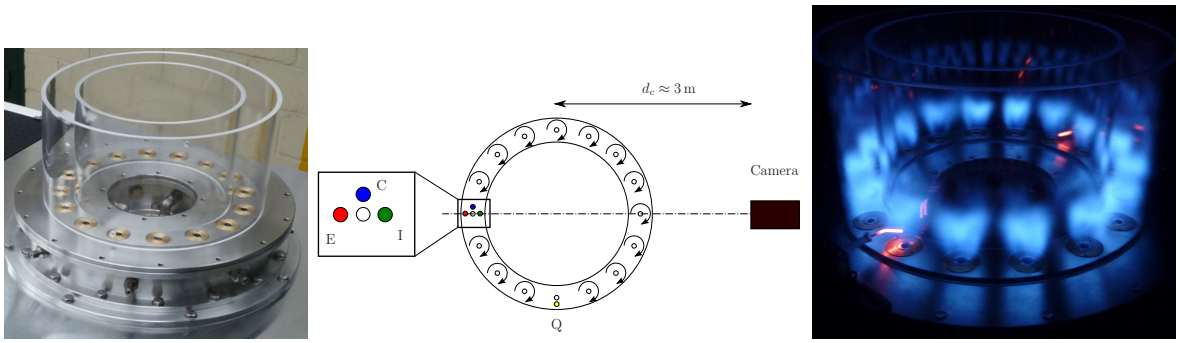

Figure 10.1: *Left : view of the annular combustion chamber. The mean diameter of the ring is 350 mm. Two spark plugs are placed in diametrically opposite positions. Right : direct true color photograph of the swirling flames in the annular chamber equipped with the 200 mm quartz tubes under steady operation at a bulk velocity* $u_b = 19.6\,m.s^{-1}$ *and an equivalence ratio* $\phi = 0.76$ *in each injection tube. The two diametrically opposed igniters can be seen in yellow/red due to their thermal radiation. Adapted from Bourgouin et al. (2013).*

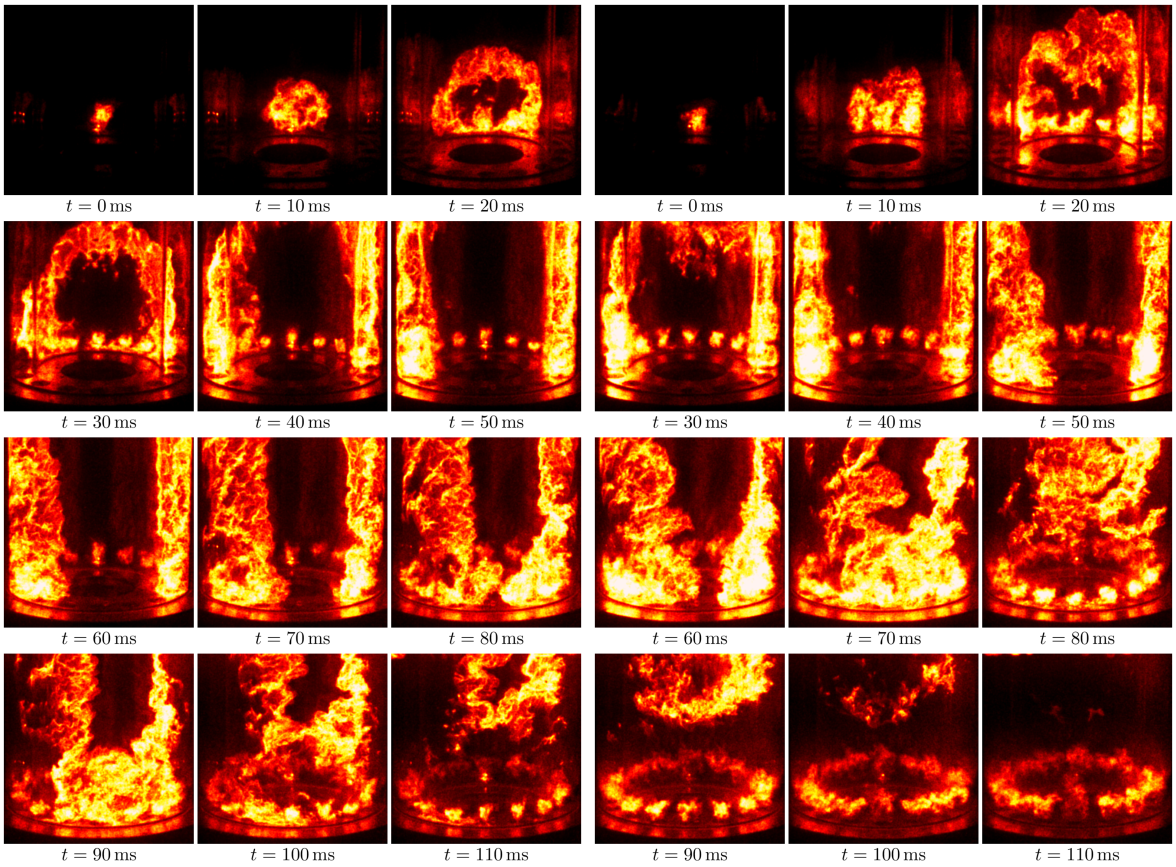

Figure 10.2: *Images of light intensity emitted by the flame during an ignition of the annular chamber at* $\phi = 0.76$. *Left:* $u_b = 12.2\,m.s^{-1}$. *Right:* $u_b = 24.5\,m.s^{-1}$. *False colors are used to improve the visualization. Yellow and dark red correspond to the highest and lowest values of light intensity. From Bourgouin et al. (2013).*

Air and propane are delivered to a premixing unit. The mixture is then conveyed to an annular plenum through eight channels which are plugged on the internal sides of this cavity. Gases in the plenum are injected into the combustion chamber through sixteen swirling injectors mounted on the flange which separates the plenum from the chamber and constitutes the chamber backplane. Each injector is made of a cylindrical tube $D = 10\,\text{mm}$ in diameter at the bottom of which is placed a swirler equipped with nine blades to set the flow in rotation. The outlet section of the injector is flush mounted to the backplane of the combustion chamber which is cooled by an internal circulation of water. When viewed from above each swirling flow rotates in the clockwise direction.

The chamber walls are made of quartz allowing optical access to the flames and transmitting its radiation in the near ultraviolet and visible ranges. This provides a full access to the combustion region (Fig. 10.1). Some reflections appear on the quartz tubes which form the combustor side walls. Figure 10.2 shows flame images recorded by the intensified CMOS camera during the propagation of the flame from the ignition kernel to the steady state operation. To improve the visualization, these images are plotted on a scale of colors where yellow corresponds to the highest intensity value while dark red represents the lowest value in flame emission. The igniter is placed in front of the camera on the opposite sector of the annular chamber. During the ignition process, the igniter generates a spark at a repetition rate of 100 Hz. The strong radiation of the spark plasma saturates some pixels of the camera sensor and it is not easy to distinguish the initial hot gas kernel, complicating the determination of the ignition instant. The initial pocket is convected by the flow and distorted by the local turbulent eddies. The delay associated with these various processes is $\tau_0 \simeq 10\,\text{ms}$. When the pocket meets favorable conditions, it expands and propagation becomes nearly isotropic and initially spherical. This defines the initial instant $t = 0$ in the following figures and it corresponds to a predefined threshold intensity level. The flame then takes the shape of a symmetric arch at instant $t = 20\,\text{ms}$. From $t = 40\,\text{ms}$ to $t = 70\,\text{ms}$ the two flame fronts are nearly vertical and the injectors are sequentially ignited by the propagating combustion front. The flame spreads more rapidly in the vicinity of the injectors and the two fronts begin to merge at time $t = 80\,\text{ms}$ and at a point that is not quite opposite to the igniter. The left side is in advance due to the swirl direction of rotation that induces a global gyration in the chamber. After merging of the left and right moving flame branches, the front is convected upwards by hot gases originating from the burners and the steady state is reached.

It is convenient to transform the images recorded by the camera to eliminate perspective effects by unwrapping the cylindrical geometry of the system. This is accomplished in Figure 10.3. These images allow direct comparisons with simulations based on a level set description of flame propagation relying on turbulent velocity estimates (Bourgouin et al. (2013)).

It is also instructive to examine the global emission signal detected by the camera. This signal is representative of the heat release rate in the system. Figure 10.4 represents on the left the integrated light intensity for a bulk velocity $u_b = 24.5\,\text{m.s}^{-1}$ and equivalence ratio $\phi = 0.76$. As explained previously a critical size c_s of the hot gas kernel is defined by an

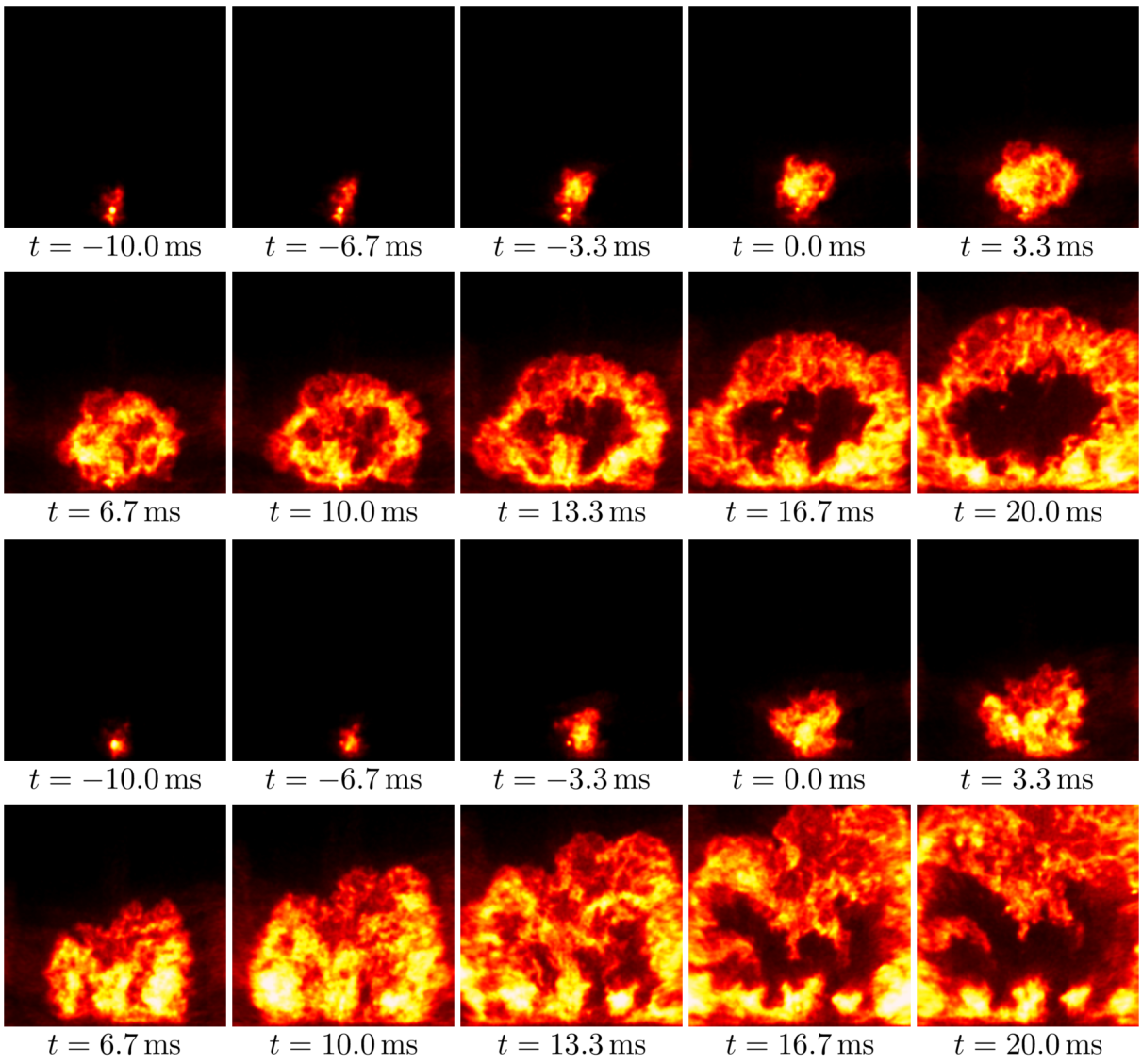

Figure 10.3: *Numerically transformed images of light intensity emitted by the flame during an ignition of the annular chamber at* $\phi = 0.76$. *False colors are used to improve the visualization. Yellow and dark red correspond to the highest and lowest values of light intensity. Upper ten images:* $u_b = 12.2\,m.s^{-1}$. *Lower ten images:* $u_b = 24.5\,m.s^{-1}$. *From Bourgouin et al. (2013).*

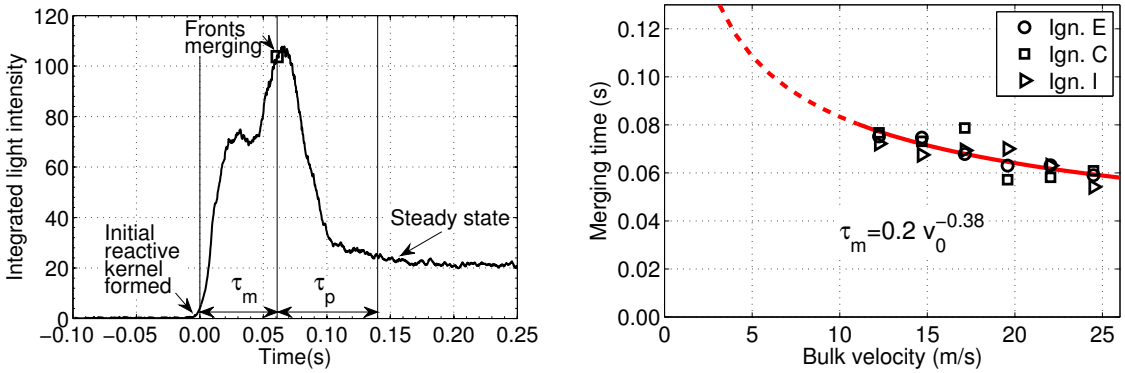

Figure 10.4: *Left : Integrated light intensity recorded by the camera during ignition for a bulk velocity $u_b = 24.5\, m.s^{-1}$. The square symbols indicate the moment where the two flame fronts merge. Right : Propagation time τ_m for six flow rates and three igniter positions. From Bourgouin et al. (2013).*

intensity threshold. This defines the instant $t = 0$ already used in Figure 10.2 to examine flame propagation. One can also define the delay τ_m from the time origin when the kernel size has reached c_s to the time where the left and right flame fronts merge. A final delay τ_p corresponds to the time duration between merging and steady state operation. The total propagation delay is then given by $\tau_t = \tau_m + \tau_p$. For a fixed value of the equivalence ratio, the steady state level is essentially proportional to the injection velocity u_b. This is coherent with the assumption that the camera signal can be qualitatively interpreted as proportional to the heat release rate. The recorded light intensity signals have a similar shape for all injection velocities explored. The frames where the fronts are merging can be manually selected and merging times τ_m can be deduced in this way as shown on the right in Figure 10.4.

10.2.2 Light round simulations in premixed conditions and comparison with experiments

The MICCA experiments constitute an interesting case for testing the ability of large eddy simulation to retrieve data gathered during light round experiments. It is possible to compare time resolved flame visualizations with LES results obtained for the same multiple-injector annular combustor geometry and operating conditions. It is probably the first time that such a direct comparison was carried out for the light-round process (Fig. 10.5). The comparison is illustrated by experimental data and calculations corresponding to an equivalence ratio $\phi = 0.76$ and a bulk velocity $u_b = 24$ m.s^{-1}. The experimental data is recorded with a high-speed intensified imaging CMOS camera at a frame rate of 6000 Hz and an exposition of 166 μs. This suitably resolves the flame during the light-round process which takes of the order of 50 ms. Calculations are carried-out with the AVBP flow solver, a code jointly developed by Cerfacs and IFP Energies Nouvelles together with the TACLES model derived at EM2C laboratory to represent the chemical conversion in the LES framework. The computational domain comprises the up-

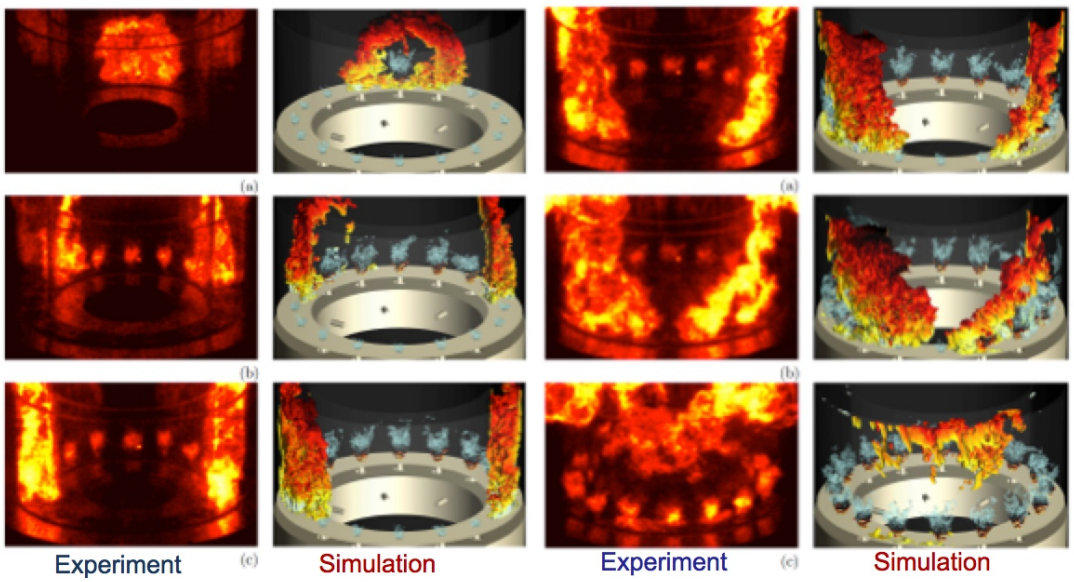

Figure 10.5: *Light round ignition of the MICCA combustor. Experiment and simulation.* $u_b = 24\ m\ s^{-1}$, $\phi = 0.76$. *Adapted from Philip et al. (2014).*

stream air and fuel manifolds, plenum, injectors and the annular chamber formed by the combustor backplane and quartz walls. The ambient atmosphere is represented by a large volume added at the exit of the combustor. The mesh comprises 310 million tetrahedra. The process is initiated by depositing a small sphere of burnt gases at the adiabatic flame temperature that is located at the position of the experimental spark ignitor. Further details and analysis may be found in Philip et al. (2015); Philip et al. (2014); Philip et al. (2015).

Figure 10.5 shows experimental data in the form of light emission images while numerical results are plotted as an isosurface of temperature colored by values of axial velocity. The structure of the flame brush at the largest scales is close to that observed experimentally, the instantaneous geometries of the flame front resemble those recorded by the high speed camera while the transit times from one injector to the next are quite similar, indicating that the LES with the selected sub-models suitably retrieves essential features of the light round process.

It is also interesting to examine the flame merging delays that are measured and simulated. Figure 10.6 shows data sets obtained under cold wall conditions and under preheated conditions. One notices that the thermal conditions at the walls have a notable influence on the propagation of the flame during the light round and on the value of the merging delay. The merging delay is longer when the chamber walls are initially cold. Preheated conditions are closest to the adiabatic wall boundary conditions used in the simulations. There is a good agreement between experimental data and the two calculated values of the merging delay.

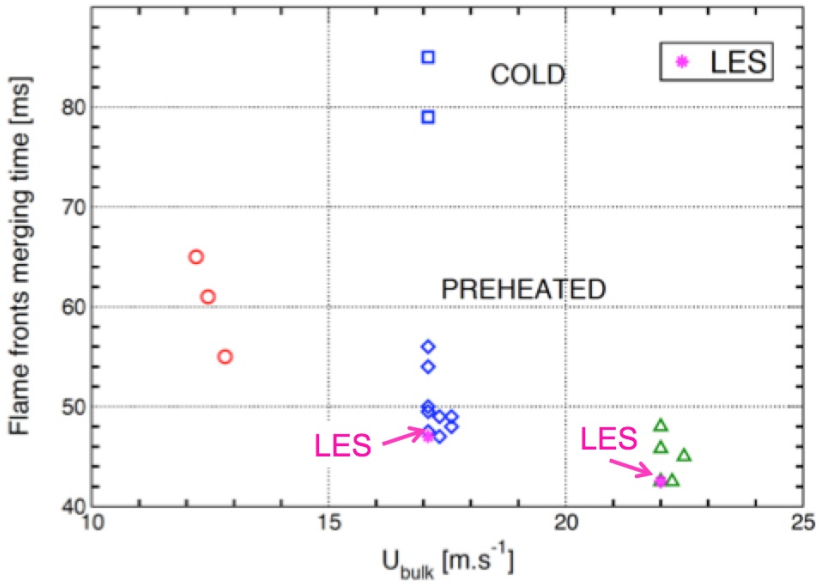

Figure 10.6: *Flame merging delay plotted as a function of the bulk injection velocities. The red circles, blue diamonds and green triangles are obtained from experiments in which the chamber walls are preheated. The blue squares correspond to experiments under cold wall conditions. The calculated merging delays are shown as magenta star symbols. Adapted from Philip et al. (2014).*

10.2.3 Ignition dynamics under liquid spray injection

It is next interesting to examine the characteristics of light round when the injection takes place in liquid form. This is accomplished by making use of a modified version of the annular combustor designated as MICCA-Spray. The liquid fuel heptane or dodecane is injected as a spray formed by hollow cone atomizers. Prieur et al. (2017b) compared the impact of the type of combustion, premixed or spray, and the influence of fuel volatility. The process was extensively characterized with high-speed measurements with an intensified camera, photomultipliers and microphone arrays placed in the plenum and in the chamber of the annular combustor. A large data set is acquired and compared when the bulk velocity, the equivalence ratio or the power are varied. An example is given in Figure 10.7.

It is found that spray combustion does not affect the basic mechanisms of the light-round. The major effect of the fuel type is to modify the delay time τ_m that is found to decrease when the volatility of the fuel is augmented and that is further decreased when fuel and oxidizer are premixed. A close-up view on the behavior of the flame propagation in an arch-like pattern is shown in Fig. 10.7. Detailed imaging of the passing flame front gives indications on the flame wrinkling. By recording the Mie scattering of the n-heptane droplets illuminated by a laser sheet, it is possible using particle image velocimetry (PIV) to observe the influence of the traveling flame front on the droplet distribution in the chamber. It is found that the propagating flame displaces the droplet spray well before the flame reaches the injector (Prieur et al. ()). Using a similar technics, the travelling velocity of the flame front can be estimated. Large eddy simulations of the light round under liquid spray injection has also been explored quite successfully by Lancien et al.

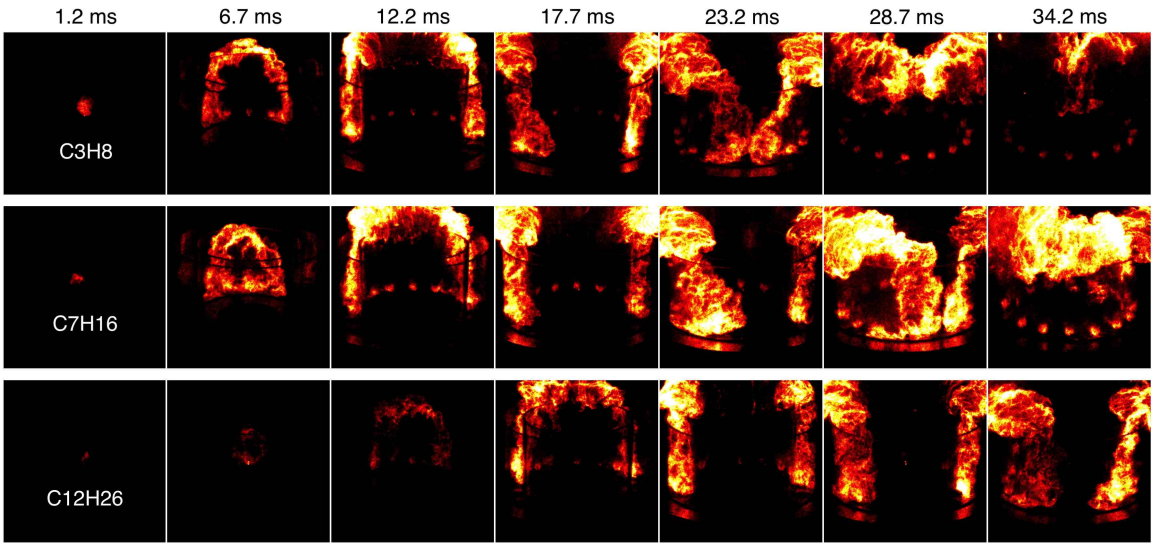

Figure 10.7: *Light emission during the light round ignition sequence of propane (top), n-heptane (middle row) and dodecane (bottom row) fuels. Yellow corresponds to high light intensity while dark red represents low light emission. Injection conditions : u_b = 31.5 m s^{-1} , ϕ= 0.90 and $\mathcal{P}$= 80 kW. From Prieur et al. (2017a).*

(2018); Lancien et al. (2019); Puggelli et al. (2020).

10.2.4 Flame structure evolution during the light-round

The high definition of the images recorded during the experimental test series that led to the publication of Prieur et al. () gives access to details of the flame shape during the ignition process of the annular chamber. In order to reduce the noise due to turbulence induced fluctuations, 50 consecutive instantaneous images, corresponding to a short time period of 8.33 ms, were recorded and averaged to get moving-averaged filtered flame shapes. This filter size was chosen so that the flame shape would barely change during this time scale. Figure 10.8 presents the filtered flame shape evolution of one injector for four different successful ignitions of the annular combustor. The initial time $t = 0$ corresponds to the ignition of this injector by the passing flame branch. One can see that the flame appears to be at first relatively compact and close to the chamber backplane. The flame luminosity extends within the injection unit through the central recirculation zone (CRZ). After 25 ms the flame lifts off from the injector, expands in a clear "M" shape and reaches its final position after 50 ms. This defines two time delays: τ_l between the time of ignition and the first flame shape switch, associated with the flame lift-off, and τ_f between the time of ignition and the stabilization of the flame in its final shape. On average, $\tau_l = 25$ ms and $\tau_f = 50$ ms.

The top of Fig. 10.9 shows two images of the flame 5 ms and 88 ms after the injector ignition. Luminosity levels are saturated in order to enhance the differences. One can see that the left flame is clearly attached to the lips of the injection unit and is even

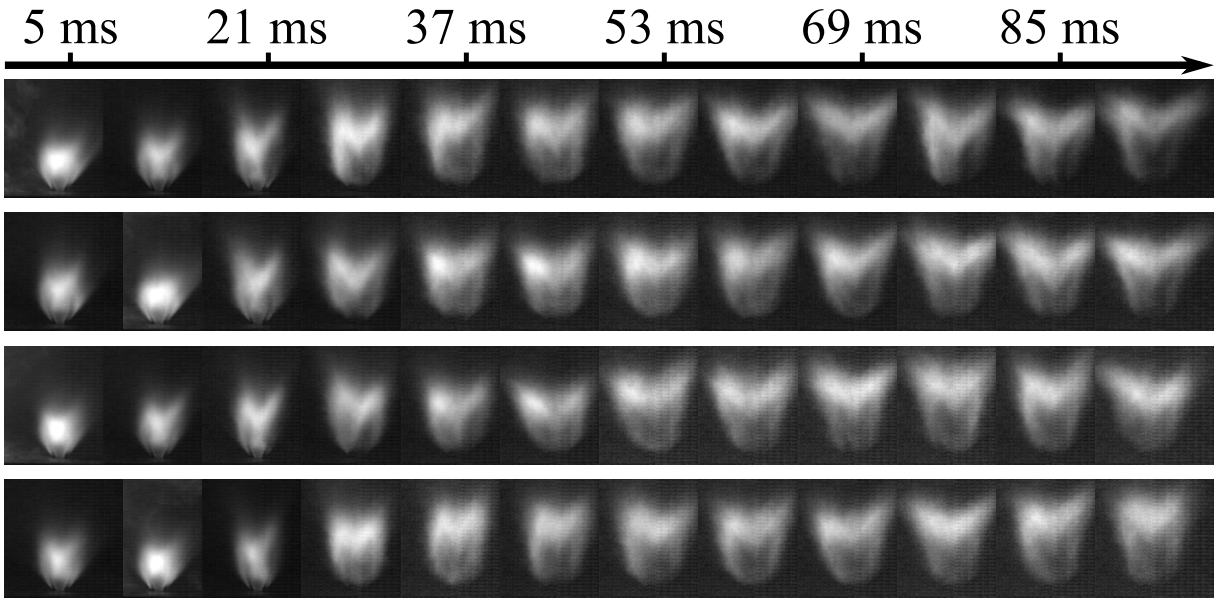

Figure 10.8: *Four ignition sequences showing the evolution of the time-averaged flame shape after the passage of the flame front. The time origin $t = 0$ corresponds to the instant when the injector is ignited by the incoming flame front.*

entering inside the injector, sucked in by the central recirculation zone (CRZ) formed by the rotating flow. After several milliseconds, the inner flame stabilized in the recirculation zone vanishes and the flame lifts off its anchoring points. Filtered Abel transform images are in both cases proposed in the lower part of Fig. 10.9, featuring two flame shapes "A" and "B". This phenomenon of upstream propagation of the flame front in the injector can be detrimental to the life duration of this unit. As the flame travels in the injector, internal metallic parts are exposed to high temperatures. Although this takes place over a period of a few milliseconds, this thermal loading taking place at every ignition might degrade the injection components. It is worth noting that this process is repeatable and not specific to the MICCA-Spray configuration.

In particular, it is interesting to see whether the evolution of flame shapes observed in a swirl spray configurations can also be observed in the case of fully premixed gaseous injection. The spray injectors are replaced by premixed injectors with the slightly different swirler geometry used in Bourgouin et al. (2013) but having about the same swirl number $S_{conv} \approx 0.7$. Figure 10.10 shows at the top the ignition of the annular combustor with these injectors for a propane/air mixture at $\phi = 0.76$ and $\mathcal{P} = 60\,\text{kW}$. One can see that flames at 120 ms and 160 ms are quite different. The same injection system is mounted on the SICCA single injector rig to examine the ignition steps. As for the spray injector, the flame is first quite compact and moves into the injection system before stabilizing and being lifted at about 40 ms. This indicates that the phenomenon observed in this study is not specific to spray swirled injection configurations.

It was already indicated in the previous paragraphs that it takes approximately $\tau_l = 25\,\text{ms}$ to expel the flame from the injection unit and that an additional delay is required for the

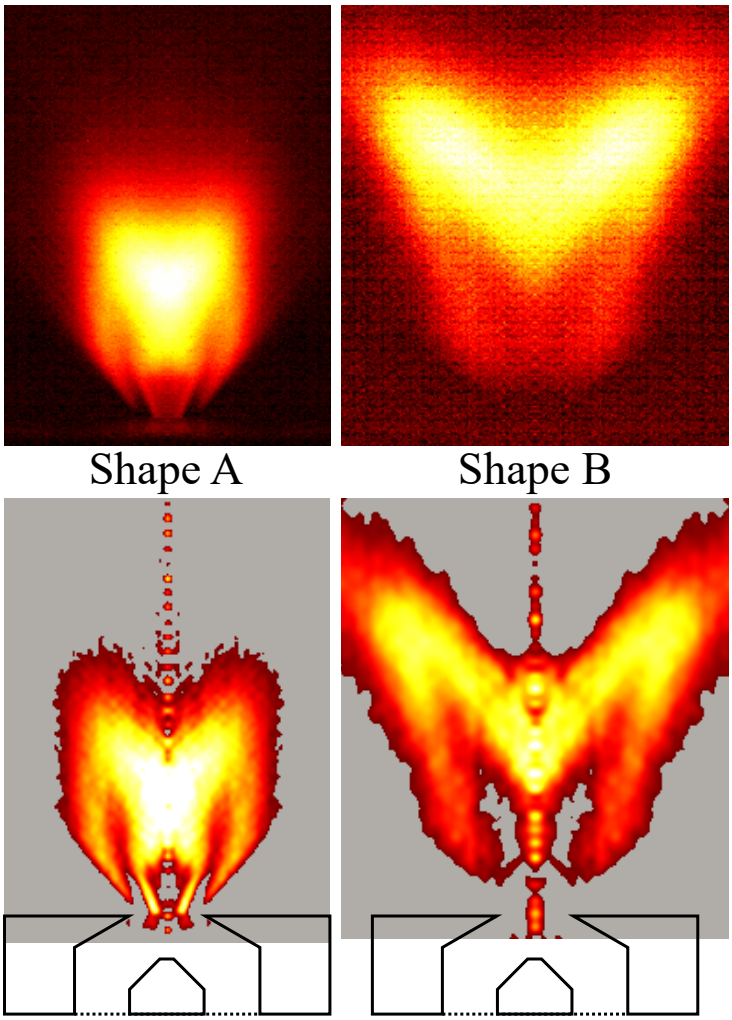

Figure 10.9: *Left: Flame shape* 5 ms *after the flame front ignites this injector (top, shape 'A') and Abel transform of the flame (bottom, shape 'A'). Right: Flame shape* 88 ms *after the flame front ignites this injector (top, shape 'B') and Abel transform of the flame (bottom, shape 'B'). Images are represented in false colors and saturated to highlight their different structures. Yellow and white correspond to high light intensities while dark red represents low light emission levels. Abel transform gives rise to errors in the near vicinity of the axis so that the values in this region should not be considered.*

flame to reach its final shape $\tau_f = 50$ ms after ignition. Figure 10.11 shows time-averaged images of three different neighboring flames in the MICCA-Spray chamber during the light-round. The averaging method over 8 ms is identical to the one used for images shown in Figs. 10.8 and 10.9. Flames are designated by letters "α", "β" and "γ", from right to left. The time step between each mean image is approximately 17 ms. The initial instant $t = 0$ corresponds to the ignition of flame "γ". Flame "α" was then ignited at $t = -8$ ms. In the first snapshot, one can see that flames "α" and "β" are adopting an "A" shape as described before. Flame "γ" is not perfectly ignited yet. At $t = 17$ ms, flame "α" switches to a "B" shape (see Fig. 10.9) while "β" and "γ" still feature an "A" shape. 17 ms later, flame "β" has switched to the "B" shape while flame "γ" is in the process of

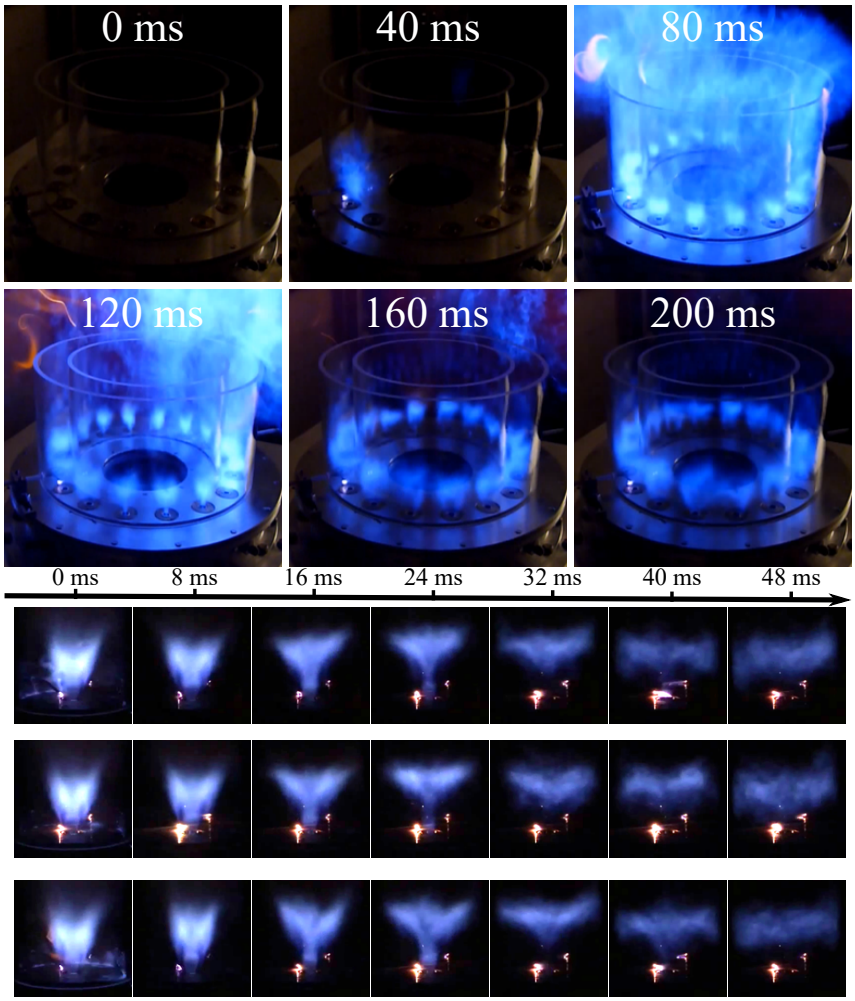

Figure 10.10: *Top: True-color low-speed images of the light-round in the MICCA combustion chamber under premixed propane-air conditions with* $\phi = 0.76$ *and* $\mathcal{P} = 60\,\mathrm{kW}$. *Bottom: Three ignition sequences of the SICCA burner equipped with the premixed swirled injector with* $\phi = 0.76$ *and* $\mathcal{P} = 3.75\,\mathrm{kW}$.

lifting-off. At $t = 51\,\mathrm{ms}$ all flames have adopted the "B" shape.

In conclusion, one can see that all the flames do not switch simultaneously from "A" to "B" shapes. The time delay τ_p between these changes is the delay for the flame front to travel from one injector to the next. The distance between two injectors is $s = (1/16)\pi D = 68\,\mathrm{mm}$ with D the mean diameter of the chamber. If one considers that the flame front absolute velocity v_f is a constant with $v_f \approx 17\,\mathrm{m\,s^{-1}}$ (see Prieur et al. ()), the time delay τ_p is 4 ms. In the annular combustor, the first flame ignited will lift-off and switch from "A" to "B" shapes after $\tau = \tau_l = 25\,\mathrm{ms}$, whereas the second one will change after $\tau = \tau_l + \tau_p = 29\,\mathrm{ms}$. The n-th flame will then change after $\tau = \tau_l + (n-1)\,\tau_p$.

Acoustic pressure signals during the light-round process are recorded using 4 microphones "MPx" in the plenum and 8 microphones "MCx" plugged on the combustor backplane (see Fig. 7). Typical pressure signals are presented in Fig. 10.12. For this specific experimental

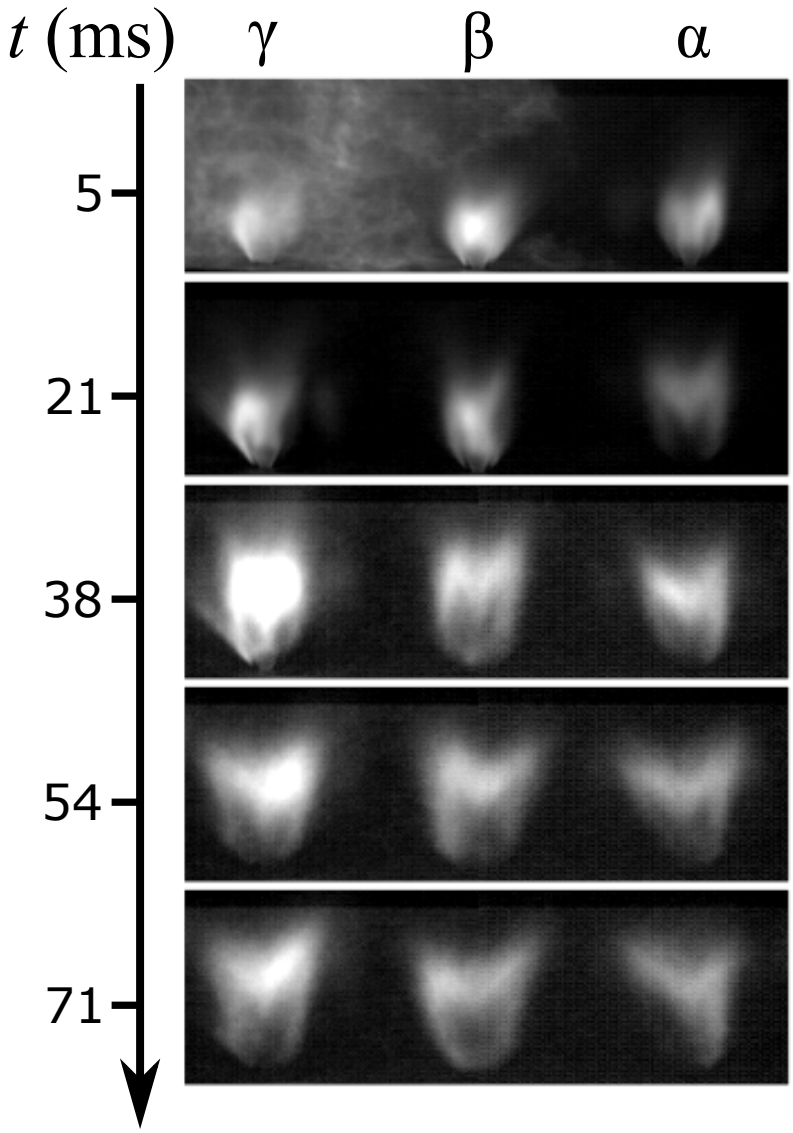

Figure 10.11: *Mean images of three consecutive flames of the annular combustor progressively switching from shape 'A' to shape "B". In the first image, the flame front propagates from right to left. The first flame to be ignited is flame "α".*

run, ignition occurred shortly at $t = 4038\,\text{ms}$. All plenum microphones show an initial rise in pressure to 130 Pa. This rise occurs over a duration of 40 ms, which corresponds to the light-round delay of the MICCA-Spray combustor at this operating point. The key information to retrieve from Fig. 10.12 is that the pressure signals recorded by the chamber microphones 'MCx', each separated by 45°, appear to be in phase. One can see that the pressure wave arrives at nearly the same instant at every sensor positions in the bottom plot in Fig. 10.12 indicating that it propagates at the speed of sound c of the medium which is typically $720\,\text{m}\,\text{s}^{-1}$ and which corresponds to a delay of 0.1 ms between two consecutive sensors. The pressure peaks in the bottom plot correspond to the ignition of the eight successive pairs of injectors in the annular combustor. This feature is underlined by the different black vertical lines in the bottom figure. The peaks are all

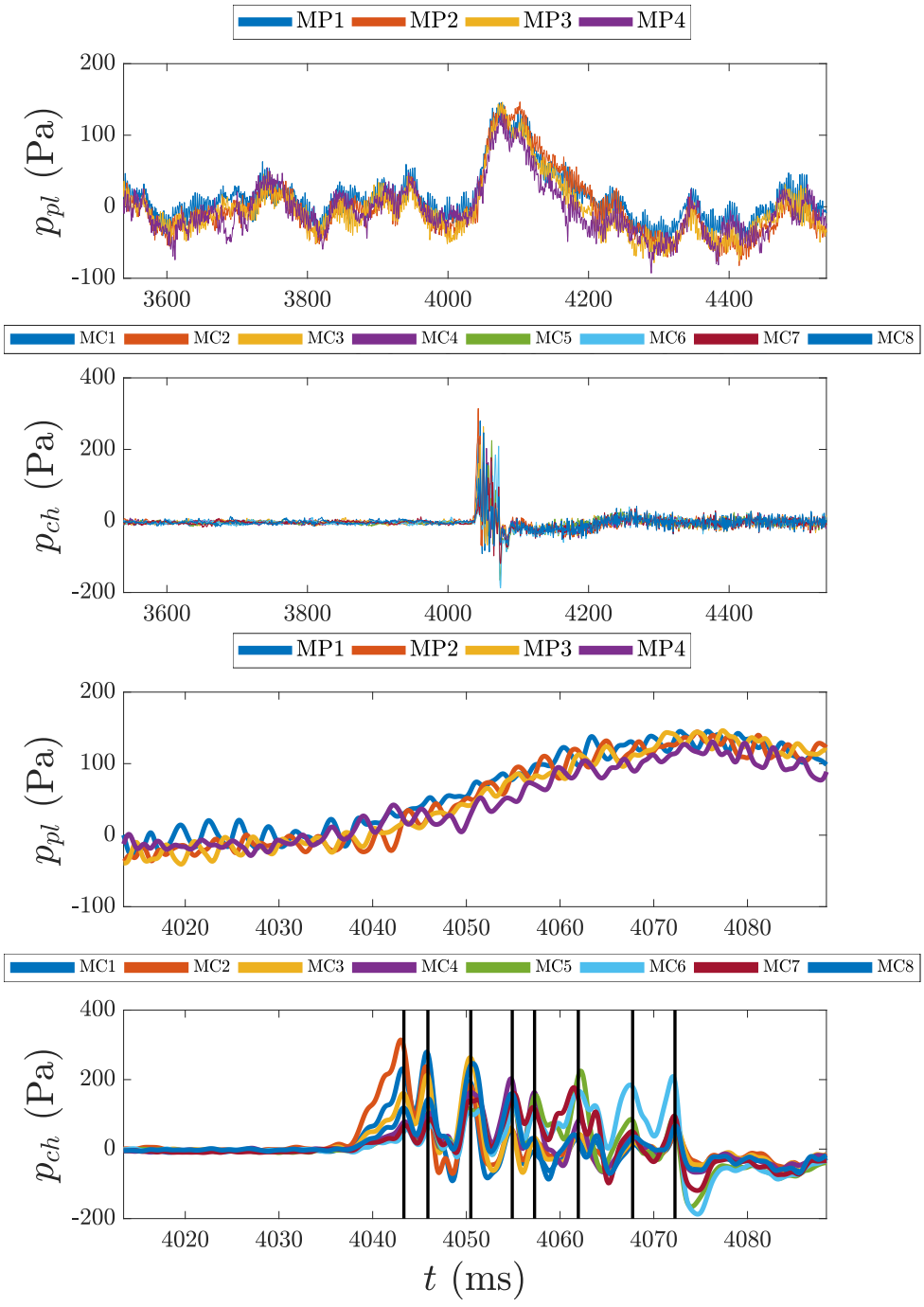

Figure 10.12: *Acoustic pressure recorded by four pressure sensors in the plenum (1st and 3rd graphs) and by eight pressure sensors in the chamber (2nd and 4th graphs) before and after the light-round. Note that the 3rd and 4th figures are expanded views of the pressure tracks in the plenum and in the chamber during ignition. In the bottom graph, the black lines correspond to successive pressure peaks, each associated to the ignition of an injector. For clarity, the signals are low-passed filtered with a cut-off frequency of* 500 Hz.

quasi-equally spaced in time and the delay is $\Delta t = 4\,\text{ms}$ which corresponds to the time for the traveling flame branch to propagate from one injector to the next.

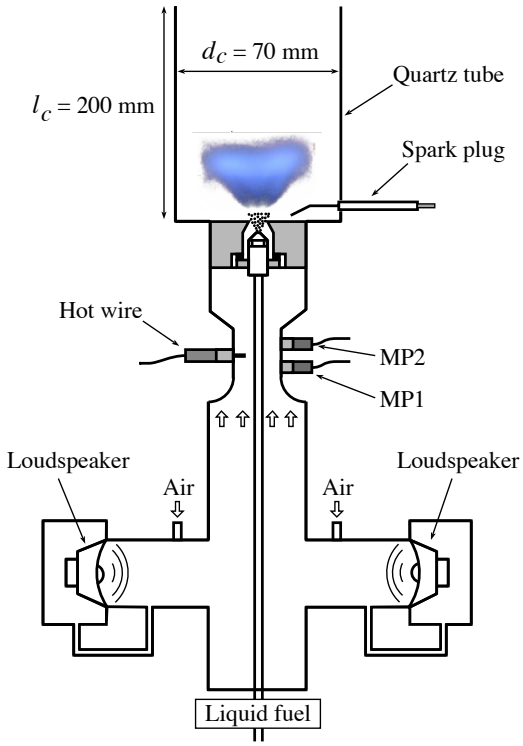

Figure 10.13: *Schematic representation of the SICCA-Spray burner with key dimensions.*

10.3 Dynamics of ignition of a single spray swirled injector

10.3.1 Experimental investigation

In order to investigate in more details this transient flame structure, and compare the behavior of one isolated injector and one flame in the annular MICCA-Spray combustor during the ignition process, the single injector system SICCA-Spray is used. It is again schematically shown in Fig. 10.13. It represents 1/16th of the MICCA-Spray annular chamber. The surface of the quartz tube forming the combustion chamber is calculated to provide a level of confinement to the flame that is close to that of the annular device. The same injection systems are used in the two rigs. The resulting flame is similar in shape to that found in the annular chamber (not shown here). More details on the characterization of the flame in SICCA-Spray are given in Prieur et al. (2017b) and in Chapters 1 and 3. Air velocity measurements in the plenum are recorded with a hot wire located 100 mm upstream from the injector exhaust section. The plenum is carefully designed to generate a flat velocity profile at the hot wire position. The average velocity measured by the hot wire during steady operation at the nominal point is $u_0 = 2.06\,\mathrm{m\,s^{-1}}$. At this position, the section is round with a diameter of 30 mm. A photomultiplier tube with an optical filter centered on the wavelength of the emission of the OH* radical is used to estimate the unsteady heat release rate during ignition. It is worth noting that, even under these non-premixed conditions, one may assume that the PM signal intensity

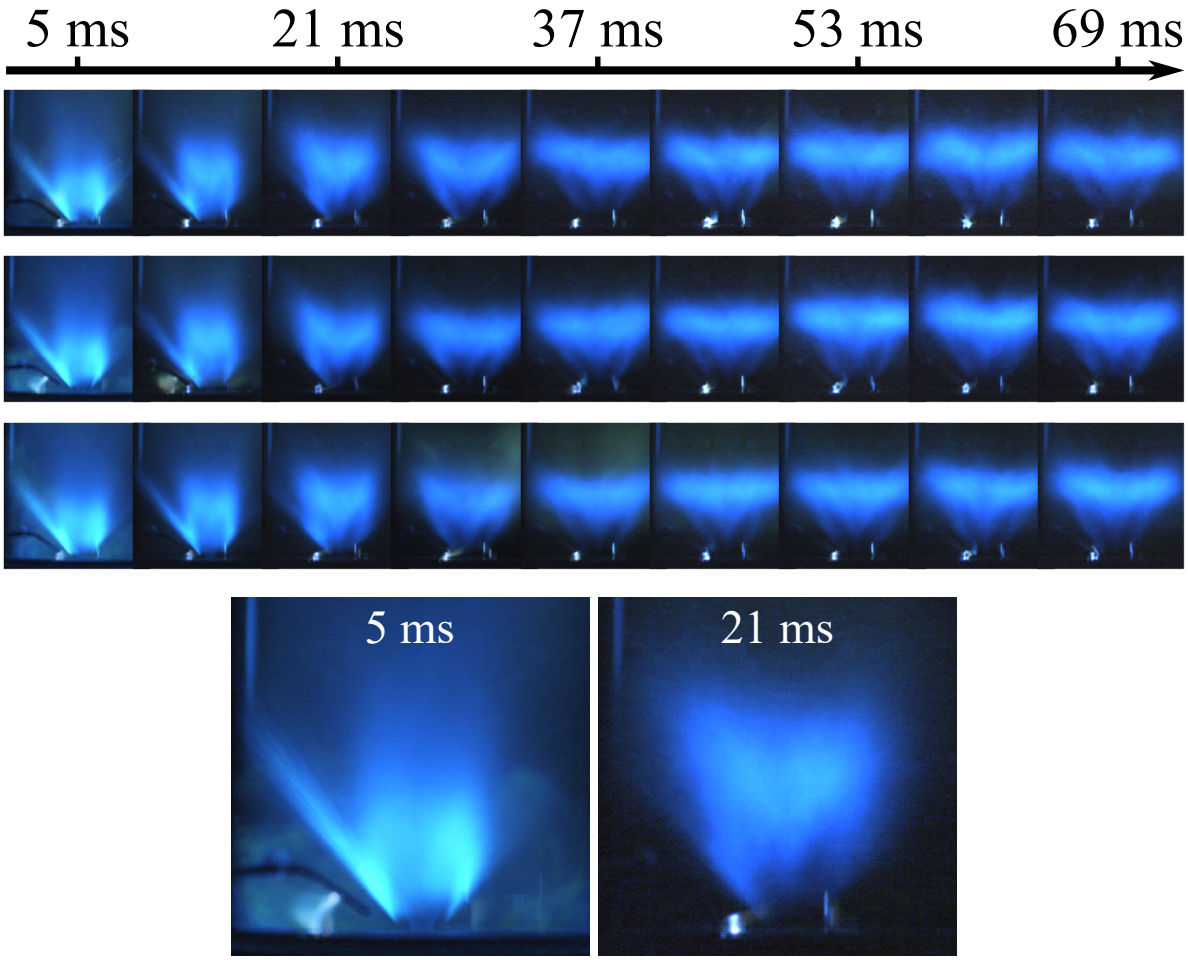

Figure 10.14: *Top: True-color ignition sequences in SICCA-Spray. Bottom: Close-up images at* $t = 5$ *and* 21 ms. *Extra white luminosity is due to the sparks used to ignite the system, which are continuously operated at a repetition rate of* 100 Hz.

provides to some extent an indication on the combustion intensity, which is linked to the flame luminosity. This was shown experimentally using a quasi-steady approach by Mirat et al. (2014) and successfully applied in Mirat et al. (2015), and is discussed at length in Chapter 2.

In subsection 10.2.4 it was found that the flame switched from shape "A" to shape "B" during the ignition of the annular chamber MICCA-Spray. This feature was characterized by a lift-off time delay $\tau_l = 25$ ms. The stabilization of the flame in its final shape requires some more time, leading to an overall time delay of $\tau_f = 50$ ms for the flame to reach its final steady state structure. The first step is to verify that the same features are found in the single injector system. Figure 10.14 presents three successful ignition runs. The same time-averaging method is used as for the data acquired in the annular chamber. One can see that the flame is first attached to the burner lips and quite compact, which can be identified as an "A" shape (Fig. 10.9). After roughly the same delay as in MICCA-Spray, the flame detaches and adopts a "B" shape. This is confirmed by larger chemiluminescence images displayed in the bottom of Fig. 10.14.

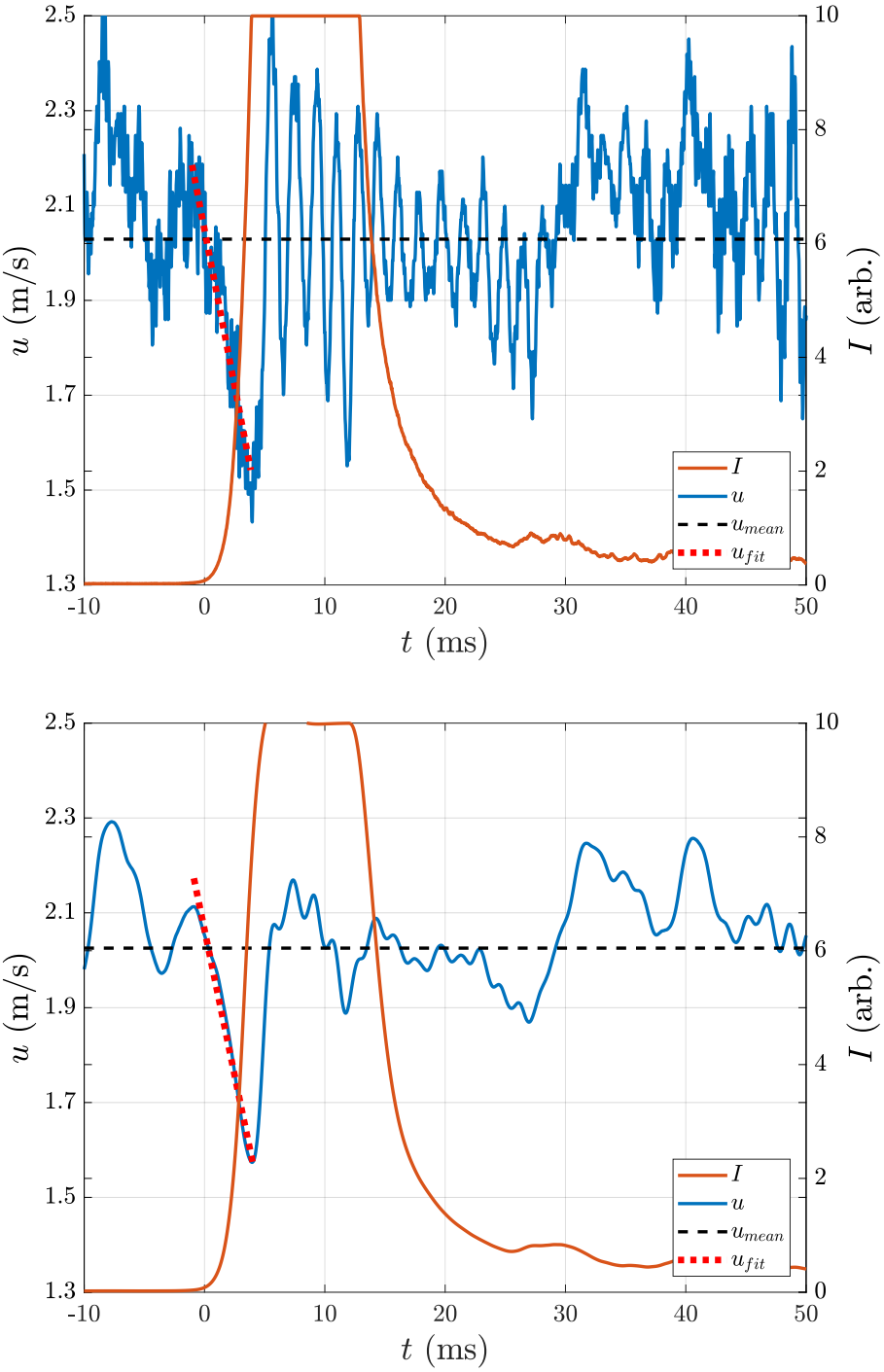

Figure 10.15: *Top: Velocity u and flame luminosity I signals during ignition of the single SICCA-Spray injector. The black dotted line corresponds to the mean velocity at nominal operating conditions. The red dotted line is a linear regression of the measured air velocity. Bottom: The signals are processed using a Butterworth low pass filter at* 200 Hz*, underlining the sudden decrease of the flowrate and its readjustment after the flame passage.*

Next, it is interesting to examine air velocity and flame luminosity measurements recorded simultaneously during several ignitions of the burner. Figure 10.15 presents typical results obtained during a period of 60 ms around the ignition time $t = 0$. The high luminosity during the ignition process is due to the burning of all the fresh mixture in the chamber resulting in a saturation of the photomultiplier signal. The important information from this measurement is the instant at which the ignition begins. One can see in the plot that, as soon as the flame luminosity I starts rising at $t = 0$, the velocity at the hot wire decreases with a constant slope. This is best seen in the bottom plot where the velocity signal has been low pass filtered to eliminate a high frequency periodic oscillation at 600 Hz already present before ignition, and associated with an acoustic resonance in the combustor. The minimum value of velocity roughly drops down to around 1.55 ms. The time of decay does not vary between each ignition and is equal to 4 ms on average (red dashed line in Fig. 10.15). After that, the air velocity rapidly increases and overshoots above its mean level before stabilizing once again around that value. This takes approximately 20 to 40 ms, defining the time delay τ_m, depending on the sequence. These time delays are of the same order of magnitude as τ_l the time delay required for flame lift-off in the MICCA-Spray set-up.

10.3.2 Mechanisms for the flame structure evolution

In this section, physical mechanisms are examined to explain the flame shape evolution observed during ignition in the two experimental configurations MICCA-Spray and SICCA-Spray. It is first observed that just after ignition the flame is initially located inside the injection unit, within the central recirculation zone. At this time, a positive spike in chamber pressure can be observed (see Fig. 10.12), as well as a drop in air flowrate (see Fig. 10.15). After a time delay $\tau_l = 25$ ms, the flame lifts-off and adopts the "B" shape described in Fig. 10.9. An additional time delay is necessary for the flame to take its final steady state shape. This occurs with a delay $\tau_f = 50$ ms after ignition in the studied conditions.

Many phenomena can intervene to drive this process and control the transition in flame shape and location:

1. The turbulent state of motion in the combustion zone, the equivalence ratio, and in the case of spray injection, the size of the fuel droplets;
2. The aerodynamics of the injector flow;
3. The thermal conditions in the flame region neighborhood.

The first two items control the flame penetration inside the injector unit while the third most probably determines the transition from this initial configuration to the final state where the flame is stabilized at a distance from the injector exhaust. This is examined in more detail in what follows.

10.3.2.1 Equivalence ratio and turbulence effects

Concerning the first set of factors, the fuel mass flow rate is most probably not affected by the ignition as the pressure loss in the fuel line is around 6 bar. However, it was shown in Prieur et al. () that the traveling flame branch, while sweeping a new injector, perturbs the cloud of liquid fuel droplets, leading to an increase in the concentration of droplets and a locally richer mixture. The decrease in air mass flow rate through the injection unit is also conducive to locally richer fuel-air mixtures in the instants following ignition. As the combustor is operated under an overall lean condition, this increase in fuel-air ratio will lead to an increase in laminar burning velocity.

Two delays related to the behavior of the droplets are however particularly relevant in this context: the convection time of a droplet through the flame τ_{cf}, and the droplet lifetime before complete evaporation τ_{vap}. The first delay τ_{cf} is the ratio between the length of the flame and the bulk velocity: $\tau_{cf} = l_f/u_b = 2\,\text{ms}$. The droplet lifetime was evaluated in Prieur et al. (2017b) at $\tau_{vap} = 0.8\,\text{ms}$ for droplets having a Sauter mean diameter typically found in MICCA-Spray. These delays are relatively small compared to the 50 ms required for the change in flame shape. Furthermore results from the premixed propane-air configuration presented previously indicate that effects of the spray are probably not driving the change in flame shape.

Turbulence in the combustion zone at the outlet of the injector will also affect the turbulent burning velocity. Following ignition and the subsequent rise in gas temperature, the turbulence level is likely to decrease, leading to lower turbulent burning velocity and local combustion intensity. The flame will have a reduced capacity to lay in the high velocity region inside the injector unit but this effect remains difficult to quantify.

10.3.2.2 Flow and injector dynamics

The injector flow dynamics is perturbed by the rise in pressure observed in Fig. 10.12 that occurs in the injector vicinity just after ignition. This pressure perturbation is associated with the rate of change of the heat release rate, and can be estimated using Eq. (10.1):

$$p'(\boldsymbol{r},t) \approx \frac{\gamma-1}{4\pi c_0^2}\,\frac{1}{|\boldsymbol{r}-\boldsymbol{r_0}|}\,\frac{d\dot{Q}'}{dt} \tag{10.1}$$

where p' designates the unsteady pressure fluctuations caused by the rate of change of the heat release rate, γ the heat capacity ratio, c_0 the speed of sound between the flame and the measurement point, $\dot{Q}'$ the integrated unsteady heat release rate of the flame and $\boldsymbol{r}$ and t are the spatial and temporal variables. In principle only valid in the far-field of a compact flame, this expression has been used under similar conditions with some success in several articles (Strahle (1978); Schuller et al. (2003); Candel et al. (2004); Noiray et al. (2007)) to estimate the near-field pressure perturbations. Using the data recorded in the ignition sequence of SICCA-Spray (Fig. 10.15), $d\dot{Q}'/dt$ can be roughly estimated at $5\,\text{MW}\,\text{s}^{-1}$, thus the unsteady pressure perturbation at the injector outlet reaches a typical

value of approximately 2 kPa.

This rise in pressure downstream of the injection unit corresponds to a decrease in pressure difference across the injector, leading to a drop in air mass flowrate observed in Fig. 10.15. The flame can then flashback in the injector, meaning that it reaches zones where the velocity is much lower than in the vicinity of the injector outlet. The pressure perturbation lasts $\tau_{\Delta P} \simeq 4\,\mathrm{ms}$, at which point a minimum of inlet flow velocity is reached. This instant corresponds to the maximum of the slope of the time evolution of the heat release rate. The flow velocity within the injector will then relax to its nominal value. The flame will be destabilized and convected at a finite velocity downstream of the injection unit, reaching its final position.

The relaxation of the air flowrate from its perturbed state to its nominal value is a function of injector geometry and flow conditions. This will induce a delay τ_{v_*}, defined as the response time of the injector to return to its nominal value at the end of the pressure perturbation. This delay can be estimated to be less than 1 ms from Fig. 10.15. Important parameters controlling this relaxation are the pressure loss in the injector and the volume of air that is perturbed by the pressure wave. A framework for the injector dynamics can be derived to represent changes in the air flowrate. It is expressed in a dimensionless form using $v_* = u/u_0$ the reduced velocity at the location of the hot wire probe. One may first consider the conservation of momentum in the injection system and write a first model thereafter called model "M1":

$$\tau \frac{dv_*}{dt} + \frac{1}{2}v_*^2 = \frac{1}{2} + \frac{\Delta p'}{\sigma \rho u_0^2} \tag{10.2}$$

where $\tau = l/(u_0\sigma) =$ is a characteristic time corresponding to the ratio of the length l of the air column displaced by the perturbation by the steady-state velocity measured by the hot wire probe $u_0 = 2.06\,\mathrm{m\,s^{-1}}$ multiplied by σ a head loss factor defined in Eq. (10.3). The difference $\Delta p'$ represents a pressure perturbation acting on the system at the injector outlet. This perturbation level and waveshape cannot be determined from the measurements performed in the present study. Using the estimation made from experimental data, it will be modeled as a triangular short pulse with a minimum $\Delta p'_{max} = -2.0\,\mathrm{kPa}$ at $t = 4\,\mathrm{ms}$ followed by a sharp return to 0 as shown in black in Fig. 10.16.

One may take $\rho = 1.2\,\mathrm{kg\,m^{-3}}$ as temperature and mean pressure in the plenum are considered to be near atmospheric conditions. The head loss coefficient $\sigma = 2.39\,10^3$ can be evaluated from the usual head loss scaling law:

$$\Delta p = \frac{1}{2}\sigma \rho u^2 \tag{10.3}$$

using the location of the hot wire probe as the reference section. Equation (10.2) can be integrated to determine the air flowrate dynamics. The velocity at the hot wire probe position is initiated at its nominal unperturbed value $u = u_0 = 2.06\,\mathrm{m\,s^{-1}}$ so that $v_*(t = 0) = 1$. Results are shown in blue in Fig. 10.16. The injector flowrate quickly responds to the pressure perturbation, with a 95% response time of 0.35 ms. The initial drop in inlet velocity, which follows the pressure perturbation, is well retrieved:

$u_{M1}^{min} = 1.69\,\mathrm{m\,s^{-1}}$ and $u_{exp}^{min} = 1.55\,\mathrm{m\,s^{-1}}$, but the subsequent behavior and oscillations are not.

In the unfiltered curves in Fig. 10.15, oscillations at $f_0 = 600\,\mathrm{Hz}$ can be observed. This frequency roughly corresponds to the longitudinal quarter wave acoustic mode of the combustion chamber of the SICCA-Spray burner, assuming a homogeneous temperature field of 950 K in the combustion chamber, which was pre-heated before the ignition sequence. To account for the oscillations in flowrate seen in the unfiltered curves in Fig. 10.15, a second model called model "M2" may be employed that comprises a second order term:

$$\frac{1}{\omega_0^2}\frac{d^2 v_*}{dt^2} + \tau\frac{dv_*}{dt} + \frac{1}{2}v_*^2 = \frac{1}{2} + \frac{\Delta p'}{\sigma\rho u_0^2} \tag{10.4}$$

In this expression, $\omega_0 = 2\pi f_0$ is the angular frequency. Equation (10.4) integrated with the initial conditions $dv_*/dt = 0$ and $v_* = 1$ yields the results plotted in Fig. 10.16. The system behaves quite similarly to model "M1" but exhibits an oscillation at 600 Hz. This oscillation, of acoustic origin, is damped, but in model "M2" only the contribution of the injector to the acoustic damping is taken into account. Neither model retrieves the low frequency oscillations at 60 Hz of the flowrate observed in Fig. 10.15. This is probably due to the approximate waveform assigned to the perturbed pressure term. However, these models account for the sudden reduction in flow velocity inside the injector and rapid return to equilibrium. In addition model "M2"' accounts for the high frequency oscillations around the steady state. The delay τ_{v_*} required for the perturbed injector flowrate to reach its steady state at the end of the pressure perturbation is shown to be small and of the order of 0.4 ms.

10.3.2.3 Effects of local thermal conditions

The third factor influencing the flame structure evolution is linked to the thermal conditions characterizing the flame neighborhood. It is well known that flames are sensitive to thermal conditions prevailing near the injector exhaust and at the surrounding boundaries. For example, the light-round time delay is modified if the chamber walls are cold Prieur et al. (2017b). Experiments (Guiberti et al. (2015)) and LES calculations (Maio et al. (2019)) have shown the influence of the boundary conditions of the chamber walls on the flame shape. Temperature measurements with thermocouples and thermochromic paint have been performed in the annular and tubular experiments under the same injection conditions (results not shown here). They indicate a maximum temperature of 900 K on the outer part of the wall and 1200 K on the inner part of the wall. These temperatures are reached after 10 minutes of operation. Note that the present experiments are all run under pre-heated conditions, the combustor having been operated for several minutes to keep the walls at the stabilized thermal conditions. The thermal inertia of the walls is large compared to the transient phenomena observed with the flames.

However, the wall temperature is much lower than the adiabatic flame temperature. The flame shape will be substantially different if the walls are nearly adiabatic or if they are isothermal and at lower temperature. One of the mechanisms involved is that the burnt

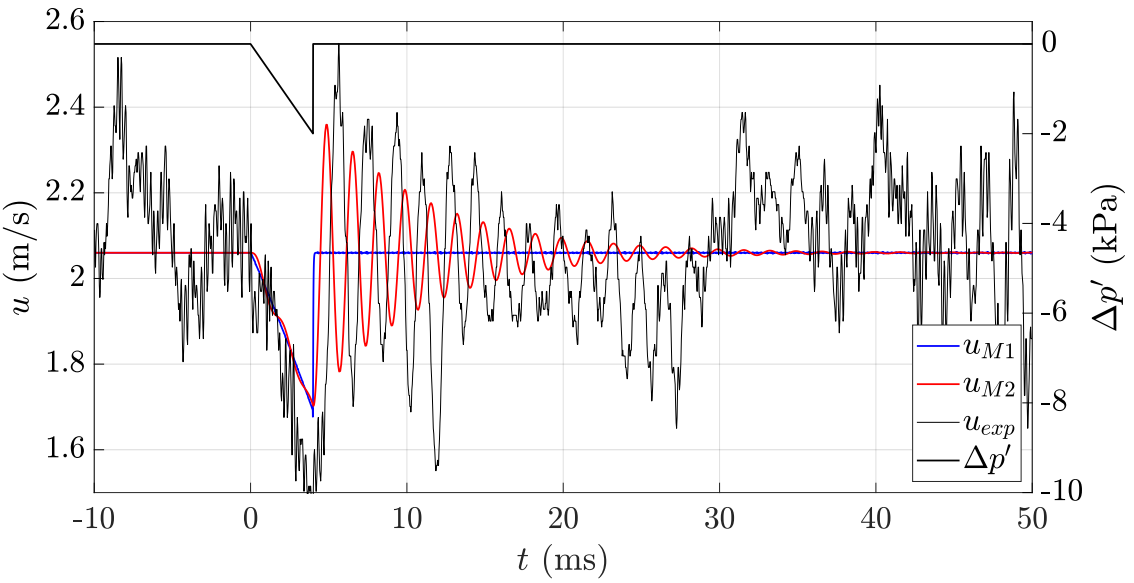

Figure 10.16: *Velocity obtained at the hot wire position using model M1 (blue, Eq. (10.2)) and M2 (red, Eq. (10.4)). The velocity measured by the hot wire is shown as a thin black line. The pressure perturbation used for the present calculation is shown as a thicker black line on top, associated with the right axis.*

gases are cooled in the outer recirculation zone before reaching the anchoring point of the flame. Under certain conditions depending on a Karlovitz number (linking a turbulent time associated to the recirculation zone and the chemical time), if this Karlovitz number exceeds a critical value (Guiberti et al. (2015)), the flame front can no longer attach to the lip of the injector. The outer part of the flame then detaches and lifts-off. In the present context, the burnt gases in the ORZ are initially not cooled by the wall, and therefore can be considered as adiabatic. The flame is then anchored at the lips of the injector. Following this first instant, the burnt gases recirculate in the outer recirculation zone and cool down. These cooled burnt gases will then affect the lower part of the flame, and more specifically the anchoring point. Several residence times characterize this cooling process and its effect on stabilization.

The residence time of the burnt gases in the ORZ can be evaluated by extrapolating from results in Guiberti et al. (2015). In this article, the swirled flame has a similar aspect to that of the present study, and the authors measured the residence time using particle image velocimetry. By normalizing the injector bulk velocity and the confinement ratio, the residence time in the SICCA-Spray setup used in the present study can be estimated: $\tau_{ORZ} = 7\,\text{ms}$. A multiple of this residence time is required for all thermal processes to reach a steady state, and for the anchoring of the flame to be affected. It should be noted that the thermal equilibrium time delay starts as soon as the combustor is ignited, and that this time delay is superimposed to the injector dynamics effects presented in section 10.3.2.2.

Recent results from high fidelity LES simulations of the ignition process in SICCA-Spray

performed by Töpperwien et al. (2020) have brought further confirmation of this thermal process affecting flame stabilization after ignition.

10.3.2.4 Time delays corresponding to the different mechanisms

There is some evidence that each of the three mechanisms mentioned at the beginning of section 10.3.2 plays a role in the change in flame structure that is observed. It is however difficult with the experimental data from the current study to evaluate the contribution of each individual mechanism. Only characteristic time delays have been evaluated with some level of confidence, and the overall time delay $\tau_f = 50\,\text{ms}$ is probably the sum of the individual contribution of each of these mechanisms. The characteristic time delay associated with the fuel droplets is 2 ms. The response of the injector to the pressure perturbation caused by the ignition spans 5 ms, and is probably responsible for the flashback of the flame. The time delay required for the thermal equilibrium to be reached in the ORZ is a multiple of τ_{ORZ}. From this, it can be estimated that five to seven residence times are required for the ORZ to fully thermalize, since $\tau_{ORZ} \approx 7\,\text{ms}$. This thermal process is most likely responsible for the lift-off of the flame and the overall time delay $\tau_f = 50\,\text{ms}$ required for the flame to reach its final position and shape.

10.4 Conclusions

This chapter is focused on the dynamics of the flame during the light-round process in annular combustors and specifically considers the evolution of the flame structure established by each injector after it is swept by the travelling flame front. Experimental observations indicate that the azimuthal sweeping of an injector by the combustion wave establishes a flame that is initially penetrating the injector unit. This flame is then expelled from this region and after a certain delay is anchored at its final position. This dynamical behavior is of practical importance because it indicates that prior to the stabilization at a distance from the injection unit, the flame takes positions that may damage the injector. Of course, this is only a model scale version of what is being used in real systems but it shows that some attention needs to be given to the injector dynamics as it is swept by the combustion wave travelling in the chamber. Similar features are observed when a single injector is ignited by a spark plug. Several mechanisms are involved in this transient phenomenon, including equivalence ratio disturbances, sudden reduction in the air flowrate caused by the unsteady pressure excursion during ignition and thermal delays in the outer recirculation zone. The dynamics of the injector response is examined by considering a simplified model representing the mass flowrate evolution after the initial disturbance induced by the sweeping of the combustion wave which induces a large negative disturbance in the mass flowrate. The velocity in the unit is reduced and allows the penetration of the flame front. The injector then rapidly responds to this perturbation by retrieving the steady state mass flowrate and the flame is expelled from this unit. Calculations based on a simplified model retrieve the aerodynamic behavior of the injector following the ignition. After a further delay required to fully thermalize gases in the outer recirculation zone, the flame reaches its final shape. Time delays associated with each mechanism are estimated

and the overall time delay is retrieved.

Chapter 11

Improvement of Lean Blow Out performance using NRP discharges

Plasma-Assisted Combustion (PAC) has shown potential in improving the ignition, extinction, and dynamic performance of combustion systems. In this work, nanosecond repetitively pulsed (NRP) spark discharges are applied to extend the lean blow out (LBO) limit of the SICCA-Spray burner. This laboratory-scale atmospheric test rig is equipped with a swirl spray injector representing in an idealized fashion a single sector of a gas turbine. Three fuels and injection conditions are considered: perfectly premixed methane-air, liquid heptane, and liquid dodecane injected as hollow cone sprays. The optimal electrode position that extends the LBO limit is found to be near the external edge of the outer recirculation zone (ORZ). Spectroscopic measurements show that the NRP sparks produce atomic species and heat the gas above the adiabatic flame temperature. High-speed chemiluminescence images of blow out sequences indicate that the flame evolves similarly for all three fuels from "M" or "V" shapes prevailing at $\phi = 0.9$ to a configuration where chemical conversion also takes place in the ORZ at $\phi = 0.63$. A low frequency combustion oscillation arises near the LBO limit ($\phi = 0.57$). Spray flames blow out at this point, while the plasma-assisted ones continue to burn. It is shown that PAC provides a significant improvement of the extinction performance, in particular when operating with liquid fuel spray injection.

This chapter reproduces an article published in Proceedings of the Combustion Institute: "Improvement of Lean Blow Out Performance of Spray and Premixed Swirled Flames using Nanosecond Repetitively Pulsed Discharges". Authors of the original article are Guillaume Vignat, Nicolas Minesi, Preethi Rajendram Soundararajan, Daniel Durox, Antoine Renaud, Victorien Blanchard, Christophe Laux and Sébastien Candel.

Contents

11.1 Introduction

Premixed and pre-vaporized lean combustion allows for reduced pollutant emissions in gas turbines and aero-engines. In order to control this type of combustion, manufacturers rely to a large extent on advances in swirling injector design to anchor compact flames with a high degree of air dilution. Although the lean stability performance of traditional swirling injectors is already quite good, an increase of the lean blow out (LBO) margin is still desirable, especially for operational and safety reasons (Dhanuka et al. (2011)). For twenty years, plasma-assisted combustion (PAC) has been considered to improve three key areas of combustion: ignition (Lefkowitz et al. (2015)), combustion instabilities (Lacoste et al. (2013); Kim et al. (2015)) and extinction (Kim et al. (2020); Barbosa et al. (2015)). Recent works in these directions are reviewed in Starikovskiy and Aleksandrov (2013); Starikovskaia (2014); Adamovich and Lempert (2015); Ju et al. (2016).

Non-equilibrium NRP (nanosecond repetitively pulsed) spark discharges last a few nanoseconds, with an overvoltage of a few kilovolts. Applied at a repetition rate in the 10 to 100 kHz range in a combustible mixture, they produce thermal, chemical, and hydrodynamic effects (Dumitrache et al. (2019); Rusterholtz et al. (2013); Pai et al. (2010)) that promote the combustion process (Bak et al. (2013); Barbosa et al. (2015); Lefkowitz et al. (2015); Kim et al. (2015)). These benefits have been extensively demonstrated at low and atmospheric pressures, and some recent studies (e.g., Boumehdi et al. (2015); Xu et al. (2016)) have also shown positive effects for the ignition of lean mixtures at pressures up to 16 bar. It was shown (Pilla et al. (2006); Bak et al. (2013)) that the discharge serves as a localized source of heat (thermal effect) and active species (chemical effect), anchoring the flame even in very lean mixtures. In a recent study, Kong et al. (2019) used a continuous AC-powered plasma in a methane-air flame and suggested that the predominant contribution might be from thermal effects, probably due to the higher duration and power of their discharge.

In most practical systems, the LBO limit is dictated by the design of the injector and operating parameters. NRP discharges have successfully been used to extend the LBO limit in laboratory scale test rigs, often with minimal modifications to the combustor. The electrode is generally located on the centerline of the burner, close to the injector outlet, inside a gas recirculation zone with low flow velocities (Barbosa et al. (2015); Lacoste et al. (2013); Rajasegar et al. (2016); Kim et al. (2020)). Even in very lean mixtures, well below the extinction limit, a reaction zone is formed in the vicinity of the electrode. The NRP discharges thus establish a pilot flame that extends the LBO limit of the combustor. It is likely, however, that combustion is incomplete under these conditions (Bak et al. (2013)).

In practical applications, specifically in aero-engines, positioning the electrode on the injector centerline may not be practical. The solid electrode will perturb the flow and symmetry, create additional flame anchoring points and also get degraded by the resulting heat fluxes. Moreover, liquid fuel atomizers are commonly located on the centerline to ensure a homogeneous spray distribution, and the discharge might form between the electrode and the atomizer head. To avoid damaging this sensitive component, in the present study, the electrode is placed close to the lateral wall and the chamber backplane, in the outer recirculation zone (ORZ). Thus, the discharges will occur in an area where the reactive species have sufficient time to mix with the fuel and oxidizer.

In this work, three fuels are considered: premixed methane-air (for a baseline), liquid heptane and liquid dodecane, which is comparatively less volatile (Prieur et al. (2017b)). We show that the LBO limit of these swirling flames is extended with NRP discharges.

11.2 Experimental Setup

11.2.1 The SICCA-Spray Combustor

Experiments are carried out at atmospheric pressure in the SICCA-Spray combustor which is slightly modified compared to previous spray ignition investigations (see Prieur et al. (2017b)). As shown in Fig. 11.1, the system consists of an air plenum followed by a swirling injection system (gray area) comprising a tangential channel swirler that leads to a convergent section with a final radius $r_{inj} = 4\,\text{mm}$. This injector has a measured swirl number of 0.68 (see Annex A.1.1 and Prieur et al. (2017b)). Liquid fuel is injected as a hollow cone spray (diamond-patterned triangle) by a simplex atomizer. When the system operates in the premixed mode, methane is mixed with the air flow using a cyclonic mixing chamber located 3 m upstream of the air plenum. A compact flame is stabilized downstream of the dump plane inside a transparent quartz confinement tube. Spray characterization, performed at the nominal operating condition (t_0 in Tab. 11.1), indicates that for both liquid fuels the mean Sauter diameter of droplets is $D_{32} \approx 30\,\mu\text{m}$ (see Prieur et al. (2017b)). NRP discharges are created between the tip of an Inconel electrode and the combustor backplane (Fig. 11.2). The electrode tip is located 5 mm above the backplane and 24 mm from the centerline of the combustor, except in Sec. 11.4 where its position is varied. Pulses of 10-ns duration with an incident amplitude of 5 kV are generated by a

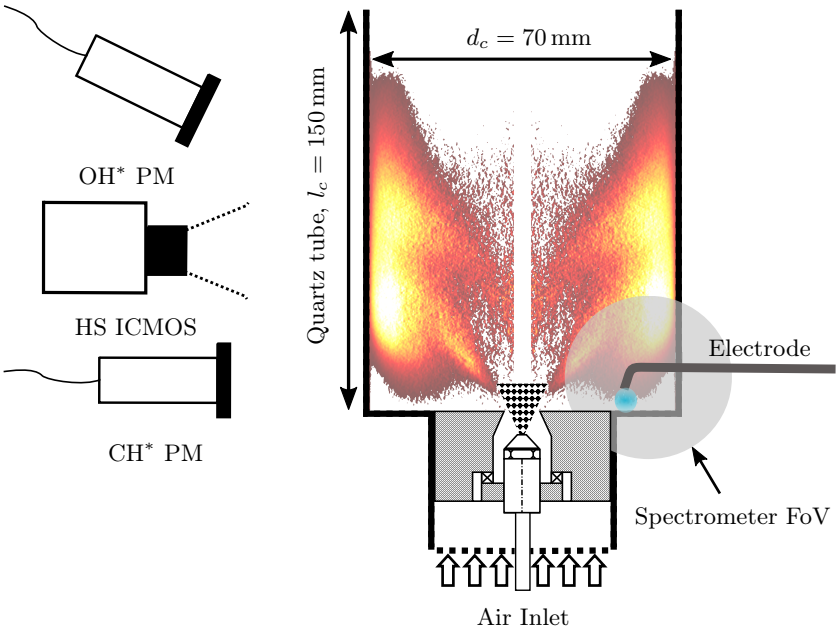

Figure 11.1: *Schematic view of the SICCA-Spray burner. The air plenum is cut for concision. Chemiluminescence diagnostics include a high-speed intensified camera (HS ICMOS) and two photomultipliers (PM). An Abel transformed flame image (see Fig. 11.5) acquired at an equivalence ratio $\phi = 0.63$ is shown in the background. A gray disk qualitatively indicates the field of view (FoV) of the spectrometer. The electrode is to scale with the flame image.*

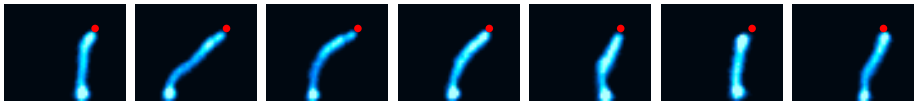

Figure 11.2: *Direct imaging of the plasma discharge using the high-speed camera at 500 fps (false colors). Exposure time is 50 µs to capture a single discharge. The red dots correspond to the tip of the electrode, the bottom of the image to the combustor backplane.*

FPG 10-30NM10 generator (FID Technology) at a repetition rate of 20 kHz.

11.2.2 Measurement equipment

A 6-meter long coaxial cable (75 Ω impedance) connects the generator and the electrode. A high voltage probe (Lecroy PPE20kV) and a current probe (Pearson 6585) are placed midway on the cable and are used to monitor the deposited energy on an oscilloscope (Lecroy HDO 6104) (Minesi et al. (2020)). Typical voltage and current curves are shown in Fig. 11.3. The deposited energy can be calculated from these curves because it has been verified that no energy is lost in the cable and because radiative losses are negligible (Maly and Vogel (1979)). In this study, the voltage is adjusted for every configuration so that the deposited energy remains constant at (5.00 ± 0.25) mJ, corresponding to an average electrical power of (100 ± 5) W.

Mass flow controllers (Bronkhorst EL-Flow) with a relative accuracy of ±7.5‰ and a repeatability better than ±2‰ monitor the flows of air and methane. A Bronkhorst

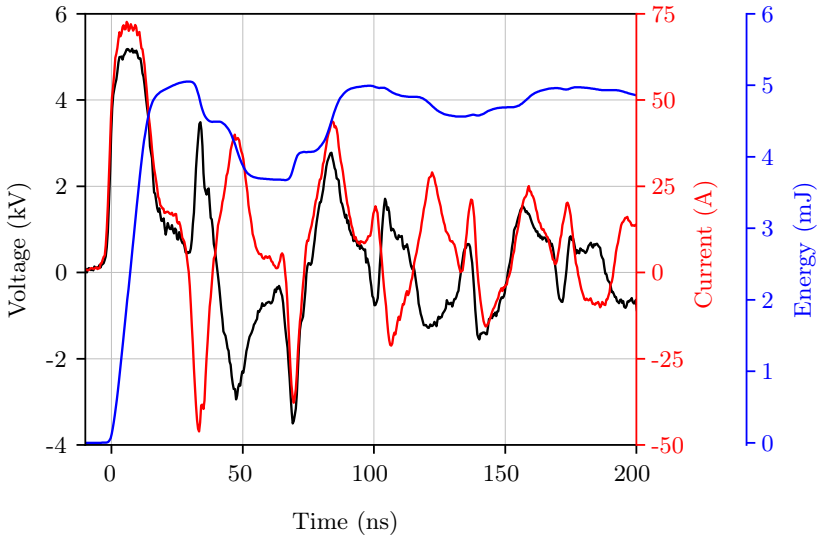

Figure 11.3: *Voltage (black) and current (red) traces recorded with NRP discharges in a dodecane flame. The energy curve (blue) is the integral of the current and voltage product. In this example,* (5.00 ± 0.25) mJ *is sent by the pulser and* (1.50 ± 0.25) mJ *is initially reflected. This energy is deposited during subsequent reflections at* $t = 90$ ns *and* $t = 180$ ns. *For detailed descriptions of the oscillograms, see Dumitrache et al. (2019); Minesi et al. (2020).*

CORI-Flow system is used for the liquid fuels (relative accuracy ±2‰, repeatability better than ±0.75‰). A high-speed intensified camera records the flame images (Photron FastCam APX-i2, 512×1024 pixels, 10−bit gray level depth, 500 images per second with an exposure time of 2 ms). It is equipped with a 45 mm lens and an optical bandpass filter centered at 431 nm to capture the emission of the CH^* radical. The field of view encompasses the whole combustion chamber, from the dump plane to the quartz tube outlet. Two photomultipliers (PM) measure the chemiluminescence signal from the flame. One is equipped with an optical bandpass interference filter centered at 308 nm to capture the emission from the OH^* radical in the flame and the other with a filter centered at 431 nm for the emission of CH^* radicals. These sensors integrate the light emission from the whole combustor volume. Their signals, along with the flowrates, are recorded at 2 kHz. The PM signals are a qualitative indicator of the instantaneous heat release rate of the flame, and are used to detect LBO when these signals drop to zero. When the discharge is active, other excited species, notably N_2^*, emit in the same spectral ranges, and electromagnetic noise, captured by the acquisition chain, is present. This is managed by appropriate electromagnetic shielding, recording the signal with a delay of 35 µs with respect to the pulsed discharge (using a BNC Model 577 gate-and-delay generator), and applying a low pass filter in post-processing. This is found sufficient to reliably detect LBO even in the presence of the discharge. An OceanOptics Maya2000Pro deep-UV spectrometer is used to analyze the spontaneous emission from the flame and the plasma. The optical train consists of a small lens and an optical fiber. The field of view (FoV) schematically shown in Fig. 11.1 encompasses the entire discharge area and some of the ORZ with an integration time including several discharges ($\approx$ 1 ms). Therefore, the spectra are representative of the brightest region of the plasma (the core) at the peak of

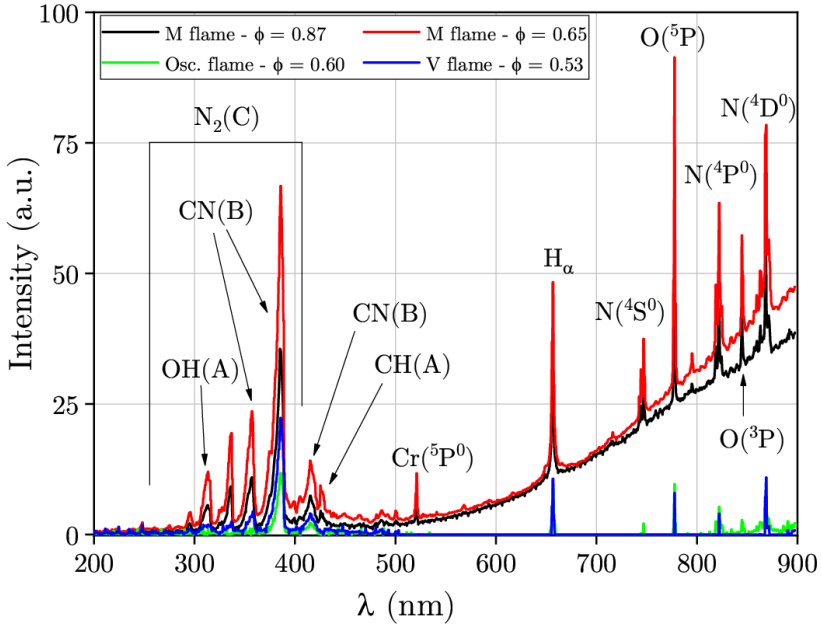

Figure 11.4: *Typical emission spectra recorded in a dodecane flame assisted by NRP discharges ($\phi = 0.87, 0.65, 0.60$ and 0.53). At 520 nm emission from Cr is visible (not to be confused for C_2 Swan emission). It originates from the erosion of the Inconel electrode ($\approx$ 20% Cr). For wavelengths longer than 500 nm, a continuum associated with thermal radiation from the burner and the quartz tube is present.*

the emission (end of the discharge).

11.2.3 Characterization of the plasma

In addition to the images in Fig. 11.2 and the electrical characterization in Fig. 11.3, optical emission spectroscopy of the plasma assisted dodecane flame is performed at four different flame operating conditions ($\phi = 0.87, 0.65, 0.60$ and 0.53). The acquired spectra displayed in Fig. 11.4 give a qualitative idea of the species excited and produced by the discharge and the flame. Typical combustion species (CH* and OH*, see Laux et al. (2003); Gaydon (1974)) are identified in these PAC spectra as well as in the spectra without PAC (not shown here). Strong peaks arising from the emission of CN^* are found, a feature also reported by Kim et al. (2006) in a plasma-assisted premixed methane-air jet flame. No significant emission from C_2^* is detected. Atomic emission from oxygen O^*, nitrogen N^*, and hydrogen H_α is observed. These features show that the NRP discharges dissociate O_2, N_2 and possibly CO_2, H_2O and the fuel.

Stark broadening of the H_α line at 656 nm is used to determine the electron number density (n_e) of the plasma (Gigosos et al. (2003)). At $\phi = 0.87$ and 0.65 (attached stable flames), $n_e = (1.4 \pm 0.2) \times 10^{17}\text{cm}^{-3}$, which corresponds to a degree of ionization about 10%. Several peaks are associated with the emission of $N_2(C)$. Using SPECAIR (Laux et al. (2003)), the rotational and vibrational temperatures are estimated: $T_{rot} = (3500 \pm 500)$K and $T_{vib} = (8000 \pm 1000)$K. As the emission is averaged in space and time by the spectrom-

Table 11.1: *Operating conditions for all fuels at the start of the air flow linear ramp (t_0) and at the end ($t_\infty = 40\,\mathrm{s}$). The bulk velocity u_b is defined at cold thermal conditions as $u_b = \dot{m}_{gas}/\pi\rho r_{inj}^2$. The fuel mass flow rate, thermal power and global equivalence ratio are respectively designated by $\dot{m}_{fuel}$, $\mathcal{P}$ and ϕ.*

	$\dot{m}_{fuel}$	$\mathcal{P}$	ϕ		u_b (m s^{-1})	
	(g h^{-1})	(kW)	t_0	t_e	t_0	t_e
CH_4	359	4.98	0.88	0.46	35	65
C_7H_{16}	400	4.95	0.87	0.45	32	62
$C_{12}H_{26}$	405	4.97	0.87	0.45	32	62

eter, the emission of $N_2(C)$ is representative of the hottest region (center) of the plasma at the end of the pulse. At this instant, $N_2(C)$ is populated by electron impact and therefore its rotational distribution mirrors that of $N_2(X)$ (Rusterholtz et al. (2013)). Owing to fast rotational-translational relaxation at atmospheric pressure, the rotational temperature of $N_2(X)$ is close to the gas temperature, therefore $T_{gas,plasma} \simeq T_{rot} = (3500 \pm 500)$K is representative of the peak temperature at the end of the discharge. The quenching of N_2 excited states by O_2 is responsible for the increase in temperature and the dissociation of O_2 (Rusterholtz et al. (2013)). Both effects are favorable for the flammability of the combustible mixture.

The temperature in the plasma $T_{gas,plasma} \approx 3500\,\mathrm{K}$, higher than the adiabatic flame temperature ($T_{ad} < 2100\,\mathrm{K}$), and the dissociation of O_2 indicate that this discharge is neither an NRP-corona nor an NRP-glow discharge (Pai et al. (2010)). n_e is between the values reported for nonequilibrium NRP-sparks (Rusterholtz et al. (2013)), and for thermal sparks (Minesi et al. (2020)). As neither N^+ emission (500 nm) nor an electron continuum is observed in the spectra, the NRP-spark is necessarily of the nonequilibrium type.

11.2.4 Lean Blow Out Procedure

To avoid changing the fuel atomization properties, which are sensitive to the flow rate for simplex atomizers Lefebvre (1989), the fuel flow rates are kept constant. They are chosen so that the thermal power is almost the same for all fuels at $\mathcal{P} \approx 5\,\mathrm{kW}$. The ratio of electrical (NRP) to thermal (combustion) power is therefore equal to 2% for all cases. The LBO limit is determined by linearly varying the air flow rate, starting from the nominal, well-characterized operating point of $\dot{m}_{air} = 1.94\,\mathrm{g\,s^{-1}}$ (Prieur et al. (2017b)) and going up to $\dot{m}_{air} = 3.77\,\mathrm{g\,s^{-1}}$ over a time period of 40 s. Before starting the air ramp, in order to ensure reproducibility, the burner is operated at the steady nominal operating point until thermal equilibrium is reached. The operating conditions are summarized in Tab. 11.1.

11.3 Experimental Results for Different Fuels

The flame evolution during the air ramp, depicted in Fig. 11.5, shows flame images for both methane and heptane. Evolution of the flame shape is essentially the same for all

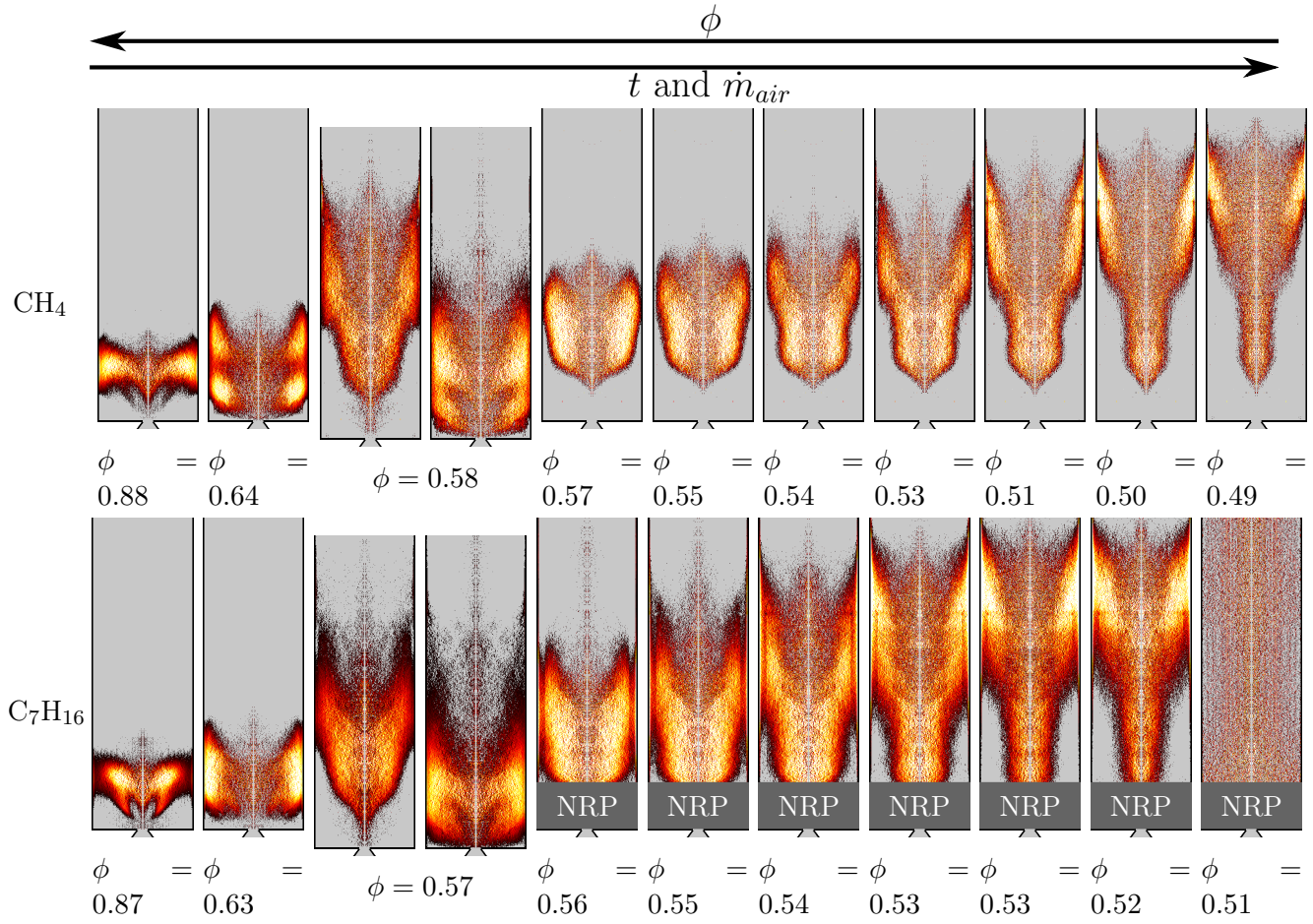

Figure 11.5: *Chemiluminescence (CH^*) images acquired using the high-speed camera. An Abel transform is performed to aid the identification of the flame shape assuming azimuthal symmetry. From left to right, the air flow is increased starting at the nominal condition of Tab. 11.1. The first line shows the blow out sequence for a methane flame without PAC. The second line that for a heptane flame, without PAC down to $\phi = 0.57$, and with PAC for leaner operating points. In the latter case, a darker band at the bottom of the combustor masks the luminosity of the discharges. The images are also noisier especially near the centerline. From $\phi = 0.62$ up to $\phi = 0.56$ for methane and from $\phi = 0.60$ up to $\phi = 0.55$ for heptane (without PAC), a low frequency oscillation is found (see Fig. 11.6). For those operating points, two opposite phase instants are shown. No change in flame shape or flame height is observed between PAC and non-assisted flames.*

three fuels with and without plasma. Starting from an "M" or "V" shaped flame at the nominal operating condition, the flame changes shape to burn both in the ORZ and at the top of the swirling jet at leaner operating points ($\phi \approx 0.64$), leading to an "M+ORZ" shape. Soon after, the flame starts to oscillate at a frequency close to 12 Hz for methane ($\phi = 0.58$), and 7 Hz for liquid fuels ($\phi = 0.57$ for heptane). These oscillations are investigated using the high speed camera. Images are processed using DMD (Dynamic Mode Decomposition, Schmid (2010)), and are shown as phase-averaged flame images in Fig. 11.6 for heptane. These low-frequency oscillations are essentially extinction and reignition in the ORZ, as the flame oscillates between an "M+ORZ" and a "tulip" shape. The ORZ reignites by the propagation of flame kernels from the downstream side to the ORZ. The overall evolution is similar for all three fuels during the oscillation, although the frequency is higher for methane. This type of low-frequency oscillations occurring close to the LBO limit is investigated in Dhanuka et al. (2011). DMD is also performed on the spark images (Fig. 11.2) acquired during the oscillation phase, but it shows no coherent motion of the spark at the frequency of the flame. These flame oscillations end either by LBO, or by stabilization of the flame in a fairly long "tulip" shape. As the air flow rate is increased, the "stem" part of the flame becomes longer, and the "petals" move downstream until LBO occurs. Flame oscillations between two stable flame regions are also reported by Kim et al. (2020) during LBO characterization of a premixed swirling flame with PAC.

As indicated previously, after the oscillations the flame either suddenly blows out or continue to burn while the equivalence ratio decreases. Table 11.2 indicates the probability $\hat{p}$ of flame blow out during the oscillations for each fuel with and without PAC. The improvement is moderate for premixed methane and air, which already features good resistance to LBO without PAC. A statistically significant extension of the LBO is observed using PAC in heptane and dodecane spray flames. For these fuels, without PAC, the flame is systematically blown out during the oscillating phase, but is much more robust with NRP discharges, leading to a significant improvement of the LBO limit.

Table 11.2: *Probability $\hat{p}$ of flame blow out during the oscillation phase for each fuel with and without PAC (lower is better). At least 10 experiments are performed for each case. The* 95% *statistical confidence interval is computed using the Clopper-Pearson method and is indicated in parenthesis.*

	$\hat{p}_{\text{no PAC}}$	$\hat{p}_{\text{PAC}}$
CH_4	$0.13\,(-0.11, +0.26)$	$0\,(+0.26)$
C_7H_{16}	$1.00\,(-0.21)$	$0.27(-0.21, +0.34)$
$C_{12}H_{26}$	$1.00\,(-0.28)$	$0.26(-0.17, +0.25)$

The improvement of the LBO limit with plasma-assistance is also represented in Fig. 11.7, where the histograms indicate the global equivalence ratio at LBO (ϕ_{LBO}) with (red) and without (black) NRP discharges. Figure 11.7 shows for each fuel the flame oscillation frequency f_{osc} as a function of ϕ (right axis, dots). In each case, a set of repeated experiments is presented. For all three fuels, the flame oscillation regime starts and ends at a leaner operating point with NRP discharges. Two observations can be drawn from these

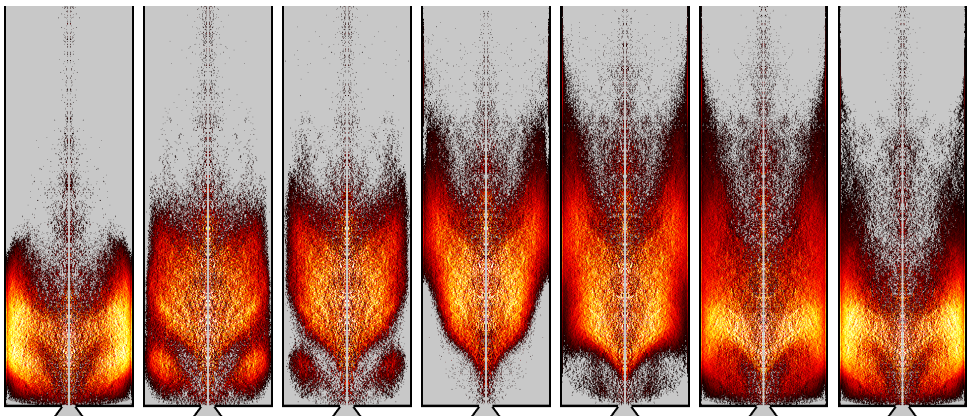

Figure 11.6: *Phase averaged images of flame oscillation with heptane fuel ($\phi = 0.57$, not PAC). Flame images are acquired using the high-speed camera and are then processed using DMD, which shows a predominant mode at* 7.5 Hz. *An Abel transform is applied.*

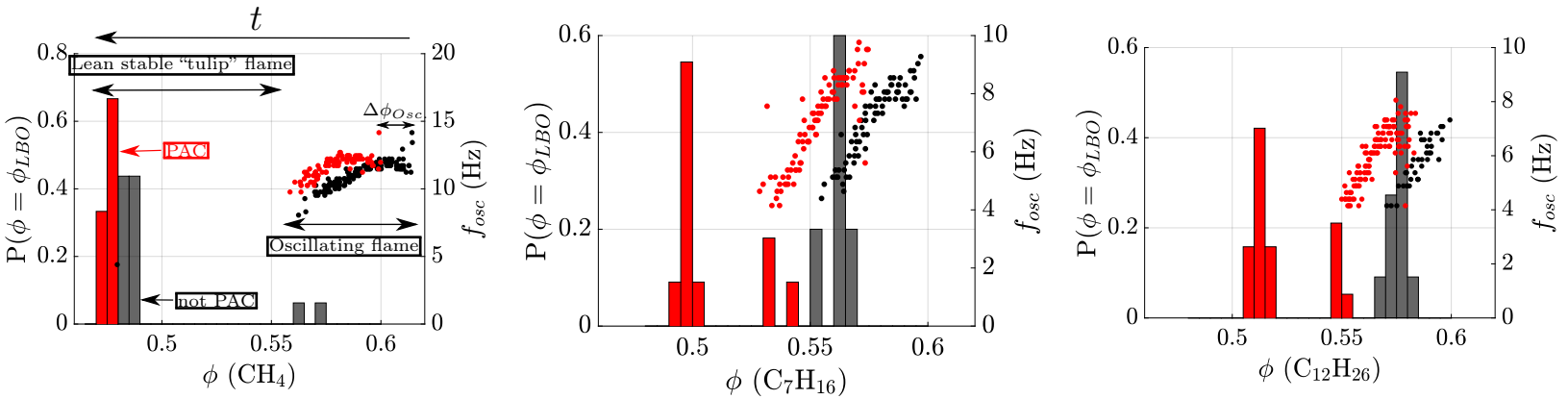

Figure 11.7: *Probability of extinction (histogram, left axis) and frequency of oscillation (dots, right axis) as a function of equivalence ratio. Experiments with (red) and without (black) plasma assistance are shown. For each experiment, a spectrogram of the OH* PM signal is computed, and during the oscillation phase depicted in Fig. 11.6, a strong peak at low frequency is visible. Each dot represents this peak frequency for an experiment, computed on a window of* 1 s*, and only during the oscillation phase. The periodogram is computed using short-time Fourier transform with a frequency resolution of* 0.25 Hz *and a temporal resolution of* 0.5 s*. This approach allows for a clear identification of the limits and frequency of the flame oscillations as a function of* ϕ*.*

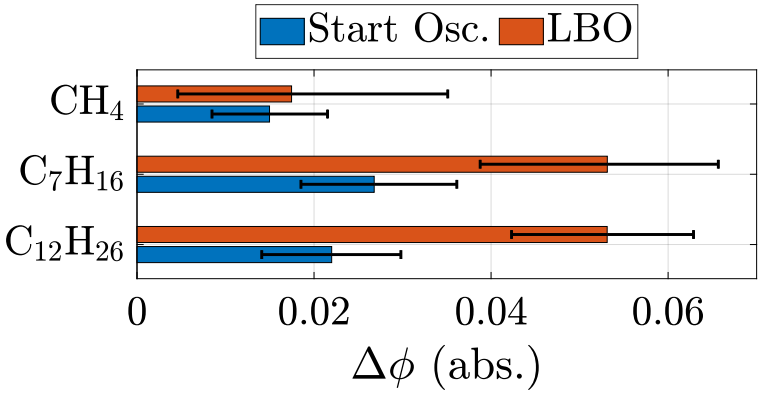

Figure 11.8: *Shift in the equivalence ratio, $\Delta\phi$, at LBO (brown) and at the start of the oscillations (blue), when NRP discharges are applied. Higher values indicate a stronger, more positive, effect of the plasma assistance. The uncertainty intervals are estimated from the repeatability of the mass flow controllers and from bootstrapping.*

results: firstly, as ϕ decreases, there is a decrease in the oscillation frequency for all three fuels. Secondly, the frequency trend is similar with and without plasma assistance.

For methane, the end of the oscillating regime is nearly the same with and without PAC. The flame stabilizes as a "tulip" shape after the oscillation. For two of the tests without NRP discharges, one observes LBO during the oscillation phase. For heptane and dodecane, without plasma assistance, LBO always occurs during flame oscillations[1]. When the NRP discharges are turned on, the flame is sustained after the oscillation phase and blows out under leaner conditions[2]. The increased LBO limit with PAC is quantified in Fig. 11.8 for all three fuels. The LBO limit (brown) is extended by $\Delta\phi = 0.05$ for both liquid fuels, and $\Delta\phi = 0.018$ for methane. The beginning of the low frequency oscillation is also delayed by $\Delta\phi \approx 0.02$ for all three fuels.

At this point, it is useful to briefly compare these values with the results of other studies of the improvement of the LBO limit by PAC in similar combustors (premixed methane-air swirling flames at atmospheric pressure). In Rajasegar et al. (2016), a variable swirl injector is used with a continuous microwave plasma discharge. The flame shape differs significantly from that of SICCA-Spray and, without plasma-assistance, LBO occurs between $0.85 < \phi_{LBO} < 1.3$ depending on the flow rate. Using PAC with an electrical to thermal power ratio of 9% yields a 43% improvement on ϕ_{LBO} in their configuration. However comparison with the present work is not possible given the difference in flame and flow topologies. The combustor used in Kim et al. (2020) is closest to SICCA-Spray. The flame shapes and LBO limits ($0.5 < \phi_{LBO} < 0.54$ without PAC) are also similar. Using a dielectric barrier discharge applied continuously, the LBO is reduced down to

[1]If the NRP discharges are turned on immediately after the extinction, the flame does not reignite.

[2]If the NRP discharges are turned off once the flame overcomes the oscillating phase, the flame continues to burn until LBO at $\phi \approx 0.52$. This indicates that the "tulip" flame can exist without plasma. However, this state cannot be reached without NRP discharges and the extinction of the "tulip" flame occurs at a leaner equivalence ratio with plasma assistance.

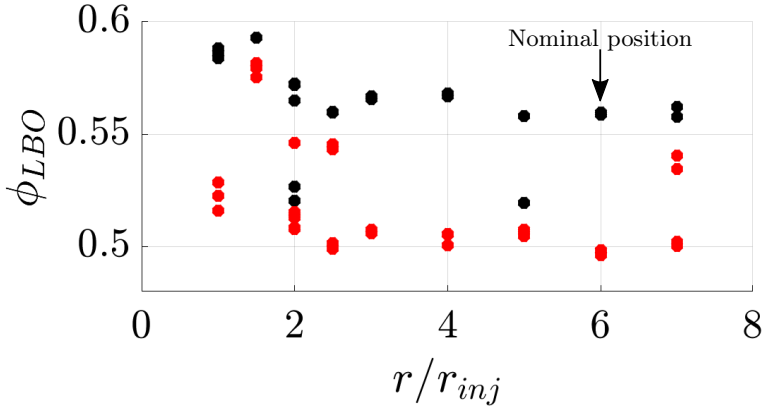

Figure 11.9: *For the experiments presented in this figure, the radial position of the electrode is varied between* $r = r_{inj} = 4\,\text{mm}$ *and* $r = 7\,r_{inj} = 28\,\text{mm}$. *The dots indicate for each electrode position the global equivalence ratio at blow out* ϕ_{LBO} *with (red) and without (black) PAC. Each dot corresponds to a single experiment.*

$0.45 < \phi_{LBO} < 0.48$ in Kim et al. (2020), which is comparable with results of the present work. In Barbosa et al. (2015), a two-stage coaxial swirling injector (propane-air) is used with NRP discharges. The LBO performance significantly depends on the air flow split between the two stages of the injector, the primary stage acting as a pilot flame. At a low power setting, PAC reduces ϕ_{LBO} for the primary stage from 2 to 0.55, a value close to what is observed in the present study.

11.4 Impact of the electrode position

As already indicated it is not possible to operate the discharges at $r/r_{inj} < 1$, because they would damage the liquid fuel atomizer head. Figure 11.9 shows the results obtained by varying the radial position of the electrode and measuring the LBO limit from repeated experiments with heptane. $r/r_{inj} = 6$ is optimal for this test rig in terms of effectiveness and repeatability. This may be linked to the structure of the flame, to the associated flow and more specifically to the location of the ORZ. The typical shape of a heptane flame at $\phi = 0.63$ is "M+ORZ" (see Fig. 11.1). From this pattern and from previously measured velocity profiles (in nonreactive, unconfined conditions in Prieur et al. (2017b), and in reactive, confined and steady conditions in Lancien (2018)), one may infer that near the combustor backplane the ORZ extends from $r/r_{inj} = 3$ to $r/r_{inj} = 6$. This region is filled with hot gases at relatively low velocity and turbulent intensity, with an augmented residence time, and a longer convective delay to the base of the flame. In the outer region, beyond $6\,r_{inj}$ the flow is cooled down by the wall. Between the injector rim and $r/r_{inj} = 2$ the flow is relatively fast, cold and turbulent. It is suggested by Kong et al. (2019) that an electrode placement in a relatively slow recirculation zone will favor plasma induced chemical effects. This explains why the electrode location at $r/r_{inj} = 6$ provides the best performance in terms of LBO improvement.

11.5 Conclusion

This study is focused on the extension of the lean blow out (LBO) limit by nanosecond repetitively pulsed (NRP) discharges in spray and perfectly premixed swirled flames at atmospheric pressure. Both liquid (heptane and dodecane) and gaseous (methane) fuels are examined. For these experiments, the fuel flow rate is kept constant, and the air flow rate is slowly increased until LBO occurs. The NRP discharges are applied at 20 kHz and the ratio of electrical to thermal power is 2%. Three phases are identified in the blow out sequence: the first stage sees flames initially in a "V" or "M" shape burning further out in the outer recirculation zone (ORZ). In the second phase, the flames oscillate at a low frequency. Perfectly premixed flames stabilize in a "tulip" shape after the oscillations (third phase), until LBO occurs. For these flames, LBO occurs at a leaner condition with the use of NRP discharges. For non-assisted spray flames, LBO systematically occurs during the oscillations. If NRP discharges are used, spray flames can be stabilized in a "tulip" shape beyond the region where oscillations occur. The LBO limit is thereby greatly extended. The position of the electrode is identified as a critical factor for the effectiveness of the PAC system. The outer edge of the ORZ is found to be the most favorable location, both in terms of LBO performance and ease of placement in many practical systems.

Conclusion

The central theme of research reported in the present thesis is that of combustion dynamics, a question that has already concentrated a large effort but that still requires considerable attention. The focal point has been to contribute to the understanding of the mechanisms giving rise to azimuthal instabilities in annular combustors. The work emphasizes the central role of the injection system, with an attempt to investigate the role of fundamental parameters like the head loss of the injection unit and the swirl number of the flow. A systematic exploration of the effects of these two parameters is initiated leading to a large set of experiments carried out in two facilities, a single sector equipped with one injector and a multiple injector annular combustor. The dialog between these two systems, already exploited in previous research in our laboratory, is here permanently established. Single sector experiments serve to guide annular system investigations. Another feature of the present effort is that experiments are accompanied by simulations which provide additional insight and complement experimental observations. This combined research has provided many new results that are listed at the end of the chapters forming this document. These results will not be reviewed exhaustively. We propose instead to discuss a few outcomes and highlights.

A first outcome is the extensive analysis of the definition of the swirl number, an important dimensionless parameter often quoted to characterize swirling injectors. The use of high fidelity simulation allows to access all variables in the flow field. The important conservation properties of the swirl number defined by Chigier and Beér (1964) are retrieved, but it is found that most of the simplifications that have been proposed over the years to compute this swirl number may yield inaccurate estimates of the original definition. To clarify the question of the swirl number, it is proposed to adopt two definitions: the original definition by Chigier and Beér (1964) has good conservation properties, but it is extremely challenging to accurately compute this swirl number from experimental data. A conventional swirl number that is widely used in practice is also evaluated as a possible replacement. It is shown to be weakly linked to the original swirl number and it is found that its value notably depends on the experimental and measurement conditions. It is important to take into account these limitations when using this number to measure the degree of rotation imparted to the flow and categorize swirling injectors.

A second outcome relates to the space-time methodology that has been devised to examine the coupling between the injected flow and the acoustic field. This novel method was shown to provide considerable insight on the processes that couple the convective motion to the acoustic disturbances that propagate on the downstream side of the flame. It was

also possible to examine the delays between initial velocity and fuel flow rate disturbances and heat release rate fluctuations and discuss the respective role of the convective and vaporization delays and find that these delays did not add up.

A third outcome concerns effects of the injector head loss on the instability process. Experiments indicate that this parameter notably changes the regions of instability, the levels of oscillation and the coupling modes.

A fourth outcome is a demonstration of the applicability of plasma assisted combustion based on nanosecond repetitive discharges to increase the lean blow out limit. This is one of the first demonstration of the applicability of such systems on a spray swirling flame. It is also found that implementing the electrode in the outer recirculation region is a viable and practical alternative to an electrode placed on the injector centerline.

A fifth outcome pertains to the high levels of azimuthal instabilities observed in MICCA-Spray. Levels of a few percent of the ambient pressure were obtained reaching up to 6 kPa. It is found as already observed in the thesis of Prieur that the very high amplitudes induce a partial extinction of the flames situated near the pressure nodal line. This line corresponds to the azimuthal velocity maximum. A novel reconstruction method based on a Fourier expansion on spatial harmonics is applied to the microphone signals and allows to track the pressure distribution deformation as the oscillation amplitude is increasing. The azimuthal velocity is deduced from this expansion allowing to estimate the velocity level that prevails when the first flame is extinguished.

There are many other outcomes of this research that are of broader interest. One of them is a method of 100 kHz laser tomography relying on tin dioxide micro-particles. This method is illustrated with a detailed examination of the reacting flow formed by a swirling injector, advanced image processing methods are used to study the dynamics of the precessing vortex core, and demonstrate its modulation in amplitude and frequency by a combustion oscillation. Another aspect that is of interest in the engineering design of swirling injectors is the numerical calculations that are carried out to understand features pertaining to the droplet spray distribution. This investigation shows that the bimodal nature of the droplet velocity distribution is linked to the existence of a liquid film formed by the spray impinging on the injector exhaust section.

Perspectives

Work reported in this thesis opens a broad range of research directions. The effort should generally focus on the link between injection and thermoacoustic coupling. In this respect, it is clear that much can be learned by combining single segment testing with annular combustor experiments. The following items are currently being investigated:

- Systematic testing in the annular system of injectors guided by the single segment experiments;
- Investigation of changes in injector parameters (swirl number and head loss);
- Effects of fuel on the nature and level of instabilities;
- Determination of the FDF of the different injectors with SICCA-Spray, but also with the new linear facility comprising three injectors TICCA-Spray (determination of FDFs in a configuration where the central flame surrounded by neighboring flames is dynamically closer to the situation prevailing in the annular combustor);
- Analysis of lean extinction phenomena with characterization in the single segment combustor injector (SICCA-Spray) and in the annular multiple-injector system MICCA-Spray;
- Further studies of light round ignition dynamics with emphasis on the analysis of the transient dynamics after initiation of an injector and further studies of thermal effects on the local establishment of the lifted flame and on the global delay corresponding to flame merging.

Combustion instabilities in annular systems

Most of the work on combustion instabilities in annular system conducted in the present work has been focused on very high amplitude oscillation leading to flame blow off and deformation of the pressure field. On this topic, a number of points remain unsettled and must be investigated if one wishes to build predictive model for such phenomenon. Blow out by transverse acoustic fluctuations should be further explored by making use of a facility allowing for transverse acoustic forcing such as the TACC linear burner at CORIA, Rouen, France. LES would also be very useful to improve out understanding of the mechanism behind flame blow off. This could be done as part of the FASMIC ANR project, a common project between Cerfacs, CORIA and EM2C. Using an acoustically forced rig would allow a much more detailed and repeatable analysis of this phenomenon. Concerning theoretical modeling, the coupling mechanisms between the acoustic field and the mean flow, taking place at a longer time scale compared to the acoustic period should be investigated.

Recent developments and experiments conducted in MICCA-Spray have also identified operating conditions where milder, near limit cycle instabilities develop. These conditions are being investigated and are more favorable for the development and validation of lower order models due to a lesser complexity.

Improving measurements of the Flame Describing Functions

Although no Flame Describing Function have been reported in the present work, the work conducted during this thesis will help for future measurements of flame dynamics. The analysis of the chemiluminescence relation to heat release rate is an important step in the more accurate determination of the flame describing function. The deployment of more advanced acoustic diagnosis in SICCA-Spray, including the integration of a series of chamber microphones will also be useful in that regard. The arrival of TICCA-Spray will also be useful as this experiment will be more representative of the boundary conditions of MICCA-Spray.

These elements have already been taken advantage of as part of the PhD thesis of Preethi Rajendram Soundararajan. FDFs are being measured to investigate the effect of fuel type and injector design on the occurence of instabilities in SICCA and MICCA. The numerical simulations of these configurations, carried out in partnership with Ermanno Lo Schiavo, Davide Laera, Laurent Gicquel and Thierry Poinsot from Cerfacs in the framework of the Annulight project, are also useful to gain a deeper understanding of the complex mechanisms responsible for the response of the flame.

Dynamics of lean blow-out

Lean blow-out has already been widely studied in the previous literature. Interesting work has been carried out at Georgia Tech with the objective of analyzing the pressure signals with a view to predicting blow-out from the precursor signals. It is noted in particular that the amplitude of oscillations detected by pressure sensors increases as one approaches the LBO limit. Although the amount of work on this issue is significant, there is little information on lean blow-out under conditions in which fuel is injected as a spray through a swirling injector. To the best of our knowledge, there are no studies available in the technical literature on LBO in annular configurations.

Preliminary work carried out on the single sector combustor (SICCA-Spray) reveals a process of quasi-periodic local extinctions and re-ignition with intense combustion phases followed by periods during which the reaction zone is reduced in size. This interesting process deserves to be studied in more detail. Other preliminary observations on MICCA-Spray reveal a mechanism in which the combustion zone evolves as an azimuthal wave.

It is clear that LBO mechanisms deserve further experiments in combination with simulations.

Characterization of light round ignition

Numerous studies have already enabled a detailed characterization of the ignition mechanism in annular combustors. Experiments have provided a fundamental information on the delay corresponding to the merging of the two flame branches originating from the core of burnt gases formed initially. This delay was found to be strongly influenced by the thermal conditions at the annular system boundaries. When the chamber walls are at room temperature, the delay is significantly longer than that obtained in a case where the walls are preheated. The ability to take into account thermal effects on flame propagation during light round stands as an important issue.

A second subject is that of the transient which follows the initiation of the injector by the passing flame. The variation in the rate of heat release induces a strong positive excursion of the pressure in the chamber which results in a negative excursion of the mass flow rate in the injector. The restoration of the flow and the return to the stabilized position of the flame are mainly determined by the response of the system and by the thermal conditions in the external recirculation regions. These mechanisms are the subject of current simulations in the Annulight framework. Further experiments are needed to support these calculations.

The role of simulation and theory

It is also apparent that considerable insight can be gained from a dialog between experiments and simulations. The joint analysis exemplified in the present work may be continued in various ways by further examination of the single injector dynamics using the novel space-time methodology devised in the present study and also by developing full annular combustor simulations aimed at retrieving azimuthal instabilities observed experimentally and reproducing parametric effects associated with injection characteristics (swirl number and head loss) and fuel composition. The flame blow-off that is found when the relative level of pressure oscillation becomes large may also be the subject of simulations.

Much remains to be done on the theoretical level to integrate knowledge generated in the present experiments. One important item would be to include the injector dynamics together with the flame dynamics in a more advanced representation of the combustion system leading to a nonlinear dispersion relation. This could then be used to predict the behavior of the combustion system and compare the results with the data gathered in the systematic experiments in the single sector system and in the annular combustor.

Appendix A

Database of experimental characterization of injection systems

Contents

This appendix gathers the large amount of velocimetry data that was acquired to characterize the different swirler introduced in Tab. 3.1. This information forms a database that can be used for a better understanding of the properties of the various injection systems, and it also may serve as a reference for future work on these injection systems. All velocity profiles reported in the present appendix were measured in unconfined conditions in SICCA-Spray using LDV.

A.1 First generation swirler: "TIMBER" with terminal plate TP1

A.1.1 Air flow rate: $\dot{m}_{air} = 1.94\,\mathrm{g\,s^{-1}}$

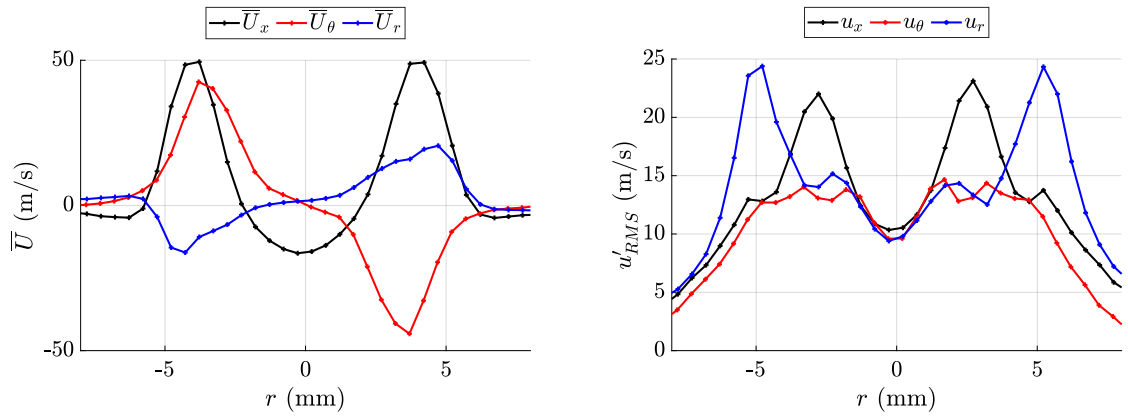

Figure A.1: *Mean and RMS velocity profiles. Swirler "TIMBER", air flow rate* $\dot{m}_{air} = 1.94\,\mathrm{g\,s^{-1}}$*, profiles measured at* $z = 2.5\,\mathrm{mm}$ *above the backplane.*

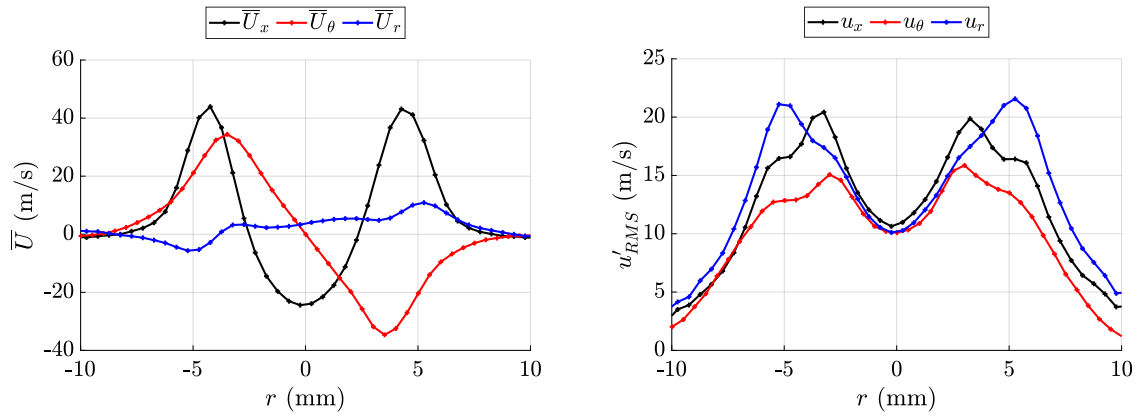

Figure A.2: *Mean and RMS velocity profiles. Swirler "TIMBER", air flow rate* $\dot{m}_{air} = 1.94\,\mathrm{g\,s^{-1}}$*, profiles measured at* $z = 5\,\mathrm{mm}$ *above the backplane.*

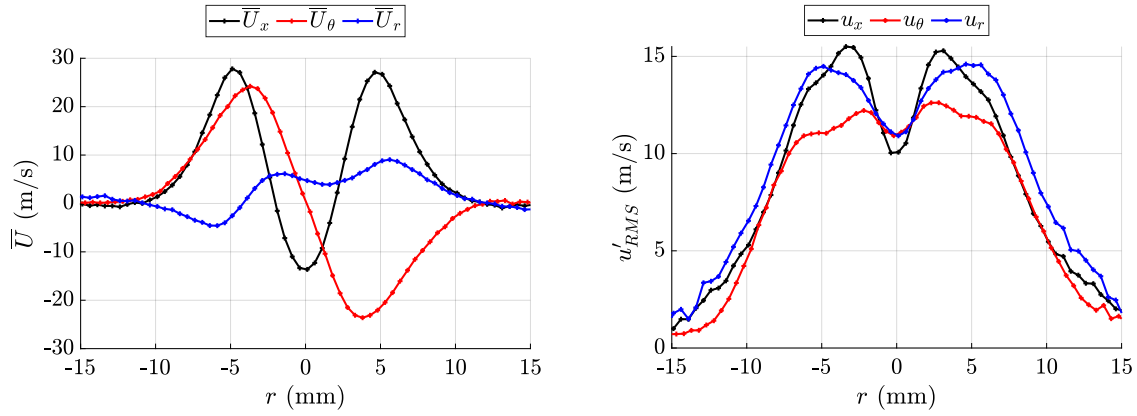

Figure A.3: *Mean and RMS velocity profiles. Swirler "TIMBER", air flow rate* $\dot{m}_{air} = 1.94\,\mathrm{g\,s^{-1}}$*, profiles measured at* $z = 10\,\mathrm{mm}$ *above the backplane.*

A.1.2 Air flow rate: $\dot{m}_{air} = 2.26\,\mathrm{g\,s^{-1}}$

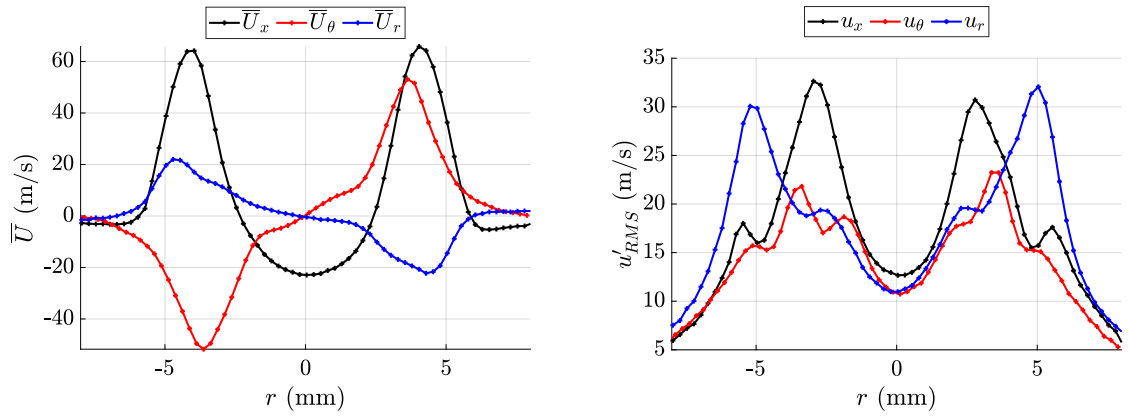

Figure A.4: *Mean and RMS velocity profiles. Swirler "TIMBER", air flow rate* $\dot{m}_{air} = 2.26\,\mathrm{g\,s^{-1}}$*, profiles measured at* $z = 2.5\,\mathrm{mm}$ *above the backplane.*

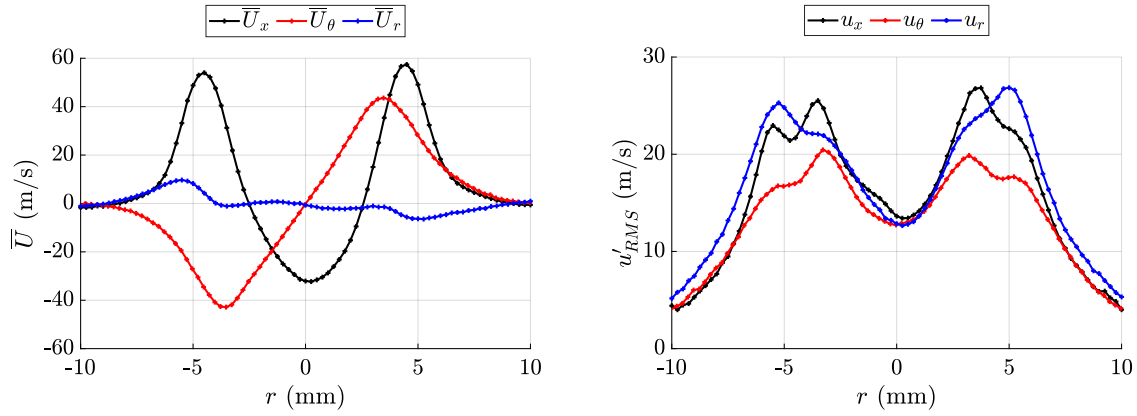

Figure A.5: *Mean and RMS velocity profiles. Swirler "TIMBER", air flow rate* $\dot{m}_{air} = 2.26\,\mathrm{g\,s^{-1}}$*, profiles measured atz* $= 5\,\mathrm{mm}$ *above the backplane.*

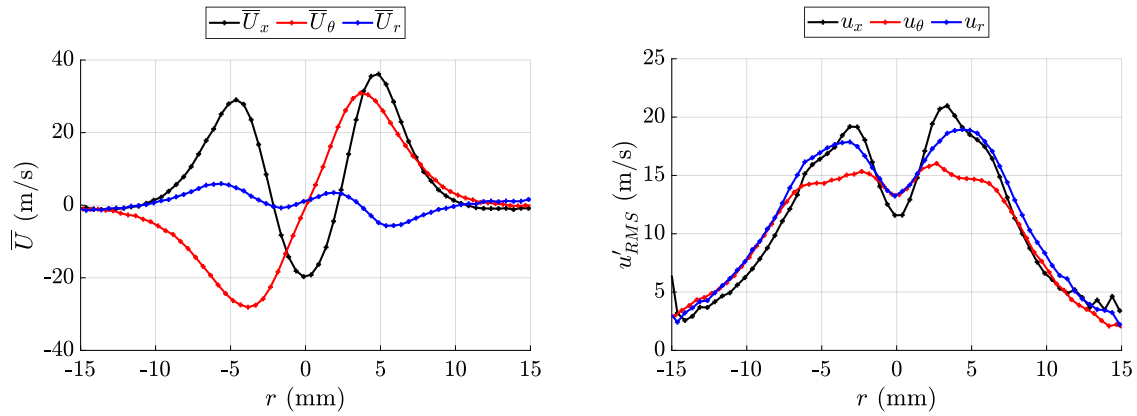

Figure A.6: *Mean and RMS velocity profiles. Swirler "TIMBER", air flow rate* $\dot{m}_{air} = 2.26\,\mathrm{g\,s^{-1}}$*, profiles measured at* $z = 10\,\mathrm{mm}$ *above the backplane.*

A.1.3 Air flow rate: $\dot{m}_{air} = 2.59\,\mathrm{g\,s^{-1}}$

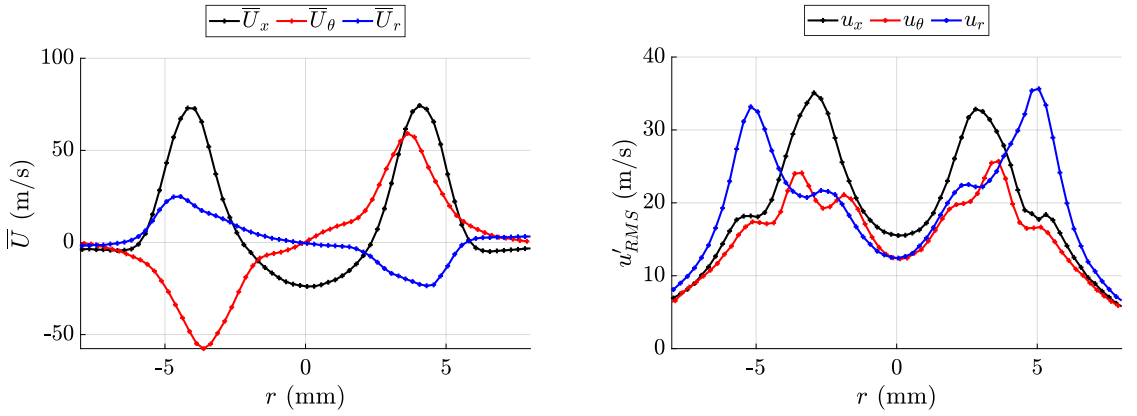

Figure A.7: *Mean and RMS velocity profiles. Swirler "TIMBER", air flow rate* $\dot{m}_{air} = 2.59\,\mathrm{g\,s^{-1}}$*, profiles measured at* $z = 2.5\,\mathrm{mm}$ *above the backplane.*

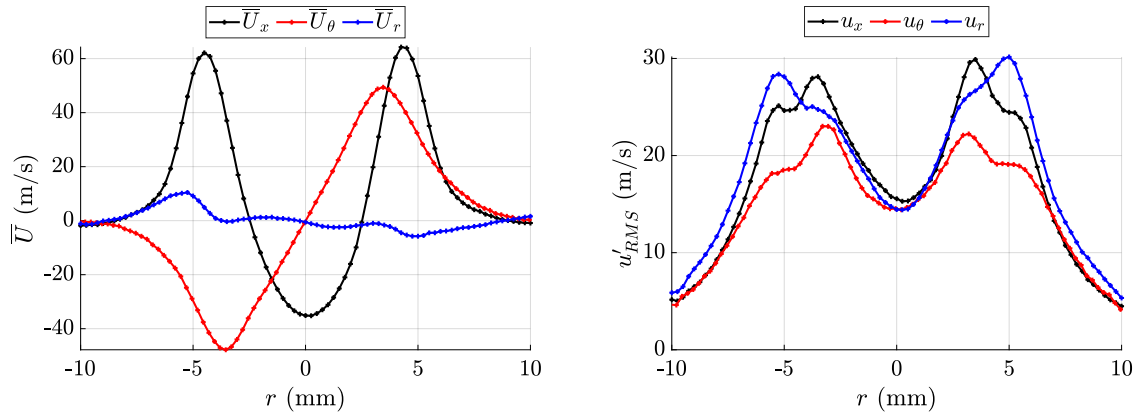

Figure A.8: *Mean and RMS velocity profiles. Swirler "TIMBER", air flow rate* $\dot{m}_{air} = 2.59\,\mathrm{g\,s^{-1}}$*, profiles measured at* $z = 5\,\mathrm{mm}$ *above the backplane.*

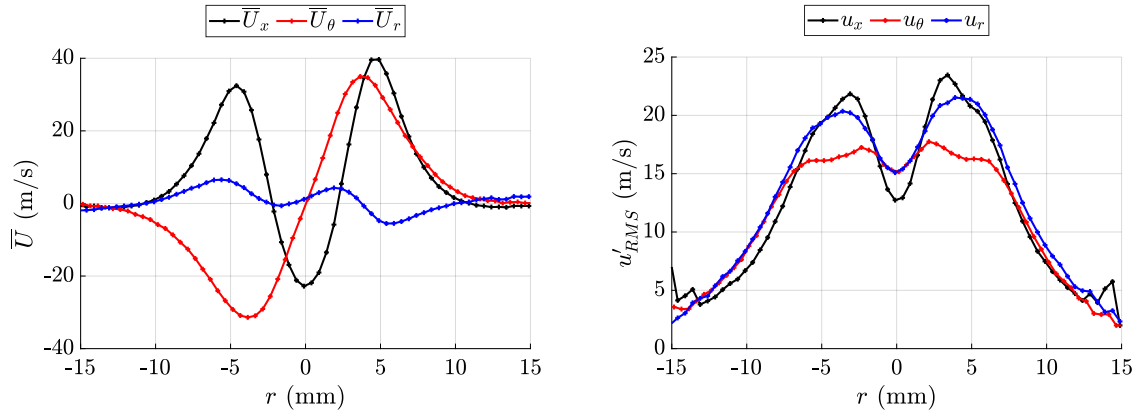

Figure A.9: *Mean and RMS velocity profiles. Swirler "TIMBER", air flow rate* $\dot{m}_{air} = 2.59\,\mathrm{g\,s^{-1}}$*, profiles measured at* $z = 10\,\mathrm{mm}$ *above the backplane.*

A.2 Second generation swirler: K with terminal plate TP1

A.2.1 Air flow rate: $\dot{m}_{air} = 2.59\,\mathrm{g\,s^{-1}}$

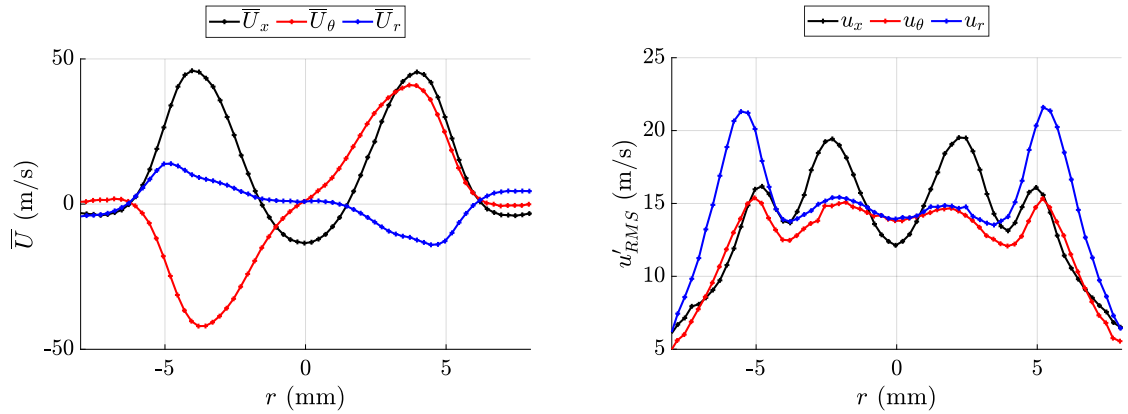

Figure A.10: *Mean and RMS velocity profiles. Swirler K, air flow rate $\dot{m}_{air} = 2.59\,\mathrm{g\,s^{-1}}$, profiles measured at $z = 2.5\,\mathrm{mm}$ above the backplane.*

A.3 Second generation swirler: K with terminal plate TP2

A.3.1 Air flow rate: $\dot{m}_{air} = 2.26\,\mathrm{g\,s^{-1}}$

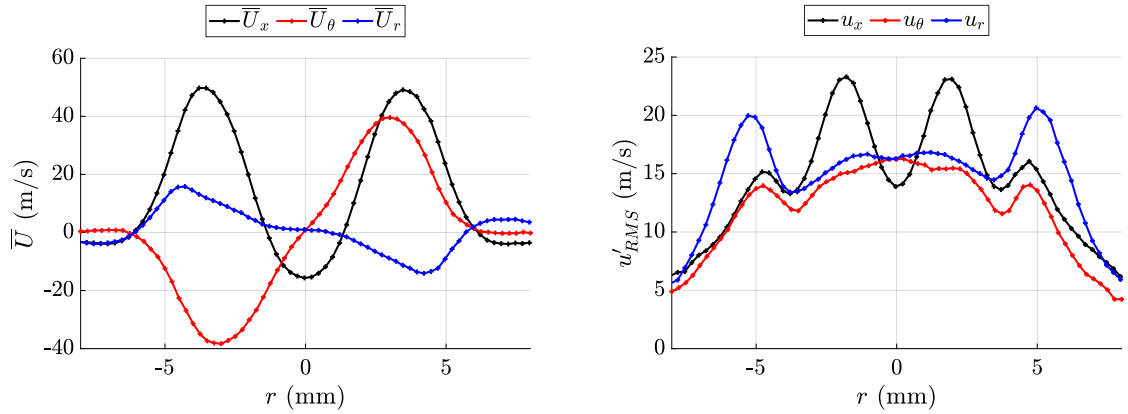

Figure A.11: *Mean and RMS velocity profiles. Swirler K, air flow rate $\dot{m}_{air} = 2.26\,\mathrm{g\,s^{-1}}$, profiles measured at $z = 2.5\,\mathrm{mm}$ above the backplane.*

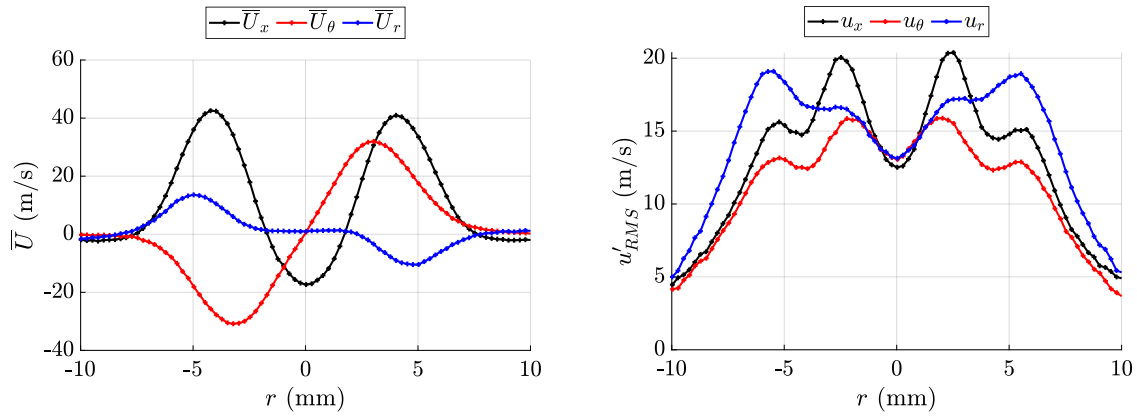

Figure A.12: *Mean and RMS velocity profiles. Swirler K, air flow rate $\dot{m}_{air} = 2.26\,\mathrm{g\,s^{-1}}$, profiles measured at $z = 5\,\mathrm{mm}$ above the backplane.*

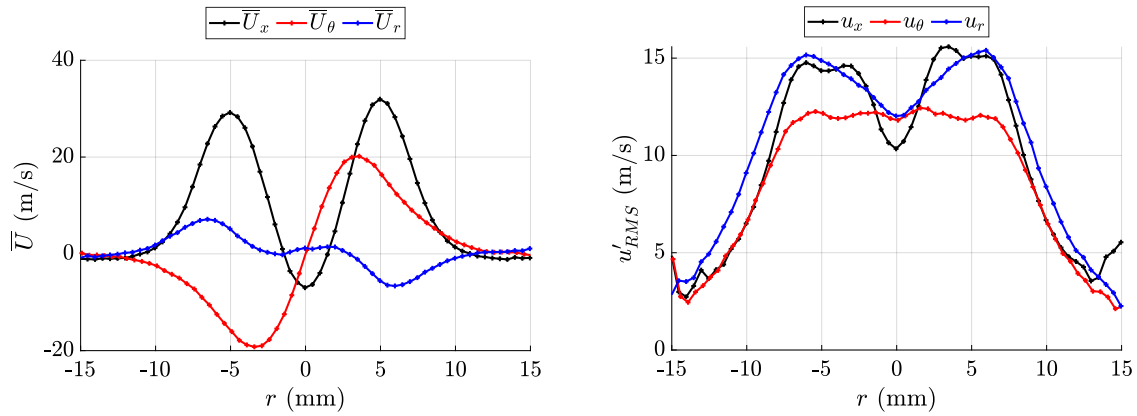

Figure A.13: *Mean and RMS velocity profiles. Swirler K, air flow rate $\dot{m}_{air} = 2.26\,\mathrm{g\,s^{-1}}$, profiles measured at $z = 10\,\mathrm{mm}$ above the backplane.*

A.3.2 Air flow rate: $\dot{m}_{air} = 2.59\,\mathrm{g\,s^{-1}}$

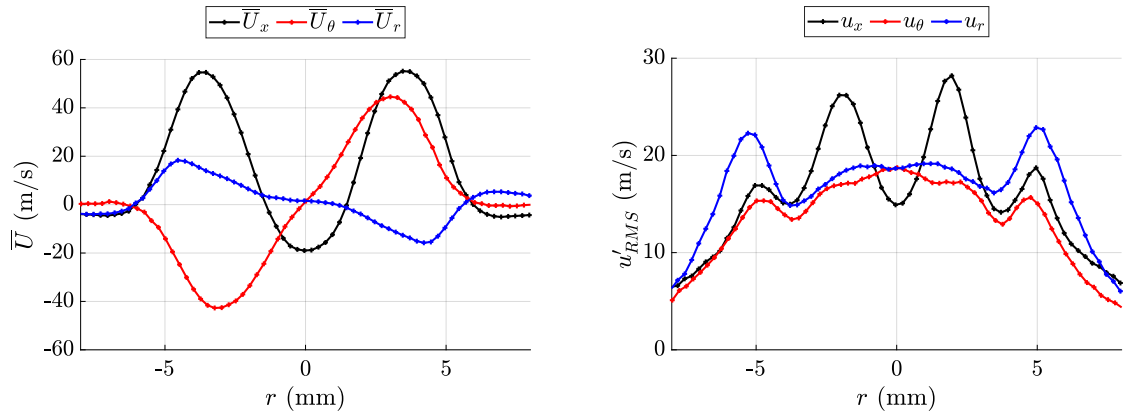

Figure A.14: *Mean and RMS velocity profiles. Swirler K, air flow rate* $\dot{m}_{air} = 2.59\,\mathrm{g\,s^{-1}}$, *profiles measured at* $z = 2.5\,\mathrm{mm}$ *above the backplane.*

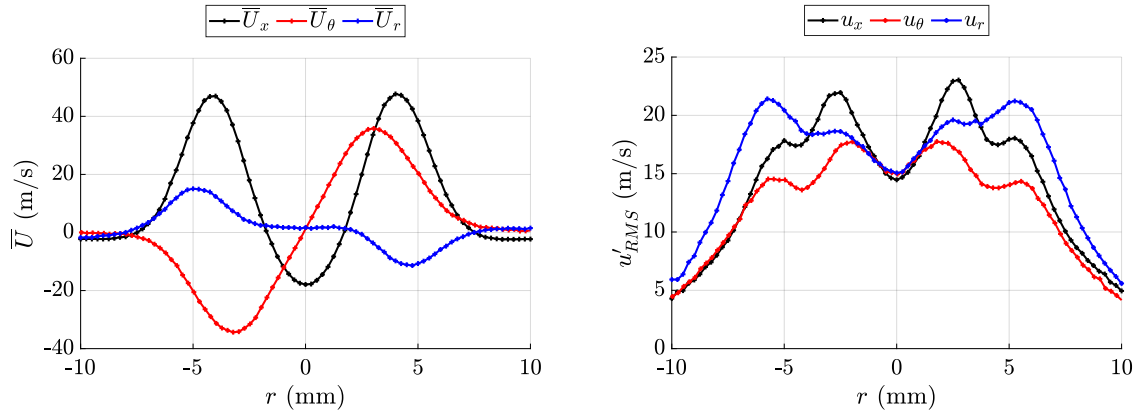

Figure A.15: *Mean and RMS velocity profiles. Swirler K, air flow rate* $\dot{m}_{air} = 2.59\,\mathrm{g\,s^{-1}}$, *profiles measured* $z = 5\,\mathrm{mm}$ *above the backplane.*

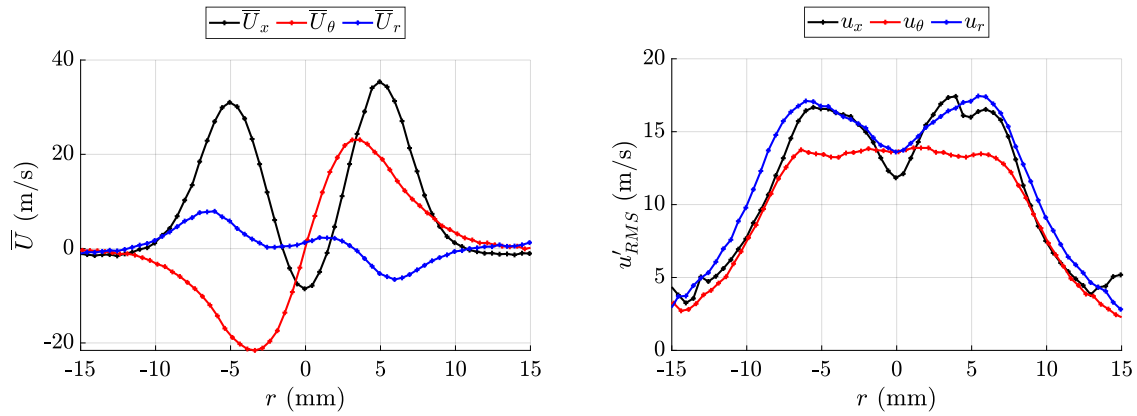

Figure A.16: *Mean and RMS velocity profiles. Swirler K, air flow rate* $\dot{m}_{air} = 2.59\,\mathrm{g\,s^{-1}}$*, profiles measured at* $z = 10\,\mathrm{mm}$ *above the backplane.*

A.4 Fourth generation swirler: 707 with terminal plate TP2

A.4.1 Air flow rate: $\dot{m}_{air} = 2.26\,\mathrm{g\,s^{-1}}$

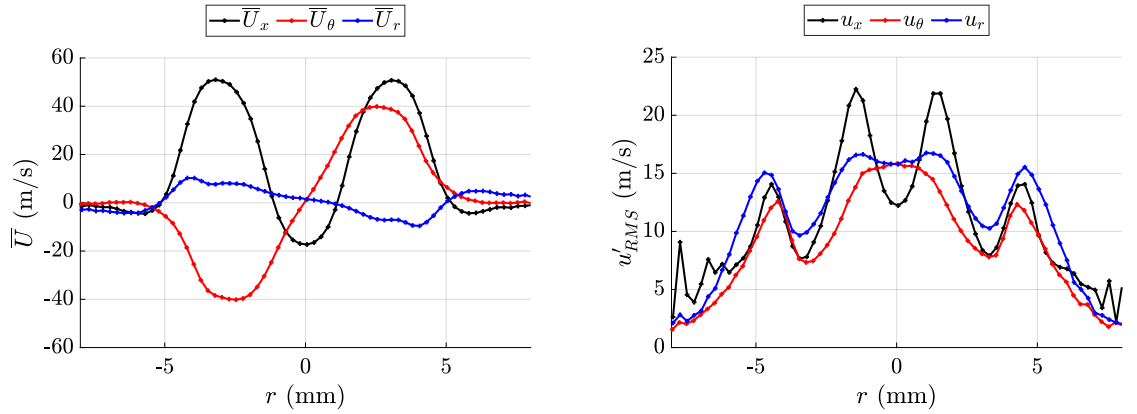

Figure A.17: *Mean and RMS velocity profiles. Swirler* 707*, air flow rate* $\dot{m}_{air} = 2.26\,\mathrm{g\,s^{-1}}$*, profiles measured at* $z = 2.5\,\mathrm{mm}$ *above the backplane.*

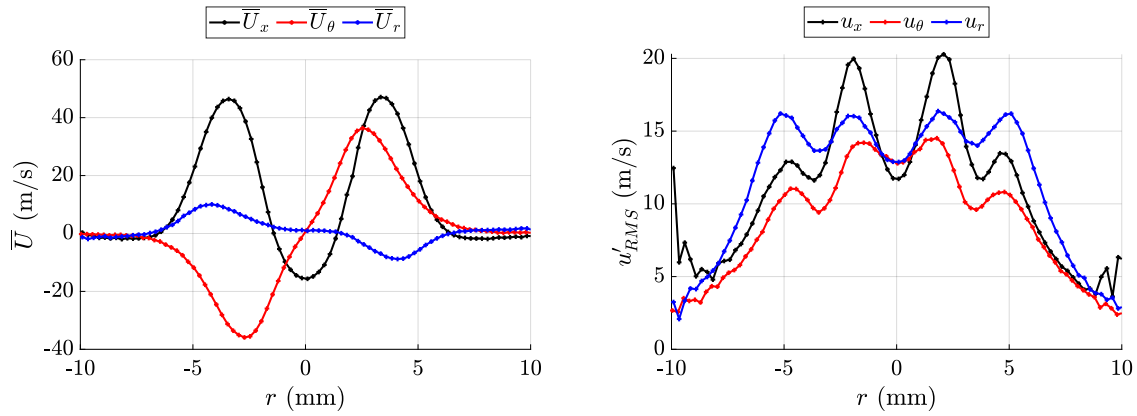

Figure A.18: *Mean and RMS velocity profiles. Swirler* 707*, air flow rate* $\dot{m}_{air} = 2.26\,\mathrm{g\,s^{-1}}$*, profiles measured at* $z = 5\,\mathrm{mm}$ *above the backplane.*

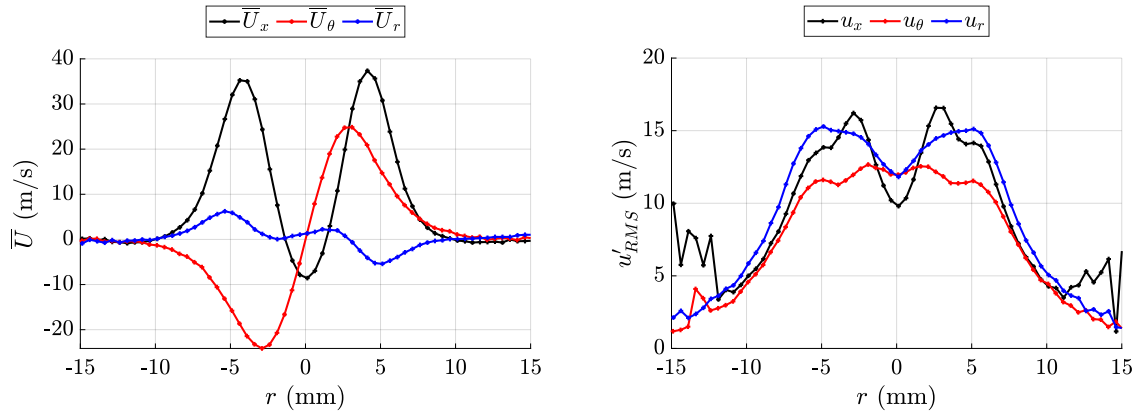

Figure A.19: *Mean and RMS velocity profiles. Swirler* 707*, air flow rate* $\dot{m}_{air} = 2.26\,\mathrm{g\,s^{-1}}$*, profiles measured at* $z = 10\,\mathrm{mm}$ *above the backplane.*

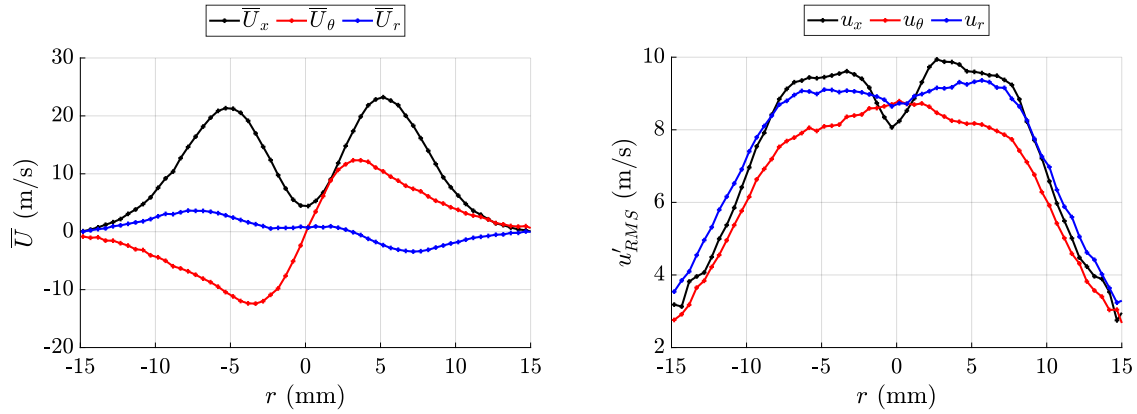

Figure A.20: *Mean and RMS velocity profiles. Swirler* 707*, air flow rate* $\dot{m}_{air} = 2.26\,\mathrm{g\,s^{-1}}$*, profiles measured at* $z = 20\,\mathrm{mm}$ *above the backplane.*

A.4.2 Air flow rate: $\dot{m}_{air} = 2.59\,\mathrm{g\,s^{-1}}$

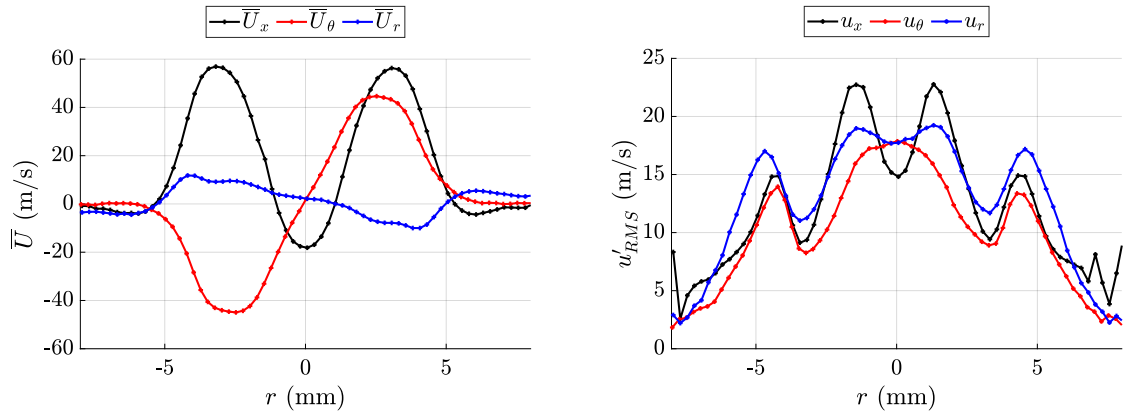

Figure A.21: *Mean and RMS velocity profiles. Swirler* 707*, air flow rate* $\dot{m}_{air} = 2.59\,\mathrm{g\,s^{-1}}$*, profiles measured at* $z = 2.5\,\mathrm{mm}$ *above the backplane.*

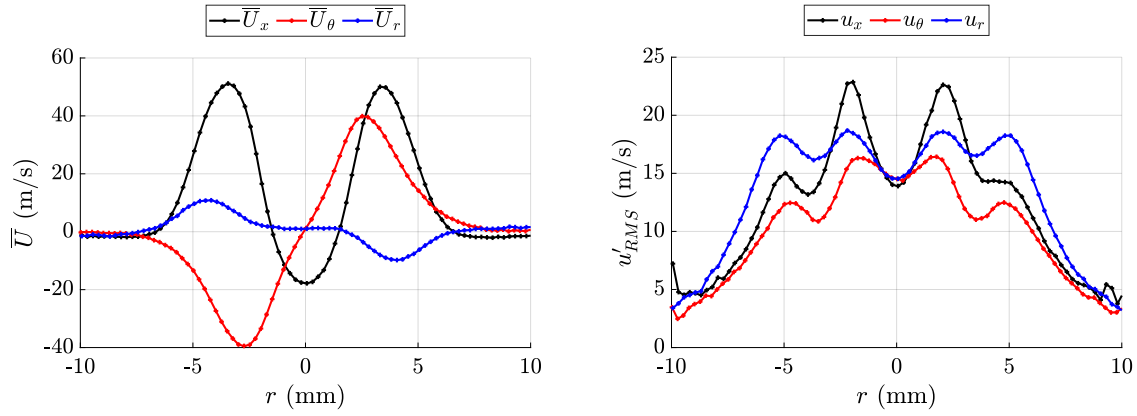

Figure A.22: *Mean and RMS velocity profiles. Swirler* 707*, air flow rate* $\dot{m}_{air} = 2.59\,\mathrm{g\,s^{-1}}$*, profiles measured at* $z = 5\,\mathrm{mm}$ *above the backplane.*

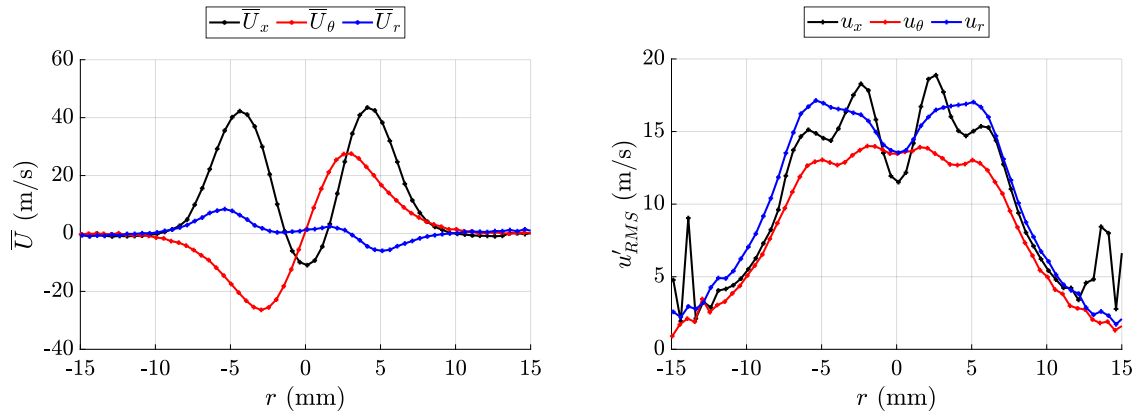

Figure A.23: *Mean and RMS velocity profiles. Swirler* 707*, air flow rate* $\dot{m}_{air} = 2.59\,\mathrm{g\,s^{-1}}$*, profiles measured at* $z = 10\,\mathrm{mm}$ *above the backplane.*

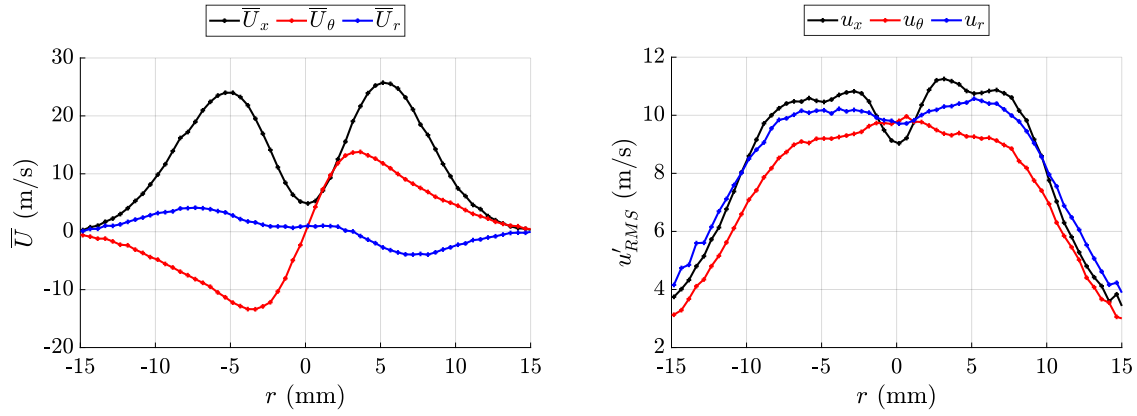

Figure A.24: *Mean and RMS velocity profiles. Swirler* 707*, air flow rate* $\dot{m}_{air} = 2.59\,\mathrm{g\,s^{-1}}$*, profiles measured at* $z = 20\,\mathrm{mm}$ *above the backplane.*

A.5 Fourth generation swirler: 712 with terminal plate TP2

A.5.1 Air flow rate: $\dot{m}_{air} = 2.26\,\mathrm{g\,s^{-1}}$

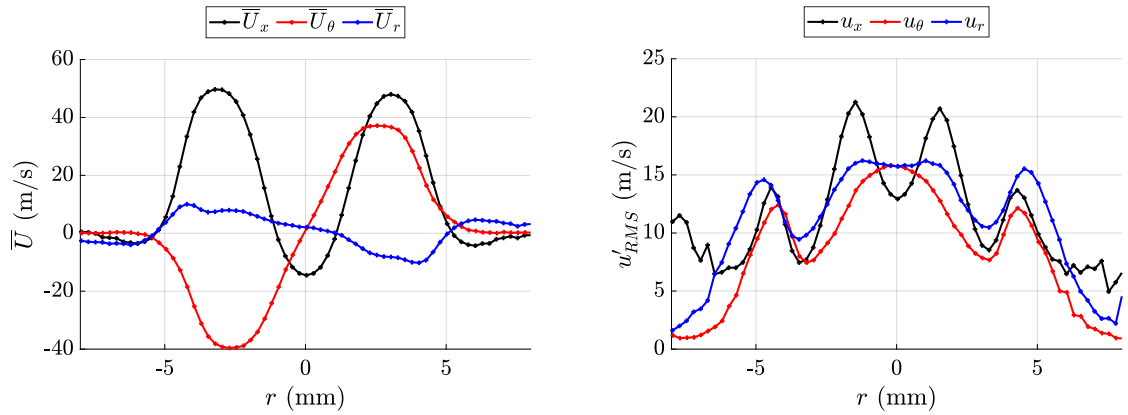

Figure A.25: *Mean and RMS velocity profiles. Swirler* 712*, air flow rate* $\dot{m}_{air} = 2.26\,\mathrm{g\,s^{-1}}$*, profiles measured at* $z = 2.5\,\mathrm{mm}$ *above the backplane.*

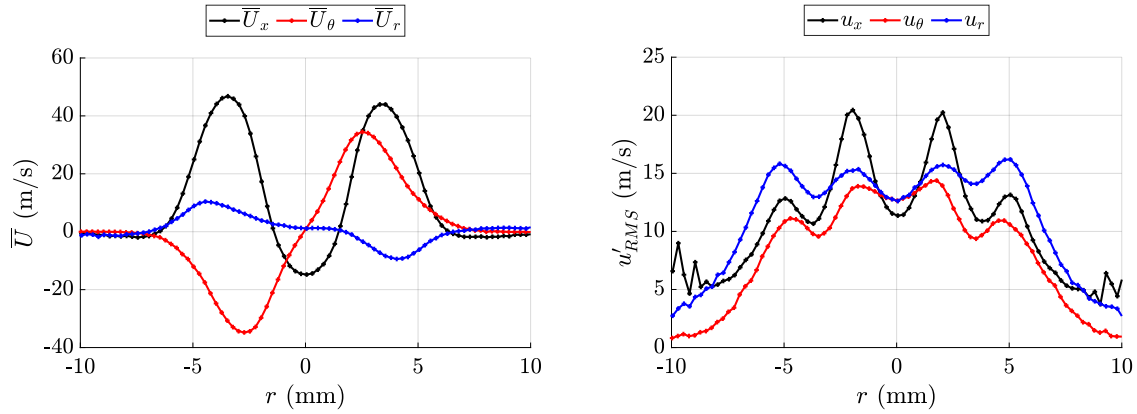

Figure A.26: *Mean and RMS velocity profiles. Swirler* 712*, air flow rate* $\dot{m}_{air} = 2.26\,\mathrm{g\,s^{-1}}$*, profiles measured at* $z = 5\,\mathrm{mm}$ *above the backplane.*

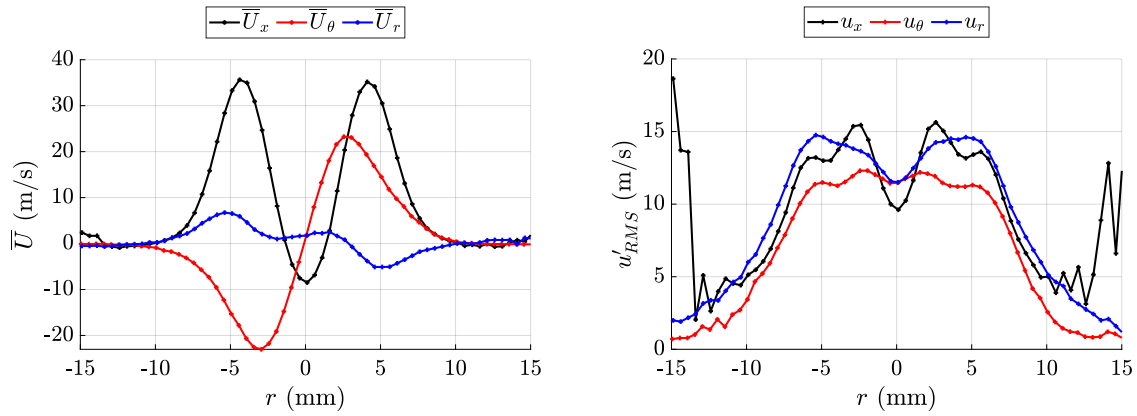

Figure A.27: *Mean and RMS velocity profiles. Swirler* 712*, air flow rate* $\dot{m}_{air} = 2.26\,\mathrm{g\,s^{-1}}$*, profiles measured at* $z = 10\,\mathrm{mm}$ *above the backplane.*

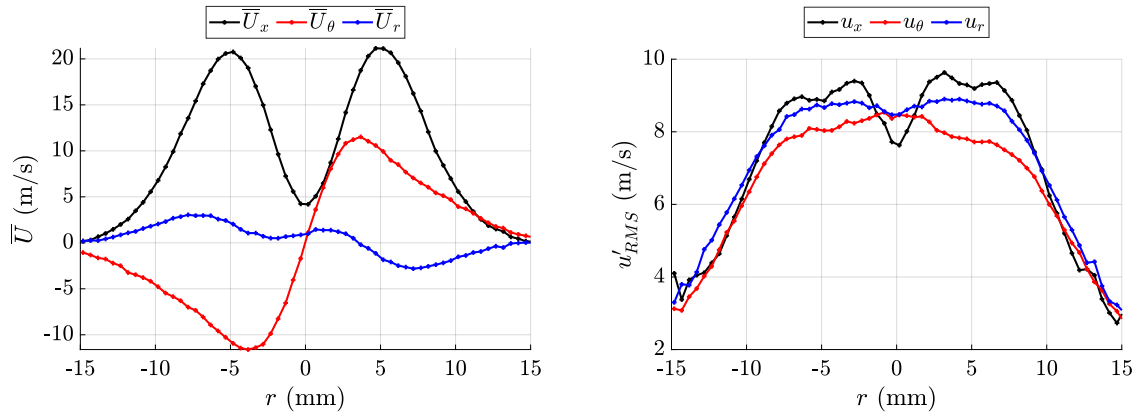

Figure A.28: *Mean and RMS velocity profiles. Swirler* 712*, air flow rate* $\dot{m}_{air} = 2.26\,\mathrm{g\,s^{-1}}$*, profiles measured at* $z = 20\,\mathrm{mm}$ *above the backplane.*

A.5.2 Air flow rate: $\dot{m}_{air} = 2.59\,\mathrm{g\,s^{-1}}$

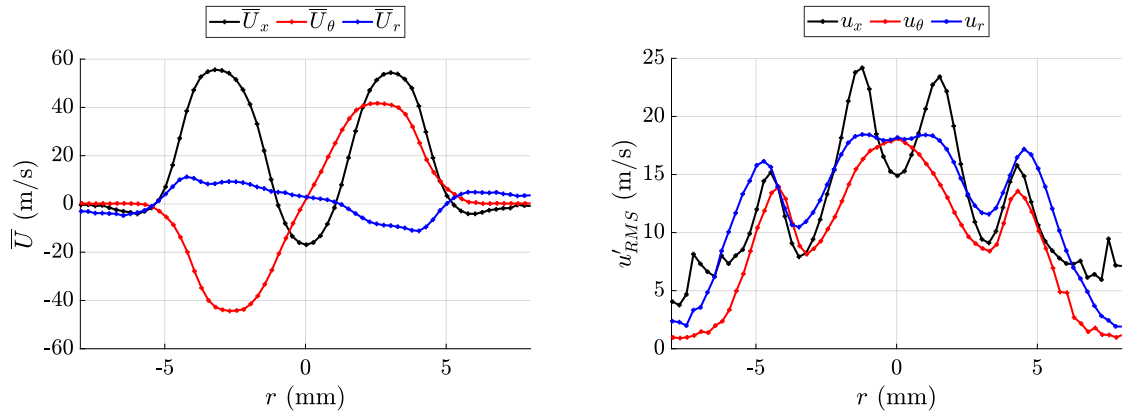

Figure A.29: *Mean and RMS velocity profiles. Swirler* 712*, air flow rate* $\dot{m}_{air} = 2.59\,\mathrm{g\,s^{-1}}$*, profiles measured at* $z = 2.5\,\mathrm{mm}$ *above the backplane.*

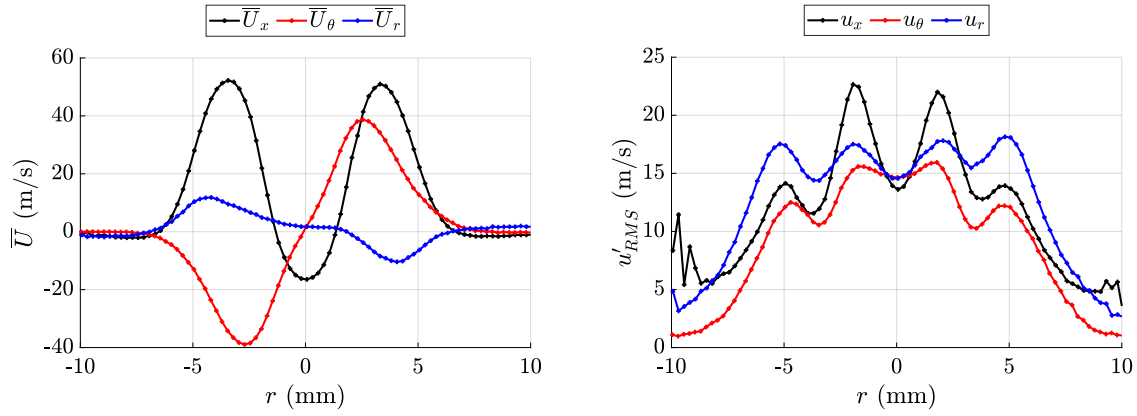

Figure A.30: *Mean and RMS velocity profiles. Swirler* 712*, air flow rate* $\dot{m}_{air} = 2.59\,\mathrm{g\,s^{-1}}$*, profiles measured at* $z = 5\,\mathrm{mm}$ *above the backplane.*

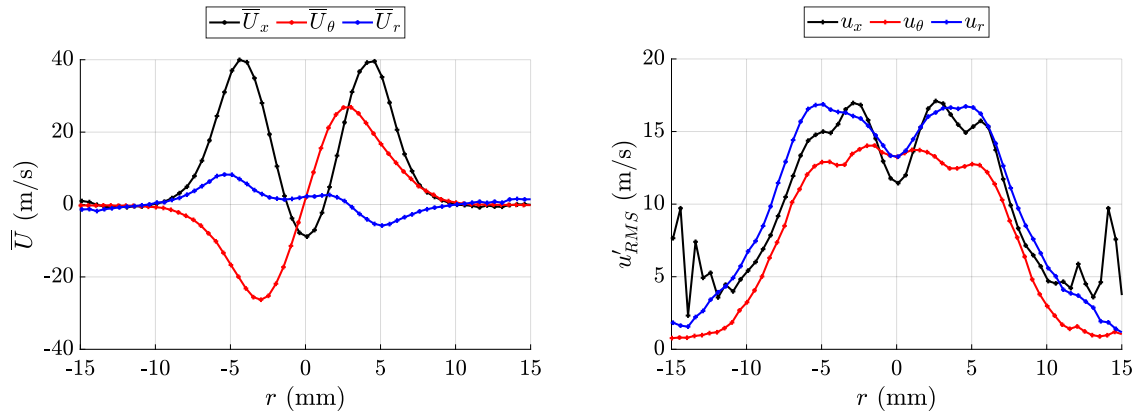

Figure A.31: *Mean and RMS velocity profiles. Swirler* 712*, air flow rate* $\dot{m}_{air} = 2.59\,\mathrm{g\,s^{-1}}$*, profiles measured at* $z = 10\,\mathrm{mm}$ *above the backplane.*

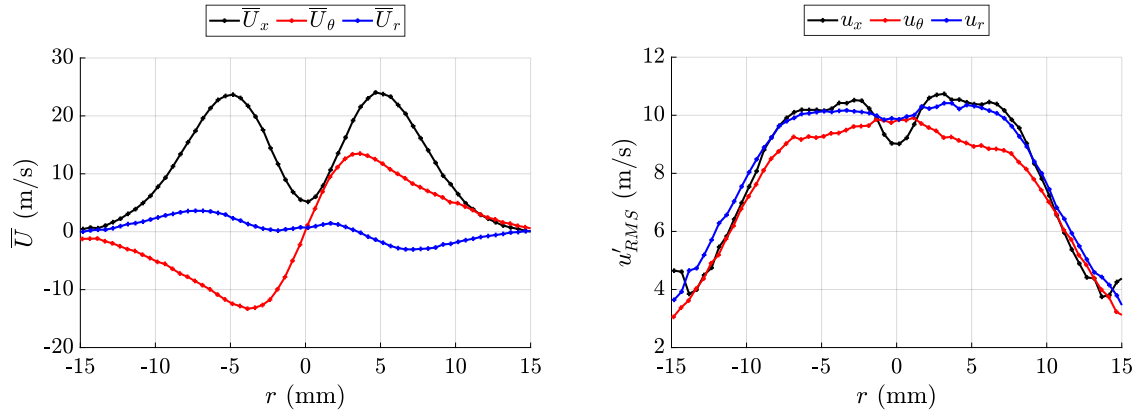

Figure A.32: *Mean and RMS velocity profiles. Swirler* 712*, air flow rate* $\dot{m}_{air} = 2.59\,\mathrm{g\,s^{-1}}$*, profiles measured at* $z = 20\,\mathrm{mm}$ *above the backplane.*

A.6 Fifth generation swirler: 716 with terminal plate TP2

A.6.1 Air flow rate: $\dot{m}_{air} = 2.26\,\mathrm{g\,s^{-1}}$

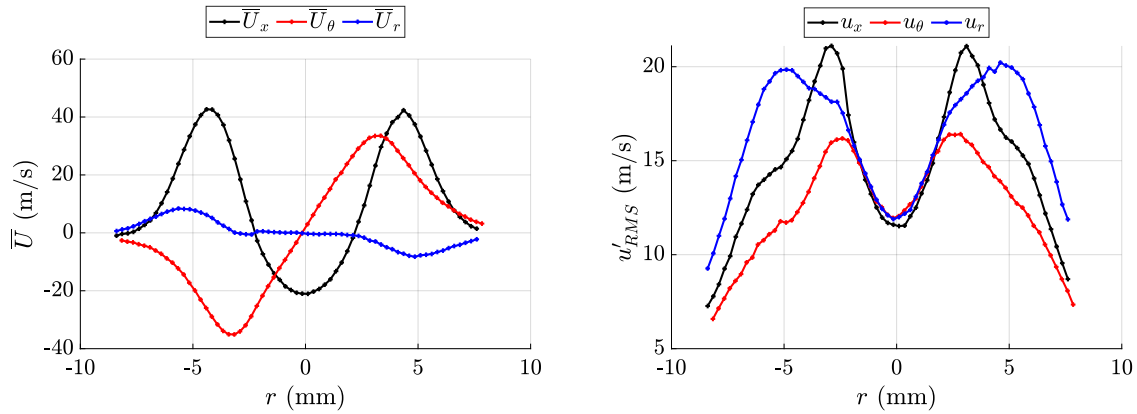

Figure A.33: *Mean and RMS velocity profiles. Swirler* 716*, air flow rate* $\dot{m}_{air} = 2.26\,\mathrm{g\,s^{-1}}$*, profiles measured at* $z = 5\,\mathrm{mm}$ *above the backplane.*

A.6.2 Air flow rate: $\dot{m}_{air} = 2.59\,\mathrm{g\,s^{-1}}$

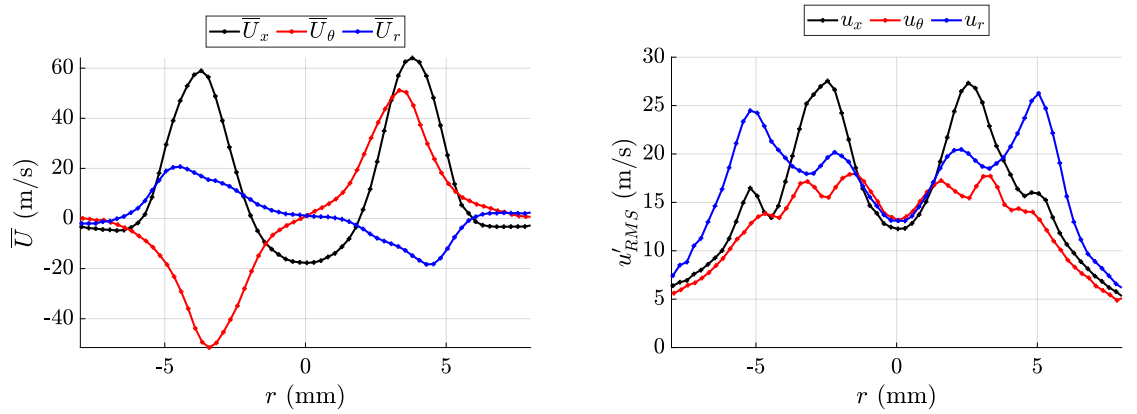

Figure A.34: *Mean and RMS velocity profiles. Swirler* 716*, air flow rate* $\dot{m}_{air} = 2.59\,\mathrm{g\,s^{-1}}$*, profiles measured at* $z = 2.5\,\mathrm{mm}$ *above the backplane.*

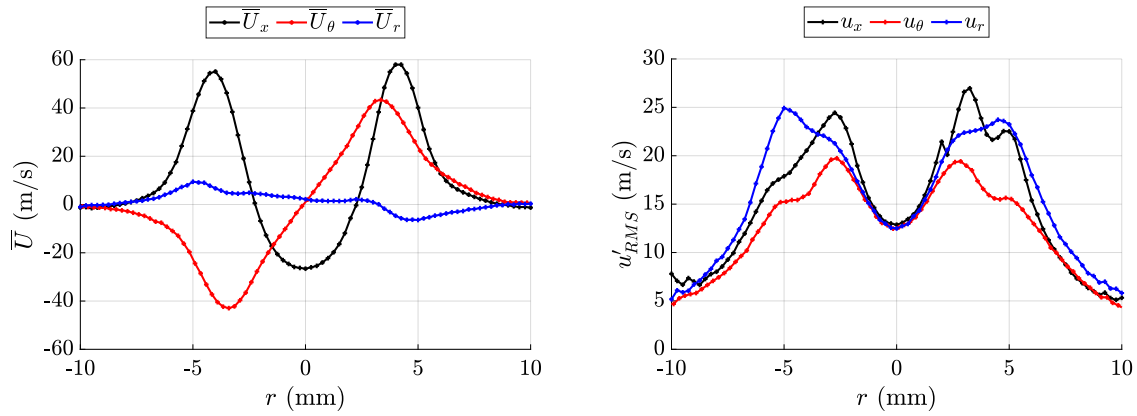

Figure A.35: *Mean and RMS velocity profiles. Swirler* 716*, air flow rate* $\dot{m}_{air} = 2.59\,\mathrm{g\,s^{-1}}$*, profiles measured at* $z = 5\,\mathrm{mm}$ *above the backplane.*

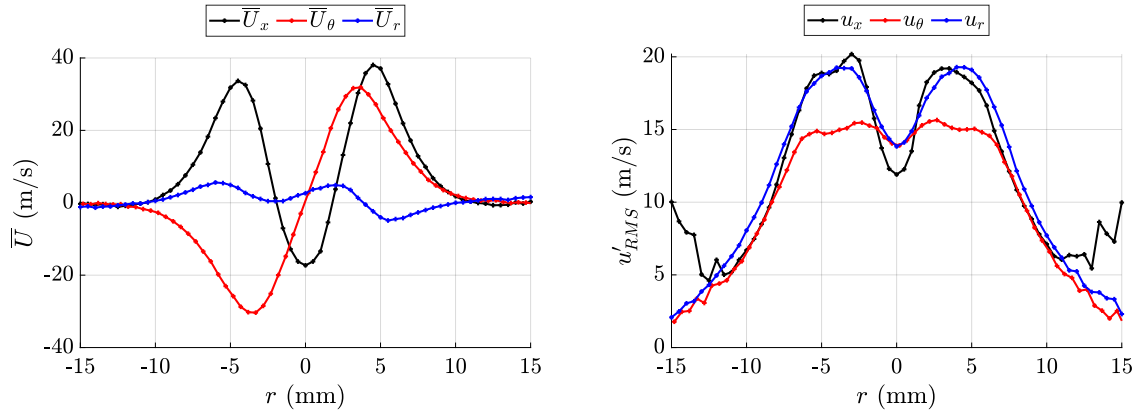

Figure A.36: *Mean and RMS velocity profiles. Swirler* 716*, air flow rate* $\dot{m}_{air} = 2.59\,\mathrm{g\,s^{-1}}$*, profiles measured at* $z = 10\,\mathrm{mm}$ *above the backplane.*

A.7 Sixth generation swirler: 713 with terminal plate TP2

A.7.1 Air flow rate: $\dot{m}_{air} = 2.59\,\mathrm{g\,s^{-1}}$

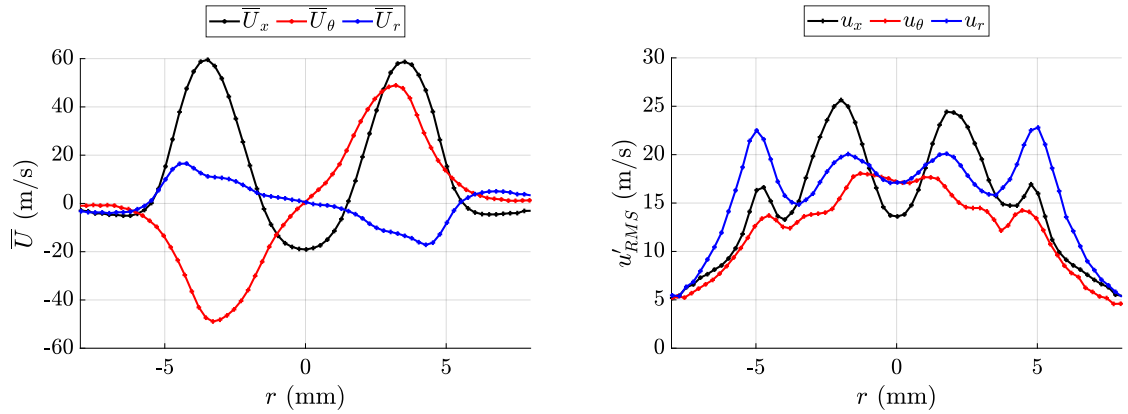

Figure A.37: *Mean and RMS velocity profiles. Swirler* 713*, air flow rate* $\dot{m}_{air} = 2.59\,\mathrm{g\,s^{-1}}$*, profiles measured at* $z = 2.5\,\mathrm{mm}$ *above the backplane.*

A.8 Sixth generation swirler: 714 with terminal plate TP2

A.8.1 Air flow rate: $\dot{m}_{air} = 2.59\,\mathrm{g\,s^{-1}}$

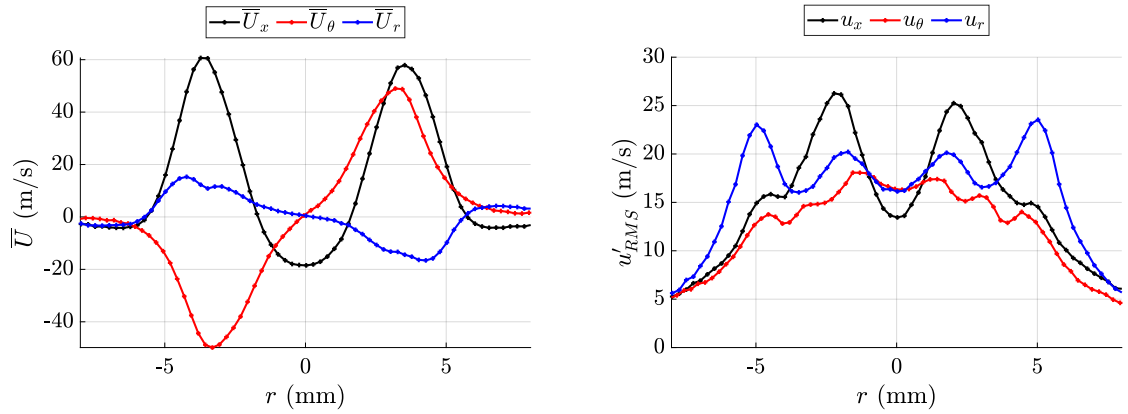

Figure A.38: *Mean and RMS velocity profiles. Swirler* 714*, air flow rate* $\dot{m}_{air} = 2.59\,\mathrm{g\,s^{-1}}$*, profiles measured at* $z = 2.5\,\mathrm{mm}$ *above the backplane.*

A.9 Sixth generation swirler: 715 with terminal plate TP2

A.9.1 Air flow rate: $\dot{m}_{air} = 2.59\,\mathrm{g\,s^{-1}}$

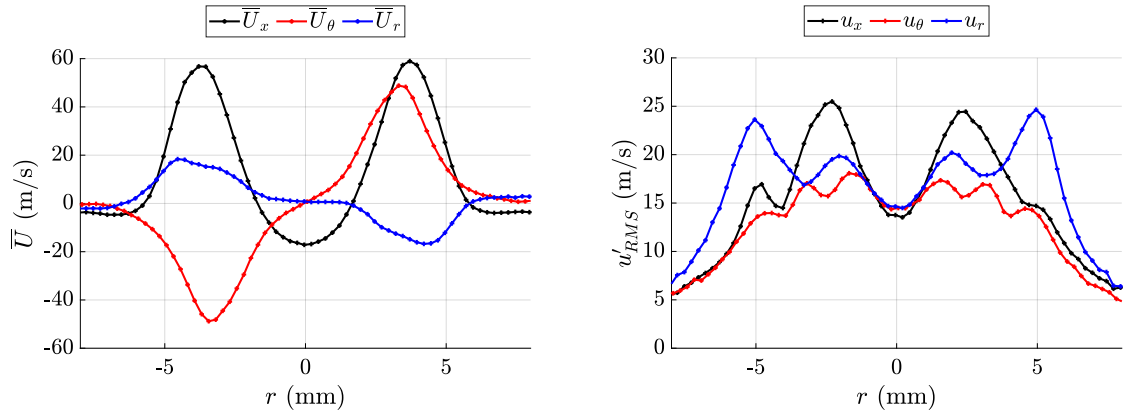

Figure A.39: *Mean and RMS velocity profiles. Swirler* 715*, air flow rate* $\dot{m}_{air} = 2.59\,\mathrm{g\,s^{-1}}$*, profiles measured at* $z = 2.5\,\mathrm{mm}$ *above the backplane.*

A.10 Sixth generation swirler: 726 with terminal plate TP2

A.10.1 Air flow rate: $\dot{m}_{air} = 2.59\,\mathrm{g\,s^{-1}}$

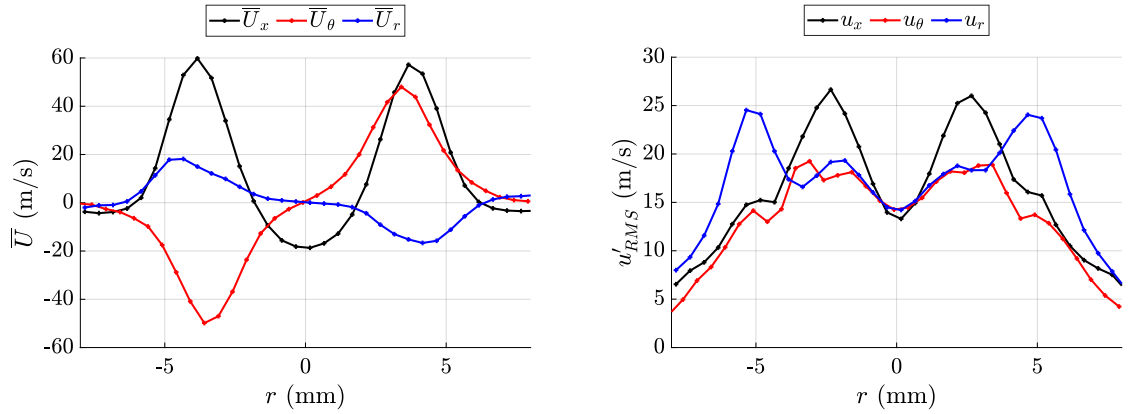

Figure A.40: *Mean and RMS velocity profiles. Swirler* 726*, air flow rate* $\dot{m}_{air} = 2.59\,\mathrm{g\,s^{-1}}$*, profiles measured at* $z = 2.5\,\mathrm{mm}$ *above the backplane.*

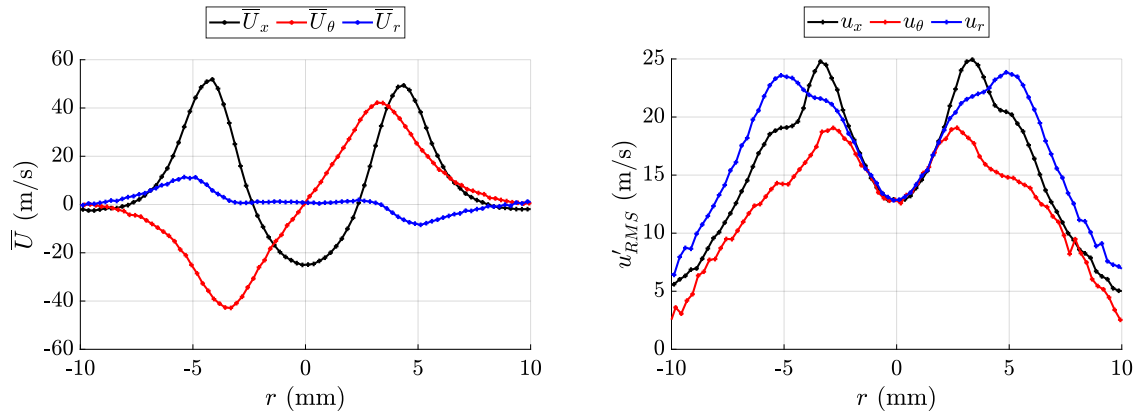

Figure A.41: *Mean and RMS velocity profiles. Swirler* 726*, air flow rate* $\dot{m}_{air} = 2.59\,\mathrm{g\,s^{-1}}$*, profiles measured at* $z = 5\,\mathrm{mm}$ *above the backplane.*

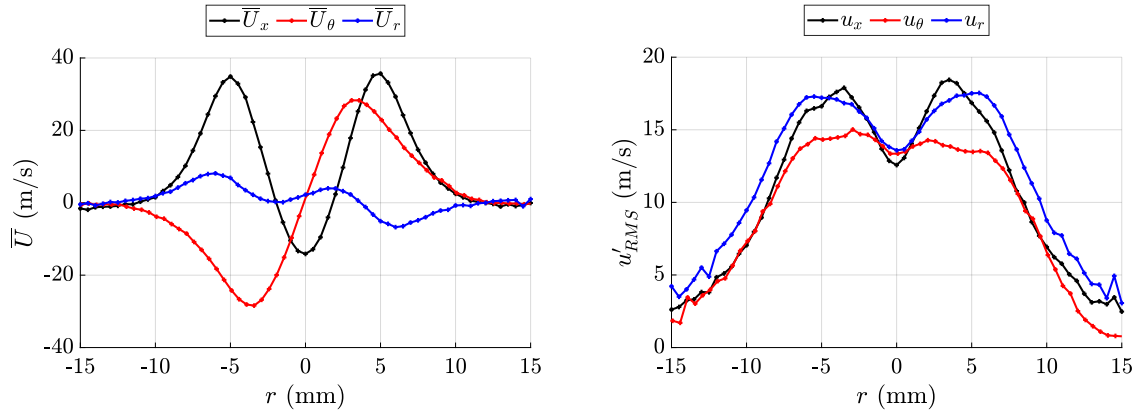

Figure A.42: *Mean and RMS velocity profiles. Swirler* 726*, air flow rate* $\dot{m}_{air} = 2.59\,\mathrm{g\,s^{-1}}$*, profiles measured at* $z = 10\,\mathrm{mm}$ *above the backplane.*

A.11 Sixth generation swirler: 727 with terminal plate TP2

A.11.1 Air flow rate: $\dot{m}_{air} = 2.59\,\mathrm{g\,s^{-1}}$

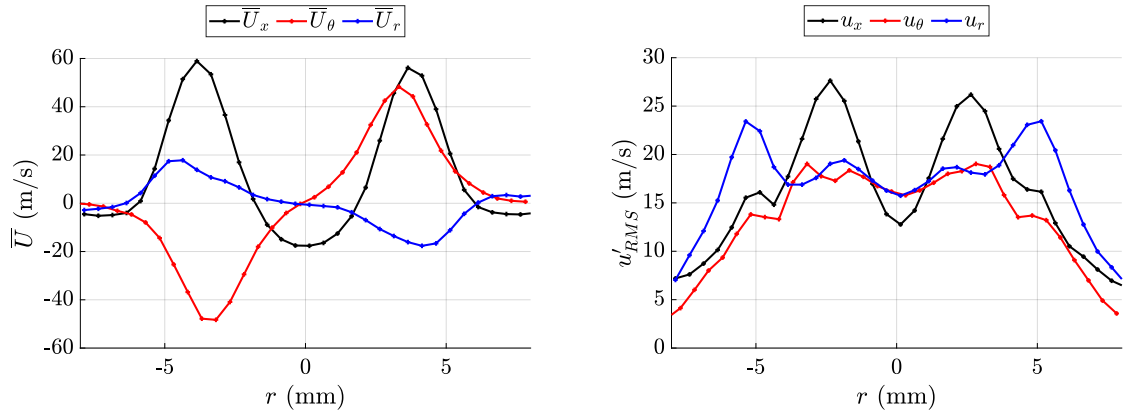

Figure A.43: *Mean and RMS velocity profiles. Swirler* 727*, air flow rate* $\dot{m}_{air} = 2.59\,\mathrm{g\,s^{-1}}$*, profiles measured at* $z = 2.5\,\mathrm{mm}$ *above the backplane.*

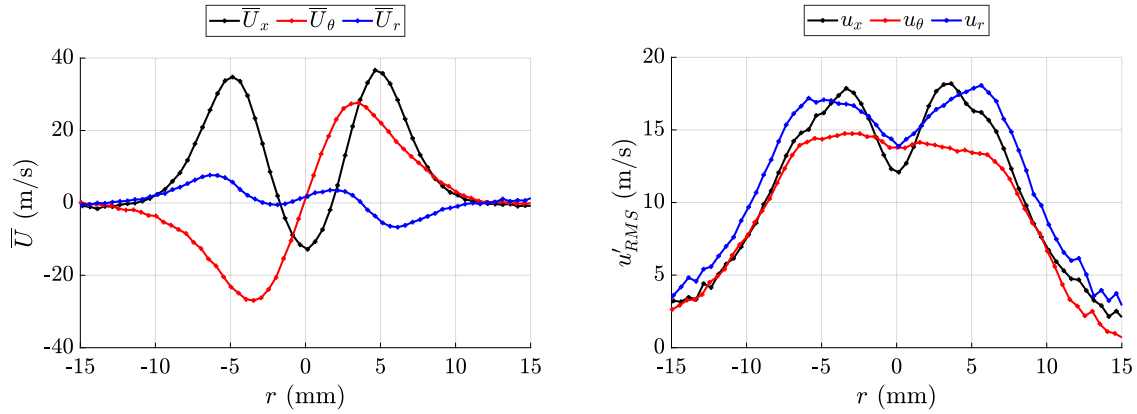

Figure A.44: *Mean and RMS velocity profiles. Swirler* 727*, air flow rate* $\dot{m}_{air} = 2.59\,\mathrm{g\,s^{-1}}$*, profiles measured at* $z = 10\,\mathrm{mm}$ *above the backplane.*

A.12 TACC injection system

The velocity profiles of the injector used by Caceres (2019); Baillot et al. (2021) in the TACC facility in CORIA, Rouen are presented below. The TACC facility is used to study the effect of transverse acoustic excitation on the dynamics of spray swirled flames similar to those found in MICCA-Spray. Clément Patat, Dr. Marcos Caceres and Pr. Françoise Baillot are gratefully acknowledged for submitting this data for inclusion in the present database.

A.12.1 Air flow rate: $\dot{m}_{air} = 1.76\,\mathrm{g\,s^{-1}}$

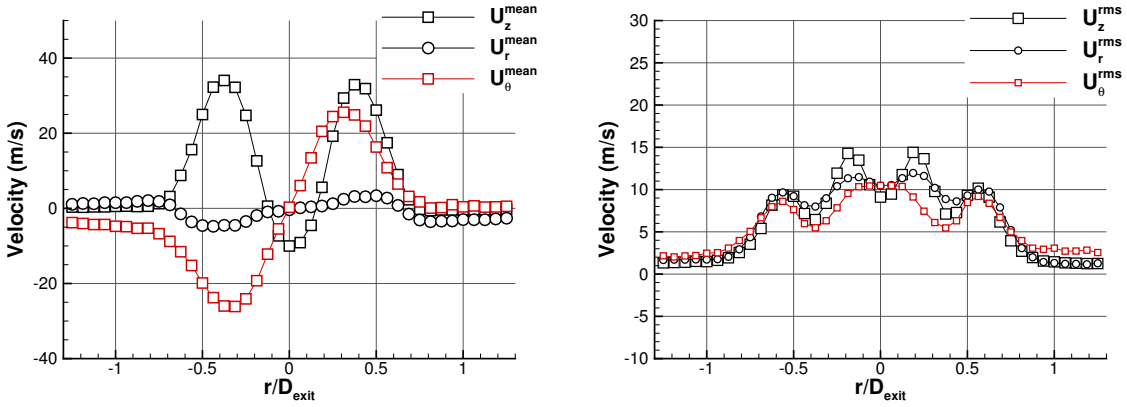

Figure A.45: *Mean and RMS velocity profiles. TACC injection system, air flow rate* $\dot{m}_{air} = 1.76\,\mathrm{g\,s^{-1}}$*, profiles measured at* $z = 3\,\mathrm{mm}$ *above the backplane.*

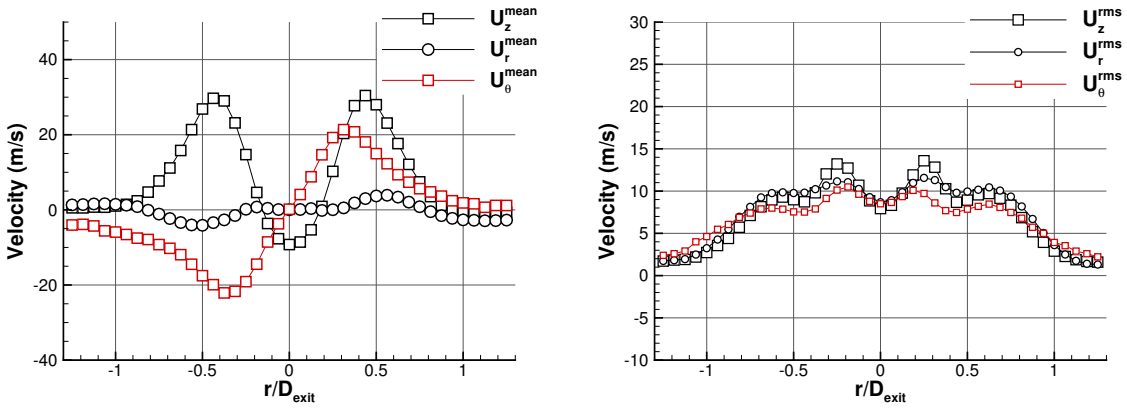

Figure A.46: *Mean and RMS velocity profiles. TACC injection system, air flow rate* $\dot{m}_{air} = 1.76\,\mathrm{g\,s^{-1}}$*, profiles measured at* $z = 6\,\mathrm{mm}$ *above the backplane.*

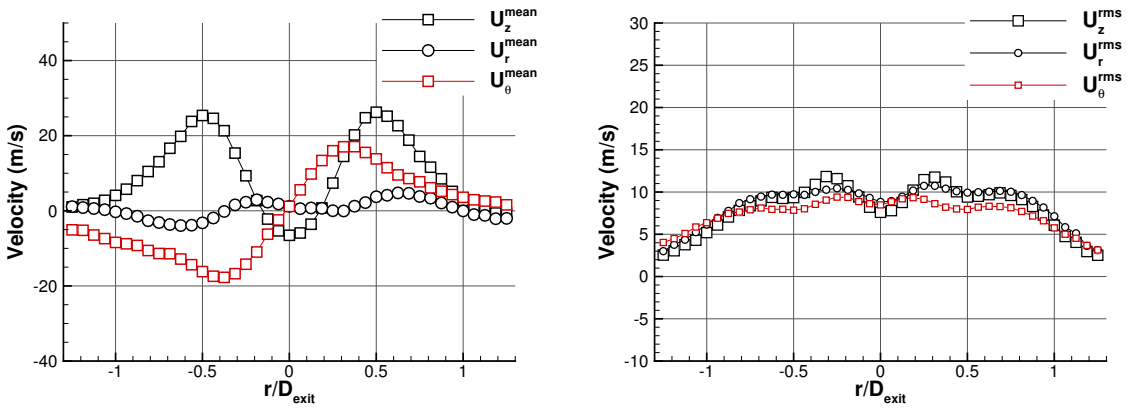

Figure A.47: *Mean and RMS velocity profiles. TACC injection system, air flow rate* $\dot{m}_{air} = 1.76\,\mathrm{g\,s^{-1}}$*, profiles measured at* $z = 9\,\mathrm{mm}$ *above the backplane.*

Appendix B

Computing the acoustic azimuthal velocity field from pressure signals in annular combustor

Combustion instabilities coupled by azimuthal acoustic modes in annular systems induce velocity oscillations in the transverse (azimuthal) direction. These oscillations reach maximum levels at the pressure field nodal line (where the pressure oscillation is at its minimum). Theses disturbances impinge on the flames and their effect is strongest in that location. It has been found that flames can be extinguished when the transverse velocity takes large values. It is then important to determine the critical value that leeds to extinction. A method is derived in this appendix to estimate the velocity oscillation in the azimuthal direction by making use of the pressure field distribution reconstructed from multiple microphone measurements.

The acoustic velocity may be deduced from the momentum balance for an annular configuration. Assuming small disturbances, neglecting viscous stresses and body forces and effects of the local mean velocity, one may use the linearized version of this equation (Poinsot and Veynante (2012)):

$$\rho_0(\theta,t)\,\frac{\partial v_\theta}{\partial t} = -\frac{1}{R}\,\frac{\partial p'}{\partial \theta} \tag{B.1}$$

where θ is the azimuthal coordinate in the annular geometry and R its median radius, ρ_0 designates the local mean value of the density, and v_θ the transverse velocity fluctuations of interest.

The present derivation relies on a representation of the acoustic field in the annular system based on the framework proposed in Eq. (9.3). In that expression the pressure field is expanded in terms of azimuthal Fourier harmonics. Eq. (9.3) is linearised at the first order in time around the instant t_0 in Eq. (B.2). $\omega(t) = 2\pi f(t)$ is the instantaneous angular frequency, $\alpha_m(t)$ the instantaneous growth rate of the m^{th} component, and $\beta(t)$

the instantaneous change in angular frequency.

$$\begin{aligned} p'(\theta,t) = & \sum_{m=-M}^{M} a_m(t_0)\, e^{-i\omega(t_0)t_0} \\ & \exp\left\{i\left[m\theta - \omega(t_0)\varepsilon + \beta(t_0)t_0\varepsilon\right] + \alpha_m(t_0)\varepsilon + O(\varepsilon^2)\right\} \\ & \varepsilon = t - t_0 \\ & \alpha_m(t_0) = \frac{1}{a_m(t_0)}\frac{da_m}{dt}(t_0) \\ & \beta(t_0) = \frac{d\omega}{dt}(t_0) \end{aligned} \tag{B.2}$$

Solving for Eq. (B.1), one obtains the first order approximation of the velocity field around t_0. It is worth noting that this expression is valid even if the density field is not uniform. One simply has to use the local value of the density field.

$$v_\theta = -\frac{1}{R\rho_0}\sum_{m=-M}^{M}\frac{im\, a_m(t)}{\alpha_m(t_0) + i\beta(t_0) - i\omega(t_0)}\exp\left\{i(m\theta - \omega(t)t)\right\} + O((t-t_0)^2) \tag{B.3}$$

In most instances, the terms α_m and β can be neglected compared to the angular frequency ω. The velocity field then takes the simpler form

$$v_\theta \simeq \frac{1}{R\rho_0}\sum_{m=-M}^{M}\frac{m\, a_m(t)}{\omega(t)}\exp\left\{i(m\theta - \omega(t)t)\right\} \tag{B.4}$$

This expression was used to determine the azimuthal velocity field appearing in Fig. 9.10.

Appendix C

Recommended procedure to compute the swirl number from CFD data

Based on the analysis of chapter 4 it is possible to formulate a set of guidelines for the computation of the swirl number in incompressible isothermal flows. These guidelines are suggested to ensure a high level of generality and reproducibility, while keeping the process straightforward in practical systems. We here consider cases where the swirl number is determined from CFD simulations and we examine unconfined and confined situations.

The computation of the conventional swirl number S_{conv} (Eq. (4.30)) is quite straightforward and is discussed in section C.1. On the other hand, determining the more general swirl number S_P^f can be challenging and requires well converged statistics. If a compressible solver is used, the presence of even minute spurious pressure oscillations can greatly impact the computation of S_P^f. For this reason, the authors highly recommend examining the axial evolution of S_P^f in a manner similar to Fig. 4.16 to check for spurious oscillations in S_P^f. The method to determine S_P^f in an unconfined configuration is presented in section C.2 before the confined case is discussed in section C.3.

C.1 Determination of the conventional swirl number S_{conv}

The determination of the conventional swirl number S_{conv} is quite straightforward. Mean velocity profiles should be acquired at an axial section located as close to the outlet of the injector as possible and can be integrated as follow:

$$S_{conv} = \frac{\int_0^{R_{lim}} \rho \, \overline{U_\theta} \, \overline{U_x} \, r^2 dr}{R_{inj} \int_0^{R_{lim}} \rho \, \overline{U_x}^2 \, r dr} \qquad (4.30 \textit{ rep.})$$

The radial integration limit R_{lim} may be determined by plotting S_{conv} for different integration radii as shown in Fig. 4.17. When quoting a value of S_{conv}, the axial section at which it is determined and the integration limit R_{lim} should be specified so that the

computation is reproducible.

C.2 Determination of S_P^f in an unconfined configuration

The calculation may proceed according to the following steps:

(1) Choose a reference radius R_{ref}. It is suggested to choose the radius of the outlet port of the injection system.

(2) Determine the far-field pressure p_∞:
- In the case of quiescent surroundings, this corresponds to the mean static pressure at infinity $p_\infty = \overline{p}(r = \infty)$.
- If a low velocity co-flow is present, $p_\infty = \overline{p}(r = \infty) + \rho(r = \infty)\overline{U_x}^2(r = \infty)$.

(3) Choose a practical integration limit R_{lim}. This should be inside the region where the numerical grid is sufficiently fine to allow an accurate calculation. It is recommended to verify this choice by plotting curves similar to those of Fig. 4.15 to check that the most of the flowrate of momentum is accounted for[1].

(4) Compute $G_{x,P}^f$, G_θ and finally S_P^f as

$$G_{x,P}^f = 2\pi \int_0^{R_{lim}} \left[\rho \left(\overline{U_x}^2 + \overline{u_x^2}\right) + (\overline{p} - p_\infty)\right] r dr \tag{C.1}$$

$$G_\theta^f = 2\pi \int_0^{R_{lim}} \rho \left(\overline{U_\theta}\,\overline{U_x} + \overline{u_\theta u_x}\right) r^2 dr \tag{C.2}$$

$$S_P^f = \frac{G_\theta^f}{R_{ref} G_{x,P}^f} \tag{C.3}$$

(5) It is recommended to calculate these terms at several axial positions downstream of the outlet port. They should be conserved.

C.3 Determination of S_P^f in a confined configuration

The procedure in this case may be as follows:

(1) Choose a reference radius R_{ref}. It is suggested to use the radius of the confinement[2].

(2) Choose a reference pressure p_{ref}. As in section 4.5.2, it is proposed to choose the sectional average of the static pressure at an axial position where the flow is established. This value may be determined by plotting the axial evolution of the sectional average of the static pressure.

[1] See footnote 1 on page 352.

[2] A hydraulic radius can be used for non-cylindrical confinements.

(3) Compute $G^f_{x,P}$, G^f_θ by integration over the whole cross-section Σ and determine S^f_P as

$$G^f_{x,P} = \int_\Sigma \left[\rho\left(\overline{U_x}^2 + \overline{u_x^2}\right) + \left(\overline{p} - p_{ref}\right)\right] dS \tag{C.4}$$

$$G^f_\theta = \int_\Sigma \rho\left(\overline{U_\theta}\,\overline{U_x} + \overline{u_\theta u_x}\right) r\, dS \tag{C.5}$$

$$S^f_P = \frac{G^f_\theta}{R_{ref} G^f_{x,P}} \tag{C.6}$$

(4) It is recommended to calculate these terms at several axial positions. Only a slow decay along the axis corresponding to the skin friction on the wall of the channel should be observed[3].

[3]See appendix **??** for a discussion on the extension of the conservation properties of the swirl number for non-cylindrical confinements.

Appendix D

Recommended procedure to compute the swirl number from experimental measurements

We consider in the present appendix cases where the swirl number is determined from experiments and we examine unconfined and confined situations.

The computation of the conventional swirl number S_{conv} (Eq. (4.30)) is quite straightforward and the reader is referred to appendix C.1 for more details. The direct determination of the more general swirl number S_P^f may only be accomplished using intrusive Pitot tubes. The formulation S_U^f (Eqs. (4.29) and (4.44)) is better suited and provides a good estimate of S_P^f. In unconfined swirling jets, recommended practices for computing S_U^f are presented in section D.1. In section D.2, we discuss the challenges associated with the determination of S_U^f in confined configurations, and suggest two methods that may be used if the experimental challenges are overcome.

D.1 Determination of the swirl number S_U^f in unconfined flows

It is assumed that measurements are obtained from laser velocimetry techniques such as Laser Doppler Velocimetry (LDV) or Particle Image Velocimetry (PIV) and that the following time averaged quantities are available: axial velocity $\overline{U_x}$ and its axial gradient; axial velocity fluctuations $\overline{u_x}$; tangential velocity $\overline{U_\theta}$; tangential velocity fluctuations $\overline{u_\theta}$; radial velocity $\overline{U_r}$ and its axial gradient; radial velocity fluctuations $\overline{u_r}$; Reynolds stress term $\overline{u_x u_\theta}$; Reynolds stress term $\overline{u_x u_r}$ and its axial gradient. Given these requirements, the preferred measurement techniques are 2-component LDV, or 3-component stereo-PIV, which give access to both Reynold stress terms $\overline{u_x u_\theta}$ and $\overline{u_x u_r}$. The swirl number may then be determined with the following steps.

(1) Choose a reference radius R_{ref}. A natural choice is the radius of the outlet port of the injection system.

(2) Choose a practical integration limit R_{lim}. The integration should be stopped where

the axial velocity and its fluctuations are close to zero (or u_∞ if applicable)[1].

(3) S_U^f can now be computed as per Eq. (4.29). First, compute G_θ^f as

$$G_\theta^f = 2\pi \int_0^{R_{lim}} \rho \left(\overline{U_\theta}\,\overline{U_x} + \overline{u_\theta u_x}\right) r^2 dr \tag{D.1}$$

(4) Compute $G_{x,U}^f$ as

$$G_{x,U}^f = 2\pi \int_0^{R_{lim}} \rho \left[\overline{U_x}^2 + \overline{u_x^2} - \frac{1}{2}\left(\overline{U_\theta}^2 + \overline{U_r}^2 + \overline{u_r^2} + \overline{u_\theta^2}\right) + \frac{r}{2}\frac{\partial}{\partial x}\left(\overline{U_x}\,\overline{U_r} + \overline{u_x u_r}\right)\right] r dr \tag{D.2}$$

(5) Compute S_U^f as

$$S_U^f = \frac{G_\theta^f}{R_{ref} G_{x,u}^f} \tag{D.3}$$

(6) It is recommended to compute these terms at several axial positions downstream of the outlet port in order to validate the calculation by checking their conservation.

D.2 Determination of the swirl number S_U^f in confined flows

The determination of the swirl number S_U^f in confined flows presents two major challenges.

- As shown in section 4.5.5, the integration of the velocity profiles must be conducted up to the wall, the radial position closest to the wall conveying a large weight in the final results. This implies that all velocities, including cross-correlations such as $\overline{u_x u_\theta}$ or the axial gradient of $\overline{u_x u_r}$ must be accurately measured near the wall with a sufficiently high resolution. Although possible in some configurations using current laser velocimetry apparatus, it remains an arduous task.
- A reference pressure needs to be determined.

Given these difficulties, numerical simulations should be considered as a practical alternative if S_P^f or S_U^f are required. We nonetheless present here two methods to determine S_U^f in confined configurations: in the simpler, but more approximate, high Reynolds number method of section D.2.1, all viscous losses are neglected. Measurements are conducted at an axial section where the flow is established, thereby removing the need for the determination of the reference pressure. A more complex method which does not involve any

[1] In practice, a good point to start is $R_{lim} \geq 2R_{ref}$. If R_{lim} is sufficiently large, G_θ^f and $G_{x,U}^f$ are independent of R_{lim}. Thus, consider plotting graphs similar to Fig. E.3, check for the following properties and increase R_{lim} until they are satisfied:

(a) All velocities and the static pressure at this position should be close to their value at $r = \infty$

(b) $2\pi R_{ref} R_{lim}\left[\rho\left(\overline{U_x}^2(x, R_{lim}) + \overline{u_x^2}(x, R_{lim})\right) + \left(\overline{p}(x, R_{lim}) - p_\infty\right)\right] \ll G_{x,P}^f(x, R_{lim})$

(c) $2\pi R_{ref} R_{lim}^2 \rho\left(\overline{U_\theta}(x, R_{lim})\,\overline{U_x}(x, R_{lim}) + \overline{u_\theta u_x}(x, R_{lim})\right) \ll G_\theta^f(x, R_{lim})$

simplifying assumptions is given in section D.2.2.

D.2.1 Simple method: high Reynolds number approach

The method presented in this section applies to confined swirling jets in configuration with a constant cross-section Σ. It is demonstrated in section 4.2, and verified in section 4.5.1 that, if viscous dissipation is negligible, the swirl number is conserved in a cylindrical duct. Similar conservation properties are demonstrated in the case of non-cylindrical confinements with constant cross-section in appendix **??**. It is then natural to attempt to measure the swirl number at an axial section where the flow is established, and where many complexities related to the radial expansion of the flow can be neglected. In particular, with the definition of the reference pressure put forward in section 4.5.2, it becomes unnecessary to determine either the static pressure or the reference pressure: $\int_\Sigma (\overline{p} - p_{ref})\, dS = 0$.

The swirl number may then be determined with the following steps.

(1) Choose a reference radius R_{ref}. It is suggested to use the radius of the confinement[2].

(2) Compute G_θ^f by integration over the entire cross-section as [3]

$$G_\theta^f = \int_\Sigma \rho \left(\overline{U_\theta}\,\overline{U_x} + \overline{u_\theta u_x}\right) r dS \tag{D.5}$$

(3) Compute $G_{x,U}^f$. The following formula only applies in axial sections where the flow is established[4].

$$G_{x,U}^f = \int_\Sigma \rho \left[\overline{U_x}^2 + \overline{u_x^2}\right] dS \tag{D.7}$$

(4) Compute S_u^f as

$$S_U^f = \frac{G_\theta^f}{R_{ref} G_{x,U}^f} \tag{D.8}$$

(5) It is recommended to compute these terms at several axial positions where the flow is established in order to validate the calculation by checking the conservation of G_θ^f, $G_{x,U}^f$ and S_U^f.

---

[2] A hydraulic radius can be used for non-cylindrical confinements.

[3] Alternatively, for a confinement with a cylindrical cross-section:

$$G_\theta^f = 2\pi \int_0^{R_c} \rho \left(\overline{U_\theta}\,\overline{U_x} + \overline{u_\theta u_x}\right) r^2 dr \tag{D.4}$$

[4] Alternatively, for a confinement with a cylindrical cross-section:

$$G_{x,U}^f = 2\pi \int_0^{R_c} \rho \left[\overline{U_x}^2 + \overline{u_x^2}\right] r dr \tag{D.6}$$

D.2.2 Complex method: injector near-field measurements

This method requires the velocity field to be measured in at least two axial section thereafter referred to as Σ_1 and Σ_2. The flow must be established at Σ_1, which serves to determine the reference pressure. Σ_2 may be found in the vicinity of the injection unit or wherever the experimenter sees fit. It is assumed here that the cross-section does not vary: $\Sigma_1 = \Sigma_2$. The difference in wall pressure between these two axial sections $\Delta P_{21} = \overline{p}(r = R_c, x = x_{\Sigma 2}) - \overline{p}(r = R_c, x = x_{\Sigma 1})$ must also be measured using a sensitive differential pressure gauge.

All steps presented in the previous section D.2.1 may be applied to the velocity field measured at section Σ_2 with the exception of step (3) where the following formula must be employed

$$\begin{aligned} G^f_{x,U}(\Sigma_2) = &\int_{\Sigma_2} \rho \left[\overline{U_x}^2 + \overline{u_x^2} - \frac{1}{2}\left(\overline{U_\theta}^2 + \overline{U_r}^2 + \overline{u_r^2} + \overline{u_\theta^2} \right) + \frac{r}{2}\frac{\partial}{\partial x}\left(\overline{U_x}\,\overline{U_r} + \overline{u_x u_r} \right) \right]\Bigg|_{\Sigma_2} dS \\ &+\Sigma_2 \Delta P_{21} - \int_{\Sigma_1} \rho \left[-\frac{1}{2}\left(\overline{U_\theta}^2 + \overline{U_r}^2 + \overline{u_r^2} + \overline{u_\theta^2} \right) + \frac{r}{2}\frac{\partial}{\partial x}\left(\overline{U_x}\,\overline{U_r} + \overline{u_x u_r} \right) \right]\Bigg|_{\Sigma_1} dS \end{aligned} \tag{D.9}$$

Alternatively to the use of Eq. (D.9), in a configuration similar to that used in the present study (depicted schematically in Fig. F.1, where the outlet of a simple cylindrical combustor is found in a quiescent atmosphere, the use of analytical jump conditions such as those presented in appendix **??** (Eqs. (F.3) or (F.6)) may be considered to determine a reference pressure and subsequently compute the swirl number using Eq. (4.44).

Appendix E

Can swirl numbers measured in a free swirling jet be extended to a confined configuration ?

In order to test the proposed swirl number computation method on a free swirling jet, it is here applied to the same injector and operating conditions, but without the quartz confinement tube. The values of S_U^f and S_{conv} for the free swirling jet are then compared to their counterpart for the confined flow. We thus examine whether swirl number measured in unconfined cases (which are generally far easier to investigate in terms of measurement apparatus) may easily be extended to a confined configuration.

To this end, LDV measurements are performed at $x = 5, 10$ and $20\,\mathrm{mm}$. As per the LDV system specifications and accounting for statistical uncertainties (assuming an underlying gaussian distribution), measurement uncertainties are under $0.25\,\mathrm{m\,s^{-1}}$ for both mean and RMS velocities. The relative measurement uncertainty for cross-correlation are better than 40% for $r < 15\,\mathrm{mm}$, but can reach up to 100% for $r > 15\,\mathrm{mm}$. Imperfections in the seeding are not accounted for. Results are presented in Fig. E.1 and E.2, and compared with the confined velocity profiles from the LES, which have been previously thoroughly validated in Fig. 4.4. In the outer regions, as could be expected, the flow differs significantly between the two configurations, and in particular, the unconfined case does not have an outer recirculation zone. The unconfined jet is also much narrower than its confined counterpart, with a weaker and narrower inner recirculation zone. The unconfined jet is not spreading as widely, and the maximum axial velocity is found to remain around $r \approx 6\,\mathrm{mm}$ at $z = 5, 10$ and $20\,\mathrm{mm}$.

Let us now compute the swirl number S_U^f (Eq. 4.29) as recommended per the procedure of appendix **??**. In the present case, the reference radius is naturally the radius of the injector $R_{ref} = R_{inj} = 5\,\mathrm{mm}$. The choice of the limit R_{lim} for the integration is based on the analysis presented in Fig. E.3. It shows the impact of R_{lim} on $G_{x,U}^f$ and G_θ^f, whose

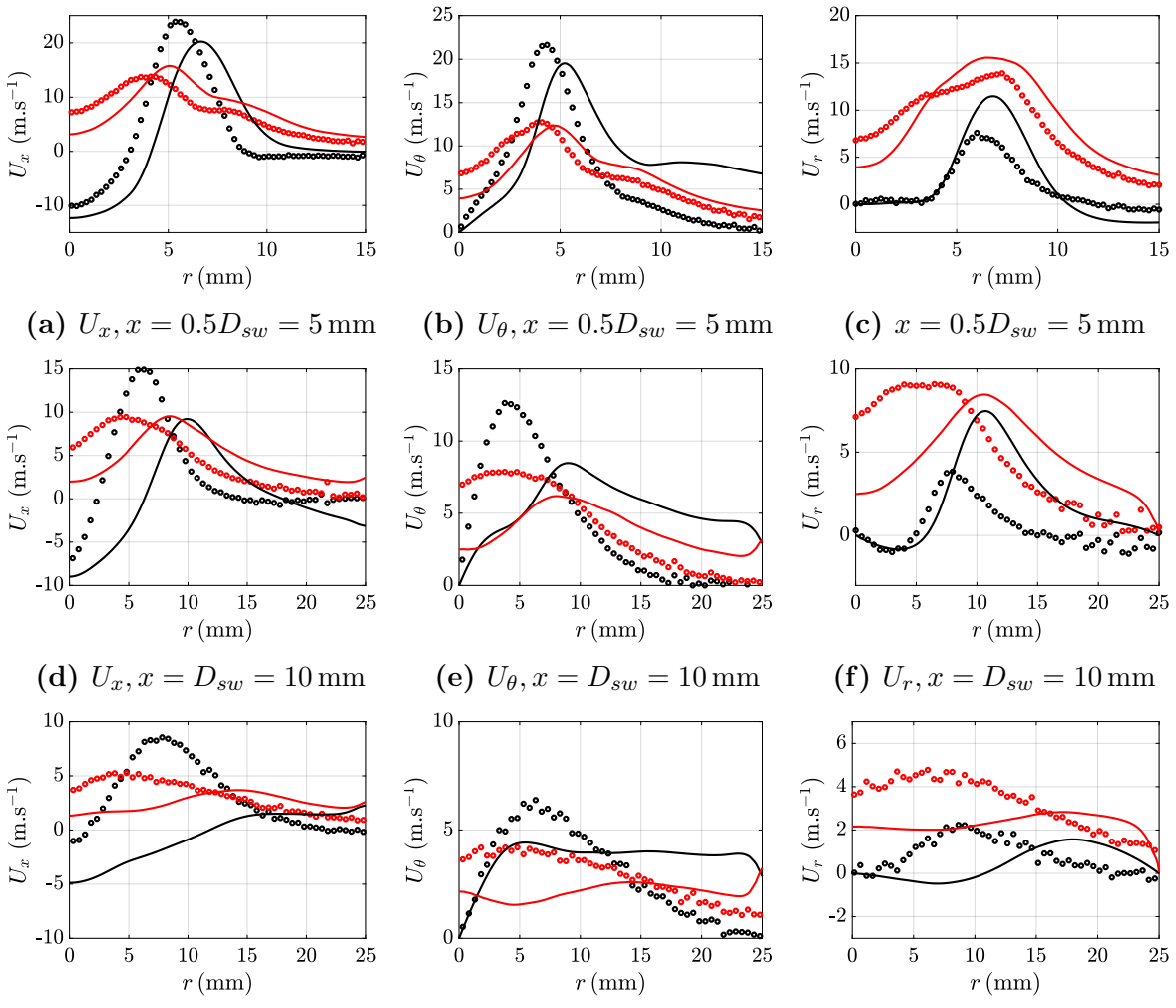

(a) $U_x, x = 0.5D_{sw} = 5\,\text{mm}$ **(b)** $U_\theta, x = 0.5D_{sw} = 5\,\text{mm}$ **(c)** $x = 0.5D_{sw} = 5\,\text{mm}$

(d) $U_x, x = D_{sw} = 10\,\text{mm}$ **(e)** $U_\theta, x = D_{sw} = 10\,\text{mm}$ **(f)** $U_r, x = D_{sw} = 10\,\text{mm}$

(g) $U_x, x = 2D_{sw} = 20\,\text{mm}$ **(h)** $U_\theta, x = 2D_{sw} = 20\,\text{mm}$ **(i)** $U_r, x = 2D_{sw} = 20\,\text{mm}$

Figure E.1: *Time averaged velocity profiles obtained using LES in the confined case (continuous lines, confinement with a* 25 mm *radius) and measured with LDV in the unconfined case (symbols). Both mean (in black) and RMS (in red) values are shown at three distances from the combustor backplane. From left to right: axial, tangential and radial velocity profiles.*

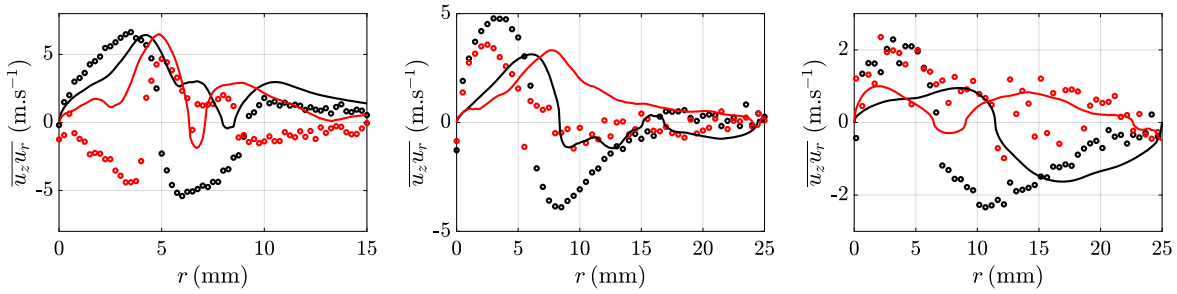

(a) $x = 0.5D_{sw} = 5\,\text{mm}$ **(b)** $x = D_{sw} = 10\,\text{mm}$ **(c)** $x = 2D_{sw} = 20\,\text{mm}$

Figure E.2: *Time averaged velocity cross-correlation profiles obtained using LES in the confined case (continuous lines, confinement with a* 25 mm *radius) and measured with LDV in the unconfined case (symbols). Both* $\overline{u_z u_r}$ *(in black) and* $\overline{u_z u_\theta}$ *(in red) values are shown at three distances from the combustor backplane.*

formulas are repeated below for a free swirling jet

$$G_{x,U}^f = 2\pi \int_0^{R_{lim}} \rho \left[\overline{U_x}^2 + \overline{u_x^2} - \frac{1}{2}\left(\overline{U_\theta}^2 + \overline{U_r}^2 + \overline{u_r^2} + \overline{u_\theta^2} \right) + \frac{r}{2}\frac{\partial}{\partial x}\left(\overline{U_x}\,\overline{U_r} + \overline{u_x u_r} \right) \right] r dr \tag{E.1}$$

$$G_\theta^f = 2\pi \int_0^{R_{lim}} \rho \left(\overline{U_\theta}\,\overline{U_x} + \overline{u_\theta u_x} \right) r^2 dr \tag{E.2}$$

The derivative of these terms with respect to R_{lim} is scaled by R_{inj} and shown alongside (dotted lines in Fig. E.3). Let us first consider $z = 10\,\text{mm}$ (black curves). From Fig. E.1, the axial velocity is close to zero after $r = 15\,\text{mm}$: $\overline{U_x}\,(z = 10, r > 15) \approx 0$. Figure E.3(b) shows that, for $R_{lim} > 15\,\text{mm}$, G_θ^f is nearly constant and $R_{inj}\,\partial G_\theta^f / \partial R_{lim}$ is small. Figure E.3(a) shows that $G_{x,U}^f(R_{lim})$ is constant around $R_{lim} = 15\,\text{mm}$. We also observe that $R_{inj}\,\partial G_{x,U}^f / \partial R_{lim} \approx 0$ at $R_{lim} = 15\,\text{mm}$. However, $G_{x,U}^f(R_{lim})$ gets smaller for larger values of R_{lim}. Given the estimated measurement uncertainties, it appears reasonable to attribute the decay of $G_{x,U}^f$ for $R_{lim} > 15\,\text{mm}$ to measurement noise. One may then chose $R_{lim}(z = 10\,\text{mm}) = 15\,\text{mm}$. The values of R_{lim} at the two other axial sections are chosen using the same process: $R_{lim}(z = 5\,\text{mm}) = 15\,\text{mm}$ and $R_{lim}(z = 20\,\text{mm}) = 25\,\text{mm}$. From Fig. E.3, one also observes that the values of $G_{x,U}^f$ and G_θ^f are fairly constant between the three axial positions $z = 5, 10$ and $20\,\text{mm}$ as is expected for a free swirling jet.

Concerning the conventional swirl number S_{conv}, we retain for both the confined flow and the free jet the same integration limit of $2R_{inj}$ (section 4.6):

$$S_{conv} = \frac{\int_0^{2R_{inj}} \rho\,\overline{U_\theta}\,\overline{U_x}\,r^2 dr}{R_{inj}\int_0^{2R_{inj}} \rho\,\overline{U_x}^2\,r dr} \tag{E.3}$$

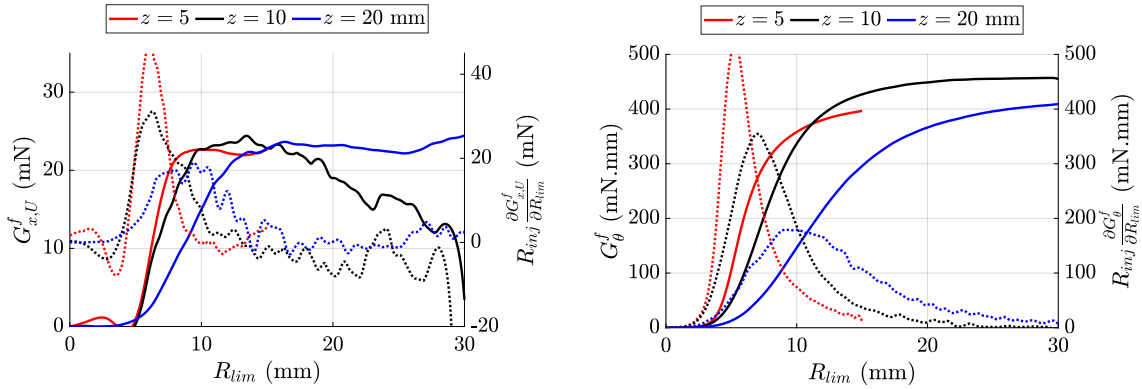

(a) $G^f_{x,P}$ **(b)** G^f_θ

Figure E.3: *Effect of integration limit on the estimated flow rates* $G^f_{x,U}$ *(left, plain line) and* G^f_θ *(right, plain line) at* $z = 5, 10$ *and* 20 mm. *The integral terms are computed by stopping the integration at various distances* R_{lim}. *As recommended in appendix* **??**, *the derivative with regards to* R_{lim} *of the momentum flowrates are shown as dotted lines. They are multiplied by the radius of the injector* R_{inj} *for scaling.*

In Fig. E.4, swirl numbers obtained in the confined case (black) using Eqs. (4.40) (S^f_P), (4.44) (S^f_U) and (4.42) (S_{conv}) are compared with swirl numbers computed in the unconfined case (red, LDV). The swirl number for the free jet, computed using Eq. (4.29) (S^f_U) are tightly grouped together as is expected from the conservation properties. However, the conventional swirl number S_{conv} (Eq. (4.30)) has a much higher variability. While the values of S_{conv} are reasonably similar between the confined and unconfined cases at $x = 2.5$ and 5 mm, S^f_U differs significantly. This could be expected because the mean velocity profiles are quite similar close to the outlet of the injector, but become quite different further downstream. This large effect of the confinement is coherent with the literature on swirling flow showing examples of such confinement induced changes in near-injector flowfields (Escudier and Keller (1985); Altgeld et al. (1983); Fu et al. (2005)).

From this, one can conclude that swirl numbers (S^f_P and S^f_U) of confined flows may not be directly compared to swirl numbers (S^f_P and S^f_U) measured in unconfined jets. On the other hand, in the present configuration, the values of the conventional swirl number S_{conv} are reasonably close provided that they are evaluated close to the outlet of the injector.

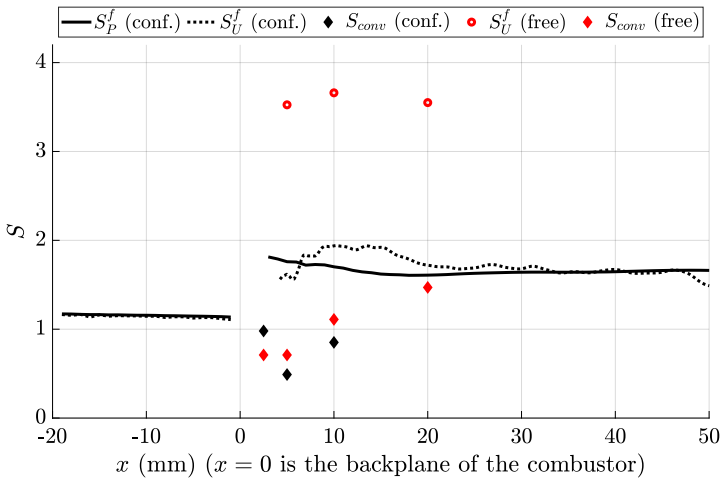

Figure E.4: *Comparison of different swirl numbers computed in the confined case (LES, black) and in the free jet (red, LDV).*

Appendix F

A jump condition to determine the reference pressure

It is worth examining the jumps in $G^f_{x,P}$ and G^f_θ at the sudden expansion. In the present appendix, these jumps are used to derive a method for determining the jump in reference pressure, which may be used as an alternative to Eq. (D.9).

The fate of swirling flows after an area change is investigated, for example, by Dellenback et al. (1988), with detailed experimental determination of velocity profiles, and correlations for vortex breakdown regimes and precessing vortex core frequency. This configuration is also studied in the vortex breakdown literature (e.g., Spall et al. (1987); Billant et al. (1998); Liang and Maxworthy (2005); Lucca-Negro and O'Doherty (2001)), the usual configuration being a swirl flow at a sudden expansion, but in water at a lower upstream Reynolds number. However, the evolution of the swirl number itself is not often considered. This matter is briefly discussed by Selle et al. (2004) and Palies et al. (2010), and there is also a recent study of the effect of a conical cup fitted to a cylindrical injector by Degenève et al. (2019). Choi et al. (2018) propose a 1D low-order model for the swirl number evolution in injectors featuring an annular cross-section with expansion and contraction. However, the pressure term is not accounted for in the swirl number formulation.

Figure 4.10 shows the sizable changes in $G^f_{x,P}$ and S^f_P at the sudden expansion, while G^f_θ only features a relatively small jump. From a straightforward application of momentum balance to the control volume defined in Fig. F.1, combined with assumptions that the flow is incompressible and isothermal, and that viscous effects can be neglected, one may write jump relations between the upstream ($-$) and downstream ($+$) sections:

$$G^f_\theta\Big|_+ = G^f_\theta\Big|_- \tag{F.1}$$

$$G^f_{x,P}\Big|_+ - G^f_{x,P}\Big|_- = 2\pi \int_{R_-}^{R_+} r\ \overline{p}|_{x=0}\ dr - \left[\Sigma|_+\, p_{ref}(+) - \Sigma|_-\, p_{ref}(-)\right] \tag{F.2}$$

where the right hand term accounts for the pressure force on the backplane and the

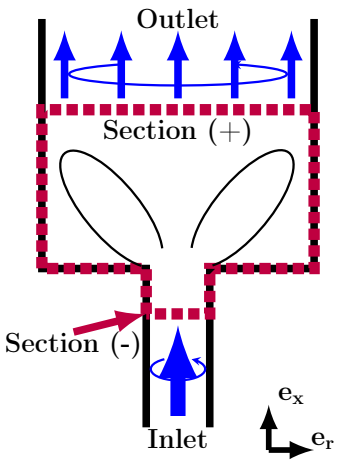

Figure F.1: *Schematic illustration of the control volumes used in Eq. (F.1) and (F.2). Sections (-) and (+) are located on the upstream and downstream side of the sudden expansion; the swirling jet and its expansion is represented by two black elliptic lines.*

change in reference pressure. $\Sigma|_+$ and $\Sigma|_-$ designate the downstream and upstream cross-sectional areas respectively. The change in the axial flux of axial momentum can thus be decomposed in two contributions: the change in reference pressure and the force exerted on the backplane. The latter is linked to the singular head loss at the sudden expansion. The change in reference pressure may be derived from the jump condition of $G^f_{x,P}$, and this process is described in what follows.

In compliance with property [P2] (section 4.5.2), two reference pressures are defined, corresponding to the upstream $(-)$ and downstream $(+)$ sections. Without any simplifying assumption, the change in reference pressure is linked to the singular head loss ΔP_{loc} at the sudden expansion by

$$p_{ref}(-) - p_{ref}(+) = \Delta P_{loc} - \frac{1}{2}\frac{\dot{m}^2}{\rho}\left(\frac{\mathrm{M}|_-}{\Sigma|_-^2} - \frac{\mathrm{M}|_+}{\Sigma|_+^2}\right) \tag{F.3}$$

The flow momentum coefficient M (Boussinesq coefficient) is defined by Idel'chik and Ginevskiy (2007)

$$\mathrm{M} = \frac{\pi {R_c}^2 \int_0^{R_c} \left[\overline{U_x}^2 + \overline{u_x^2}\right] r dr}{\left(\int_0^{R_c} \overline{U_x} r dr\right)^2} \tag{F.4}$$

and used to estimate the singular head loss coefficient ξ_{loc} under the assumption that $\mathrm{M}|_-$ is close to unity

$$\xi_{loc} = \frac{2\rho\,\Sigma|_-^2}{\dot{m}^2}\Delta P_{loc} \simeq (3\,\mathrm{M}|_- - 2)\left[1 - \frac{2\,\Sigma|_-}{3\,\Sigma|_+}\right] + \frac{\Sigma|_-^2}{\Sigma|_+^2} - \frac{4\,\Sigma|_-}{3\,\Sigma|_+} \tag{F.5}$$

Using these relationships a jump condition for the reference pressure is obtained based

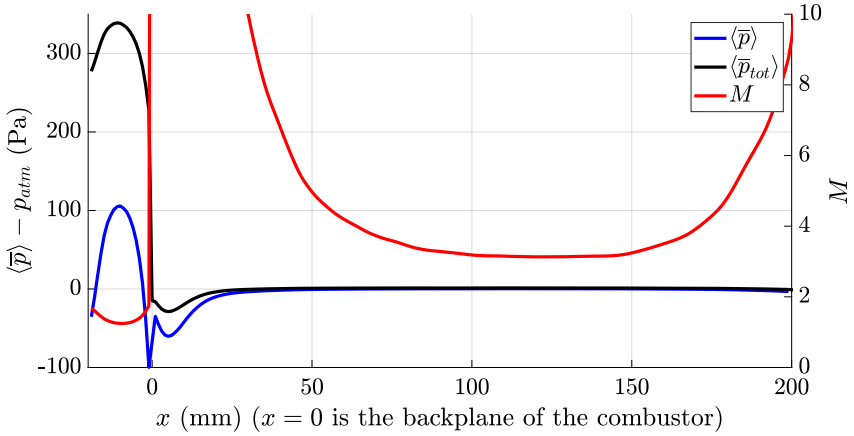

Figure F.2: *Axial evolution of the section averaged static (blue) and total (black) pressure* $\langle\overline{p}_{tot}\rangle = \langle\overline{p} + {}^1\!/\!_2\rho\left(\overline{U}^2 + \overline{u^2}\right)\rangle$ *in the system (left axis). The atmospheric pressure* $p_{atm} = 101\,325\,\mathrm{Pa}$ *is removed. Values of the Boussinesq momentum coefficient M (red) are given in the right axis.*

only on the upstream Boussinesq coefficient $\mathrm{M}|_-$ and well-known geometric and operational parameters. Figure F.2 shows that in the present case, the Boussinesq coefficient M, section averaged total $\langle\overline{p}_{tot}\rangle$ and static $\langle\overline{p}\rangle$ pressures can be considered to be constant where the flow is established. This is coherent with previous experimental measurements in Scott and Bartelt (1976); Kitoh (1991) where the shape of the velocity profiles is found to be conserved.

In the present case, the simulation yields $\Delta P_{loc} = 317\,\mathrm{Pa}$, and the Boussinesq coefficients $\mathrm{M}|_- = 1.3$ and $\mathrm{M}|_+ = 3.2$. The estimate for ΔP_{loc} from Eq. (F.5) is 318 Pa. In section 4.5.2, the reference pressures were chosen as $p_{ref}(+) = 101\,325.3\,\mathrm{Pa}$ in the downstream duct and $p_{ref}(-) = 101\,405\,\mathrm{Pa}$ in the cylindrical injector, which gives $p_{ref}(-) - p_{ref}(+) = 80\,\mathrm{Pa}$. Equation (F.3) yields $p_{ref}(-) - p_{ref}(+) = 88\,\mathrm{Pa}$.

In practive, Eq. (F.3) may be used to estimate the reference pressure. For example, for a ducted swirling flow exhausting to a quiescent atmosphere, the reference pressure in the duct may be readily estimated by recasting Eq. (F.3) and (F.5):

$$p_{ref} \simeq p_{atm} + \frac{\dot{m}^2}{\rho\Sigma^2}\left[\mathrm{M} - 1\right] \tag{F.6}$$

where M is the Boussinesq coefficient computed at an axial section where the flow is established in the duct.

Appendix G

Effect of non-axisymmetry of the flow and confinement on the swirl number

All theoretical developments and results presented in Chapter 4 specifically apply to axisymmetric flows. In the case of confined flows, this implies in particular that the confinement must be cylindrical with a circular cross section. In the present appendix, it is shown that previous developments and results extend to non-axisymmetric confinements which are often encountered in practical configurations.

The derivation relies on the Reynolds average Navier-Stokes equations expressed in a cylindrical reference frame. For a stationnary incompressible flow these equations write

$$\frac{1}{r}\frac{\partial(r\overline{U_r})}{\partial r}+\frac{\partial\overline{U_x}}{\partial x}+\frac{1}{r}\frac{\partial\overline{U_\theta}}{\partial\theta}=0 \tag{G.1}$$

$$\begin{aligned}\overline{U_r}\frac{\partial\overline{U_r}}{\partial r}+\overline{U_x}\frac{\partial\overline{U_r}}{\partial x}+\frac{\overline{U_\theta}}{r}\frac{\partial\overline{U_r}}{\partial\theta}-\frac{\overline{U_\theta}^2}{r}&=-\frac{1}{\rho}\frac{\partial\overline{p}}{\partial r}\\ -\left[\frac{\partial\overline{{u_r}^2}}{\partial r}+\frac{\partial\overline{u_r u_x}}{\partial x}+\frac{1}{r}\frac{\partial\overline{u_r u_\theta}}{\partial\theta}+\frac{1}{r}\left(\overline{{u_r}^2}-\overline{{u_\theta}^2}\right)\right]&\\ +\frac{1}{\rho}\left[\frac{1}{r}\frac{\partial r\overline{\tau_{rr}}}{\partial r}+\frac{1}{r}\frac{\partial\overline{\tau_{r\theta}}}{\partial\theta}+\frac{\partial\overline{\tau_{rx}}}{\partial x}-\frac{1}{r}\overline{\tau_{\theta\theta}}\right]&\end{aligned} \tag{G.2}$$

$$\begin{aligned}\overline{U_r}\frac{\partial\overline{U_\theta}}{\partial r}+\overline{U_x}\frac{\partial\overline{U_\theta}}{\partial x}+\frac{\overline{U_\theta}}{r}\frac{\partial\overline{U_\theta}}{\partial\theta}+\frac{\overline{U_r}\,\overline{U_\theta}}{r}&=-\frac{1}{\rho r}\frac{\partial\overline{p}}{\partial\theta}\\ -\left[\frac{\partial\overline{u_\theta u_x}}{\partial x}+\frac{1}{r^2}\frac{\partial(r^2\overline{u_r u_\theta})}{\partial r}+\frac{1}{2r}\frac{\partial\overline{u_\theta^2}}{\partial\theta}\right]+\frac{1}{\rho}\left[\frac{1}{r^2}\frac{\partial r^2\overline{\tau_{\theta r}}}{\partial r}+\frac{1}{r}\frac{\partial\overline{\tau_{\theta\theta}}}{\partial\theta}+\frac{\partial\overline{\tau_{\theta x}}}{\partial x}\right]&\end{aligned} \tag{G.3}$$

$$\begin{aligned}\frac{\overline{U_\theta}}{r}\frac{\partial\overline{U_x}}{\partial\theta}+\overline{U_r}\frac{\partial\overline{U_x}}{\partial r}+\overline{U_x}\frac{\partial\overline{U_x}}{\partial x}=-\frac{1}{\rho}\frac{\partial\overline{p}}{\partial x}\\ -\left[\frac{\partial\overline{u_x^2}}{\partial x}+\frac{1}{r}\frac{\partial(r\overline{u_r u_x})}{\partial r}+\frac{1}{r}\frac{\partial(\overline{u_\theta u_x})}{\partial\theta}\right]+\frac{1}{\rho}\left[\frac{1}{r}\frac{\partial r\overline{\tau_{rx}}}{\partial r}+\frac{1}{r}\frac{\partial\overline{\tau_{\theta x}}}{\partial r}+\frac{\partial\overline{\tau_{xx}}}{\partial x}\right]\end{aligned} \tag{G.4}$$

Let Σ designate a duct cross-section orthogonal to the axis $\mathbf{x}$, and integrate Eq. (G.4) multiplied by r over this cross-section. After some straightforward calculations one finds

$$\begin{aligned}\frac{d}{dx}\int_\Sigma\left[(\overline{p}-p_\infty)+\rho(\overline{U_x}^2+\overline{u_x^2})\right]dS=\frac{d}{dx}\int_\Sigma\overline{\tau_{xx}}dS\\ +\int_0^{2\pi}\left(R_c(\theta)\,\overline{\tau_{rx}}|_{r=R_c(\theta)}+\overline{\tau_{\theta x}}|_{r=R_c(\theta)}\right)d\theta-\int_0^{2\pi}\int_0^{R_c(\theta)}\rho\left[\frac{\partial\overline{U_x}\,\overline{U_\theta}}{\partial\theta}+\frac{\partial\overline{u_x u_\theta}}{\partial\theta}\right]drd\theta\end{aligned} \tag{G.5}$$

The right hand term in this equation is equal to zero if viscous losses are neglected and no-slip boundary conditions are assumed at the wall. Similarly, multiplying Eq. (G.3) by r^2 and integrating over the cross-section yields

$$\begin{aligned}\frac{d}{dx}\int_\Sigma\rho r\,\left(\overline{U_\theta}\,\overline{U_x}+\overline{u_r u_\theta}\right)\,dS=\int_0^{2\pi}\left(R_c{}^2(\theta)\,\overline{\tau_{r\theta}}|_{r=R_c(\theta)}+R_c(\theta)\,\left.\frac{\partial\overline{\tau_{\theta\theta}}}{\partial\theta}\right|_{r=R_c(\theta)}\right)d\theta\\ +\frac{d}{dx}\left(\int_\Sigma r\,\overline{\tau_{\theta x}}\,dS\right)-\int_0^{2\pi}\int_0^{R_c(\theta)}\frac{r}{2}\frac{\partial}{\partial\theta}\left(\overline{U_\theta}^2+\overline{u_\theta}^2\right)drd\theta\end{aligned} \tag{G.6}$$

Again, if viscous losses are neglected and no-slip boundary conditions are assumed at the wall, the right hand term vanishes in this equation. In a non-circular constant cross-section confinement Σ, the axial flow rates of axial momentum and of the angular momentum axial component can be recast as

$$G^f_{x,P}=\int_\Sigma\left[\rho\left(\overline{U_x}^2+\overline{u_x^2}\right)+\overline{p}-p_\infty\right]dS \tag{G.7}$$

$$G^f_\theta=\int_\Sigma\rho r\,\left[\overline{U_\theta}\,\overline{U_x}+\overline{u_r u_\theta}\right]dS \tag{G.8}$$

These definitions share the same conservation properties that apply to the axisymmetric case. If the boundary around the cross-section Σ is designated as $\partial\Sigma$, then

$$\frac{d}{dx}G^f_{x,P}=\frac{d}{dx}\int_\Sigma\overline{\tau_{xx}}dS+\int_{\partial\Sigma}\left(r\,\overline{\tau_{rx}}+\overline{\tau_{\theta x}}\right)\,d\sigma \tag{G.9}$$

$$\frac{d}{dx}G^f_\theta=\frac{d}{dx}\int_\Sigma r\,\overline{\tau_{\theta x}}dS+\int_{\partial\Sigma}\left(r^2\,\overline{\tau_{r\theta}}+r\frac{\partial\overline{\tau_{\theta\theta}}}{\partial\theta}\right)\,d\sigma \tag{G.10}$$

These results indicate that the properties used in the discussion of Chapter 4 are easily extended to non perfectly axisymmetric swirling flows. Eqs. (4.35) and (4.55) are also easily extended to this case. This extension is useful for example when the injector is placed in a single sector rig having a square cross section, or in an actual annular combustor.

References

Pubchem, tin(iv) oxide. *(p. 165, 169, 171)*

Abramzon, B. and W. A. Sirignano (1989). Droplet vaporization model for spray combustion calculations. *International Journal of Heat and Mass Transfer 32*(9), 1605–1618. *(p. 59, 60)*

Acharya, V. and T. Lieuwen (2020). Nonlinear response of swirling premixed flames to helical flow disturbances. *Journal of Fluid Mechanics*. *(p. 187)*

Adamovich, I. V. and W. R. Lempert (2015). Challenges in understanding and predictive modeling of plasma assisted combustion. *53rd AIAA Aerospace Sciences Meeting 57*(1), 14001. *(p. 300)*

Ahmed, S. F., R. Balachandran, T. Marchione, and E. Mastorakos (2007). Spark ignition of turbulent nonpremixed bluff-body flames. *Combustion and Flame 151*, 366–385. *(p. 274)*

Ahmed, S. F. and E. Mastorakos (2006). Spark ignition of lifted turbulent jet flames. *Combustion and Flame 146*(1-2), 215–231. *(p. 274)*

Airbus (2019). Airbus 2019-2038 Global Market Forecast. Technical report. *(p. 1)*

Albayrak, A., M. P. Juniper, and W. Polifke (2019). Propagation speed of inertial waves in cylindrical swirling flows. *Journal of Fluid Mechanics 879*, 85–120. *(p. 7)*

Albrecht, H.-E., M. Borys, N. Damaschke, and C. Tropea (2003). *Phase Doppler Systems*, pp. 409–490. Springer Berlin Heidelberg. *(p. 46, 48)*

Alekseenko, S. V., V. M. Dulin, Y. S. Kozorezov, and D. M. Markovich (2012). Effect of high-amplitude forcing on turbulent combustion intensity and vortex core precession in a strongly swirling lifted propane/air flame. *Combustion Science and Technology 184*(10-11), 1862–1890. *(p. 187)*

Altgeld, H., W. P. Jones, and J. Wilhelmi (1983). Velocity measurements in a confined swirl driven recirculating flow. *Experiments in Fluids 1*(2), 73–78. *(p. 37, 96, 124, 358)*

Apeloig, J. M., F. X. D'Herbigny, F. Simon, P. Gajan, M. Orain, and S. Roux (2015). Liquid-fuel behavior in an aeronautical injector submitted to thermoacoustic instabilities. *Journal of Propulsion and Power 31*(1), 309–319. *(p. 21)*

Bach, E., J. Kariuki, J. R. Dawson, and E. Mastorakos (2013). Spark ignition of single bluff-body premixed flames and annular combustors. In *51st AIAA Meeting, Grapevine, Texas*. *(p. 275)*

Baillot, F. and F. Lespinasse (2014). Response of a laminar premixed V-flame to a high-frequency transverse acoustic field. *Combustion and Flame 161*(5), 1247–1267. *(p. 7, 252)*

Baillot, F., C. Patat, M. Caceres, J.-B. Blaisot, and E. Domingues (2021). Saturation

phenomenon of swirling spray flames at pressure antinodes of a transverse acoustic field. *Proceedings of the Combustion Institute*. *(p. 37, 341)*

Bak, M. S., S. Kyun Im, M. G. Mungal, and M. A. Cappelli (2013). Studies on the stability limit extension of premixed and jet diffusion flames of methane, ethane, and propane using nanosecond repetitive pulsed discharge plasmas. *Combustion and Flame 160*(11), 2396–2403. *(p. 300, 301)*

Ballal, D. R. and A. H. Lefebvre (1975). The influence of spark discharge characteristics on minimum ignition energy in flowing gases. *Combustion and Flame 24*(C), 99–108. *(p. 274)*

Ballal, D. R. and A. H. Lefebvre (1978a). Ignition of liquid fuel sprays at subatmospheric pressures. *Combustion and Flame 31*(C), 115–126. *(p. 274)*

Ballal, D. R. and A. H. Lefebvre (1979). Ignition and flame quenching of flowing heterogeneous fuel-air mixtures. *Combustion and Flame 35*(C), 155–168. *(p. 274)*

Ballal, D. R. and A. H. Lefebvre (1981). A general model of spark ignition for gaseous and liquid fuel-air mixtures. *Symposium (International) on Combustion 18*(1), 1737–1746. *(p. 274)*

Ballal, D. R. and A. H. A. H. Lefebvre (1977). Ignition and Flame Quenching in Flowing Gaseous Mixtures. *Proceedings of the Royal Society of London A: Mathematical, Physical and Engineering Sciences 357*(1689). *(p. 274)*

Ballal, D. R. and A. H. A. H. Lefebvre (1978b). Ignition and flame quenching of quiescent fuel mists. *Proceedings of the Royal Society of London. A. Mathematical and Physical Sciences 364*(1717), 277–294. *(p. 274)*

Ballester, J. and T. García-Armingol (2010). Diagnostic techniques for the monitoring and control of practical flames. *Progress in Energy and Combustion Science 36*(4), 375–411. *(p. 64, 65)*

Balusamy, S., A. Cessou, and B. Lecordier (2011). Direct measurement of local instantaneous laminar burning velocity by a new PIV algorithm. *Experiments in Fluids 50*(4), 1109–1121. *(p. 164, 189)*

Barbosa, S., G. Pilla, D. A. Lacoste, P. Scouflaire, S. Ducruix, C. O. Laux, and D. Veynante (2015). Influence of nanosecond repetitively pulsed discharges on the stability of a swirled propane air burner representative of an aeronautical combustor. *Philosophical Transransactions of the Royal Society of London A 373*(2048), 20140335. *(p. 300, 301, 311)*

Barré, D., L. Esclapez, M. Cordier, E. Riber, B. Cuenot, G. Staffelbach, B. Renou, A. Vandel, L. Y. M. Gicquel, and G. Cabot (2014). Flame propagation in aeronautical swirled multi-burners: Experimental and numerical investigation. *Combustion and Flame 161*, 2387–2405. *(p. 274)*

Bauerheim, M., M. Cazalens, and T. Poinsot (2015). A theoretical study of mean azimuthal flow and asymmetry effects on thermo-acoustic modes in annular combustors. *Proceedings of the Combustion Institute 35*(3), 3219–3227. *(p. 7, 251)*

Bauerheim, M., A. Ndiaye, P. Constantine, S. Moreau, and F. Nicoud (2016). Symmetry breaking of azimuthal thermoacoustic modes: The UQ perspective. *Journal of Fluid Mechanics 789*(3), 534–566. *(p. 7, 251)*

Bauerheim, M., J. F. Parmentier, P. Salas, F. Nicoud, and T. Poinsot (2014). An analytical model for azimuthal thermoacoustic modes in an annular chamber fed by

an annular plenum. *Combustion and Flame*. *(p. 7, 211)*

Bauerheim, M., P. Salas, F. Nicoud, and T. Poinsot (2014). Symmetry breaking of azimuthal thermo-acoustic modes in annular cavities: A theoretical study. *Journal of Fluid Mechanics 760*, 431–465. *(p. 7, 251)*

Baya Toda, H., O. Cabrit, G. Balarac, S. Bose, J. Lee, H. Choi A N, and F. Nicoud (2010). A subgrid-scale model based on singular values for LES in complex geometries. In *Center for Turbulence Research Proceedings of the Summer Program*. *(p. 50, 96, 136, 198)*

Beer, J. M. and N. A. Chigier (1972). *Combustion aerodynamics*. *(p. 122, 123)*

Bellucci, V., C. O. Paschereit, P. Flohr, and F. Magni (2001). On the use of helmholtz resonators for damping acoustic pulsations in industrial gas turbines. In *ASME Turbo Expo 2001*, Number 2001-GT-0039, New Orleans, LA, USA. *(p. 210)*

Bernier, D., F. Lacas, and S. Candel (2004). Instability mechanisms in a premixed prevaporized combustor. *Journal of Propulsion and Power 20*(4), 648–656. *(p. 20, 21, 32, 196, 207)*

Bilger, R., S. Stårner, and R. Kee (1990). On reduced mechanisms for methane air combustion in nonpremixed flames. *Combustion and Flame 80*(2), 135–149. *(p. 203)*

Billant, P., J.-M. Chomaz, and P. Huerre (1998). Experimental study of vortex breakdown in swirling jets. *Journal of Fluid Mechanics 376*, 183–219. *(p. 123, 124, 136, 140, 166, 361)*

Boileau, M., G. Staffelbach, B. Cuenot, T. Poinsot, and C. Bérat (2008). LES of an ignition sequence in a gas turbine engine. *Combustion and Flame 154*, 2–22. *(p. 274)*

Bonciolini, G., D. Ebi, U. Doll, M. Weilenmann, and N. Noiray (2019). Effect of wall thermal inertia upon transient thermoacoustic dynamics of a swirl-stabilized flame. *Proceedings of the Combustion Institute 37*(4), 5351–5358. *(p. 43, 251)*

Borghesi, G., F. Biagioli, and B. Schuermans (2009). Dynamic response of turbulent swirling flames to acoustic perturbations. *Combustion Theory and Modelling 13*(3), 487–512. *(p. 6)*

Bothien, M. R., N. Noiray, and B. B. Schuermans (2013). A Novel Damping Device for Broadband Attenuation of Low-Frequency Combustion Pulsations in Gas Turbines. *Journal of Engineering for Gas Turbines and Power 136*(4), 041504. *(p. 251)*

Boudy, F., D. Durox, T. Schuller, G. Jomaas, and S. Candel (2011). Describing function analysis of limit cycles in a multiple flame combustor. *Journal of Engineering for Gas Turbines and Power 133*. *(p. 6)*

Boujo, E., A. Denisov, B. B. Schuermans, and N. Noiray (2016). Quantifying acoustic damping using flame chemiluminescence. *Journal of Fluid Mechanics 808*, 245–257. *(p. 239, 244, 245)*

Boumehdi, M. A., S. A. Stepanyan, P. Desgroux, G. Vanhove, and S. M. Starikovskaia (2015). Ignition of methane- and n-butane-containing mixtures at high pressures by pulsed nanosecond discharge. *Combustion and Flame 162*(4), 1336–1349. *(p. 300)*

Bourgouin, J.-F. (2014). *Dynamique de flamme dans les foyers annulaires présentant des injecteurs multiples*. Ph. D. thesis, Ecole Centrale Paris, Chatenay-Malabry. *(p. 228, 232, 236, 240)*

Bourgouin, J.-F., D. Durox, J. P. Moeck, T. Schuller, and S. Candel (2013). Self-sustained instabilities in an annular combustor coupled by longitudinal and az-

imuthal acoustic modes. In *Proceedings of the ASME Turbo Expo 2013. (p. 8, 9, 16, 17)*

Bourgouin, J.-F., D. Durox, J. P. Moeck, T. Schuller, and S. Candel (2015a). A new pattern of instability observed in an annular combustor: The slanted mode. *Proceedings of the Combustion Institute 35*(3), 3237–3244. *(p. 10, 17, 19)*

Bourgouin, J.-F., D. Durox, J. P. Moeck, T. Schuller, and S. Candel (2015b). Characterization and modeling of a spinning thermoacoustic instability in an annular combustor equipped with multiple matrix injectors. *Journal of Engineering for Gas Turbines and Power 137*(2), 021503. *(p. 10, 17, 20, 211, 250, 251, 253, 259, 260, 262)*

Bourgouin, J.-F., D. Durox, T. Schuller, J. Beaunier, and S. Candel (2013). Ignition dynamics of an annular combustor equipped with multiple swirling injectors. *Combustion and Flame 160*, 1398–1413. *(p. 9, 10, 52, 54, 275, 276, 277, 278, 279, 283)*

Bourgouin, J.-F., J. P. Moeck, D. Durox, T. Schuller, and S. Candel (2013). Sensitivity of swirling flows to small changes in the swirler geometry. *Comptes Rendus Mécanique 341*(1-2), 211–219. *(p. 15, 134, 251)*

Boutier, A. and J.-M. Most (2012). Vélocimétrie laser Doppler. In A. Boutier (Ed.), *Vélocimétrie laser pour la mécanique des fluides*, pp. 51–169. Hermès Science. *(p. 46, 48)*

Boyer, L. (1980). Laser tomographic method for flame front movement studies. *Combustion and Flame 39*(3), 321–323. *(p. 164)*

Caceres, M. (2019). *Impact of transverse acoustic modes on linearly arranged two-phase flow swirling flames*. Ph. D. thesis, Normandie Université. *(p. 7, 37, 341)*

Candel, S. (2002). Combustion dynamics and control: Progress and challenges. *Proceedings of the Combustion Institute 29*(1), 1–28. *(p. 4, 7, 210)*

Candel, S., D. Durox, and T. Schuller (2004). Flame Interactions as a Source of Noise and Combustion Instabilities. In *10th AIAA/CEAS Aeroacoustics Conference*, Reston, Virigina. American Institute of Aeronautics and Astronautics. *(p. 292)*

Candel, S., D. Durox, T. Schuller, J.-F. Bourgouin, and J. P. Moeck (2014). Dynamics of Swirling Flames. *Annual Review of Fluid Mechanics 46*, 147–73. *(p. 6, 20, 122, 165, 186, 250)*

Candel, S., D. Durox, T. Schuller, P. Palies, J.-F. Bourgouin, and J. P. Moeck (2012). Out of Equilibrium Dynamics Progress and challenges in swirling flame dynamics. *Compte Rendus Mécanique 340*, 758–768. *(p. 134, 165, 250)*

Cassidy, J. J. and H. T. Falvey (1970). Observations of unsteady flow arising after vortex breakdown. *Journal of Fluid Mechanics 41*(4), 727–736. *(p. 165)*

Cavaliere, D. E., J. Kariuki, and E. Mastorakos (2013). A comparison of the blow-off behaviour of swirl-stabilized premixed, non-premixed and spray flames. *Flow, Turbulence and Combustion 91*(2), 347–372. *(p. 163)*

CERFACS (2020). http://www.cerfacs.fr/avbp7x/. *(p. 50)*

Champion, M., B. Deshaies, and G. Joulin (1988). Relative influences of convective and diffusive transports during spherical flame initiation. *Combustion and Flame 74*(2), 161–170. *(p. 274)*

Champion, M., B. Deshaies, G. Joulin, and K. Kinoshita (1986). Spherical flame ini-

tiation: Theory versus experiments for lean propaneair mixtures. *Combustion and Flame 65*(3), 319–337. *(p. 274)*

Chang, F. and V. K. Dhir (1995). Mechanisms of heat transfer enhancement and slow decay of swirl in tubes using tangential injection. *International Journal of Heat and Fluid Flow 16*(Issue 2), 78–87. *(p. 122)*

Chatterjee, A. (2000). An introduction to the proper orthogonal decomposition. *Current Science 78*(7), 808–817. *(p. 49)*

Chaussonnet, G. (2014). *Modeling of liquid film and breakup phenomena in Large-Eddy Simulations of aeroengines fueled by airblast atomizers*. Ph. D. thesis, Université de Toulouse. *(p. 60)*

Chaussonnet, G., E. Riber, O. Vermorel, B. Cuenot, S. Gepperth, and R. Koch (2013). Large Eddy Simulation of a prefilming airblast atomizer. In *ILASS: Europe 2013, 25th European Conference on Liquid Atomization and Spray Systems, Chania, Greece, 1-4 September 2013*, Number September, pp. 1–4. *(p. 60, 198)*

Chauveau, C., M. Birouk, F. Halter, and I. Gökalp (2019). An analysis of the droplet support fiber effect on the evaporation process. *International Journal of Heat and Mass Transfer 128*, 885–891. *(p. 113)*

Chen, L. D. and W. Roquemore (1986). Visualization of jet flames. *Combustion and Flame 66*(1), 81–86. *(p. 164)*

Chen, L. D., J. P. Seaba, W. M. Roquemore, and L. P. Goss (1989). Buoyant diffusion flames. *Symposium (International) on Combustion 22*(1), 677–684. *(p. 132)*

Chen, R.-H. and J. F. Driscoll (1989). The role of the recirculation vortex in improving fuel-air mixing within swirling flames. *Symposium (International) on Combustion 22*(Issue 1), 531–540. *(p. 122)*

Chen, R.-H., J. F. Driscoll, J. Keller, M. Namazian, and R. W. Schefer (1990). A comparison of bluff-body and swirl-stabilized flames. *Combustion Science and Technology 71*(4-6), 197–217. *(p. 132)*

Chigier, N. A. and J. M. Beér (1964). Velocity and static-pressure distributions in swirling air jets issuing from annular and divergent nozzles. *Journal of Basic Engineering 86*(4), 788–796. *(p. vii, 25, 123, 124, 133, 134, 145, 146, 153, 156, 313)*

Chigier, N. A. and A. Chervinsky (1967a). Aerodynamic study of turbulent burning free jets with swirl. *Proceedings of the combustion institute*, 489 – 499. *(p. 123, 153, 156)*

Chigier, N. A. and A. Chervinsky (1967b). Experimental investigation of swirling vortex motion in jets. *Journal of Applied Mechanics 34*(2), 443–451. *(p. 123, 125, 126, 127, 128, 130, 133, 149, 153, 156)*

Choi, J., E. Jung, S. Kang, and H. Do (2018). Modeling Swirl Decay Rate of Turbulent Flows in Annular Swirl Injectors. *AIAA Journal 56*(12), 4910–4926. *(p. 133, 361)*

Chung, J. Y. and D. A. Blaser (1980a). Transfer function method of measuring in duct acoustic properties. i. theory. *The Journal of the Acoustical Society of America 68*(3), 907–913. *(p. 219)*

Chung, J. Y. and D. A. Blaser (1980b). Transfer function method of measuring in duct acoustic properties. ii. experiment. *The Journal of the Acoustical Society of America 68*(3), 914–921. *(p. 219)*

Claypole, T. and N. Syred (1981). The effect of swirl burner aerodynamics on nox formation. *Symposium (International) on Combustion 18*(Issue 1), 81–89. *(p. 132, 156)*

Colin, O. and M. Rudgyard (2000). Development of High-Order Taylor Galerkin Schemes for LES. *Journal of Computational Physics 162*(2), 338–371. *(p. 50, 136)*

Collin-Bastiani, F., J. Marrero-Santiago, E. Riber, G. Cabot, B. Renou, and B. Cuenot (2019). A joint experimental and numerical study of ignition in a spray burner. *Proceedings of the Combustion Institute 37*(4), 5047–5055. *(p. 56, 274)*

Cordier, M., A. Vandel, G. Cabot, B. Renou, and A. M. Boukhalfa (2013). Laser-induced spark ignition of premixed confined swirled flames. *Combustion Science and Technology 185*(3), 379–407. *(p. 274)*

Cosic, B., J. Moeck, and C. Paschereit (2014). Nonlinear instability analysis for partially premixed swirl flames. *Combustion Science and Technology 186*, 713–736. *(p. 6)*

Crocco, L. (1951). Aspects of combustion stability in liquid propellant rocket motors. 1. Fundamentals-low frequency instability with monopropellants. *Journal of the American Rocket Society 21*(6), 163–178. *(p. 4, 20)*

Crocco, L. (1952). Aspects of combustion stability in liquid propellant rocket motors. 2. Low frequency instability with bipropellants-high frequency instability. *Journal of the American Rocket Society 22*(1), 7–16. *(p. 4, 20)*

Crocco, L. (1965). Theoretical studies on liquid-propellant rocket instability. *Symposium (International) on Combustion 10*(1), 1101–1128. *(p. 4, 20, 60)*

Crocco, L. and S. Cheng (1953). High-frequency combustion instability in rocket motor with concentrated combustion. *Journal of the American Rocket Society 23*(5), 301–&. *(p. 4)*

Crocco, L. and S. I. Cheng (1956). *Theory of combustion instability in liquid propellant rocket motors*, Volume Agardograph No 8. Butterworths Science. *(p. 4, 197)*

Crocco, L, L. and W. Sirignano (1966). Effect of transverse velocity component on nonlinear behavior of short nozzles. *AIAA Journal 4*(8), 1428. *(p. 4)*

Culick, F. E. C. (1976). Nonlinear behavior of acoustic waves in combustion chambers-I. *Acta Astronautica 3*(9-10), 715–734. *(p. 4, 265)*

Culick, F. E. C. (1988). Combustion Instabilities in Liquid-Fueled Propulsion System - an Overview. In *AGARD 72B Specialists' Meeting of the Propulsion and Energetics Panel 450. (p. 4, 226, 265)*

Culick, F. E. C. (2001). *Dynamics of combustion systems: Fundamentals, acoustics and control*. NASA Glenn Research Center. *(p. 7, 226)*

Cunha Caldeira Mesquita, L., A. Vié, and S. Ducruix (2017). Two-Phase Flow Large Eddy Simulations of a Staged Multipoint Swirling Burner: Comparison Between Euler-Euler and Euler-Lagrange Descriptions. In *Proceedings of the ASME Turbo Expo*, pp. V04BT04A024. *(p. 56)*

Daviller, G., M. Brebion, P. Xavier, G. Staffelbach, J.-D. Müller, and T. Poinsot (2017). A Mesh Adaptation Strategy to Predict Pressure Losses in LES of Swirled Flows. *Flow, Turbulence and Combustion 99*(1), 93–118. *(p. 55, 137)*

Dawson, J. R. and N. A. Worth (2014). Flame dynamics and unsteady heat release rate of self-excited azimuthal modes in an annular combustor. *Combustion and Flame 161*(10), 2565–2578. *(p. 8)*

Dawson, J. R. and N. A. Worth (2015). The effect of baffles on self-excited azimuthal modes in an annular combustor. *Proceedings of the Combustion Institute 35*(3), 3283–3290. *(p. 8)*

de la Cruz García, M., E. Mastorakos, and A. P. Dowling (2009). Investigations on the self-excited oscillations in a kerosene spray flame. *Combustion and Flame 156*(2), 374–384. *(p. 20, 32, 196)*

De Rosa, A. J., S. J. Peluso, B. D. Quay, and D. A. Santavicca (2015). The Effect of Confinement on the Structure and Dynamic Response of Lean-Premixed, Swirl-Stabilized Flames. *Journal of Engineering for Gas Turbines and Power 138*(6), 061507. *(p. 251)*

Degenève, A., P. Jourdaine, C. Mirat, J. Caudal, R. Vicquelin, and T. Schuller (2019). Effects of a Diverging Cup on Swirl Number, Flow Pattern, and Topology of Premixed Flames. *Journal of Engineering for Gas Turbines and Power 141*, 031022–1. *(p. 133, 361)*

Degenève, A., R. Vicquelin, C. Mirat, B. Labegorre, P. Jourdaine, J. Caudal, and T. Schuller (2019). Scaling relations for the length of coaxial oxy-flames with and without swirl. *Proceedings of the Combustion Institute 37*(4), 4563–4570. *(p. 189)*

Dellenback, P. A., D. E. Metzger, and P. G. Neitzel (1988). Measurements in turbulent swirling flow through an abrupt axisymmetric expansion. *AIAA Journal 26*(6), 669–681. *(p. 361)*

Delprat, N., P. Guillemain, B. Escudie, R. Kronland-Martinet, P. Tchamitchian, and B. Torresani (1992). Asymptotic Wavelet and Gabor Analysis: Extraction of Instantaneous Frequencies. *IEEE Transactions on Information Theory 38*(2), 644–664. *(p. 178)*

Deshaies, B. and G. Joulin (1984). On the Initiation of a Spherical Flame Kernel. *Combustion Science and Technology 37*(3-4), 99–116. *(p. 274)*

Dhanuka, S. K., J. E. Temme, and J. F. Driscoll (2011). Lean limit combustion instabilities of a lean premixed prevaporized gas turbine combustor. *Proceedings of the Combustion Institute 33*(2), 2961–2966. *(p. 300, 307)*

Ding, Y. (2018). *Use of flame chemiluminescence and ionization current for the combustion status monitoring of a domestic gas boiler*. Ph. D. thesis, Université Paris-Saclay. *(p. 65)*

Ding, Y., D. Durox, N. Darabiha, and T. Schuller (2019). Chemiluminescence of Burner-Stabilized Premixed Laminar Flames. *Combustion Science and Technology 191*(1), 18–42. *(p. 64, 65)*

Docquier, N. and S. Candel (2002). Combustion control and sensors: A review. *Progress in Energy and Combustion Science 28*(2), 107–150. *(p. 64, 65, 74)*

Dowling, A. P. (1997). Nonlinear self-excited oscillations of a ducted flame. *Journal of Fluid Mechanics 346*, 271–290. *(p. 6)*

Dowling, A. P. and S. R. Stow (2003). Acoustic Analysis of Gas Turbine Combustors. *Journal of Propulsion and Power 19*(5), 751–764. *(p. 6)*

Dring, R. P. and M. Suo (1978). Particle trajectories in swirling flows. *Journal of Energy 2*(4), 232–237. *(p. 104, 107, 177)*

Dumitrache, C., A. Gallant, N. Minesi, S. Stepanyan, G. D. Stancu, and C. O. Laux (2019). Hydrodynamic regimes induced by nanosecond pulsed discharges in air:

Mechanism of vorticity generation. *Journal of Physics D: Applied Physics 52*(36), 364001. *(p. 300, 303)*

Dumont, J.-P. and R. Borghi (1986). A Qualitative Study by Laser Tomography of the Structure of Turbulent Flames. *Combustion Science and Technology 48*(3-4), 107–128. *(p. 164, 165, 169)*

Durox, D. and S. Ducruix (2000). Concerning the Location of the Schlieren Limit in Premixed Flames. *Combustion and Flame 120*, 595–598. *(p. 164)*

Durox, D., S. Ducruix, and F. Lacas (1999). Flow seeding with an air nebulizer. *Experiments in Fluids 27*(5), 408–413. *(p. 46)*

Durox, D., J. P. Moeck, J.-F. Bourgouin, P. Morenton, M. Viallon, T. Schuller, and S. Candel (2013). Flame dynamics of a variable swirl number system and instability control. *Combustion and Flame 160*(9), 1729–1742. *(p. 6, 132, 210, 251)*

Durox, D., K. Prieur, T. Schuller, and S. Candel (2016). Different Flame Patterns Linked With Swirling Injector Interactions in an Annular Combustor. *Journal of Engineering for Gas Turbines and Power 138*(10), 101504. *(p. 9, 10, 32, 134, 253)*

Durox, D., T. Schuller, N. Noiray, A. Birbaud, and S. Candel (2009). Rayleigh criterion and acoustic energy balance in unconfined self-sustained oscillating flames. *Combustion and Flame 156*(1), 106–119. *(p. 239)*

Durox, D., T. Schuller, N. Noiray, and S. Candel (2009). Experimental analysis of nonlinear flame transfer functions for different flame geometries. *Proceedings of the Combustion Institute 32*(1), 1391–1398. *(p. 201, 243)*

EASA (2019). *European Aviation Environmental Report 2019*. Number 1. *(p. 1)*

Ebi, D. and N. T. Clemens (2016). Simultaneous high-speed 3D flame front detection and tomographic PIV. *Measurement Science and Technology 27*(3), 035303. *(p. 163, 164)*

Eckstein, J., E. Freitag, C. Hirsch, and T. Sattelmayer (2006). Experimental study on the role of entropy waves in low-frequency oscillations in a RQL combustor. *Journal of Engineering for Gas Turbines and Power 128*(2), 264–270. *(p. 20, 21, 32, 104, 196, 207)*

Escudier, M. P. and J. J. Keller (1985). Recirculation in swirling flow: A manifestation of vortex breakdown. *AIAA Journal 23*(1), 111–116. *(p. 7, 36, 37, 96, 124, 140, 358)*

Evesque, S., W. Polifke, and C. Pankiewitz (2003). Spinning and Azimuthally Standing Acoustic Modes in Annular Cavities. In *9th AIAA/CEAS Aeroacoustics Conference and Exhibit*, pp. AIAA 2003–3182. *(p. 7)*

Fanaca, D., P. R. Alemela, C. Hirsch, and T. Sattelmayer (2010). Comparison of the flow field of a swirl stabilized premixed burner in an annular and a single burner combustion chamber. *Journal of Engineering for Gas Turbines and Power 132*(7). *(p. 7, 32, 37, 96, 251)*

Farokhi, S., R. Tagavi, and E. J. Rice (1989). Effect of initial swirl distribution on the evolution of a turbulent jet. *AIAA Journal 27*(6), 700–706. *(p. 124)*

Franzelli, B., A. Vié, B. Fiorina, and N. Darabiha (2013). Large Eddy Simulation of Swirling Kerosene/Air Spray Flame Using Tabulated Chemistry. In *Proceedings of the ASME TurboExpo*, pp. V01AT04A034. *(p. 104)*

Froessling, N. (1938). Über die Verdunstung Fallender Tropfen. *Gerlands Beitrage zur*

Geophysik 52, 107–216. *(p. 59, 60)*

Froud, D., A. Beale, T. O'Doherty, and N. Syred (1996). Studies of helmholtz resonance in a swirl/furnace system. *Symposium (International) on Combustion 26*(2), 3355–3362. *(p. 166)*

Froud, D., T. O'Doherty, and N. Syred (1995). Phase averaging of the precessing vortex core in a swirl burner under piloted and premixed combustion conditions. *Combustion and Flame 100*(3), 2–11. *(p. 166)*

Fu, Y., J. Cai, S. M. Jeng, and H. Mongia (2005). Confinement effects on the swirling flow of a counter-rotating swirl cup. In *Proceedings of the ASME Turbo Expo*, pp. GT2005–68622. *(p. 37, 96, 358)*

Gajan, P., A. Strzelecki, B. Platet, R. Lecourt, and F. Giuliani (2007). Investigation of Spray Behavior Downstream of an Aeroengine Injector with Acoustic Excitation. *Journal of Propulsion and Power 23*(2), 390–397. *(p. 21, 104)*

Galazka, Z., R. Uecker, D. Klimm, K. Irmscher, M. Pietsch, R. Schewski, M. Albrecht, A. Kwasniewski, S. Ganschow, D. Schulz, C. Guguschev, R. Bertram, M. Bickermann, and R. Fornari (2014). Growth, characterization, and properties of bulk SnO2 single crystals. *Physica Status Solidi (A) Applications and Materials Science 211*(1), 66–73. *(p. 171)*

Gallaire, F., M. Ruith, E. Meiburg, J.-M. Chomaz, and P. Huerre (2006). Spiral vortex breakdown as a global mode. *Journal of Fluid Mechanics 549*, 71–80. *(p. 165)*

García-Armingol, T., J. Ballester, and A. Smolarz (2013). Chemiluminescence-based sensing of flame stoichiometry: Influence of the measurement method. *Measurement: Journal of the International Measurement Confederation 46*(9), 3084–3097. *(p. 74)*

García-Armingol, T., Y. Hardalupas, A. M. Taylor, and J. Ballester (2014). Effect of local flame properties on chemiluminescence-based stoichiometry measurement. *Experimental Thermal and Fluid Science 53*, 93–103. *(p. 64, 65, 80)*

Gatti, M., R. Gaudron, C. Mirat, L. Zimmer, and T. Schuller (2019). Impact of swirl and bluff-body on the transfer function of premixed flames. *Proceedings of the Combustion Institute 37*, 51977–5204. *(p. 6)*

Gaudron, R. (2018). *Réponse acoustique de flammes prémélangées soumises à des ondes sonores harmoniques*. Ph. D. thesis, Université Paris-Saclay. *(p. 45)*

Gaudron, R., M. Gatti, C. Mirat, and T. Schuller (2019). Flame describing functions of a confined premixed swirled combustor with upstream and downstream forcing. *Journal of Engineering for Gas Turbines and Power 141*(5). *(p. 37, 38)*

Gaydon, A. G. (1974). *The Spectroscopy of Flames*. Springer Netherlands. *(p. 69, 304)*

Ghani, A., T. Poinsot, L. Gicquel, and J. D. Müller (2016). LES Study of Transverse Acoustic Instabilities in a Swirled Kerosene/Air Combustion Chamber. *Flow, Turbulence and Combustion 96*(1), 207–226. *(p. 165, 187)*

Ghirardo, G. and M. P. Juniper (2013). Azimuthal instabilities in annular combustors: Standing and spinning modes. *Proceedings of the Royal Society A: Mathematical, Physical and Engineering Sciences 469*(2157). *(p. 7, 18, 251)*

Ghirardo, G., M. P. Juniper, and J. P. Moeck (2016). Weakly nonlinear analysis of thermoacoustic instabilities in annular combustors. *Journal of Fluid Mechanics 805*(3), 52–87. *(p. 6, 7)*

Giauque, A., L. Selle, L. Gicquel, T. Poinsot, H. Buechner, P. Kaufmann, and W. Krebs

(2005). System identification of a large-scale swirled partially premixed combustor using LES and measurements. *Journal of Turbulence 6*, N21. *(p. 187)*

Gicquel, L. Y., G. Staffelbach, and T. Poinsot (2012). Large Eddy Simulations of gaseous flames in gas turbine combustion chambers. *Progress in Energy and Combustion Science 38*(6), 782–817. *(p. 6)*

Gigosos, M. A., M. Á. González, and V. Cardeñoso (2003). Computer simulated Balmer-alpha, -beta and -gamma Stark line profiles for non-equilibrium plasmas diagnostics. *Spectrochimica Acta - Part B Atomic Spectroscopy 58*(8), 1489–1504. *(p. 304)*

Gilchrist, R. T. and J. W. Naughton (2005). Experimental study of incompressible jets with different initial swirl distributions: Mean results. *AIAA Journal 43*(4), 741–751. *(p. 124)*

Granet, V., O. Vermorel, T. Léonard, L. Gicquel, and T. Poinsot (2010). Comparison of nonreflecting outlet boundary conditions for compressible solvers on unstructured grids. *AIAA Journal 48*(10), 2348–2364. *(p. 55)*

Greiffenhagen, F., J. Peterleithner, J. Woisetschläger, A. Fischer, J. Gürtler, and J. Czarske (2019). Discussion of laser interferometric vibrometry for the determination of heat release fluctuations in an unconfined swirl-stabilized flame. *Combustion and Flame 201*, 315–327. *(p. 66)*

Greiffenhagen, F., J. Woisetschläger, J. Gürtler, and J. Czarske (2020). Quantitative measurement of density fluctuations with a full-field laser interferometric vibrometer. *Experiments in Fluids 61*(1), 1–15. *(p. 163)*

Guedot, L., G. Lartigue, and V. Moureau (2018). Modeling and Analysis of the Interactions of Coherent Structures with a Spray Flame in a Swirl Burner. pp. 15–26. Springer, Cham. *(p. 104)*

Guethe, F., D. Guyot, G. Singla, N. Noiray, and B. Schuermans (2012). Chemiluminescence as diagnostic tool in the development of gas turbines. *Applied Physics B: Lasers and Optics 107*(3), 619–636. *(p. 65)*

Guiberti, T. F., D. Durox, P. Scouflaire, and T. Schuller (2015). Impact of heat loss and hydrogen enrichment on the shape of confined swirling flames. *Proceedings of the Combustion Institute 35*(2), 1385–1392. *(p. 43, 294, 295)*

Guo, S., C. F. Silva, A. Ghani, and W. Polifke (2019). Quantification and Propagation of Uncertainties in Identification of Flame Impulse Response for Thermoacoustic Stability Analysis. *Journal of Engineering for Gas Turbines and Power 141*(2). *(p. 6)*

Gupta, A. K., D. G. Lilley, and N. Syred (1984). *Swirl Flows*. Abacus Press. *(p. 122, 123, 126, 133)*

Han, X. and A. S. Morgans (2018). Non-linear Interactions of Two Premixed Flames Explored by Large Eddy Simulation with External Acoustic Forcing. *Combustion Science and Technology 190*(3), 424–435. *(p. 7)*

Hardalupas, Y. and M. Orain (2004). Local measurements of the time-dependent heat release rate and equivalence ratio using chemiluminescent emission from a flame. *Combustion and Flame 139*(3), 188–207. *(p. 64, 65)*

Hardalupas, Y., A. M. K. P. Taylor, and J. H. Whitelaw (1992). Particle Dispersion in a Vertical round Sudden-Expansion Flow. *Philosophical Transactions of the Royal Society A: Mathematical, Physical and Engineering Sciences 341*(1662), 411–442.

(p. 103)

Harrje, D. J. and F. H. Reardon (1972). Liquid propellant rocket instability. Technical Report Report SP-194, NASA. *(p. 4, 210, 211)*

Harvey, J. K. (1962). Some observations of the vortex breakdown phenomenon. *Journal of Fluid Mechanics 14*(4), 585–592. *(p. 124)*

Hermeth, S., G. Staffelbach, L. Y. Gicquel, V. Anisimov, C. Cirigliano, and T. Poinsot (2014). Bistable swirled flames and influence on flame transfer functions. *Combustion and Flame 161*(1), 184–196. *(p. 218)*

Hertzberg, J. R., M. Namazian, and L. Talbot (1984). A laser tomographic study of a laminar flame in a Karman vortex street. *Combustion Science and Technology 38*(3-4), 205–216. *(p. 164)*

Higgins, B., M. Q. McQuay, F. Lacas, J. C. Rolon, N. Darabiha, and S. Candel (2001). Systematic measurements of OH chemiluminescence for fuel-lean, high-pressure, premixed, laminar flames. *Fuel 80*(1), 67–74. *(p. 64)*

Hoenig, C. L. and A. W. Searcy (1966). Knudsen and Langmuir Evaporation Studies of Stannic Oxide. *Journal of the American Ceramic Society 49*(3), 128–134. *(p. 171)*

Hopfinger, E. J. and J. C. Lasheras (1996). Explosive breakup of a liquid jet by a swirling coaxial gas jet. *Physics of Fluids 8*(7), 1696–1698. *(p. 111)*

Huang, Y. and V. Yang (2009). Dynamics and stability of lean-premixed swirl-stabilized combustion. *Progress in Energy and Combustion Science 35*(4), 293–364. *(p. 4, 7, 186, 196)*

Hubbard, G. L., V. E. Denny, and A. F. Mills (1975). Droplet evaporation: Effects of transients and variable properties. *International Journal of Heat and Mass Transfer 18*(9), 1003–1008. *(p. 59)*

Hurle, I., R. Price, T. Sugden, and A. Thomas (1968). Sound emission from open turbulent premixed flames. *Proceedings of the Royal Society of London. Series A. Mathematical and Physical Sciences 303*(1475), 409–427. *(p. 64)*

Idel'chik, I. E. and A. S. Ginevskiy (2007). *Handbook of hydraulic resistance*. Begell House. *(p. 362)*

Innocenti, A., A. Andreini, B. Facchini, and A. Peschiulli (2017). Numerical analysis of the dynamic flame response of a spray flame for aero-engine applications. *International Journal of Spray and Combustion Dynamics 9*(4), 310–329. *(p. 196, 202)*

Iudiciani, P. and C. Duwig (2011). Large eddy simulation of the sensitivity of vortex breakdown and flame stabilisation to axial forcing. *Flow, Turbulence and Combustion 86*(3-4), 639–666. *(p. 187)*

Jaegle, F., O. Cabrit, S. Mendez, and T. Poinsot (2010). Implementation methods of wall functions in cell-vertex numerical solvers. *Flow, Turbulence and Combustion 85*(2), 245–272. *(p. 55, 96, 136)*

Jaegle, F., J.-M. Senoner, M. García, F. Bismes, R. Lecourt, B. Cuenot, and T. Poinsot (2011). Eulerian and Lagrangian spray simulations of an aeronautical multipoint injector. *Proceedings of the Combustion Institute 33*(2), 2099–2107. *(p. 56, 104)*

Jones, W. P., A. J. Marquis, and K. Vogiatzaki (2014). Large-eddy simulation of spray combustion in a gas turbine combustor. *Combustion and Flame 161*(1), 222–239. *(p. 196)*

Ju, Y., J. K. Lefkowitz, C. B. Reuter, S. H. Won, X. Yang, S. Yang, W. Sun, Z. Jiang, and Q. Chen (2016). Plasma Assisted Low Temperature Combustion. *Plasma Chemistry and Plasma Processing 36*(1), 85–105. *(p. 300)*

Juniper, M. P. and R. Sujith (2018). Sensitivity and Nonlinearity of Thermoacoustic Oscillations. *Annual Review of Fluid Mechanics 50*(1), 661–689. *(p. 251)*

Keller, J., M. Gebretsadik, P. Habisreuther, F. Turrini, N. Zarzalis, and D. Trimis (2015). Numerical and experimental investigation on droplet dynamics and dispersion of a jet engine injector. *International Journal of Multiphase Flow 75*, 144–162. *(p. 104)*

Keller, J. J. (1995). Thermoacoustic oscillations in combustion chambers of gas turbines. *AIAA Journal 33*(12), 2280–2287. *(p. 3)*

Kim, G. T., C. S. Yoo, S. H. Chung, and J. Park (2020). Effects of non-thermal plasma on the lean blowout limits and CO/NOx emissions in swirl-stabilized turbulent lean-premixed flames of methane/air. *Combustion and Flame 212*, 403–414. *(p. 300, 301, 307, 310, 311)*

Kim, W., H. Do, M. G. Mungal, and M. A. Cappelli (2006). Plasma-discharge stabilization of jet diffusion flames. *IEEE Transactions on Plasma Science 34*(6), 2545–2551. *(p. 304)*

Kim, W., J. Snyder, and J. Cohen (2015). Plasma assisted combustor dynamics control. *Proceedings of the Combustion Institute 35*(3), 3479–3486. *(p. 300)*

Kim, W., S. Zhang, P. Palies, J. Cohen, S. Liljenberg, and D. Hautman (2012). The behavior of liquid fuel sprays in acoustically-forced air swirler flows. In *Proceedings of the ASME Turbo Expo*, Volume GT2012-689. *(p. 21, 104)*

King, L. V. (1914). On the convection of heat from small cylinders in a stream of fluid: determination of the convection constants of small platinium wires, with application to hot-wire anemometry. *Proceedings of the Royal Society A 90*(622), 563–570. *(p. 44)*

Kitano, T., K. Kaneko, R. Kurose, and S. Komori (2016). Large-eddy simulations of gas- and liquid-fueled combustion instabilities in back-step flows. *Combustion and Flame 170*, 63–78. *(p. 21, 196, 202)*

Kitoh, O. (1991). Experimental study of turbulent swirling flow in a straight pipe. *Journal of Fluid Mechanics 225*, 445–479. *(p. 146, 363)*

Kojima, J., Y. Ikeda, and T. Nakajima (2000). Spatially resolved measurement of OH^*, CH^*, and C_2^* chemiluminescence in the reaction zone of laminar methane/air premixed flames. *Proceedings of the Combustion Institute 28*(2), 1757–1764. *(p. 64, 65, 74)*

Komarek, T. and W. Polifke (2010). Impact of swirl fluctuations on the flame response of a perfectly premixed swirl burner. *Journal of Engineering for Gas Turbines and Power 132*(6), 1–7. *(p. 7)*

Kong, C., Z. Li, M. Aldén, and A. Ehn (2019). Stabilization of a turbulent premixed flame by a plasma filament. *Combustion and Flame 208*, 79–85. *(p. 300, 311)*

Konrad, W., N. Brehm, F. Kameier, C. Freeman, and I. J. Day (1998). Combustion Instability Investigations on the BR710 Jet Engine. *Journal of Engineering for Gas Turbine and Power 120*(1), 34–40. *(p. 32, 196)*

Kopitz, J., A. Huber, T. Sattelmayer, and W. Polifke (2005). Thermoacoustic stability

analysis of an annular combustion chamber with acoustic low order modeling and validation against experiment. In *Proceedings of the ASME Turbo Expo 2005, Vol 2*, pp. 583–593. *(p. 7)*

Krebs, W., P. Flohr, B. Prade, and S. Hoffmann (2002). Thermoacoustic stability chart for high-intensity gas turbines combustion systems. *Combustion Science and Technology 174*(7), 99–128. *(p. 3, 8, 251)*

Kreith, F. and O. K. Sonju (1965). The decay of a turbulent swirl in a pipe. *Journal of Fluid Mechanics 22*(2), 257–271. *(p. 146)*

Kriebel, A. R. (1961). Particle Trajectories in a Gas Centrifuge. *Journal of Basic Engineering 83*(3), 333. *(p. 104, 107, 177)*

Kuenne, G., A. Ketelheun, and J. Janicka (2011). LES modeling of premixed combustion using a thickened flame approach coupled with FGM tabulated chemistry. *Combustion and Flame 158*(9), 1750–1767. *(p. 166)*

Kypraiou, A.-M., N. A. Worth, and E. Mastorakos (2016). Experimental Investigation of the Response of Premixed and Non-premixed Turbulent Flames to Acoustic Forcing. In *54th AIAA Aerospace Sciences Meeting*, Reston, Virginia. American Institute of Aeronautics and Astronautics. *(p. 163)*

Lacoste, D. A., J. P. Moeck, D. Durox, C. O. Laux, and T. Schuller (2013). Effect of nanosecond repetitively pulsed discharges on the dynamics of a swirl-stabilized lean premixed flame. *Journal of Engineering for Gas Turbines and Power 135*(10). *(p. 300, 301)*

Laera, D., K. Prieur, D. Durox, T. Schuller, S. M. Camporeale, and S. Candel (2017). Impact of Heat Release Distribution on the Spinning Modes of an Annular Combustor With Multiple Matrix Burners. *Journal of Engineering for Gas Turbines and Power 139*(5), 051505. *(p. 10, 20, 251)*

Laera, D., T. Schuller, K. Prieur, D. Durox, S. M. Camporeale, and S. Candel (2017). Flame Describing Function analysis of spinning and standing modes in an annular combustor and comparison with experiments. *Combustion and Flame 184*, 136–152. *(p. 6, 20, 212, 251)*

Lamoreaux, R. H., D. L. Hildenbrand, and L. Brewer (1987). High-Temperature Vaporization Behavior of Oxides II. Oxides of Be, Mg, Ca, Sr, Ba, B, Al, Ga, In, Tl, Si, Ge, Sn, Pb, Zn, Cd, and Hg. *Journal of Physical and Chemical Reference Data 16*(3), 419–443. *(p. 171)*

Lancien, T. (2018). *Numerical study of two-phase ignition in annular multi-burner combustors*. Ph. D. thesis, Université Paris-Saclay. *(p. 311)*

Lancien, T., N. Dumont, K. Prieur, D. Durox, S. Candel, O. Gicquel, and R. Vicquelin (2016). Uncertainty quantification of injected droplet size in mono-dispersed Eulerian simulations. In *9th International Conference on Multiphase Flow. (p. 24, 86)*

Lancien, T., K. Prieur, D. Durox, S. Candel, and R. Vicquelin (2018). Large Eddy Simulation of Light-Round in an Annular Combustor with Liquid Spray Injection and Comparison with Experiments. *Journal of Engineering for Gas Turbines and Power 140*(2). *(p. 165, 172, 173, 176, 282)*

Lancien, T., K. Prieur, D. Durox, S. Candel, and R. Vicquelin (2019). Leading point behavior during the ignition of an annular combustor with liquid n-heptane injectors.

Proceedings of the Combustion Institute 37(4), 5021–5029. *(p. 282)*

Lang, W., T. Poinsot, and S. Candel (1987). Active control of combustion instability. *Combustion and Flame 70*(3), 281–289. *(p. 210)*

Lauer, M., M. Zellhuber, T. Sattelmayer, and C. J. Aul (2011). Determination of the heat release distribution in turbulent flames by a model based correction of OH* chemiluminescence. *Journal of Engineering for Gas Turbines and Power 133*(12). *(p. 65, 69, 74, 76, 80)*

Laurent, C., M. Bauerheim, T. Poinsot, and F. Nicoud (2019). A novel modal expansion method for low-order modeling of thermoacoustic instabilities in complex geometries. *Combustion and Flame 206*, 334–348. *(p. 227)*

Laux, C. O., T. G. Spence, C. H. Kruger, and R. N. Zare (2003). Optical diagnostics of atmospheric pressure air plasmas. *Plasma Sources Science and Technology 12*(2), 125–138. *(p. 304)*

Lecordier, B., M. Mouqallid, S. Vottier, E. Rouland, D. Allano, and M. Trinite (1994). CCD Recording method for cross-correlation PIV development in unstationary high speed flow. *Experiments in Fluids 17*(3), 205–208. *(p. 164)*

Lecourt, R., G. Linassier, and G. Lavergne (2011). Detailed characterisation of a swirled air/kerosene spray in reactive and non-reactive conditions downstream from an actual turbojet injection system. In *Proceedings of the ASME Turbo Expo*, Volume 2, Vancouver, Canada, pp. 185–194. *(p. 32, 104)*

Lee, D. S., D. W. Fahey, P. M. Forster, P. J. Newton, R. C. Wit, L. L. Lim, B. Owen, and R. Sausen (2009). Aviation and global climate change in the 21st century. *Atmospheric Environment 43*(22-23), 3520–3537. *(p. 1)*

Lee, J. G. and D. A. Santavicca (2003). Experimental Diagnostics for the Study of Combustion Instabilities in Lean Premixed Combustors. *Journal of Propulsion and Power 19*(5), 735–750. *(p. 80)*

Lee, J.-Y., E. Lubarsky, and B. T. Zinn (2005). "Slow" active control of combustion instabilities by modification of liquid fuel spray properties. *Proceedings of the Combustion Institute 30*(2), 1757–1764. *(p. 21, 104)*

Lee, S. Y. and S. U. Ryu (2006). Recent progress of spray-wall interaction research. *(p. 60)*

Lee, T., J. Park, D. Han, and K. T. Kim (2019). The dynamics of multiple interacting swirl-stabilized flames in a lean-premixed gas turbine combustor. *Proceedings of the Combustion Institute 37*(4), 5137–5145. *(p. 32)*

Lefebvre, A. H. (1989). *Atomization and Sprays*. Taylor & Francis. *(p. 103, 113, 305)*

Lefebvre, A. H. (1995). The role of fuel preparation in low-emission combustion. *Journal of Engineering for Gas Turbines and Power 117*(4), 617–654. *(p. 101)*

Lefebvre, A. H. and D. R. Ballal (2010). *Gas turbine combustion : alternative fuels and emissions*. Taylor & Francis. *(p. 1, 40, 103, 105, 250, 274)*

Lefkowitz, J. K., P. Guo, T. Ombrello, S. H. Won, C. A. Stevens, J. L. Hoke, F. Schauer, and Y. Ju (2015). Schlieren imaging and pulsed detonation engine testing of ignition by a nanosecond repetitively pulsed discharge. *Combustion and Flame 162*(6). *(p. 300)*

Leitgeb, T., T. Schuller, D. Durox, F. Giuliani, S. Köberl, and J. Woisetschläger (2013). Interferometric determination of heat release rate in a pulsated flame. *Combustion*

and Flame 160(3), 589–600. *(p. 66)*

Lemaire, R. and S. Menanteau (2017). Assessment of radiation correction methods for bare bead thermocouples in a combustion environment. *International Journal of Thermal Sciences 122*, 186–200. *(p. 43)*

Lespinasse, F., F. Baillot, and T. Boushaki (2013). Responses of V-flames placed in an HF transverse acoustic field from a velocity to pressure antinode. *Comptes Rendus - Mecanique 341*(1-2), 110–120. *(p. 37)*

Lewis, B. and G. Elbe (1987). *Combustion, Flames and Explosions of Gases* (New York: ed.). *(p. 274)*

Li, G. and E. J. Gutmark (2005). Effect of exhaust nozzle geometry on combustor flow field and combustion characteristics. *Proceedings of the Combustion Institute*. *(p. 7, 37, 96, 124)*

Li, J., F. Richecoeur, and T. Schuller (2012). Determination of Heat Release Rate Disturbances in Unconfined Flames Based on Fluctuations in the Travel Time of Ultrasonic Waves. *Combustion Science and Technology 184*(4), 533–555. *(p. 66)*

Li, J., F. Richecoeur, and T. Schuller (2013). Reconstruction of heat release rate disturbances based on transmission of ultrasounds: Experiments and modeling for perturbed flames. *Combustion and Flame 160*(9), 1779–1788. *(p. 66)*

Liang, H. and T. Maxworthy (2005). An experimental investigation of swirling jets. *Journal of Fluid Mechanics 525*, 115–159. *(p. 101, 123, 124, 165, 166, 175, 176, 178, 361)*

Lieuwen, T., H. Torres, C. Johnson, and B. Zinn (2001). A mechanism of combustion instability in lean premixed gas turbine combustors. *Journal of Engineering for Gas Turbines and Power 123*(1), 182–189. *(p. 6)*

Lieuwen, T. and V. Yang (2005). *Combustion instabilities in gas turbine engines, Operational experience, Fundamental mechanisms, and modeling*, Volume 210 of *Progress in Astronautics and Aeronautics*. American Institute of Aeronautics and Astronautics, Inc. *(p. 4, 20)*

Lieuwen, T. C. and V. Yang (2006). *Combustion Instabilities In Gas Turbine Engines*. Reston ,VA, USA: AIAA. *(p. 210)*

Lilley, D. G. (1977). Swirl flows in combustion: A review. *AIAA Journal 15*(8), 1063–1078. *(p. 122, 133)*

Lo Schiavo, E., D. Laera, E. Riber, L. Gicquel, and T. Poinsot (2020). Effect of liquid fuel wall interaction on thermoacoustic instabilities in swirling spray flames. *Combustion and Flame 219*, 86–101. *(p. 202, 207)*

Lucca-Negro, O. and T. O'Doherty (2001). Vortex breakdown: A review. *Progress in Energy and Combustion Science 27*(4), 431–481. *(p. 123, 124, 165, 361)*

Machover, E. and E. Mastorakos (2016). Spark ignition of annular non-premixed combustors. *Experimental Thermal and Fluid Science 73*, 64–70. *(p. 8, 275)*

Machover, E. and E. Mastorakos (2017a). Experimental investigation on spark ignition of annular premixed combustors. *Combustion and Flame 178*, 148–157. *(p. 8, 275)*

Machover, E. and E. Mastorakos (2017b). Numerical Investigation of the Stochastic Behavior of Light-Round in Annular Non-Premixed Combustors. *Combustion Science and Technology 189*(9), 1467–1485. *(p. 8)*

Mahmud, T., J. S. Truelove, and T. F. Wall (1987). Flow Characteristics of Swirling

Coaxial Jets From Divergent Nozzles. *Journal of Fluids Engineering 109*(3), 275–282. *(p. 133, 134, 146, 147)*

Maio, G., M. Cailler, R. Mercier, and B. Fiorina (2019). Virtual chemistry for temperature and CO prediction in les of non-adiabatic turbulent flames. *Proceedings of the Combustion Institute 37*(2), 2591–2599. *(p. 294)*

Malbois, P., E. Salaün, B. Rossow, G. Cabot, L. Bouheraoua, S. Richard, B. Renou, and F. Grisch (2019). Quantitative measurements of fuel distribution and flame structure in a lean-premixed aero-engine injection system by kerosene/OH-PLIF measurements under high-pressure conditions. *Proceedings of the Combustion Institute 37*(4), 5215–5222. *(p. 32)*

Maly, R. and M. Vogel (1979). Initiation and propagation of flame fronts in lean CH4-air mixtures by the three modes of the ignition spark. *Symposium (International) on Combustion 17*(1), 821–831. *(p. 302)*

Manoharan, K., M. Frederick, S. Clees, J. O'Connor, and S. Hemchandra (2020). A weakly nonlinear analysis of the precessing vortex core oscillation in a variable swirl turbulent round jet. *Journal of Fluid Mechanics 884*, A29. *(p. 101, 165, 186)*

Marble, F. and D. Cox (1953). Servo-stabilization of low-frequency oscillations in a liquid bipropellant rocket motor. *Journal of the American Rocket Society 23*(2), 85. *(p. 4)*

Marchioli, C. (2017). Large-eddy simulation of turbulent dispersed flows : a review of modelling approaches. *Acta Mechanica 228*, 741–771. *(p. 59)*

Marley, J. A. and T. C. MacAvoy (1961). Growth of Stannic Oxide Crystals from the Vapor Phase. *Journal of Applied Physics 32*(12), 2504–2505. *(p. 171)*

Mason, D., S. Clees, M. Frederick, and J. O'Connor (2019). The effects of exit boundary condition on precessing vortex core dynamics. In *Proceedings of the ASME Turbo Expo*, Volume 4B-2019. American Society of Mechanical Engineers (ASME). *(p. 37)*

Mastorakos, E. (2017). Forced ignition of turbulent spray flames. *Proceedings of the Combustion Institute 36*(2), 2367–2383. *(p. 274)*

Mattingly, J. and G. Oates (1986). An experimental investigation of the mixing of coannular swirling flows. *AIAA Journal 24*(5), 785–792. *(p. 127, 130, 131, 132, 147, 149, 154)*

Mazur, M., H. T. Nygård, J. R. Dawson, and N. A. Worth (2019). Characteristics of self-excited spinning azimuthal modes in an annular combustor with turbulent premixed bluff-body flames. *Proceedings of the Combustion Institute 37*(4), 5129–5136. *(p. 8, 251)*

McDonnell, V. G., C. D. Cameron, and G. S. Samuelsen (1990). Symmetry assessment of an air-blast atomizer spray. *Journal of Propulsion and Power 6*(4), 375–381. *(p. 104, 105, 119)*

McDonnell, V. G., G. S. Samuelsen, M. R. Wang, C. H. Hong, and W. H. Lai (1994). Interlaboratory comparison of phase Doppler measurements in a research simplex atomizer spray. *Journal of Propulsion and Power 10*(3), 402–409. *(p. 107)*

McManus, K. R., T. Poinsot, and S. Candel (1993). A review of active control of combustion instabilities. *Progress in Energy and Combustion Science 19*, 1–29. *(p. 210)*

Mensah, G. A., L. Magri, A. Orchini, and J. P. Moeck (2019). Effects of Asymmetry on Thermoacoustic Modes in Annular Combustors: A Higher-Order Perturba-

tion Study. *Journal of Engineering for Gas Turbines and Power 141*(4), 041030. *(p. 251)*

Méry, Y. (2018). Dynamical response of a perfectly premixed flame and limit behavior for high power density systems. *Combustion and Flame 192*, 410–425. *(p. 3)*

Miles, P. C. and F. C. Gouldin (1998). Premixed turbulent flame/flow interaction: Simultaneous measurements of velocity and flamelet position. *AIAA Journal 36*(7), 1178–1189. *(p. 164)*

Minesi, N., S. A. Stepanyan, P. Mariotto, G. D. Stancu, and C. O. Laux (2020). Fully ionized nanosecond discharges in air: the thermal spark. *Plasma Sources Science and Technology 29*, 085003. *(p. 302, 303, 305)*

Mirat, C., D. Durox, and T. Schuller (2014). Analysis of the spray and transfer function of swirling spray flames from a multi-jet steam assisted liquid fuel injector. In *Proceedings of the ASME Turbo Expo 2014*, Number GT2014-25111. *(p. 65, 256, 289)*

Mirat, C., D. Durox, and T. Schuller (2015). Stability analysis of a swirl spray combustor based on flame describing function. *Proc. Combust. Inst. 35*(3), 3291–3298. *(p. 65, 256, 289)*

Mitchell, C., L. Crocco, and W. Sirignano (1969). Nonlinear oscillations in liquid rocket combustion chambers. *Astronautica Acta 14*(5), 409. *(p. 4)*

Moeck, J. P., J.-F. Bourgouin, D. Durox, T. Schuller, and S. Candel (2012). Nonlinear interaction between a precessing vortex core and acoustic oscillations in a turbulent swirling flame. *Combustion and Flame 159*(8), 2650–2668. *(p. 134, 166, 187)*

Moeck, J. P., D. Durox, T. Schuller, and S. Candel (2019). Nonlinear thermoacoustic mode synchronization in annular combustors. *Proceedings of the Combustion Institute 37*(4), 5343–5350. *(p. 10, 20, 251)*

Moeck, J. P., M. Paul, and C. O. Paschereit (2010). Thermoacoustic Instabilities in an Annular Rijke Tube. In *Proceedings of the ASME Turbo Expo 2010*, pp. 1219–1232. *(p. 7)*

Mouqallid, M., B. Lecordier, and M. Trinite (1994). High Speed Laser Tomography Analysis of Flame Propagation in a Simulated Internal Combustion Engine - Applications to Nonuniform Mixture. In *SAE Technical Paper*, pp. 941990. *(p. 164)*

Muthuselvan, G., K. D. Ghate, M. S. Rao, V. S. Iyengar, S. Thirumalachari, and S. Kothandaraman (2018). Experimental study of spray breakup phenomena in small-scale simplex atomizers with andwithout air swirl. *Atomization and Sprays 28*(4), 299–320. *(p. 112)*

Naegeli, D. W. and L. G. Dodge (1991). Ignition Study in a Gas Turbine Combustor. *Combustion Science and Technology 80*(4-6), 165–184. *(p. 274)*

Najm, H. N., P. H. Paul, C. J. Mueller, and P. S. Wyckoff (1998). On the Adequacy of Certain Experimental Observables as Measurements of Flame Burning Rate. *Combustion and Flame 113*(3), 312–332. *(p. 66)*

Neophytou, A., E. S. Richardson, and E. Mastorakos (2012). Spark ignition of turbulent recirculating non-premixed gas and spray flames: A model for predicting ignition probability. *Combustion and Flame 159*(4), 1503–1522. *(p. 274)*

Noiray, N., M. Bothien, and B. Schuermans (2011). Investigation of azimuthal staging concepts in annular gas turbines. *Combustion Theory and Modelling 15*(5), 585–606.

(p. 7, 18, 210)

Noiray, N., D. Durox, T. Schuller, and S. Candel (2007). Passive control of combustion instabilities involving premixed flames anchored on perforated plates. *Proceedings of the Combustion Institute 31*(1), 1283–1290. *(p. 292)*

Noiray, N., D. Durox, T. Schuller, and S. Candel (2008). A unified framework for nonlinear combustion instability analysis based on the flame describing function. *Journal of Fluid Mechanics 615*, 139. *(p. 6, 212, 266, 268)*

Noiray, N. and B. Schuermans (2012). Theoretical and experimental investigations on damper performance for suppression of thermoacoustic oscillations. *Journal of Sound and Vibration 331*(12), 2753–2763. *(p. 210)*

Noiray, N. and B. Schuermans (2013a). Deterministic quantities characterizing noise driven Hopf bifurcations in gas turbine combustors. *International Journal of Non Linear Mechanics 50*, 152–163. *(p. 242)*

Noiray, N. and B. Schuermans (2013b). On the dynamic nature of azimuthal thermoacoustic modes in annular gas turbine combustion chambers. *Proceedings of the Royal Society of London A: Mathematical, Physical and Engineering Sciences 469*(2151). *(p. 7, 251)*

Nygård, H. T., M. Mazur, J. R. Dawson, and N. A. Worth (2019). Flame dynamics of azimuthal forced spinning and standing modes in an annular combustor. *Proceedings of the Combustion Institute 37*(4), 5113–5120. *(p. 8, 18, 19)*

Oberleithner, K., M. Sieber, C. N. Nayeri, C. O. Paschereit, C. Petz, H.-C. Hege, B. R. Noack, and I. Wygnanski (2011). Three-dimensional coherent structures in a swirling jet undergoing vortex breakdown: Stability analysis and empirical mode construction. *Journal of Fluid Mechanics 679*, 383–414. *(p. 124, 165, 178)*

O'Connor, J., V. Acharya, and T. Lieuwen (2015). Transverse combustion instabilities: Acoustic, fluid mechanic, and flame processes. *Progress in Energy and Combustion Science 49*, 1–39. *(p. 7, 37, 251)*

O'Connor, J., N. A. Worth, and J. R. Dawson (2013). Circumferential Instability in a Model Annular Gas Turbine. *Proceedings of ASME Turbo Expo 2013*, GT2013–95897. *(p. 37)*

Oefelein, J. C. and V. Yang (1993). Comprehensive review of liquid-propellant combustion instabilities in F-1 engines. *Journal of Propulsion and Power 9*(5), 657–677. *(p. 210)*

Orchini, A., G. A. Mensah, and J. P. Moeck (2019). Effects of nonlinear modal interactions on the thermoacoustic stability of annular combustors. *Journal of Engineering for Gas Turbines and Power 141*(2), 1–14. *(p. 251)*

Örlü, R. and P. H. Alfredsson (2008). An experimental study of the near-field mixing characteristics of a swirling jet. *Flow, Turbulence and Combustion 80*(3), 323–350. *(p. 122, 125, 127, 128)*

Osborne, J. R., S. A. Ramji, C. D. Carter, and A. M. Steinberg (2017). Relationship between local reaction rate and flame structure in turbulent premixed flames from simultaneous 10 kHz TPIV, OH PLIF, and CH2O PLIF. *Proceedings of the Combustion Institute 36*(2), 1835–1841. *(p. 163)*

Otsu, N. (1979). Threshold selection method for gray level histograms. *IEEE Transactions on Systems, Man and Cybernetics SMC-9*(1), 62–66. *(p. 189)*

Pai, D. Z., D. A. Lacoste, and C. O. Laux (2010). Transitions between corona, glow, and spark regimes of nanosecond repetitively pulsed discharges in air at atmospheric pressure. *Journal of Applied Physics 107*(9), 93303. *(p. 300, 305)*

Palies, P., D. Durox, T. Schuller, and S. Candel (2010). The combined dynamics of swirler and turbulent premixed swirling flames. *Combustion and Flame 157*(9), 1698–1717. *(p. 7, 204, 205, 361)*

Palies, P., D. Durox, T. Schuller, and S. Candel (2011). Nonlinear combustion instability analysis based on the flame describing function applied to turbulent premixed swirling flames. *Combustion and Flame 158*(10), 1980–1991. *(p. 6, 238)*

Palies, P., D. Durox, T. Schuller, P. Morenton, and S. Candel (2009). Dynamics of premixed confined swirling flames. *Comptes Rendus Mécanique 337*(6-7), 395–405. *(p. 134)*

Panda, J. and D. K. McLaughlin (1994). Experiments on the instabilities of a swirling jet. *Physics of Fluids 6*(1), 263–276. *(p. 124)*

Pankiewitz, C. and T. Sattelmayer (2003). Time domain simulation of combustion instabilities in annular combustors. *Journal of Engineering for Gas Turbines and Power 125*(3), 677–685. *(p. 7)*

Park, S. H. and H. D. Shin (1993). Measurements of entrainment characteristics of swirling jets. *International Journal of Heat and Mass Transfer 36*(Issue 16), 4009–4018. *(p. 122)*

Paulhiac, D. (2015). Modélisation de la combustion d'un spray dans un brûleur aéronautique. *(p. 56, 199)*

Peterleithner, J., N. V. Stadlmair, J. Woisetschläger, and T. Sattelmayer (2016). Analysis of measured flame transfer functions with locally resolved density fluctuation and OH-Chemiluminescence Data. *Journal of Engineering for Gas Turbines and Power 138*(3), 1–9. *(p. 65, 66, 74, 80)*

Philip, M. (2016). *Dynamique de l'allumage circulaire dans les foyers annulaires multi-injecteurs*. Ph. D. thesis, École Centrale Paris. *(p. 135, 137)*

Philip, M., M. Boileau, R. Vicquelin, E. Riber, T. Schmitt, B. Cuenot, D. Durox, and S. Candel (2015). Large Eddy Simulations of the ignition sequence of an annular multiple-injector combustor. *Proceedings of the Combustion Institute 35*(3), 3159–3166. *(p. 280)*

Philip, M., M. Boileau, R. Vicquelin, T. Schmitt, D. Durox, J. F. Bourgouin, and S. Candel (2014). Simulation of the ignition process in an annular multiple-injector combustor and comparison with experiments. *Journal of Engineering for Gas Turbines and Power 137*(3), 031501. *(p. 280, 281)*

Philip, M., M. Boileau, R. Vicquelin, T. Schmitt, D. Durox, J.-F. Bourgouin, and S. Candel (2015). Ignition sequence in a multi-injector combustor. *Physics of Fluids 26*(9). *(p. 280)*

Pilla, G., D. Galley, D. Lacoste, F. Lacas, D. Veynante, and C. Laux (2006). Stabilization of a turbulent premixed flame using a nanosecond repetitively pulsed plasma. *IEEE Transactions on Plasma Science 34*(6), 2471–2477. *(p. 300)*

Poinsot, T. (2017). Prediction and control of combustion instabilities in real engines. *Proceedings of the Combustion Institute 36*(1), 1–28. *(p. 4, 6, 7, 20, 210, 250)*

Poinsot, T. and S. Lele (1992). Boundary conditions for direct simulations of com-

pressible viscous flows. *Journal of Computational Physics 101*(1), 104–129. *(p. 55, 136)*

Poinsot, T. and D. Veynante (2012). *Theoretical and numerical combustion*. R.T. Edwards. *(p. 55, 64, 211, 226, 266, 345)*

Polifke, W., A. Fischer, and T. Sattelmayer (2003). Instability of a premix burner with nonmonotonic pressure drop characteristic. *Journal of Engineering for Gas Turbine and Power 125*, 21–27. *(p. 211, 218)*

Pope, S. B. (2000). *Turbulent Flows*. Cambridge University Press. *(p. 126)*

Prieur, K. (2017). *Dynamique de la combustion dans un foyer annulaire multi injecteurs diphasique*. Ph. D. thesis, Université Paris Saclay. *(p. 86, 87, 108)*

Prieur, K., D. Durox, J. Beaunier, T. Schuller, and S. Candel (2017a). Ignition dynamics in an annular combustor for liquid spray and premixed gaseous injection. *Proceedings of the Combustion Institute 36*(3), 3717–3724. *(p. 10)*

Prieur, K., D. Durox, J. Beaunier, T. Schuller, and S. Candel (2017b). Ignition dynamics in an annular combustor for liquid spray and premixed gaseous injection. *Proceedings of the Combustion Institute 36*(3), 3717–3724. *(p. 105, 163, 165, 172, 173, 281, 288, 294, 301, 305, 311)*

Prieur, K., D. Durox, and T. Schuller (2016). Influence of cup angle on the Flame Describing Function of a swirled injector with liquid fuel. In *Thermoacoustic instabilities in gas turbines and rocket engines: industry meets academia*, Number October. *(p. 12, 24, 86, 87, 198, 212)*

Prieur, K., D. Durox, T. Schuller, and S. Candel (2017a). A hysteresis phenomenon leading to spinning or standing azimuthal instabilities in an annular combustor. *Combustion and Flame 175*, 283–291. *(p. 10, 19, 20, 198, 214, 217, 253, 282)*

Prieur, K., D. Durox, T. Schuller, and S. Candel (2017b). Strong Azimuthal Combustion Instabilities in a Spray Annular Chamber With Intermittent Partial Blow-Off. *Journal of Engineering for Gas Turbine and Power 140*(3), 031503. *(p. 43, 197, 206, 212, 250, 251, 252, 253, 255, 259, 260, 262, 265, 292)*

Prieur, K., D. Durox, T. Schuller, and S. Candel (2018). Strong Azimuthal Combustion Instabilities in a Spray Annular Chamber With Intermittent Partial Blow-Off. *Journal of Engineering for Gas Turbines and Power 140*(3), 031503. *(p. 10, 22, 24, 86)*

Prieur, K., G. Vignat, D. Durox, T. Schuller, and S. Candel. Flame and spray dynamics during the light-round process in an annular system equipped with multiple swirl spray injectors. *Journal of Engineering for Gas Turbines and Power 141*(6), 061007. *(p. 10, 163, 165, 172, 173, 281, 282, 285, 292)*

Puggelli, S., T. Lancien, K. Prieur, D. Durox, S. Candel, and R. Vicquelin (2020). Impact of wall temperature in large eddy simulation of light-round in an annular liquid fueled combustor and assessment of wall models. *Journal of Engineering for Gas Turbines and Power 142*(1). 011018. *(p. 282)*

Putnam, A. (1971). *Combustion driven oscillations in industry*. Elsevier. *(p. 7)*

Rajamanickam, K. and S. Basu (2017). Insights into the dynamics of spray-swirl interactions. *Journal of Fluid Mechanics 810*, 82–126. *(p. 103, 107)*

Rajamanickam, K. and S. Basu (2018). Insights into the dynamics of conical breakdown modes in coaxial swirling flow field. *Journal of Fluid Mechanics 853*, 72–110.

(p. 166)

Rajasegar, R., C. M. Mitsingas, E. K. Mayhew, S. Hammack, H. Do, and T. Lee (2016). Effects of continuous volumetric direct-coupled nonequilibrium atmospheric microwave plasma discharge on swirl-stabilized premixed flames. *IEEE Transactions on Plasma Science 44*(1), 39–48. *(p. 301, 310)*

Rayleigh (1878). The explanation of certain acoustical phenomena. *Nature 18*(455), 319–321. *(p. 3)*

Renaud, A., S. Ducruix, and L. Zimmer (2017). Bistable behaviour and thermo-acoustic instability triggering in a gas turbine model combustor. *Proceedings of the Combustion Institute 36*(3), 3899–3906. *(p. 20, 218)*

Renaud, A., S. Ducruix, and L. Zimmer (2019). Experimental Study of the Precessing Vortex Core Impact on the Liquid Fuel Spray in a Gas Turbine Model Combustor. *Journal of Engineering for Gas Turbines and Power 141*(11), 111022. *(p. 104, 186, 187)*

Ribeiro, M. M. and J. H. Whitelaw (1980). Coaxial jets with and without swirl. *Journal of Fluid Mechanics 96*(Issue 4), 769–795. *(p. 122, 127, 133)*

Rock, N., B. Emerson, J. Seitzman, and T. Lieuwen (2020). Near-lean blowoff dynamics in a liquid fueled combustor. *Combustion and Flame 212*, 53–66. *(p. 189)*

Rose, W. G. (1962). A Swirling Round Turbulent Jet. *Journal of Applied Mechanics* (December). *(p. 123, 145, 153, 156)*

Roux, S., G. Lartigue, T. Poinsot, U. Meier, and C. Bérat (2005). Studies of mean and unsteady flow in a swirled combustor using experiments, acoustic analysis, and large eddy simulations. *Combustion and Flame 141*(1-2), 40–54. *(p. 166)*

Rusterholtz, D. L., D. A. Lacoste, G. D. Stancu, D. Z. Pai, and C. O. Laux (2013). Ultrafast heating and oxygen dissociation in atmospheric pressure air by nanosecond repetitively pulsed discharges. *Journal of Physics D: Applied Physics 46*(46), 464010. *(p. 300, 305)*

Samaniego, J. M., F. N. Egolfopoulos, and C. T. Bowmanâ (1995). CO_2^* chemiluminescence in premixed flames. *Combustion Science and Technology 109*(1-6), 183–203. *(p. 74)*

Sanchez, P. S. (2012). *Modeling the dispersion and evaporation of sprays in aeronautical combustion chambers*. Ph. D. thesis, Université de Toulouse. *(p. 56, 60)*

Sanjosé, M., J. Senoner, F. Jaegle, B. Cuenot, S. Moreau, and T. Poinsot (2011). Fuel injection model for Euler Euler and Euler Lagrange large eddy simulations of an evaporating spray inside an aeronautical combustor. *International Journal of Multiphase Flow 37*(5), 514–529. *(p. 111)*

Sarpkaya, T. (1971). On stationary and travelling vortex breakdowns. *Journal of Fluid Mechanics 45*(Issue 3), 545–559. *(p. 140)*

Sattelmayer, T. and W. Polifke (2003). Assessment of methods for the computation of the linear stability of combustors. *Combustion Science and Technology 175*(3), 453–476. *(p. 6)*

Schiller, L. and A. Naumann (1935). A Drag Coefficient Correlation. *Zeitschrift des Vereins Deutscher Ingenieure 77*, 318–320. *(p. 56)*

Schmid, P. J. (2010). Dynamic mode decomposition of numerical and experimental data. *Journal of Fluid Mechanics 656*, 5–28. *(p. 15, 49, 199, 264, 307)*

Schofield, K. (2020). Trace species reported combustion behavior and their chemistry. In *Combustion Emissions*, pp. 23–467. *(p. 171)*

Schuermans, B., F. Guethe, D. Pennell, D. Guyot, and C. O. Paschereit (2010). Thermoacoustic Modeling of a Gas Turbine Using Transfer Functions Measured Under Full Engine Pressure. *Journal of Engineering for Gas Turbines and Power 132*(11), 111503. *(p. 6)*

Schuermans, B. B., V. Bellucci, and C. O. Paschereit (2003). Thermoacoustic modeling and control of multi burner combustion systems. In *American Society of Mechanical Engineers, International Gas Turbine Institute, Turbo Expo (Publication) IGTI*, Volume 2, pp. 509–519. *(p. 7)*

Schuermans, B. B., W. Polifke, and C. O. Paschereit (1999). Modeling transfer matrices of premixed flames and comparison with experimental results. In *Proceedings of the ASME Turbo Expo*, Volume 2. American Society of Mechanical Engineers (ASME). *(p. 3)*

Schuller, T., D. Durox, and S. Candel (2003). Self-induced combustion oscillations of laminar premixed flames stabilized on annular burners. *Combustion and Flame 135*(4), 525–537. *(p. 6, 292)*

Schuller, T., D. Durox, P. Palies, and S. Candel (2012). Acoustic decoupling of longitudinal modes in generic combustion systems. *Combustion and Flame 159*(5), 1921–1931. *(p. 211)*

Scott, C. J. and K. W. Bartelt (1976). Decaying annular swirl flow with inlet soild body rotation. *Journal of Fluids Engineering, Transactions of the ASME 98*(1), 33–40. *(p. 146, 363)*

Selle, L., G. Lartigue, T. Poinsot, R. Koch, K. U. Schildmacher, W. Krebs, B. Prade, P. Kaufmann, and D. Veynante (2004). Compressible large eddy simulation of turbulent combustion in complex geometry on unstructured meshes. *Combustion and Flame 137*(4), 489–505. *(p. 165, 166, 361)*

Sharma, S., K. Ghate, T. Sundararajan, and S. Sahu (2019). Effects of air swirler geometry on air and spray droplet interactions in a spray chamber. *Advances in Mechanical Engineering 11*(5), 168781401985097. *(p. 103)*

Sheen, H., W. Chen, S. Jeng, and T. Huang (1996). Correlation of swirl number for a radial-type swirl generator. *Experimental Thermal and Fluid Science 12*(Issue 4), 444–451. *(p. 133)*

Shum-Kivan, F., J. Marrero Santiago, A. Verdier, E. Riber, B. Renou, G. Cabot, and B. Cuenot (2017). Experimental and numerical analysis of a turbulent spray flame structure. *Proceedings of the Combustion Institute 36*(2), 2567–2575. *(p. 55, 56, 196, 198)*

Silva, C. F., F. Nicoud, T. Schuller, D. Durox, and S. Candel (2013). Combining a Helmholtz solver with the flame describing function to assess combustion instability in a premixed swirled combustor. *Combustion and Flame 160*(9), 1743–1754. *(p. 6)*

Sirignano, W. and L. Crocco (1964). A shock wave model of unstable rocket combustor. *AIAA Journal 2*(7), 1285–1296. *(p. 4)*

Sislian, J. and R. Cusworth (1986). Measurements of mean velocity and turbulent intensities in a free isothermal swirling jet. *AIAA Journal 24*(2), 303–309. *(p. 133)*

Smith, D. A. and E. E. Zukoski (1985). Combustion Instability Sustained by Unsteady

Vortex Combustion. In *21st Joint Propulsion Conference*, pp. AIAA–85–1248. *(p. 6)*

Smith, G. P., D. M. Golden, M. Frenklach, N. W. Moriarty, B. Eiteneer, M. Goldenberg, T. C. Bowman, R. K. Hanson, S. Song, W. C. J. Gardiner, V. V. Lissianski, and Z. Qin. http://www.me.berkeley.edu/gri_mech/. *(p. 169)*

Smith, T. E., I. P. Chterev, B. L. Emerson, D. R. Noble, and T. C. Lieuwen (2018). Comparison of Single- and Multinozzle Reacting Swirl Flow Dynamics. *Journal of Propulsion and Power 34*(2), 384–394. *(p. 32)*

Spalding, D. (1953). The combustion of liquid fuels. *Symposium (International) on Combustion 4*(1), 847–864. *(p. 59)*

Spall, R. E., T. B. Gatski, and C. E. Grosch (1987). A criterion for vortex breakdown. *Physics of Fluids 30*(11 , Nov. 1987), 3434–3440. *(p. 123, 361)*

Staffelbach, G., L. Y. Gicquel, G. Boudier, and T. Poinsot (2009). Large Eddy Simulation of self excited azimuthal modes in annular combustors. *Proceedings of the Combustion Institute 32*(2), 2909–2916. *(p. 20, 21, 251)*

Starikovskaia, S. M. (2014). Plasma assisted ignition and combustion: nanosecond discharges and development of kinetic mechanisms. *Journal of Physics D: Applied Physics 47*(15), 353001. *(p. 300)*

Starikovskiy, A. and N. Aleksandrov (2013). Plasma assisted ignition and combustion. *Progress in Energy and Combustion Science 39*(1), 61–110. *(p. 300)*

Steenbergen, W. and J. Voskamp (1998). The rate of decay of swirl in turbulent pipe flow. *Flow Measurement and Instrumentation 9*(Issue 2), 67–78. *(p. 122, 146)*

Stöhr, M., K. Oberleithner, M. Sieber, Z. Yin, and W. Meier (2018a). Experimental Study of Transient Mechanisms of Bistable Flame Shape Transitions in a Swirl Combustor. *Journal of Engineering for Gas Turbines and Power 140*(1), 011503. *(p. 163)*

Stöhr, M., K. Oberleithner, M. Sieber, Z. Yin, and W. Meier (2018b). Experimental Study of Transient Mechanisms of Bistable Flame Shape Transitions in a Swirl Combustor. *Journal of Engineering for Gas Turbines and Power 140*(1). *(p. 165, 166)*

Stöhr, M., R. Sadanandan, and W. Meier (2011). Phase-resolved characterization of vortex-flame interaction in a turbulent swirl flame. *Experiments in Fluids 51*(4), 1153–1167. *(p. 165, 166, 175, 178, 181)*

Stow, S. R. and A. P. Dowling (2001). Thermoacoustic oscillations in an annular combustor. In *Proceedings of the ASME Turbo Expo*, Volume 2. American Society of Mechanical Engineers (ASME). *(p. 7)*

Strahle, W. C. (1978). Combustion noise. *Progress in Energy and Combustion Science 4*(3), 157–176. *(p. 292)*

Summerfield, M. (1951). A theory of unstable combustion in liquid propellent rocket systems. *Journal of the American Rocket Society 21*(5), 108–114. *(p. 210, 211)*

Sutton, G. and O. Biblarz (1949). *Rocket propulsion elements*. New-York, NY, USA: John Wiley and Sons. *(p. 210, 211)*

Syred, N. (2006). A review of oscillation mechanisms and the role of the precessing vortex core (PVC) in swirl combustion systems. *Progress in Energy and Combustion Science 32*(2), 93–161. *(p. 101, 165, 166, 176, 187, 191)*

Syred, N. and J. M. Beer (1972). Damping of precessing vortex cores by combustion in

swirl generators. *Astronautica Acta 17*(4-5), 783–801. *(p. 166)*

Syred, N. and J. M. Beér (1974). Combustion in swirling flows: A review. *Combustion and Flame 23*(Issue 2), 143–201. *(p. 122, 126)*

Syred, N., N. A. Chigier, and J. M. Beér (1971). Flame stabilization in recirculation zones of jets with swirl. *Symposium (International) on Combustion 13*(Issue 1), 617–624. *(p. 122, 133)*

Tachibana, S., K. Saito, T. Yamamoto, M. Makida, T. Kitano, and R. Kurose (2015). Experimental and numerical investigation of thermo-acoustic instability in a liquid-fuel aero-engine combustor at elevated pressure: Validity of large-eddy simulation of spray combustion. *Combustion and Flame 162*(6), 2621–2637. *(p. 20, 21, 56, 104, 196, 202)*

Tacina, R. (1990). Low nox potential of gas turbines engines. In *AIAA Aerospace Sciences Meeting (90-0550)*, Reno, Nevada. *(p. 1)*

Tammisola, O. and M. P. Juniper (2016). Coherent structures in a swirl injector at Re = 4800 by nonlinear simulations and linear global modes. *Journal of Fluid Mechanics 792*, 620–657. *(p. 101, 186)*

Tang, P. K. and W. A. Sirignano (1973). Theory of a generalized helmholtz resonator. *Journal of Sound and Vibration 26*(2), 247–262. *(p. 210)*

Terhaar, S., B. C. Bobusch, and C. O. Paschereit (2012). Effects of outlet boundary conditions on the reacting flow field in a swirl-stabilized burner at dry and humid conditions. *Journal of Engineering for Gas Turbines and Power 134*(11). *(p. 7, 37, 96, 124)*

Terhaar, S., B. Ćosić, C. O. Paschereit, and K. Oberleithner (2016). Suppression and excitation of the precessing vortex core by acoustic velocity fluctuations: An experimental and analytical study. *Combustion and Flame 172*, 234–251. *(p. 186, 187, 191)*

Terhaar, S., K. Oberleithner, and C. O. Paschereit (2015). Key parameters governing the precessing vortex core in reacting flows: An experimental and analytical study. *Proceedings of the Combustion Institute 35*(3), 3347–3354. *(p. 166, 186, 187)*

Thumuluru, S. K. and T. Lieuwen (2009). Characterization of acoustically forced swirl flame dynamics. *Proceedings of the Combustion Institute 32 II*, 2893–2900. *(p. 6)*

Tiribuzi, S. (2007). Numerical Assessment of SCAP: A Passive System for Preventing Thermoacoustic Oscillations in Gas Turbine Annular Combustors. In *ASME Turbo Expo 2007*, Number GT2007-280639, Montreal, Canada. *(p. 210)*

Toh, I., D. Honnery, and J. Soria (2010). Axial plus tangential entry swirling jet. *Experiments in Fluids 48*(Issue 2), 309–325. *(p. 124, 133, 136, 150)*

Töpperwien, K., F. e. Collin Bastiani, E. Riber, B. e. e. Cuenot, G. Vignat, K. Prieur, D. Durox, S. Candel, and R. Vicquelin (2020). Large eddy simulation of flame dynamics during the ignition of a swirling injector unit and comparison with experiments. In *Proceedings of the ASME Turbo Expo 2020*. *(p. 296)*

Tran, N. (2009). *Influence of inlet acoustic boundary condition on large amplitude combustion instabilities : design of a robust impedance control system*. Ph. D. thesis. *(p. 42)*

Tsien, H. (1952). Servostabilization of combustion in rocket motors. *Journal of the American Rocket Society 22*(5), 256. *(p. 4)*

Upton, T. D., D. D. Verhoeven, and D. E. Hudgins (2011). High-resolution computed tomography of a turbulent reacting flow. *Experiments in Fluids 50*(1), 125–134. *(p. 164)*

Urzay, J., M. Bassenne, G. I. Park, and P. Moin (2014). Characteristic regimes of subgrid-scale coupling in LES of particle-laden turbulent flows. In *Center for Turbulence Research Proceedings of the Summer Program. (p. 199)*

Valera-Medina, A., N. Syred, P. Bowen, and A. Crayford (2011). Studies of swirl burner characteristics, flame lengths and relative pressure amplitudes. *Journal of Fluids Engineering 133(10)*(101302). *(p. 122)*

Vanierschot, M., J. S. Müller, M. Sieber, M. Percin, B. W. van Oudheusden, and K. Oberleithner (2020). Single and double helix vortex breakdown as two dominant global modes in turbulent swirling jet flow. *Journal of Fluid Mechanics 883*, A31. *(p. 101, 166, 186)*

Vignat, G., D. Durox, K. Prieur, and S. Candel (2019). An experimental study into the effect of injector pressure loss on self-sustained combustion instabilities in a swirled spray burner. *Proceedings of the Combustion Institute 37*(4), 5205–5213. *(p. 172, 173)*

Vignat, G., D. Durox, A. Renaud, and S. Candel (2020). High Amplitude Combustion Instabilities in an Annular Combustor Inducing Pressure Field Deformation and Flame Blow Off. *Journal of Engineering for Gas Turbine and Power 142*(1), 011016. *(p. 105, 173)*

Vigueras-Zuñiga, M. O., A. Valera-Medina, and N. Syred (2012). Studies of the precessing vortex core in swirling flows. *Journal of Applied Research and Technology 10*(5), 755–765. *(p. 166)*

Wang, H., V. G. McDonnell, W. A. Sowa, and S. Samuelsen (1994). Experimental Study of a Model Gas Turbine Combustor Swirl Cup, Part 11: Droplet Dynamics. *Journal of Propulsion and Power 10*(4), 446–452. *(p. 111)*

Wang, S., S. Y. Hsieh, and V. Yang (2005). Unsteady flow evolution in swirl injector with radial entry. I. Stationary conditions. *Physics of Fluids 17*(4), 045106. *(p. 165, 166)*

Wang, S., Z. Rusak, R. Gong, and F. Liu (2017). On the three-dimensional stability of a solid-body rotation flow in a finite-length rotating pipe. *Journal of Fluid Mechanics 797*, 284–321. *(p. 165)*

Weber, R. and J. Dugué (1992). Combustion accelerated swirling flows in high confinements. *Progress in Energy and Combustion Science 18*(Issue 4), 349–367. *(p. 122, 124, 130, 132, 148, 154)*

Wolf, P., R. Balakrishnan, G. Staffelbach, L. Y. M. Gicquel, and T. Poinsot (2012). Using LES to Study Reacting Flows and Instabilities in Annular Combustion Chambers. *Flow, Turbulence and Combustion 88*(1-2), 191–206. *(p. 21, 251)*

Wolf, P., G. Staffelbach, L. Y. Gicquel, J.-D. Müller, and T. Poinsot (2012). Acoustic and Large Eddy Simulation studies of azimuthal modes in annular combustion chambers. *Combustion and Flame 159*(11), 3398–3413. *(p. 21, 210, 251)*

Worth, N. A. and J. R. Dawson (2013a). Modal dynamics of self-excited azimuthal instabilities in an annular combustion chamber. *Combustion and Flame 160*(11), 2476–2489. *(p. 8, 9, 14, 250)*

Worth, N. A. and J. R. Dawson (2013b). Self-excited circumferential instabilities in a model annular gas turbine combustor: Global flame dynamics. *Proceedings of the Combustion Institute 34*(2), 3127–3134. *(p. 8, 14, 18, 37, 251)*

Worth, N. A. and J. R. Dawson (2017). Effect of equivalence ratio on the modal dynamics of azimuthal combustion instabilities. *Proceedings of the Combustion Institute 36*(3), 3743–3751. *(p. 8, 231)*

Worth, N. A. and J. R. Dawson (2019). Characterisation of flame surface annihilation events in self excited interacting flames. *Combustion and Flame 199*, 338–351. *(p. 7, 32)*

Worth, N. A., J. R. Dawson, J. A. Sidey, and E. Mastorakos (2017a). Azimuthally forced flames in an annular combustor. *Proceedings of the Combustion Institute 36*(3), 3783–3790. *(p. 8)*

Worth, N. A., J. R. Dawson, J. A. Sidey, and E. Mastorakos (2017b). Azimuthally forced flames in an annular combustor. *Proceedings of the Combustion Institute 36*(3), 3783–3790. *(p. 18, 250, 251)*

Xu, D. A., D. A. Lacoste, and C. O. Laux (2016). Ignition of Quiescent Lean Propane Air Mixtures at High Pressure by Nanosecond Repetitively Pulsed Discharges. *Plasma Chemistry and Plasma Processing 36*(1), 309–327. *(p. 300)*

Yajnik, K. and M. Subbaiah (1973). Experiments on swirling turbulent flows. part 1. similarity in swirling flows. *Journal of Fluid Mechanics 60*(Issue 4), 665–687. *(p. 123)*

Yang, D., D. Laera, and A. S. Morgans (2019). A systematic study of nonlinear coupling of thermoacoustic modes in annular combustors. *Journal of Sound and Vibration 456*, 137–161. *(p. 6)*

Yang, D. and A. S. Morgans (2018). Low-order network modeling for annular combustors exhibiting longitudinal and circumferential modes. In *Proceedings of the ASME Turbo Expo 2018*. *(p. 20)*

Yang, V. and W. E. Anderson (1995). *Liquid Rocket Engine Combustion Instability*. Washington DC, USA: AIAA. *(p. 210)*

Ye, C., G. Wang, Y. Fang, C. Ma, L. Zhong, and S. Moreau (2018). Ignition dynamics in an annular combustor with gyratory flow motion. In *Proceedings of the ASME Turbo Expo*, pp. GT2005–68622. *(p. 275)*

Yin, Z. and M. Stöhr (2020). Time-frequency localisation of intermittent dynamics in a bistable turbulent swirl flame. *Journal of Fluid Mechanics 882*, A301–A3042. *(p. 163, 166, 178, 187)*

Yu, K. H., K. J. Wilson, and K. C. Schadow (1998). Liquid-fueled active instability suppression. In *Symposium (International) on Combustion*, Volume 27, pp. 2039–2046. *(p. 21)*

Zhang, Y., D. Shimokuri, Y. Mukae, and S. Ishizuka (2005). Flow field in swirl-type tubular flame burner. *JSME International Journal Series B Fluids and Thermal Engineering 48*(4), 830–838. *(p. 132, 156)*

Zhao, D. and X. Y. Li (2015). A review of acoustic dampers applied to combustion chambers in aerospace industry. *Progress in Aerospace Science 74*, 114–130. *(p. 210)*

Zhao, D. and A. S. Morgans (2009). Tuned passive control of combustion instabilities using multiple helmholtz resonators. *Journal of Sound and Vibration 320*(4), 744–

757. *(p. 210)*

Zhu, M., A. P. Dowling, and K. N. Bray (2000). Self-excited Oscillations in Combustors with spray atomisers. In *Proceedings of the ASME Turbo Expo*. *(p. 21)*

Zhu, M., A. P. Dowling, and K. N. Bray (2005). Transfer function calculations for aeroengine combustion oscillations. *Journal of Engineering for Gas Turbine and Power 127*(1), 18–26. *(p. 196, 202)*

Zinn, B. and L. Crocco (1968). Nozzle boundary condition in nonlinear rocket instability problem. *Astronautica Acta 13*(5-6), 489. *(p. 4)*

Zinn, B. and E. Powell (1970). Application of the Galerkin Method in the Solution of Combustion Instability Problems. In *Proceedings of the Nineteenth International Astronautical Congress on Propulsion, Re-Entry Physics 3*, pp. 59–73. *(p. 4, 226, 265)*

Zukoski, E. E. (1988). Afterburners. In G. C. Oates (Ed.), *Aerothermodynamics of Aircraft Engine Components* (AIAA Educa ed.)., pp. 76. New York. *(p. 6)*

université PARIS-SACLAY

ÉCOLE DOCTORALE
Sciences mécaniques et énergétiques, matériaux et géosciences (SMEMAG)

Titre: Dynamique de l'injection et des flammes de spray swirlées et couplage azimutal dans les foyers annulaires

Mots clés: Foyers annulaires, Injecteur aéronautique, Flamme swirlée, Flamme de spray, Instabilités de combustion

Résumé: Le déploiement de technologies à faibles émissions dans les moteurs d'avion ne nécessite pas seulement que les nouvelles conceptions émettent des quantités réduites de polluants, mais également que leur comportement dynamique (allumage, extinction et instabilités de combustion) soit compatible avec les normes de sécurité élevées en vigueur dans l'aéronautique. Ce travail de recherche se concentre sur ces derniers aspects. Une chambre annulaire transparente équipée de 16 injecteurs swirlés représentant à échelle réduite le foyer d'un moteur d'hélicoptère est utilisée conjointement avec un système à un seul secteur pour étudier les problèmes dynamiques. Théorie, expérimentation et simulation aux grandes échelles sont combinées pour examiner une gamme de questions ayant trait à la dynamique de l'injecteur, à la structure de l'écoulement, à la détermination du niveau de rotation, aux caractéristiques du spray, au couplage entre l'injection et le champ acoustique. Une base de données d'injecteurs est introduite pour étudier l'impact des paramètres d'injection sur la dynamique de la combustion. Ces injecteurs sont examinés dans des conditions stables et instables en combinant des diagnostics laser et des simulations permettant la caractérisation de comportements spécifiques à la dynamique du spray et du système d'injection. Un résultat important est que la présence d'un film liquide formé sur la paroi de l'injecteur induit une distribution multimodale des vitesses des gouttelettes. Une nouvelle méthode est introduite pour examiner le comportement spatio-temporel de l'écoulement et de la flamme lorsque l'injecteur est soumis à des modulations axiales. Une étude du processus par lequel les perturbations convectives se couplent au champ acoustique permet d'examiner les délais qui contrôlent l'instabilité de combustion et d'identifier les rôles respectifs de la convection et de l'évaporation des gouttes. La tomographie à grande vitesse reposant sur des particules de SnO_2 fournit des résultats majeurs sur la structure du noyau tourbillonnaire en précession et montre son comportement sous forçage acoustique. L'impact de la perte de charge de l'injecteur sur les instabilités de combustion est examiné à l'aide de plusieurs systèmes d'injection avec des niveaux de rotation semblables. Il est démontré que ce paramètre joue un rôle majeur dans le couplage entre la flamme et le plenum. Les résultats précédents sont utilisés pour guider les expériences sur la chambre de combustion annulaire. L'accent est mis sur les oscillations de combustion de grande amplitude couplées par un mode azimutal stationnaire induisant une extinction de flamme au voisinage de la ligne nodale de pression. La déformation du champ acoustique est suivie à l'aide d'un développement en série d'harmoniques azimutaux permettant la détermination des conditions critiques conduisant à ce phénomène. De nouveaux résultats sont également présentés sur la dynamique transitoire d'un injecteur lors de l'allumage et sur l'extinction pauvre avec une preuve de concept de la possibilité d'étendre la limite d'extinction par des décharges plasma nanosecondes.

Title: Injection and combustion dynamics in swirled spray flames and azimuthal coupling in annular combustors

Keywords: Annular combustors, Aeronautical injectors, Swirled flame, Spray flame, Combustion dynamics

Abstract: The deployment of low-emission technologies in aero-engines does not only require that new designs produce reduced amounts of pollutants, but also that their dynamical behavior (ignition, blow-off, and combustion instabilities) be compatible with the high safety standards prevailing in aeronautics. This research is focused on the latter aspect of combustor design. A transparent annular combustor equipped with 16 swirled spray injectors is used to represent at the laboratory scale the combustion chamber of a jet engine. This system is used in conjunction with a single sector rig to investigate dynamical issues. Theory, experimentation and large eddy simulation are combined to examine a range of items pertaining to the injector dynamics, flow structure, swirl number determination, spray characteristics, and coupling between injector flow and acoustic field. A database of injectors is introduced to investigate the impact of injection parameters on combustion dynamics. These injectors are examined under steady and unsteady conditions by combining laser diagnostics and high-fidelity simulations which allows the characterization of spray-specific behaviors of relevance to the dynamics of injection systems. One important result is that the presence of a liquid film formed on the wall of the injection unit gives rise to a multi-modal distribution of droplet velocities. A novel method is introduced to examine the space-time behavior of the flow and flame of a swirling injector submitted to axial modulations. A detailed investigation of the process by which convective perturbations couple with the acoustic field allows to examine the time lags that control combustion instabilities and sort out the respective roles of convection and fuel droplet evaporation. High speed tomography relying on SnO_2 microparticles provides major results on the Precessing Vortex Core structure and show its behavior under acoustic forcing. The impact of injector head loss on combustion instabilities is examined using several injection systems with similar levels of swirl. The head loss is shown to play a major role in the coupling between the flame and the upstream plenum. The previous results obtained in a single sector rig are used to guide experiments on the annular combustor. The focus is placed on high amplitude combustion oscillations coupled by a standing azimuthal mode inducing flame blow-off near the pressure nodal line. The deformation of the acoustic distribution is tracked using a novel expansion on azimuthal harmonics allowing the determination of the critical conditions leading to this phenomenon. New results are also presented about the transient dynamics of an injector during ignition and about lean blow out with a proof of concept extension of the LBO limit by nanosecond plasma discharges.

Université Paris-Saclay
Espace Technologique / Immeuble Discovery
Route de l'Orme aux Merisiers RD 128 / 91190 Saint-Aubin, France